CRANFIELD INSTITUTE OF TECHNOLOGY

SCHOOL OF MECHANICAL ENGINEERING

Ph.D THESIS

1991-92

A. TOURLIDAKIS

NUMERICAL MODELLING OF VISCOUS TURBOMACHINERY FLOWS WITH A PRESSURE CORRECTION METHOD

Supervisors: Professor R. L. ELDER

Dr M.LOBO

MARCH 1992

ABSTRACT

A fully elliptic computational method for the analysis of steady viscous flow in high speed subsonic centrifugal compressor impellers with tip leakage, is presented. A generalised curvilinear, non-orthogonal grid is utilised and the time-averaged Navier-Stokes equations are transformed and expressed in a fully conservative form. The discretisation of the governing equations is performed through finite volume integration. The solution procedure employs a non-staggered variable arrangement and a SIMPLE based method for coupling the velocity and pressure fields. The turbulence effects are simulated with the use of the k-ϵ model, modified to account for rotation and streamline curvature, and the near-wall viscous phenomena are modelled through the wall function method.

The numerical model is implemented for the flow prediction in a series of two and three dimensional test cases. Incompressible flow predictions in two-dimensional cascades and three-dimensional ducting systems with different geometrical features and inlet conditions are initially performed and the numerical results are compared against available experimental data. The final objective of the present study is achieved through the comparative study of the predictions obtained against the results of Eckardt's experimental investigation of the viscous compressible flow in a high speed radial impeller operating at design condition and in a backswept impeller at design and off-design conditions. In addition, the flow is simulated in the passages of the Rolls Royce GEM impeller which was tested at Cranfield at design and off-design flow rates.

A jet/wake pattern was discerned in all the simulated centrifugal compressor cases and a good overall agreement was achieved with the measured wake formation and development; and, encouraging results were obtained on the evolution of the secondary flows. The tip leakage effects influenced the loss distribution, the size and the location of the wake flow pattern at the rotor exit. The effects of the flow mass rate on the detailed flow pattern and on the compressor performance have been well represented. In certain cases, the quality of the present predictions is an improvement over that obtained by other "state-of-the-art" Navier-Stokes solvers. In conclusion, the developed finite volume flow model has captured a large number of complex flow phenomena encountered in the tested impellers and is expected to provide a useful aerodynamic analysis tool for stationary or rotating, axial or radial turbomachinery components.

Acknowledgements

I would like to express my sincere gratitude to my supervisor Professor R.L. Elder for his continuous guidance and support throughout the course of this doctoral study. Many thanks are due to Dr M. Lobo for his technical advice and the proof-reading of this thesis.

Various people have contributed towards improvements in the content of this dissertation through useful discussions, comments and suggestions. Among them I would like to thank Mr W.J. Calvert from R.A.E., Professor P. Stow and Dr B.L. Lapworth from Rolls-Royce plc, and Professor A. Goulas who was my former supervisor at the University of Thessaloniki, Greece. The excellent teaching of Professor P.L. Roe on Computational Fluid Dynamics and of Professor G.P. Hammond on Boundary Layer Theory and Turbulence stimulated my interest and enhanced my understanding of these subjects.

I feel indebted to all my friends and colleagues at Cranfield who have been a source of support, company and interesting discussions.

Last but not least, this project would had never been completed without the continuous encouragement which I received from my family and my friends in Greece to whom I dedicate this piece of work with my deepest appreciation.

Αντώνιος Τουρλιδάκης
Μάρτιος 1992.

Antonios Tourlidakis
Cranfield, March 1992.

CONTENTS

LIST OF FIGURES

Figure 5.14: Rhoden's cascade, 20° camber, $a_1 = 45°$. (a) Computational grid. (b) C_p coefficient along the blade surfaces.

Figure 5.14: Rhoden's cascade, 20° camber, $a_1 = 45°$. (c) Predicted C_p coefficient contours. (d) Predicted velocity vectors.

Figure 5.15: Rhoden's cascade, 20° camber, $a_1 = 50°$. (a) Computational grid. (b) C_p coefficient along the blade surfaces.

Figure 5.15: Rhoden's cascade, 20° camber, $a_1 = 50°$. (c) Predicted C_p coefficient contours. (d) Predicted velocity vectors.

Figure 5.16: Rhoden's cascade, 20° camber, $a_1 = 55°$. (a) Computational grid. (b) C_p coefficient along the blade surfaces.

Figure 5.16: Rhoden's cascade, 20° camber, $a_1 = 55°$. (c) Predicted C_p coefficient contours. (d) Predicted velocity vectors.

Figure 5.17: Rhoden's cascade, 20° camber, $a_1 = 60°$. (a) Computational grid. (b) C_p coefficient along the blade surfaces.

Figure 5.17: Rhoden's cascade, 20° camber, $a_1 = 60°$. (c) Predicted C_p coefficient contours. (d) Predicted velocity vectors.

Figure 5.18: Rhoden's cascade, 20° camber, $a_1 = 60°$. (a) Predicted streamlines along the suction side. (b) Predicted velocity vectors along the suction side.

Figure 5.19: Rhoden's cascade, 20° camber. Comparison between the measured and predicted outlet flow angle.

Figure 5.20: Rhoden's cascade, 30° camber, $a_1 = 35°$. (a) Computational grid. (b) C_p coefficient along the blade surfaces.

Figure 5.20: Rhoden's cascade, 30° camber, $a_1 = 35°$. (c) Predicted C_p coefficient contours. (d) Predicted velocity vectors.

Figure 5.21: Rhoden's cascade, 30° camber, $a_1 = 40°$. (a) Computational grid. (b) C_p coefficient along the blade surfaces.

Figure 5.21: Rhoden's cascade, 30° camber, $a_1 = 40°$. (c) Predicted C_p coefficient contours. (d) Predicted velocity vectors.

Figure 5.22: Rhoden's cascade, 30° camber, $a_1 = 45°$. (a) Computational grid. (b) C_p coefficient along the blade surfaces.

Figure 5.22: Rhoden's cascade, 30° camber, a_1 = 45°. (c) Predicted C_p coefficient contours. (d) Predicted velocity vectors.

Figure 5.23: Rhoden's cascade, 30° camber, a_1 = 50°. (a) Computational grid. (b) C_p coefficient along the blade surfaces.

Figure 5.23: Rhoden's cascade, 30° camber, a_1 = 50°. (c) Predicted C_p coefficient contours. (d) Predicted velocity vectors.

Figure 5.24: Rhoden's cascade, 30° camber, a_1 = 55°. (a) Computational grid. (b) C_p coefficient along the blade surfaces.

Figure 5.24: Rhoden's cascade, 30° camber, a_1 = 55°. (c) Predicted C_p coefficient contours. (d) Predicted velocity vectors.

Figure 5.25: Rhoden's cascade, 30° camber, a_1 = 60°. (a) Computational grid. (b) C_p coefficient along the blade surfaces.

Figure 5.25: Rhoden's cascade, 30° camber, a_1 = 60°. (c) Predicted C_p coefficient contours. (d) Predicted velocity vectors.

Figure 5.26: Rhoden's cascade, 30° camber, a_1 = 60°. (a) Predicted streamlines along the suction side. (b) Predicted velocity vectors along the suction side.

Figure 5.27: Rhoden's cascade, 30° camber. Comparison between the measured and predicted outlet flow angle.

Figure 5.28: Rhoden's cascade, 40° camber, a_1 = 40°. (a) Computational grid. (b) C_p coefficient along the blade surfaces.

Figure 5.28: Rhoden's cascade, 40° camber, a_1 = 40°. (c) Predicted C_p coefficient contours. (d) Predicted velocity vectors.

Figure 5.29: Rhoden's cascade, 40° camber, a_1 = 45°. (a) Computational grid. (b) C_p coefficient along the blade surfaces.

Figure 5.29: Rhoden's cascade, 40° camber, a_1 = 45°. (c) Predicted C_p coefficient contours. (d) Predicted velocity vectors.

Figure 5.30: Rhoden's cascade, 40° camber, a_1 = 50°. (a) Computational grid. (b) C_p coefficient along the blade surfaces.

Figure 5.30: Rhoden's cascade, 40° camber, a_1 = 50°. (c) Predicted C_p coefficient contours. (d) Predicted velocity vectors.

Figure 7.3 : Computational grid at the measurement planes.

Figure 7.4a: Computational blade to blade grid.

Figure 7.4b: Computational meridional grid

Figure 7.5 : Computational grid at the tip clearance gap.

Figure 7.6a: Radial impeller, design condition. Measured contours of meridional velocity $V_m/(\Omega*R_2)$.

Figure 7.6b: Radial impeller, design condition. Predicted contours of meridional velocity $V_m/(\Omega*R_2)$.

Figure 7.7 : Radial impeller, design condition. Contours of meridional velocity $V_m/(\Omega*R_2)$. (a) Measured. (b) Predicted.
(c) Predicted by Moore et al (1980b).

Figure 7.8 : Radial impeller, design condition. Contours of meridional velocity $V_m/(\Omega*R_2)$. (a) Rotating shroud, no tip leakage. (b) Rotating shroud, 1% tip leakage. (c) Rotating shroud, 2% tip leakage. (d) Stationary shroud, no tip leakage. (e) Stationary shroud, 1% tip leakage. (f) Stationary shroud, 2% tip leakage.

Figure 7.9a: Radial impeller, design condition. Pressure distribution p/P_0 on the shroud wall.

Figure 7.9b: Radial impeller, design condition. Three-dimensional pressure distribution p/P_0.

Figure 7.10: Radial impeller, design condition. Velocity vectors on blade-to-blade surfaces.

Figure 7.11: Radial impeller, design condition. Velocity vectors on meridional surfaces.

Figure 7.12: Radial impeller, design condition. Predicted secondary velocity vectors at the rotor exit. (a) 20 x 20 x 50 grid. (b) 32 x 32 x 65 grid.

Figure 7.13: Radial impeller, design condition. Predicted streamlines.

Figure 7.14: Radial impeller, design condition. Distribution of P_{rel}/P_0 at the rotor exit. (a) Measured. (b) Predicted with 1% tip leakage. (c) Predicted without tip leakage.

Figure 7.14: Radial impeller, design condition. Distribution of P_{rel}/P_0 at the rotor exit. (a) Measured. (b) Predicted with 1% tip leakage. (d) Predicted by Rhie et al (1984).

Figure 7.15a: Backswept impeller, design condition. Measured meridional velocity $V_m/(\Omega*R_2)$.

Figure 7.15b: Backswept impeller, design Condition. Predicted contours of meridional velocity $V_m/(\Omega*R_2)$.

Figure 7.16: Backswept impeller, design condition. Distribution of meridional velocity $V_m/(\Omega*R_2)$ at plane IV. (a) Measured. (b) Predicted. (c) Predicted by Hah et al (1988).

Figure 7.17: Backswept impeller, design condition. Distribution of meridional velocity $V_m/(\Omega*R_2)$ at plane V. (a) Measured. (b) Predicted. (c) Predicted by Hah et al (1988).

Figure 7.18a: Backswept impeller, design condition. Pressure distribution p/P_0 on the shroud wall.

Figure 7.18b: Backswept impeller, design condition. Three dimensional pressure distribution p/P_0.

Figure 7.19: Backswept impeller, design condition. Velocity vectors on blade-to-blade surfaces.

Figure 7.20: Backswept impeller, design condition. Velocity vectors on meridional surfaces.

Figure 7.21: Backswept impeller, design condition. Predicted streamlines.

Figure 7.22: Backswept impeller, choking condition. Distribution of P_{rel}/P_0 at the rotor exit. (a) Measured. (b) Predicted with 1% tip leakage. (c) Predicted without tip leakage.

Figure 7.23a: Backswept impeller, choking condition. Measured meridional velocity $V_m/(\Omega*R_2)$.

Figure 7.23b: Backswept impeller, choking condition. Predicted contours of meridional velocity $V_m/(\Omega*R_2)$.

Figure 7.24: Backswept impeller, choking condition. Three dimensional pressure distribution p/P_0.

Figure 7.25: Backswept impeller, choking condition. Velocity vectors on blade-to-blade surfaces.

Figure 7.26: Backswept impeller, choking condition. Velocity vectors on meridional surfaces.

Figure 7.27: Backswept impeller, choking condition. Predicted streamlines.

Figure 7.28: Backswept impeller, choking condition. Distribution of P_{rel}/P_0 at the rotor exit. (a) Measured. (b) Predicted with 1% tip leakage. (c) Predicted by Dawes (1987).

Figure 7.29: Backswept impeller, adiabatic efficiency.

Figure 7.30: GEM impeller. (a) Measurement Planes. (b) Velocity triangle.

Figure 7.31a: GEM impeller, peak efficiency condition. Measured relative velocity V_R distribution in m/s.

Figure 7.31b: GEM impeller, peak efficiency condition. Predicted relative velocity V_R distribution in m/s.

Figure 7.32: GEM impeller, peak efficiency condition. Turbulence intensity % at section C.

Figure 7.33: GEM impeller. Static pressure p/P_0 on the shroud wall. (a) Peak efficiency condition. (b) Choking condition.

Figure 7.34: GEM impeller, peak efficiency condition. Relative total pressure P_{rel}/P_0 on the shroud wall.

Figure 7.35: GEM impeller, peak efficiency condition. Velocity vectors on blade-to-blade surfaces.

Figure 7.36: GEM impeller, peak efficiency condition. Velocity vectors on meridional surfaces.

Figure 7.37a: GEM impeller, near surge condition. Measured relative velocity V_R distribution in m/s.

Figure 7.37b: GEM impeller, near surge condition. Predicted relative velocity V_R distribution in m/s.

Figure 7.38: GEM impeller, near surge condition. Relative flow angle Θ distribution at section A. (a) Measured. (b) Predicted.

Figure 7.39: GEM impeller, near surge condition. Relative flow angle Θ distribution at section D. (a) measured. (b) Predicted.

Figure 7.40: GEM impeller, near surge condition. Velocity vectors on blade-to-blade surfaces.

Figure 7.41: GEM impeller, near surge condition. Velocity vectors on meridional surfaces.

Figure 8.1 : Unsteady flow prediction. Variation of the inlet total pressure.

Figure 8.2 : Unsteady flow prediction. Passing wake in front of a stator.

NOMENCLATURE

a,b,c,d	: Positive constants, eqs. (4.2.8) and (4.2.9)
a_1	: Inlet flow angle in a cascade
A_w	: Area of the control volume face lying on the wall
a	: Coefficients of the disctrete algebraic eq. (3.4.1)
a^c	: Convective parts of the finite difference coefficients
a^p	: Coefficients of the pressure correction eq. (3.6.11)
A	: Area
$\underline{\underline{A}}$	: Matrix of algebraic equations system coefficients
$\underline{\underline{A}}$	: Transformation matrix
B,C,D	: Constants in velocity correction equations
c	: Blade chord
C	: Final destination of an iterative path
C_0,C_1,C_2	: Successive extrema of an iterative path
C_p	: Pressure coefficient; specific heat at constant pressure
C_μ,C_1,C_2	: Constants in k-ϵ model
c_i^j	: Discretised metric coefficients scaled by the Jacobian
D	: Square duct or channel width
$\bar{e}_1,\bar{e}_2,\bar{e}_3$	: Cartesian unit vectors
E	: Log-law constant
E	: Function of under-relaxation factor, eq. (3.4.8)
e,w,n,s,f,b	: Points at the control volume faces
E,W,N,S,F,B	: Neighbouring grid points
f	: Instantaneous flow variable
$\bar{f}$,f′	: Reynolds mean and fluctuating components
$\tilde{f}$,f″	: Favre mean and fluctuating components
f^ξ, f^η, f^ζ	: Interpolation factors in the ξ,η,ζ direction
$\vec{F}=(F_1,F_2,F_3)$	: Body force
F_1,F_2,F_3	: Mass fluxes in the ξ, η and ζ directions
$\bar{\bar{f}}$	: General vector quantity in Gauss's theorem expression
g^{ij} (i=1,2,3 and j=1,2,3)	: Components of the metric coefficients tensor

G_C : Rotation and curvature modification term

G_k : Rate of production of turbulent kinetic energy

h^{ij} : Metric coefficients

i,j,k : Coordinate direction indices

I : Rothalpy; Discretised flux

I_b, I_u : Flux from a bounded and an unbounded scheme

I^c : Convective flux

I^d, I^{dc}, I^{do} : Diffusive, cross-diffusive and orthogonal-diffusive flux

$\mathbf{I}$: Unit matrix

J : Jacobian of coordinate transformation

k : Turbulence kinetic energy

l_m : Mixing length

m_p : Mass imbalance in the pressure correction equation

$\tilde{m}_p$: Integrated mass source based on $\tilde{U}, \tilde{V}, \tilde{W}$ velocities

M_{in} : Mass flux through inner plane

$\vec{n} = (n_1, n_2, n_3)$: Normal unit vector

N : Number of grid points or unknown values of Φ

N : A very big number, eg. 10^{30}

p : Static pressure

P : Total pressure; Grid point inside the control volume

P_{rel} : Relative total pressure

p' : Pressure correction

Pe : Peclet number

Pr : Prandtl number

$p(\xi), r(\xi), q(\xi), s(\xi)$: Control functions given by eqs. (4.2.21) and (4.2.23)

$P(\xi,\zeta), Q(\xi,\eta)$: Control functions for the grid generation procedure

Q_{ij} (i=1,2,3 and j=1,2,3) : Interpolation factors for the QUICK scheme

$\vec{r}$: Position vector

R : Gas constant; Radius of streamline curvature; Distance from the axis of rotation

R_1, R_2, R_3, R_4 : Geometrical quantities, Eqs (4.2.22) and (4.2.24)

R_2 : Distance of the impeller exit from the axis of rotation

Re : Reynolds number

s : Cascade space or pitch; Entropy

s_η : Geometrical quantity defined by eq. (4.2.12)

S_I : Source term in the energy equation

S_P : Explicit part of the source term used in eq. (3.4.1)

S_{ui} : Source term of the u_i momentum equation

$S_{\epsilon P}', S_{\epsilon P}''$: Parts of the linearised source term of the ϵ equation

S_Φ : Source term of the dependent variable Φ equation

S_Φ', S_Φ'' : Parts of the linearised source term

$\underline{S}$: Matrix of constant terms, eq. (3.4.3)

t : Time

t_0 : Initial time

T : Static temperature

T_0 : Inlet total temperature

T_u : Inlet turbulence intensity

T_w : Wall shear force

u,v,w or u_j (j=1,2,3) : Cartesian velocity components

U,V,W or U_j (j=1,2,3) : Curvilinear velocity components

u_{in}' : Fluctuation of the inlet velocity

u_τ : Friction velocity

U_p : Velocity component parallel to the wall

u^+ : Non-dimensional velocity

u',v',w' : Corrections to the velocity components

$\tilde{U},\tilde{V},\tilde{W}$: Pseudo-velocity components

V : Volume

V_{eff} : Effective or total velocity

V_m : Meridional velocity

V_R : Relative velocity

V_α : Absolute velocity

x,y,z or x_j (j=1,2,3) : Cartesian coordinates

$x_{\xi\xi}, x_{\eta\eta}, x_{\xi\eta}$: Second derivatives

X : Distance from the side wall of the curved duct

x : Grid point in a Cartesian system

y^+ : Non-dimensional distance normal to wall

α : Under-relaxation factor

α, β, γ : Coefficients of the eqs. (4.2.5) and (4.2.6)

Γ : Diffusion coefficient for general transport equation

δ : Deviation angle

δ_0, m, b : Parameters used in NASA's rule for deviation angle

δ_{ij} : Kronecker delta (1 if i=j, 0 otherwise)

δn : Normal distance from the wall

$(\delta x_i)_e^{\xi_j}$, $(\delta x_i)_w^{\xi_j}$, ... : Difference in x_i along the ξ_j coordinate at e,w,.. faces

Δp : One dimensional pressure correction

δs : Distance of the first grid line from the wall

Δt : Time interval for Reynolds or Favre averaging

Δt^* : Reference time interval, eq. (3.4.10)

$\delta x, \delta y$: Differences in the Cartesian coordinates x and y

$\delta\xi, \delta\eta, \delta\zeta$: Distances between grid points or control volume dimensions in curvilinear coordinate directions

ΔU : One dimensional velocity correction, 2-d

ΔV : Volume of the control cell

ΔW : One-dimensional velocity correction, 3-d

ϵ : Dissipation rate of turbulence energy

ϵ_c : Value for the convergence criterion, eq. (3.7.1)

ϵ_{ijk} : 1 if ijk cyclic, -1 if ijk anti-cyclic, 0 otherwise

θ : Intersection angle of the grid lines with the boundaries

Θ : Relative flow angle

κ : Von Karman's constant

λ : Second coefficient of viscosity

λ : Blending factor, eq. (3.5.14)

Λ_w : Parameter in the log-law eqs. (6.2.5) and (6.2.6)

Δ : Inverse transformation matrix

μ : Dynamic viscosity

ξ,η,ζ or ξ_j (j=1,2,3) : Curvilinear coordinates

ξ_{max},η_{max} : Maximum values of ξ and η.

$\xi_{xx},\xi_{yy},\eta_{xx},\eta_{yy}$: Second derivatives

ρ : Density

ρ' : Density fluctuation

$\rho\overline{u_i'u_j'}$: Components of the Reynolds stress tensor

$\rho\overline{u_i'\Phi'}$: Components of the turbulent flux tensor

σ : Cascade solidity

σ_k,σ_ϵ : Effective Prandtl number for k and ϵ

σ_Φ^T : Turbulent Prandtl number for Φ

τ : Shear stress

τ_θ : Shear stress component normal to streamline curvature

τ_Ω : Shear stress component normal to coriolis acceleration

ϕ : Blade camber angle

Φ : General scalar quantity

Φ_{ref} : Reference value of Φ for checking convergence

$\underline{\Phi}$: Matrix of unknown dependent Φ values.

ω : Over-relaxation factor

$\vec{\Omega}=(\Omega_1,\Omega_2,\Omega_3)$: Rotational speed vector

Ω : Magnitude of the rotational speed vector

I,II,III,IV,V : Measurement stations at Eckardt's impeller

A,B,C,D : Measurement stations at GEM impeller

Subscripts

P : Control grid point

E,W,N,S,F,B : Neighbouring grid points

e,w,n,s,f,b : Surfaces of the computational cell

i,j,k : Coordinate direction indices

0	: Upstream reference condition
c	: Values at centre
in	: Values at inlet
out	: Values at outlet
eff	: Effective value
T	: Turbulent
x,y,z	: Partial derivatives in respect to x,y,z
w	: Value at a solid wall
Φ	: Related to scalar Φ
ξ,η,ζ	: Partial derivatives in respect to ξ,η,ζ

Superscripts

i,j,k	: Coordinate direction indices
—	: Value obtained by simple averaging
*	: Arising from the initial guess or the solution of momentum equations
p	: Associated with pressure
u,v,w	: Associated with Cartesian velocity components
x,y,z	: Associated with Cartesian coordinate directions
k,ϵ	: Associated with turbulence scalars k and ϵ
Φ	: Associated with arbitrary scalar Φ
n	: Iteration level

Abbreviations

LHS	: Left hand side
PS	: Pressure surface
RHS	: Right hand side
SS	: Suction surface

CHAPTER 1

Introduction

1.1 Introduction

Centrifugal compressors currently find a wide range of applications due to their ability to achieve high pressure ratios per stage resulting in lightweight and compact compression systems. Despite their popularity in small gas-turbine engines and turbochargers, however, they tend to be less efficient than their axial counterparts largely due to the limited effort which has been devoted for their development and for establishing a better understanding of the complicated flow phenomena occurring in the rotating curved passages of the impellers. The aerodynamics of the impeller are very complex and involve boundary layer transition, growth and separation on the various surfaces, shock waves, unsteady and turbulence effects, secondary flows due to rotation, passage curvature and tip leakage and eventually the deterioration of the streamwise velocity profile and the formation of wake patterns in the impeller passages. The process of wake formation is associated with entropy production and high losses and affects the efficiency and the operating range of both the rotating impeller and the downstream diffuser. The wake pattern has been found to exist in most of the published flow data of experimentally investigated radial impellers and is linked with loss processes resulting in engine fuel consumption requirements that are higher than is desirable.

There is therefore an urgent demand for the improvement of the aerodynamic performance of centrifugal impellers which is strongly associated with seeking ways to control the flow phenomena involved and especially to eliminate the wake formation and at the same time maintaining the levels of diffusion in the rotating passages of the impeller. In addition to improving impeller flow, a uniform impeller

exit velocity profile would result in both an increase in the pressure rise which can be obtained from the downstream diffuser and an improvement in the operating range.

To achieve these objectives it is essential to fully understand all the flow phenomena and their interaction, occurring in the rotating passages. The most appropriate ways forward appear to be firstly the acquisition of measurement data of the internal flow field using non-intrusive techniques and secondly the theoretical analysis of the flow using three-dimensional, compressible and viscous flow solution methods which during the past decade have shown promising developments.

The resort to experimental processes for obtaining internal flow data is a reliable way to systematically study and collect quantitative design information about the effect of different geometrical and operating conditions on the compressor's performance. During the initial stages of the centrifugal compressor's development, this experimental data reduction contributed substantially towards a significant improvement in efficiency and pressure loading. However, nowadays any fractional efficiency gain can only be achieved through substantial effort in obtaining high quality detailed flow data from within the passages which is required to provide details of the various flow phenomena occurring, and subsequently much more work is required in accommodating these data in the design process. This iterative "built and test" route is usually accompanied by high costs of preparing the test models, building the necessary experimental equipment and for repeated testing and also requires long times for achieving the final design.

During the last decade, advanced computational techniques have been developed and have become a significant part of the modern design procedures. In many cases, the utilization of flow analysis computer programs has facilitated the identification of deficiencies in the preliminary designs of turbomachinery components and has shortened drastically the development times for the delivery of a new product by limiting the necessity for testing only in the final phase. The use

of Computational Fluid Dynamics (CFD) methods can provide much more detailed information than the current experimental techniques, in much reduced time scales. The effects of different upstream or downstream conditions, the impact of alternative geometrical configurations, the study of ideal boundary conditions which cannot be modelled in an experiment, are examples of areas where the application of CFD can provide enhanced aerodynamic understanding and effectively large scale reductions in the development time and costs for a new design. Nevertheless, despite these successes, the computational cost is still large and can be prohibitive. However, the computer technology, which has advanced dramatically during the last few years, and the availability of new more economical numerical approaches, which continuously emerge, provide a very favourable environment for the wider application of the computational techniques for the flow analysis in complex systems.

The dominant role of CFD as a modern design technology of air breathing engines will not mean the abandonment of the experimental approach as their development cannot proceed without validation against high quality and thorough experimental information from modern high performance impellers. A thorough investigation of the already existing data, at least in the open literature, reveals that the length and the depth of our data base is very limited and much more systematic effort is necessary to render available "benchmark" data for the evaluation and the definition of the limitations of the computer viscous flow solution methods, the calibration of the physical models which are employed and the development of more sophisticated approaches insofar as the various aspects of physical modelling is concerned.

Taking into account all the above incentives, the aim of the current doctoral research programme has been the development of a reliable three-dimensional, viscous, compressible flow computational analysis method capable of the following:

(i) to predict the most significant phenomena and their interaction which occurs inside the passages of centrifugal compressor configurations,

(ii) to perform parametric studies of the effect of different inlet conditions and

different geometrical shapes on the local and global features of the flow field,
(iii) to be applicable to other turbomachinery components, and to form the basis for simulating stage interaction within multistage machines,
(iv) to be sufficiently flexible and robust such that the computer code can be used by a wide range of turbomachinery design offices,
(v) to form a computational core for any theoretical investigation of alternative numerical discretisation schemes, physical models and solution procedures which may influence the accuracy, stability and the economy of the method.

The route which has to be followed in order that the above objectives can be accomplished, involves a step by step development of the method, with increasing complexity of the analysis at each step. A thorough comparison of the current predictions against those available in the literature or in-house experimental and predicted results will also be required.

1.2 Historic development of the flow prediction methods in Turbomachinery flows

The field of Computational Fluid Dynamics constitutes a new emerging technology which currently finds application and contributes to a wide range of fields which incorporate transport phenomena in fluids. Researchers also receive support and feedback from different fields. The application of CFD in the turbomachinery and gas turbine technological field has some special characteristics which are derived firstly from the highly competitive and demanding nature of this technology and secondly from the complexity of the flow phenomena which are involved inside the various components. Both of the above issues have contributed significantly by posing challenging benchmarks which have led towards substantial developments in CFD during the last two decades. Consequently the review which follows is concentrated mainly on the presentation of methodologies which are commonly encountered in the gas turbine aerodynamic design, research and development. The methods are presented in a sequence of increasing degree of

complexity and level of approximation of the flows which can be handled.

1.2.1 Streamfunction methods

A historical contribution which greatly influenced the aerodynamic analysis and design of turbomachines, was the theory for steady, inviscid, three-dimensional flow in subsonic and supersonic axial, radial or mixed-flow turbomachine passages, which was presented by Wu (1952). The solution of the direct and the inverse problem is obtained by the appropriate combination of flows on two families of relative stream surfaces, namely S1 and S2. Thus, the solution of the three-dimensional flow is greatly simplified mathematically into a number of solutions of two-dimensional flows on a number of S1 (blade to blade) surfaces, which are placed from hub to tip, and a number of S2 (hub to tip) surfaces, which are located from one blade to another. The successive solution of the flow equations on different stream surfaces of both families and combination of the obtained results yields either a quasi three-dimensional solution which assumes that the S1 surfaces are axisymmetric and thus only one S2 stream surface is required in the computations, or a fully three-dimensional solution. During the iterative procedure the stream surfaces must be allowed to move and adjust their "shape" according to the solutions obtained in the other family of surfaces.

The implementation of this method was delayed until the development of computer capabilities permitted Katsanis (1966) to apply Wu's ideas to obtain a quasi three-dimensional solution by using a single meridional hub to tip surface and three S1 blade to blade surfaces: one at the hub, one at the mean streamline of the meridional plane and one at the casing. Marsh (1966) introduced the calculation approach called "matrix through flow" method, by solving the streamsurface equations on the meridional surface, assuming pitchwise averaged flow quantities and using a fixed grid, via a matrix inversion approach. Marsh presented a general computer program for the estimation of the subsonic through-flow pattern through axial, radial and mixed flow turbomachines. Hirsch and Warzee (1980) published

a quasi 3-D flow calculation inside a centrifugal impeller employing a finite element discretisation scheme and based on a density-averaged, pitch-averaged meridional flow calculation which replaced the S2 streamsurface flow analysis. Using the "matrix through flow" method, Goulas (1980) obtained a quasi three-dimensional solution in a centrifugal impeller by calculating a dissipative force based on the stress tensor. Adler and Krimerman (1980) obtained full three-dimensional solutions in subsonic centrifugal compressors using a finite element discretisation approach, drawing the conclusion that inviscid models cannot accurately represent separated flow regions and especially the wake region in the radial discharge of the impeller. Wu's general theory was extended recently by Wu et al (1990) to predict the quasi- and full three-dimensional rotational flow in transonic turbomachines.

Most of the computational methods which have evolved from Wu's theory depend strongly on empiricism to account for the viscous effects of flow deviation and blockage and their predictive capability is restricted in separated flow regions. Despite the popularity these methods experienced a decade ago, the trend nowadays is towards their replacement by Euler and Reynolds-averaged Navier-Stokes solution methods.

1.2.2 Potential methods

The inviscid potential theory is the simplest one to describe the fluid flow and assumes that the flow is irrotational. The velocity components are related to a potential and the set of Euler equations reduces to a single equation for the velocity potential. Compressibility effects are fully taken into account. Pioneering work on such methods has been performed by Murman and Cole (1971) and Jameson (1975). The potential equation is elliptic in subsonic regions and hyperbolic in supersonic flow regions. Moreover if shocks are present, special treatment is entailed. However, it is possible to maintain the discretisation techniques which are applicable to subsonic regions in all flow regions, by either introducing some kind of upwinding in the evaluation of the mass flux or of the density, or by adding some

artificial viscosity terms. For the solution of the potential flow equation, there are various methods available which are based on the line relaxation (SLOR) methods or approximate factorisation algorithms (AF) which are derivatives of the Alternating-Direction-Implicit algorithm (ADI) and are very widely used for transonic calculations. For the acceleration of the convergence rates, Jameson (1979) applied successfully a multi-grid process for the solution of the conservative form of the potential equation. Potential methods have reached a mature level of development and they are very useful for the flow analysis in the subsonic, fully supersonic and low transonic (i.e. free of strong shocks) flow regimes during the preliminary design stages.

1.2.3 Euler equations - Time Marching methods

Time marching methods are very well-established for solving the system of Euler equations which constitutes the highest level of approximation for the description of non-viscous flows. The main advantage of these methods is their ability to calculate mixed subsonic and supersonic flows since the nature of the equations solved is hyperbolic, providing automatic shock capturing. Another useful feature of this class of methods is the simplicity of the solution procedure and the physical insight thereby gained. The prescription of a pressure ratio instead of a mass flow which most other methods require, enables the relatively easy computation of the choking mass flow. An arbitrary guess of the flow field is used as a starting point and the solution is allowed to evolve with time until the steady state is reached where the "steady" conservation equations are valid for each control element. The continuity equation is used for the calculation of the density unlike the pressure based relaxation techniques which utilize the continuity to update the pressure field.

The numerous schemes which have been developed for the time marching solution of the Euler equations can be classified into two major categories: explicit and implicit. A scheme is explicit when the dependent variables at a given grid point

are calculated only from values at the previous time step. In an implicit scheme the variables at each grid point are linked to those of the neighbouring grid points at the current time step and a matrix inversion is usually necessary. For stability reasons, the explicit schemes are limited by the magnitude of the allowed time step. For turbomachinery applications, the explicit schemes proved to have better success than the implicit schemes.

The methods which have been used to achieve stability for explicit schemes are as follows:

- Addition of large numerical damping terms to the equations e.g. Lax (1954), McDonald (1971). These schemes are very simple and robust but are only first order accurate in time and space and consequently require very large number of grid points to achieve sufficiently accurate solutions.
- Schemes with only one time level at each time step and a second order of temporal and spatial accuracy, e.g. Ni (1981), Delaney (1982). Although both Ni's and Delaney's methods appear to be successful they do not seem to have been adopted by other researchers.
- Two or more step predictor - corrector schemes e.g. McCormack (1969), Thompkins and Tong (1978). This scheme tends to be second order accurate both in space and time. A disadvantage of this type of scheme is that each time step is split into a predictor and a corrector level and there is the need for all flow properties to be stored at two time levels.
- Deferred correction schemes in which there is progressive cancellation of the numerical damping of "Lax" type during the calculation process, e.g. Denton (1982). Eventually the obtained solution is second order accurate in space. This scheme has the advantages of simplicity, speed and is possibly the most widely used in turbomachinery applications.

1.2.4 Viscous-Inviscid interaction methods

The absence of the viscous terms from the Euler equations limits their

accurate applicability to flow regimes and conditions where viscous effects are unimportant. The major impact of the viscous effects is the reduction of the effective passage area which is important for compressors where the boundary layers are relatively thicker and in transonic flows where small area changes are essential and can dramatically alter the flow field. Euler solvers have a restricted capability to simulate off-design flows where the boundary layers can be excessively separated in parts of the flow field. In the viscous-inviscid interaction methods there is an iterative coupling between the boundary layer displacement effects and the inviscid bulk of the flow. This can be achieved either by adding the boundary layer displacement thickness to the blade geometry, Calvert (1982), thus requiring the regeneration of the mesh which is to be used for the Euler analysis, or by introducing a transpiration model which simulates the effects of the displacement by adding appropriate mass flux through the blade surfaces, Singh (1982), as a boundary condition during the implementation of the Euler solver. For the calculation of the boundary layers usually an integral method is preferred. The viscous-inviscid interaction methodologies are much more economical than the solution of the Navier-Stokes equations but they can be applied to flow situations where viscous and inviscid flow regimes can be distinguished.

1.2.5 Navier-Stokes methods

The state of the art in turbomachinery computations is the three-dimensional viscous flow analysis using the Reynolds-averaged Navier-Stokes equations with a turbulence model since the direct simulation of turbulence cannot be supported by the computer resources available today. A unique set of flow equations is valid to all flow regions and can automatically capture the viscous effects without requiring in addition boundary layer computations as in the interaction techniques or empirical correlations which are commonly utilized in the Throughflow methods, Denton (1978). However, for the bulk of the design process the lower-level calculation methods offer simplicity, speed and reasonable accuracy in the preliminary design stage, while the Navier-Stokes solvers are used as a "numerical wind tunnel" to

verify thoroughly the final design.

The time marching method has been successfully applied for the numerical solution of the Navier-Stokes equations. The numerical schemes which have been developed for the solution of the Euler equations can be adapted for the simulation of high speed, compressible and viscous flows which are described by the Navier-Stokes equations, where for the discretisation of the viscous and thermal diffusion terms a central discretisation strategy is always followed.

Among others, the full Navier-Stokes equations were solved by Beam and Warming (1978) and Briley and McDonald (1977). Dawes (1986) developed a solver based on the thin-layer approximation to the full Navier-Stokes equations where the diffusion term was neglected in the flow direction parallel to the wall. This approach was later extended, Dawes (1988), to form a computational tool for the full Navier-Stokes analysis inside various types of turbomachinery with considerable success.

The application of the time marching method for incompressible flows requires special adaptation since the assumption of a constant density would remove the continuity equation from the calculation procedure and there would not be any guarantee that the velocity field obtained from the solution of the momentum equations, would satisfy the mass conservation condition. In order to resolve this problem alternative strategies were considered, one of the most important being the "pressure correction" method.

1.3 The Pressure Correction method

An alternative approach to the time marching procedure for the solution of the steady state time-averaged Navier-Stokes equations is the, so called, "pressure correction" approach which was implemented with a great deal of success initially for incompressible recirculating flow calculations and later for compressible flow prediction. Instead of marching the unsteady flow equations forward in time till the

flow field converges to the steady state solution, an iterative relaxation methodology is utilized, whereby the solution of the steady equations is promoted through successive corrections to the flow field till the error in the satisfaction of the flow equation is minimised. Usually the solution algorithm is based on a semi-implicit scheme which utilizes the continuity equation for the derivation of a Poisson type equation for the calculation of the pressure in order to satisfy a divergence free velocity field. In the first step a guessed pressure field is the pre-condition for the solution of the momentum equations which are decoupled and expressed in a linearised form and in the second step an equation for the pressure or pressure correction is solved to update the pressure field and promote the satisfaction of the continuity condition. The density is then calculated using the perfect gas law. The SIMPLE algorithm of Patankar and Spalding (1972) provided a remarkably successful implicit scheme and has dominated the field of numerical simulation of incompressible flows. Although the relaxation process which is used has not a direct physical interpretation, with some extra analysis it may be seen that this iterative process is similar to a time-marching approach which retains in the equation the transient term and proceeds in time updating the flow quantities, Van Doormaal and Raithby (1984).

For cases in which the main flow direction does not change, the full flow equations can be parabolised by neglecting the diffusive terms in the through-flow direction. In this "purely parabolic" formulation, Patankar and Spalding (1972), the flow conditions are transferred downstream only and consequently, as in two-dimensional boundary layer calculations, the solution can be obtained with only one iteration of the forward marching process. However, in many flow situations there is a dominant flow direction in which there is negligible reverse flow and the downstream conditions influence the upstream flow only through the transmission of pressure "signals" such as in flows with streamline curvature in the streamwise direction. A solution approach to this class of flows which are called "partially parabolic" was originated by Pratap and Spalding (1976), who presented a multi-pass algorithm for establishing a three-dimensional flow field in Cartesian coordinates.

This procedure was expanded by Moore and Moore (1979a and 1979b) who expressed the equations in orthogonal curvilinear coordinates allowing the treatment of the compressible flow field in arbitrarily shaped configurations. This method used a two dimensional pressure correction on each cross-stream plane which was not coupled to the streamwise pressure gradient unlike the procedure of Pratap and Spalding. After a complete pass of the marching procedure, a three-dimensional correction was employed. The storage of the dependent flow variables in all of the above methods is performed in staggered locations on the grid in order to render the coupling between the pressure and the velocity field possible and remove the unphysical pressure oscillations. This approach is inconvenient and sometimes its success, as far as the coupling is concerned, is limited when it is applied for the solution of the flow equations expressed in generalised form to describe the flow in arbitrarily shaped geometries. Hence, Rhie and Chow (1983) presented a numerical scheme which allowed coupling of the velocity and the pressure fields when a non-staggered grid arrangement was employed for the flow prediction in two-dimensional cascades with trailing edge separation. In this case all the flow variables are stored and calculated at the same grid location. The Rhie and Chow scheme has been proven to be very efficient and nowadays is widely used in many applications of pressure correction computations which tend to utilize collocated grids. Beyond the aforementioned references, the pressure correction has been further developed and established as a very reliable tool for the analysis of low-speed recirculating flows. However, the evidence for its implementation in centrifugal compressors and especially in transonic and supersonic flows, as it will be discussed in the next section, is rather very scant.

The first attempt to simulate the flow in a centrifugal compressor configuration using the solution of the time-averaged Navier-Stokes equations, was performed by Moore and Moore (1980a) who implemented their partially parabolic procedure for the incompressible flow prediction in a low speed shrouded impeller. Although the turbulence, compressibility and tip leakage effects were neglected, this simulation represented a major step towards the application of Navier-Stokes analysis

in centrifugal compressors. The pioneering work of Moore and Moore continued further, Moore and Moore (1980b), with the extension of their method to compute the turbulent, compressible flow in a high speed impeller with tip leakage and a stationary shroud. The computed and experimentally defined three-dimensional viscous flow data and the overall thermodynamic performance of the compressor were compared favourably. Rhie et al (1984) extended a partially parabolic procedure for the analysis of the three-dimensional flow in ducting systems, Rhie (1985), and implemented this technique for the flow prediction in a high speed impeller with tip leakage. This was the first attempt in which the two-equation k-ϵ turbulence model was used in realistic impeller geometries and flow conditions. The above methods provide sufficient solutions at design conditions where reversed flows are minimised but, increasingly, the parabolic or partially parabolic assumption becomes a limitation at off-design conditions. This implies that all the terms, including the streamwise diffusive term, should be retained in the time averaged Navier-Stokes equations which consequently obtain an elliptic form and can capture reversed flows with the penalty of substantial increase in the required computational effort. Hah et al (1988) developed a fully elliptic three-dimensional viscous flow analysis method with a finite volume relaxation procedure and a modified k-ϵ model and presented comparisons between numerical and experimental data for the detailed flowfields and overall performance of a backswept impeller at design, choke and near-surge operating conditions. This methodology was used later by Hah and Krain (1990) for the flow analysis in a high efficiency and high pressure ratio modern backswept impeller. Moore and Moore (1987) now with an elliptic computational algorithm, predicted flow at design and off-design operating conditions, accurately calculating the relative total pressure losses and the wake size in an impeller without an inducer but with a radial inlet.

All the above methods are based on the pressure correction relaxation approach for solving the Reynolds-averaged Navier-Stokes equations. Dawes (1988) presented the results obtained for the flow inside a backswept impeller at its choking operating condition using his time marching process for the solution of the fully

three-dimensional equations of motion expressed in a finite volume form. For the prediction of the turbulence effects on the main flow a mixing-length closure was employed and for the acceleration of the convergence rates, a multigrid algorithm was implemented. Casey et al (1990) presented the results and the experience gained from the use of this computer code in the design and analysis process of industrial centrifugal compressors.

1.4 Pressure Correction in high speed flows

The time marching approach has been widely researched and successfully implemented to handle high speed transonic and supersonic flows. The system of the partial differential equations which describe the steady compressible flows changes its type from elliptic for subsonic flows to hyperbolic for supersonic flows. If a pressure correction analysis is to be applied, this type of change should be taken into account through appropriate numerical adjustments in order to avoid instability and ensure convergence. A common numerical treatment is the linearisation of the mass flux in terms of independent linearisation of the density and velocity, and also the upwinding of the density which, however, tends to smear the shock waves. Another numerical practice is the solution of the momentum equations to yield Cartesian momentum components instead of velocity components and this provides better coupling between the dependent variables during the relaxation process and also avoids the strong under-relaxation of the density field, McGuirk and Page (1989).

Among other researchers who extended the pressure correction method to treat transonic and supersonic flows, Rhie (1986) developed an upwind scheme incorporating an implicit treatment of the density in the pressure correction procedure. Rhie used a multigrid algorithm to accelerate the convergence rates. Hah (1987) extended his implicit, finite volume relaxation methodology to handle transonic and supersonic flows by using a multistage operator splitting to ensure coupling of the velocity, density and pressure fields, and a higher order upwinding for the discretisation of the convective term. Shyy (1988) presented a pressure

correction algorithm with a staggered grid and a second order accurate discretisation of the momentum equations, adopting an adaptive meshing strategy hence avoiding the use of explicit damping in order to capture shocks. Shyy claims that his algorithm is fully applicable to viscous transonic and supersonic problems and is very competitive with the time marching approach.

1.5 Contributions of the present study

In general the methods which were discussed in the previous sections are based on different model assumptions and numerical solution procedures. Despite their successes, they have their own limitations especially insofar as the accurate prediction of the losses, the secondary flows, the separated flow regions and the transitional boundary layers are concerned.

Many predictive problems are encountered in the qualitative and many more in the quantitative representation of the entropy production mechanisms occurring in the rotating impeller passages and only few authors provide satisfactorily accurate loss predictions. A clear definition of the level of "reality" to which the physical models, and especially the turbulence models employed, are able to represent the true physics of the process, and of the borders of their practical applicability, is still not possible. Beyond the uncertainties of the physical models, there are drawbacks associated with the accuracy and the stability of the numerical discretisation schemes and the robustness of the solution methods which are currently in development or in use. Much more work is also required to produce more economical algorithms taking into account the developments in the architecture of the modern computer systems.

Following the above incentives, work continues on the further development and verification of already existing computational methods and on the derivation of alternative schemes since the most suitable way forward is still not clear and well-defined. From this point of view, theoretical methods for the prediction of flows in

centrifugal compressors based on the solution of the system of the Navier-Stokes equations, have been initiated at Cranfield Institute of Technology with the work of Lapworth (1987) who presented a computational method to handle incompressible flows in shrouded centrifugal impellers. Taking into account this background and the general environment and policies for continuity and consistency of Cranfield's turbomachinery research activities, the present work has been aimed towards the development of this method to high speed subsonic flows in centrifugal compressors with or without tip leakage and with stationary shroud walls. This goal has been pursued in this study, through successive developments which are described in the following chapters. Initially, the computer code has been implemented for the prediction of two-dimensional cascade flows and three-dimensional ducting flows which present some of the features which might be encountered in centrifugal compressor flows. Ultimately, the final objective has been achieved through the validation study and comparison of the predictions obtained with the proposed method against the results of Eckardt's experimental investigation, Eckardt (1976 and 1980), of the flow in high speed radial and backswept impellers, at design and off-design conditions, and against the experimental results obtained at Cranfield, Forster (1988a and 1988b), for the flow within the passages of the Rolls Royce GEM impeller.

The main features of the proposed computational method are as follows:

a) Solution of the fully elliptic time-averaged Navier-Stokes equations,

b) finite volume discretisation,

c) use of a pressure correction approach to solve the system of the equations,

d) use of a generalised coordinate system and a structured general or boundary-fitted grid system,

e) fully conservative form of the equations and use of the Cartesian velocity components as unknowns in the momentum equations,

f) collocated variable arrangement on the computational grid and adoption of an appropriate interpolation practice to prevent decoupling between velocity and pressure fields,

g) use of a simplified form of the energy equation or the assumption of a constant rothalpy and the perfect gas law in order to update the density,

h) use of the two-equation k-ϵ turbulence model with wall functions,

i) first order Upwind, Hybrid and Quadratic Upwind numerical schemes for the discretisation of the convective term,

j) spatial marching from the inlet to the outlet plane with the implementation of an Alternating Direction Implicit (ADI) scheme at each cross-plane and the Tri-Diagonal-Matrix-Algorithm (TDMA) for the solution of the system of algebraic equations at each grid line,

k) simulation of the tip leakage flow as part of the general procedure,

l) option of a stationary or rotating shroud wall.

Specific contributions of the present study are:

- The proposal of a relaxation scheme to predict compressible subsonic flows.
- The presentation of the flow model and the finite volume discretisation procedure in generalised coordinates.
- The adjustment and implementation of a grid generation technique based on the solution of elliptic partial differential equations, for the boundary fitted meshing of arbitrary two-dimensional geometries.
- The assessment of the effects of the under-relaxation factors on the speed of convergence and the application of an alternative acceleration technique in two-dimensional problems.
- The comparison of the performance of three different numerical schemes with different degree of upwinding of the convective term.
- The assessment of the effect of tip-leakage flow and the boundary condition for the shroud on the centrifugal impeller's performance and flow phenomena.
- The assessment of the effect of the flow mass rate on the flow evolution and entropy production in the rotating passage.
- The effect of the backsweep on the flow features inside the passages of a centrifugal impeller.
- The extension and modification of the model for its application in axial flow

compressors and ducting systems.

- The extension of the current model to predict unsteady flows.

Eventually, the outcome of the present study is a robust and accurate general computational tool for the time-averaged Navier-Stokes analysis and flow prediction in high speed centrifugal impellers which can be incorporated in the design process facilitating the qualitative description of expected flow features, the comparative assessment of alternative aerodynamic design strategies for a specific Turbomachinery product and the thorough quantitative investigation and verification of the final design.

1.6 Structure of the thesis

To summarise this thesis, Chapter 2 presents the system of the governing equations. An introduction to turbulence modelling and a presentation of the flow equations for the description of the turbulent flow, follows. The grid system which is used in the current work and the form of the transformed equations, are then discussed. A brief derivation of the transformed equations in a general coordinate system is finally presented.

Chapter 3 describes the spatial discretisation process of the governing equations. Then follows a discussion which elucidates the selection of the numerical schemes which are used for compromising between accuracy and stability during the discretisation of the non-linear convective term. The derivation of the current pressure correction algorithm and the general relaxation process which are utilized for the numerical solution of the flow equations adopted in the present work, are presented.

In Chapter 4, a general elliptic grid generation procedure is presented and is utilized to provide two-dimensional boundary fitted grids whose lines intersect the blade walls in a perpendicular direction.

The final objective of the present work is pursued through a step by step procedure, with increased degree of complexity, which validates and illustrates the applicability of the general method in simpler flow situations which incorporate flow patterns encountered also in radial stages.

In Chapter 5 the application of the incompressible derivative of the model is implemented for the flow prediction in two-dimensional cascades. A series of cascades with different blade geometry and inlet flow conditions are considered. The results which are obtained from the flow analysis as compared against available experimental data, are discussed. The effect of the under-relaxation parameters on the computational economy of the method is investigated and the applicability of a novel method for the acceleration of the relaxation process is assessed.

In Chapter 6, the method is implemented for the laminar and turbulent flow analysis in a series of complex three-dimensional stationary ducting systems.

In Chapter 7, the implementation of the computational model for the flow prediction in a radial and two backswept high speed centrifugal impellers at design and off-design conditions, is described. The results which are obtained are compared critically against experimental data and predictions by other researchers and discussions follow.

In Chapter 8, conclusions from the present work are drawn and proposals for possible future extensions of the present method and research work are suggested.

CHAPTER 2

Computational model

2.1 Introduction

The system of governing Navier-Stokes equations is presented in a Cartesian form. For the analysis of high Reynolds number turbulent flows, the available computer resources do not allow the full simulation of all eddies which cover a wide range of time and length scales. Hence, an averaging procedure of the governing equations is required which results in a form which relates averaged flow quantities and in addition incorporates some extra unknown terms: the Reynolds stresses and the turbulent heat flux which are correlations of fluctuating components.

The simulation of these terms is carried out through the adoption of an appropriate turbulence model. A brief review of the current trends on turbulence modelling follows and the models which are selected to be implemented in the present study, are presented.

The ability of a computational model to treat arbitrary geometrical configurations is of great importance and is closely linked to the combination of the grid system and the form of the governing equations which are selected. In the present study, the equations are transformed in a generalised coordinate system obtaining a semi-Cartesian form which ensures the satisfaction of the conservative property. This transformation is described and the form of the system of the transformed flow equations is given.

2.2 Governing equations. Navier-Stokes equations

The equations which govern three-dimensional, steady and compressible flows are the Navier-Stokes equations expressing the conservation of mass, momentum and energy.

It has been found that in turbomachinery applications where the flow has to be predicted in rotating passages, a relative frame of reference rotating with the passage is more convenient for adoption. Consequently the velocity components appearing in the following equations are the relative ones and the energy equation is formulated in terms of the conservation of a scalar quantity called rothalpy and is the equivalent of the total enthalpy in a rotating frame of reference. Additionally the Coriolis and the centrifugal forces must be included in the momentum equations.

Expressed in a Cartesian coordinate system these equations are as follows:

Conservation of mass:

$$\frac{\partial \rho}{\partial t} + \frac{\partial (\rho u_j)}{\partial x_j} = 0 \qquad (2.2.1)$$

Conservation of momentum:

$$\frac{\partial (\rho u_i)}{\partial t} + \frac{\partial (\rho u_i u_j)}{\partial x_j} = -\frac{\partial p}{\partial x_i} + \frac{\partial \tau_{ij}}{\partial x_j} + F_i \qquad i=1,2,3 \qquad (2.2.2)$$

Conservation of energy:

$$\frac{\partial (\rho I)}{\partial t} + \frac{\partial (\rho u_j I)}{\partial x_j} = \frac{\partial}{\partial x_j}\left(\frac{\mu}{Pr}\frac{\partial I}{\partial x_j}\right) + S_I \qquad (2.2.3)$$

where u_j (j=1,2,3) stands for the cartesian velocity components u, v and w, which are respectively parallel to the axes of the Cartesian system x_j (j=1,2,3) which stands for x, y and z and correspond to the fixed unit vectors $\bar{e}_j$ (j=1,2,3). Additionally ρ is the fluid density, p is the thermodynamic (static) pressure and Pr is the Prandtl number of the fluid. The term τ_{ij} is the viscous stress tensor given by Newton's law of viscosity:

$$\tau_{ij} = \mu\left(\frac{\partial u_i}{\partial x_j} + \frac{\partial u_j}{\partial x_i}\right) + \lambda\frac{\partial u_k}{\partial x_k}\delta_{ij} \qquad (2.2.4)$$

where δ_{ij} is the Kronecker delta ($\delta_{ij}=1$ if i=j and $\delta_{ij}=0$ if i≠j), μ is the dynamic viscosity and λ is the second coefficient of viscosity given by:

$$\lambda = -\frac{2}{3}\mu \qquad (2.2.5)$$

The term F_i is the component of the centrifugal plus the coriolis forces' vector to the i direction and is defined in tensor form as:

$$F_i = -2\rho\,\varepsilon_{ijk}\Omega_j u_k - \rho\,(\Omega_n x_n)\,\Omega_i + \rho\,(\Omega_m\Omega_m)\,x_i \qquad (2.2.6)$$

where ϵ_{ijk} is the alternating tensor which obtains the value 1 if ijk cyclic (123, 231, 312), -1 if ijk anti-cyclic (321, 132, 213) and 0 otherwise.
The term Ω_j is the component of the rotational speed vector $\vec{\Omega}$ to the j direction.

The rothalpy is defined as follows:

$$I = C_pT + \frac{1}{2}(u_k u_k) - \frac{1}{2}(\vec{\Omega}\times\vec{r})\cdot(\vec{\Omega}\times\vec{r}) \qquad (2.2.7)$$

$$\text{where :} \qquad \vec{r} = x_j\vec{e}_j$$

where T is the static temperature and C_p is the specific heat at constant pressure of the fluid. In the current study the rotation is assumed to be around the z axis. If the rotational speed becomes equal to zero then the rothalpy becomes equal to the total enthalpy.

The term S_I which appears in the energy equation has the following form:

$$S_I = \frac{\partial}{\partial x_j}\left[\frac{\mu}{Pr}\cdot\frac{\partial}{\partial x_j}\left(\frac{u_k u_k}{2}\right)\right] + \frac{\partial}{\partial x_j}\left[\frac{\mu}{Pr}\cdot\frac{\partial}{\partial x_j}\left(\frac{\Omega^2 r^2}{2}\right)\right] + \frac{\partial}{\partial x_j}(\tau_{ji}\cdot u_i) \qquad (2.2.8)$$

This is a small term and can be neglected without any serious loss of accuracy. The derivation of the energy equation is performed in Appendix A.

The perfect gas law which relates the static pressure, the static temperature and the density of the gas is given by the relation:

$$p = \rho RT \qquad (2.2.9)$$

where R is the gas constant.

The whole set of the equations in Cartesian coordinates can be written in the form of a single general equation for the transport of an arbitrary scalar dependent variable Φ:

$$\frac{\partial}{\partial x}(\rho u\Phi) + \frac{\partial}{\partial y}(\rho v\Phi) + \frac{\partial}{\partial z}(\rho w\Phi) = \frac{\partial}{\partial x}\left(\Gamma_\Phi \frac{\partial \Phi}{\partial x}\right) + \qquad (2.2.10)$$

$$+ \frac{\partial}{\partial y}\left(\Gamma_\Phi \frac{\partial \Phi}{\partial y}\right) + \frac{\partial}{\partial z}\left(\Gamma_\Phi \frac{\partial \Phi}{\partial z}\right) + S_\Phi(x,y,z)$$

or:

$$\frac{\partial(\rho u_j \Phi)}{\partial x_j} = \frac{\partial}{\partial x_j}\left(\Gamma_\Phi \frac{\partial \Phi}{\partial x_j}\right) + S_\Phi(x,y,z) \qquad (2.2.11)$$

where Γ_Φ is the diffusion coefficient and S_Φ is the source term. The unsteady term $\partial/\partial t$ is dropped from the above equation since only steady state flows are considered in the present study. The LHS term is the convection term and the first term on the RHS is the diffusion term.

2.3 Navier-Stokes equations for turbulent flow

The time-dependent three-dimensional Navier-Stokes equations describe both laminar and turbulent flows completely. However, the time and space scales associated with the turbulent motion are so small even for simple flows, that the required large number of grid points and the small size of time-steps render the direct simulation of turbulent flows beyond the possibilities of the present computers. The most advanced approach today is the so called "large eddy simulation" which involves the solution of the unsteady Navier-Stokes equations for the prediction of the motion of the large eddies and the modelling of the smallest eddies, Schumann and Friedrich (1986).

For engineering calculations of industrial applications encountered in turbomachinery, which involve turbulent flows, the main trend is the description of the flow motion in terms of time-averaged quantities rather than instantaneous. The time-averaging of the Navier-Stokes equations gives rise to the Reynolds equations of motion which include Reynolds stress gradients and heat flux quantities linked with the turbulent motion. Hence, the number of unknowns increases above the number of the available equations and the problem is then to formulate a turbulence model to describe the Reynolds stresses and the turbulent heat flux quantities through certain assumptions, "closing" by this mean the system of equations.

The derivation of the Reynolds equations is performed by decomposing the dependent variables in the conservation equations into time-mean and fluctuating components and then time averaging the entire equation.

For compressible flows, two different averaging types are used, the Reynolds averaging and the density-weighted procedure suggested by Favre (1965). The two formulations become identical when the density fluctuations can be neglected. The Reynolds mean $\bar{f}$ and the Favre mean $\tilde{f}$ are defined as:

$$\bar{f} = \frac{1}{\Delta t} \int_{t_0}^{t_0+\Delta t} f \cdot dt \qquad (2.3.1)$$

and

$$\tilde{f} = \frac{1}{\bar{\rho}\Delta t} \int_{t_0}^{t_0+\Delta t} f\rho \cdot dt \qquad (2.3.2)$$

where Δt is required to be large compared to the period of the randfom turbulence fluctuations, and $\bar{\rho}$ is the Reynolds mean density.

The instantaneous randomly varying variable f can be considered as the summation of a time-averaged mean value plus a fluctuating component about the

average:

Reynolds decomposition:

$$f = \bar{f} + f' \qquad (2.3.3)$$

Favre decomposition:

$$f = \tilde{f} + f'' \qquad (2.3.4)$$

where f′ and f″ are the Reynolds and Favre fluctuating components of the flow variable f, respectively.

By definition the following relations are valid for the fluctuating values f′ and f″:

$$\bar{f'} = \frac{1}{\Delta t}\int_{t_0}^{t_0+\Delta t} f'dt \equiv 0 \qquad (2.3.5)$$

and

$$\overline{\rho f''} = \frac{1}{\Delta t}\int_{t_0}^{t_0+\Delta t} \rho f''dt \equiv 0 \qquad (2.3.6)$$

It can be shown that:

$$\tilde{f} = \bar{f} + \frac{\overline{\rho' f'}}{\bar{\rho}} \qquad (2.3.7)$$

When the fluid is incompressible, $\rho'=0$ and hence $\bar{f}=\tilde{f}$ and the two time averaging procedures provide the same result.

In the case of a Reynolds averaging applied for compresible flows, the density fluctuations ρ' cause new correlations to appear in the mean equations which become quite complex. The use of a mass-weighted averaging (Favre procedure) provides a more compact form of the mean equations which remain similar to the Reynolds form with uniform density.

In most of the turbomachinery applications of advanced Computational Fluid

Dynamics methods, presented till now, a Reynolds time-averaging is employed and the terms involving the density fluctuations are neglected from the mean equations. The same practice is followed in the present study where a Reynolds averaging is utilized and the neglect of the density fluctuations gives rise to a tidy form of the mean flow equations which is similar to the equations describing incompressible flow. Another reason for the above mentioned assumption is the development of a compressible flow model from an incompressible one used in the previous work by Lapworth (1987).

The replacement of the dependent variables with their time averages plus their fluctuations according to relation (2.3.3) in the Navier-Stokes equations and the time averaging of each of these equations using the above mentioned assumptions, produces the Reynolds form of the governing equations which are as follows:

Mass conservation:

$$\frac{\partial \overline{\rho}}{\partial t} + \frac{\partial (\overline{\rho}\overline{u}_j)}{\partial x_j} = 0 \qquad (2.3.8)$$

Momentum conservation:

$$\frac{\partial (\overline{\rho}\overline{u}_i)}{\partial t} + \frac{\partial (\overline{\rho}\overline{u}_i\overline{u}_j)}{\partial x_j} = -\frac{\partial \overline{p}}{\partial x_i} + \frac{\partial}{\partial x_j}\left(\overline{\tau_{ij}} - \overline{\rho}\ \overline{u_i' u_j'} \right) + F_i \qquad (2.3.9)$$

where:

$$\overline{\tau_{ij}} = \mu \left(\frac{\partial \overline{u}_i}{\partial x_j} + \frac{\partial \overline{u}_j}{\partial x_i} - \frac{2}{3}\delta_{ij}\frac{\partial \overline{u}_k}{\partial x_k} \right) \qquad (2.3.10)$$

Scalar conservation:

$$\frac{\partial (\overline{\rho}\overline{\Phi})}{\partial t} + \frac{\partial (\overline{\rho}\overline{u}_j\overline{\Phi})}{\partial x_j} = \frac{\partial}{\partial x_j}\left(\Gamma_\Phi \frac{\partial \overline{\Phi}}{\partial x_j} - \overline{\rho}\ \overline{u_j'\Phi'} \right) + \overline{S}_\Phi \qquad (2.3.11)$$

In the subsequent expressions, the overbar will be neglected from the time-

averaged flow parameters.

The above Reynolds equations governing now the conservation of time-averaged quantities, are very similar to those governing the conservation of the instantaneous variables with the only difference the appearance in the momentum equations of the apparent stress $-\rho\overline{u_i'u_j'}$ gradients due to the transport of momentum by turbulent fluctuations, called Reynolds stresses, and the apparent turbulent heat-flux components $-\rho\overline{u_i'\Phi'}$ arising in the Reynolds scalar equation.

These statistical terms are new unknowns and thus the Reynolds equations cannot be solved in the above form. Consequently additional relations and assumptions are required to relate the new turbulent quantities with the mean flow local features. A remedy to this "closure" problem is most usually achieved through the use of appropriate turbulence modelling.

2.4 Turbulence modelling

The most commonly used way of turbulence models classification is the one based on the number of differential equations solved in addition to the mean flow equations, Nallasamy (1987):

(i) Zero equation models.

(ii) One equation models.

(iii) Two equation models.

(iv) Stress equation models.

(v) Algebraic stress models.

Most of the models, (i)-(iii), use the Boussinesq eddy viscosity concept based on the assumption that the Reynolds stresses and the turbulent scalar fluxes follow the same type of stress-strain relation as the laminar flow:

$$-\rho\overline{u_i'u_j'} = \mu_T\left(\frac{\partial u_i}{\partial x_j} + \frac{\partial u_j}{\partial x_i}\right) - \frac{2}{3}\delta_{ij}\left(\frac{\partial u_k}{\partial x_k} + \rho\overline{u_k'u_k'}\right) \qquad (2.4.1)$$

$$-\rho\overline{u_j'\Phi'} = \Gamma_\Phi^T \frac{\partial \Phi}{\partial x_j} \qquad where \qquad \Gamma_\Phi^T = \frac{\mu_T}{\sigma_\Phi^T}$$

where μ_T is the turbulent or eddy viscosity which is defined through the turbulence model and σ_Φ^T is the turbulent Prandtl number for the transport of scalar Φ. The term $-2/3\rho\delta_{ij}\overline{u'_k u'_k}$ can be assumed as an extra normal pressure due to turbulence. One of the great advantages of this assumption is that the turbulent equations obtain the same form as the laminar equations having the molecular viscosity μ replaced by an effective viscosity $\mu_{eff}=\mu+\mu_T$ and the diffusion coefficient Γ_Φ by an effective diffusion coefficiect $\Gamma_{\Phi,eff}=\Gamma_\Phi+\Gamma_\Phi^T$ and allows the use of the same solution procedure.

The zero-equation or algebraic models are the simplest ones and calculate the turbulent viscosity using an algebraic expression. The first turbulence model proposed, the Prandtl's mixing length hypothesis, Prandtl (1925), for two-dimensional thin shear layer flows, relates the eddy viscosity distribution to the mean strain $\partial u/\partial y$:

$$\mu_T = \rho l_m u_T \qquad (2.4.2)$$

where l_m is an empirically user-prescribed "mixing length" which can be viewed as a transverse distance over which particles maintain their original momentum; and u_T is a velocity scale of turbulence given by:

$$u_T = l_m \left|\frac{\partial u}{\partial y}\right| \qquad (2.4.3)$$

The main disadvantage of the model is that the evaluation of the mixing length becomes difficult especially in three-dimensional flows since in most of the cases a boundary layer thickness needs to be defined. The mixing length models assume that the flow is in local equilibrium with the mean flow field. The history and the transport effects of turbulence are not taken into account.

Another algebraic model which is widely used, is the Baldwin and Lomax

(1978) turbulence model. This model defines a two-layer eddy viscosity distribution. The length scale's distribution is calculated using the vorticity values and thus the boundary layer thickness is not required. Despite their drawbacks, the algebraic turbulence models are used by many researchers mainly because of their simplicity and computational economy.

The one equation model usually requires the solution of a transport equation for the turbulent kinetic energy k which is derived from the Navier-Stokes equations. In this way the transport properties of the turbulence are taken into account. The velocity scale u_T of the turbulent motion is then given by:

$$u_T = C_\mu^{\frac{1}{4}} \sqrt{K} \qquad (2.4.4)$$

where C_μ is a constant value; and, the length scale is determined through a mixing length distribution assumption which is empirical and flow dependent. The one equation models are not very popular since they do not perform much better than the zero equation models despite the extra required computational effort.

The two equation models are the models which are widely used in engineering calculations. Additionally to the transport equation for the velocity scale as the turbulent kinetic energy is, an additional differential equation is solved for the calculation of a length scale. A very popular two-equation model is the k-ϵ turbulence model in which the second partial differential equation is derived for the transport of the rate of dissipation of turbulence energy ϵ, Launder and Spalding (1974). The k-ϵ model is a more realistic model than the algebraic models since the non-equilibrium and the transport properties of turbulence are simulated and there is no more need for a mixing length distribution definition. The standard k-ϵ model has been modified by researchers to include effects of streamline-curvature, rotation, buoyancy, low-Reynolds-number and near-wall effects on the turbulence structure and has been used widely for the flow prediction in turbomachinery configurations.

The major practical drawback of the two-equation models is the assumption of the validity of Boussinesq's approximation on which these models rely. In the two-equation models the individual Reynold's stresses $-\rho\overline{u'_i u'_j}$ are related to only one velocity scale $k^{1/2}$ where in actual flows the scales may develop differently in each direction. The different development of the individual stresses can be considered by introducing transport equations for each $-\rho\overline{u'_i u'_j}$, Launder et al (1975). The exact form of these equations may be derived but the closure problem is now referring to the simulation of the higher order fluctuating components correlations. An additional equation for the dissipation rate of turbulence energy is solved to provide information about the length scale distribution. These models are called "Reynolds stress" models and seem to be the most advanced turbulence models with better chances of giving more satisfactory answers than the other models for the unsolved problem of turbulence if the time averaging of the Navier-Stokes equations philosophy is to be retained as the core of the solution methodology. The main disadvantage of the Reynolds-stress models is that they are very "expensive" in terms of computational effort because of the requirement to solve differential transport equations for each of the Reynolds stresses.

If the diffusion and convection terms in the equation for $-\rho\overline{u'_i u'_j}$ are substituted by certain model approximations, then the equations become algebraic and contain the production terms appearing in the Reynolds stress equations. These turbulence models are called Algebraic Stress Models and they are mainly eddy viscosity formulations where beyond the solution of the transport equations for k and ϵ, an algebraic system of equations needs to be solved additionally to yield values for the Reynolds stresses. These models are appropriate whenever the transport of $-\rho\overline{u'_i u'_j}$ is not important but on the other hand the effects of non-isotropic fields, body force and wall damping on the flow pattern can be incorporated in the source terms of the algebraic system. Representative Algebraic Stress Models have been proposed by Launder and Ying (1973) and by Demuren and Rodi (1984).

In the area of the turbulent flow prediction in turbomachinery applications, the way forward insofar as the selection of the appropriate turbulence model is concerned, is still not clear since there are different trends and different research groups use different models in their methods. In general, the two main competitors are the algebraic or zero equation models and the two-equation k-ϵ based models modified appropriately to incorporate the effect of rotation and curvature on the turbulence structure. Moore and Moore (1980b), use a mixing length model. The most popular zero equation model is the Baldwin-Lomax (1978) two-layer model, which has been widely used by several researchers, Dawes (1986), Davis et al (1988), and is currently assumed to be the industrial model because of its simplicity and computational economy. The two-equation k-ϵ model has been extensively used in other fluid engineering applications, during the last two decades, but only recently has its use been established in the area of three-dimensional turbomachinery flow predictions. Rhie et al (1984) used the k-ϵ model with an explicit modification of the turbulence generation term to include the effects of the streamline curvature and rotation on the turbulence structure. The two-equation k-ϵ model with a low-Reynolds-number modification was used by Hah et al (1990) for the flow prediction in a transonic compressor. Hah (1984) used an algebraic stress model modified for the effects of streamline curvature and rotation.

In the present study the two-equation k-ϵ turbulence model, Launder and Spalding (1974), suitably adjusted to include the effects of rotation and streamline curvature in the case of three-dimensional rotating centrifugal impeller passages, is selected in order to pursue the realistic simulation of the turbulence effects on the mean flow characteristics.

2.5 The two-equation k-ϵ model

The form of the standard k-ϵ turbulence model which is adopted in the present work is that of Launder and Spalding (1974) but modified to account

empirically for the effects of the streamline curvature and the rotation, on the local turbulence.

In the k-ϵ model the turbulent viscosity is given by the formula:

$$\mu_T = \rho C_\mu \frac{k^2}{\epsilon} \qquad (2.5.1)$$

where k is the kinetic energy of turbulence defined as:

$$k = \frac{1}{2}\overline{u_k' u_k'} \qquad (2.5.2)$$

and ϵ is the dissipation rate of the turbulence energy defined as:

$$\epsilon = \frac{\mu}{\rho}\cdot\overline{\frac{\partial u_i'}{\partial x_j}\frac{\partial u_i'}{\partial x_j}} \qquad (2.5.3)$$

At high Reynolds numbers the transport of the turbulent kinetic energy k and of the dissipation rate of the turbulence energy ϵ, are governed by the following equations:

$$\frac{\partial(\rho u_j k)}{\partial x_j} = \frac{\partial}{\partial x_j}\left(\frac{\mu_T}{\sigma_k}\frac{\partial k}{\partial x_j}\right) + G_k - \rho\epsilon + G_c \qquad (2.5.4)$$

$$\frac{\partial(\rho u_j \epsilon)}{\partial x_j} = \frac{\partial}{\partial x_j}\left(\frac{\mu_T}{\sigma_\epsilon}\frac{\partial \epsilon}{\partial x_j}\right) + \frac{\epsilon}{k}(C_1 G_k - C_2\rho\epsilon + G_c) \qquad (2.5.5)$$

where G_k is the generation rate of turbulence obtained by:

$$G_k = \mu_T\left(\frac{\partial u_i}{\partial x_k} + \frac{\partial u_k}{\partial x_i}\right)\frac{\partial u_i}{\partial x_k} \qquad (2.5.6)$$

The constants appearing in the equations obtain the values given in the following table:

C_μ	C_1	C_2	σ_k	σ_ϵ
0.09	1.44	1.92	1.0	1.3

The term G_c is given by a semi-empirical relation which is calculated explicitly during the numerical procedure and is used to take into account the effects of streamline curvature and rotation on the turbulence structure and will be discussed in Section 7.4.

2.6 Turbulent flow near the walls

In the near-wall regions the local Reynolds number of turbulence is small enough and the viscous phenomena become dominant. In a numerical solution procedure the proper resolution of the wall layer requires a substantially fine grid near the wall which increases the computational time significantly. Thus, most of the computational schemes tend to avoid the problem by utilizing the "wall-function" approach to bridge the whole of the wall layer to the fully turbulent region taking advantage of the Couette-flow behaviour which the fluid exhibits close to the wall.

According to Bradshaw (1978), within the linear sublayer ($y^+ \leq 3$) of a turbulent boundary layer, there is purely viscous flow described by:

$$u^+ = y^+ \qquad (2.6.1)$$

where:

$$u^+ = \frac{U_p}{u_T}, \qquad y^+ = \frac{\rho\, u_T\, \delta n}{\mu}, \qquad u_T = \sqrt{\frac{\tau_w}{\rho}} \qquad (2.6.2)$$

δn is the normal distance from the wall and U_p is the velocity parallel to the wall.

In the fully turbulent region, $y^+ \geq 50$, the velocity is assumed to follow a logarithmic law:

$$u^+ = \frac{1}{\kappa} \ln (E y^+) \qquad (2.6.3)$$

where κ is von Karman's constant equal to 0.41 and E is a function of the wall roughness, found equal to 9.0 for a smooth wall.

The buffer layer which exists between the linear sublayer and the log-law region, where there is a smooth change of the velocity profiles, is ignored in engineering computations. If continuity is to be retained in the values of u^+, the transition point is found to be at $y^+ \approx 11.5$.

The above relations based on a velocity profile assumption in the near-wall layer, are used to provide a shear stress τ_w which is used in the descritized Navier-Stokes equations to define a wall diffusion flux. The definition of the friction velocity u_T yields:

$$\tau_w = \rho u_T^2 \qquad (2.6.4)$$

In the k-ϵ model the shear stress τ_w can be calculated explicitly assuming that in the wall-layer the total shear stress is uniform and that the generation and dissipation of the turbulence kinetic energy are in balance (equilibrium). The friction velocity is then linked to the turbulence kinetic energy through the following expression:

$$u_T^2 = k \sqrt{C_\mu} \qquad (2.6.5)$$

The substitution of the equations (2.6.5) and (2.6.2) into the definition of u^+ and y^+ yields:

$$u^+ = \frac{\rho U_p C_\mu^{\frac{1}{4}} \sqrt{K}}{\tau_w} \qquad (2.6.6)$$

Replacing the u^+ and y^+ into the law of the wall expressions, the following relations for calculating the shear stress are obtained:

$$y^+ = \frac{\rho\, C_\mu^{\frac{1}{4}} \sqrt{k}\, \delta n}{\mu} \qquad (2.6.7)$$

$$\tau_w = \frac{\mu U_p}{\delta n} \quad if \quad y^+ < 11.5 \qquad (2.6.8)$$

$$\tau_w = \frac{\kappa C_\mu^{\frac{1}{4}} \sqrt{k} \rho U_p}{\ln\left(E C_\mu^{\frac{1}{4}} \sqrt{k} \rho\, \delta n/\mu\right)} \quad if \quad y^+ \geq 11.5 \qquad (2.6.9)$$

Hence, the shear stress on the wall can be calculated through the values of the flow variables at the grid node next to the wall.

The application of the wall functions in the current Computational Fluid Dynamics methods reduces the computational effort required to incorporate the wall effects on the turbulent flow but its validity in three-dimensional flows with curvature and rotation is doubtful or at least insufficient for the accurate representation of the tip leakage flows. Another shortcoming of the wall function approach, as it is used with the standard k-ϵ model, is that it is valid only in the fully turbulent flow region and cannot be valid through the laminar and transitional regions. Many researchers have extended the k-ϵ model including additional terms in the transport equations for k and ϵ to maintain the low Reynolds number and the near-wall damping effects on the near-wall turbulence in place of the wall functions. An extended review of Low-Reynolds-Number turbulence models may be found in the paper by Schreurer et al (1984).

In the present study, the wall function approach in a general form for complex geometries has been fully adopted since the Computer resources were limited especially at the outset of the research programme.

2.7 Grid system - Form of the governing equations

The flow in the vicinity of a solid wall is very critical and determines the

flow features through the entire flow domain. There are severe gradients of most of the flow parameters especially when the flow is turbulent and in many engineering applications, global parameters such as the heat transfer coefficient of a turbine blade surface, the drag coefficient of a cascade airfoil section etc., are highly dependent on the flow features in the near wall region. Thus, an accurate representation of the boundary conditions in these areas are of high importance for any numerical method which attempts to predict the flow. An irregularly shaped flow domain which is commonly encountered in most practical applications renders the above representation even more difficult. When standard finite difference techniques are implemented to solve the flow conservation equations in a Cartesian system the irregular boundary is approximated through a stepwise representation in which the boundary conditions cannot be represented accurately.

This problem is overcome, by using the so called "Boundary Fitted Coordinates" (BFC) approach in which the boundaries coincide with lines of a structured mesh which covers the irregular domain. This method retains all the simplicity of the finite difference methods and additionally takes into account the constraints caused by the irregular shape of the boundary insofar as the accurate description of the boundary conditions is concerned.

There are two types of Boundary Fitted Coordinates: orthogonal and generalised. A BFC system is orthogonal, when the angle between the tangents to the coordinate lines is equal to 90°. The term "generalised" or "general" is used when the angle between the tangents to the coordinate lines is arbitrary. There is a special category of general BFC where the grid lines are perpendicular only on the boundaries of the flow domain.

In the present study, a general system of Boundary Fitted Coordinates is employed since the generation of orthogonal grids is difficult in highly irregular shapes and especially in the three-dimensional space.

Since the Boundary Fitted Coordinate approach has been adopted, a transformation of the equations from the "physical space" to an "imaginary" or

"computational space" is necessary. Demirdzic (1982) has conducted an extensive study of the possible forms of the governing differential equations when a general, non-orthogonal coordinate system is used. One of the most important factors influencing the choice of the form of the governing equations is the degree of their "conservative" property. Depending on the way the divergence operator is expressed in a generalised coordinate system, the governing equations can have either a "weak conservation" form if some of the terms are not under the differential operator, or a "strong conservation" form if all the terms arising from the divergence operator are under differential operators. The "strong conservation" form guarantees overall conservation of the transported quantity since when the differential equations are integrated over a finite number of control volumes, the resulting fluxes will cancel in pairs at all interior control volume faces and only the boundary fluxes remain. In a "weak conservation" form the integration of the governing equations causes remained undifferentiated terms so that overall conservation is not guaranteed. In the case of the momentum equation, which describes the conservation of a vector quantity, the velocity components are conserved only if the direction of resolution is spatially constant. When the directions of resolution vary in space then in the transformed equations for the velocity components, undifferentiated terms will appear and these equations are said to be of a "semi-strong" conservation form.

The "strong conservation" form of the transformed equations is therefore adopted in the present study. The simplest form of the governing generalised equations results when vector and tensor components are referred to a fixed base. A very straightforward choice is to use orthogonal, Cartesian base vectors, in which case there is no difference between covariant and contravariant velocity components. In this case the unknown quantities in the momentum equations are the Cartesian velocity components and the form of the generalised equation is called "semi-Cartesian". The implementation of the boundary conditions is also easier in the case of Cartesian velocity components. A problem arising immediately is that the velocity components do not follow the local coordinate directions, and decoupling between

the pressure and the velocity fields and pressure oscillations may occur when standard numerical solution techniques are used, Rhie and Chow (1983). The arrangement of the variables' location on the general grid and manner in which the pressure equation is derived are crucial for the numerical solution of such an equations' set form and will be discussed in the next chapter. In the next section the derivation of the equations in the general system will be presented and the final form of the governing equations will be given.

2.8 Transformation of the basic equations

For the expression of the general transport law 2.2.11 from the Cartesian physical space (x,y,z) to the computational space (ξ,η,ζ), where ξ, η and ζ are new independent local variables in the generalised boundary fitted coordinate system, a transformation $\xi=\xi(x,y,z)$, $\eta=\eta(x,y,z)$ and $\zeta=\zeta(x,y,z)$ has to be implemented in both a one-to-one and onto fashion.

If $\mathbf{x}$ is a grid point in the Cartesian system, then $\underline{\mathbf{A}}\mathbf{x}$ is the corresponding point in the computational coordinate system (ξ,η,ζ), where $\underline{\mathbf{A}}$ is the transformation matrix given by:

$$\underline{\mathbf{A}} = \begin{vmatrix} x_\xi & y_\xi & z_\xi \\ x_\eta & y_\eta & z_\eta \\ x_\zeta & y_\zeta & z_\zeta \end{vmatrix} \qquad (2.8.1)$$

One important parameter for the transformation is the Jacobian J which is the determinant of the matrix $\underline{\mathbf{A}}$ and is given by:

$$J = x_\xi (y_\eta z_\zeta - z_\eta y_\zeta) - y_\xi (x_\eta z_\zeta - z_\eta x_\zeta) + z_\xi (x_\eta y_\zeta - y_\eta x_\zeta) \qquad (2.8.2)$$

The Jacobian at each point expresses the ratio of the control cell's volume in the physical to the corresponding volume in the computational space and must obtain no-zero positive values for a transformation without any singularities.

The inverse transformation from the curvilinear to the Cartesian coordinate system is determined via an analogous matrix $\underline{\Delta}$:

$$\underline{\Delta} = \begin{vmatrix} \xi_x & \eta_x & \zeta_x \\ \xi_y & \eta_y & \zeta_y \\ \xi_z & \eta_z & \zeta_z \end{vmatrix} \qquad (2.8.3)$$

The points $\Delta(\Delta x)$ and x must coincide for all grid points x in the Cartesian system. Thus the following expression is valid:

$$\underline{\Delta} \cdot \underline{A} = \underline{I} \qquad (2.8.4)$$

where $\underline{I}$ is the unit matrix and:

$$\underline{\Delta} = \underline{A}^{-1} \qquad (2.8.5)$$

This relation is used to yield a series of relationships between the coordinate transformation components:

$$\xi_x = J^{-1}(y_\eta z_\zeta - z_\eta y_\zeta) \;,\; \eta_x = J^{-1}(z_\xi y_\zeta - y_\xi z_\zeta) \;,\; \zeta_x = J^{-1}(y_\xi z_\eta - z_\xi y_\eta) \quad (2.8.6)$$

$$\xi_y = J^{-1}(x_\zeta z_\eta - z_\zeta x_\eta) \;,\; \eta_y = J^{-1}(x_\xi z_\zeta - z_\xi x_\zeta) \;,\; \zeta_y = J^{-1}(x_\eta z_\xi - z_\eta x_\xi) \quad (2.8.7)$$

$$\xi_z = J^{-1}(x_\eta y_\zeta - y_\eta x_\zeta) \;,\; \eta_z = J^{-1}(x_\zeta y_\xi - y_\zeta x_\xi) \;,\; \zeta_z = J^{-1}(x_\xi y_\eta - y_\xi x_\eta) \quad (2.8.8)$$

The metrics x_ξ, y_ξ ... etc can be approximated using an appropriate finite difference scheme utilizing the coordinates of the corresponding points in the physical and in the computational space. The metrics ξ_x, ξ_y, ... etc are then evaluated using the above relations.

For the transformation of the partial derivatives $\partial/\partial x_i$, the chain rule is employed in a fully conservative form, Lapworth (1987):

$$\frac{\partial \Phi}{\partial x_i} = \frac{1}{J}\left[\frac{\partial (J\xi_{x_i}\Phi)}{\partial \xi} + \frac{\partial (J\eta_{x_i}\Phi)}{\partial \eta} + \frac{\partial (J\zeta_{x_i}\Phi)}{\partial \zeta}\right] \qquad (2.8.9)$$

This form of the chain rule is necessary for the generalised flow equations to obtain the same "strong conservation" law form as the Cartesian flow equations.

The velocity components U, V and W which are used in the generalised system when transforming the flow conservation equations, are related to the Cartesian ones, u, v and w, by:

$$U = J(\xi_x u + \xi_y v + \xi_z w) \qquad (2.8.10)$$

$$V = J(\eta_x u + \eta_y v + \eta_z w) \qquad (2.8.11)$$

$$W = J(\zeta_x u + \zeta_y v + \zeta_z w) \qquad (2.8.12)$$

or in a compact form:

$$U_i = J\frac{\partial \xi_i}{\partial x_j} u_j \qquad (2.8.13)$$

where there is a summation over the repeated index j.

The components U, V and W have an important physical meaning. In fact $U/J\sqrt{\xi_x^2+\xi_y^2+\xi_z^2}$ is the velocity component normal to the constant ξ planes in the physical space, $V/J\sqrt{\eta_x^2+\eta_y^2+\eta_z^2}$ is the velocity component normal to the constant η planes and $W/J\sqrt{\zeta_x^2+\zeta_y^2+\zeta_z^2}$ is the velocity component normal to the constant ζ surfaces. In other words U, V and W are the contravariant velocity components scaled by the Jacobian of the transformation.

The Cartesian velocity components may be expressed by the inverse relations:

$$u = J^{-1}(x_\xi U + x_\eta V + x_\zeta W) \qquad (2.8.14)$$

$$v = J^{-1}(y_\xi U + y_\eta V + y_\zeta W) \qquad (2.8.15)$$

$$w = J^{-1}(z_\xi U + z_\eta V + z_\zeta W) \qquad (2.8.16)$$

The application of the above transformation relations onto the general transport equation for the scalar quantity Φ provides the transport equation in the generalised coordinate system.

Convection term

The convection term of the general transport equation for the scalar Φ in a Cartesian system has the form:

$$\frac{\partial(\rho u_j \Phi)}{\partial x_j} = \frac{\partial(\rho u \Phi)}{\partial x} + \frac{\partial(\rho v \Phi)}{\partial y} + \frac{\partial(\rho w \Phi)}{\partial z} \qquad (2.8.17)$$

The expression of the derivatives in this relation according to the conservative chain rule, equation (2.8.9), results after rearranging in the final convection term form in the general system:

$$\frac{\partial(\rho u_j \Phi)}{\partial x_j} = \frac{1}{J}\frac{\partial(\rho U_j \Phi)}{\partial \xi_j} = \frac{1}{J}\frac{\partial(\rho U \Phi)}{\partial \xi} + \frac{1}{J}\frac{\partial(\rho V \Phi)}{\partial \eta} + \frac{1}{J}\frac{\partial(\rho W \Phi)}{\partial \zeta}$$

(2.8.18)

Diffusion Term

If the chain rule expressions are used twice for the transformation of the diffusion term, the resulting diffusion term in the generalised coordinate system obtains the following form:

$$\frac{\partial}{\partial x_j}\left(\Gamma_\Phi \frac{\partial \Phi}{\partial x_j}\right) = \frac{1}{J}\frac{\partial}{\partial \xi}\left[J\Gamma_\Phi\left(g^{11}\frac{\partial \Phi}{\partial \xi} + g^{12}\frac{\partial \Phi}{\partial \eta} + g^{13}\frac{\partial \Phi}{\partial \zeta}\right)\right]$$

$$+ \frac{1}{J}\frac{\partial}{\partial \eta}\left[J\Gamma_\Phi\left(g^{21}\frac{\partial \Phi}{\partial \xi} + g^{22}\frac{\partial \Phi}{\partial \eta} + g^{23}\frac{\partial \Phi}{\partial \zeta}\right)\right] \qquad (2.8.19)$$

$$+ \frac{1}{J}\frac{\partial}{\partial \zeta}\left[J\Gamma_\Phi\left(g^{31}\frac{\partial \Phi}{\partial \xi} + g^{32}\frac{\partial \Phi}{\partial \eta} + g^{33}\frac{\partial \Phi}{\partial \zeta}\right)\right]$$

where the metric components g^{ij} are given by the relation:

$$g^{ij} = \frac{\partial \xi_i}{\partial x_k}\frac{\partial \xi_j}{\partial x_k} \qquad (2.8.20)$$

where there is a summation over the repeated index k, e.g.:

$$g^{21} = \frac{\partial \xi_2}{\partial x_1}\frac{\partial \xi_1}{\partial x_1} + \frac{\partial \xi_2}{\partial x_2}\frac{\partial \xi_1}{\partial x_2} + \frac{\partial \xi_2}{\partial x_3}\frac{\partial \xi_1}{\partial x_3} = \eta_x\xi_x + \eta_y\xi_y + \eta_z\xi_z = g^{12}$$

(2.8.21)

Finally, in a compact form, the transformed diffusion term may be expressed as:

$$\frac{\partial}{\partial x_j}\left(\Gamma_\Phi \frac{\partial \Phi}{\partial x_j}\right) = \frac{1}{J}\frac{\partial}{\partial \xi_j}\left(\Gamma_\Phi J g^{\overset{i}{\overset{=}{j}}\overset{i}{\overset{=}{k}}}\frac{\partial \Phi}{\partial \xi_k}\right) \qquad (2.8.22)$$

where there is a summation over both the j and k indices.

General equation

Eventually the transformation of the general transport equation to the curvilinear coordinate system may be expressed as follows:

$$\frac{\partial(\rho U_j \Phi)}{\partial \xi_j} = \frac{\partial}{\partial \xi_j}\left(J\,\Gamma_\Phi\, g^{jk}\frac{\partial \Phi}{\partial \xi_k}\right) + J \cdot S_\Phi(\xi,\eta,\zeta) \qquad (2.8.23)$$

where the term $S_\Phi(\xi,\eta,\zeta)$ is the transformed source term obtained by applying the chain rules for the transformation of the Cartesian derivatives appearing in the source term $S_\Phi(x,y,z)$.

Equation (2.8.23) retains the same fully conservative form as the general Cartesian transport equation and consequently the numerical solution procedure used for the Cartesian form of the equations can be directly implemented to the generalised equations. In addition, the common general form of all the transport equations, facilitates the application of the same solution method for all these flow equations. The Cartesian velocity components u, v and w are retained as unknowns in the transformed momentum equations (semi-Cartesian form). However, the fluxes are calculated by using the contravariant velocity components U, V and W.

CHAPTER 3

Numerical Solution

3.1 Introduction

In this chapter, the details and the sequence of the numerical procedure steps which are followed for the solution of the system of the governing partial differential equations, are presented.

The full form of the governing equations is provided in order to facilitate the description of the discretisation practices which are utilized.

Firstly the flow domain is covered with a structured grid and the general equations are integrated over each control volume, which is constructed on the computational grid, and become algebraic by using certain assumptions concerning the local spatial variation of the various parameters involved.

The numerical differencing schemes used for the discretisation of the convective, the diffusive and the source terms and their properties are then discussed.

The main characteristic of the solution procedure of the current method is the use of the continuity equation to derive an equation for the approximation of the pressure field. The mathematical details of the implementation of a calculation procedure for a pressure field which ensures the satisfaction of both the continuity and the momentum equations, the associated difficulties and the remedies which are proposed are explained.

Eventually, the general relaxation methodology is described and discussed.

3.2 Expanded form of the governing equations

The compact form of the governing equations can be rewritten as follows:

$$\frac{1}{J}\frac{\partial(\rho U_j)}{\partial \xi_j} = 0 \qquad (3.2.1)$$

$$\frac{1}{J}\frac{\partial}{\partial \xi_j}\left(\rho U_j u_i - J(\mu+\mu_T) g^{jk}\frac{\partial u_i}{\partial \xi_k} \right) = S_{u_i} \qquad i = 1,2,3 \qquad (3.2.2)$$

$$\frac{1}{J}\frac{\partial}{\partial \xi_j}\left(\rho U_j \Phi - J\Gamma_\Phi g^{jk}\frac{\partial \Phi}{\partial \xi_k} \right) = S_\Phi \qquad (3.2.3)$$

Each of these equations will now be expressed in its expanded form, which will constitute the starting point in the discretisation procedure which follows.

Continuity equation

$$\frac{\partial(\rho U)}{\partial \xi} + \frac{\partial(\rho V)}{\partial \eta} + \frac{\partial(\rho W)}{\partial \zeta} = 0 \qquad (3.2.4)$$

where U, V and W are related to the contravariant velocity components and are defined through the relations (2.8.13):

$$U_i = J\left(\frac{\partial \xi_i}{\partial x_k} u_k\right) \qquad (3.2.5)$$

Momentum equations

u - momentum

$$\frac{\partial}{\partial \xi}\left[\rho U u - J(\mu+\mu_T)\left(g^{11}\frac{\partial u}{\partial \xi} + g^{12}\frac{\partial u}{\partial \eta} + g^{13}\frac{\partial u}{\partial \zeta}\right)\right] +$$

$$+ \frac{\partial}{\partial \eta}\left[\rho V u - J(\mu+\mu_T)\left(g^{21}\frac{\partial u}{\partial \xi} + g^{22}\frac{\partial u}{\partial \eta} + g^{23}\frac{\partial u}{\partial \zeta}\right)\right] +$$

$$+ \frac{\partial}{\partial \zeta}\left[\rho W u - J(\mu+\mu_T)\left(g^{31}\frac{\partial u}{\partial \xi} + g^{32}\frac{\partial u}{\partial \eta} + g^{33}\frac{\partial u}{\partial \zeta}\right)\right] = \qquad (3.2.6)$$

$$= JF_1 - J\left(\frac{\partial p}{\partial \xi}\xi_x + \frac{\partial p}{\partial \eta}\eta_x + \frac{\partial p}{\partial \zeta}\zeta_x\right) + \frac{\partial}{\partial \xi_s}\left[J(\mu+\mu_T)\frac{\partial \xi_s}{\partial x_p}\left(\frac{\partial u_p}{\partial \xi_1}\frac{\partial \xi_1}{\partial x} - \right.\right.$$

$$\left.\left. - \frac{2}{3}\delta_{1p}\left(\frac{\partial u_m}{\partial \xi_n}\frac{\partial \xi_n}{\partial x_m}\right)\right)\right]$$

<u>v-momentum</u>

$$\frac{\partial}{\partial \xi}\left[\rho Uv - J(\mu+\mu_T)\left(g^{11}\frac{\partial v}{\partial \xi} + g^{12}\frac{\partial v}{\partial \eta} + g^{13}\frac{\partial v}{\partial \zeta}\right)\right] +$$

$$+ \frac{\partial}{\partial \eta}\left[\rho Vv - J(\mu+\mu_T)\left(g^{21}\frac{\partial v}{\partial \xi} + g^{22}\frac{\partial v}{\partial \eta} + g^{23}\frac{\partial v}{\partial \zeta}\right)\right] +$$

$$+ \frac{\partial}{\partial \zeta}\left[\rho Wv - J(\mu+\mu_T)\left(g^{31}\frac{\partial v}{\partial \xi} + g^{32}\frac{\partial v}{\partial \eta} + g^{33}\frac{\partial v}{\partial \zeta}\right)\right] = \qquad (3.2.7)$$

$$= JF_2 - J\left(\frac{\partial p}{\partial \xi}\xi_y + \frac{\partial p}{\partial \eta}\eta_y + \frac{\partial p}{\partial \zeta}\zeta_y\right) + \frac{\partial}{\partial \xi_s}\left[J(\mu+\mu_T)\frac{\partial \xi_s}{\partial x_p}\left(\frac{\partial u_p}{\partial \xi_1}\frac{\partial \xi_1}{\partial y} - \right.\right.$$

$$\left.\left. - \frac{2}{3}\delta_{2p}\left(\frac{\partial u_m}{\partial \xi_n}\frac{\partial \xi_n}{\partial x_m}\right)\right)\right]$$

<u>w-momentum</u>

$$\frac{\partial}{\partial \xi}\left[\rho Uw - J(\mu+\mu_T)\left(g^{11}\frac{\partial w}{\partial \xi} + g^{12}\frac{\partial w}{\partial \eta} + g^{13}\frac{\partial w}{\partial \zeta}\right)\right] +$$

$$+ \frac{\partial}{\partial \eta}\left[\rho Vw - J(\mu+\mu_T)\left(g^{21}\frac{\partial w}{\partial \xi} + g^{22}\frac{\partial w}{\partial \eta} + g^{23}\frac{\partial w}{\partial \zeta}\right)\right] +$$

$$+ \frac{\partial}{\partial \zeta}\left[\rho Ww - J(\mu+\mu_T)\left(g^{31}\frac{\partial w}{\partial \xi} + g^{32}\frac{\partial w}{\partial \eta} + g^{33}\frac{\partial w}{\partial \zeta}\right)\right] = \qquad (3.2.8)$$

$$= JF_3 - J\left(\frac{\partial p}{\partial \xi}\xi_z + \frac{\partial p}{\partial \eta}\eta_z + \frac{\partial p}{\partial \zeta}\zeta_z\right) + \frac{\partial}{\partial \xi_s}\left[J(\mu+\mu_T)\frac{\partial \xi_s}{\partial x_p}\left(\frac{\partial u_p}{\partial \xi_1}\frac{\partial \xi_1}{\partial z} - \right.\right.$$

$$\left.\left. - \frac{2}{3}\delta_{3p}\left(\frac{\partial u_m}{\partial \xi_n}\frac{\partial \xi_n}{\partial x_m}\right)\right)\right]$$

Scalar equation

$$\frac{\partial}{\partial \xi}\left[\rho U\Phi - \Gamma_\Phi J\left(g^{11}\frac{\partial \Phi}{\partial \xi} + g^{12}\frac{\partial \Phi}{\partial \eta} + g^{13}\frac{\partial \Phi}{\partial \zeta}\right)\right] +$$

$$+ \frac{\partial}{\partial \eta}\left[\rho V\Phi - \Gamma_\Phi J\left(g^{21}\frac{\partial \Phi}{\partial \xi} + g^{22}\frac{\partial \Phi}{\partial \eta} + g^{23}\frac{\partial \Phi}{\partial \zeta}\right)\right] + \qquad (3.2.9)$$

$$+ \frac{\partial}{\partial \zeta}\left[\rho W\Phi - \Gamma_\Phi J\left(g^{31}\frac{\partial \Phi}{\partial \xi} + g^{32}\frac{\partial \Phi}{\partial \eta} + g^{33}\frac{\partial \Phi}{\partial \zeta}\right)\right] = J\cdot S_\Phi$$

where the metric components g^{jk} are defined through the relation (2.8.20), or in an expanded form:

$$g^{11} = \xi_x^2 + \xi_y^2 + \xi_z^2$$

$$g^{12} = g^{21} = \xi_x\eta_x + \xi_y\eta_y + \xi_z\eta_z$$

$$g^{13} = g^{31} = \xi_x\zeta_x + \xi_y\zeta_y + \xi_z\zeta_z \qquad (3.2.10)$$

$$g^{22} = \eta_x^2 + \eta_y^2 + \eta_z^2$$

$$g^{33} = \zeta_x^2 + \zeta_y^2 + \zeta_z^2$$

$$g^{23} = g^{32} = \eta_x\zeta_x + \eta_y\zeta_y + \eta_z\zeta_z$$

The momentum equations have as unknowns the Cartesian velocity

components and are much more complex than the transport equation for a scalar Φ containing all the three derivatives of all the three velocity components. The transformation also gives rise to three pressure gradients to be present in each of the three momentum equations. However, despite the large number of terms appearing, the momentum equations have a relatively simple form, and by using certain assumptions, exhibit similarity to the equations expressed in the Cartesian system and hence, a similar discretisation route can be followed.

3.3 Discretisation procedure

3.3.1 Finite Volume integration

The system of governing equations which has been presented in the previous section describes the variation of flow parameters in the continuous space. For the numerical solution of this system the continuous information becomes discretised, with the density of the discretisation depending on the available computer resources in terms of memory, storage and run time requirements. Various methods of discretisation for fluid flow problems exist, the most important being the Finite Difference (FDM), the Finite Volume (FVM) and the Finite Element Methods (FEM). In the current study, a finite volume approach is chosen for the discretisation of the flow equations, in which the system of the algebraic equations is obtained by integrating the governing differential equations over finite volumes - cells, fulfilling, by this means, the requirement for local conservation of the flow parameters. Nowadays, finite volume methods are very popular and well established for the discretisation of fluid flow problems. With the introduction of appropriate transformations in generalised coordinate systems, they are very competitive to finite element methods as far as accuracy in the description of external irregular geometries is concerned.

The first step for the implementation of most current numerical methods is the covering of the flow domain with a grid which implies that the discretised information is obtained on characteristic points of this grid whereby the continuous

information is subsequently calculated through an appropriate interpolation method. The most common type of grid which is encountered in three-dimensional flow computations using the finite volume method is a structured mesh consisting of a network of three families of lines whose intersection nodes are the so-called grid nodes, each of which is enclosed by its own hexahedral control volume. In the present study, the control volume boundaries are assumed to be located in the middle of the distance between adjacent grid nodes. An example of such a grid is illustrated in Figure 3.1a. The generalised transformation, which was described in the previous chapter, expresses the equations in terms of general coordinates and maps the irregular grid in the physical space, as shown in Figure 3.1a, into the computational space where the grid is regular and in the general case consists of rectangular control volumes, as illustrated in Figure 3.1b.

Figure 3.2 focuses on the control volume surrounding the grid point P. With E,W,N,S,F,B are denoted the neighbouring grid points per two in the ξ, η and ζ directions respectively, and with e,w,n,s,f,b the location of the corresponding cell faces. With the use of Gauss's theorem:

$$\int_V div\vec{f}\, dV = \int_A \vec{f}\cdot\vec{n}\, dA \qquad (3.3.1)$$

where A is the area of the surface which encloses the volume V and $\vec{n}$ is the outward unit normal vector to that surface, the volume integrals on the left-hand-side of the transport equations can be expressed as surface integrals over the six faces of each control volume or computational cell:

$$\int_V div\vec{f}\, dV = \int_{A_e} f_e dA - \int_{A_w} f_w dA + \int_{A_n} f_n dA - \int_{A_s} f_s dA + \int_{A_f} f_f dA - \int_{A_b} f_b dA \qquad (3.3.2)$$

where, eg. f_w is the component of $\vec{f}$ normal to the "w" face of the control volume and A_w is the area of that cell face.

The integration of the transport equations (3.2.4) to (3.2.9) over the control volume which encloses the grid node P, using the above equation, can be expressed in the following form:

$$I_e - I_w + I_n - I_s + I_f - I_b = \int_{\Delta V_p} S_\Phi \cdot dV \qquad (3.3.3)$$

where I_i are the surface integrals of the terms under the divergence operator on the LHS of the transport equations. Each of these terms consists of two parts: the convective term I^c which has the general form $\rho U_i u_j$ and the diffusive term I^d. The diffusive term can be split up into two parts: the "orthogonal" or "normal" diffusive term I^{do} which includes the terms multiplied by g^{11}, g^{22} and g^{33}, and the cross diffusive I^{dc} term which includes the rest of the diffusion terms due to the non-orthogonal intersection of the grid lines. Thus:

$$I = I^c + I^d = I^c + I^{do} + I^{dc} \qquad (3.3.4)$$

3.3.2 Discretisation of the metric coefficients

For the description of the discretisation of each of the I terms appearing in equation (3.3.3), it is necessary to evaluate numerically the geometrical quantities or metric coefficients which appear in the transport equations and this constitutes the topic of the current section.

The construction of each control volume is performed by using segments of straight lines which join the cell vertices. In Figure 3.3a, a two dimensional projection of a ζ=const surface is shown together with graphical illustration of the basic geometrical parameters that will be utilized. In the Figure 3.3b the three faces e, n and f of a general three-dimensional control volume are depicted along with the appropriate notation. The only geometrical information about the grid which enters the computations, are the differences of Cartesian coordinates at specific locations of the control cell necessary for the definition of involved distances and face areas and the magnitude of the cell's volume. These differences in the Cartesian coordinates can be expressed as follows:

$$(\delta x_i)^{\xi}_{e}=x_{i_E}-x_{i_P} \qquad (\delta x_i)^{\eta}_{e}=(x_{i_n}-x_{i_s})_{e} \qquad (\delta x_i)^{\zeta}_{e}=(x_{i_t}-x_{i_b})_{e}$$

$$(\delta x_i)^{\xi}_{n}=(x_{i_e}-x_{i_w})_{n} \qquad (\delta x_i)^{\eta}_{n}=x_{i_N}-x_{i_P} \qquad (\delta x_i)^{\zeta}_{n}=(x_{i_t}-x_{i_b})_{n} \qquad (3.3.5)$$

$$(\delta x_i)^{\xi}_{f}=(x_{i_e}-x_{i_w})_{f} \qquad (\delta x_i)^{\eta}_{f}=(x_{i_n}-x_{i_s})_{f} \qquad (\delta x_i)^{\zeta}_{f}=x_{i_P}-x_{i_P}$$

where $(\delta x_i)_e^{\xi j}$ represents the difference in the Cartesian coordinate x_i, where x_i denotes x, y or z, along the computational coordinate ξ_j at the "e" face of the control volume. Similar definitions arise for the rest of the control faces (w, s and b).

The metric coefficients multiplied by the Jacobian are denoted with c_i^j and are discretised in the following manner:

$$c_1^1=J\xi_x=y_\eta z_\zeta-z_\eta y_\zeta=\frac{1}{\delta\eta\delta\zeta}\left[(\delta y)^{\eta}(\delta z)^{\zeta}-(\delta z)^{\eta}(\delta y)^{\zeta}\right]=\frac{1}{\delta\eta\delta\zeta}b_1^1$$

$$c_2^1=J\xi_y=x_\zeta z_\eta-z_\zeta x_\eta=\frac{1}{\delta\eta\delta\zeta}\left[(\delta x)^{\zeta}(\delta z)^{\eta}-(\delta z)^{\zeta}(\delta x)^{\eta}\right]=\frac{1}{\delta\eta\delta\zeta}b_2^1$$

$$c_3^1=J\xi_z=x_\eta y_\zeta-y_\eta x_\zeta=\frac{1}{\delta\eta\delta\zeta}\left[(\delta x)^{\eta}(\delta y)^{\zeta}-(\delta y)^{\eta}(\delta x)^{\zeta}\right]=\frac{1}{\delta\eta\delta\zeta}b_3^1$$

$$c_1^2=J\eta_x=z_\xi y_\zeta-y_\xi z_\zeta=\frac{1}{\delta\xi\delta\zeta}\left[(\delta z)^{\xi}(\delta y)^{\zeta}-(\delta y)^{\xi}(\delta z)^{\zeta}\right]=\frac{1}{\delta\xi\delta\zeta}b_1^2$$

$$c_2^2=J\eta_y=x_\xi z_\zeta-z_\xi x_\zeta=\frac{1}{\delta\xi\delta\zeta}\left[(\delta x)^{\xi}(\delta z)^{\zeta}-(\delta z)^{\xi}(\delta x)^{\zeta}\right]=\frac{1}{\delta\xi\delta\zeta}b_2^2 \qquad (3.3.6)$$

$$c_3^2=J\eta_z=x_\zeta y_\xi-y_\zeta x_\xi=\frac{1}{\delta\xi\delta\zeta}\left[(\delta x)^{\zeta}(\delta y)^{\xi}-(\delta y)^{\zeta}(\delta x)^{\xi}\right]=\frac{1}{\delta\xi\delta\zeta}b_3^2$$

$$c_1^3=J\zeta_x=y_\xi z_\eta-z_\xi y_\eta=\frac{1}{\delta\xi\delta\eta}\left[(\delta y)^{\xi}(\delta z)^{\eta}-(\delta z)^{\xi}(\delta y)^{\eta}\right]=\frac{1}{\delta\xi\delta\eta}b_1^3$$

$$c_2^3 = J\zeta_y = x_\eta z_\xi - z_\eta x_\xi = \frac{1}{\delta\xi\delta\eta}\left[(\delta x)^\eta (\delta z)^\xi - (\delta z)^\eta (\delta x)^\xi\right] = \frac{1}{\delta\xi\delta\eta} b_2^3$$

$$c_3^3 = J\zeta_z = x_\xi y_\eta - y_\xi x_\eta = \frac{1}{\delta\xi\delta\eta}\left[(\delta x)^\xi (\delta y)^\eta - (\delta y)^\xi (\delta x)^\eta\right] = \frac{1}{\delta\xi\delta\eta} b_3^3$$

where $\delta\xi$, $\delta\eta$ and $\delta\zeta$ represent the grid spacing in the computational space along the coordinates ξ, η and ζ respectively. The actual values of $\delta\xi$, $\delta\eta$ and $\delta\zeta$ do not affect the computation of the flow field and can obtain arbitrary values. It should be noted that the nine c_i^j need to be defined at all six control volume faces. The terms b_i^j have a significant physical meaning and represent the projection of a constant ξ_i characteristic surface of the control volume (eg. a cell face) onto the constant x_j Cartesian plane.

The volume of the computational cell in the physical space is given by the expression:

$$\Delta V_P = J_P(\delta\xi\delta\eta\delta\zeta)_P \qquad (3.3.7)$$

3.3.3 Discretisation of the convective term

The numerical representation of the convective term of the transport equations require the computation of the computational velocities U, V and W on all six cell faces.

Firstly, the continuity equation which contains only convective terms will be considered. If eg. the convective term at the "e" face of the cell represents the mass flux through this face and is defined as:

$$I_e^c = \int_{A_e} \rho U dA = F_{1e} = (\rho U \delta\eta\delta\zeta)_e = \left[\rho J(\xi_x u + \xi_y v + \xi_z w)\delta\eta\delta\zeta\right]_e =$$

$$= \rho_e\left(b_1^1 u + b_2^1 v + b_3^1 w\right)_e$$

On the "w" cell surface the term F_{1w} is calculated by using the same formula but with the values of u_i and b_i^j defined onto this surface. In the other two directions η

and ζ, the mass fluxes are defined by the following similar expressions:

$$F_2 = \rho V \delta\xi\delta\zeta = \rho\left(ub_1^2 + vb_2^2 + wb_3^2\right) \qquad (3.3.9)$$

$$F_3 = \rho W \delta\xi\delta\eta = \rho\left(ub_1^3 + vb_2^3 + wb_3^3\right)$$

Effectively the continuity equation obtains the following form:

$$F_{1e} - F_{1w} + F_{2n} - F_{2s} + F_{3f} - F_{3b} = 0 \qquad (3.3.10)$$

For the discretisation of the convective terms of the general transport equation, a similar procedure is followed. In this case the mean value theorem is utilized; eg :

$$\Phi_e = \frac{\int_{A_e} \rho U \Phi \, dA}{\int_{A_e} (\rho U dA)_e} = \frac{\int_{A_e} \rho U \Phi \, dA}{F_{1e}} \qquad (3.3.11)$$

Subsequently the convective term I_e^c is estimated by employing the expression:

$$I_e^c = \int_{A_e} (\rho U \Phi) \, dA = F_{1e} \Phi_e \qquad (3.3.12)$$

Similar expressions are used for the rest of the cell faces:

$$I_w^c = \int_{A_w} (\rho U \Phi) \, dA = F_{1w} \Phi_w$$

$$I_n^c = \int_{A_n} (\rho V \Phi) \, dA = F_{2n} \Phi_n$$

$$I_s^c = \int_{A_s} (\rho V \Phi) \, dA = F_{2s} \Phi_s \qquad (3.3.13)$$

$$I_f^c = \int_{A_f} (\rho W \Phi) \, dA = F_{3f} \Phi_f$$

$$I_b^c = \int_{A_b} (\rho W \Phi)\, dA = F_{3b}\Phi_b$$

For the calculation of the mass and the convective fluxes through the cell faces, the values of the velocity components and the general scalar quantity Φ are required to be estimated on these faces by using corresponding values stored at the surrounding grid nodes. This estimation is performed by using certain interpolation practices as it will be analysed in the following sections.

3.3.4 Discretisation of the diffusion term

The diffusion term of the transport equations consists of two parts: the "normal" diffusion terms which incorporate the first derivative of Φ in the direction normal to the cell faces, and the "cross" diffusion term which contains first derivatives of Φ in directions "crossing" the cell faces, eg. the normal diffusion term of the "e" face is given by the expression:

$$I_e^{do} = \int_{A_e} J\Gamma_\Phi \left(g^{11} \frac{\partial \Phi}{\partial \xi} \right) dA \qquad (3.3.14)$$

and the cross diffusion term is defined as follows:

$$I_e^{dc} = \int_{A_e} J\Gamma_\Phi \left(g^{12} \frac{\partial \Phi}{\partial \eta} + g^{13} \frac{\partial \Phi}{\partial \zeta} \right) dA \qquad (3.3.15)$$

The diffusion term at the "w" face is obtained by using similar expressions. For the rest of the faces the diffusion term is divided into the above mentioned two parts by using the formulas:

<u>"n" and "s" faces:</u>

$$I^{do} = \int_A J\Gamma_\Phi \left(g^{22} \frac{\partial \Phi}{\partial \eta} \right) dA \qquad I^{dc} = \int_A J\Gamma_\Phi \left(g^{21} \frac{\partial \Phi}{\partial \xi} + g^{23} \frac{\partial \Phi}{\partial \zeta} \right) dA \qquad (3.3.16)$$

"f" and "b" faces:

$$I^{do} = \int_A J\Gamma_\Phi \left(g^{33} \frac{\partial \Phi}{\partial \zeta} \right) dA \qquad I^{dc} = \int_A J\Gamma_\Phi \left(g^{31} \frac{\partial \Phi}{\partial \xi} + g^{32} \frac{\partial \Phi}{\partial \eta} \right) dA \qquad (3.3.17)$$

The calculation of the first derivatives of Φ "normal" to the cell faces are performed by using simple central differencing scheme, eg.:

$$\left(\frac{\partial \Phi}{\partial \xi} \right)_e = \frac{\Phi_E - \Phi_P}{(\delta \xi)_e} \qquad (3.3.18)$$

For the calculation of the two cross derivatives at each cell face, values of Φ at the middle of the cell edges have to be employed, eg:

$$\left(\frac{\partial \Phi}{\partial \eta} \right)_e = \frac{(\Phi_n - \Phi_s)_e}{(\delta \eta)_e} \qquad \left(\frac{\partial \Phi}{\partial \zeta} \right)_e = \frac{(\Phi_f - \Phi_b)_e}{(\delta \zeta)_e} \qquad (3.3.19)$$

The values $(\Phi_n-\Phi_s)_e$ and $(\Phi_f-\Phi_b)_e$ which are used in the above approximations, are obtained from the nodal values of the neighbouring points, through appropriate interpolations as it will be discussed in Section 3.5.4.

By using the definitions of g^{ij}, c_i^j and b_i^j of Sections 3.2 and 3.3.2, the discretised and integrated form of the diffusion term is obtained, eg. at the "e" control volume face, by:

$$I_e^d = I_e^{do} + I_e^{dc} = \int_{A_e} \Gamma_\Phi J g^{11} \frac{\partial \Phi}{\partial \xi} dA + \int_{A_e} \Gamma_\Phi J \left(g^{12} \frac{\partial \Phi}{\partial \eta} + g^{13} \frac{\partial \Phi}{\partial \zeta} \right) dA = \qquad (3.3.20)$$

$$= \left(\frac{\Gamma_\Phi}{\Delta V} \right)_e h^{11} (\Phi_E - \Phi_P) + \left(\frac{\Gamma_\Phi}{\Delta V} \right)_e h^{12} (\Phi_n - \Phi_s)_e + \left(\frac{\Gamma_\Phi}{\Delta V} \right)_e h^{13} (\Phi_f - \Phi_b)_e$$

The diffusion terms are approximated in a similar manner at the rest of the cell faces.

The metric coefficients h^{ij} appearing in the above equations are calculated through the relations:

$$h^{11} = b_1^1 b_1^1 + b_2^1 b_2^1 + b_3^1 b_3^1 \qquad h^{22} = b_1^2 b_1^2 + b_2^2 b_2^2 + b_3^2 b_3^2$$

$$h^{12} = h^{21} = b_1^1 b_1^2 + b_2^1 b_2^2 + b_3^1 b_3^2 \qquad h^{33} = b_1^3 b_1^3 + b_2^3 b_2^3 + b_3^3 b_3^3 \qquad (3.3.21)$$

$$h^{13} = h^{31} = b_1^1 b_1^3 + b_2^1 b_2^3 + b_3^1 b_3^3 \qquad h^{23} = h^{32} = b_1^2 b_1^3 + b_2^2 b_2^3 + b_3^2 b_3^3$$

The metric coefficients b_i^j which are employed for the estimation of the h^{ij} coefficients are approximated at each control volume face following the practice which was introduced in Section 3.3.2.

3.3.5 Discretisation of the source term

The rest of the terms in the transport equations which are not included in the convective and diffusive terms, are assumed to constitute the source terms. In a finite volume discretisation process, the volume integral of the source term is approximated by:

$$\int_{\Delta V_P} S_\Phi \cdot dV = \int_{\Delta V_P} S_\Phi \cdot J \delta\xi \delta\eta \delta\zeta = S_{\Phi P} \cdot \Delta V_P \qquad (3.3.22)$$

where $S_{\Phi P}$ is the value of the source at the node P which represents the whole control volume and, ΔV_P is the volume of the control cell which surrounds the node P. If the source term S_Φ is a function of the dependent variable Φ, then the source term is linearised into two distinct parts, Patankar (1980):

$$S_\Phi = S_\Phi' + S_\Phi'' \cdot \Phi \qquad (3.3.23)$$

The sign of S_Φ'' should be always negative to ensure realistic solutions. In the case of such a linearisation, the discretisation of the source term is performed according to:

$$\int_{\Delta V_P} S_\Phi dV = \int_{\Delta V_P} (S_\Phi' + S_\Phi'' \cdot \Phi) \cdot J d\xi d\eta d\zeta = (S_{\Phi P}' + S_{\Phi P}'' \cdot \Phi_P) \cdot \Delta V_P \qquad (3.3.24)$$

The pressure terms in the momentum equations are separated from the source term because of their significance in the derivation of the numerical scheme for the

calculation of the pressure as it will be discussed in Section 3.6.2. However, these terms are integrated in the same manner as the source terms in the discretisation process of the momentum equations, eg. of the u-momentum equation:

$$-\int_{\Delta V_P} J\left(\frac{\partial p}{\partial \xi}\xi_x + \frac{\partial p}{\partial \eta}\eta_x + \frac{\partial p}{\partial \zeta}\zeta_x\right)\delta\xi\delta\eta\delta\zeta = -(p_e-p_w)\left(b_1^1\right)_P - (p_n-p_s)\left(b_1^2\right)_P - (p_f - p_b)\left(b_1^3\right)_P \qquad (3.3.25)$$

where the coefficients b_i^j are given from the expressions (3.3.6) and approximated at the central node P as it was explained in the Section 3.3.2.

3.4 Solution of the algebraic equations system

3.4.1 General form of the equations

The control volume discretisation of all the different terms of the transport equation has been presented in the previous sections. If all these discretised terms are combined together, then the full discretised form of the transport equation will be obtained. The result of this combination is a discrete equation which has the typical following form:

$$a_P\Phi_P = \sum_k a_k\Phi_k + S_P \qquad (3.4.1)$$

where the coefficients a_k which are multiplied by the values of the dependent variable Φ at the neighbouring "k" mesh points around the grid node P and S_p is the explicit part of the discretised source term at P. The term a_p is the coefficient of Φ_p and if the linearisation process of the source term is taken into account, a_p is obtained from the expression:

$$a_P = \sum_k a_k - S_\Phi'' \qquad (3.4.2)$$

In the present study, the coefficients a_k consist of contributions from the convective and "normal" diffusive terms which are approximated numerically as it was described in Section 3.3.4.

The total number of grid points which are involved in the above discrete equation depends on the interpolation scheme which is adopted for the estimation of the values of Φ at locations on the cell faces, from the nodal values at points surrounding the central point P. The minimum number of grid nodes involved, is 5 in two-dimensional flows and 7 in three dimensional ones, and that happens when the grid is orthogonal and the values at the control volume faces are obtained by using linear interpolation. When the grid becomes non-orthogonal, these minimum values become 9 and 19 for 2-d and 3-d cases respectively.

If the grid which is employed in the computations consists of N nodes, then a system of N equations of the discrete form of equation (3.4.1) with N unknowns is formed with the general form:

$$\underline{\underline{A}} \cdot \underline{\Phi} = \underline{S} \qquad (3.4.3)$$

where $\underline{\underline{A}}$ is the matrix of the coefficients which has a special diagonal form, $\underline{\Phi}$ is the column matrix containing the unknown values of the dependent variable Φ and $\underline{S}$ is a column matrix which includes the explicitly calculated S_p term of the discrete equations. In the present study, the matrix $\underline{\underline{A}}$ obtains either a five-diagonal or a seven-diagonal form for two- and three-dimensional computations respectively. This is due to the fact that only convective and "normal" diffusive terms from the grid points linked directly with the central node P, are considered in the LHS of the equation (3.4.1) while the cross diffusion terms and the terms arising when higher order interpolation practices are followed and involve more grid points, are calculated explicitly and are added to the S_p term in the RHS of the discrete equation.

The solution of the system of the algebraic equations (3.4.3) can be performed by using various methods. One class of such techniques involve the direct inversion of the matrix $\underline{\underline{A}}$ using any of the several available methods. This type of technique is not very popular because it is very expensive in terms of computational

effort especially for three-dimensional grids. In addition, the coefficients a_i are functions of the dependent variable Φ and this non-linear behaviour, especially due to the appearance of the convective term, renders the direct methods inefficient and the utilization of an appropriate iterative approach is usually required.

In the flow problems encountered in the present study, there is a dominant flow direction and the system of the algebraic equations is solved two-dimensionally at each of the cross-stream planes. If the primary flow direction follows the ζ computational coordinate, the equations are solved at each successive ξ-η plane assuming the values of Φ_B and Φ_F known from the solution on the previous plane at the current iteration level and from the solution on the next plane obtained at the previous iteration respectively.

At each cross-plane a "Line-By-Line" marching procedure is followed whereby a line of constant ξ or η is chosen assuming that the Φ's along neighbouring lines are known from their latest updates. In this case, the general system of equations for all grid points is divided into a number of systems, one for each line at each cross-flow plane, which obtains a special tri-diagonal form since only two neighbouring points with unknown values are considered at each internal grid point and the rest of the neighbouring nodes are treated explicitly. An appropriate direct method called Tri-Diagonal-Matrix-Algorithm - described in Appendix B - is employed to solve the system of algebraic equations at each line. The above procedure is followed at each constant ζ plane for the lines of constant ξ and afterwards is repeated for the lines in the other cross direction η. A large number of traverses is required to obtain exact solutions for the dependent variables but since the problem is non-linear and the values of the coefficients are temporary it is obviously not important to achieve a convergent solution each time the line-by-line process is implemented at each cross-plane. In the present study, the marching is implemented just once for all the dependent flow variables.

Alternative methods can be incorporated in the general computational

procedure for the solution of the system of discretised equations, like the method of conjugate gradients, Hestens and Stiefel (1952), the method of Stone (1968), etc.

3.4.2 The use of under-relaxation

The change in the magnitude of the dependent variables between successive iterations should remain relatively small in order to avoid divergence of the solution procedure which may occur. In strongly non-linear problems the use of the under-relaxation is an appropriate computational tool for the slowing down of these changes. In the current approach, the implementation of the under-relaxation procedure is performed by using the general discrete equation (3.4.1) which yields:

$$\Phi_P = \frac{\sum_k a_k \Phi_k + S_p}{a_p} \qquad (3.4.4)$$

which is equivalent to the relation:

$$\Phi_P = \Phi_P^* + \left(\frac{\sum_k a_k \Phi_k}{a_p} + S_p - \Phi_P^* \right) \qquad (3.4.5)$$

where Φ_P^* is the value of the dependent variable Φ at the point P obtained at the previous iteration and the terms in the parentheses represent the change in the magnitude of Φ_P due to the current iteration. .This change can be reduced if it is multiplied by a factor α which is called under-relaxation factor and obtains values between 0 and 1. When $\alpha=1$ the value of Φ_P is given by the relation (3.4.4) and when $\alpha=0$ the value of Φ_P does not change from iteration to iteration ($\Phi_P=\Phi_P^*$).

With the introduction of the under-relaxation factor α the relation (3.4.5) becomes:

$$\Phi_P = \Phi_P^* + \alpha \left(\frac{\sum_k a_k \Phi_k}{a_p} + S_p - \Phi_P^* \right) \qquad (3.4.6)$$

and eventually:

$$\frac{a_P}{\alpha}\Phi_P = \sum_k a_k\Phi_k + S_P + \left(\frac{1-\alpha}{\alpha}\right)a_P\Phi_P^* \qquad (3.4.7)$$

The under-relaxation factor has an important physical meaning as it is explained by Raithby and Doormal (1984) and can be compared to a time marching procedure for the computation of a steady state flow field. With the introduction of the E factor which is defined as:

$$E = \frac{1-\alpha}{\alpha} \qquad (3.4.8)$$

the equation (3.4.7) obtains the following form:

$$a_P\left(1 + \frac{1}{E}\right)\Phi_P = \sum_k a_k\Phi_k + S_P + \frac{a_P}{E}\Phi_P^* \qquad (3.4.9)$$

which is exactly the equation which is obtained if the transient term is retained in the general transport equation. Each iteration proceeds through a time step Δt which is proportional to a reference time interval Δt^*, i.e.:

$$\Delta t = E\cdot\Delta t^* \qquad where \qquad \Delta t^* = \frac{\rho\cdot\Delta V_P}{a_P} \qquad (3.4.10)$$

which is associated to the required time to convect and diffuse a change of Φ across the control volume which surrounds the node P.

Large values of the under-relaxation factor α and consequently of the E factor, is equivalent to large time steps and if α is kept uniform through the whole flow field then the time step will differ from one point to another and in general the changes in the values of Φ will advance with different speed. Similar interpretations and conditions can be derived as far as the stability criteria concern in the case of the implementation of an explicit numerical technique for the calculation of Φ.

There is no general rule for the selection of the optimum underrelaxation factor for each dependent variable Φ. The optimum value is estimated through

empirical means and trials and depends on the nature and the complexity of the problem, the numerical solution methodology which is utilized and the grid spacing.

3.5 Numerical differencing schemes

3.5.1 Introduction

The finite volume discretisation procedure of the transport equations, gives rise to convective and diffusive fluxes which need to be calculated at the faces of the control volume and involve the estimation of the values of the dependent variables at these locations. These values at the cell faces have to be expressed in terms of the values at the neighbouring grid points in order that discrete equations of the form of equation (3.4.1) to be derived at each grid point for each dependent variable. There are a variety of interpolation techniques which are also known as "numerical differencing schemes", which can be utilised to calculate the values of the dependent variables at the cell faces. Each of these techniques is characterised by different features, degree of complexity, degree of accuracy, level of physical interpretation and their role is vital both to the accuracy of the obtained solution and to the stability of the employed computational solution method. At this point it has to be underlined that the field of the interpolation practices especially when the non-linear convection term is present, has attracted the interest of many researchers and there is a considerable accumulation of research work and contribution on this subject. Hence, this section is not aiming to review the current "state of the art" in numerical differencing schemes, but tends to provide only the basic principles and the formulation of the schemes which are implemented in the current work. Firstly the required properties of the numerical schemes are identified, Peric (1985), and discussed and afterwards appropriate schemes which are selected for the convective term, are described.

3.5.2 Required properties of the numerical schemes

Conservative Property: According to Roach (1982), a numerical scheme possesses

the conservative property "if it preserves certain integral conservation relations of the continuum equation". It is essential for a solution methodology to conserve the flow quantities which follow conservation laws such as the mass, the momentum, the energy etc. When a finite volume approach is used, all the inner fluxes through common faces of neighbouring control volumes should cancel thus providing the discrete integral equation for the global conservation for the whole flow domain. This can only be accomplished if the flux through any control volume face is discretised in a unique fashion for the two adjacent cells.

Boundedness: When a value of a dependent variable at a grid node is affected by the conditions at the surrounding grid points only through convection and diffusion, then an increase in the value at this point should cause an increase at the neighbouring points, assuming that the other conditions remain unchanged. That means that the values of a transported quantity Φ in the interior of a flow domain will be between the minimum and the maximum of Φ encountered at the domain's boundaries, in the absence of any sources. In order that the above physical requirements to be satisfied, all the coefficients a_i which appear in the discrete transport equation (3.4.1) should maintain the same sign, Patankar (1980). In general the boundedness criterion is not satisfied in a straightforward manner by most of the available differencing schemes and a failure to do so produces "wiggles" or "overshoots" under certain circumstances.

Transportive property: A numerical scheme possesses the transportive property if the effect of a perturbation in a transport property is advected only in the direction of the velocity, Roach (1982). The numerical scheme should account for the important physical phenomenon where for high speed flows the changes at a node will have very weak or no influence on upstream regions while will have a significant impact on the downstream regions. If the fluid is stagnant the influence should be equal to all directions. When the transport equations do not satisfy this property which is called transportiveness criterion accounting for the above mentioned features, then unrealistic results are produced from the numerical method.

3.5.3 Differencing schemes for the convective term

The discretisation of the convective fluxes have been described in Section 3.3.3. Hereafter, methods which are used in order to express the required value of the dependent variable Φ at locations on the cell faces (i.e., the term Φ_e of the relation (3.3.12)), are briefly described below.

Central Differencing Scheme

The simplest interpolation practice for the calculation of the value Φ_e at the "e" control volume boundary, is to extract this value from a linear interpolation between the values of the bracketing nodes P and E, Figure 3.4a:

$$\Phi_e = \Phi_E f_P^\xi + \Phi_P\left(1-f_P^\xi\right) \qquad (3.5.1)$$

where f_p^ξ is an interpolation factor associated with the node P and the ξ direction and is defined as:

$$f_P^\xi = \frac{\overline{Pe}}{\overline{Pe} + \overline{eE}} = \frac{\xi_e - \xi_P}{\xi_E - \xi_P} \qquad (3.5.2)$$

where the overbar denotes distance. The interpolation coefficients f_p^η and f_p^ζ are defined in an analogous manner. As mentioned previously, the a_i coefficients consist of convective and normal diffusive contributions a_i^c and a_i^{do}:

$$a_I = a_I^c + a_I^{do} \qquad (3.5.3)$$

The convective contributions a_i^c in the case of a central differencing scheme, are defined as follows:

$$a_E^c = -F_{1e} f_P^\xi \qquad a_W^c = +F_{1w}\left(1 - f_W^\xi\right)$$

$$a_N^c = -F_{2n} f_P^\eta \qquad a_S^c = +F_{2s}\left(1 - f_S^\eta\right) \qquad (3.5.4)$$

$$a_F^c = -F_{3f} f_P^\zeta \qquad a_B^c = +F_{3b}\left(1 - f_B^\zeta\right)$$

$$a_P^C = \sum_k a_k^C \qquad k = E, W, N, S, F, B$$

From the above relations it can be observed that some of the a_i^c coefficients are always negative and if the flow is convection dominated then the whole corresponding a_i coefficients become negative. In this case unbounded solutions are possible and this is because at high Peclet numbers (Peclet number Pe is an expression of the local Reynolds number based on the local grid size) the transportive property is not satisfied by employing unphysically downstream influence in the original formulation of the differencing scheme. For small Pe numbers the central differencing scheme is stable and accurate, Patankar (1980). In terms of Taylor series truncation error analysis, the central differencing provides a second order accurate scheme.

Upwind Differencing Scheme:

In the upwind differencing scheme the value of the transported property Φ at the cell face "e" is regarded to be equal to the value of Φ at the upstream grid point of the same local coordinate direction, Figure 3.4b:

$$\Phi_e = \begin{cases} \Phi_P & if \quad F_{1e} > 0 \\ \Phi_E & if \quad F_{1e} < 0 \end{cases} \qquad (3.5.5)$$

The convective contributions a_i^c to the total a_i coefficients are given by the following relations:

$$a_E^C = \max(0, -F_{1e}) \qquad a_W^C = \max(0, F_{1w})$$

$$a_N^C = \max(0, -F_{2n}) \qquad a_S^C = \max(0, F_{2s}) \qquad (3.5.6)$$

$$a_F^C = \max(0, -F_{3f}) \qquad a_B^C = \max(0, F_{3b})$$

$$a_P^C = \sum_k a_k^C \qquad k = E, W, N, S, F, B$$

All the above coefficients are positive and, unless there is a strong negative contribution, this guarantees the boundedness of the numerical solution. In the upwind scheme, there is full consideration of the transportive property. The truncation error analysis neglects the term incorporating the second derivative of Φ and hence the scheme is first order accurate and it suffers from excessive numerical diffusion. Especially when the flow direction is oblique to the grid lines and there is a strong gradient of Φ in the cross-flow direction, then the upwind scheme introduces significant numerical smearing or numerical diffusion in high Pe number regions, Leschziner (1980), whose results are equivalent to those from the presence of an unphysical diffusion process. This "false" diffusion is maximum when the angle between the flow direction and the grid lines is 45°. However, this numerical diffusion offers to the flow prediction computer codes the favourable advantage of stability. Remedies to this problems can be found by resorting to either grid refinement which reduces the Peclet number or grid lines' alignment with the flow direction.

Quadratic Upwind Numerical Scheme:

The Quadratic Upwind differencing scheme was suggested by Leonard (1979) and is well-known as the QUICK scheme. The value of the dependent variable Φ at the control volume boundary "e" is determined assuming a variation according to a quadratic parabolic function which passes through the points E and P from both sides of "e" and from the upstream point W or EE according to the direction which the flow follows (Figure 3.4c). The formulas which describe the values Φ_e are more cumbersome than those for the previous schemes and are as follows:

$$\Phi_e = Q_{11}^e \Phi_E + Q_{12}^e \Phi_W + (1-Q_{11}^e-Q_{12}^e)\,\Phi_P \qquad if \quad F_{1e} > 0 \qquad (3.5.7)$$

$$\Phi_e = Q_{21}^e \Phi_P + Q_{22}^e \Phi_{EE} + (1-Q_{21}^e-Q_{22}^e)\,\Phi_E \qquad if \quad F_{1e} < 0$$

where the interpolation coefficients Q_{ij} are defined from the relations:

$$Q_{11}^e = \frac{(\xi_e-\xi_P)\cdot(\xi_e-\xi_W)}{(\xi_E-\xi_P)\cdot(\xi_E-\xi_W)}$$

$$Q_{12}^e = \frac{(\xi_e-\xi_P)\cdot(\xi_e-\xi_E)}{(\xi_P-\xi_W)\cdot(\xi_E-\xi_W)} \qquad (3.5.8)$$

$$Q_{21}^e = \frac{(\xi_e-\xi_E)\cdot(\xi_e-\xi_{EE})}{(\xi_E-\xi_P)\cdot(\xi_{EE}-\xi_P)}$$

$$Q_{22}^e = \frac{(\xi_e-\xi_E)\cdot(\xi_e-\xi_P)}{(\xi_{EE}-\xi_E)\cdot(\xi_{EE}-\xi_P)}$$

These interpolation coefficients are defined at all cell faces. The same treatment applies to the "w" control volume boundary yielding similar expressions to those obtained for the "e" face by replacing the indices e,E,P,W,EE with the new indices w,P,W,WW,E respectively. Similar expressions arise for the rest of the control volume faces. For the case of a uniform grid the Q_{ij} coefficients obtain constant values equal for all the faces, which are given by:

$$Q_{11} = \frac{3}{8} \qquad Q_{12} = -\frac{1}{8} \qquad Q_{21} = \frac{3}{8} \qquad Q_{22} = -\frac{1}{8} \qquad (3.5.9)$$

The convective contributions a_i^c to the coefficients a_i of the general discrete equation (3.4.1) are given by the following expressions:

$$a_E^c = -\max(0, F_{1e})\,Q_{11}^e + \min(0, F_{1w})\,Q_{22}^w - \min(0, F_{1e})\,(1-Q_{21}^e-Q_{22}^e)$$

$$a_W^c = -\max(0, F_{1e})\, Q_{12}^e - \min(0, F_{1w})\, Q_{21}^w + \max(0, F_{1w})\,(1 - Q_{11}^w - Q_{12}^w)$$

$$a_N^c = -\max(0, F_{2n})\, Q_{11}^n + \min(0, F_{2s})\, Q_{22}^s - \min(0, F_{2n})\,(1 - Q_{21}^n - Q_{22}^n) \quad (3.5.10)$$

$$a_S^c = -\max(0, F_{2n})\, Q_{12}^n - \min(0, F_{2s})\, Q_{21}^s + \max(0, F_{2s})\,(1 - Q_{11}^s - Q_{12}^s)$$

$$a_F^c = -\max(0, F_{3f})\, Q_{11}^f + \min(0, F_{3b})\, Q_{22}^b - \min(0, F_{3f})\,(1 - Q_{21}^f - Q_{22}^f)$$

$$a_B^c = -\max(0, F_{3f})\, Q_{12}^f - \min(0, F_{3b})\, Q_{21}^b + \max(0, F_{3b})\,(1 - Q_{11}^b - Q_{12}^b)$$

The terms a_{EE}^c, a_{WW}^c, a_{FF}^c, a_{BB}^c, a_{NN}^c and a_{SS}^c are treated explicitly and their contribution is taken into account in the source term of the discrete equation. The transportive property is not fully satisfied since weighted downstream influence is considered irrespectively of the Peclet number magnitude.The QUICK scheme contains negative coefficients a_i^c for the downstream nodes, i.e., the term a_N^c becomes negative when the coefficient F_{2n} is positive and in the case of a uniform grid this coefficient would be equal to $-(3/8)F_{2n}$. In this case if the Peclet number is greater than 8/3, the coefficient a_E becomes negative. The QUICK scheme is third order accurate on uniform grids and provides faster response to grid refinement on improving the accuracy of the numerical solution. However, boundedness problems may be encountered, Leschziner (1980).

3.5.4 Differencing scheme for the diffusive term

The discretisation of the "normal" diffusive term was described in Section 3.3.4. The "normal" derivatives at the cell faces are approximated by using a second order accurate central differencing scheme and considering the equation (3.3.19), then the contributions of the normal diffusion terms to the a_i coefficients of the discrete equation (3.4.1) are defined as follows:

$$a_E^{do} = \left(\frac{\Gamma_\Phi}{\Delta V}\right)_e h_e^{11} \qquad a_W^{do} = \left(\frac{\Gamma_\Phi}{\Delta V}\right)_w h_w^{11}$$

$$a_N^{do} = \left(\frac{\Gamma_\Phi}{\Delta V}\right)_n h_n^{22} \qquad a_S^{do} = \left(\frac{\Gamma_\Phi}{\Delta V}\right)_s h_s^{22} \qquad (3.5.11)$$

$$a_F^{do} = \left(\frac{\Gamma_\Phi}{\Delta V}\right)_f h_f^{33} \qquad a_B^{do} = \left(\frac{\Gamma_\Phi}{\Delta V}\right)_b h_b^{33}$$

These coefficients are always positive and the satisfaction of the boundedness property is left to the convective contributions described in the previous section.

As it was mentioned in Section 3.4.1, the cross-diffusion terms are treated explicitly and are added to the source term of the discrete equation (3.4.1). However, their estimation requires additional interpolations in order to approximate quantities such as $(\Phi_n-\Phi_s)_e$ which appear in the discrete form of the cross-diffusion terms. In the current work, the most straightforward approach is employed where a double linear interpolation is performed. For example, the terms $(\Phi_n-\Phi_s)_e$ and $(\Phi_f-\Phi_b)_e$ at the "e" boundary, are evaluated by the expressions:

$$(\Phi_n-\Phi_s)_e = (\Phi_n-\Phi_s)_P\left(1-f_P^\xi\right) + (\Phi_n-\Phi_s)_E f_P^\xi \qquad (3.5.12)$$

$$(\Phi_f-\Phi_b)_e = (\Phi_f-\Phi_b)_P\left(1-f_P^\xi\right) + (\Phi_f-\Phi_b)_E f_P^\xi$$

where the values Φ_n, Φ_s, Φ_f, Φ_b at the "e" cell face are calculated using a central differencing scheme which was described in the previous section, i.e.:

$$\Phi_n = \Phi_N f_P^\eta + \Phi_P\left(1-f_P^\eta\right) \qquad \Phi_f = \Phi_F f_P^\zeta + \Phi_P\left(1-f_P^\zeta\right) \qquad (3.5.13)$$

The differences are defined in a unique manner at each face and hence the scheme is conservative.

3.5.5 The Hybrid scheme

As it was described in the previous section, the upwind scheme is unconditionally bounded but introduces large amounts of false diffusion. The use of higher order schemes, although providing more accurate solutions, is often associated with boundedness problems. One of the methods employed as a remedy to the above problems, is the expression of the flux at the cell face by blending a flux I_b obtained by a less accurate but bounded scheme, with a flux I_u obtained by a more accurate but not always bounded scheme:

$$I = \lambda I_u + (1-\lambda) I_b \qquad (3.5.14)$$

The hybrid differencing scheme which was introduced by Spalding (1972) implements the above principle by blending the convective flux obtained by the upwind scheme as the bounded term I_b and the convective flux which is derived through a central differencing as the unbounded term I_u. In diffusion dominated flows, when $Pe<2$, the coefficient λ becomes equal to unity and the central differencing scheme is utilised exclusively, while in convection dominated flows, when $Pe>2$, the coefficient λ is given zero value and the convective fluxes are estimated by the upwind scheme.

The coefficients a_i of the discrete equation (3.4.1) are calculated according to the following relations:

$$a_E = a_E^{do} A(|Pe^e|) + \max(-F_{1e}, 0)$$

$$a_W = a_W^{do} A(|Pe^w|) + \max(F_{1w}, 0)$$

$$a_N = a_N^{do} A(|Pe^n|) + \max(-F_{2n}, 0) \qquad (3.5.15)$$

$$a_S = a_S^{do} A(|Pe^s|) + \max(F_{2s}, 0)$$

$$a_F = a_F^{do} A(|Pe^f|) + \max(-F_{3f}, 0)$$

$$a_B = a_B^{do} A(|Pe^b|) + \max(F_{3b}, 0)$$

where the coefficients a_i^{do} are estimated by using the expressions (3.5.11) and the mass fluxes F_i from (3.3.8) and (3.3.9). The Peclet number Pe is calculated at each face as the ratio of F_i and a_i^{do}, i.e.:

$$Pe^s = \frac{F_{2s}}{\left(\frac{\Gamma_\Phi}{\Delta V}\right)_s h_s^{22}} \qquad (3.5.16)$$

The term A(| Pe |) is a function which for the hybrid scheme is defined as:

$$A(|Pe|) = \max\left(0 , \frac{|Pe|}{2}\right) \qquad (3.5.17)$$

For the upwind scheme, the coefficients a_i are directly composed from the normal diffusive contribution a_i^{do} and the convective one a_i^c. By comparing the relations which are obtained with the expressions (3.5.6), the function A(| Pe |) is equal to unity.

3.6 The calculation of the pressure field

3.6.1 The Pressure Correction method

One of the main features of the current computational method is the utilisation of the continuity equation as the basis for establishing the correct pressure field through the iterative numerical procedure. The derivation of models which employ the continuity equation for the pressure field calculation has attracted the interest of many researchers, mainly aiming to predict low speed incompressible flows where the pressure affects the density very weakly but its effect on the velocity is very strong, and gave rise to the so-called pressure correction methods, Caretto et al (1972), Patankar et al (1972), Connell et al (1986), Van Doormaal et al (1984).

The numerical implementation of the available pressure correction methods

is closely associated with the relative storage locations of the velocity components and pressure values on the computational grid and special attention is required for the accomplishment of the correct coupling between the velocity and pressure fields. When the coupling is not appropriate, pressure oscillations are produced which are unrealistic and this happens especially when all the variables are stored at the same grid location. One of the first methods for the calculation of the pressure, is due to Harlow and Welch (1965) who first introduced the idea of the staggered grid where the location of the velocity components and their control volumes are displaced from the grid node to a location between the pressures which act as the driving force for the local flow, Figure 3.5 (MAC method). Alternative arrangements of the dependent variables on the grid system have been proposed, Rhie and Chow (1983), Hirt et al (1974), which contain different degree of complexity in the numerical treatment for preventing decoupling problems.

Several pressure correction strategies have emerged which vary in the way of deriving the process for the pressure field computation. One of the most extensively used pressure correction techniques is the SIMPLE algorithm (Semi-Implicit-Method-for-Pressure-Linked-Equations) of Caretto et al (1972), Patankar and Spalding (1972), which is based on a staggered grid arrangement and the iterative approximation of the pressure field through an equation for the pressure correction which is derived by combining the discrete continuity and momentum equations. The SIMPLE algorithm formed the basis for the development of several alternative algorithms with specific improved capabilities, such as SIMPLER [Patankar (1980)], SIMPLEC [Van Doormaal and Raithby (1984)], PISO [Issa (1982)] etc.

The pressure correction scheme which is employed in the current study is based on the SIMPLE algorithm with suitable adjustments to extent its applicability to generalised coordinate systems. In addition, a collocated grid arrangement is selected because of its simplicity in terms of computer coding, together with an appropriate technique based on the numerical handling of the mass fluxes entering

the discretised continuity equation, to prohibit the decoupling between the pressure and the velocity fields associated with such a dependent variable arrangement.

3.6.2 The SIMPLE pressure correction method

The general discrete equation (3.4.1) is modified slightly in the case of the momentum equations by explicitly expressing the pressure terms separating them from the source term for the purpose of the following analysis. If the discretisation formula (3.3.25) for the pressure term is taken into consideration, the three discretised momentum equations obtain the following form:

$$a_P^u u_P = \sum_k a_k u_k + S_P^u - \Delta V_P(\xi_x p_\xi + \eta_x p_\eta + \zeta_x p_\zeta)_P$$

$$a_P^v v_P = \sum_k a_k v_k + S_P^v - \Delta V_P(\xi_y p_\xi + \eta_y p_\eta + \zeta_y p_\zeta)_P \qquad (3.6.1)$$

$$a_P^w w_P = \sum_k a_k w_k + S_P^w - \Delta V_P(\xi_z p_\xi + \eta_z p_\eta + \zeta_z p_\zeta)_P$$

The first step of the algorithm is a predictor stage. Assuming a pressure field p^*, which is obtained either from an initial guess or from the previous iteration, the solution of the momentum equations (3.6.1) will provide values for the velocity field u^*, v^* and w^*. From these values the curvilinear velocity components U^*, V^* and W^* are calculated. These velocity components will not satisfy the discretised continuity equation which is expressed through (3.3.10) but a mass source will be produced which is practically the error in the satisfaction of the continuity equation:

$$m_p = F_{1e}^* - F_{1w}^* + F_{2n}^* - F_{2s}^* + F_{3f}^* - F_{3b}^* \qquad (3.6.2)$$

The corrector step which follows is aiming towards the elimination of this mass source by adjusting appropriately the pressure and thereby the velocity field.

For this purpose, corrections u′, v′, w′ and p′ are added to the u*, v*, w* and p* values respectively providing the flow field values u, v, w, and p, in order to promote the satisfaction of both the continuity and the momentum equations. Hence:

$$u = u^* + u' \qquad v = v^* + v' \qquad w = w^* + w' \qquad p = p^* + p' \qquad (3.6.3)$$

Both the set of values u,v,w,p and the set u*,v*,w*,p* satisfy the momentum equations and their substitution into the expressions (3.6.1) and the consideration of the relations (3.6.2), gives rise to three equations which relate each Cartesian velocity correction to the pressure correction:

$$a_P^u u'_P = \sum_k a_k u'_k - \Delta V_P \left(\xi_x p'_\xi + \eta_x p'_\eta + \zeta_x p'_\zeta\right)_P$$

$$a_P^v v'_P = \sum_k a_k v'_k - \Delta V_P \left(\xi_y p'_\xi + \eta_y p'_\eta + \zeta_y p'_\zeta\right)_P \qquad (3.6.4)$$

$$a_P^w w'_P = \sum_k a_k w'_k - \Delta V_P \left(\xi_z p'_\xi + \eta_z p'_\eta + \zeta_z p'_\zeta\right)_P$$

The final solution is not affected if the first term on the RHS of the above equations containing the contributions of the velocity corrections of the neighbouring nodes, is neglected since the corrections u′, v′ and w′ become equal to zero in the converged solution. Consequently, explicit relations between each of the corrections u′, v′, w′ and the pressure correction values p′ arise whose substitutions in the relations (3.6.3) produces the following expressions for the corrected u, v, and w velocities:

$$u = u^* + \left(B^u p'_\xi + C^u p'_\eta + D^u p'_\zeta\right)$$

$$v = v^* + \left(B^v p'_\xi + C^v p'_\eta + D^v p'_\zeta\right) \qquad (3.6.5)$$

$$w = w^* + \left(B^w p'_\xi + C^w p'_\eta + D^w p'_\zeta\right)$$

where:

$$B^u = -\xi_x \frac{\Delta V_P}{a_P^u} \qquad C^u = -\eta_x \frac{\Delta V_P}{a_P^u} \qquad D^u = -\zeta_x \frac{\Delta V_P}{a_P^u}$$

$$B^v = -\xi_y \frac{\Delta V_P}{a_P^v} \qquad C^v = -\eta_y \frac{\Delta V_P}{a_P^v} \qquad D^v = -\zeta_y \frac{\Delta V_P}{a_P^v} \qquad (3.6.6)$$

$$B^w = -\xi_z \frac{\Delta V_P}{a_P^w} \qquad C^w = -\eta_z \frac{\Delta V_P}{a_P^w} \qquad D^w = -\zeta_z \frac{\Delta V_P}{a_P^w}$$

The corresponding curvilinear U, V and W values are obtained by substituting the relation (3.6.5) into the expressions (3.2.5) :

$$U = U^* + J(B^u\xi_x + B^v\xi_y + B^w\xi_z)\,p'_\xi + \underline{J(C^u\xi_x + C^v\xi_y + C^w\xi_z)\,p'_\eta}$$

$$+ \underline{J(D^u\xi_x + D^v\xi_y + D^w\xi_z)\,p'_\zeta}$$

$$V = V^* + \underline{J(B^u\eta_x + B^v\eta_y + B^w\eta_z)\,p'_\xi} + J(C^u\eta_x + C^v\eta_y + C^w\eta_z)\,p'_\eta \qquad (3.6.7)$$

$$+ \underline{J(D^u\eta_x + D^v\eta_y + D^w\eta_z)\,p'_\zeta}$$

$$W = W^* + \underline{J(B^u\zeta_x + B^v\zeta_y + B^w\zeta_z)\,p'_\xi} + \underline{J(C^u\zeta_x + C^v\zeta_y + C^w\zeta_z)\,p'_\eta}$$

$$+ J(D^u\zeta_x + D^v\zeta_y + D^w\zeta_z)\,p'_\zeta$$

The terms with the underbar are the cross-pressure terms which appear due to the non-orthogonality of the grid system. In order to simplify the above expressions, the cross-pressure terms are eliminated without affecting the converged solution where the pressure correction p′ becomes equal to zero. Consequently, simplified formulas for U, V and W can be derived:

$$U = U^* + Bp'_\xi \qquad V = V^* + Cp'_\eta \qquad W = W^* + Dp'_\zeta \qquad (3.6.8)$$

where:

$$B = J(B^u\xi_x + B^v\xi_y + B^w\xi_z)$$

$$C = J(C^u \eta_x + C^v \eta_y + C^w \eta_z) \qquad (3.6.9)$$

$$D = J(D^u \zeta_x + D^v \zeta_y + D^w \zeta_z)$$

The substitution of the corrected curvilinear velocity components U, V, and W into the discretised continuity equation results in a discrete equation for the pressure correction p′:

$$a_P^P \, p_P' = \sum_k a_k^P \, p_k' - m_p \qquad (3.6.10)$$

where m_p is the mass imbalance based on the starred curvilinear velocities and is given from the relation (3.6.2).

The coefficients a_i^P are given from the expressions:

$$a_E^P = -(\rho B)_e \delta\eta\delta\zeta/(\delta\xi)_e \qquad a_W^P = -(\rho B)_w \delta\eta\delta\zeta/(\delta\xi)_w$$

$$a_N^P = -(\rho C)_n \delta\xi\delta\zeta/(\delta\eta)_n \qquad a_S^P = -(\rho C)_s \delta\xi\delta\zeta/(\delta\eta)_s \qquad (3.6.11)$$

$$a_F^P = -(\rho D)_f \delta\xi\delta\eta/(\delta\zeta)_f \qquad a_B^P = -(\rho D)_b \delta\xi\delta\eta/(\delta\zeta)_b$$

$$a_P^P = a_E^P + a_W^P + a_N^P + a_S^P + a_F^P + a_B^P$$

The discrete equation (3.6.10) for the pressure correction p′ presents a similar form to the general discrete equation (3.4.1) and its solution is performed by using the same technique which was described in Section 3.4. The solution of (3.6.10) provides values for the pressure correction p′ which is used to correct the pressure and the U, V and W curvilinear velocities. The Cartesian velocity components u, v and w are calculated through the general transformation relations (2.8.14) to (2.8.16). Although the corrected flow field will satisfy the continuity equation, in general will fail to satisfy the momentum equations which need to be solved again assuming the corrected pressure values. This procedure is repeated till the error in the mass conservation becomes negligible and this implies that the

velocities obtained from the solution of the momentum equations satisfy the continuity condition as well and ensures the correctness of the computed pressure field.

3.6.3 Non-staggered grid and pressure oscillations

In the present study, a non-staggered grid arrangement is utilised where all the dependent variables are stored at the same grid location - nodal location - and the same control volume is used for the finite volume discretisation of the transport equations for all the dependent variables. This approach is very convenient because it simplifies the computer coding since a great deal of computations need to be performed once at each iteration. For example, the convective contributions a_i^c to the general coefficients a_i are the same for all the dependent variables and also the normal diffusive contributions differ only in the definition of the diffusion coefficient Γ_ϕ.

Despite its aforementioned advantages, a straightforward non-staggered variable arrangement is associated with an important drawback: the velocity and the pressure fields may decouple from each other because the pressure derivative $\partial p/\partial \xi_j$ at the grid nodes is performed using a $2\text{-}\Delta\xi_j$ difference. Hence, if a "zig-zag" pressure field arises during the iterative procedure in the ξ_j direction, the momentum equations will not "sense" this pressure oscillation and similar response is expected from the pressure correction equation which is formed irrespectively with the actual values of the pressure field.

A remedy to this fundamental problem was proposed by Rhie (1981) and Rhie and Chow (1983) who employed a non-staggered grid for the two-dimensional computation of the flow past an isolated aerofoil. The main idea of the suggested scheme is the calculation of the curvilinear velocities at the cell faces which enter the continuity equation through the mass source m_p, by using a more complicated scheme than the linear interpolation between the nodal values, which senses the

oscillatory pressure behaviour. The formula which is suggested, i.e. for the "e" cell face, is as follows:

$$U_e^* = \overline{U_e^*} + \overline{B_e}\left[\left(\frac{\partial p^*}{\partial \xi}\right)_e - \overline{p_\xi^*}\right] \qquad (3.6.12)$$

Similar expressions are proposed for U_w^*, V_n^*, V_s^*, W_f^* and W_b^*. The term $\overline{U}_e^*$ is obtained by linearly interpolating the values of U^* at the grid points P and E. The extra term proposed by Rhie and Chow contains the difference of a 1-$\Delta\xi$ pressure difference at the cell face "e", Figure 3.6, given by:

$$\left(\frac{\partial p}{\partial \xi}\right)_e = \frac{p_E - p_P}{(\delta\xi)_e} \qquad (3.6.13)$$

and the interpolated at the face "e" value of a 2-$\Delta\xi$ pressure differences defined at the nodes P and E:

$$\overline{p_\xi^*} = f_{1P}(p_\xi^*)_E + (1-f_{1P})(p_\xi^*)_P \qquad (3.6.14)$$

where: $\quad (p_\xi^*)_E = \dfrac{p_{EE} - p_P}{\delta\xi_e + \delta\xi_{ee}} \qquad (p_\xi^*)_P = \dfrac{p_E - p_W}{\delta\xi_e + \delta\xi_w}$

When an oscillatory pressure field emerges, the Rhie and Chow term obtains a relatively large value which affects eventually the mass source m_p through the value of U_e^*. Thus, the pressure correction value at the node P will tend to smooth and finally remove the oscillation as the iterative process advances. The Rhie and Chow term becomes negligible in smoothly varying pressure fields.

The Rhie and Chow scheme has been adopted in the present work and has been proven to be a very effective and reliable tool for suppressing any unphysical pressure oscillation arising due to decoupling between the pressure and velocity fields.

3.7 Solution procedure

In the previous sections the numerical discretisation procedure of the transport equations was presented. With the implementation of the appropriate boundary conditions which will be described in following sections according to the application area of the proposed computational model, an effective numerical strategy can be now applied in order to iteratively promote the elliptic flow field values effectively ensuring the satisfaction of all the governing equations.

The flow quantities are fixed at the inlet plane and a space marching process is implemented at each cross-stream plane form the inlet to the outlet curvilinear plane of the flow domain.

The entire solution algorithm can be outlined as follows:

1. All the flow parameters are given initial approximate values usually by extrapolating the inlet values to the interior of the flow domain. Although the converged solution is independent of the initial "guess" for the flow field, a bad initial field can cause divergence problems.
2. The solution procedure begins on the first cross-stream plane after the inlet.
3. For a given pressure field p^* the momentum equations are solved yielding values for the Cartesian components u^*, v^* and w^* and from the transformation relations the values of U^*, V^* and W^* are obtained.
4. The continuity condition is enforced by solving the pressure correction equation. The pressure and the velocities are updated accordingly.
5. If the k-ϵ turbulence model is used, the equations (2.5.4) and (2.5.5) are solved and the turbulence viscosity is updated through the relation (2.5.1).
6. The energy equation is solved in the case of compressible flow computations and the static temperature field is obtained through the rothalpy values. The density is then calculated through the perfect gas law.
7. The computational domain is shifted to the next cross-stream plane and the sequence from step 3 to step 6 is repeated until the outlet plane has been reached.

8. If the outlet station has been reached then the convergence criteria are checked.

9. The one-pass completed through the steps 2 to 8 is repeated until a convergent solution is accomplished.

The solution of the system of the discrete equations for each dependent variable, at each cross-plane is carried out using an alternating direction Successive Line Under Relaxation method with the use of the Tri-Diagonal-Matrix-Algorithm as it was discussed in Section 3.4.

The solution is supposed to have converged when all the flow variables satisfy the condition:

$$\sum_{n} |a_P\Phi_P - \sum_{k} a_k\Phi_k - S_P| < e_c\Phi_{ref} \qquad (3.7.1)$$

where the summation is over all the grid points n, ϵ_c is an appropriately small value and Φ_{ref} is a typical reference value of Φ arising in the flow field, i.e. the value of Φ at the inlet.

CHAPTER 4

Numerical grid generation

4.1 Introduction

A grid generation method based on the solution of a system of coupled elliptic Poisson type equations is implemented for the numerical construction of two-dimensional meshes in the irregularly shaped flow passage between adjacent cascade blades. The main features of the computational methodology which is utilised, are the control of the grid spacing of the first grid line from the blade wall surfaces and the enforcement of the angle at which grid lines intersect the blade walls and the periodic boundaries to be orthogonal. The method is iterative and has been found to be a very reliable tool for generating smooth boundary fitted general grids.

4.2 Grid generation algorithms
- Current theoretical model

In Computational Fluid Dynamics, the generation of appropriate meshes plays a critical role in the accurate numerical representation of the flow phenomena under consideration. The mesh which is utilised in a flow computation and thereby the procedure involved for the generation of this mesh, has to fulfill certain conditions as far as the spacing, the orthogonality, the smoothness and the alignment with the local flow direction, are concerned.

A grid generation method should be capable of providing grids which are in general non-uniform and concentrated in areas where significant changes in the flow variables are expected to occur. A drawback of the non-uniformity of the grid spacing is that it causes the employed numerical differencing schemes to lose

accuracy in terms of Taylor series truncation error analysis.

The orthogonality of the grid lines eliminates the appearance of the cross-diffusion terms and it is a desirable feature although difficult and sometimes impossible to be achieved. The current flow computational model has the capability of handling non-orthogonal meshes and thus the grid generation procedure is not required to provide orthogonal meshes. However, the orthogonality of the grid lines with the blade wall surfaces is a very attractive feature and facilitates the proper definition of the wall boundary conditions.

A smooth grid is a grid with small relative change in the direction of the grid lines from one cell to another and affects the accuracy of the interpolation methods which are used to approximate values of the dependent variables at cell face locations.

The alignment of the grid lines with the flow direction significantly influences the accuracy of the numerical solution as it was described in Section 3.5.3 and reduces the false diffusion. The problem in this case is that the flow pattern is not known "a priori" and the grid may need to be respecified after preliminary flow computations. An ideal way to achieve this property is the utilisation of an adaptive grid strategy where the grid changes during the iterative flow calculation process according to certain criteria, Dawes (1991). However, this technique is rather cumbersome and requires significant effort to be implemented robustly in a finite volume solver. The grids which are used in the present work remain fixed during the flow calculations.

The essential influence of the computational grid on the accuracy and stability of the numerical flow prediction models has caused the methods for constructing meshes to attract considerable research and implementation interest and significant progress has been achieved in the recent years. Very good references on this progress can be found in the report NASA CP-2166 (1980) and the book of

Thompson (1982) on Grid Generation Techniques in CFD.

Grid generation procedures can be classified into two major categories: algebraic techniques, in which the coordinates are determined through interpolations, and techniques involving partial differential equations. In the latter case, the physical coordinates are obtained as a solution of these equations which can be achieved either by comformal mapping or by numerically solving elliptical, Thompson et al (1974) , hyperbolic or parabolic partial differential equations, Thompson (1984).

The current method of grid generation involves solving a system of elliptical differential equations.

The grid generation algorithm is based on the transformation $\xi=\xi(x,y)$ and $\eta=\eta(x,y)$ which performs the mapping between a physical space x, y and a computational space ξ, η for $0<\xi<\xi_{max}$ and $0<\eta<\eta_{max}$ (Figure 4.1). The grid is constructed from two families of lines: the lines of constant ξ in the blade to blade direction and the η = constant lines in the streamwise direction.

Elliptical grid generation techniques are aiming towards the definition of the (x,y) pairs of physical coordinates corresponding to the (ξ,η) computational points by iteratively solving the system of partial differential equations:

$$\xi_{xx} + \xi_{yy} = P(\xi,\eta) \qquad (4.2.1)$$

$$\eta_{xx} + \eta_{yy} = Q(\xi,\eta) \qquad (4.2.2)$$

where the double subscripts denote second derivatives.

When the above coordinate transformation is performed, the following relations are valid:

$$\xi_x = \frac{y_\eta}{J} \qquad \xi_y = \frac{-x_\eta}{J} \qquad \eta_x = \frac{-y_\xi}{J} \qquad \eta_y = \frac{x_\xi}{J} \qquad (4.2.3)$$

where:

$$J = x_\xi y_\eta - x_\eta y_\xi \qquad (4.2.4)$$

is the Jacobian of the coordinate transformation.

By applying the relations (4.2.3) and (4.2.4) to the system (4.2.1) and (4.2.2) the transformed Poisson equations are derived:

$$\alpha x_{\xi\xi} - 2\beta x_{\xi\eta} + \gamma x_{\eta\eta} = -J^2(Px_\xi + Qx_\eta) \qquad (4.2.5)$$

$$\alpha y_{\xi\xi} - 2\beta y_{\xi\eta} + \gamma y_{\eta\eta} = -J^2(Py_\xi + Qy_\eta) \qquad (4.2.6)$$

where:

$$\alpha = x_\eta^2 + y_\eta^2 \qquad \beta = x_\xi x_\eta + y_\xi y_\eta \qquad \gamma = x_\xi^2 + y_\xi^2 \qquad (4.2.7)$$

The inhomogenous terms-functions P and Q are defined in such a way that the generated grid satisfies certain geometrical constraints and properties, i.e. to be finer in certain regions of highly varying flow parameters or to be perpendicular to the solid walls etc. The P and Q functions can be assumed to be given by:

$$P(\xi,\eta) = p(\xi)\cdot e^{-a\eta} + r(\xi)\cdot e^{-c(\eta_{max}-\eta)} \qquad (4.2.8)$$

$$Q(\xi,\eta) = q(\xi)\cdot e^{-b\eta} + s(\xi)\cdot e^{-d(\eta_{max}-\eta)} \qquad (4.2.9)$$

where a, b, c and d are positive constants.

In the present study, the calculation of the functions P and Q is performed automatically during the iterative process according to Sorenson (1980), in such a way that the grid is adjusted to satisfy certain geometrical conditions at the blade walls and the periodic boundaries.

The first geometrical constraint which is imposed is that the spacing along ξ=const lines between the wall at η=0 and the next grid point is user-prescribed and equal to δs. This requirement is essential for the level of resolution of the flow

analysis and especially for the turbulent flow calculation in the near wall flow regions. The prescribed value of δs determines the y^+ and consequently whether the first point away from the wall is located in the laminar sublayer, in the buffer layer or in the fully turbulent boundary layer zone.

If δx and δy are the coordinate differences along this interval, the spacing δs is defined as:

$$(\delta s)_{\eta=0} = \sqrt{(\delta x)^2_{\eta=0} + (\delta y)^2_{\eta=0}} \qquad (4.2.10)$$

In the limit as $\delta x \to 0$ and $\delta y \to 0$, the following differential relation is obtained:

$$(ds)_{\eta=0} = \sqrt{(dx)^2_{\eta=0} + (dy)^2_{\eta=0}} = \sqrt{(x_\xi d\xi + x_\eta d\eta)^2_{\eta=0} + (y_\xi d\xi + y_\eta d\eta)^2_{\eta=0}} \qquad (4.2.11)$$

and because ξ=const then $d\xi=0$ and the above relation becomes:

$$(ds)_{\xi=const} = \sqrt{(x_\eta)^2_{\eta=0} + (y_\eta)^2_{\eta=0}} \cdot d\eta \qquad and$$

$$\left(\frac{ds}{d\eta}\right)_{\xi=const} = \sqrt{(x_\eta)^2_{\eta=0} + (y_\eta)^2_{\eta=0}} = (s_\eta)_{\eta=0} \qquad (4.2.12)$$

The second geometric requirement is the imposition of the angle at which the lines of ξ=const intersect the lines of $\eta=0$, to be equal to a specified value θ ($\theta=90°$ in the present study and the lines are perpendicular). This requirement facilitates significantly the definitions of the appropriate boundary conditions along the $\eta=0$ boundary during the calculation of the flow field. It is kown that:

$$(\vec{\nabla}\xi \vec{\nabla}\eta)_{\eta=0} = (|\vec{\nabla}\xi||\vec{\nabla}\eta|\cos\theta)_{\eta=0} \rightarrow (\xi_x\eta_x + \xi_y\eta_y)_{\eta=0} = \left(\sqrt{\xi_x^2+\eta_x^2}\sqrt{\xi_y^2+\eta_y^2}\cos\theta\right)_{\eta=0}$$

$$\rightarrow (x_\xi x_\eta + y_\xi y_\eta)_{\eta=0} = -\left(\sqrt{(x_\eta^2+y_\eta^2)(x_\xi^2+y_\xi^2)}\cos\theta\right)_{\eta=0} \qquad (4.2.13)$$

All the derivatives in the ξ direction can be easily defined on the $\eta=0$ boundary. By solving the equations (4.2.12) and (4.2.13), the values x_η and y_η are expressed as:

$$(x_\eta)_{\eta=0} = \left(\frac{s_\eta(-x_\xi \cos\theta - y_\xi \sin\theta)}{\sqrt{(x_\xi^2 + y_\xi^2)}} \right)_{\eta=0} \qquad (4.2.14)$$

$$(y_\eta)_{\eta=0} = \left(\frac{s_\eta(-y_\xi \cos\theta + x_\xi \sin\theta)}{\sqrt{(x_\xi^2 + y_\xi^2)}} \right)_{\eta=0} \qquad (4.2.15)$$

In a similar manner, the same geometrical requirements from the grid, apply to the $\eta=\eta_{max}$ boundary yielding expressions for x_η and y_η:

$$(x_\eta)_{\eta=\eta_{max}} = \left(\frac{s_\eta(-x_\xi \cos\theta - y_\xi \sin\theta)}{\sqrt{(x_\xi^2 + y_\xi^2)}} \right)_{\eta=\eta_{max}} \qquad (4.2.16)$$

$$(y_\eta)_{\eta=\eta_{max}} = \left(\frac{s_\eta(-y_\xi \cos\theta + x_\xi \sin\theta)}{\sqrt{(x_\xi^2 + y_\xi^2)}} \right)_{\eta=\eta_{max}} \qquad (4.2.17)$$

The above defined values x_η and y_η at the $\eta=0$ and $\eta=\eta_{max}$ boundaries are used for the estimation of the functions P and Q which is performed in the following sequence:

The coefficients r and s in equations (4.2.8) and (4.2.9) are negligible at the boundary $\eta=0$ and hence:

$$P(\xi,0) = p(\xi) \qquad Q(\xi,0) = q(\xi) \qquad (4.2.18)$$

Consequently the transformed Poisson equations (4.2.5) and (4.2.6) obtain the following form:

$$\alpha x_{\xi\xi} - 2\beta x_{\xi\eta} + \gamma x_{\eta\eta} = -J^2 \left[p(\xi) \cdot x_\xi + q(\xi) \cdot x_\eta \right] \qquad (4.2.19)$$

$$\alpha y_{\xi\xi} - 2\beta y_{\xi\eta} + \gamma y_{\eta\eta} = -J^2 \left[p(\xi) \cdot y_\xi + q(\xi) \cdot y_\eta \right] \qquad (4.2.20)$$

The only unknowns in the above system of equations are the values of $p(\xi)$ and $q(\xi)$ which can be obtained from the solution of this system:

$$p(\xi) = \left(\frac{y_\eta R_1 - x_\eta R_2}{J}\right)_{\eta=0} \qquad q(\xi) = \left(\frac{-y_\xi R_1 + x_\xi R_2}{J}\right)_{\eta=0} \qquad (4.2.21)$$

where:

$$R_1 = \left(\frac{-(\alpha x_{\xi\xi} - 2\beta x_{\xi\eta} + \gamma x_{\eta\eta})}{J^2}\right)_{\eta=0} \qquad R_2 = \left(\frac{-(\alpha y_{\xi\xi} - 2\beta y_{\xi\eta} + \gamma y_{\eta\eta})}{J^2}\right)_{\eta=0}$$

(4.2.22)

The same procedure applies to the top boundary $\eta=\eta_{max}$ and gives rise to the following relations:

$$r(\xi) = \left(\frac{y_\eta R_3 - x_\eta R_4}{J}\right)_{\eta=\eta_{max}} \qquad s(\xi) = \left(\frac{-y_\xi R_3 + x_\xi R_4}{J}\right)_{\eta=\eta_{max}} \qquad (4.2.23)$$

where:

$$R_3 = \left(\frac{-(\alpha x_{\xi\xi} - 2\beta x_{\xi\eta} + \gamma x_{\eta\eta})}{J^2}\right)_{\eta=\eta_{max}} \qquad R_4 = \left(\frac{-(\alpha y_{\xi\xi} - 2\beta y_{\xi\eta} + \gamma y_{\eta\eta})}{J^2}\right)_{\eta=\eta_{max}}$$

(4.2.24)

Consequently the functions $P(\xi,\eta)$ and $Q(\xi,\eta)$ are fully defined if the a, b, c and d constants appearing in the relations (4.2.8) and (4.2.9), are given certain values. From these relations it can be observed that the effect of p, q, r and s which incorporate the geometrical constraints, decays exponentially in the direction away from the boundaries. The constants a, b, c and d determine the strength of this decay; large values, i.e. 0.8 , cause enhanced decay and hence reduced propagation of the geometric effects in the interior domain facilitating the convergence of the solution procedure. The opposite consequences are caused by small values of the constants, i.e. 0.2. In the present study typical values of a=b=c=d=0.6 have been employed.

At the boundaries $\eta=0$ and $\eta=\eta_{max}$, Dirichlet conditions are implemented whereby the points remain fixed at their initial location on the boundary during the

iterative procedure. At the inlet and outlet boundaries where $\xi=0$ and $\xi=\xi_{max}$ respectively, a Neumann condition is applied whereby the points are allowed to move by adjusting their position according to simple extrapolation from the neighbouring interior grid points.

Since the pairs (x,y) are fixed at $\eta=0$ and $\eta=\eta_{max}$, the derivatives x_ξ, $x_{\xi\xi}$, y_ξ, $y_{\xi\xi}$ remain unchanged on these boundaries. The derivatives x_η and y_η are calculated by using the expressions (4.2.14) to (4.2.17) and the cross derivatives $x_{\xi\eta}$ and $y_{\xi\eta}$ are estimated by differencing the x_η and y_η values along the ξ coordinate. The second derivatives $x_{\eta\eta}$ and $y_{\eta\eta}$ need to be updated at each iteration by using the following expressions, Sorenson (1980):

$$(x_{\eta\eta})_{\eta=0} = (-7x_{\eta=0}+8x_{\eta=1}-x_{\eta=2}) / (2\Delta\eta^2) - 3(x_\eta)_{\eta=0}/\Delta\eta$$

$$(y_{\eta\eta})_{\eta=0} = (-7y_{\eta=0}+8y_{\eta=1}-y_{\eta=2}) / (2\Delta\eta^2) - 3(y_\eta)_{\eta=0}/\Delta\eta \qquad (4.2.25)$$

$$(x_{\eta\eta})_{\eta=\eta_{max}} = (-7x_{\eta=\eta_{max}}+8x_{\eta=\eta_{max-1}}-x_{\eta=\eta_{max-2}}) / (2\Delta\eta^2) + 3(x_\eta)_{\eta=\eta_{max}}/\Delta\eta$$

$$(y_{\eta\eta})_{\eta=\eta_{max}} = (-7y_{\eta=\eta_{max}}+8y_{\eta=\eta_{max-1}}-y_{\eta=\eta_{max-2}}) / (2\Delta\eta^2) + 3(y_\eta)_{\eta=\eta_{max}}/\Delta\eta$$

A very small relaxation factor is used when the values of the functions p, q, r and s are updated because these values change substantially from iteration to iteration and may cause divergence problems.

For the solution of the transformed Poisson equations a simple Gauss-Seidel point over-relaxation solution method is employed very effectively as it will be shown in the next section.

The complete iterative process which is followed for the solution of the transformed Poisson equations can be outlined as follows:

1. Given the cascade geometry, the desired distribution of the grid points on the $\eta=0$ and $\eta=\eta_{max}$ boundaries is defined. The interior initial grid is computed by

interpolating between the two boundaries which have the same ξ value. An exponential clustering is used around the leading and trailing edges and at the near wall regions employing a simple method which will be described in the next section. In addition, the spacing Δs and the angle θ are defined. The derivatives which are fixed during the iterative process are calculated and the functions p, q, r and s are given initial values.

2. The values of $x_{\eta\eta}$ and $y_{\eta\eta}$ are computed on the boundaries according to the expressions (4.2.25) and the values of p, q, r and s are updated assuming the expressions (4.2.21) and (4.2.23), and by using under-relaxation. The values of P and Q are then updated at each grid point through the expressions (4.2.8) and (4.2.9).

3. The transformed Poisson equations (4.2.5) and (4.2.6) are solved and the coordinates x and y are updated by using a point over-relaxation solution method which sweeps the whole flow field in a point by point fashion.

The grid which is obtained from the step 3 is used as the initial grid of the step 1 for the next iteration. The steps 2 and 3 are repeated as many times as it is necessary for a convergent solution to be accomplished. The convergence criterion is given by:

$$\max \left[\, abs(x_i^n - x_i^{n-1}) \, \right] < \epsilon_c \quad for \quad all \quad x_i \qquad (4.2.26)$$

where x_i stands for both x and y; the superscript n denotes the current iteration level and n-1 denotes the previous one; and, ϵ_c is a small value, typically 10^{-6}.

4.3 Results and discussions

The grid generation procedure which has been described in the previous section, is implemented for the construction of two dimensional boundary fitted meshes which are necessary for the cascade flow predictions which will be described in the next chapter. The blade profile which is used in the cascade blades is the NGTE 10C4/30C50 profile which is described in Appendix C. The chord of the blades is 0.1 m, the space to chord ratio is equal to 1.0 and the upstream and

downstream of the cascade passage regions are extented to one chord length in the axial direction. The angle between the direction of the upstream and the downstream regions with the axial direction is always taken equal to the blade angle at the leading and the trailing edges respectively.

The initial grids are constructed by assuming three separate regions: the upstream region, the blade to blade region and the downstream region (Figure 4.2). The coordinates of the grid points on the upper and lower boundary are defined by the same law in such a way that there is an exponential reduction in the grid spacing towards the leading and trailing edges from both sides. The stretching transformation which is used to yield the appropriate grid point distributions in the three discrete domains, results from the family of general transformations proposed by Roberts (1971). The grid lines of constant ξ are perpendicular to the x-axis connecting the corresponding points of the upper and the lower boundary, and thus all their points obtain the same x coordinate. The position of the interior points of each pitchwise line can be determined by assuming an exponential variation of the grid spacing in the η direction which reduces towards the blade walls.

The grid generation method is applied to produce grids for four different stagger angles of the cascade, equal to: i) 15°, ii) 30°, iii) 45° and iv) -15°. Each of these grids consists of 70 points in the streamwise direction 20 of which are located in the upstream region, 20 in the downstream region, and 30 in the blade to blade direction. The initial grids together with the computed boundary fitted grids are depicted in the Figures 4.3 to 4.10. The computational times required to achieve convergence were respectively: i) 27, ii) 28, iii) 31 and iv) 30 seconds of CPU time on a DEC 5000/200 computer system. Figure 4.11 shows the convergence history for the four different grids indicating the degree of difficulty for achieving convergence in respect with the level of the stagger angle.

The effect of the grid size on the convergence history of the grid generation methodology is illustrated in Figure 4.12 for the construction of three meshes of

different sizes: 50 x 30, 70 x 30 and 90 x 30, and a stagger angle of 15°. The number of iterations to obtain convergence increases as the size of the grid increases. Of course the computational time required for each iteration is larger for the finer meshes.

The over-relaxation factor ω is used to accelerate the convergence rates of the solution of the system of the Poisson equations, by updating the x and y coordinates through the expressions:

$$x = x^{n-1} + \omega (x^n - x^{n-1}) \qquad and \qquad y = y^{n-1} + \omega (y^n - y^{n-1}) \qquad (4.3.1)$$

The effect of the over-relaxation factor on the convergence history of the grid generation of a 70 x 30 grid covering the passage between cascade blades at a stagger angle of 15°, is shown in Figure 4.13. As shown in Figure 4.14, an optimum over-relaxation factor can be derived for this case which is equal to 1.61. When the over-relaxation factor is increasing towards 1.7 the method does not converge while when it is close to 1.0 it converges very slowly.

In general, the implementation of the method to different configurations with varying degree of complexity, has proven that the proposed scheme is a very reliable, robust and excessively fast tool for generating two-dimensional BFC grids in cascade configurations. The grids which are obtained are smooth and fulfil the orthogonality condition of the grid lines at the blade walls. In addition, the proposed grid generation algorithm is found to be much more effective than the method suggested and developed previously at Cranfield by Lapworth (1987). The Neumann condition which was incorporated into that method, gave rise to enhanced divergence problems especially at high blade stagger angles, as the author of the present thesis has experienced.

CHAPTER 5

Two-dimensional cascade flow computations

5.1 Introduction

In this chapter, the computational method which has been presented in the previous chapters, is implemented for the two dimensional flow prediction in cascades. Rows of blades are encountered in almost every turbomachinery configuration and the introduction of the cascade model has played a vital role in the analysis and design of the blading of modern engines. In this chapter the elliptic flow model is applied to compressor cascades only. Another reason for the incorporation of the two dimensional cascade flow analysis in the present study is that it forms the basis for the development of the final three-dimensional model.

The theoretical assumptions and the form of the governing equations in a two dimensional plane are presented. The simplified form of the pressure correction scheme and a global pressure correction process which ensures stability during the calculation procedure are examined. The boundary conditions and the special treatment of the periodic and the solid wall boundaries are considered. Subsequently, the model is validated through its application for the flow prediction under certain conditions in low speed compressor cascade configurations for which experimental results have been reported in the literature. The comparisons between the predictions and the experimental results, in general, exhibit good correlation.

5.2 Theoretical model

The two-dimensional model is derived by neglecting the third coordinate z and any variations associated with this coordinate direction from the equations (3.2.4) to (3.2.9). Moreover because all cases considered in this chapter are of low speed the flow may be assumed to be incompressible and the energy equation may be removed from the computations. The physical flow domain is assumed to be on the x - y coordinate plane and the curvilinear coordinates are ξ and η. Using the above assumptions, the governing equations obtain the following simplified form:

Continuity:

$$\frac{\partial(\rho U_j)}{\partial \xi_j} = 0 \qquad (5.2.1)$$

u_i - Momentum:

$$\frac{\partial(\rho U_j u_i)}{\partial \xi_j} = \frac{\partial}{\partial \xi_j}\left(J(\mu+\mu_T)\, g^{jk}\frac{\partial u_i}{\partial \xi_k}\right) - J(p_\xi \xi_{x_i} + p_\eta \eta_{x_i}) + J\cdot S_{u_i} \qquad (5.2.2)$$

General Transport equation:

$$\frac{\partial(\rho U\Phi)}{\partial \xi} + \frac{\partial(\rho V\Phi)}{\partial \eta} = \frac{\partial}{\partial \xi}\left(J\Gamma_\Phi g^{11}\frac{\partial \Phi}{\partial \xi}\right) + \frac{\partial}{\partial \eta}\left(J\Gamma_\Phi g^{22}\frac{\partial \Phi}{\partial \eta}\right) + J\cdot S_\Phi(\xi,\eta) \qquad (5.2.3)$$

The curvilinear velocity components U and V are linked to the Cartesian velocities u and v through the relations:

$$U = J\,(\,\xi_x u + \xi_y v\,) \qquad V = J\,(\,\eta_x u + \eta_y v) \qquad (5.2.4)$$

The metric coefficients ξ_x, η_x, ξ_y, η_y and the Jacobian of the coordinate transformation are defined through the following relations:

$$\xi_x = \frac{y_\eta}{J} \qquad \xi_y = -\frac{x_\eta}{J}$$

$$\eta_x = -\frac{y_\xi}{J} \qquad \eta_y = \frac{x_\xi}{J} \qquad (5.2.5)$$

$$J = x_\xi y_\eta - x_\eta y_\xi$$

The components of the metric tensor g^{ij} are defined as:

$$g^{11} = \xi_x^2 + \xi_y^2$$

$$g^{22} = \eta_x^2 + \eta_y^2 \qquad (5.2.6)$$

$$g^{12} = g^{21} = \xi_x\eta_x + \xi_y\eta_y$$

The finite volume discretisation of the two dimensional transport equation is performed in an exactly similar manner to the three dimensional one and provides the following algebraic equation:

$$a_P\Phi_P = a_E\Phi_E + a_W\Phi_W + a_N\Phi_N + a_S\Phi_S + S_\Phi \qquad (5.2.7)$$

The coefficients a_i of the above equations are obtained from the three dimensional coefficients by suppressing the third coordinate direction through setting $\delta\zeta$ equal to unity.

The diffusion terms are discretised by using central difference approximations and for the discretisation of the convective terms the first order accurate Upwind, the Hybrid or the QUICK differencing schemes are appropriately utilised. The solution methodology is based on a space marching of the flow domain following a line by line of constant ξ sweeping in the streamwise direction. The Tri-Diagonal-Matrix-Algorithm (TDMA) is employed for the solution of the algebraic system of the equations at each line.

5.3 The pressure correction scheme

The pressure correction scheme which is used in the two-dimensional computations is a SIMPLE based scheme as it was described in Section 3.6.2. In order to suppress the pressure oscillations arising due to the decoupling of the pressure and the velocity field associated with the collocated grid arrangement, the modification proposed by Rhie and Chow, as was explained in Section 3.6.3, is employed in a 2-d fashion. The pressure correction scheme showed very good behaviour in suppressing the local pressure oscillations and coupling the velocity and the pressure fields. The storage of all the variables at the same grid location simplified the computer coding.

The failure of the staggered grid arrangement to deliver a pressure field which satisfies the periodicity condition has been reported previously by Mirzaborzog (1987) and Lapworth (1988) in their two dimensional cascade analyses. As a remedy to this problem, Mirzaborzog suggested a joint SIMPLE/SIMPLER pressure correction scheme in which the SIMPLER algorithm, Patankar (1980), was applied outside the blade to blade passage where the periodicity condition was implemented directly as a boundary condition for the pressure. The SIMPLE procedure was retained within the blade passage. Lapworth, by using the relations of Rhie and Chow, derived a pressure correction equation in terms of p rather than p' and this was claimed to have advantages over the corresponding equation in terms of p' because this formulation allowed the periodicity condition to be implemented directly as a boundary condition for the pressure equation.

Following the same procedure as for the derivation of the three-dimensional pressure correction, the velocity components u^* and v^* obtained from the solution of the momentum equations with a pressure field p^*, in general, do not satisfy the continuity equation and a mass-source is produced which is given by the relation:

$$m_P = F_{1e}^* - F_{1w}^* + F_{2n}^* - F_{2s}^* \qquad (5.3.1)$$

where the fluxes F_i are defined in the expressions (3.3.8) and (3.3.9) where $\delta\zeta$ is set

equal to 1 and the velocity component W is set equal to 0. The purpose of the pressure correction scheme is the elimination of this mass source through the appropriate adjustment of the pressure and the velocity field by adding corrections u′, v′ and p′ to the u^*, v^* and p^* values respectively. Following the analysis explained in Section 3.6.2, the corrected Cartesian velocity components u and v are related to pressure correction gradients as follows:

$$u = u^* + (B^u p'_\xi + C^u p'_\eta)$$

$$v = v^* + (B^v p'_\xi + C^v p'_\eta) \qquad (5.3.2)$$

where:

$$B^u = -\xi_x \frac{\Delta V_P}{a_P^u} \qquad C^u = -\eta_x \frac{\Delta V_P}{a_P^u}$$

$$B^v = -\xi_y \frac{\Delta V_P}{a_P^v} \qquad C^v = -\eta_y \frac{\Delta V_P}{a_P^v} \qquad (5.3.3)$$

where the volume ΔV_p of each computational cell in the physical space is now defined as:

$$\Delta V_P = J_P (\delta\xi\delta\eta)_P \qquad (5.3.4)$$

The corresponding corrected two-dimensional curvilinear velocity components U and V are given by the simplified formulas:

$$U = U^* + B\, p'_\xi \qquad V = V^* + C\, p'_\eta \qquad (5.3.5)$$

where:

$$B = J\,(\, B^u \xi_x + B^v \xi_y\,) \qquad C = J\,(\, C^u \eta_x + C^v \eta_y\,) \qquad (5.3.6)$$

The two dimensional pressure correction equation is obtained by substituting the relations (5.3.5) into the discretised continuity equation (5.3.1) and by using the relations (3.3.8) and (3.3.9) for the definition of the mass fluxes in a 2-d fashion:

$$a_P^P p_P' = a_E^P p_E' + a_W^P p_W' + a_N^P p_N' + a_S^P p_S' - m_p \qquad (5.3.7)$$

where the coefficients a_i^P are obtained from those in Section 3.6.2 by setting $\delta\zeta$ equal to unity:

$$a_E^P = -(\rho B)_e \frac{\delta\eta}{(\delta\xi)_e} \qquad a_W^P = -(\rho B)_w \frac{\delta\eta}{(\delta\xi)_w}$$

$$a_N^P = -(\rho C)_n \frac{\delta\xi}{(\delta\eta)_n} \qquad a_S^P = -(\rho C)_s \frac{\delta\xi}{(\delta\eta)_s} \qquad (5.3.8)$$

$$a_P^P = a_E^P + a_W^P + a_N^P + a_S^P$$

and the mass imbalance m_p is based on the starred curvilinear velocities and is obtained from the relation (5.3.1).

A global pressure correction step is implemented at each cross line of constant ξ in order to accelerate the establishment of the pressure field and to suppress instabilities in the values of the flow variables especially during the first iterations of the relaxation procedure. The mass flux through the inlet plane is equal to the mass flux through the cross stream plane at station ξ. This condition can be expressed in the following discretised form:

$$M_{in} = \sum_{inlet} (\rho U)\,\Delta\eta = \sum_{\xi} \rho\,(U^* + \Delta U)\,\Delta\eta \qquad (5.3.9)$$

where the summations are over each grid point in the cross stream line. With the assumption of a constant velocity ΔU, the above relation provides the one dimensional correction:

$$\Delta U = \frac{M_{in} - \sum_{\xi} \rho U^* \Delta\eta}{\sum_{\xi} \rho \Delta\eta} \qquad (5.3.10)$$

By applying a simplified streamwise momentum equation, this velocity correction is linked with an one dimensional global pressure correction given by the relation,

Lapworth (1987):

$$\Delta p = -\Delta U \frac{\sum_{\xi} \rho\left[J^{-1}(x_\xi^2 + y_\xi^2)U + (x_\xi u^* + y_\xi v^*)\right]\Delta\eta}{\sum_{\xi} J\Delta\eta} \qquad (5.3.11)$$

The correction Δp calculated at each station ξ is also added at all the following downstream stations in order to preserve the pressure gradients which are involved in the momentum equations.

Despite its effectiveness in stabilising the iterative process, it is found that the global correction constrains the velocity profile by adding a uniform velocity correction to all the grid points of the cross-station and causes the residual to oscillate around higher values than those obtained in cases where the global correction is implemented only during the initial stages of the relaxation solution method.

5.4 Boundary conditions

A unique solution to the governing equations may only be achieved if a consistent set of boundary conditions is specified. For low speed flow through a cascade, the following boundary conditions suffice to provide a unique solution:

At the upstream inlet boundary, the velocity components u and v are uniformly fixed according to the Reynolds number and the flow angle at the cascade inlet. The static pressure is only unique up to the addition of an arbitrary constant, since the flow is assumed to be incompressible. The magnitude of the inlet static pressure is arbitrarily chosen to be equal to zero. The value of the turbulent kinetic energy at the inlet boundary, is calculated from the inlet turbulence intensity which is obtained from the experimental conditions. For isotropic turbulence, the turbulence intensity is defined as:

$$T_u = \frac{\overline{(u_{in}'^2)}^{\frac{1}{2}}}{U_{in}} * 100 \qquad (5.4.1)$$

where U_{in} and u_{in}' are the mean and fluctuating velocities in the streamwise direction; and the overbar denotes quantities obtained by time-averaging. From the definition of the turbulence kinetic energy and the assumption of an isotropic turbulence, the inlet value of k is given by:

$$k_{in} = \frac{3}{2}(\overline{u_{in}'^2}) \qquad (5.4.2)$$

By combining this equation with the definition of the turbulence intensity, eq. (5.4.1), the inlet value of the k is defined as follows:

$$k_{in} = \frac{3}{2}\left(\frac{T_u \cdot U_{in}}{100}\right)^2 \qquad (5.4.3)$$

The value of the dissipation rate of the turbulent energy ϵ is determined either by assuming a mixing length value at the inlet or a level of an inlet uniform eddy viscosity in respect to the laminar one. From the values of k_{in} and μ_T, a uniform inlet distribution for ϵ can be specified from the relation (2.5.1), which may be reexpressed as:

$$\epsilon_{in} = \frac{C_\mu \rho k_{in}^2}{\mu_T} \qquad (5.4.4)$$

At the downstream outlet boundary which is usually taken one blade chord downstream of the blade trailing edge, the values of all the dependent variables are defined by linearly extrapolating their values from the adjacent interior domain.

The blade to blade flow passage is in fact one of a series of similar passages separated by the airfoils which are placed parallel to each other and comprise the whole cascade. The assumption of repeating flow conditions are valid in most of the cascade experiments especially in the passages located in the middle of the cascade where the effects of the side walls of the experimental setup are negligible. In order to simplify and reduce the computational effort required to handle the whole

cascade, only one representative flow passage between two adjacent blades is considered and periodic boundary conditions are implemented in the upstream and downstream of the blades regions. This implies that in these regions, the corresponding values of the dependent variables on the first and last constant η lines have to be equal. In the present method, the imposition of the periodic boundary conditions is performed explicitly by linearly interpolating the values of the variables at the $\eta=2$ and $\eta=\eta_{max-1}$, at each constant ξ line.

On the solid walls, the no-slip condition is applied and this sets all velocity values to zero. The pressure is calculated by a Neumann boundary condition which assumes a zero pressure gradient in the direction normal to the wall. The boundary fitted grid which is generated as it was described in Chapter 4, provides lines of constant ξ which fall orthogonally on the blade walls. This property facilitates the application of the above boundary condition and does not require any kind of interpolation:

$$\frac{\partial p}{\partial n} = \frac{\partial p}{\partial \xi}\frac{\partial \xi}{\partial n} + \frac{\partial p}{\partial \eta}\frac{\partial \eta}{\partial n} = \frac{\partial p}{\partial \eta} = 0 \qquad (5.4.5)$$

where n is a local physical coordinate normal to the wall.

In order to resolve the viscous effects in the near wall region where large gradients of the flow variables occur, a large number of grid points is required. The use of the wall functions which has been adopted in the present study as it was discussed in Section 2.6, facilitates the economical resolution of these regions with the penalty of reduced accuracy. An alternative method to deal with the near wall regions, could be the application of a low-Reynolds-number modification of the standard k-ϵ model which accounts for the damping effects due to the wall proximity and the low-Reynolds number viscous effects on the local flow. This approach does not require the use of wall functions and is expected to provide better resolution in the near wall regions with the expense of increased computational cost due to the finer grids which need to be employed.

The implementation of the wall function in the momentum equations is performed by adjusting the source in the grid points next to the wall to take into account the effect of the wall shear stress as it is determined through the profile assumptions by the relations (2.6.2) and (2.6.3). In order to include the effect of the wall shear stress into the near wall discretisation, the shear stress τ_w, based on the total velocity $V_{eff} = \sqrt{u^2+v^2}$ which is assumed to be approximately parallel to the wall in the near wall region, is resolved into two components along the x and y Cartesian directions:

$$\tau_w^u = \tau_w \frac{u}{V_{eff}} \qquad \tau_w^v = \tau_w \frac{v}{V_{eff}} \qquad (5.4.6)$$

With this approach, the velocity component normal to the wall is treated in the same way as the tangential one. However, the normal velocity component is much smaller than the tangential one and any inaccuracy introduced by this approach is considered to be less significant than the approximations already accepted with the adoption of the wall function method. For the test cases which have been considered in the present study, the difference between the flow field resulting from this approximation and the one where only the tangential component of the wall shear stress is considered, was found to be negligible.

The implementation of the wall function method to the near wall flow region lying e.g., along the "north" boundary of the flow domain is performed by deeming, for simplicity, that the shear wall force T_w acts in the direction opposite to the total velocity vector V_{eff}. The magnitude of this force is equal to the product of the wall shear stress τ_w and the area A_w, assuming a width equal to unity in the two dimensional case, i.e.:

$$T_w = \tau_w A_w \qquad (5.4.7)$$

Its components in the x and y direction are obtained if the shear stress τ_w is expressed in terms of its components in these directions:

$$T_w^u = \tau_w^u A_N \qquad T_w^v = \tau_w^v A_N \tag{5.4.8}$$

where the area A_w is defined as follows:

$$A_w = \left(\sqrt{(\delta x)^2 + (\delta y)^2} \right)_{\eta=\eta_{max}} = \left(\sqrt{x_\xi^2 + y_\xi^2} \right)_{\eta=\eta_{max}} (\delta \xi)_{\eta=\eta_{max}} \tag{5.4.9}$$

The influence of the wall shear force is introduced into the near wall discretisation by setting $a_N=0$ which breaks the link between the wall node N and the adjacent node P and by modifying the source term of the discretised momentum equations at the point P. Considering the linearisation process of the source term as it has been described in Section 3.3.5 the term S_p'' of the momentum equations is modified as follows:

$$S_p'' = S_p'' - \frac{\tau_w}{V_{eff}} \sqrt{x_\xi^2+y_\xi^2}\, \delta\xi \tag{5.4.10}$$

The generation and the dissipation of the turbulent kinetic energy arising in the transport equation for k, in the next to the wall grid line are modified taking into account the wall shear stress as calculated from the wall function relations (2.6.8) and (2.6.9). The k-source terms may by expressed using the wall shear stress as follows:

$$S_{kP} = (G - \rho e)_P \Delta V_P = \left(\tau_w \frac{\partial V_{eff}}{\partial n} - \frac{C_\mu \rho^2 k^2}{\mu_T} \right)_P \cdot \Delta V_P = \tag{5.4.11}$$

$$= \left(\tau_w - \frac{C_\mu \rho^2 k^2}{\tau_w} \right)_P \cdot \Delta V_P \left(\frac{\partial V_{eff}}{\partial n} \right)_P$$

The linearisation of the S_{kP} source term is performed as follows:

$$S_{kp}' = \frac{\Delta V_p}{\left(\sqrt{x_\eta^2+y_\eta^2} \right)_n \delta\eta} \tau_w V_{eff} \tag{5.4.12}$$

$$S''_{kp} = -\frac{\Delta V_p}{\left(\sqrt{x_\eta^2+y_\eta^2}\right)_n \delta\eta} C_\mu \rho^2 k_p \frac{V_{eff}}{\tau_w} \qquad (5.4.13)$$

The dissipation rate of the turbulent energy ϵ is given the value defined from the relation, Launder and Spalding (1974):

$$\epsilon_p = \frac{\left(k_p \sqrt{C_\mu}\right)^{\frac{3}{2}}}{\kappa\, \delta n} \qquad (5.4.14)$$

The value ϵ_p is required to be fixed for the grid points next to the wall and this is performed through the following adjustment procedure of the ϵ-equation source terms:

$$S'_{\epsilon P} = N\, \epsilon_P \qquad S''_{\epsilon P} = -N \qquad (5.4.15)$$

where N is a very large number ,e.g. $N = 10^{30}$, which causes the remaining terms in the finite difference equation to become negligible compared to $S_{\epsilon p}'$ and $S_{\epsilon p}''$ and ensures that the solution provides the value of ϵ at the node P to be equal to the specified value ϵ_p.

The turbulent viscosity is set equal to zero on the wall and hence the effective viscosity is obtained only from the molecular one.

5.5 Validation of the model

A numerical investigation has been performed in which the present Navier-Stokes procedure was used to analyse a series of compressor cascade viscous flows for which corresponding experimental data are available. The objective of this investigation is to determine the capability of the proposed computational methodology to predict cascade flow phenomena over a wide range of flow conditions over the entire incidence range. The results of these calculations demonstrate that the current viscous flow solver is capable of predicting cascade airfoil pressure distributions and turning angles with good accuracy. The total pressure loss tends to be overpredicted largely due to the numerical diffusion errors

associated with the currently employed numerical schemes and the inadequacy of the wall function method to accurately represent all the viscous phenomena occurring in the boundary layer region of the cascade blade.

The computational model is implemented for the flow prediction in three different low speed compressor cascade configurations: i) The NGTE 10C4/30C50 cascade, Felix and Emery (1957), ii) the NACA-65 cascade, Felix and Emery (1957), and iii) a series of three cascades of C4 profile with different camber angles, which were tested by Rhoden (1956) for the entire range of incidence angles. The coordinates of the blade suction and pressure sides of the above cascades are given in Appendix C. For each of these cascades, comparisons are carried out between the predicted and the measured values in terms of the pressure coefficient distribution along the blade pressure and suction sides and the deviation angle at the cascade exit.

5.5.1 Low speed NGTE 10C4/30C50 compressor cascade

The first two digits, 10, in the designation of the NGTE 10C4/30C50 cascade, specify the value of the maximum thickness of the blade in percent chord; the term C4 refers to the type of the thickness distribution; 30 is the camber angle in degrees; the following letter C indicates that the blade mean line is a circular arc; and 50 refers to the distance in percent chord, of the point of maximum camber from the leading edge. The main geometric and aerodynamic parameters of the test case are given in Table 5.1.

The pressure coefficient C_p is defined as follows:

$$C_p = \frac{P_{in} - p}{\frac{1}{2}\rho U_{in}^2} \qquad (5.5.4)$$

where P_{in} is the value of total pressure at the cascade inlet.

At the outset of this study, a grid refinement study was undertaken to provide an estimation of the computational grid spacing which was required to yield grid independent solutions, and its effect on the predicted pressure distribution and deviation angle. For this purpose, grid refinements were performed both in the streamwise and blade-to-blade directions. Figure 5.1 shows the predicted deviation angle as a function of the different grid sizes which were used in the flow analysis around the NGTE 10C4/30C50 cascade at an incidence of 0°.

TABLE 5.1

Chord c	5 inch
Stagger angle	15.0°
Camber angle	30.0°
Blade inlet angle	30.0°
Blade outlet angle	0.0°
Space/chord ratio	1.0
Reynolds number based on chord	280000
Air inlet angle	30.0°
Flow incidence angle	0.0°

For the grid refinement study , calculations were performed using eight different grids with: 50 x 20, 50 x 28, 80 x 20, 80 x 28, 80 x 45, 100 x 20, 100 x 28 and 100 x 45 grid points in the streamwise and blade to blade directions respectively. The predicted value of the deviation angle is found to be in a band of 0.3 degrees. Figure 5.2 illustrates the effect of the different grid spacing on the prediction of the pressure coefficient distribution. From this figure it may be deduced that despite the variation of the grid point densities in both directions, grid independent solutions are obtained and the grid with the minimum number of grid

points can be used to provide reliably accurate predictions of the pressure distribution along the blade surfaces. The same conclusion can be drawn from the prediction of the deviation angle as shown in Figure 5.1.

Subsequently, a numerical investigation was undertaken for the comparative study of the predictions by using the three different numerical schemes - Upwind, Hybrid and QUICK - for the discretisation of the convective term as described in Chapter 3. The results of this study are compared in Figure 5.3 where the predicted pressure distributions along the suction and the pressure sides of the cascade blade are compared with the available experimental data, Felix and Emery (1957). The calculated values do not quite achieve the same peak values near the leading edge as the experimental results, especially on the pressure side of the blade. This is attributed to the "bluntness" of the leading edge and the large flow gradients occurring in this region. However, the predicted values do demonstrate the same qualitative shape as the experimental results especially in the suction side of the blade. Along the remainder of the blade surface the calculated and measured values are in good agreement. The Kutta condition is approached at the trailing edge, but it is not satisfied exactly since the construction of the grid in this region is such that there is no grid point to coincide with the trailing edge point. The three numerical schemes provide very close distributions with the QUICK appearing to provide a tangibly better peak at the suction side of the leading edge.

The accurate prediction of the deviation angle at cascades, which is the difference between the outlet flow angle and the blade mean line angle at the trailing edge, is very essential both in the design and in the analysis of turbomachinery components. Obviously, the deviation angle is a measure of the guidance capacity of the cascade passages and is dependent upon cascade geometry parameters, the flow incidence angle and the Reynolds number of the passing flow. Figure 5.4 compares the predicted deviation angle variation with incidence against the experimental data provided by Felix and Emery (1957). The results show a good qualitative agreement with the experimental values, although the computed values

are slightly shifted from the measured ones especially at high negative incidences giving rise to a maximum discrepancy between the two sets of data, of around 1°.

The variation of the deviation angle in respect with the chord to space ratio - which is called solidity - is shown in Figure 5.5 where it is compared with data from empirical correlations which are derived from a number of experimental results. The first is the NASA correlation, NASA SP-36 (1965), and the second is the Carter's rule, Carter (1950). According to the NASA's correlation, the deviation angle is given by:

$$\delta = \delta_0 + m\frac{\phi}{\sigma^b} \qquad (5.5.2)$$

where the values of δ_0, m and b vary with the inlet flow angle and ϕ is the camber angle of the blade.

The Carter's correlation relates the deviation angle with the square root of the solidity:

$$\delta = m\phi/\sqrt{\sigma} \qquad (5.5.3)$$

where σ is the cascade solidity σ=c/s and m is a factor which varies with the blade setting angle. These two correlations do not give exactly the same values of deviation angle for a given value of solidity. The numerical results are obtained by assuming a constant chord length with the cascade space varying and by considering a constant flow angle of 30°. In general, the predictions show a better agreement with the NASA's correlation than with the Carter's rule. Taking into consideration the difference between the two correlations, the approximate agreement of the computed variation with the NASA correlation is assumed to be satisfactory.

The results which have been presented till this point, have been obtained on boundary fitted grids generated through the very fast and robust elliptic numerical method which was presented in the previous chapter. The computational time for the grid generation process is, as it was mentioned in the previous chapter, of the order

of a few seconds and is considered to be negligible as compared with the time taken by the flow computation. Figure 5.6 compares the pressure distribution which is obtained by using two different types of meshes: a boundary fitted mesh with the grid lines perpendicular to the blade surfaces, which was generated through the aforementioned elliptic iterative scheme, and an H-type grid which is constructed algebraically by joining with straight lines corresponding points of the outer boundary in the blade to blade direction and by dividing these lines into intervals which correspond to those intervals defined at the inlet grid line. These two grids are similar to those illustrated in Figures 4.4 and 4.3 respectively. Figure 5.6a presents results from computations which were carried out on 50 x 22 grids and Figure 5.6b shows the same set of results on finer grids consisted from 80 x 28 grid points. For the currently tested flow configuration, the H-type shear grid appears to provide better flow resolution and to achieve a better peak in C_p distribution around the suction side of the leading edge, than the boundary fitted grid, especially when the finer grid is considered.

The convergence history with and without the global pressure correction scheme described in Section 5.3 is depicted in Figure 5.7 where only the residuals of the momentum equations are considered. As it was mentioned in Section 5.3, the global pressure correction keeps the residuals at quite a high level when compared to those obtained without the global pressure correction scheme. However, the use of the global pressure correction was found to facilitate the stabilisation of the iterative procedure especially in the initial iteration steps and in off-design cases for which the solution is prone to divergence.

The computer code used to analyse the cascade flows was run on a DEC 5000/200 Workstation. As an example, a convergent solution has been obtained in approximately 820 iterations of the calculation procedure taking 11.4 minutes of CPU time for a typical 50 x 22 grid. This corresponds to 0.00075 seconds per grid point per iteration. According to the author's experience, a cascade can be analysed over the entire incidence range by using eight discrete points, in approximately two

and a half hours of real time. In addition to the flow analysis routines, a good deal of effort has been devoted to the development of software tools for the graphical representation of the predicted flow field in terms of flow velocity vectors, pressure contours, C_p and flow angle distributions etc, which enhance the understanding and the physical interpretation of the numerical results and assist the debugging and the further development of the flow model.

5.5.2 Low speed NACA 65-($12A_{10}$)10 cascade

This cascade airfoil has a typical NACA 65-series section which presents similar performance characteristics, that is, turning angles, drag coefficients and operating ranges with the NGTE 10C4/30C50 cascade according to comparative low-speed cascade tests conducted by Felix and Emery (1957). The detailed description of the blade geometry is given in Appendix C. The major geometric and aerodynamic parameters of this test case are the same as those used for the NGTE cascade test case of the previous section and are given in Table 5.1.

The comparison between the pressure distributions predicted by the solver and those experimentally measured, is illustrated in Figure 5.8. The predicted results are obtained by using the Upwind, the Hybrid and the QUICK numerical schemes which do not present significant differences between their predictions. The disagreement between the predicted and measured C_p coefficient around the leading edge, especially on the pressure side of the blade, is considered to arise due to the inadequacy of the grid points density in this area to resolve the large gradients of the flow parameters. The NACA cascade presents a lower loading in the leading edge region than the NGTE cascade because of its smaller radius at the leading edge.

The grid which was used in the computations consists of 70 points in the streamwise direction and 28 points in the blade-to-blade direction and is shown in Figure 5.9. The predicted velocity vector diagram is presented in Figure 5.10 where

the growth of the boundary layer along the suction side and the formation of the wake in the cascade discharge are easily identified. The C_p coefficient contour plot is also illustrated in Figure 5.11 where the acceleration of the flow on the suction side and the blade to blade loading are very clearly observed.

5.5.3 Rhoden's cascades

Rhoden (1956) conducted experimental work which consisted of the separate testing of three cascades of axial-flow compressor blades with camber angles of 20°, 30° and 40° respectively covering a wide range of Reynolds number and also a range of air flow inlet angles from 35° to 60°. The three blade shapes were the C4 profile of the National Gas Turbine Establishment of Great Britain based on circular arc camber lines. The blade chord was 0.1524m (6 inch) and the space to chord ratio was equal to 1. The numerical investigation which is presented hereafter aims at the simulation of the three aforementioned cascades for a set of six different inlet flow angles - except for the 40° camber angle case where only four inlet angles were examined - covering the entire incidence range, and correspond to the highest Reynolds number case from Rhoden's experimental results. Thus, in total, sixteen different configurations are tested with the currently proposed Navier-Stokes method and the predicted results are compared with the corresponding experimental data demonstrating the capabilities and identifying the limitations of the flow model. The results are presented and analysed in the next three different sections which correspond to the 20°, 30° and 40° camber angle of the tested blades. The pressure coefficient C_p on the blade surfaces for the following sets of results is defined as the difference between the static pressure at the point on the blade surface and the static pressure at the cascade outlet, expressed as a fraction of the outlet dynamic head:

$$C_p = \frac{p - p_{out}}{\frac{1}{2}\rho U_{out}^2} \qquad (5.5.4)$$

where p_{out} and U_{out} are the mass averaged static pressure and velocity values at the

plane located one chord downstream from the trailing edge.

The computational grid which has been used for all the following test cases, consists of 50 lines in the streamwise direction 20 of which are located in the blade passage, 15 in the upstream region and 15 in the downstream region, with 24 lines employed in the blade-to-blade direction.

20° camber angle

The cascade was set to a stagger angle of 34° which resulted in a blade angle of 44° at the inlet. The air inlet flow angle varied from 35° to 60° corresponding to incidence angles from -9° to +16° in increments of 5°. The Reynolds number based on the blade chord length for each inlet flow angle condition is given in table 5.2.

TABLE 5.2

a_1	35°	40°	45°	50°	55°	60°
Re	395200	432000	470000	473000	505000	281200

The computational grids for each case are illustrated in Figures 5.12a to 5.17a where the grid lines in the upstream of the blade passage region, are set to approximately align with the inlet flow direction.

Figures 5.12b to 5.17b compare the predicted C_p coefficient along the blade surfaces against the experimentally measured ones. There is an increasing cascade loading observed as the incidence angle increases. In general, the predicted results demonstrate very good agreement with the measured values all over the range of incidence variation. For the cases of 35°, 40° and 45° inlet flow angle, there is slight disagreement around the leading edge region - this is probably due to the local grid structure which is not sufficiently fine to resolve the large flow gradients which are present. Also the skewness of the grid is very high in this region and might

cause significant numerical diffusion errors. Apart from the above two reasons, the numerical treatment of the change from a periodic to a solid wall boundary is very critical and it was found that it can alter the whole pressure distribution pattern. For the cases of the 50°, 55° and 60° inlet flow angles which correspond to positive incidence angles of 6°, 11° and 16° respectively, there is better agreement than that of the previous cases, between the predictions and the experimental data, even in the leading edge region. This shows a general trend of the computer code, which was observed in other cases as well; increasingly better results are obtained as the incidence angle increases and the stagnation point moves towards the pressure surface of the blade. In the case of the 11° incidence angle, the turbulent boundary layer separates from the suction side and there is a region of flow recirculation as can be observed from the vector plot in Figure 5.16d. The C_p coefficient distribution presents an almost constant value at the recirculation area which is slightly lower than the experimentally measured one. This is probably due to the inadequacy of the k-ϵ turbulence model to deal with this kind of recirculating flow conditions in combination with the highly diffusive upwind definition of the convective term. More severe conditions of separation are predicted in the case of the 16° incidence where the largest part of the convex surface is stalled. In this case the computed pressure coefficient is in a good correlation with the experimentally defined values. In Figure 5.18a, the streamline pattern around the suction surface of the blade is depicted, where the flow recirculation region is very clearly identified. The corresponding vector plot diagram is depicted in Figure 5.18b.

The pressure coefficient C_p contour plots for each inlet flow angle are illustrated in Figures 5.12c to 5.17c.

The velocity vector diagrams are presented in Figures 5.12d to 5.17d.

The predicted deviation angle distribution with incidence as compared with the measured one, is provided in Figure 5.19. There is a very good agreement between these two sets of data in terms of the qualitative shape of the distributions. In addition, the disagreement in the actual levels is less than 0.8° and is worst in the cases of the -9° and -4° incidences.

From the above presented results for the 20° camber angle, it can be concluded that the Navier-Stokes model shows a good capability of predicting accurately most of the flow characteristics in the cascade passage, using a relatively coarse grid. In addition, the computer code was proved to be very robust in the calculation of very difficult cases such as those of +11° and +16° incidence, where the flow is severely stalled and unsteady. However, in the latter two test cases the Hybrid scheme was insufficient to stabilise the iterative process. Hence, the Upwind scheme had to be employed in combination with much lower relaxation factors than the ones usually used. The implementation of the current model in lower Reynolds number flows, failed to predict laminar separation regions mainly because of the inadequacy of the wall function approach involved in the computations. For these cases, a Low-Reynolds number modification to the k-ϵ model associated with a grid refinement to cover even the laminar sublayer region of the boundary layer, is expected to provide a better flow resolution and to capture the effects of the viscous phenomena in the proximity of the wall.

30° camber angle

This cascade configuration was set to a stagger angle of 36° providing a blade angle of 51° at the inlet. The flow angle at the inlet covered a range from 35° to 60° which correspond to incidence angles from -16° to +9° in increments of 5°. Table 5.3 presents the Reynolds number based on the blade chord length for each inlet flow angle.

The computational grids which are employed in the computations are shown in Figures 5.20a to 5.25a.

Figures 5.20b to 5.25b show comparisons between the predicted C_p coefficient along the blade surfaces and the experimentally measured ones. In general, there is a good correlation in most of the incidence angle conditions with small discrepancies in the area of the leading edge of the blade as in the previous test cases. Especially in the cases of inlet flow angle 35° and 40° where there is an

inversion in the cascade loading along the initial 20% and 10% of the blade chord respectively, the negative loading is underestimated. In the case of the highest incidence +9°, there is a turbulent flow separation from the convex surface of the blade close to the trailing edge which renders the pressure coefficient almost constant in this region in contrast with the high gradient which appears in the upstream region of the blade. The streamline pattern in this region is depicted in Figure 5.26a where the closed streamlines indicate the recirculated flow region and the corresponding velocity vector plot is presented in Figure 5.26b.

TABLE 5.3

a_1	35°	40°	45°	50°	55°	60°
Re	401000	408500	474000	478000	475000	506500

The pressure coefficient C_p contour plots for each inlet angle are illustrated in Figures 5.20c to 5.25c.

The predicted velocity vectors at each grid point of the flow domain are depicted in Figures 5.20d to 5.25d. In the latter figure, the vectors indicate the separation region on the suction side in the vicinity of the trailing edge.

The predicted deviation angle distribution, with incidence as compared with the measured one, is provided in Figure 5.27 where similar trends with those observed in the cascade of 20° camber are identified. There is a very good qualitative agreement between the computed and the experimentally defined shape of the deviation angle variation. However, the model tends to underpredict the actual levels of the deviation angle at high negative incidences and overpredict them at high positive angles. The discrepancy is within 1° and is judged to be acceptable taking into account the uncertainties associated with the experimental procedures.

40° camber angle

The 40° cascade was set to a stagger angle of 38° giving a blade inlet angle of 58°. The inlet flow angle varied from 40° to 55° in increments of 5° corresponding to an incidence angle variation from -18° to -3°. The Reynolds number for each of the above flow angles is presented in Table 5.4.

The 50 x 24 boundary fitted grids which are used for the flow analyses are shown in Figures 5.28a to 5.31a.

The predicted pressure coefficient C_p along the pressure and suction sides of the blade are compared against Rhoden's experimental results in Figures 5.28b to 5.31b. This cascade delivers a higher loading than the previous two tested for the same incidence angle because of the higher camber angle of the blade. The predicted results exhibit a fairly good agreement with the corresponding test data in most of the cases apart from some discrepancies which appear around the leading edge of the blade. There is a remarkable agreement in the pressure distribution for the inlet flow angle of 50° as it is shown in Figure 5.30b.

The contour plots of the pressure coefficient C_p for each inlet angle are shown in Figures 5.28c to 5.31c which are typical for low speed compressor passages.

TABLE 5.4

a_1	40°	45°	50°	55°
Re	425000	474000	493000	517000

Figures 5.28d to 5.31d, the computed velocity vectors inside the blade passage for each case of inlet flow angle, are illustrated.

The variation of the predicted deviation angle with varying incidence as it is compared with the measured one, is given in Figure 5.32 where it appears that the computational model captures fairly successfully the qualitative characteristics of this distribution. However, there is a departure of around 1° from the test data in the worst case of very high negative incidence angle.

5.6 The effect of under-relaxation

In this section the effect of the under-relaxation parameters α_u and α_p for the velocity and the pressure correction respectively on the rate of convergence of the computational method are studied. The laminar flow prediction through the NGTE 10C4/30C50 cascade using a 50 x 24 BFC grid and the hybrid numerical scheme, is utilised as a typical example to demonstrate general trends and the significance of the selection of the appropriate relaxation factors on the computational economy and efficient usage of the model.

For this particular study, the convergence criterion is that the absolute value of the maximum difference of the flow field values u, v and p, between consecutive iterations, should be less than a specified small number, 0.0001 in the current case.

Figure 5.33 illustrates the required number of iterations for convergence, as a function of the under-relaxation factor used for the solution of the pressure correction equation. Each of the four different curves corresponds to a factor of 0.3, 0.5, 0.7 and 0.9 respectively chosen as under-relaxation parameter for the solution of the momentum equations. From the variations presented in this graph, it can be discerned that for a given under-relaxation factor for the momentum equations, there is an optimum factor α_p for the pressure correction which offers the quickest convergence and in addition, there is a "band" of suitable α_p values which can be used. In the current study, this band was found to be fairly narrow and there is an upper limit for α_p close to a value of 0.3 beyond which the method fails to converge or crashes completely for much larger values of α_p. There is an optimum set of under-relaxation parameters α_u and α_p which provides quickest convergence. This set is problem dependent and in the currently investigated case is α_p=0.3 and α_u=0.7. However, the conservative choice of the set α_u=0.6 and α_p=0.2 was judged to offer good convergence rates and proved to be very safe for most of the calculations presented in the previous paragraphs. In Figure 5.34, the variation of the convergence rate with the relaxation factor α_u assuming a typical value for a_p equal to 0.25, is depicted. The shape of the curve indicates the existence of an

optimum value for the factor α_u, equal to 0.7, for the specified value of α_p. A similar pattern is followed in the variation of α_u for each value of the under-relaxation factor α_p within the "band" in which a solution can be obtained.

The above features were also encountered by Peric (1985) who studied the effects of the under-relaxation factors used in an elliptic relaxation methodology for the laminar flow prediction in a cavity with inclined side walls and a moving lid. In this investigation, it was concluded that the width of the "band" of the α_p values which can be used with given α_u factors, depends on the non-orthogonality of the grid. The width becomes narrower as the grid becomes more non-orthogonal. A similar trend became apparent when the current model was implemented in cascade flow cases with high inlet flow angles (greater than 50°) and the generated grid was highly distorted in the upstream of the blade passage region in order to align with the flow direction, e.g. the grid in Figure 5.25a for the 30° cambered Rhoden's cascade. In these cases an under-relaxation factor of 0.1 for the pressure correction was proved to be fairly safe in order to guarantee convergence in reasonably fast rates. For the transport equations for k and ϵ, the value of the under-relaxation factor was set equal to 0.5.

5.7 Acceleration of the iterative solution

An accelerative numerical procedure aiming towards the reduction of the number of iterations required for a convergent solution, has been incorporated as an option in the proposed two-dimensional flow model. This technique was proposed by M.Lobo (1991) and is based on the prediction of the final destination of the iterative path which each of the flow variables follows, by examining a few typical points of the path. Obviously, this preassumes that a certain iterative pattern is followed which is true for quite a large number of cases. For a typical problem, the iterative path consists of two distinct phases: an unsteady phase occurring due to the influence of the different boundary conditions which lasts till these influences have been properly assimilated, and a second steady phase which exhibits a certain pattern

which, in general, can differ from one case to another.

The use of a multigrid approach which is a very well established technique can accelerate the unsteady phase through the rapid transmission of the boundary effects. The currently implemented novel approach is focused on the steady phase and attempts to estimate the asymptotic values which the variables may obtain when convergence is accomplished. Lobo defined various iterative paths which may be encountered in CFD problems and proposed appropriate formulas for the approximate estimation of the convergent solution. In the current computational method, it has been found that the flow variables follow a long-period oscillatory pattern and not a monotonically varying one because the dependent flow variables converge to their final solution at different rates. A typical variation pattern of the velocity component u obtained from a cascade flow simulation at a specified monitoring grid location, is depicted in Figure 5.35.

The centre of the oscillatory path is determined through the assumption that the amplitude of successive waves decays exponentially. If C_0, C_1 and C_2 represent successive extrema, the guess for the final destination of the iterative path will be:

$$C = \frac{C_2 + C_1 \cdot \frac{C_2 - C_1}{C_0 - C_1}}{1 + \frac{C_2 - C_1}{C_0 - C_1}} \qquad (5.7.1)$$

This formula is applied to all points of the flow field at the stage when every single point has encountered a third extremum of its iterative path. In addition, the acceleration process ensures that the amplitude of the successive extrema is indeed decaying. Because of the long period of the oscillatory pattern, the acceleration cannot be implemented until the iterates are already a fairly considerable fraction of the path towards convergence.

Figures 5.36 and 5.37 present convergence rates for accelerated and unaccelerated procedures for two different sets of under-relaxation factors. In the

first case the relaxation factors are set equal to 0.8, 0.8 and 0.3 for the calculation of the u and v velocity components and the pressure correction respectively. The corresponding values for the second case are 0.6, 0.6 and 0.2. For the first 207 iterations in the first case and 283 in the second, the two curves are identical because only at this stage all the grid points have experienced a third extremum in their iterative paths. Thereafter the acceleration process converges much faster yielding a benefit of 32% and 29.4% in terms of the number of iterations for convergence in each of the two cases respectively. The benefit in terms of CPU time is slightly less if the additional floating point operations required for the acceleration procedure are included. The incorporation of this acceleration process into the Computer program causes also a relatively small increase of the required Computer memory.

5.8 Conclusions

In this chapter, the implementation of the proposed computational methodology to predict two-dimensional, low-speed flows in the passages of compressor cascade blades, is presented. The theoretical simplifications to the three dimensional flow model presented in the previous chapters and the application of the required boundary conditions, are explained and discussed. The computational grid which is utilised in the computations is a boundary fitted grid with the grid lines intersecting the blade surfaces and the periodic boundaries perpendicularly and is generated through the robust computational procedure described in Chapter 4. The predictive capabilities of the 2-d model are assessed through a number of comparisons of the computed flow parameters with experimental data, available in the literature, corresponding to different blade profiles, cascade settings and flow conditions in terms of inlet flow angle and Reynolds number. There is a fairly good correlation of the predicted pressure coefficient distributions on the blade surfaces, with the measured data. The discrepancies which are observed in the leading edge region are attributed to reasons inherent into the grid construction process around this area and to the numerical treatment of the change from a periodic to a solid wall

boundary condition. The predicted deviation angle for the different configurations examined, is in good agreement with empirical correlations or alternatively with experimental data. However differences arise at high negative values of incidence. In some of these cases, large flow separation areas have been predicted on the suction surface of the blade. The computer code tends to overpredict the total pressure loss coefficient due to the highly diffusive numerical schemes which are employed for the discretisation of the convection term of the flow equations and to the inaccuracies from the introduction of the wall function method to bridge the first grid point away from the wall with the wall surface.

The effects of the under-relaxation parameters on the rate of convergence have been identified and an optimum set of values, which is problem dependent, has been determined. A novel accelerative method has been implemented and certain improvements in the computational economy of the suggested flow model have been accomplished.

CHAPTER 6

Flow in three-dimensional ducts

6.1 Introduction

The proposed mathematical flow model was implemented for the flow prediction in two dimensional cascade configurations as was described in the previous chapter. However, the flow phenomena through the complex geometry of a centrifugal impeller are highly three dimensional and a numerical model of greater complexity is required. In this chapter, the three dimensional model is applied for the flow prediction in three dimensional flows through ducting systems which exhibit some of the features that are likely to be encountered in the modelling of centrifugal compressor flows. The additional model considerations which are required in addition to those described previously, the boundary conditions and the calculation procedure for this class of flows, are presented.

The assessment of the applicability of the current method to three-dimensional duct flows, is performed through a set of steady state incompressible flow test cases where the basic physical elements associated with centrifugal compressors are encompassed. Each test case is selected to examine a particular feature of the model as independently as possible from the other features. Two laminar and two turbulent flows are considered passing through straight ducts. The flow in a 90° curved passage with rectangular cross-section is used as a benchmark to test the behaviour of the proposed methodology in curvature dominated flows where a pressure gradient is applied in the cross-stream direction. The turbulent flow in a series of low-aspect ratio planar diffusers with different exit to inlet area ratios are studied for two different Reynolds numbers.

The predicted results are compared against exact solutions for the laminar flow test cases whereas for the turbulent flows the computed results are compared either with experimental results or with previous numerical computations obtained by other methods. In general, satisfactory agreement has been obtained in most of the examined cases.

6.2 Implementation of Boundary Conditions

Inlet Boundaries

The values of all the flow variables are usually obtained by referring to available experimental data or through analytical relations taking into account other given conditions when the required information is not complete. The turbulence kinetic energy k, is fixed to a uniform value based on a level of turbulence intensity when no other measured distribution of k is provided. As it was described in Section 5.4, the inlet turbulence dissipation rate ϵ can be either calculated by considering an eddy viscosity level or through the assumption of a distribution of the length scale l_m, via the relationship:

$$\epsilon \propto \frac{k^{\frac{3}{2}}}{l_m} \qquad (6.2.1)$$

A two-dimensional control cell, placed next to an inlet boundary, is depicted in Figure 6.1. As it can be observed, the spacing between B and P is approximately half of the distance between the nodes P and F and therefore the point P is located in the middle of the "central-line" bf of the control volume. In this way, the flow variables at P are more realistically representative of the constant values which are assumed to prevail in the control volume as they are used for the explicit computation of some parts of the source term. This practice is consistently followed to all control volumes adjacent to any boundary of the computational domain. The boundary nodes are placed at the boundary control volume faces and the known flow quantities are assigned to them. No modifications are necessary to the discretised equations for the inlet boundary cells, since the weighting factors used for the

interpolations, as it was described in Section 3.5.3, ensure both the accurate computation of the inlet convective flux, since the cell face values in the interpolation formulas correspond to the boundary values, and the correct estimation of the diffusion terms.

The inlet mass fluxes are not required to be corrected and thus the velocity corrections for boundary cell faces are neglected, which is equivalent to a zero pressure correction gradient boundary condition for the pressure correction equation. This is automatically arranged by setting the coefficients a_i^p corresponding to the boundary node equal to zero. This is the practice which is adopted in the present study, where the simplified, without the cross derivative terms in the relations (3.6.7), pressure correction equation is used, which subsequently is equivalent to setting to zero the gradient in the coordinate direction ξ_j and not along the direction normal to the boundary. This has no significant effect on the converged solution, but may cause difficulties at highly non-orthogonal grids.

Outlet Boundaries

The outlet boundary is located sufficiently far downstream from the region of interest, Figure 6.2, at a location where there is no recirculation and the flow is everywhere directed outwards, so that any inaccuracy in the definition of the outlet conditions will not be allowed to travel far upstream if the Reynolds number is large.

When an upwind scheme is employed for the definition of the convective flux, the downstream grid points are not considered and the coefficients a_i^c which correspond to the outlet boundary will be zero for all the neighbouring control volumes. Consequently, only the diffusion part of the a_i coefficients remains which becomes negligible when the local Reynolds number is high. As a result, the outlet boundary values can be estimated by extrapolation from upstream. In most cases it is found sufficient to consider the outlet values equal to the values at the adjacent

upstream plane which is equivalent to zero gradient in the ξ_i direction, for all flow variables except pressure. For the pressure values a linear or a quadratic extrapolation is found to be more realistic especially when there is a pressure gradient at the exit region. The overall continuity is ensured through the global velocity and pressure correction procedure applied at each cross plane, as it is described in Section 6.3. In the cases where the values of the dependent variables are known at the exit, these values are fixed as such and no extrapolation practice is followed.

Symmetry Boundaries

The conditions which are valid at a plane of symmetry are the setting of no convective and no diffusion flux of the dependent variables along the normal to the symmetry plane directions.

The values of the dependent variables at the symmetry boundary are calculated from the interior nodal values by imposing the requirement for a zero normal gradient:

$$\frac{\partial \Phi}{\partial \vec{n}} = 0 \qquad (6.2.2)$$

where $\vec{n}$ is the coordinate normal to the symmetry plane. For the situation shown as an example in Figure 6.3 where the "b" face lies on a symmetry plane, the above equation is equivalent to:

$$\left(\frac{\partial \Phi}{\partial \zeta}\right)_b = \left(\frac{\partial \Phi}{\partial \xi}\right)_b \cos\theta_{13} + \left(\frac{\partial \Phi}{\partial \eta}\right)_b \cos\theta_{23} \qquad (6.2.3)$$

where θ_{13} and θ_{23} are the angles between the positive parts of ξ and η and the inward part of ζ. When the grid is orthogonal at the symmetry plane (as it happens in all the cases where a symmetry plane was employed in the computations of the current study) then the simplified zero gradient condition along the coordinate which intersects the symmetry plane applies:

$$\left(\frac{\partial \Phi}{\partial \zeta}\right)_b = 0 \qquad (6.2.4)$$

Solid walls

The velocity components u_i and the corresponding fluxes F_i, are set to be equal to zero on the solid walls. The link between the grid points located adjacent to a wall with those located on the wall boundary, breaks by setting the corresponding coefficient a_i equal to zero and incorporating the diffusive contribution due to the wall shear stress into the source term of the momentum equations according to the analysis presented in Section 5.4 for two-dimensional flow. In the case of turbulent flows, the wall function method is adopted to define empirically the shear stress as it was explained in Section 2.6. The wall function assumption is based on Couette flow analysis for fully developed flow which, although a realistic assumption for parallel near-wall flows, may be greatly erroneous in case of recirculating flows where large gradients along the wall prevail. The general application of the method in three dimensional flows, can be summarised as follows:

The wall shear stress is written as a function of the component $\vec{U}_p$ of the velocity vector $\vec{U}$ which is parallel to the wall, Figure 6.4:

$$\vec{\tau}_w = -\Lambda_w (\vec{U}_p)_P \qquad (6.2.5)$$

where:

$$\Lambda_w = \frac{\mu}{\delta n} \qquad if \quad y_P^+ < 11.6 \qquad (6.2.6)$$

$$\Lambda_w = \frac{\kappa \rho C_\mu^{\frac{1}{4}} k_P^{\frac{1}{2}}}{\ln[E y_P^+]} \qquad if \quad y_P^+ > 11.6 \qquad (6.2.7)$$

where:

$$y_P^+ = \frac{\rho\, C_\mu^{\frac{1}{4}}\, k_P^{\frac{1}{2}}\, \delta n}{\mu} \qquad (6.2.8)$$

The shear force $\vec{T}_w$ is assumed to act in the direction opposite to $\vec{U}_p$, Figure 6.4, and is equal to:

$$\vec{T}_w = \vec{\tau}_w A_w = -\Lambda_w A_w (\vec{U}_p)_P \qquad (6.2.9)$$

where A_w is the area of the control volume face lying on the wall. The analysis of $\vec{T}_w$ in each of the x_i directions is performed by expressing $\vec{U}_p$ in terms of its Cartesian components:

$$T_{w_i} = -\Lambda_w A_w (U_{P_i})_P \qquad (6.2.10)$$

The velocity component $\vec{U}_p$ is obtained by the total velocity vector $\vec{U}=(u_1,u_2,u_3)$ as follows:

$$\vec{U}_P = \vec{U} - (\vec{U}\cdot\vec{n})\cdot\vec{n} \qquad (6.2.11)$$

where $\vec{n}=(n_1,n_2,n_3)$ is the normal to the wall unit vector defined by the vector product of two cell face "central lines", e.g. from $(\overline{ew})_b$ and $(\overline{ns})_b$ for the cell illustrated in Figure 6.4.

Eventually each shear stress component in the x_i direction is given by the relation:

$$T_{w_i} = -\Lambda_w A_w \left(u_i - n_i \sum_{j=1}^{3} u_j n_j \right) \qquad (6.2.12)$$

The force T_{wi} is subsequently added to the source term of the momentum equation for u_i after appropriate linearisation through the relation (3.3.24).

The near-wall treatment for the k transport equation is performed through the adjustment of the source term for the boundary control volume adjacent to the wall, by following the analysis leading to the relation (5.4.11) used for the two-dimensional flow predictions where ΔV_p is now the volume of the three-dimensional control volume.

The value of the dissipation rate of the turbulence energy ϵ is fixed at the control volumes next to the wall, to a value determined explicitly by the relation (5.4.14) by means of a linearised source term, relation (5.4.15).

6.3 Calculation of the pressure field

The pressure field is calculated by using a SIMPLE based pressure correction approach as it is described in Section 3.6.2 with the amendment proposed by Rhie and Chow (1983) in order to couple the pressure and the velocity fields and to remove the oscillations which might arise during the calculation process due to the non-staggered location of the flow variables on the computational grid, as it was discussed in Section 3.6.3. The three dimensional implementation of the pressure calculation procedure differs slightly from the one used in the cascade computations. Specifically, the three-dimensional pressure field is generated using a three-step procedure.

In the first step, a one-dimensional global correction is implemented at each cross-stream plane. A uniform velocity correction is obtained by applying global conservation of mass:

$$\Delta W = \frac{M_{in} - \sum_{\zeta} \rho W^* \delta\xi\delta\eta}{\sum_{\zeta} \rho\delta\xi\delta\eta} \qquad (6.3.1)$$

which ensures that the mass flux M_{in} through the inlet plane is equal to the mass flux through each cross-stream plane at station of constant ζ, which has been considered as the coordinate in the approximate streamwise direction. The generalised coordinates ξ and η are assumed to be the cross stream coordinates and the summation is over each grid point in the cross plane.

A one dimensional correction to the pressure is obtained from the solution of an approximate integrated streamwise momentum equation, Lapworth (1987), and is given by the expression:

$$\Delta p = -\Delta W \cdot \frac{\sum_{\zeta} \rho\left[J^{-1}\left(x_\zeta^2+y_\zeta^2+z_\zeta^2\right) w + \left(x_\zeta u^*+y_\zeta v^*+z_\zeta w^*\right)\right]}{\sum_{\zeta} J\delta\xi\delta\eta} \qquad (6.3.2)$$

The pressure correction Δp calculated at station ζ is also added to all downstream stations preserving the existing pressure gradients which are practically "sensed" by the momentum equations. The one-dimensional corrections to the velocity and pressure are equivalent to those used in the two dimensional analysis of the previous chapter and have been found to accelerate the establishment of the correct pressure field.

In the second step, a two-dimensional elliptic pressure correction is performed to the cross-stream velocities and pressure in order to promote the satisfaction of the local conservation of mass, through the solution of the equation (3.6.10) which is derived in the previous chapter. A brief review of this step which has also been discussed in Sections 3.6.2 and 3.6.3, is as follows:

The values u^*, v^* and w^* obtained from the solution of the momentum equations are utilised for the estimation of the curvilinear velocities U^*, V^* and W^* at the grid nodes through the relation (3.2.5). Subsequently the above components are approximated at the control volume faces by applying the expression (3.6.12), Rhie and Chow (1983):

$$U^* = \overline{U}^* - B\left(\overline{p_\xi}^* - \frac{\partial p^*}{\partial \xi}\right) \qquad V^* = \overline{V}^* - C\left(\overline{p_\eta}^* - \frac{\partial p^*}{\partial \eta}\right) \qquad W^* = \overline{W}^* - D\left(\overline{p_\zeta}^* - \frac{\partial p^*}{\partial \zeta}\right)$$

(6.3.3)

where the coefficients B, C and D are given by the expressions (3.6.9). Correction are then added to U^*, V^* and W^* in order that local continuity be satisfied:

$$U = U^* + B \cdot p'_\xi \qquad V = V^* + C \cdot p'_\eta \qquad W = W^* + D \cdot p'_\zeta \qquad (6.3.4)$$

where p' is the correction to the value of p^*. The substitution of U, V and W given from the previous relations into the discretised continuity equation provides an equation for the pressure correction, equation (3.6.10). The solution of this equation

is performed two dimensionally at each constant ζ plane, assuming $p'_F=p'_B=0$, and provides values for p' which are used to correct the cross-stream general velocity components U and V. The pressure correction values are under-relaxed before updating the pressure for stability reasons. Usually an under-relaxation factor of 0.2 is used taking into account the conclusions of Section 5.6 for the two dimensional cascade analysis.

In the third step, a three-dimensional correction to the pressure field alone is executed for the acceleration of the elliptic pressure effects transmission. The combination of the relations (6.3.3) and (6.3.4), provides the relations:

$$U = \tilde{U} + Bp_\xi \qquad V = \tilde{V} + Cp_\eta \qquad W = \tilde{W} + Dp_\zeta \tag{6.3.5}$$

where:

$$\tilde{U} = \overline{U^*} - B\overline{p_\xi^*} \qquad \tilde{V} = \overline{V^*} - C\overline{p_\eta^*} \qquad \tilde{W} = \overline{W^*} - D\overline{p_\zeta^*} \tag{6.3.6}$$

An equation for the pressure field itself is obtained by substituting the above relations $\tilde{U}$, $\tilde{V}$ and $\tilde{W}$ into the discrete continuity equation:

$$a_p^p = \sum_k a_k^p p_k - \tilde{m}_p \tag{6.3.7}$$

where $\tilde{m}_p$ is the integrated local mass imbalance based on the general velocity components $\tilde{U}$, $\tilde{V}$ and $\tilde{W}$, which are updated after the second pressure correction step. The coefficients a_k^p which appear in the above equation for pressure are identical to those encountered in the pressure correction equation (3.6.10) used in the second step, and consequently have to be computed only once.

6.4 Computational Results

6.4.1 Laminar Flow Test Cases

The laminar flows between two parallel plates and in a circular pipe are considered. These cases belong to a small number of flows for which analytic

solutions exist. For both calculations the Hybrid numerical scheme is utilized.

The flow between parallel plates is a two dimensional one. However, the results are obtained by fixing suitably the three-dimensional computer code, assuming just 5 grid points in the infinitely expanded third direction and considering the side boundaries to be symmetry planes. The orthogonal grid which is used consists of 16 x 5 grid points in the cross section of the channel and 88 grid points streamwise, covering a region of 60 channel widths in the flow direction. The outline of the grid is illustrated in Figure 6.5. The Reynolds number based on the channel width D and the mean velocity W_{in}, is equal to 100. This test case is chosen in order to examine whether the non-orthogonal diffusion and pressure terms are coded correctly and vanish eventually from the computations. In the current study the whole width is considered despite the existing symmetry, in order to provide an additional check of the symmetry of the profiles along the width of the channel and reveal any existing computational errors. Uniform velocity profiles at the inlet and zero axial gradients at the outlet are prescribed, with the initial values set to: $u=v=p=0$ and $w=W_{in}$. The predicted velocity profiles are symmetrical indeed and there is no variation in the third direction. The predicted parabolic velocity profile in the fully developed region is in excellent agreement with the analytic solution as shown in Figure 6.6. In addition, the calculated pressure drop and shear stress are within less than 1% agreement with the values given from the analytic solution for these parameters, Schlichting (1979). The cross-stream velocity components are predicted to be negligible in the fully developed region.

The second laminar flow test case deals with the developing flow prediction in a circular pipe. This test case is especially designed to test the performance of the current method on non-orthogonal grid systems at the cross-stream plane. Only one quarter of the cross-section is considered in the computations because of flow symmetry. The grid which is used to cover this cross-stream plane, illustrated in Figure 6.7, consists of 16 x 16 points and is generated algebraically to provide equal physical spacing in both constant ξ and η directions. This grid is highly non-

orthogonal around the point C at 45° from the horizontal direction. In the streamwise direction, 88 axial stations are used covering a distance of 60 pipe diameters. The Reynolds number of the flow based on the diameter of the pipe, is equal to 100 and the boundary and initial conditions are identical to those described above for the flow between two parallel plates. The solution procedure was found to be stable, and no effect of grid non-orthogonality on accuracy was observed. The predicted velocity profile of the fully developed flow is in excellent agreement with the analytic solution and is identical for every direction which passes through the axis of the pipe. This is illustrated in Figure 6.8 where the predicted velocity profiles along the AB at 0° and AC at 45° lines of Figure 6.7, coincide with the analytically derived parabolic profile. The pressure drop and the shear stress on the pipe walls are computed to be in very good agreement with the corresponding analytically obtained values.

6.4.2 Turbulent Flow test cases

6.4.2.1 Flow between parallel plates

The flow between parallel plates is predicted for the turbulent regime to assess the accuracy of the proposed scheme when the additional scalar equations k and ϵ are solved. The computational grid is the same as in the laminar case covering the whole width of the passage despite the flow symmetry in order to reveal any computational errors encountered in the coding associated with the turbulent scalars and the wall functions. The inlet profiles are uniform and are given from the following relations:

$$u_{in}=v_{in}=p_{in}=0 \ , \quad w_{in}= W_{in} \ , \quad k_{in}=\frac{3}{2}(T_u \cdot W_{in})^2 \ , \quad \epsilon_{in}=\frac{C_\mu \rho k_{in}^2}{\mu_{T_{in}}} \qquad (6.4.1)$$

where T_u is the inlet turbulent intensity taken to be 0.03 and μ_{Tin} is an inlet value for the eddy viscosity equal to 50 for the present test case. The Reynolds number based on the width of the passage is equal to 20,000.

The computed velocity profiles obtained at each cross section are found to be symmetric around the mid-width plane of the passage as expected. The velocity profile in the fully developed flow regime is shown in Figure 6.9 and is compared with the three-dimensional numerical solution of Peric (1985). The profile of the turbulence kinetic energy k normalised by the square of the friction velocity u_T given by:

$$u_\tau = \sqrt{\frac{\tau_w}{\rho}} \qquad (6.4.2)$$

where τ_w is the wall shear stress, is presented in Figure 6.10. The turbulence mixing length l_m defined as:

$$l_m = C_\mu \frac{\epsilon^{\frac{3}{2}}}{k} \qquad (6.4.3)$$

normalised by the half-width of the channel, is depicted in Figure 6.11 as a function of the distance from the wall. Finally the turbulent kinematic viscosity normalised by the friction velocity u_T and the half-width of the channel, is illustrated in Figure 6.12. In all of the above comparisons, a satisfactory agreement with the results obtained by Peric who used a different pressure correction approach for the flow analysis, can be observed everywhere across the channel.

6.4.2.2 Developing turbulent flow in a straight duct of square cross-section

As a second three-dimensional turbulent flow test case, the developing turbulent flow in a straight duct of square cross-section is simulated. The turbulent flow in a straight duct of non-circular cross-section is characterised by the presence of transverse mean secondary flow even in the fully developed flow regions. This secondary flow defined by Prandtl as secondary flow of the second kind, is a result of Reynolds stress gradients in the corner region. Although the magnitude of the secondary velocity is only a small percentage (2-3%) of the streamwise bulk

velocity, it exerts a significant influence on the global and local properties of the flow. The contours of the axial mean velocity bulge outwards near the corners as a result of the transport of high-momentum fluid from the core fluid to the corner regions through the circulatory transverse flow.

Although experimental investigations on fully developed flows in non-circular ducts were conducted by many workers, available experimental data are scarce for the case of developing turbulent flow. Gessner, Po and Emery (1979), reported a thorough experimental investigation on the three-dimensional developing flow in a square duct at a Reynolds number of 250,000. Melling and Whitelaw (1976), performed Laser Doppler measurements at two axial stations of the square duct at a Re = 42,000. The experimental data from both the above investigations have been used by many workers especially for the validation of turbulence models and are used for comparisons with the present predictions.

It is generally accepted that a turbulence model using the assumption of an isotropic eddy viscosity, as the k-ϵ model, can not predict the secondary motion and a more refined modelling of the turbulent stresses is necessary, Launder and Ying (1973), Naot and Rodi (1982), Demuren and Rodi (1984). There have been several attempts to analyse the nature of the turbulent flow in non-circular ducts. Due to the complex nature of the secondary motion in these flows various ways of modelling the Reynolds stresses have been proposed based on simplifications of the transport equations for these stresses , giving rise to Algebraic Stress Models. At this stage, however, only results obtained with the use of the k-ϵ model will be presented. However, it should be mentioned that the adoption of an Algebraic Stress Turbulence Model and its incorporation in the current computational model which uses a non-staggered grid arrangement is not straightforward and special care should be taken on where the Reynolds stresses are located on this grid. The author of the present work experienced an apparent oscillatory distribution of the transverse velocities when the Reynolds stresses are located at the same location with the rest of the flow variables. A remedy to this problem might be either the staggering of

the locations of the Reynolds stresses from the grid nodes where all the flow variables are stored, Choi et al (1989), or the implementation of special interpolation techniques and other numerical measures if the collocated variable approach is to be retained for the Reynolds stresses as well, Obi et al (1991), Cho and Fletcher (1991).

Figure 6.14a shows the predicted axial centreline velocity compared with the experimental data obtained by Gessner et al. There is an increase in the centreline velocity as far as z/D = 40 as a result of the boundary layer growth on the walls confining and accelerating the core fluid. Subsequently the centreline velocity decreases as a result of the redistribution of the momentum across the duct through the secondary circulatory motion. The predictions agree with the measurements quite well in the initial part of the duct but indicate their peak value at z/D = 35. After this station the centreline velocity reduces and tends asymptotically to the value measured for the fully developed turbulent flow. The corresponding predictions for the experiment carried out by Melling and Whitelaw are shown in Figure 6.14b. The centreline velocity along the duct presents a trend similar to that of the previous experiment. The peak of the ratio W/W_{in} occurs at z/D = 25 and it becomes almost constant before it falls gradually.

The boundary layer development along the duct for the flow conditions of Gessner, Po and Emery (1979), can be observed in Figure 6.15. The axial velocity profiles are plotted against the distance from the wall bisector. The gap between the predicted values and the experimental data is greater at the z/D = 24 and z/D = 40 stations. This occurs due to the insufficiency of the k-ϵ model to deal with the turbulence-driven secondary flows and the subsequent bulging of the axial velocity contours outwards to the corner bisector and inwards to the wall bisector.

The grid employed for the simulation of the experiment performed by Gessner et al had 14 by 14 nodes covering one quarter of the cross-plane because of the symmetry of the flow and 48 planes covering 60 widths length of the duct, Figure

6.13. The computations were performed on a DEC 5000/200 computer system and reached convergence after 520 iterations requiring 10760 sec of CPU time or 0.0022 sec per grid point per iteration.

6.4.2.3 Flow in a curved passage of rectangular cross-section

In order to check the capability of the presented computational method to treat strong curvature in the longitudinal direction, the turbulent flow in a 90 deg bend of rectangular cross-section was calculated.

This calculation simulated the experimental conditions reported by Pratap (1975). Figure 6.16 shows the configuration of the curved duct. The test section of the duct was rectangular and the height and the width were equal to 1.22 m and 0.304 m respectively. The duct curved through 90 deg with a centre line radius of 2.52 m.

The flow domain for which computations have been carried out consisted of a 1.22 m long straight section and the 90 degrees of the curved duct. Only half of the width was considered because of the symmetry of the flow. The grid which was employed consisted of 14 nodes in the ξ, 16 nodes in the η and 34 nodes in the streamwise ζ direction. The polar angle between the cross-sectional planes in the curved part was equal to 3.75 degrees. The grid was not uniform more points being clustered in the near-wall region.

The Reynolds number based on the hydraulic diameter of the duct and the mean velocity was 700,000. A uniform static pressure was specified at the inlet plane of the calculation domain and the rest of the flow conditions were fixed according to the experimental measurements at the location 1.22 m upstream of the curved part. At the solid walls, the no-slip condition is considered with the pressure gradient normal to the wall set equal to zero. At the symmetry plane, the normal velocity component, u in this case, is set equal to zero with the rest of the flow variables extrapolated from the adjacent plane. At the outlet plane, the flow variables are

extrapolated from their values at the upstream grid nodes. In the initial "guess", the velocities are taken from the inlet profile, with the flow direction changed smoothly through 90° around the bend and no cross flow is assumed present.

The predictions showed a complex three-dimensional flow pattern due to the secondary motion driven by the strong pressure gradient induced by the curvature. Two counter-rotating vortices were found to exist with a maximum velocity of the secondary motion about 20% of the maximum primary velocity. This secondary motion is shown, for the 75 deg plane, in Figure 6.17 where only half of the duct is plotted. As a result of this secondary motion, the primary velocity profiles were distorted and showed a maximum towards the inside of the curved duct. Figures 6.18 and 6.19 show the streamwise velocity profiles at the 11.35 deg and the 33.75 deg planes for distances X = 0.01 m and X = 0.02 m from the side wall of the duct. The velocities were non-dimensionalised with the magnitude of the total velocity W_c at the centre of the corresponding cross-sectional plane. The velocity shows a peak near the inner wall of the duct which occurred due to the pressure gradient developed from the inner to the outer wall and was caused by the curvature of the bend. This pressure distribution is presented in Figures 6.20 and 6.21 in terms of a C_p coefficient defined as:

$$C_p = \frac{p - p_c}{\frac{1}{2}\rho W_c^2} \qquad (6.4.4)$$

where index "c" denotes values at the centre of the cross-stream plane.

The C_p coefficient presents its maximum at the outer wall and this value reduces towards the inner wall due to the action of the centrifugal forces. The results obtained are in very good agreement with the measured values in most of the cross-sections of the duct.

The calculations were performed on a DEC 5000/200 computer system and convergent solution was obtained after 560 iterations of the marching procedure and

took 9300 sec of CPU time corresponding to 0.00206 sec per grid point per iteration.

6.4.2.4 Flow in low-aspect-ratio diffusers

To check the capability of the present analysis to treat flows with streamwise diffusion, the turbulent flow in low-aspect-ratio diffusers was studied. McMillan and Johnston (1970), (1973), conducted an experimental investigation of air flows in low-aspect-ratio rectangular diffusers of different outlet to inlet area ratios and for different Reynolds numbers. Figure 6.22 shows the configuration of the diffuser.

The present calculation simulated the experimental conditions reported by McMillan and Johnston (1970), for three diffusers of outlet to inlet area ratios equal to 2.1 : 1, 2.7 : 1 and 3 : 1 and with a fully developed turbulent flow at the inlet of the diffuser.

The computational inlet plane was located $0.8*W_1$ lengths upstream of the diffuser inlet section following the calculations performed by Rhie (1985), for the same test case. Only one quarter of the whole diffuser configuration was considered in the computations because the flow was symmetrical in both the cross-stream directions. A grid of 25 x 10 x 52 was used. Figure 6.23 shows the static pressure distribution along the diffuser for Re = 20,600 and Re = 50,600 in the case of the unstalled diffuser of an area ratio of 2.1 : 1. The local pressure recovery is expressed in terms of a C_p coefficient defined as:

$$C_p = \frac{p - p_{in}}{\frac{1}{2}\rho W_{in}^2} \qquad (6.4.5)$$

where p is the local static pressure, p_{in} is the inlet static pressure and W_{in} is the area-averaged inlet velocity. The C_p coefficient increases along the diffuser obtaining higher values for the higher Reynolds number. Generally the predicted values are in good agreement with the corresponding measured data. For the outlet to inlet area ratio of 2.7 : 1, the diffuser was characterised experimentally to operate in transitory

stall regime and flow separations were predicted for both Reynolds numbers. The predicted C_p distributions for this case are compared against the experimental results in Figure 6.24 where satisfactory agreement is demonstrated. For the area ratio of 3 : 1, transitory stall was reported experimentally for the lower Reynolds number, but fully developed stall for the higher Reynolds number where the flow separates from one wall but follows along the other. This is called bi-stable and cannot be treated using the current solution methodology which is steady and a symmetric boundary condition is enforced to the solution. However, the predicted pressure recovery is in reasonable agreement with the corresponding measured data, Figure 6.25.

At this stage it should be mentioned that the elliptic nature of the set of equations which is employed in the current computations was able to deal with separated flow regions irrespective of the size of these regions, as it was found in the cascade flow computations of the previous chapter as well. There is no special treatment, in the current method, which is activated when flow separation is experienced at the outlet boundary. This situation usually leads to divergence of the computational procedure and hence care should be taken to expand the computational geometry sufficiently far downstream, as it was mentioned in Section 6.2, in order to allow flow reattachment upstream of the outlet plane and within the computational regime. In the cases of the 2.7 : 1 and 3 : 1 area ratios diffusers where flow separation was predicted, a constant area rectangular duct was added downstream of the diffuser discharge to avoid flow separation at the outlet plane of the computational domain which might occur during the calculation procedure.

The necessary CPU time was typically around 20300 seconds on a DEC 5000/200 computer system for 710 iterations, corresponding to 0.0022 seconds per grid point per iteration.

6.5 Conclusions

The implementation of the proposed flow model to predict three-dimensional duct flows has been presented in this chapter. The appropriate boundary conditions valid for various boundaries and the amended form of the pressure correction scheme, are presented. The model has been validated through its application for the flow prediction in two laminar and totally ten different turbulent flow cases. The laminar flow cases have proven that the computer code can be used reliably to predict with very high accuracy laminar flows even on highly non-orthogonal grids which is inevitable feature in most of the finite volume flow computations through complex ducting configurations used in turbomachines. The turbulence scalars are well-correlated with other predictions at the fully developed regime of the straight channel flow. However, the use of the standard k-ϵ model is inadequate for the accurate computation of corner flows. The flow model yields good predictions in the case of the bended duct where is required to treat strong curvature in the longitudinal direction which causes strong pressure gradients on the cross stream planes. When a strong streamwise diffusion is present, the flow may separate and the elliptic nature of the form of the governing equations which are employed, allows the model to deal with these separated flow regions independently of their size.

CHAPTER 7

Flow in centrifugal compressors

7.1 Introduction

The three-dimensional elliptic code, developed for this thesis, which has sofar been applied to predict two-dimensional compressor cascade flows and three-dimensional duct flows, is now implemented for modelling the flow through the complex passages of a series of centrifugal compressors. The effects of compressibility are considered through the solution of the energy equation for the transport of rothalpy and the perfect gas law. The tip clearance effects on the relative flow pattern are important and are appropriately simulated. In the cases which are tested the casing wall is stationary and the magnitude of the tip gap can be adjusted.

In this chapter, a brief review of the experimental attempts to map the internal flow field through the passages of centrifugal compressors, is presented. Subsequently, theoretical calculations with the current method are performed and the results are compared critically with available experimental data and with results from other computational models. Three high-speed subsonic compressors with different geometrical and operating characteristics are analysed at design and off-design conditions. In all cases, a jet/wake flow pattern is pronounced and strong secondary flows are discerned. The predictive capability of the current flow model is judged to be fairly satisfactory taking into account the limitations of the physical models and the numerical schemes involved in the computations.

7.2 Summary of experimental investigations

Each of the computational tools presented in the review of Chapter 1 and implemented for the flow prediction in centrifugal compressors, is based on different theoretical model assumptions and numerical methodologies and has its own limitations. Hence, despite the predictive successes, much more work is required for more accurate predictions of the turbulent flow field and for the identification and quantification of the loss mechanisms especially at off-design conditions.

The further development of advanced computational tools can not progress without their validation against high quality, detailed and extensive data on modern impellers. A thorough examination of the already existing data reveals that the length of our database is very limited and much more effort is required for the acquisition of "benchmark" data for the evaluation of the computational viscous flow methods, the calibration of the physical models which are employed and the development of more sophisticated approaches in terms of physical modelling.

The "state of the art" in the technology of centrifugal compressors during the seventies, is presented in the AGARD CP-282 (1980) and in the ASME Conference Proceedings on performance prediction of centrifugal pumps and compressors, ASME (1980). A number of good summary articles have been presented as part of the von Karman Institute lecture series on flow in Centrifugal Compressors (1984). Elder and Forster (1987) provide a description of a series of investigations in a variety of low speed and high speed impellers. A few historical notes are summarised here.

Hamrick et al (1954) studied the internal flow field of a 48 inch (1.2102m) diameter radial inlet impeller and presented results in the form of relative velocity and relative pressure loss contours. With the use of a total pressure probe within the passage, they obtained a comprehensive map of the total pressure losses through the impeller for a wide range of mass flows. A significant observation of this study was the absence of low-energy fluid on the pressure side and the appearance of the high

loss region at the shroud towards the suction surface of the blades. From the pressure contours along the geometric streamlines, pressure gradients normal to these streamlines could be calculated and the corresponding secondary flow patterns could be plotted.

Fowler (1966) tested a 78 inch (1.9812m) diameter impeller rotating at low speeds of 30 to 70 rpm. The flow measurements in the rotating frame were carried out by placing a technician at the centre of the rig who rotated with the blade passages!! Using low inertia wool tufts they were able to photograph the strong unsteady flow and using hot wires they measured the flow velocities in several planes of the rotating passage.

Eckardt (1976), performed detailed measurements, using a Laser-2-Focus velocimeter, in a high speed impeller with a radial discharge. This non intrusive measurement technique was used for the first time to plot the flow velocity through the impeller passages for five measurement planes. Eckardt observed flow separation from the blade suction side and the rapid development of a wake pattern in the impeller's radial part. Just before the separation point, a sharp drop in fluctuation intensity along the shroud was identified which was attributed to the turbulence stabilisation due to the effects of channel curvature and Coriolis forces. The effects of the blade backsweep on the performance and on the local flow phenomena of the same high speed impeller were presented by Eckardt (1980). The potential flow model, Schuster and Schmidt-Eisenlohr (1980), which was used to predict the above mentioned flow fields, proved inadequate to describe the separated flow regions and the distortion of the streamwise velocity profile at the impeller exit.

Krain (1988) presented results of laser measurements in the blade passages of a backswept impeller. Despite the distortions of the throughflow field and the substantial diffusion of the relative flow, a smooth velocity profile was observed at the rotor discharge that was quite different from the typical jet/wake flow pattern found in all the previous investigations. The work of Eckardt and Krain contributed

towards the understanding of the effects of geometry on the obtained flow field and the quality and comprehensiveness of the provided experimental data attracted the interest of several flow modellers to use them for "benchmark" comparisons against their theoretical results.

Moore and Johnson (1983) carried out detailed flow measurements in a low speed shrouded impeller using pressure probes which were rotating with the impeller. They measured all three velocity components and the rotary stagnation pressure with 5-hole pressure probes which rotated with the impeller. The action of the secondary flows at the surfaces of the blade moving low relative stagnation pressure fluid to increase the boundary layer thickness and the size of the wake, was clearly observed. The same research compressor was used later by Farge et al (1989) to study the effects of the tip-leakage and by Johnson and Farge (1991) to study the effects of inlet distortion on the internal flow field.

Fagan and Fleeter (1990) performed a series of experiments using Laser Doppler Velocimetry in order to investigate the 3-D flow field in the passages of a low speed research mixed-flow centrifugal compressor at its design point. The application of a modern viscous flow model to predict the compressor flow field was moderately successful and the requirement for improvements in accuracy and further development of the model, was underlined.

Joslyn, Brasz and Dring (1990) described the outset of a centrifugal compressor research programme at United Technologies Research Centre with detailed static pressure distributions and surface flow visualisation on an unshrouded centrifugal compressor impeller.

The new low-speed centrifugal compressor facility at NASA Lewis Research Centre, Hathaway et al (1991), has been built to provide a more detailed understanding of the complex nature of the flow phenomena occurring in the curved rotating passages of centrifugal compressors and to obtain high quality "benchmark"

experimental data for the verification of three-dimensional Navier-Stokes solvers.

The experimental work at Cranfield continues providing three-dimensional flow data in a small high-speed impeller, Ahmed and Elder (1990), using a novel Doppler anemometer, and obtaining a series of Laser Transit Anemometry measurements inside the blade passages of a high speed Rolls-Royce impeller of current in service engines, at 80% speed and at two operating conditions, Forster (1988a) and (1988b). The measured flow field data in this impeller, indicate a curvature dominated flow, with a wake flow pattern observed on the casing wall of its radial discharge and a jet pattern close to the hub wall.

The above studies have shown that a jet/wake flow pattern is present at the outlet of a centrifugal compressor impeller which causes penalties in efficiency. The major mechanisms which contribute to the formation and development of the wake include the secondary flows induced by the curvature from axial to radial and in the tangential direction, and by the rotation of the impeller; boundary layer growth on the suction and pressure sides of the blades and on the hub and casing walls; flow separation on the suction side towards the shroud wall; operating speed, flow rate and geometry of the blade passage; and tip leakage flows in the case of unshrouded impellers. In an unshrouded impeller the casing wall moves relative to the other three walls of the channel and the boundary layer on it modifies the flow in the channel. In addition, the existing running clearance between the impeller blades and the stationary casing wall allows fluid to pour past the blade, against the direction of rotation, from the high to low pressure face. The tip leakage flow displaces the wake from the casing-suction surface corner region towards the middle of the passage location, Goto (1990).

The complicated interactions of the above flow phenomena render the accurate theoretical representation of the flow field in a centrifugal compressor a significantly difficult task. The losses in stage performance associated with this flow field provide a challenging incentive for viscous flow models to contribute towards

the achievement of improved compressors aerodynamic performance through the further physical insight and understanding of the complex flow features.

7.3 Model Assumptions

The flow in centrifugal compressor impellers has been investigated using the compressible flow model which was presented in Chapter 2. The calculation of the rothalpy values is performed through the solution of the partial differential equation 2.2.3. In addition, an alternative form of the energy equation can be utilized in the computer code which assumes that the rothalpy remains constant inside the impeller passage. The latter assumption although not strictly valid in the boundary layer regions, is more economical in terms of computational effort because it does not require the solution of the energy equation and was found to give almost identical results for the parameters which were compared. The results which are presented in the following sections are obtained by solving the energy equation in order to be consistent with the presented theoretical model.

The numerical scheme which is used in the computations presented in this chapter is the Upwind numerical scheme which is known to be more stable than other schemes and is capable of providing the computer code with very good robustness. Obviously, there are some penalties in terms of accuracy which are discussed in Lapworth (1987). A compromise which is chosen is to use the Hybrid scheme for the discretisation of the convective terms on the cross planes and to use the Upwind scheme to discretize the streamwise convective terms.

The calculation of the source term of the governing equations, Section 3.2, is the most expensive part of the computations and requires approximately 50% of the total computational effort. In the current three-dimensional computations the "compressible part" of the source term of the i-momentum equation which expresses the transformed divergence of the dilation term, has the form:

$$\frac{\partial}{\partial \xi_s}\left[(\mu+\mu_T)\cdot\frac{\partial \xi_s}{\partial x_p}\left(-\frac{2}{3}\delta_{ip}\left(\frac{\partial u_m}{\partial \xi_n}\cdot\frac{\partial \xi_n}{\partial x_m}\right)\right)\right] \qquad (7.3.1)$$

This consists of 27 terms in total and is neglected in the computations without any serious penalties in the accuracy of the predictions for the subsonic flows which have been studied in this chapter. The inclusion of the above term in the equations causes an increase in computational time of around 22%.

During the computer code development, the updating of the density values was initially performed after the end of each complete sweep. This approach worked successfully in the cases of the radial and the backswept impellers tested by Eckardt (Sections 7.5.1 and 7.5.2). However, in the case of the Rolls-Royce GEM impeller (Section 7.5.3) where the flow velocities are higher and the degree of non - orthogonality of the grid is also higher than in the impellers tested by Eckardt, the above relaxation practice was not satisfactory and in some cases caused divergence. The approach of updating the density values after the computation at each cross-flow plane, proved to be more stable and provided faster convergence.

The computer code which has been developed provides the option of a stationary or a rotating shroud in the absolute frame of reference and the level of the tip clearance gap can be adjusted appropriately. At the upstream inlet boundary, the flow can be considered axial or with a preswirl and the boundary layer features can be adjusted.

7.4 Turbulence model

The k-ϵ turbulence model which was used successfully in the previous chapters, is retained for the impeller flow computations. However, the standard k-ϵ turbulence model is modified to account for the effects of the streamline curvature and coriolis acceleration on the transport equations for the scalars k and ϵ. Wilcox and Chambers (1977), using a physical argument, showed that curvature and rotation

primarily affect the turbulent kinetic energy, and derived appropriate terms to account for these effects. They claim that with proper consideration of the physics of turbulent flow with streamline curvature, two equation turbulence models can naturally predict flows with streamline curvature and coordinate-system rotation. The model which they proposed, is expected to apply naturally and not in an empirical manner, in two-dimensional flows but its direct applicability in 3-D flows has not been assessed through comparisons with experimental turbulence data and can only be speculative.

The additional terms to the k and ϵ equations which were suggested by Wilcox and Chambers, are adopted in the present study in a form suitable for centrifugal compressor flows which has been provided by Rhie et al (1984). The modification to the standard k-ϵ model is performed by adjusting the equations (2.5.4) and (2.5.5) for the transport of k and ϵ to include the additional contribution G_c due to the effects of streamline curvature and rotation on the local turbulence structure. The term G_c is given by:

$$G_c = 9\,\Omega\,\tau_\Omega - \frac{9\,V_{eff}\tau_\theta}{2R} \qquad (7.4.1)$$

where τ_Ω and τ_θ are the local mean shear stress components normal to the coriolis acceleration and streamline curvature respectively; V_{eff} is the local velocity and R is the local streamline radius of curvature. In order to simplify the implementation of this modification, the streamwise local coordinates ζ are assumed to be approximate streamlines for the evaluation of the radius R, which is an acceptable assumption taking into account the empirical nature of the above approximation and the relatively coarse grids which are used in the computations.

7.5 Predicted Centrifugal Compressor Flows

The computational method presented in the Chapters 2 and 3 is implemented for the prediction of the flow in a radial centrifugal compressor operating at its

design point and in a backswept impeller at its design and choking conditions. These two impellers were experimentally tested by Eckardt (1976) and (1980). Eventually the flow through the Rolls-Royce GEM impeller is also simulated. Experimental tests for this impeller, operating at its design and near surge conditions, were carried out at Cranfield by Forster (1988a) and (1988b).

7.5.1 Eckardt's Radial impeller

7.5.1.1 Boundary conditions and computational grid

As a first test case, the current method is applied for the prediction of the flow in the high-speed centrifugal compressor impeller for which Eckardt (1976) performed detailed flow investigations. These data were selected for their high quality which render this centrifugal compressor flow one of the most carefully documented in the literature. From the laser and hot wire anemometry results combined with instantaneous pressure measurements, the relative velocity profiles show the development of a jet/wake flow pattern and the mixing of the jet and the wake in the impeller discharge flow.

The geometry of the impeller, provided in Appendix D, is constructed according to Schuster et al (1980) and is described by equations for elliptic-shaped blade camber lines in cylindrical sections, and for circular-arc hub and shroud lines. An alternative source of reference from which the impeller geometry can be reconstructed, has been provided by Moore (1976). An outline of the three dimensional complete impeller geometry is shown in Figure 7.1. The grid system which is employed in the computations is obtained using the above profile equations and by fitting cubic splines through the added thicknesses which are taken approximately from Eckardt's plotted graphs of the streamwise velocity distribution, Eckardt (1976), since they could not be obtained from any other source. The grid is constructed using cross-stream planes through the impeller in such a way that five of the computational planes are coincident with the five measurement stations for which measured velocity data from laser traverses are available, thus allowing a

direct comparison between the computed and the measured results. Figure 7.2a shows the geometrical domain and the outline of the grid which is used to cover the impeller passage, the upstream region and the vaneless diffuser. The shroud and the vaneless diffuser downstream of the impeller are stationary and the impeller is assumed to operate with a clearance gap of 1% of the local blade height.

The location of the five measurement stations is indicated schematically in Figure 7.2b and the computational grid which covers each of these stations is presented in Figure 7.3. The blade to blade surfaces are covered with grids similar to the one which is illustrated in Figure 7.4a for the mid span surface and the meridional grid surfaces are covered with the grid shown in Figure 7.4b.

The computations start with axial flow upstream of the impeller inlet, proceed through the rotor passage to its radial exit and march from the impeller outlet at radius R_2 = 0.2 m to the constant area diffuser up to a radius ratio of R/R_2 = 1.35.

The three dimensional structured grids which are used in the computations are constructed algebraically with simple rules and exponential clustering of the grid points in the near wall regions. In the blade to blade planes, the grid is of a shear-type. Previous studies of the Eckardt's impeller, Hah et al (1988), showed that relatively coarse grids can capture most of the flow phenomena occurring inside this impeller geometry. Two different computational grids consisting of 20 x 20 x 50 points and 32 x 32 x 65 points, are employed for the present study. The predictions based on the fine grid present negligible changes compared to those obtained on the coarse one and hence the 20 x 20 x 50 grid can be assumed to provide solutions which are almost grid independent. The results which are presented in the next section have been obtained on this coarse mesh. In the streamwise direction 28 cross-planes are located inside the rotor passage. Three of the grid points in the hub to shroud direction are located in the tip region.

The flow is modelled at the compressor's maximum efficiency condition, that

is, a rotational speed of 14000 rpm and a mass-flow rate of 5.31 kg/s. The impeller tip speed is equal to 293.2 m/s and the measured values of total-to-total pressure ratio and efficiency are equal to 2.094 and 0.88 respectively.

At the inlet of the flow domain a total pressure equal to 1.0133 bar and a uniform total temperature equal to 288.1 K are taken. The flow upstream of the impeller is assumed to be axial and in the absence of information on the velocity profile, an inlet boundary layer thickness of 15% of the hub to shroud distance is defined on the shroud surface and a thickness of 1% on the hub. A uniform static pressure is maintained at the inlet. The turbulence parameters are kept uniform at the inlet based on an inlet turbulence level of 4%. The rothalpy profile at the inlet plane is calculated through the velocity components and pressure values at the inlet plane.

The flow is simulated in the rotating frame of reference where it is assumed to be steady, and the velocity components of the momentum equations are the relative ones. The absolute velocity on the stationary shroud and the diffuser walls are set equal to zero. This is equivalent to setting the relative velocity vector equal to $-\vec{\Omega}x\vec{R}$ in the grid points which are located on these boundaries where $\vec{R}$ is the local radius from the axis of rotation. The relative velocity is set equal to zero on the impeller blades and on the hub. The walls are assumed to be adiabatic. Along the periodic boundaries upstream and downstream of the impeller passage a circumferentially repeating condition is imposed for all flow variables.

The periodic boundary condition is also employed for the grid points which are located in the tip gap. The grid which is located in the tip clearance gap presents the structure which is illustrated in Figure 7.5. The blade is considered to have a sharp edge at the tip which is found to be an appropriate assumption which does not introduce significant errors in the case where the blade thickness is small at the blade tip as is the case in many centrifugal impellers. This assumption simplifies the computer coding because it treats the tip region without any alterations of the

general computational procedure apart from the implementation of the periodicity boundary condition in this region. In the case of axial flow compressors and especially turbines where the blade thickness is considerable at the tip, the assumption of a sharp edge will cause a highly non-orthogonal grid in the clearance region and poor grid resolution for the flow phenomena occurring in the gap. In this case a different approach has to be followed which utilizes an additional structured grid to cover the tip gap which cannot be treated directly by the general computational procedure but it requires additional coding.

At the exit of the flow domain, all the independent variables are obtained by extrapolating their values from the plane immediately upstream.

7.5.1.2 Computational results

The predicted primary velocity contour plots at the five measurement planes are illustrated in Figure 7.6b. The contour lines are produced by fitting cubic splines through the computational values obtained at the 20 x 20 grid points in each of the measurement planes. The results are compared with Eckardt's measurements as they are presented in contour plots by Moore and Moore (1980b) and shown in Figure 7.6a. The velocities are normalised by the impeller tip speed $\Omega * R_2$.

At all stations the velocity distribution demonstrates a large region with potential flow characteristics. One of the major features of the flow is the boundary layer thickening on the casing wall commencing at station III and its rapid growth at the downstream stations.

The substantial blockage caused by the growing wake, results in the displacement of the main flow towards the pressure side of the hub wall. This can be observed from the velocity contours. For example, consider the 0.4 contour which follows an anti-clockwise motion in the impeller passage, its position is found near the suction/shroud corner at plane II, moves towards the suction side at plane III,

occupies the hub/suction corner at plane IV and eventually moves to the pressure side of the passage to occupy the largest area of the cross-stream plane at plane V.

The wake is located near the shroud-suction corner and grows rapidly after the plane III. A jet flow pattern is also captured at the suction side of the hub wall at plane V, indicated by the contour $V_m/(\Omega^*R_2) = 0.5$. In general, good agreement is shown at all the meridional planes. The discrepancies observed at plane I could be attributed to errors in the blade thickness distribution around the blade leading edge which has been estimated empirically from Eckardt's presented graphs and to the assumptions which have been made about the boundary layer thickness at the upstream inlet boundary of the passage.

The distribution of the streamwise velocity at station V, obtained by Moore and Moore (1980b) from a computation with a stationary shroud and 1% tip clearance using a partially parabolic approach with a mixing length turbulence model, is illustrated in Figure 7.7. When this plot is compared with the current predictions and the corresponding experimental data, it can be concluded that the current method is capable of providing a better agreement with the experimental data for the exit velocity distribution than Moore's partially parabolic method.

The results of a study of the effects of the tip clearance magnitude and the boundary condition for the shroud wall, which is assumed to rotate with the impeller or remain stationary, are illustrated in Figure 7.8. For each shroud boundary condition, the tip clearance size is considered to be successively equal to 0%, 1% and 2% of the local blade height, yielding totally six different test cases. In the case of 1% tip leakage, 3 grid points are uniformly distibuted in the tip gap whereas in the case of the 2% gap, 4 points are used. In the case of zero clearance, the stationary shroud causes the wake region to move away from the suction/shroud corner where it is found when the shroud rotates with the impeller. The increase in the tip gap tends to influence the position of the wake which, in the case of a rotating shroud, is carried away from the suction/shroud corner region towards the

shroud wall in a clockwise manner, or moves further towards the mid passage region of the shroud wall when the casing remains stationary. In addition the area of the low velocity region increases slightly as the tip gap increases.

The calculated static pressure distribution on the shroud wall normalised by the inlet total pressure, is compared with the measured values in Figure 7.9a. The contours demonstrate very good agreement and exhibit the development of the blade to blade pressure gradients and the steep pressure rise in the radial part of the impeller to yield a 1.5 pressure ratio at the impeller discharge. The colour plot of Figure 7.9b shows a three-dimensional view of the non-dimensional static pressure distribution on the walls of the impeller passage.

The blade-to-blade predicted velocity vectors at mid-span, near-hub and in the middle of the tip-gap surfaces are presented in Figure 7.10. Velocity vectors in the meridional planes near the pressure, the suction and on the mid-pitch surface are shown in Figure 7.11. Low energy fluid is transported radially towards the shroud surface close to the blade surfaces and afterwards it moves across near the shroud forming two counter-rotating vortices which dump this boundary layer fluid into the wake region. This motion explains the rapid increase in the wake size between planes III and V.

The secondary flow pattern predicted at the impeller outlet plane is shown in Figure 7.12a. Three discrete secondary flows can be observed, as previously found in Rhie et al (1984); a major anticlockwise vortex moves along the hub, pressure side and casing wall, a weaker second motion dumps low energy fluid into the wake region from the suction surface and finally the tip leakage flow increases the wake size. It appears that air or relatively high energy from the pressure side of the passage, pours the clearance space, expands into the area of the suction surface, and moves the low-energy air along the shroud. The same pattern is more clearly observed when a fine grid of 32 x 32 x 65 is used in the computations and is depicted in Figure 7.12b.

A qualitative approach for the visualisation of the secondary flows in the impeller is performed by defining the trajectories of particles which are released at various locations of the cross-stream computational plane at the entrance of the passage, as shown in Figure 7.13. The particle trajectory prediction model, Tan (1988), is based on the solution of a set of particle equations of motion in the flowfield obtained with the current flow model. The particles are assumed to be spheres of 5 μm diameter and of uniform density of approximately two orders of magnitude greater than the air density. It can be discerned that the particles which are located very close to the shroud wall are driven by the tip clearance flow and move along the shroud opposite to the direction of rotation.

The loss analysis at the impeller exit is performed through the definition of the relative total pressure. According to Eckardt (1976) the relative total pressure P_{rel} referred to the inlet stagnation pressure P_0 is given by:

$$\frac{P_{rel}}{P_0} = e^{-\frac{s}{R}}$$

where R is the gas constant and s is the entropy distribution which is related to the static pressure p and static temperature T through the relation:

$$s = C_p \ln\left(\frac{T}{T_0}\right) - R \ln\left(\frac{p}{P_0}\right)$$

where T_0 is the inlet stagnation temperature. By definition the isobars $P_{rel}/P_0=1.0$ enclose areas of isentropic fluid.

The predicted and experimental relative total pressure distribution normalised by the isentropic total pressure, at plane V, is illustrated in Figures 7.14a and 7.14b. Both of the plots show the high-loss region in the position where the wake appears in the velocity contour plots, Figure 7.6. Despite the $\pm 2\%$ uncertainty of the measured values, it is felt that the experimental results agree closely with those computed using the proposed method although there currently exists in the predictions a spreading of the contours representing the relative total pressure levels from 0.90 to 0.96 which in the experimental results appear to be condensed in a

smaller area exhibiting a more rapid change from the inviscid to the wake flow region. In addition, the shape of the contour lines in this region indicates that the secondary flow along the shroud wall which accumulates low energy fluid into the wake region, is underpredicted in the computations. This spreading and difference in shape of the contour lines can be attributed to the limitations of the currently used turbulence model which is based on the assumption of an eddy viscosity which is unique for all Reynolds stresses and its calibration is originated from different flow conditions than those encountered in rotating impeller passages. Additionally the differences between the experimental and the computational results are due to the strong numerical diffusion introduced implicitly through the upwind definition of the convective flux.

Interestingly, calculation with a stationary shroud and without tip leakage produces the relative total pressure distribution shown in Figure 7.14c where the relative total pressure contour levels have been increased, especially in the wake region, illustrating the impact of the tip leakage on the loss production in the impeller.

The results which were obtained by Rhie et al (1984) using a partially parabolic approach, are shown in Figure 7.14d. There is a good agreement with the current predictions of Figure 7.14b both qualitative and quantitative. However, there are slight differences and it can be observed that the present flow model predicts a larger isentropic region in the hub - pressure side corner, than that provided by Rhie et al, which is in closer ageement with the measured pattern. From this comparison it can also be concluded that the partially-parabolic procedure is efficient as long as the leading edge effects remain relatively small which is the case for this impeller which has a lightly loaded inducer at design point. The large leading edge losses which were present in the Ghost impeller inducer studied by Lapworth (1988) with an elliptic flow model and Moore and Moore (1980a) with a partially parabolic process, caused an improved performance of the elliptic method for the loss prediction at the impeller's exit as compared to the partially parabolic approach.

Acceptable convergence was obtained using 695 iterations of the marching procedure and required 8.9 hours of CPU time on a DEC 5000/200 computer system, corresponding to 0.0023 seconds per grid point per iteration.

7.5.2 Backswept impeller

7.5.2.1 Operating and boundary conditions and computational grid

Centrifugal compressors with backswept blades at impeller exit have gradually replaced compressors with radially ending blades, because they offer improved efficiency and operating range as they present a better aerodynamic load distribution and reduced impeller tip Mach numbers. The second centrifugal impeller for which the present computational method is implemented, is a typical high-speed backswept impeller for which Eckardt (1980) described detailed measurements. Hah et al (1988) assess critically the quality of these test data and their uncertainties and utilize them to validate their computations using a Navier-Stokes method.

The backswept impeller is very similar to the radial one described in Section 7.5.1 and its geometry is constructed according to Schuster and Schmidt-Eisenlohr (1980) and is described in Appendix D. Both impellers have the same tip diameters, shroud contours, axial lengths and blade numbers (20 blades). The blade camber lines of the backswept impeller have an elliptic shape in cylindrical sections which follows the same construction relations as the radial impeller.

The backward curvature commences at $R/R_2 = 0.8$ and terminates at a blade exit angle of 60° (30° of backsweep). The inducer inlet area is reduced in the backswept impeller and the hub profile is different from that of the radial impeller.

The compressor operates at a rotational speed of 14000 rpm firstly at its maximum efficiency condition at a mass-flow rate of 4.54 kg/s. The rest of the inlet conditions and all the boundary conditions are identical to those used for the radial impeller and are described in Section 7.5.1.1. The 20 x 20 x 50 computational grid

is also similar to that used for the radial impeller.

7.5.2.2 Computational results for Design condition

The primary velocity contour plots at the five measurement planes are shown in Figure 7.15 where they are also compared against the corresponding Eckardt's measurements (1980).

The observed velocity distribution is similar to that found in the radial impeller. The velocity distribution exhibits potential flow features at planes I and II within the axial inducer. The blade-to-blade loading increases at plane III and the low energy flow area near the shroud wall thickens. The velocity distribution in planes IV and V show the wake development and the jet/wake structure at the impeller discharge. Comparing these velocity distributions with the corresponding distributions for the radial impeller, it can be observed that there is a circumferential unloading especially near the hub surface and a smoothing of the steep velocity gradients which occurs towards the exit of the backswept rotor. The backwards channel curvature appears to enhance the mixing process and consequently an extended potential flow area appears at the rotor exit. The above observation agrees with the results of the experimental investigations of Adler and Levy (1979) and Eckardt (1980), which show that the blade backward-curvature destabilizes the shear layers, weakens the secondary flows and reduces the feeding of the low-energy fluid into the wake. In general, good agreement between the predicted and the measured values is shown. Figure 7.16 and 7.17 compare the predicted streamwise velocity profiles at stations IV and V with the experimental distributions and the distributions predicted by Hah et al (1988) using a fully elliptic model. As it can be noticed, the present model provides a better correlation with the experimental profiles than Hah's distribution which appear to yield a rather smooth wake whose location is shifted towards the middle of the casing wall.

The computed static pressure distribution on the shroud wall in terms of isobaric lines of pressure ratio p/P_0 is illustrated in Figure 7.18a where a very good

agreement exists with the corresponding measured results. Figure 7.18b illustrates the three-dimensional distribution of the non-dimensional static pressure on the blade surfaces and on the casing wall. The predicted pressure values within the inducer develop similarly to those in the radial rotor. In the downstream radial region, the pressure rise is governed by centrifugal forces yielding a steep rise in the radial direction.

The blade-to-blade pressure variation in the radial region of the impeller characterises the local energy transfer rate and is smoother (less abrupt) in the backswept than in the radial impeller.

The developed secondary flow patterns are similar to those predicted for the radial discharge impeller. The calculated velocity vectors in three blade to blade and three meridional grid surfaces are illustrated in Figures 7.19 and 7.20 respectively. The calculated particle trajectories in the passage of the backswept impeller are shown in Figure 7.21. The trajectories of the particles which are released from the hub boundary layer region roll in a clockwise manner opposite to the direction of the rotation. As they emerge radially from the rotor outlet they cannot maintain their already low radial momentum and are carried away tangentially by the high momentum fluid.

The predicted relative total pressure distribution normalised by the isentropic total pressure, at plane V, is illustrated in Figure 7.22, where it is compared with the measured distribution. The position of the predicted wake is shifted towards the suction/shroud corner of the impeller outlet. The discrepancies between the predicted and the experimental data can be attributed to the uncertainties in the experimental data, the limitation of the turbulence model which is employed and the inaccuracy of the first order numerical scheme which is used for the discretization of the convective term. Other areas of uncertainty are in the inlet conditions of the impeller, the blade geometry and thickness definition and the quite crude simulation of the tip clearance flow using only three grid points.

A calculation without tip-leakage provides a distribution with higher levels of relative total pressure contours as illustrated in Figure 7.22c. The clearance jet causes the formed wake to move towards the centre of the shroud wall.

7.5.2.3 Computational Results for Off-design condition

Figure 7.23 shows contours of the meridional velocity in the five cross-planes at which Eckardt performed laser two-spot traverses. The experimental results have been obtained from Eckardt (1980) and Dawes (1987).

A strong wake develops on the shroud wall towards the suction surface and grows rapidly between planes III and IV. The rate of growth decreases downstream of the plane IV till the exit of the rotor. The growing of the wake displaces the main flow towards the pressure side of the passage and a jet-wake pattern is clearly observed.

The three-dimensional distribution of the non-dimensional static pressure distribution p/P_0 on the walls of the impeller passage, is given in Figure 7.24. The predicted pressure rise for this operating condition presents the same characteristics to those which have been predicted for the design condition, Figure 7.9b, but with actual pressure levels significantly lower.

The secondary flows in the impeller follow similar patterns to those predicted in the radial impeller and are discussed in Section 7.5.1.2. The blade to blade velocity vectors in grid surfaces which are located close to the hub, mid-span and inside the clearance gap are shown in Figure 7.25. The flow vectors in meridional planes near the pressure, the suction and the mid-pitch of the impeller passage are plotted in Figure 7.26. The trajectories of solid particles which are released at the leading edge cross-flow plane close to the suction surface of the blade, are shown in Figure 7.27. The trajectories of the particles which start from the near-hub region roll in a clockwise manner and follow the vortex which appears to carry low energy

fluid from the hub along the suction surface. As soon as these particles reach the downstream vaneless diffuser, they turn very abruptly to the tangential direction as they are carried away by the high momentum fluid coming from the neighbouring leading passage.

The relative total pressure distribution at plane V is shown in Figure 7.28. The agreement between the predicted and the measured values is remarkable and the position of the wake away from the suction/shroud corner is accurately predicted. As expected, the level of losses is larger than at design condition, Figure 7.22, and demonstrate the capability of the present method to respond to the increase in the mass flow. Figure 7.28c compares the same distribution to that presented by Dawes (1987) who used his time-marching Navier-Stokes analysis assuming no clearance gap. Again, the current model appears to capture more accurately the location of the wake region on the casing wall than Dawes's flow model.

The ability of the method to "sense" the change in the flow mass rate can also be exhibited in Figure 7.29 where the predicted adiabatic efficiency figures for the design and near choke conditions are compared with the measured efficiency curve as it is presented in Hah et al (1988). The experimental data for the rotor efficiency values are based on total pressure measurements at $R/R_2 = 1.075$ and temperature traverses at $R/R_2 = 1.687$. The numerical results are calculated by mass-averaging the predicted flow-field values at $R/R_2 = 1.0795$.

A very good agreement appears to be accomplished despite the various assumptions involved in the description of the inlet conditions and of the impeller geometry and the inherent limitations of the turbulence model.

7.5.3 Rolls Royce GEM impeller

7.5.3.1 Introduction

The GEM impeller was tested at Cranfield and is part of the axial + centrifugal compression system of a currently in service GEM engine. The impeller has a pressure ratio of 3.5 with a $\Delta H/U^2$ of 0.70 and represents the duty of a typical High Pressure stage of current axial + centrifugal compression systems. The impeller has a design tip speed of 586.75 m/s and a specific speed of 71.0 (Ai-Research definition). The impeller was designed in the early seventies using the latest "Quasi 3D" streamline curvature techniques, Birdi (1991). The geometry of the impeller was generated by using straight line ruling between the hub and the shroud. The unshrouded impeller has 19 blades, an axial inlet with a radius of 62.23 mm at the hub and 81.91 mm at the shroud, and discharges the air radially at a radius of 126.7 mm. The impeller has a backsweep angle of 40° from the radial direction and the current measurements were carried out using a vaneless radial diffuser downstream of the rotor.

Laser anemometry investigations were conducted at 80% speed (28300 rpm) and at two operating points on the impeller characteristic, one at peak efficiency and the other at a point near surge. A fairly comprehensive mapping of the flow patterns has been achieved at five planes, three of which are within the impeller, one just upstream of the blade leading edge and one immediately over the impeller exit. In this section, results are presented for the three planes inside the rotating passage and for the plane upstream of the leading edge, Figure 7.30a. The measurement system provides information about the magnitude V_α and the direction (α) of the mean absolute velocity vectors and its turbulent components, Figure 7.30b. The magnitude V_R and the direction (Θ) of the relative velocity vector are subsequently obtained from the local absolute velocity and the circumferential velocity. The error of the absolute velocity measurements is below ± 1 percent and the uncertainty of the absolute flow angle measurement is less ± 1 degree.

7.5.3.2 Computational grid - Boundary conditions

The geometry of the impeller is constructed according to data obtained from Rolls Royce, Pinot (1991). The shroud and the vaneless diffuser downstream of the rotor passage are stationary and the impeller is assumed to operate with a linearly distributed tip clearance between 1.2% of the local blade height at the leading edge and 2.9% at the trailing edge. The flow proceeds from the impeller discharge at radius R_2=126.7 mm to the diffuser up to a radius ratio of R/R_2=1.2.

The computations are carried out on three-dimensional structured grids of H-type. After a grid refinement study, it was found that a computational grid of 20 x 20 x 70 yields solutions which are sufficiently grid independent. In the streamwise direction 40 cross-planes are located inside the rotor passage. The locations of the five cross-stream planes at which laser traverses have been performed, coincide with grid planes in order to allow a direct comparison between the predicted and the experimentally obtained data. Three of the grid points in the spanwise direction are uniformly distributed in the tip gap region. An exponential clustering of the grid nodes has been implemented in the near wall regions of the blade to blade and hub to shroud direction, in order to facilitate the proper resolution of the viscous effects and the high gradients of the flow parameters occurring in these regions.

The compressor is simulated to operate at a rotational speed of 28300 rpm firstly at its peak efficiency condition at a mass flow rate of 0.823 kg/s and secondly at a point near surge at a mass flow rate of 0.705 kg/s.

At the inlet of the flow domain a uniform total pressure equal to 1.0132 bar and a uniform total temperature equal to 289.2 K are fixed. The flow is assumed to be axial and an inlet turbulent boundary layer thickness of 16% of the hub to shroud distance is defined on the shroud surface and a thickness of 5% on the hub. The turbulence parameters are kept uniform at the inlet based on an inlet turbulence intensity of 5%.

Damaged Page(s)

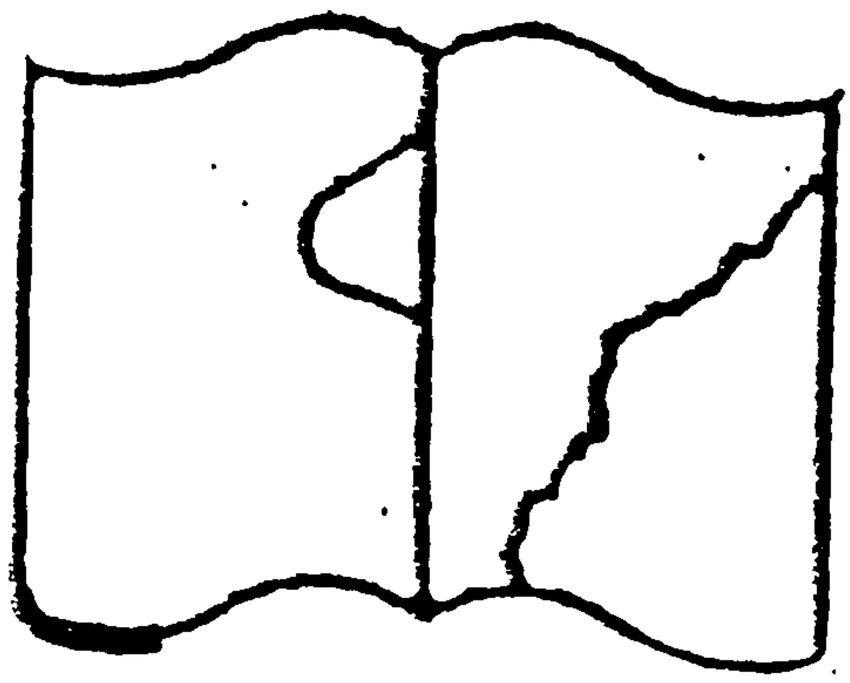

The boundary conditions which are applicable on the hub, shroud, blade and diffuser walls are identical to those applied in the study of Eckardt's impeller and are discussed in section 7.5.1.1. The periodic boundaries and the tip clearance region are treated similarly by explicitly imposing a circumferentially repeating condition for all the flow variables. At the exit of the computational domain, all the flow variables are updated through extrapolations from their upstream values.

In the following computations, sufficiently convergent solutions were obtained after 720 iterations of the marching procedure and required 8.94 hours of CPU time on a DEC 5000/200 computer system, which corresponds to 0.0023 seconds per grid point per iteration.

7.5.3.3 Computational results for Peak Efficiency condition

The predicted flow presents "potential flow" features at plane A just upstream of the axial inducer, as shown in Figure 7.31b. From the experimental results which are depicted in Figure 7.31a it can be clearly observed that the blade relative velocity is highest in the suction/shroud corner and decreases across the passage to the hub/pressure corner. The actual levels of the predicted relative velocity compare favourably with the measured ones, but the jet location is not picked up from the viscous computations. The main reasons which contribute to this are: (1) the poor modelling of the inlet conditions for which there is no information about the level of the blockage which is quite significant due to the extended intake, (2) the assumptions in the representation of the leading edge profile and local blade thickness distribution in this region.

At plane B the flow presents the same potential flow characteristics with a jet pattern closely attached onto the suction side towards the casing wall, Figure 7.31b. The measured velocities, as illustrated in Figure 7.31a, are generally "potential" in character with the highest velocity in the suction/shroud corner. However, there is a noticeable drop in expected velocity at the 2.03 mm depth (26%) especially in the

shroud/pressure corner. There is good correlation between predicted and measured values.

At plane C, the measured relative velocity pattern, as depicted in Figure 7.31a, shows the highest velocity contour to emerge in the hub/suction region and although no measurements were obtained in the shroud/suction corner, the contours suggest that velocity values in this region would be lower. There is a region of lower throughflow velocity on the shroud near the mid passage. The magnitude of this velocity is found to be only 42% of the highest velocity and this region is confined to the measurement section closest to the shroud (21%) depth.

The predicted jet pattern moves along the suction side of the blade to occupy the hub/suction corner of the passage, as depicted in Figure 7.31b. The level of the velocity is underpredicted in this region. On the shroud wall there is a deterioration of the relative velocity profile giving rise to the development of a wake pattern in the mid distance between the blades. The level of this profile deepening is accurately simulated. In Figure 7.32 a comparison between the predicted and the measured turbulence intensity is depicted. The lowest turbulence is on the hub and high turbulence region is captured on the shroud wall and is in very good correlation with the wake position according to the relative velocity contour plot. A very good agreement has been accomplished as far as the actual measured levels of turbulence intensity are concerned.

At station D, continuing its anti-clockwise movement inside the impeller passage, the computed jet flow pattern is attached very close to the whole hub wall, Figure 7.31b. The experimental plot of Figure 7.31a, exhibits a deficit in blade relative velocity for the centre of the blade to blade span near the casing wall. The calculated wake appears to be attached on to the shroud wall and there is good correlation to the measured values.

The distribution of the predicted static pressure normalised by the inlet total pressure, on the shroud wall, is illustrated in Figure 7.33a. The blade loading and

the rapid increase of the pressure in the radial impeller discharge can be observed. The predicted mass-averaged value of the pressure ratio p/P_0 at the rotor exit is equal to 1.6711 corresponding to a measured value of 1.7.

The relative total pressure distribution normalised by the isentropic total pressure, at the exit plane of the impeller, is shown in Figure 7.34. The location of the high loss region coincides with the region where the wake is observed in the laser measurements. On the hub/pressure corner of the passage, the loss presents its minimum value. The comparison of this distribution for the GEM impeller against the results presented in Figure 7.14 for the Eckardt radial impeller at its design condition, show similar qualitative loss distribution at the impeller exit. However, the Eckardt impeller appears to be more efficient than the GEM operating at its peak efficiency condition at 80% speed. The above description is consistent with the efficiency figures which were quoted from measurements for the two impellers.

Figure 7.35 shows the velocity vectors at blade to blade computational surfaces located near the hub, at the mid-span and in the mid-height of the tip gap. The flow passes over the blade tip from the pressure to the suction surface of the blade, opposite to the direction of the rotation. The meridional velocity vectors at meridional grid surfaces which are close to the pressure, the suction and the mid pitch surfaces of the passage are given in Figure 7.36.

7.5.3.4 Computational results for Near surge operating condition

At section A, the magnitude of the measured blade relative flow velocity presents its peak value in the shroud/suction corner and decreases across the passage to the hub/pressure corner, Figure 7.37a. The velocity pattern shows a slight discontinuity near the shroud/pressure corner region which was not present at peak efficiency. The predicted flow characteristics at this station, are "potential" with the existence of a jet pattern close to the shroud/suction corner. The location of the jet and the actual values of the magnitude of the relative velocity are in good agreement

to the measured data, Figure 7.37b.

The lines of constant relative flow angle, called "isoclines", can be utilized for the secondary flow analysis. According to the analysis presented by Krain (1988), the shape of these isoclines yields information about the vortex flow within the impeller. A real vortex is composed from a solid-body vortex and a potential one. The isoclines are parallel in the solid-body vortex area and obtain an elliptic shape in the potential vortex area. The vortex centre is located in the middle of the parallel isoclines.

The measured flow angle distribution is illustrated in Figure 7.38 where it is compared against the computationally obtained distribution. The highest angles measured angles are found along the shroud wall and the lowest angles in the mid-passage region near the hub. The predictions show that there is an increase of the "slip" towards the shroud wall as is observed in the experiment but in general the level of the predicted relative angles is higher than the measured ones which present their minimum on the hub wall.

In station B, the experimental velocity contours show a somewhat complicated pattern as illustrated in Figure 7.37a. On the hub the velocity decreases from 183 m/s on the suction side to 145 m/s on the pressure side. At mid passage the velocity remains almost constant at approximately 150 m/s. On the casing wall the velocity is generally lower with a local region of much lower velocity near the mid passage (93 m/s). According to the predictions shown in Figure 7.37b, a jet appears towards the suction side of the blade in the middle of the distance between the hub and the tip unlike the experimentally detected jet location towards the hub wall of the suction side. Also a wake pattern is predicted to emerge on the shroud wall towards its pressure side. The agreement at this station is not as precise as at the other stations.

The flow in station C is characterised by the existence of a strong wake pattern in the middle of the shroud wall, Figure 7.37b. The "depth" of the wake is

accurately captured by the computational model, but its location is predicted closer to the suction side. The absence of experimental information in the hub area is likely to hide the true magnitude of the jet pattern velocity which appears to be slightly over-predicted.

At station D , close to the impeller exit, the relative velocity contours are very similar to those measured at the higher flow condition with a region of low velocity in the middle of the shroud surface and generally increasing velocities towards the hub, Figure 7.37a. There is a remarkable agreement of the predicted velocity distribution with the experimental one, as shown in Figure 7.37b. A jet/wake flow pattern is pronounced with the wake being present in the middle of the casing wall and the jet on the hub wall as indicated by the contour levels of 160 m/s in the two passage corners of the hub wall.

Figure 7.39a, illustrates the measured blade relative flow angle contours with a general flow angle of 33° to 40° and with a region of high angle, up to 78°, on the shroud. The region of high "slip" coincides with the region of lowest streamwise velocity. The secondary flow pattern is dominated by a clockwise passage vortex which moves fluid towards the pressure side along the casing and towards the suction side along the hub. The predicted flow angle distribution is shown in Figure 7.39b. As found in the optical measurements as well, the angle remains almost unchanged and equal to 40° to most of the cross-section and increases rapidly towards the shroud wall.

The non-dimensional static pressure distribution on the shroud wall is represented in Figure 7.33b where is compared with the distribution obtained at the near peak efficiency condition and similar trends can be observed.

The blade to blade velocity vectors are shown in Figure 7.40 and the velocity vectors on meridional surfaces are plotted in Figure 7.41.

7.5.3.5 General remarks

The main flow characteristics which are predicted at the near surge condition are very similar to those at near peak efficiency operating condition: the jet flow pattern follows an anti-clockwise motion, the wake is located on the shroud wall where the low energy fluid from the hub and blade surface boundary layers, is directed due to the secondary flows and the tip leakage action. This flow pattern is very consistent with previous observations in radial impellers, Eckardt (1976), Moore and Johnson (1983), and is characteristic of the curvature dominated flows as the mean Rossby number of the current impeller indicates. The onset of flow separation for the near surge condition is captured in an earlier location (station B) than in the design condition where the flow appears separated at station C.

The relative flow angle increases from the hub to the casing wall where the "slip" is very high and the predicted values are close to the observed ones. Although the main trends of the relative flow angle distribution at all the measurement planes are captured by the computational model, there are slight discrepancies in the actual distribution. The strength of the secondary flow at the impeller exit is under-predicted, Birdi (1991), as it was found as well in the previous investigation of Eckardt's impeller.

The predicted turbulence intensity level, which is slightly higher for the near surge condition, increases rapidly in the wake region and presents a rather smooth distribution in the rest of the cross-sections. The excessive fluctuations are restricted in the wake region attached on the shroud showing a very weak turbulence damping due to the Coriolis effects.

The tip leakage flow contributes to the migration of the wake towards the centre of the shroud wall. This motion is under-predicted in the current computations. It is thought that the magnitude of the tip gap which is used in the simulation is less than the real one which was kept relatively high, especially in the radial discharge of the rotor, due to mechanical constraints.

7.6 Conclusions

The computer code developed is capable of predicting the involved flow phenomena occurring in high speed subsonic centrifugal compressor configurations with both stationary and rotating parts and with or without tip leakage.

The method can be applied to different centrifugal compressor designs and at different operating conditions providing a great deal of detailed information about the complex flowfield patterns occurring in centrifugal compressors.

For the test cases related to Eckardt's impellers, the development of a strong wake on the shroud wall near the suction surface is pronounced. The behaviour of this wake is affected by the backward curvature at the radial part of the rotating channel which tends to smooth the circumferential pressure and velocity gradients. The classical jet/wake flow pattern is clearly observed. The influence of the increase in flow rate has been well represented and good predictions of the efficiency are now possible. In general, good agreement is achieved with the measured meridional velocity distributions at the five measurement planes and with the measured pressure rise distribution. The code provides substantial insight into the evolution of the secondary flows in the impeller which affect the wake formation and location.

The computational method can capture the effects of the tip leakage which decreases the efficiency and shifts the wake towards the centre of the casing wall. Nevertheless, it is felt that a more refined tip leakage calculation is required with more grid points located in the tip gap and more accurate representation of the blade thickness distribution near the blade tip. A second step is the abandonment of the wall functions which are extracted from two-dimensional turbulent boundary layer profile considerations.

The computed flow field data in the high-speed Rolls-Royce GEM impeller, indicate a curvature dominated flow with a wake flow pattern observed on the casing wall of its radial discharge and a jet pattern close to the hub wall. The

implementation of the computational model for the flow analysis in the GEM impeller was less successful than in Eckardt's impellers with the main reasons for that being the existing uncertainties in the inlet conditions, the running tip clearances and the level of completeness of the available experimental data. Nevertheless, good agreement has been accomplished for most of the predicted flow parameters with the available experimental results and a comprehensive map of the flow field for two operating conditions has been obtained.

In general, the proposed computational model which has been used for the theoretical analysis of the centrifugal compressor impellers, has provided much more detailed information and good overall agreement with the experimentally captured flow features. However, further work is required for a more accurate representation of the secondary flows and the loss production mechanisms occurring in the rotating passage.

The results of the research work which has been presented in this chapter have been presented and published in the European Conference on Turbomachinery, which was held in London in March 1991, Tourlidakis and Elder (1991), and in the 10th International Symposium for Air Breathing Engines, which was held in Nottingham in September 1991, Birdi, Forster and Tourlidakis (1991).

CHAPTER 8

Conclusions and suggestions for further work

8.1 Conclusions

A detailed investigation of the problem of fluid flow in the geometrically complex passages of centrifugal compressors and other turbomachinery components has been performed. As a result a three-dimensional model for the viscous and compressible flow prediction in high speed centrifugal compressors with or without tip leakage has been developed, validated and implemented. The set of Reynolds averaged Navier-Stokes equations in a strong conservation form and the finite volume discretisation procedure in physical space which is utilized, have been presented and discussed. The computational method is based on an elliptic relaxation pressure correction method which uses generalised coordinates which allow the treatment of arbitrarily shaped geometries, collocated variables storage which minimises the effort for the estimation of the coefficients of the discretised equations and the two equation k-ϵ turbulence model. The pressure correction algorithm is based on the SIMPLE method and on the scheme proposed by Rhie and Chow (1983) as a remedy for the pressure oscillations and the decoupling between the pressure and the momentum fields which might arise during the iterative procedure due to the collocated variable arrangement on the computational grid. The calculation of the flow field is performed through a space marching of the flow domain along a selected curvilinear coordinate and update of the dependent variables at each "cross" plane.

The assessment of the flow model has been carried out through its implementation for the flow prediction in a series of two- and three-dimensional test cases.

The initial study involved the computation of two-dimensional, low-speed compressor cascade flows through a series of totally five different cascades operating at design and off-design conditions, which has shown that the proposed model can capture most of the flow phenomena occurring in the cascade passages. The validation study has been based largely on the comparison of the current numerical results against published experimental data for the pressure coefficient distribution along the blade surfaces and the deviation angle variation with incidence and cascade solidity. In general, accurate results and satisfactory agreement has been achieved taking into consideration the limitations of the turbulence model and the wall function approach, and in addition the model has been proven to be very robust as it was implemented to a variety of cascades with widely varying geometrical features and flow conditions. However, the use of boundary fitted coordinates which are orthogonal at the solid boundaries, did not exhibit any tangible advantage over the utilization of simple H-type grids.

The effect of the under-relaxation parameters is very significant on the computational economy of the method and an optimum range of values is proposed. A novel acceleration approach has been adopted and improvements in the speed of convergence have been obtained. The grids which were used in the flow computations were generated through an elliptic grid generation algorithm which involves the solution of a system of Poisson type equations with control functions which ensure orthogonality of the grid lines on the airfoil walls and provide a pre-defined grid spacing of the first grid line from the solid boundaries. The robustness and the effectiveness of the grid generation method was tested for various cascade geometries and flow angle settings.

The validation of the three-dimensional flow model was performed through its implementation to simulate various flows in ducting systems of different geometrical configurations. Two laminar and two turbulent flows were considered in order to assess and verify various features of the method. For the laminar cases, the fully developed profiles were in excellent agreement with the corresponding

analytical solutions. The k-ϵ model was thoroughly tested and the distributions of the turbulence scalars were compared against other numerical results in the case of the developing flow between two parallel plates. However, its predictive capability in corner flows is limited and more refined models have to be adopted with special care if the non-staggered grid of the current method is to be retained in order to avoid spatial oscillations in the velocity field. Accurate results were obtained from the turbulent flow modelling inside a strongly curved duct of rectangular cross-section where a pressure gradient is present in the cross-stream direction and strong secondary flows exist which is one of the features likely to be encountered in centrifugal compressor flows. The turbulent flow simulation through low-aspect-ratio planar diffusers with three different outlet to inlet area ratios and for two Reynolds numbers, provided encouraging results in terms of pressure coefficient distribution. In the cases when separation was present on the side walls due to the strong streamwise diffusion, the results are slightly less accurate than those obtained when the flow remained attached.

Finally, the proposed Navier-Stokes solver has been implemented for the simulation of the viscous compressible flow through different impellers operating at design and off-design flow rates. Firstly, the flow through Eckardt's high speed radial impeller and downstream diffuser was tested at design condition. Subsequently, the flow through Eckardt's backswept rotor and vaneless diffuser was simulated at design and near-choke flow rates. Eventually, the Rolls Royce GEM impeller of a currently in service engine, which was experimentally investigated at Cranfield, was modelled at a point near peak efficiency and at a point near surge at its 80% speed.

A jet/wake flow pattern was discerned in all test cases. The analysis provided encouraging results about the wake formation and development and the evolution of secondary flows. The tip leakage effects were found to be significant and influenced the loss distribution, the size and the position of the low-energy fluid region at the rotor exit. The effects of the flow mass rate on the detailed flow patterns such as the streamwise velocity distribution, and on the compressor performance have been

fairly represented. Despite the small number of grid points which were employed in the simulations, the simplified modelling of the tip clearance region and the numerical mixing due to the first order upwind definition of the convective fluxes, the current model provided good qualitative and quantitative agreement with the experimental data. Moreover, the quality of the present numerical results is comparable and in certain cases improved to that obtained by "state-of-the-art" Navier-Stokes computational tools which are available and are currently used in the analysis and design of modern gas turbine engine components. However, the accuracy of the modified (for curvature and rotation) two equation k-ϵ model could not be assessed thoroughly due to lack of detailed experimental evidence on the distribution of the turbulent quantities inside the rotating passage which is quite complicated technically to be achieved.

In summary, the developed finite volume, elliptic flow model has captured a large number of complex flow phenomena encountered in the tested centrifugal compressors and has been proven to be a robust flow analysis tool which can be easily adjusted to simulate the flow through a wide range of stationary or rotating axial or radial turbomachinery components.

8.2 Suggestions for future work

1. Unsteady Flows and Rotor-Stator interaction study.

The flow inside turbomachinery components is in most cases unsteady. A single stage of a turbomachine consists of one row of stationary blades (stators) and one row of moving blades (rotors) and one of the main sources of unsteadiness is the interaction between the stator wakes and the rotor. The stator wakes, which can be considered to be approximately steady in the stator frame of reference, are unsteady in the rotating with the rotor frame of reference as the rotor passes through these wakes and cuts them into pieces. During the last decade, there has been an increasing interest and effort, e.g. Rai (1987), Giles (1988) etc, in the unsteady interaction between the viscous flow fields through rotor and stator passages. These

studies can provide valuable information about the deformation of wakes, their transport through the blade rows and their influence on boundary layer behaviour, and separation. In addition, the better understanding of the unsteady interaction between the centrifugal compressor rotor and its downstream diffuser could lead to gains in performance and operating range of modern compressors.

The computer code which has been developed in the course of work presented in this thesis, can be extended to simulate unsteady flow fields, rotor/stator interaction and multistage machines. The first step of this development which is the incorporation of the additional complexity of unsteadiness in the computer code has already been performed. The unsteady term is retained in the governing equations and is treated through a fully implicit, first order in time, numerical scheme. At each time step, the solution of the flow field has to converge before it proceeds to the next time step. Two cases of a two dimensional implementation of the unsteady code, are given in Figures 8.1 and 8.2.

In the first case, the inlet total pressure which is imposed at the inlet boundary of the flow domain of a low speed NGTE 10C4/30C50 cascade passage, varies periodically in a sinusoidal fashion. Figure 8.1, illustrates the C_p coefficient (expressing dynamic head) variation at different instances during a complete period. As it can be observed, there is a significant change in the distribution pattern from one instance to another. One important conclusion of this study is that the pressure wave was found to travel with the speed of sound in the flow domain, and the disturbance in the velocity field with the convective speed of the fluid.

In the second example, a simplified stator/rotor interaction case is considered. The incoming wakes are specified as unsteady boundary condition at the inlet of the flow domain of a 20° camber stalled NGTE cascade. Another assumption is that the stator/rotor pitch ratio is 1:1 which allows the use of periodic boundary conditions. In Figure 8.2, the calulated C_p coefficient distribution is presented for different instances which correspond to different locations of the centreline of the passing wakes upstream of the cascade.

2. Modelling of multistage compressors

With appropriate modifications the current method can be utilized for the complete Navier-Stokes analysis of steady flow in multistage compressors since the computer time is still expensive and prohibitive for an unsteady analysis in the way which has been described in the previous section. The first task, which has already been carried out, is the enhancement of the computational method to handle in a unique procedure more than one blade rows which can be either stationary or rotating. The second task towards a multistage capability is the treatment of the grid inter-plane which separates the grids which are used to cover successive rows. For this purpose, a simple circumferential mass-averaging of the flow variables can apply and the obtained quantities can fixed as input for the next stage analysis. Similar applications of already existing Euler or Navier-Stokes methods can be found in Denton (1990) and Dawes (1990) respectively.

3. Acceleration of the current method

The speed and the storage capacity of available computer systems and the cost per calculation are significant constraining factors on the use of CFD technology for design. The implementation of the three-dimensional computer program as an analysis and design tool on a routine basis is still expensive in terms of computational cost. This cost is proportional to the number of grid points to a power of approximately 2. As a matter of fact, the computer technology has been progressing rapidly and has been contributing to a continous reduction of the cost per computation rendering CFD an increasingly attractive alternative to model scale testing in the design process. However, further improvements can be achieved by using appropriate numerical acceleration techniques. The effectiveness of the acceleration technique which was presented in Chapter 5, is to be assessed in three-dimensional flows. Another alternative is the use of a multigrid acceleration approach which is reported, Vanka (1987), NASA CP-2202 (1982), to offer significant savings in computer time costs when compared to conventional solution techniques. In the multigrid approach, a sequence of coarser grids is employed to damp the low frequency error component of the solution. The expected reduction in

the run-times of the code will allow local grid refinement studies to facilitate in improving accuracy.

4. Turbulence modelling

The lack of detailed experimental data on turbulent quantities in the complex viscous flows environment of the examined centrifugal compressors did not allow a detailed assessment of the k-ϵ turbulence model and the modifications to account for curvature and rotation. The low-speed centrifugal compressor facility at NASA Lewis Research Centre, Hathaway et al (1991), is expected to provide "benchmark" data for verification of three-dimensional viscous flow models and to facilitate the development of more sophisticated models of the physical phenomena encountered in centrifugal compressors.

Despite the most wide use and the successes of the k-ϵ turbulence model and the associated wall function approach in many applications, they have proven to fail in many complex flows. According to a review presented by Lakshminarayana (1991) the model fails for flow with rotation, curvature, strong swirl, three-dimensionality, and shock induced separation. When these extra complex strain effects are present, the Reynolds stress closure equations can provide a more rigorous approach. The full Reynolds stress model, Launder et al (1976), provides a more realistic physical simulation of turbulence but is very complex, the least tested model so far and still very expensive in terms of computational time. A compromise for the current computer code would be the use of the k-ϵ model coupled with an Algebraic Reynolds Stress Model, which does not entail considerable additional resources and has proven to capture directly rotation and curvature effects, Warfield and Lakshminarayana (1987).

5. Transonic and Supersonic flows

The flow in a turbomachine can be subsonic, transonic or supersonic; some turbomachinery flows include all of these regimes. There are only a few reports of application of the pressure correction method to predict transonic and supersonic flows and to capture accurately shock waves, as it was described in Chapter 1. Work

on numerical investigations continues at Cranfield for the extension of the current method and the assessment of its capability to handle the above flow regimes.

6. Study of Tip Leakage Flows

The computer code which has been developed in the course of work presented in the present thesis, is currently used for the study of tip clearance effects in axial flow compressors in the framework of a collaborative European sponsored research project, Dunker (1991), in which Cranfield Institute of Technology participates as a partner. One of the other partners, who are the National Technical University of Athens, Greece, installed the computer code on an Alliant FX-80 computer and modified it in order to attain improved computational efficiency in terms of run times and to utilize the Alliant's vector/parallel capabilities. In addition, the tip-clearance region has been modelled with an extension of the computational domain to cover the tip region with an H-type grid taking into account the real tip geometry and abandoning the assumption of a rounded to a single point tip, Papailiou (1991).

7. Numerical schemes

The use of the Upwind numerical scheme was necessitated for stability reasons, despite the inaccuracies which are introduced and the strong numerical diffusion. More work is still required in order to investigate the applicability of alternative more accurate schemes which are available and are based either on a higher order differencing definition of the convective flux or on vector differencing which accounts for misalignment of the dominant flow direction with the grid lines. The capabilities of the developed flow model are expected to be enhanced by the introduction of such numerical schemes taking appropriate numerical measures which ensure stability of the solution procedure. In addition, the current computer program can be used for comparison studies of the performance of alternative numerical schemes on predicting certain complex flows.

8. Pre- and Post- processing enhancement

The CFD codes of the next generation will consist of enhanced pre- and post-processing facilities including interactive geometry and mesh generation, graphics and visualisation, video technology and database management systems linked with the flow solvers in an integrated software environment. Only very recently, such integrated CFD systems for 3D turbomachinery applications have started to emerge, Hirsch et al (1991).

REFERENCES

Adler D. and Levy Y. (1979)
"A Laser-Doppler Investigation of the Flow inside a Backswept, Closed, Centrifugal Impeller", IMechE Journal of Mechanical Engineering Science, Vol. 21, No. 1.

Adler D. and Krimerman Y. (1980)
"Comparison Between the Calculated Subsonic Inviscid Three-Dimensional Flow in a Centrifugal Impeller and Measurements", ASME CP Performance Prediction on Centrifugal Pumps and Compressors, pp.19-26.

Ahmed N.A. and Elder R.L. (1990)
"Flow Investigation in a Small High Speed Impeller Passage Using laser Anemometry", ASME paper 90-GT-233.

AGARD-CP-282 (1980)
"Centrifugal Compressors, Flow Phenomena and Performance", Brussels.

Anderson D.A., Tannehill J.C. and Pletcher R.H. (1984)
"Computational Fluid Mechanics and Heat Transfer", McGraw-Hill Book Co..

ASME (1980)
"Performance Prediction of Centrifugal Pumps and Compressors", presented at the 25th Annual International Gas Turbine Conference and Exhibit and the 22nd Annual Fluids Engineering Conference, New Orleans, Louisiana.

Baldwin B.S. and Lomax H. (1978)
"Thin Layer Approximation and Algebraic Model for Separated Turbulent Flows", AIAA paper No. 78-257.

Beam R.M. and Warming R.F. (1978)
"An Implicit Factorised Scheme for the Compressible Navier-Stokes equations", AIAA Journal, Vol. 16, pp. 393-401.

Birdi K. (1991)
Private Communication.

Birdi K., Forster C.P. and Tourlidakis A. (1991)
"Comparison of the Experimentally Defined and Computed Flow Field in the Rolls Royce GEM Impeller", 10th International Symposium for Air-Breathing Engines, Nottingham U.K..

Bradshaw P. (1978)
"Turbulence, Topics in Applied Physics, Vol. 12", Ed. P. Bradshaw, Second Edition, Springer-Verlag, New-York.

Briley W.R. and McDonald H. (1977)
"Solution of the Multidimensional Navier-Stokes equations by a Generalised Implicit Method", Journal of Computational Physics, vol. 24, pp. 372-397.

Calvert W.J. (1982)
"An Inviscid-Viscous Interaction Treatment to predict the Blade-to-Blade Performance of Axial Compressors with Leading Edge Normal Shock Waves", ASME paper No 82-GT-135.

Calvert W.J. (1988)
Private Communication.

Caretto L.S., Gosman A.D., Patankar S.V. and Spalding D.B. (1972)
"Two calculation procedures for steady three-dimensional flows with recirculation", Proceedings of the Third International Conference on Numerical Methods in Fluid Dynamics, Springer-Verlag, New York.

Carter A.D.S. (1950)
"The Low Speed Performance of related Aerofoils in Cascade", Aeronautical Research Council, ARC/CP-29.

Casey M.V., Dalbert P. and Roth P. (1990)
"The use of a 3D Viscous Flow Calculations in the Design and Analysis of Industrial Centrifugal Compressors", ASME paper 90-GT-2.

Cho N.H. and Fletcher C.A.J. (1991)
"Computation of Turbulent Conical DIffuser Flows Using a non-Orthogonal Grid System", Computers and Fluids, Vol. 19, No. 3/4, pp. 347-361.

Choi Y.D., Iacovides H. and Launder B.E. (1989)
"Numerical Computation of Turbulent Flow in a Square-Sectioned 180° Bend", Transactions of ASME, Journal of Fluids Engineering, Vol. 111.

Connell S.D. and Stow P. (1986)
"The Pressure Correction Method", Computers and Fluids, Vol. 14, No. 1, pp. 1-10.

Davis R.L., Hobbs D.E. and Weingold H.D. (1988)
"Prediction of Compressor Cascade Performance Using a Navier-Stokes Technique", ASME paper No 88-GT-96.

Dawes W.N. (1986a)
"Computation of Off-Design Flows in a Transonic Compressor Rotor", ASME Journal of Engineering for Gas Turbines and Power, Vol. 108, pp. 144-150.

Dawes W.N. (1986b)
"A Numerical Analysis of the Three-Dimensional Viscous Flow in a Transonic Compressor Rotor and Comparison with Experiment", ASME paper No 86-GT-16.

Dawes W.N. (1987)
" Application of a Three-Dimensional Viscous Compressible Flow Solver to a High-Speed Centrifugal Compressor Rotor - Secondary Flow and Loss Generation", IMechE paper C261/87.

Dawes W.N. (1988)
"Development of a 3D Navier Stokes Solver for Application to all Types of Turbomachinery", ASME paper No 88-GT-70.

Dawes W.N. (1990)
"Towards Improved Throughflow Capability: The Use of 3D Viscous Flow Solvers in a Multistage Environment", ASME paper No 90-GT-18.

Dawes W.N. (1991)
"The Simulation of Three- Dimensional Viscous Flow in Turbomachinery geometries Using a Solution-Adaptive Unstructured Mesh Methodology", ASME paper 91-GT-91.

Delaney R.A. (1982)
"Time-Marching Analysis of Steady Transonic Flow in Turbomachinery Cascades Using a Hopscotch Method", ASME paper No 82-GT-152.

Demirdzic I.A. (1982)
"A Finite Volume Method for Computation of Fluid Flow in Complex Geometries", PhD Thesis, Mechanical Engineering Department, Imperial College of Science and Technology, University of London.

Demuren A.O. and Rodi W. (1984)
"Calculation of Turbulence-driven Secondary Flows in Ducts of non-circular Cross-section", Journal of Fluid Mechanics, Vol. 140, pp. 189-222.

Denton J.D. (1978)
"Throughflow Calculations for Transonic Axial Flow Turbines", Transactions of the ASME, Journal of Engineering for Power, Vol. 100, pp. 212-218.

Denton J.D. (1982)
"An Improved Time-Marching Method for Turbomachinery Flow Calculation", ASME paper No 82-GT-239.

Denton J.D. (1990)
"The Calculation of Three Dimensional Viscous Flow Through Multistage Turbomachines", ASME paper No 90-GT-19.

Dunker R.J. (1991)
"European Collaboration - A Changing Scene in Aero-Engine Research", 10th International Symposium for Air Breathing Engines, Nottingham.

Eckardt D. (1976)
"Detailed Flow investigations Within a High-Speed Centrifugal Compressor Impeller", ASME J. Fluids Engg., Vol. 98, pp. 390-402.

Eckardt D. (1980)
"Flow Field Analysis of Radial and Backswept Centrifugal Compressor Impellers. Part I: Flow Measurements Using a Laser Velocimeter", ASME CP Performance Prediction on Centrifugal Pumps and Compressors, pp. 77-86.

Elder R.L and Forster C.P. (1987)
"Measurements in Centrifugal Compressors" ,von Karman Institute for Fluid Dynamics Lecture Series 1987-01.

Fagan J.R. and Fleeter S. (1990)
"Impeller Flow Field Measurement and Analysis", ASME paper 90-GT-146.

Farge T.Z., Johnson M.W. and Maskoud T.M.A. (1989)
"Tip LEakage in a Centrifugal Impeller", ASME Journal of Turbomachinery, Vol. 111, No 3, pp. 244-249.

Favre A. (1965)
"Équations des Gaz Turbulents Compressibles: 1. Formes Générales", Journal de Méchanique, Vol. 4, pp. 361-390.

Felix A.R. and Emery J.C. (1957)
"A Comparison of Typical National Gas Turbine Establishment and NACA Axial-Flow Compressor Blade Sections", NACA TN 3937.

Forster C.P. (1988a)
"Laser Anemometry Study of the GEM 2 Impeller: Measurements at 80% Speed Near Peak Efficiency", Internal Report, Cranfield Institute of technology, TR/88/3.

Forster C.P. (1988b)
"Laser Anemometry Study of the GEM 2 Impeller: Measurements at 80% Speed Near Surge", Internal Report, Cranfield Institute of technology, TR/88/7.

Fowler H.S. (1966)
"An Investigation of the Flow Processes in a Centrifugal Compressor Impeller", National Research Council of Canada report, N.R.C. No. 9199.

Gessner F.B., Po J.K. and Emery A.F. (1979)
"Measurements of Developing Turbulent Flow in a Rectangular Duct", Turbulent Shear Flows I (Edited by Durst et al) Springer-Verlag.

Giles M.B. (1988)
"Stator/Rotor Interaction in a Transonic Turbine", AIAA paper 88-3093.

Goto A. (1990)
"Study of Internal Flows in a Mixed-Flow Pump Impeller at Various Tip Clearances Using 3D Viscous Flow Computations", ASME paper 90-GT-36.

Goulas A. (1980)
"Flow in Centrifugal Compressor Impellers - A Theoretical and Experimental Study", AGARD - CP - 282.

Hah C. (1984)
"A Navier-Stokes Analysis of Three-Dimensional Turbulent Flows Inside Turbine Blade Rows at Design and Off-Design Conditions", ASME Journal of Engineering for Gas Turbines and Power, Vol. 106, pp. 421-429.

Hah C. (1987)
"Calculation of Three-Dimensional Viscous Flows in Turbomachinery with an Implicit Relaxation Method", AIAA Journal of Propulsion, Vol. 3, No 5, pp. 415-422.

Hah C., Bryans A.C., Moussa Z. and Tomsho M.E. (1988)
"Application of Viscous Flow Computations for the Aerodynamic Performance of a Backswept Impeller at Various Operating Conditions", ASME Journal of Turbomachinery, Vol. 110, pp. 303-311.

Hah C. and Krain H. (1990)
"Secondary Flows and Vortex Motion in a High-Efficiency Backswept Impeller at Design and Off-Design Conditions", ASME Journal of Turbomachinery, Vol. 112, pp. 7-13.

Hah C. and Wennerstrom A.J. (1990)
"Three-Dimensional Flowfields Inside a Transonic Compressor with Swept Blades", ASME paper no 90-GT-359.

Hamrick J.T., Mizisin J. and Michel D.J. (1954)
"Study of Three-Dimensional Internal Flow Distribution Based on Measurements in a 48-inch Radial-Inlet Centrifugal Impeller", NACA TN 3101.

Harlow F.H. and Welch J.E. (1965)
"Numerical calculations of time-dependent viscous incompressible flow of fluid with free surface", The Physics of Fluids, Vol. 8, pp. 2182-2189.

Hathaway M.D., Wood J.R. and Wasserbauer C.A. (1991)
"NASA Low-Speed Centrifugal Compressor for 3-D Viscous Code Assessment and Fundamental Flow Physics Research", ASME paper No 91-GT-140.

Hestenes M.R. and Stiefel E. (1952)
"Methods of Conjugate Gradients for Solving Linear Systems", NBS J. Res., Vol. 49.

Hirsch Ch., Lacor C., Dener C., and Vucinic D. (1991)
"An Integrated CFD System for 3D Turbomachinery Applications", AGARD-PEP, 77th Symposium on CFD Techniques for Propulsion Applications, San Antonio, Texas.

Hirsch Ch. and Warzee G. (1980)
"Quasi 3-D Finite Element Computation of Flows in Centrifugal Compressors", ASME CP Performance Prediction on Centrifugal Pumps and Compressors, pp. 69-75.

Hirt C.W., Amsden A.A., Cook J.L. (1974)
"An Arbitrary Langrangian-Eulerian computing Method for All Flow Speeds", J. of Comp. Physics, Vol. 14, pp. 227.

Issa R.I. (1982)
"Solution of the Implicitly discretised Fluid Flow Equations by Operator-Splitting", Fluids Section report FS/82/15, Mech. Eng. Dept., Imperial College, London.

Jameson A. (1975)
"Transonic Potential Flow Calculations Using Conservative Form", Proc. AIAA, Second Computational Fluid Dynamics Conference, Hartford, pp. 148-161.

Jameson A. (1979)
"Acceleration of Transonic Potential Flow Calculations on Arbitrary Meshes Using the Multi-grid Method", AIAA paper 79-1458, AIAA 4th Computational Fluid Dynamics Conference.

Johnson M.W. and Farge T.Z. (1991)
"The Effect of Hub Total Pressure Deficient Radial Inlet Distortion on Centrifugal Impeller Flow", Proceeding of IMechE, European Conference on Turbomachinery, IMechE paper No C423/012.

Joslyn H.D., Brasz J.J. and Dring R.P. (1990)
"Centrifugal Compressor Impeller Aerodynamics (an Experimental Investigation)", ASME paper 90-GT-128.

Katsanis T. (1966)
"Use of Arbitrary Quasi-Orthogonals for Calculating the Flow Distribution in a Turbomachine", J.Engg. for Power, Vol. 88, pp. 197-202.

Krain H. (1988)
"Swirling Impeller Flow", ASME Journal of Turbomachinery, Vol. 110, pp 122-128.

Lakshminarayana B. (1991)
"An Assessment of Computational Fluid Dynamics Techniques in the Analysis and Design of Turbomachinery - The 1990 Freeman Scholar Lecture", ASME Journal of Fluids Engineering, Vol. 113, pp. 315-352.

Lapworth B.L. (1987)
" Three-Dimensional Elliptic Computations for Viscous Turbomachinery Flows", PhD Thesis, Cranfield Institute of technology.

Lapworth B.L. (1988)
"Examination of Pressure Oscillations Arising in the Computation of Cascade Flow Using a Boundary-Fitted Co-ordinate System", International Journal for Numerical Methods in Fluids, Vol. 8, pp. 387-404.

Lapworth B.L. and Elder R.L. (1988)
"Computation of the Jet-Wake Flow Structure in a Low Speed Centrifugal Impeller, ASME paper No 88-GT-217.

Launder B.E., Reece B.J. and Rodi W. (1975)
"Progress in the Development of a Reynolds Stress Turbulence Closure Model", Journal of Fluid Mechanics, Vol. 68, part 3, pp. 537-566.

Launder B.E. and Spalding D.B. (1974)
"The Numerical Computation of Turbulent Flows", Comp. Meth. in Appl. Mech. Engg., Vol. 3, pp. 269-289.

Launder B.E. and Ying W.M. (1973)
"Prediction of Flow and Heat Transfer in Ducts of Square Cross-section", Heat and Fluid Flow, Vol. 3, No 2, pp. 115-121.

Lax P.D. (1954)
"Weak Solutions of Nonlinear Hyperbolic Equations and Their Numerical Computation", Communications on Pure and Applied Mathematics, Vol. 7, pp. 159-193.

Leonard B.P. (1979)
"A Stable and Accurate Convective Modelling procedure Based on Quadratic Upstream Interpolation", Comp. Meth. Appl. Mech. Engg., Vol. 19, pp. 59-98.

Leschziner M.A. (1980)
"Practical Evaluation of Three Finite Difference Schemes for the Computation of Steady-State Recirculating Flows", Computer Methods in Applied Mechanics and Engineering, Vol. 23, pp. 293-312.

Lobo M. (1991)
"Numerical Schemes for Turbomachinery Flows with Emphasis on Computational Economy", Internal Report, School of Mechanical Engineering, Cranfield Institute of Technology.

Marsh H. (1966)
"A Digital Computer Program for the Through-Flow Mechanics in an Arbitrary Turbomachine Using the Matrix Method", A.R.C. R. & M. No 3509.

McCormack R.W. (1969)
"The Effect of Viscosity in Hypervelocity Impact Cratering", AIAA Paper 69-354.

McDonald P.W. (1971)
"The Computation of Transonic Flow Through Two Dimensional Gas Turbine Cascades", ASME paper No 71-GT-89.

McGuirk J. and Page G. (1989)
"Shock Capturing Using a Pressure-Correction Method", AIAA paper No AIAA-89-0561.

McMillan O.J. and Johnston J.P. (1970)
"Performance of Low - Aspect - Ratio diffusers With Fully developed Turbulent Inlet Flows", Stanford University, Thermosciences Div. Report PD-14.

McMillan O.J. and Johnston J.P. (1973)
"Performance of Low - Aspect - Ratio Diffusers with Fully Developed Inlet Flows, Part I - some Experimental Results", J. of Fluids Engg., Vol. 95, pp. 385-392.

Melling A. and Whitelaw J.H. (1976)
"Turbulent Flow in a Rectangular Duct", J. of Fluids Engg., Vol. 78, part 2, pp. 289-315.

Mirzabozorg M.A.S. (1987)
"Measurement and Computation of the Flow in an Axial Blade Row", PhD thesis, Cranfield Institute of Technology.

Moore J. (1976)
"Eckardt's impeller - A Ghost from Ages Past", Cambridge University Engineering Department, CUED/A - Turbo/TR 83.

Moore J. and Johnson M.W. (1983)
"Secondary Flow Mixing Losses in a Centrifugal Impeller", ASME Journal of Engineering for Power, Vol. 105, pp. 24-32.

Moore J. and Moore J.G. (1979a)
"A Calculation Procedure for Three-Dimensional, Viscous, Compressible Duct Flow. Part I - Inviscid Flow Considerations', ASME Journal of Fluids Engg, Vol. 101, pp. 415-422.

Moore J. and Moore J.G. (1979b)
"A Calculation Procedure for Three-Dimensional, Viscous, Compressible Duct Flow. Part II -Stagnation Pressure Losses in a Rectangular Elbow', ASME Journal of Fluids Engg, Vol. 101, pp. 423-428.

Moore J. and Moore J.G. (1980a)
"Calculations of Three-Dimensional Viscous Flow and Wake Development in a Centrifugal Impeller", ASME CP Performance Prediction of Centrifugal Pumps and Compressors", pp. 61-67.

Moore J. and Moore J.G. (1980b)
"Three-Dimensional, Viscous Flow Calculations for Assessing the Thermodynamic Performance of Centrifugal Compressors - Study of the Eckardt Compressor", AGARD - CP - 282.

Moore J. and Moore J.G. (1987)
"3-D Viscous Flow Calculations at Design and Off-Design Conditions for the NACA-48-inch Radial Inlet Centrifugal Impeller", ISABE-87-7008.

Murman and Cole (1971)
"Calculation of Plane Steady Transonic Flows", AIAA Journal, Vol. 9, pp. 114-121.

Nallasamy M. (1987)
"Turbulence Models and their Applications to the Prediction of Internal Flows: A Review", Computers and Fluids, Vol. 15, No 2, pp. 151-194.

Naot D. and Rodi W. (1982)
"Numerical Simulations of Secondary Currents in Channel Flow", Journal of Hydraulics, Div. ASCE, Vol. 108, pp. 948-968.

NASA CP-2166 (1980)
"Numerical Grid Generation Techniques".

NASA CP-2202 (1982)
"Multigrid Methods".

NASA SP-36 (1965)
"Aerodynamic Design of Axial-Flow Compressors".

Ni R.H. (1981)
"A Multiple-Grid Scheme for Solving the Euler Equations", AIAA paper 81-1025.

Obi S., Peric M. and Scheuerer G. (1991)
"Second-Moment Calculation Procedure for Turbulent Flows with Collocated Variable Arrangement", AIAA Journal, Vol. 29, No. 4.

Papailiou K.D. (1991)
Private Communication.

Patankar S.V. (1980)
"Numerical Heat Transfer and Fluid Flow", McGraw-Hill, New York.

Patankar S.V. and Spalding D.B. (1972)
"A calculation procedure for Heat, Mass and Momentum Transfer in Three-Dimensional Parabolic Flows"; Int. J. Heat Mass Transfer, Vol. 15, pp. 1787-1806.

Patel V.C., Rodi W. and Scheuerer G.. (1984)
"Turbulence Models for Near-Wall and Low Reynolds Number Flows: A Review", AIAA Journal, Vol. 23, No 9, pp. 1308-1319.

Peric M. (1985)
"A Finite Volume Method for the Prediction of Three-Dimensional Fluid Flow in Complex Ducts", PhD Thesis, Imperial College, University of London.

Pinot P. (1991)
Private Communication.

Prandtl L. (1925)
"Bericht uber Untersuchungen zur ausgebilteten Turbulenz", ZAMM Vol. 5, No. 2.

Pratap V.S. (1975)
"Flow and Heat Transfer in Curved Ducts", Imperial College of Science and Technology, Report No. HTS/75/25.

Pratap V.S. and Spalding D.B. (1976)
"Fluid Flow and Heat Transfer in Three-Dimensional Duct Flows", Int. J. Heat Mass Transfer, Vol. 19, pp. 1183-1188.

Rai M.M. (1987)
"Unsteady Three-Dimensional Navier-Stokes Simulations of Turbine Rotor-Stator Interaction", AIAA paper 87-2058.

Rhie C.M. (1981)
"A Numerical Study of the Flow Past as Isolated Airfoil with Separation", PhD Thesis, Dept. of Mech. and Ind. Engg., Univ. of Illinois at Urbana-Champaign.

Rhie C.M. and Chow W.L. (1983)
"Numerical Study of the Turbulent Flow Past an Airfoil with Trailing Edge Separation", AIAA Journal, Vol. 21, No 11, pp. 1525-1532.

Rhie C.M., Delaney R.A. and McKain T.F. (1984)
"Three-Dimensional Viscous Flow analysis for Centrifugal Impellers", AIAA paper 84-1296.

Rhie C.M. (1985)
"A Three-Dimensional Passage Flow Analysis Method Aimed At Centrifugal Impellers", Computers and Fluids, Vol. 13, No 4, pp. 443-460.

Rhie C.M. (1986)
"A Pressure Based Navier-Stokes Solver Using the Multigrid Method", AIAA paper No AIAA-86-0207.

Rhoden H.G. (1956)
"Effects of Reynolds Number on the Flow of Air through a Cascade of Compressor Blades", A.R.C. R. & M.No. 2919.

Roach P.J. (1982)
"Computational Fluid Dynamics", Hermosa Publishers, New Mexico.

Roberts G.O. (1971)
"Computational Meshes for Boundary Layer Problems", Proceedings of Second International Conference on Numerical Methods in Fluid Dynamics, Lecture Notes in Physics, Vol. 8, Springer-Verlag, pp. 171-177.

Schlichting H. (1979)
"Boundary Layer Theory", McGraw Hill Book Co., Seventh Edition.

Schuster P. and Schmidt-Eisenlohr U. (1980)
"Flow Field Analysis of Radial and Backswept Centrifugal Compressor Impellers. Part 2: Comparison of Potential Flow Calculations and Measurements", ASME CP Performance Prediction of Centrifugal Pumps and Compressors, pp. 87-95.

Schumann U. and Friedrich R. (1986)
"Direct and Large Eddy Simulation of Turbulence", Proceedings of the European Colloquium No. 199, Munich 1985, Friedr. Vieweg & Sohn Braunschweig/Wiesbaden.

Shyy W. (1988)
"A numerical Study of Two-Dimensional Compressible Navier-Stokes Flows", Numerical Heat Transfer, Vol. 14, pp. 323-341.

Singh U.K. (1982)
"A Computation and Comparison with Measurements of Transonic Flow in Axial Compressor Stage with Shock and Boundary Layer Interaction", ASME Journal of Engineering for Power, Vol. 104.

Sorenson R.L. (1980)
"A Computer Program to Generate Two-dimensional Grids about Airfoils and Other Shapes by the use of the Poisson's Equation", NASA TM-81198.

Spalding D.B. (1972)
"A Novel Finite-Difference Formulation for Differential Expressions Involving Both First and Second Derivatives", Int. J. Num. Meth. Eng., Vol. 4, pp. 551-559.

Stone H.L. (1968)
"Iterative Solution of Implicit Approximations of Multidimensional Partial Differential Equations", SIAM Journal of Numerical Analysis, Vol. 5.

Tan S.C. (1988)
"A Study of Particle Trajectories In a Gas Turbine Intake", PhD thesis, Cranfield Institute of Technology.

Thomas L.H. (1949)
"Elliptic Problems in Linear Difference Equations over a Network", Watson Sci. Comput. Lab. Rept., Columbia University, New York.

Thompkins W.T. and Tong S.S. (1978)
"Inverse or Design Calculations for Non-Potential Flow in Turbomachinery Blade Passages", ASME paper No 81-GT-78.

Thompson J.F. (1982)
"Numerical Grid Generation", Ed. J.F. Thompson, Elsevier Science Publication Company.

Thompson J.F. (1984)
"Grid Generation Techniques in Computational Fluid Dynamics", AIAA Journal, Vol. 22, No. 11, pp. 1505-1523.

Thompson J.F., Thames F.C. and Mastin C.W. (1974)
"Automatic Numerical Generation of Body-Fitted Curvilinear Coordinate System for Field Containing any Number of Arbitrary Two dimensional Bodies", J. Comp. Physics, Vol. 15, pp. 299-319.

Tourlidakis A. and Elder R.L. (1991)
"Computations of Three-Dimensional Viscous Turbulent Flows in Centrifugal Compressors with Tip Leakage", Proceedings of the IMechE, European Conference on Turbomachinery, IMechE paper No C423/050.

Van Doormaal J.P. and Raithby G.D. (1984)
"Enhancements of the Simple Method for Predicting Incompressible Fluid Flows", Numerical Heat Transfer, Vol. 7, No 2, pp. 147-163.

Vanka S.P. (1987)
"Block-Implicit Computation of Viscous Internal Flows - Recent Results", AIAA paper, AIAA-87-0058.

von Karman Institute for Fluid Dynamics Lecture Series 1984-07, May 1984.

Warfield M. and Lakshminarayana B. (1987)
"Calculation of Rotating Turbulent Flow with an Algebraic Reynolds Stress Model", AIAA Journal, Vol. 25, No. 7, pp. 957-964.

Wilcox D.C. and Chambers T.L. (1977)
"Streamline Curvature Effects on Turbulent Boundary Layers", AIAA Journal, Vol. 15, No. 4, pp. 574-580.

Wu C.H. (1952)
"A General Theory of Three-Dimensional Flow in Subsonic and Supersonic Turbomachines of Axial, Radial and Mixed-Flow Types", NACA-TN-2407.

Wu C.H., Wang Z. and Chen H. (1990)
"Three-Dimensional Flow in Transonic Turbomachines. Part II: Full 3D flow in CAS Rotor Obtained by Using a Number of S1 and S2 Stream Filaments", ASME paper 90-GT-13.

APPENDIX A

Energy equation

The conservation equation for energy expressed in terms of static enthalpy, presents the following form, Anderson et al (1984):

$$\rho \frac{Dh}{Dt} = - \nabla q + \frac{\partial Q}{\partial t} + \Phi + \frac{Dp}{Dt} \qquad (A.1)$$

where:

$$q = - k\nabla T = - \frac{k}{C_p}\nabla h = -\frac{\mu}{P_r}\nabla h \qquad (A.2)$$

$$\Phi = \tau_{ij}\cdot\frac{\partial u_i}{\partial x_j} = \tau_{ij}\cdot\nabla\vec{V} \qquad (A.3)$$

$$\left(\frac{D}{Dt}\right) = \left(\frac{\partial}{\partial t} + \vec{V}\cdot\nabla \right) \qquad (A.4)$$

where V is the relative velocity vector. The momentum equation is given in the following form, Anderson et al (1984):

$$\rho \frac{D\vec{V}}{Dt} = \rho \vec{f} + \nabla \Pi_{ij} \qquad (A.5)$$

where:

$$\Pi_{ij} = -p\delta_{ij} + \mu\left[\left(\frac{\partial u_i}{\partial x_j}+\frac{\partial u_j}{\partial x_i}\right) - \frac{2}{3}\delta_{ij}\frac{\partial u_k}{\partial x_k} \right] = -p\delta_{ij} + \tau_{ij} \qquad (A.6)$$

If the momentum equation is projected to the direction of the relative velocity, the following relation is obtained:

$$\rho \vec{V}\frac{D\vec{V}}{Dt} = \rho \vec{V}\vec{f} + \vec{V}\cdot\nabla \Pi_{ij} \rightarrow \rho \frac{D(V^2/2)}{Dt} = \rho \vec{V}\vec{f} - \vec{V}\cdot\nabla p + \vec{V}\cdot\nabla\tau_{ij} \qquad (A.7)$$

In addition the following relation is valid:

$$\rho \frac{D(\Omega^2 r^2/2)}{Dt} = \rho \Omega^2 \vec{r} \frac{D\vec{r}}{Dt} = \rho \Omega^2 \vec{r} \vec{V} = \rho (\vec{\Omega}\vec{\Omega}) \vec{r} \vec{V} \qquad \text{(A.8)}$$

Combining the relations (A.1), (A.7) and (A.8), the following equation is obtained:

$$\rho \frac{Dh}{Dt} + \rho \frac{D(V^2/2)}{Dt} - \rho \frac{D(\Omega^2 r^2/2)}{Dt} = -\nabla q + \frac{\partial Q}{\partial t} + \nabla(\tau_{ij} \cdot \vec{V}) + \qquad \text{(A.9)}$$
$$+ \frac{\partial p}{\partial t} + \rho \vec{V} \vec{f} + \vec{V} \cdot \nabla \tau_{ij} - \rho (\vec{\Omega}\vec{\Omega}) \vec{r} \vec{V}$$

Using the definition of rothalpy I, the above relation becomes:

$$\rho \frac{DI}{Dt} = -\nabla q + \frac{\partial Q}{\partial t} + \nabla(\tau_{ij} \cdot \vec{V}) + \frac{\partial p}{\partial t} + \rho \vec{f} \vec{V} - \rho (\vec{\Omega}\vec{\Omega}) \vec{r} \vec{V} \qquad \text{(A.10)}$$

where rothalpy I is given by:

$$I = C_p T + \frac{1}{2} V^2 - \frac{1}{2} \Omega^2 r^2 = h + \frac{1}{2} V^2 - \frac{1}{2} \Omega^2 r^2 \qquad \text{(A.11)}$$

The forces $\vec{f}$ which appear in the above equations are the Coriolis and the centrifugal forces:

$$\vec{f} = -2 \cdot \vec{\Omega} x \vec{V} - \vec{\Omega} x (\vec{\Omega} x \vec{r}) \quad \rightarrow \qquad \text{(A.12)}$$
$$\rho \vec{f} \vec{V} = -2\rho (\vec{\Omega} x \vec{V}) \cdot \vec{V} - \rho \vec{\Omega} \cdot (\vec{\Omega} \vec{r}) \cdot \vec{V} + \rho \vec{r} \cdot (\vec{\Omega}\vec{\Omega}) \cdot \vec{V}$$

The first term of the RHS of the above relation is equal to 0.

The substitution of this relation to the energy equation (A.10) provides the following form of the energy equation:

$$\rho \frac{DI}{Dt} = \nabla(\frac{\mu}{P_r} \nabla h) + \frac{\partial Q}{\partial t} + \frac{\partial p}{\partial t} - \rho \vec{\Omega} (\vec{\Omega} \vec{r}) \vec{V} + \nabla \tau_{ij} \vec{V} \qquad \text{(A.13)}$$

If the unsteady terms are neglected and the vectors $\vec{\Omega}$ and $\vec{r}$ are assumed perpendicular which is the case in the current study, the above relation obtains the form:

$$\rho\frac{DI}{Dt} = \nabla(\frac{\mu}{P_r}\nabla I) - \nabla(\frac{\mu}{P_r}\nabla(\frac{V^2}{2})) + \nabla(\frac{\mu}{P_r}\nabla(\frac{\Omega^2 r^2}{2})) + \nabla(\tau_{ij}\vec{V}) \qquad (A.14)$$

The comparison between equation (A.14) and the equation (2.2.3), gives rise to the definition of the S_I term:

$$S_I = -\nabla(\frac{\mu}{P_r}\nabla(\frac{V^2}{2})) + \nabla(\frac{\mu}{P_r}\nabla(\frac{\Omega^2 r^2}{2})) + \nabla(\tau_{ij}\vec{V}) \qquad (A.15)$$

APPENDIX B

Tri-Diagonal-Matrix-Algorithm

The adoption of the "Line-by-Line" marching procedure at each cross-plane of the flow domain, as it was discussed in Section 3.4.1, causes the coefficients matrix $\underline{A}$ of the system of algebraic equations (3.4.3) to obtain a tridiagonal form. On each line, the discretised flow equations may be expressed in the form:

$$d_i\Phi_i = a_i\Phi_{i+1} + b_i\Phi_{i-1} + c_i \qquad \text{(B.1)}$$

where the terms involving neighbouring values of Φ not on the line have been taken explicitly into the source term c_i. Hence, the system of algebraic equations 3.4.3 obtains the following form for each grid line:

$$\begin{vmatrix} d_1 & a_1 & 0 & \cdots & 0 \\ b_2 & d_2 & a_2 & & \vdots \\ 0 & b_3 & d_3 & a_3 & \vdots \\ \vdots & & & & 0 \\ 0 & \cdots & 0 & b_m & d_m \end{vmatrix} \cdot \begin{vmatrix} \Phi_1 \\ \Phi_2 \\ \Phi_3 \\ \vdots \\ \Phi_m \end{vmatrix} = \begin{vmatrix} c_1 \\ c_2 \\ c_3 \\ \vdots \\ c_m \end{vmatrix} \qquad \text{(B.2)}$$

Matrix $\underline{A}$ is a tridiagonal matrix and a rapid technique for solving this type of system of equations was suggested by Thomas (1949) and is known as Thomas algorithm or Tri-Diagonal-Matrix-Algorithm (TDMA).

The system of equations is put into an upper triangular form by replacing the main diagonal elements d_i with:

$$d_i - \frac{b_i}{d_{i-1}}a_{i-1} \qquad i=2,3,\ldots,m \qquad \text{(B.3)}$$

and the source term elements c_i with:

$$c_i - \frac{b_i}{d_{i-1}}c_{i-1} \qquad i=2,3,\ldots,m \qquad \text{(B.4)}$$

The Φ_i values are subsequently computed using back substitution starting

with:

$$\Phi_m = \frac{c_m}{d_m} \tag{B.5}$$

and continuing with:

$$\Phi_i = \frac{c_i - a_i \Phi_{i+1}}{d_i} \qquad i=m-1,m-2,.....,1 \tag{B.6}$$

APPENDIX C

Description of blade geometry of C4 and NACA 65-($12A_{10}$)10 aerofoils

The thickness distribution of the C4 aerofoil is calculated from analytical relations as a function of the fractional distance p from the leading edge along the camber line of the blade and the designated maximum thickness of the blade t_{max}, Calvert (1988):

$$t = 2(28.110p^3-25.281p^2-6.563p+15.492p^{\frac{1}{2}})\frac{t_{max}}{10} \quad if \quad p<0.3$$

$$t = 2(3.448p^3-14.632p^2+7.848p+3.869)\frac{t_{max}}{10} \quad if \quad p\geq 0.3$$

The coordinates of the NACA 65-($12A_{10}$)10 are given in the following table:

SUCTION SIDE		PRESSURE SIDE	
x/c	y/c	x/c	y/c
0.0	0.0	0.0	0.0
0.161	0.971	0.839	-0.371
0.374	1.227	1.126	-0.387
0.817	1.679	1.683	-0.395
1.981	2.599	3.019	-0.367
4.399	4.035	5.601	-0.243
6.868	5.178	8.132	-0.090
9.361	6.147	10.639	0.057
14.388	7.734	15.612	0.342
19.477	8.958	20.553	0.594
24.523	9.915	25.477	0.825
29.611	10.640	30.389	1.024
34.706	11.153	35.294	1.207
39.804	11.479	40.196	1.373
44.904	11.598	45.096	1.542
50.000	11.488	50.000	1.748
55.087	11.139	54.913	2.001
60.161	10.574	59.839	2.278
65.214	9.801	64.786	2.559
70.245	8.860	69.755	2.804
75.256	7.808	74.744	2.932
80.242	6.607	79.758	2.945
85.204	5.272	84.796	2.804
90.154	3.835	89.846	2.369
95.096	2.237	94.904	1.555
100.068	0.134	99.932	-0.134

L.E. radius = 0.666 Slope through L.E. radius = 0.505

APPENDIX D

Geometry of Eckardt's radial and backswept impellers

The main dimensions of Eckardt's radial and backswept impellers are presented in Figure D.1. The radial impeller is noted with the letter O and the backswept with the letter A. Both impellers have 20 blades and an identical shroud contour which consists of a straight line segment and two circular arcs with radius 59 mm and 85 mm respectively. The blade camber lines have ellipsoidal shapes in cylindrical sections. The ellipse can be reconstructed using the relation:

$$\frac{(Y-a)^2}{a^2} + \frac{X^2}{b^2} = 1 \qquad (D.1)$$

where the circumferential half-axis a of the ellipse is proportional to the radius R from the axis of rotation:

$$\begin{aligned} a &= 4.7693 \cdot R \ \ mm \\ b &= 220.579 \ \ mm \end{aligned} \qquad (D.2)$$

The hub profile of the radial impeller consists of a circular arc with a radius of 141 mm and a straight line segment at the impeller discharge.

The hub profile of the backswept impeller is provided in Table D.1.

Z in mm	R in mm
0	60.000
20	64.818
40	71.153
60	79.962
80	92.484
95	105.681
105	117.500
115	133.782
120	145.005
125	160.750
130	200.000

TABLE D.1 Hub profile of Backswept Impeller

The circumferential backsweep of the backswept rotor commences at a radius of R = 160 mm and its distribution as a function of radius is given in Table D.2.

R in mm	ϵ in deg	β_b in deg
160	0.000	90.000
170	0.204	82.239
180	0.908	73.213
190	2.092	64.805
200	3.663	60.000

TABLE D.2 Backsweep angle Distribution

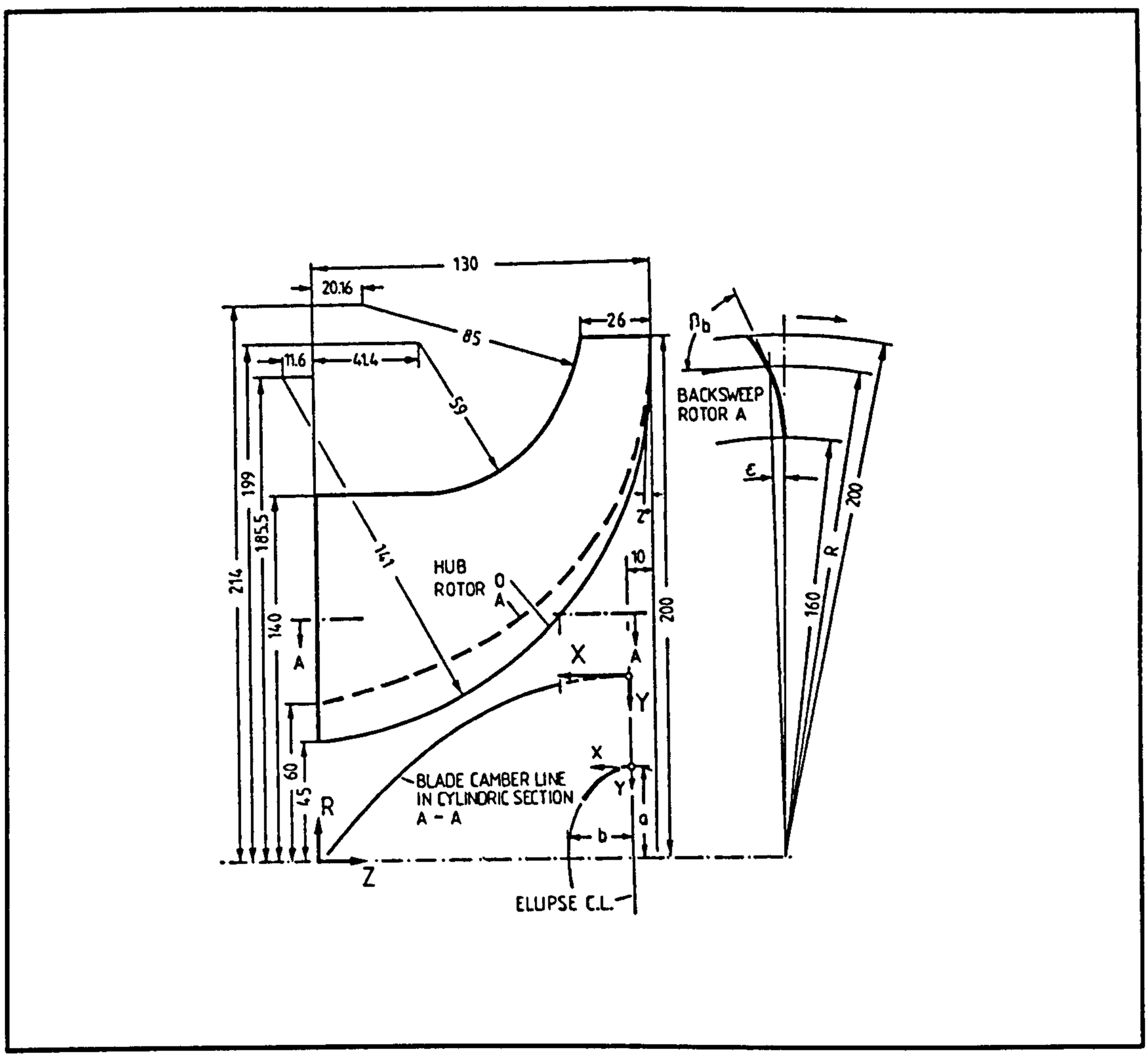

FIGURE D.1 Geometry of Eckardt's radial and backswept impellers

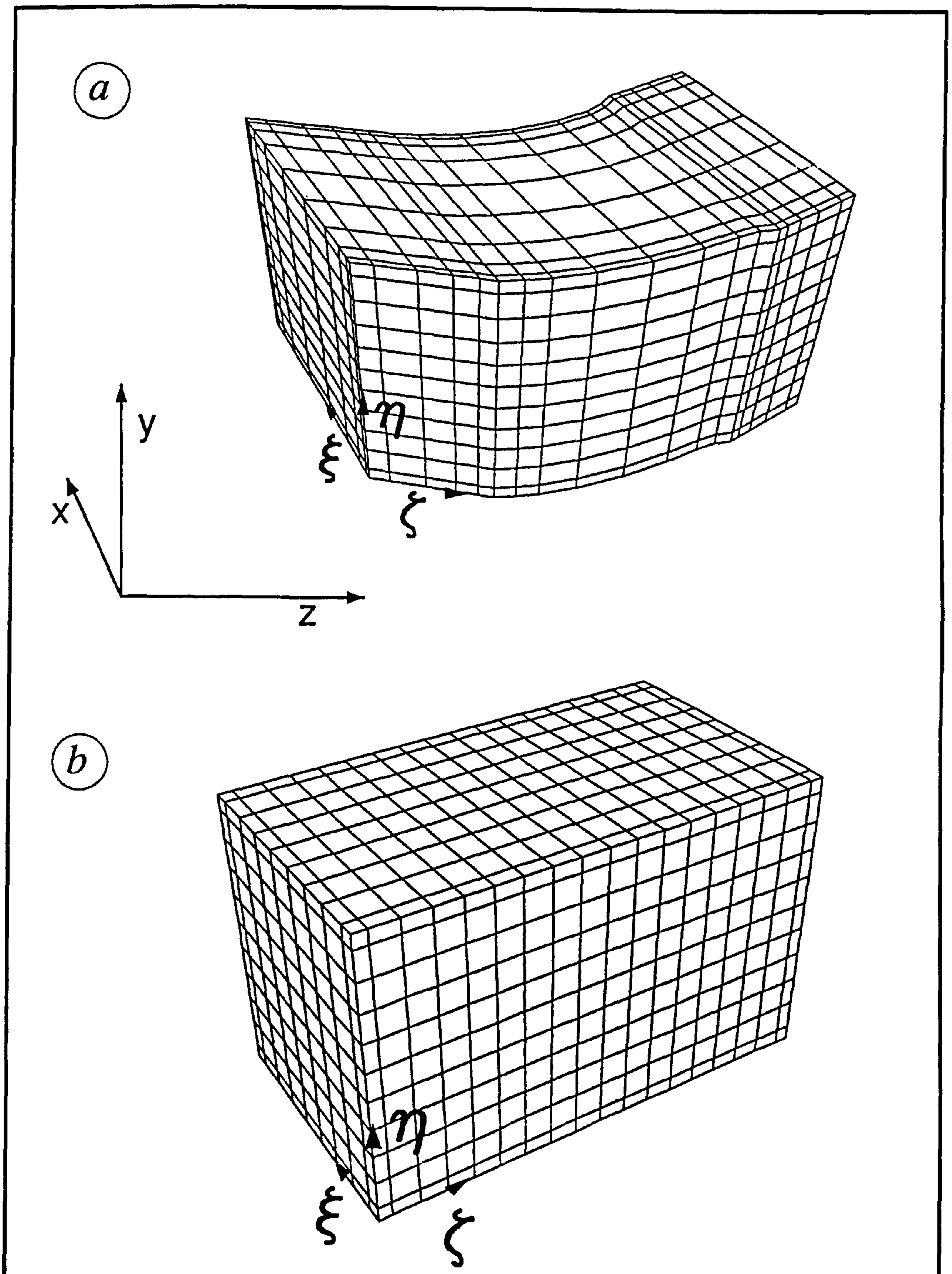

Figure 3.1 : (a) Computational grid in physical space.
(b) Computational grid in computational space.

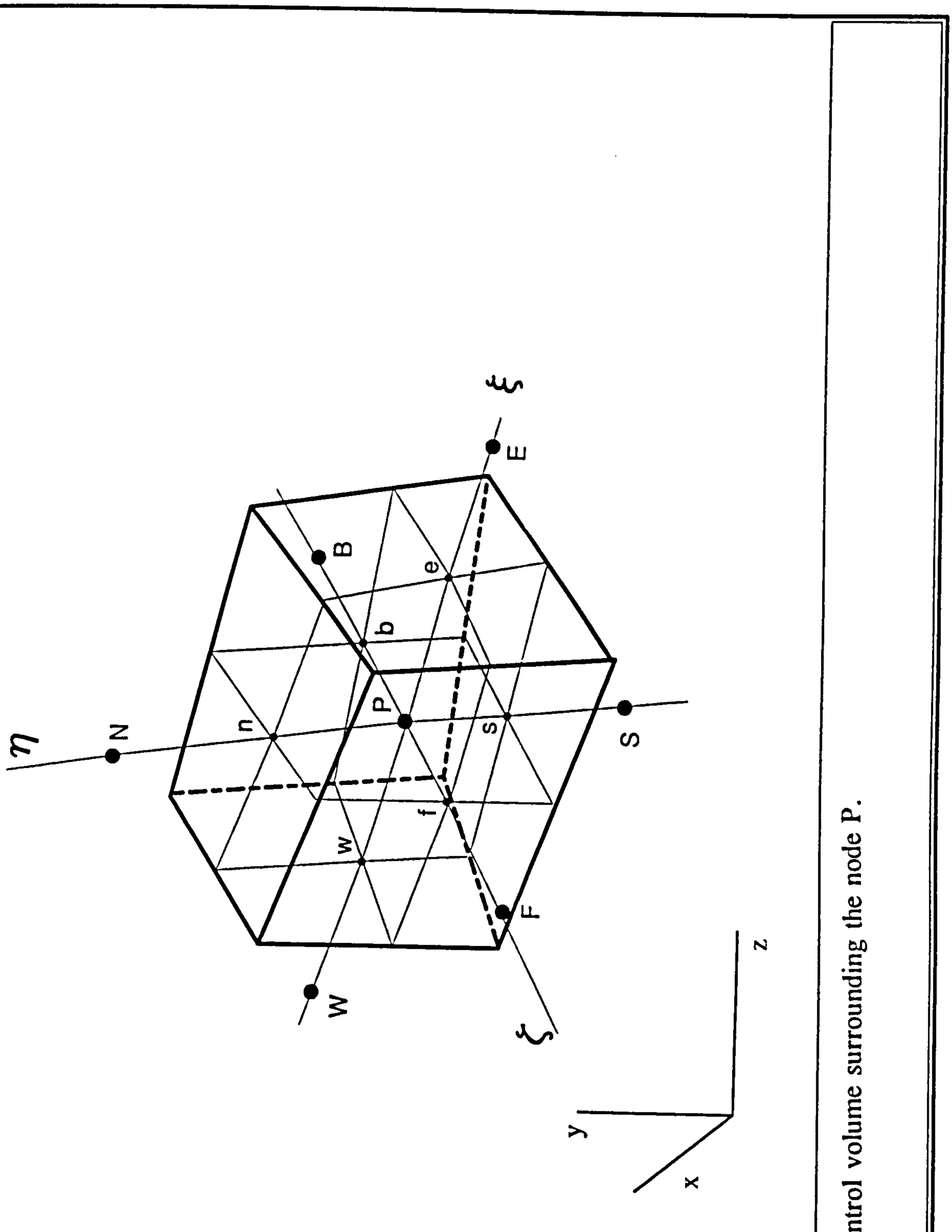

Figure 3.2 : Control volume surrounding the node P.

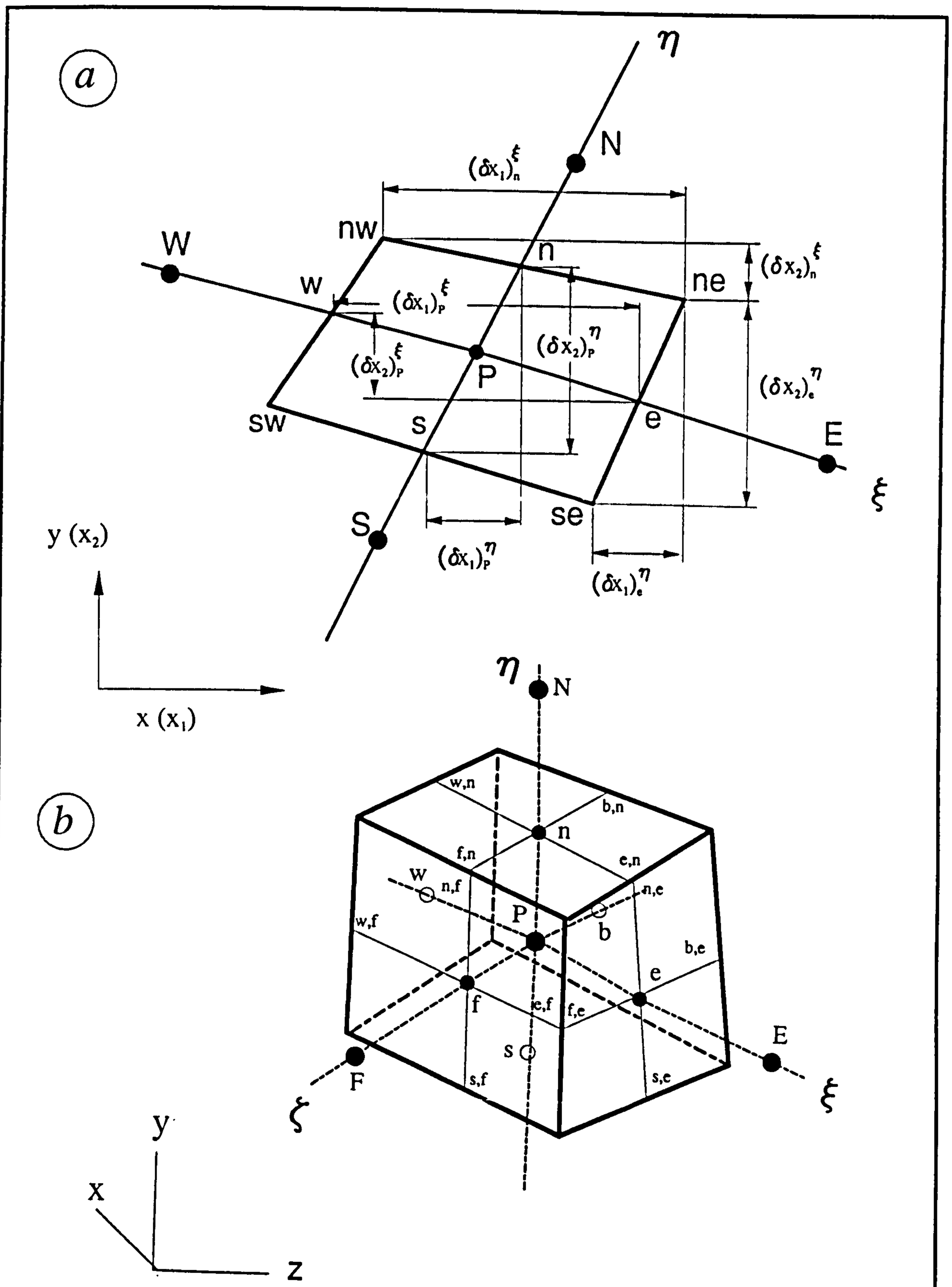

Figure 3.3 : (a) Basic geometrical parameters of the control volume.
(b) Faces "e", "n" and "f" of the control volume.

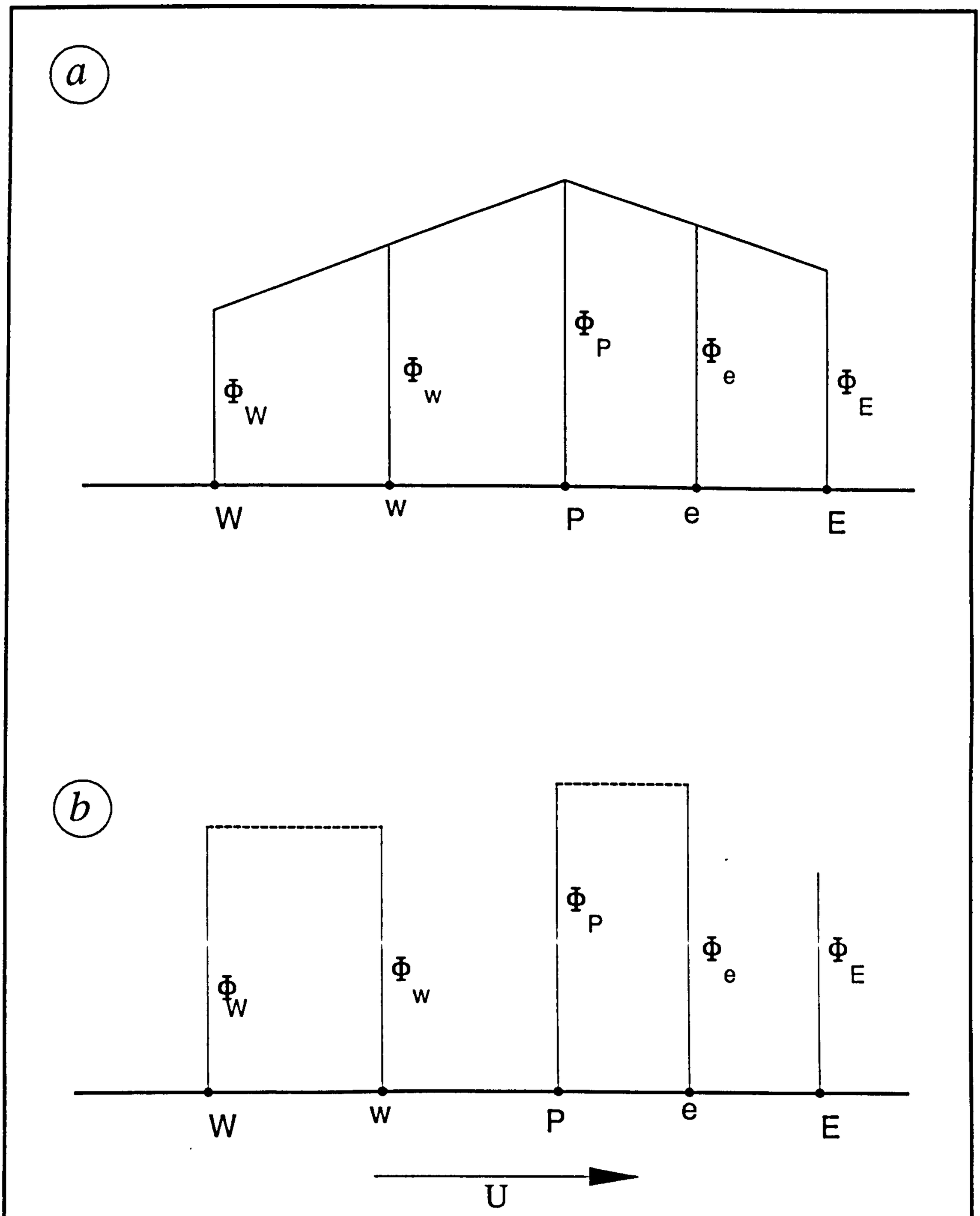

Figure 3.4 : (a) Interpolation practice used in the Central difference scheme.
(b) Interpolation practice used in the Upwind scheme.

c

i

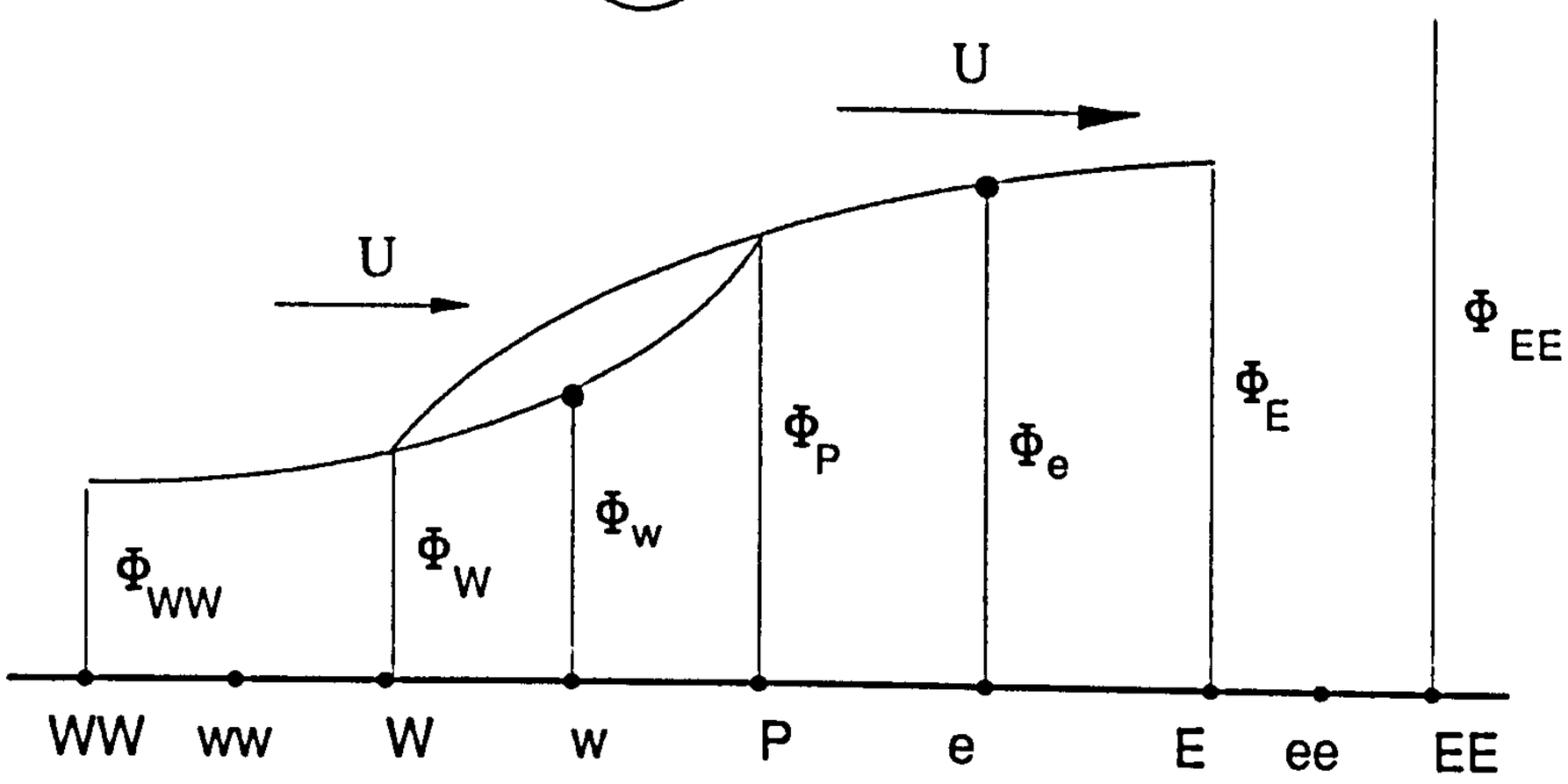

ii

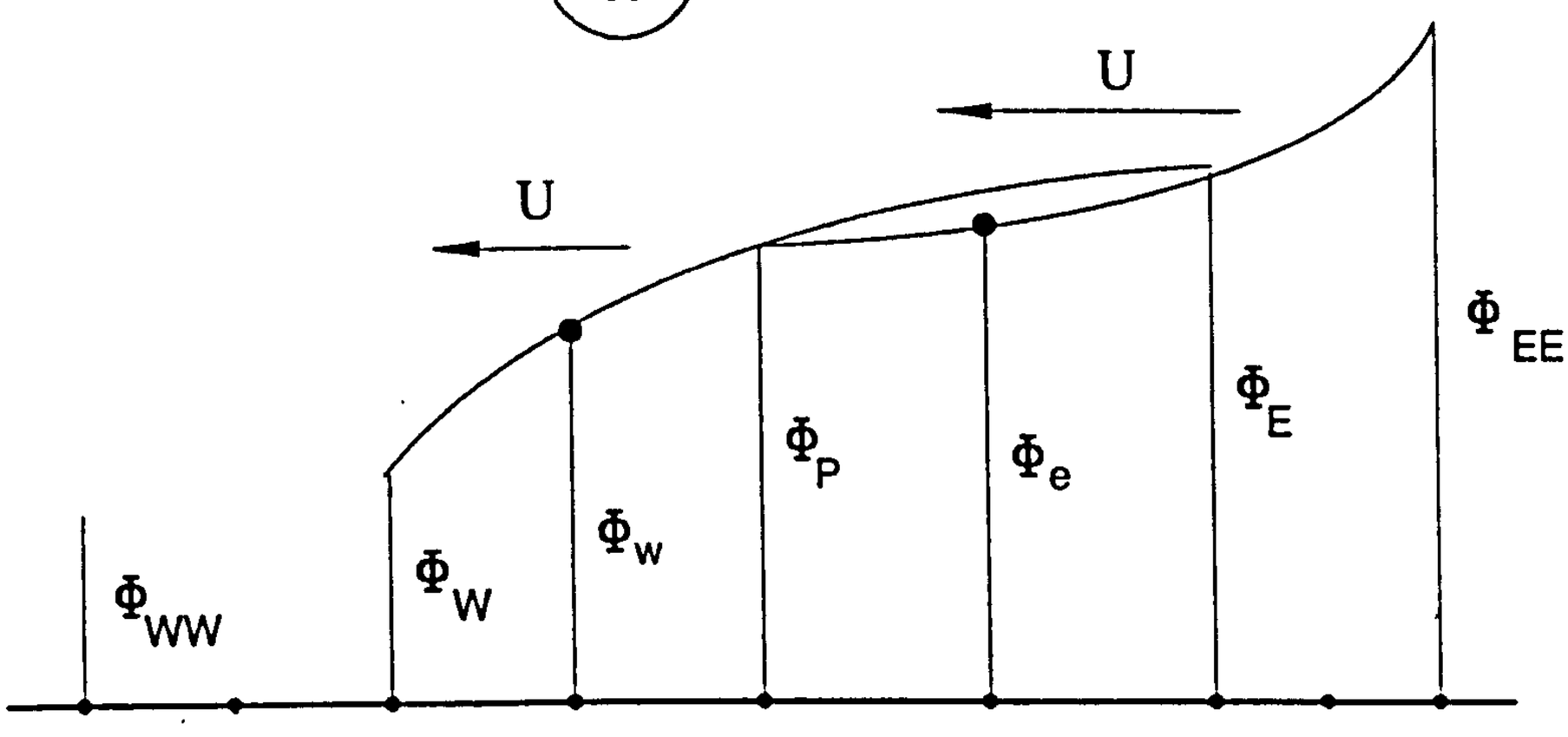

Figure 3.4 : (c) Interpolation practice used in the QUICK scheme for i) positive, and ii) negative convective velocity.

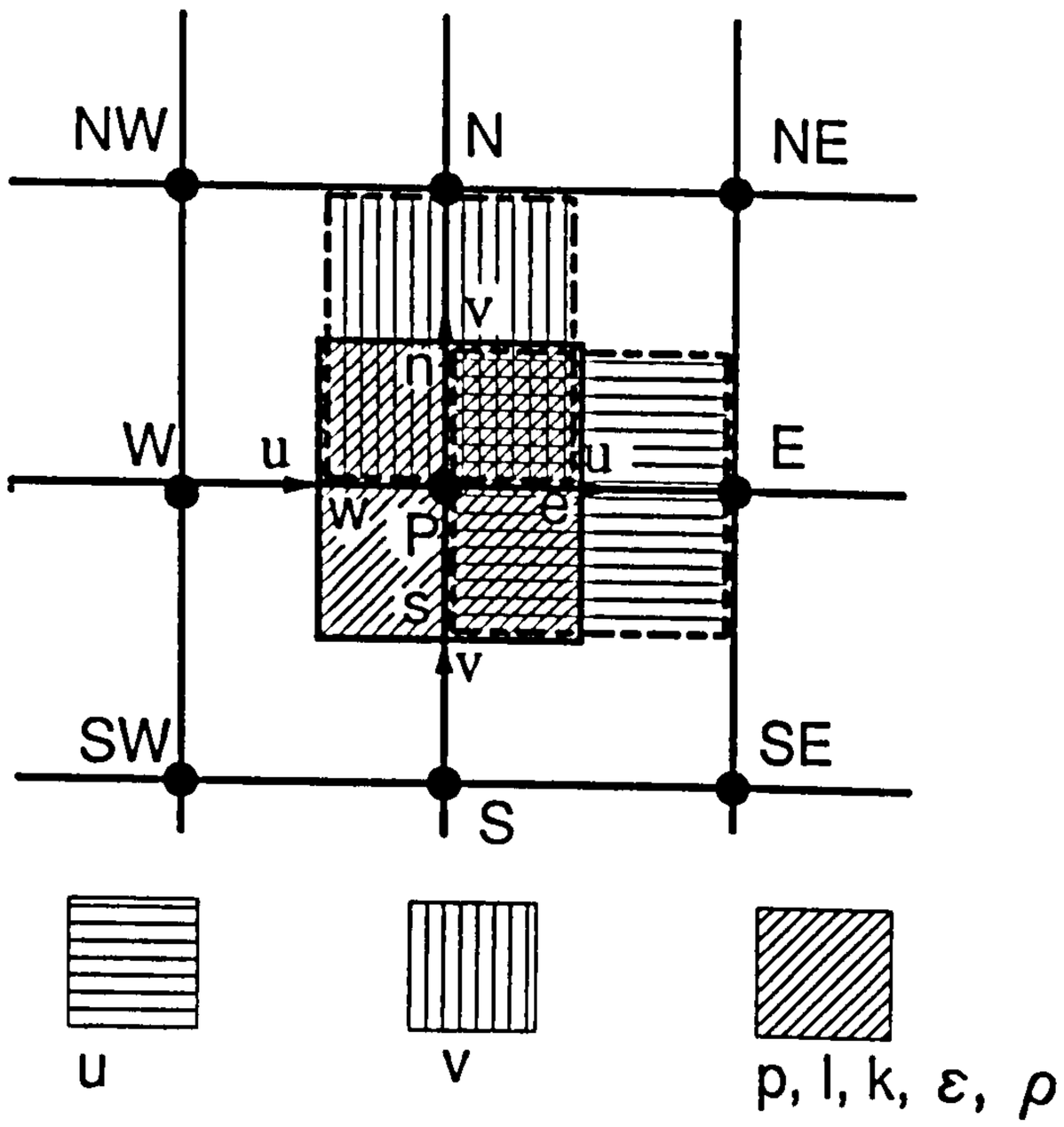

Figure 3.5 : Control volumes for the dependent variables on a staggered grid.

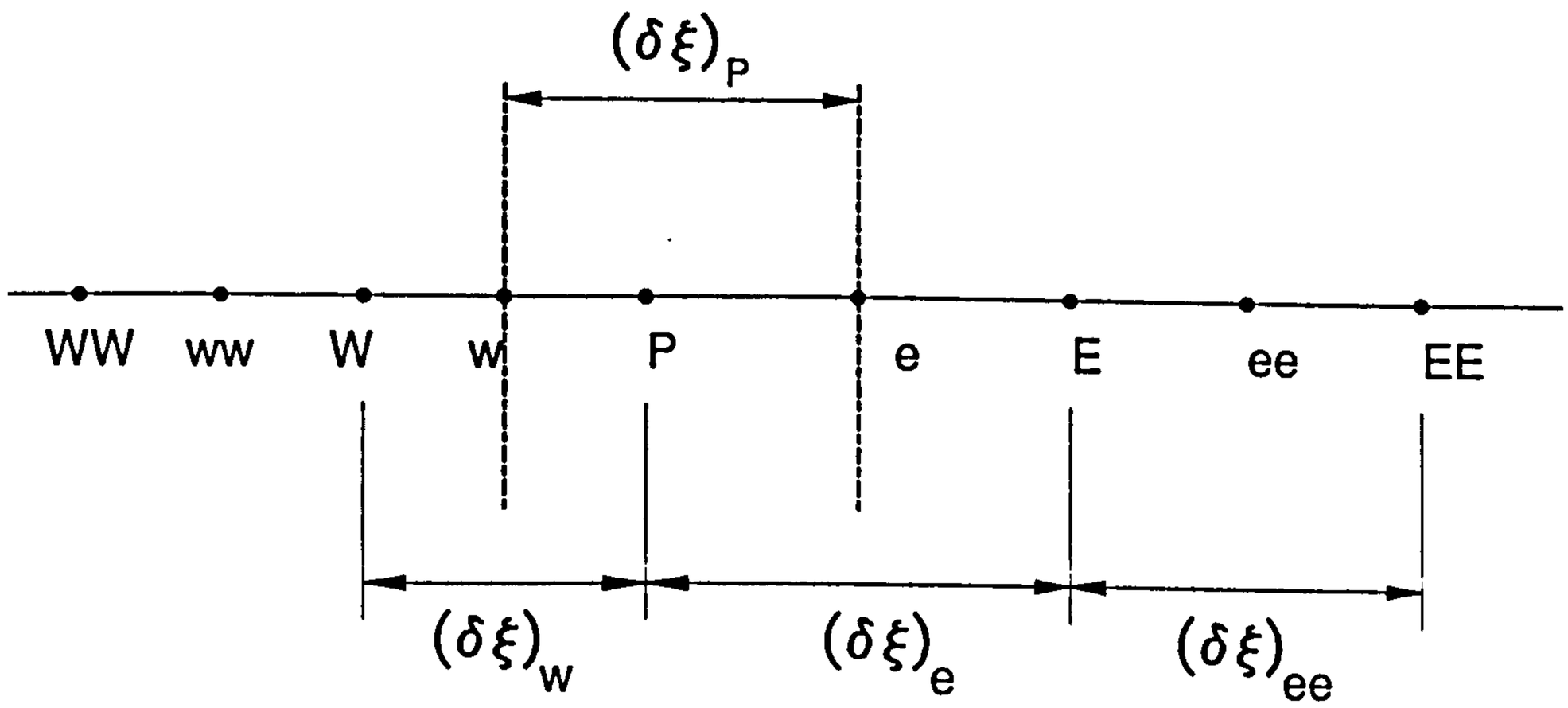

Figure 3.6 : Neighbouring points of node P for the implementation of the Rhie and Chow scheme.

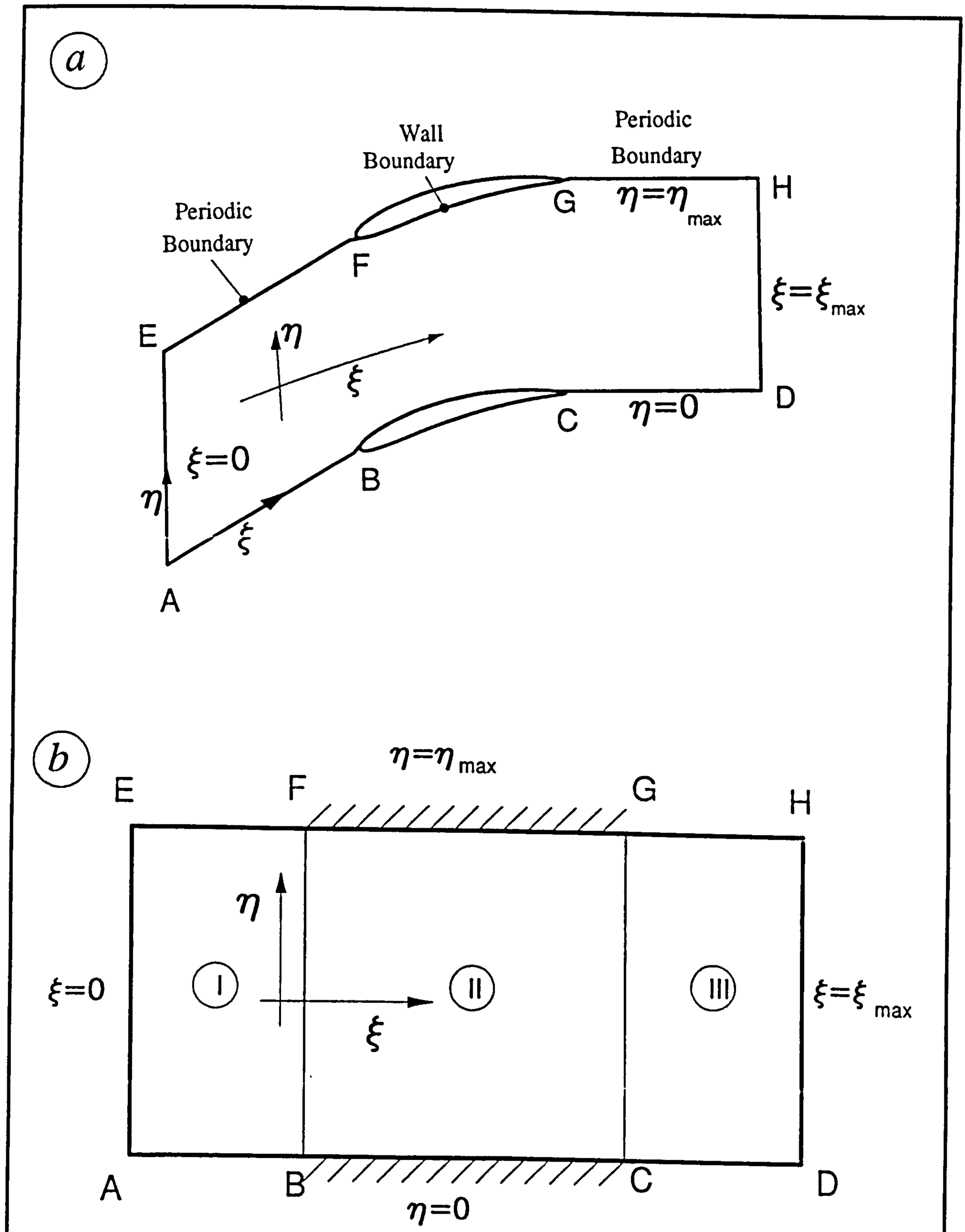

Figure 4.1 : Topology and notation for grid generation.
(a) Physical space. (b) Computational space.

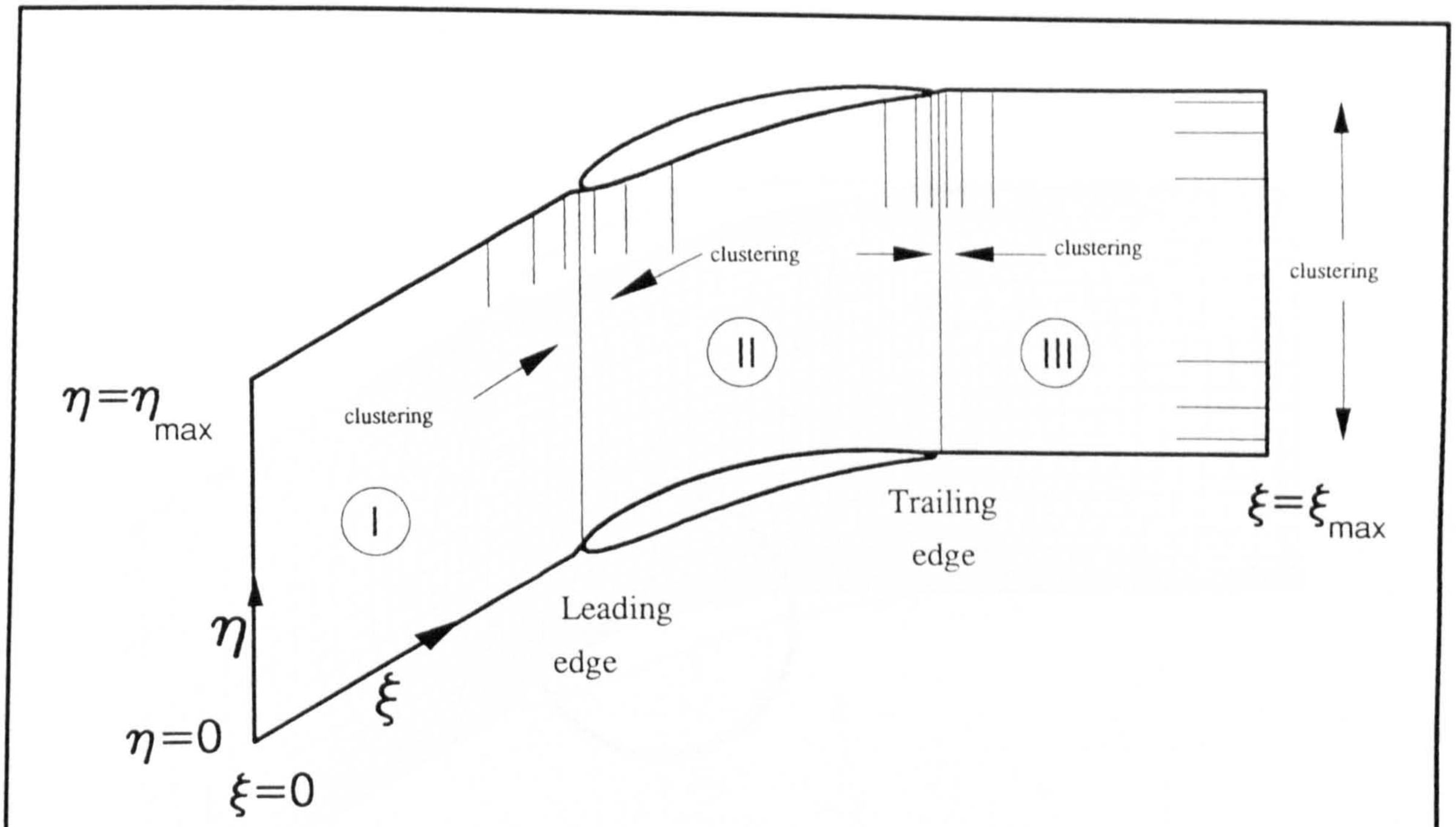

Figure 4.2 : Regions and features of the grid.

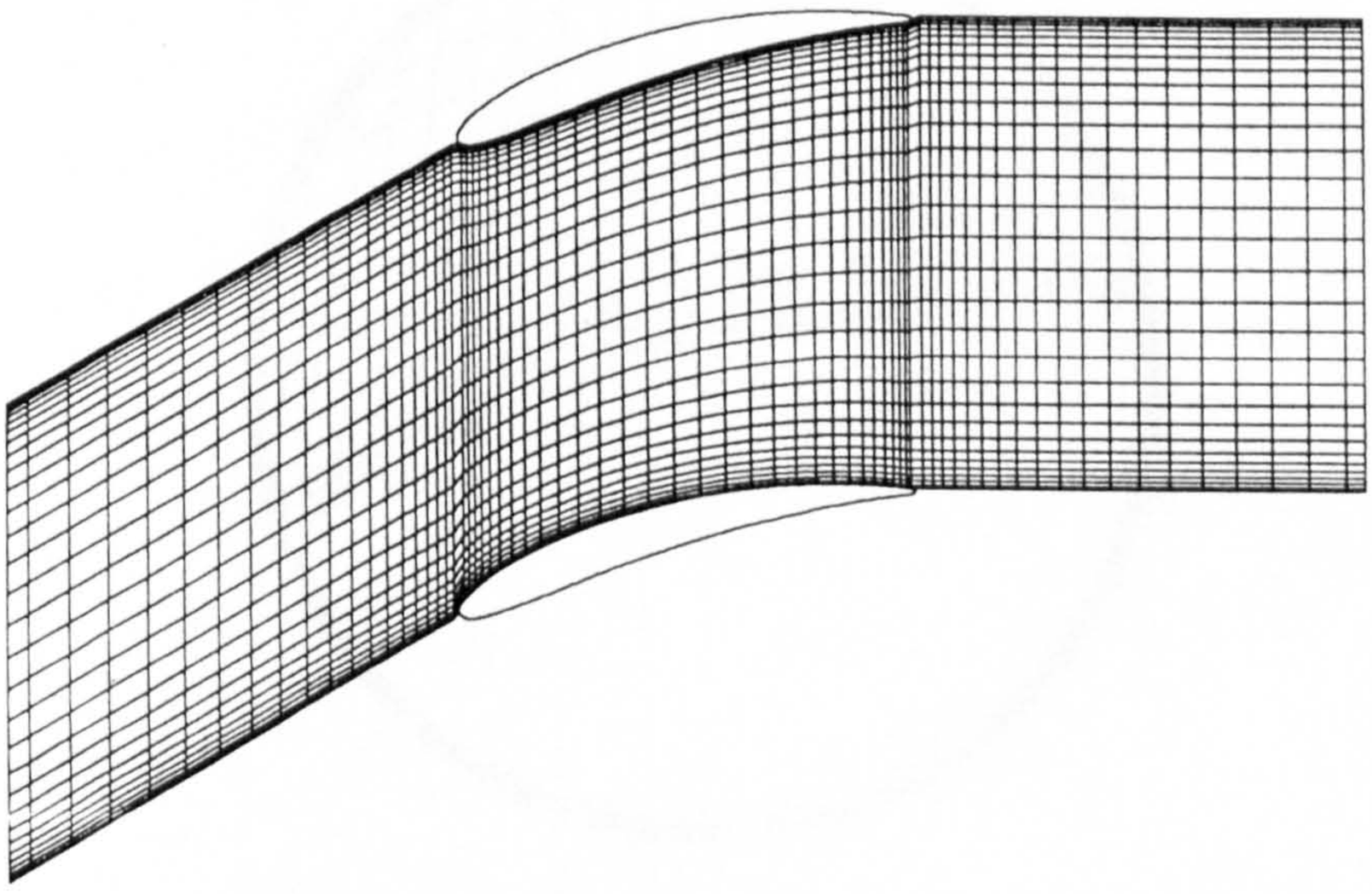

Figure 4.3 : Initial grid for NGTE 10C4/30C50 cascade, stagger angle = 15°.

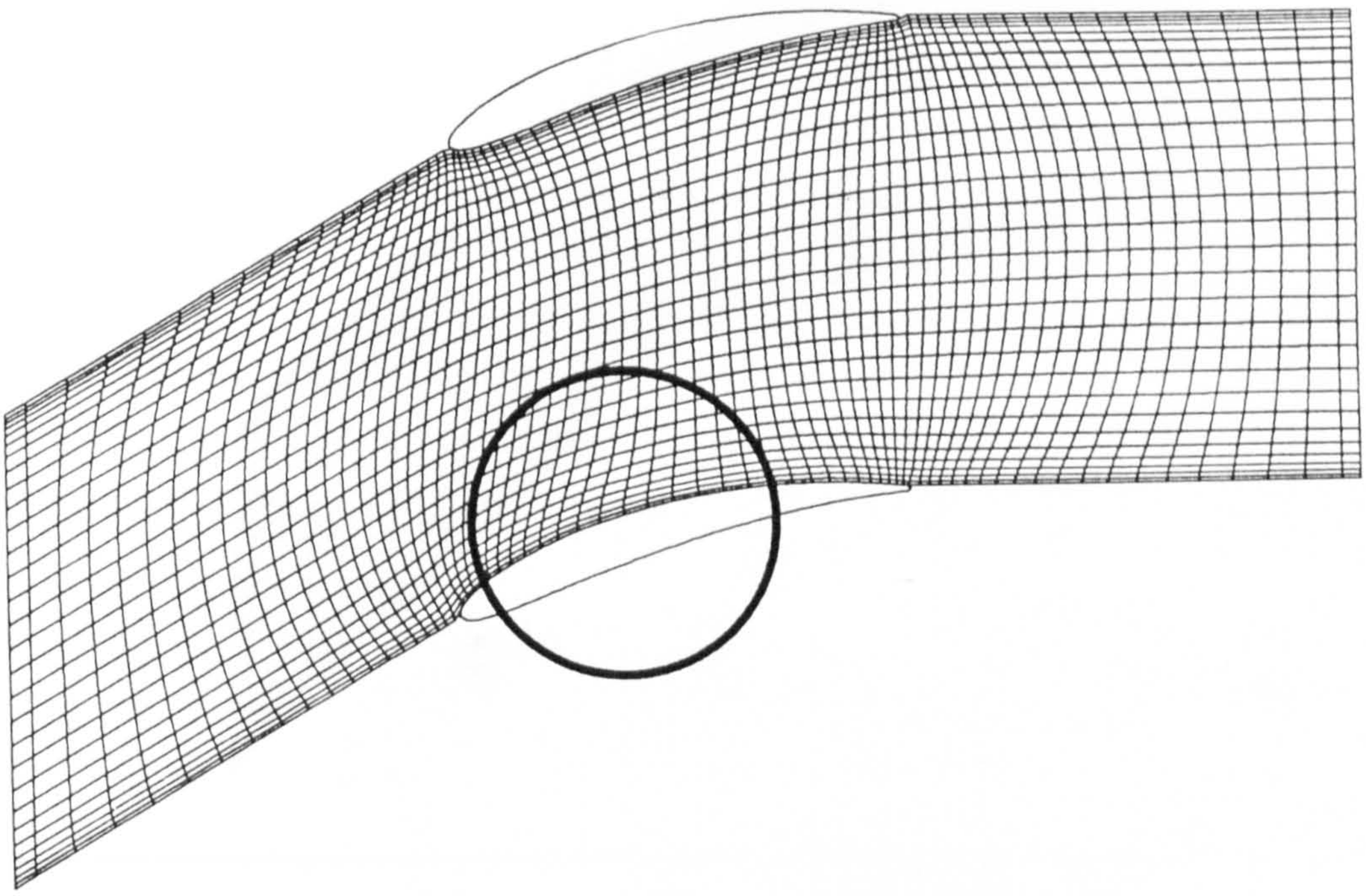

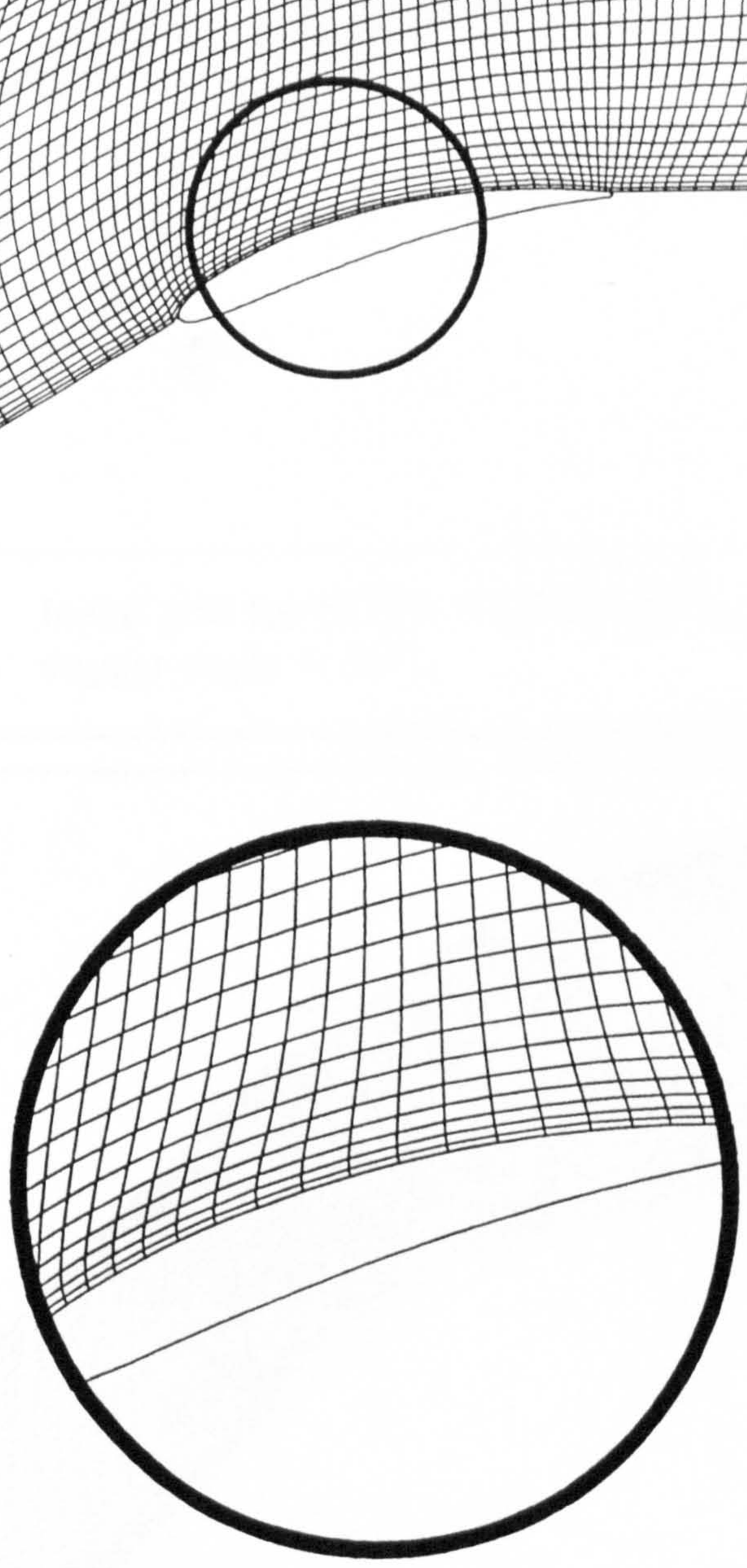

Figure 4.4 : Generated grid for NGTE 10C4/30C50 cascade, stagger angle = 15°.

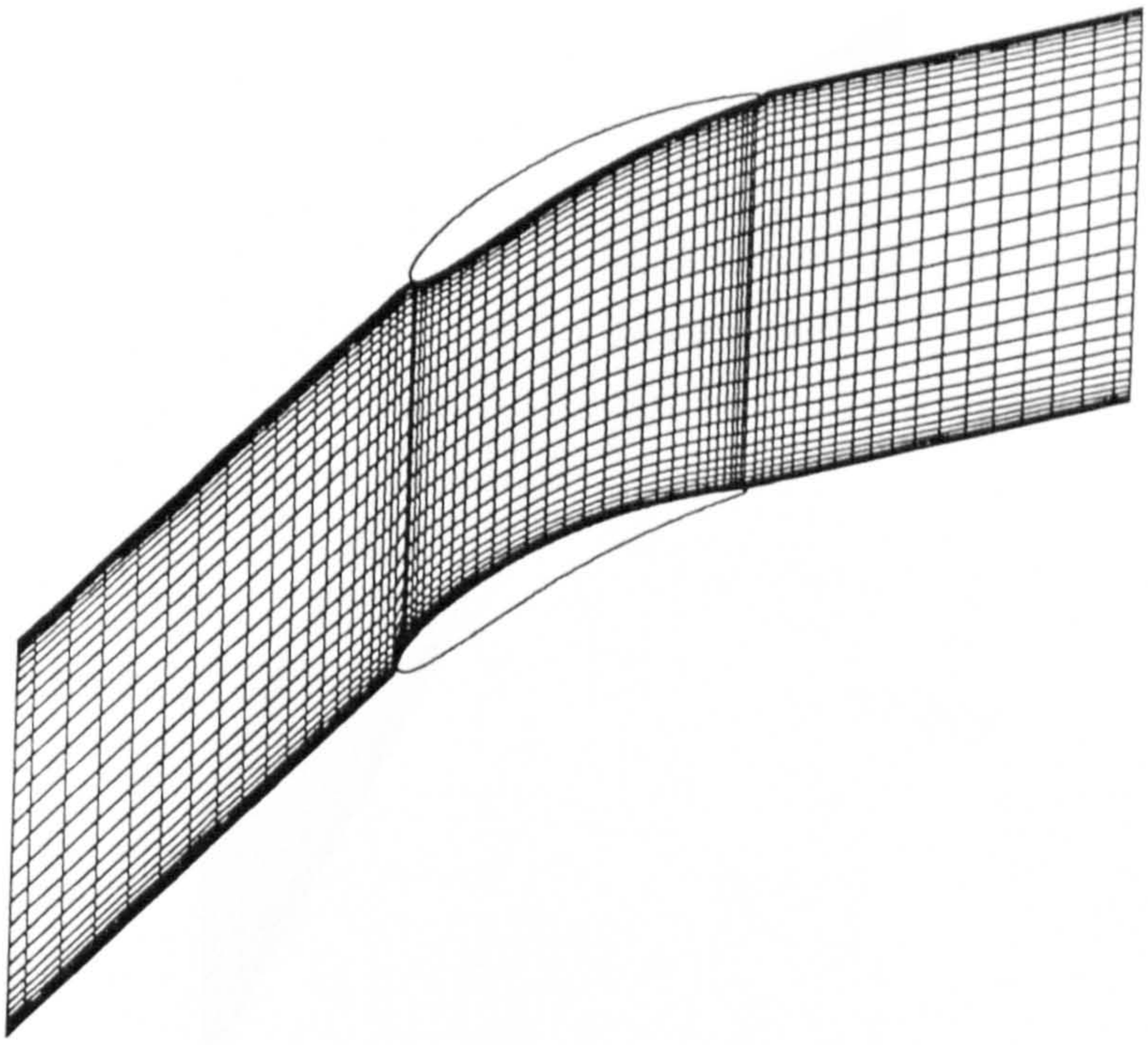

Figure 4.5 : Initial grid for NGTE 10C4/30C50 cascade, stagger angle = 30°.

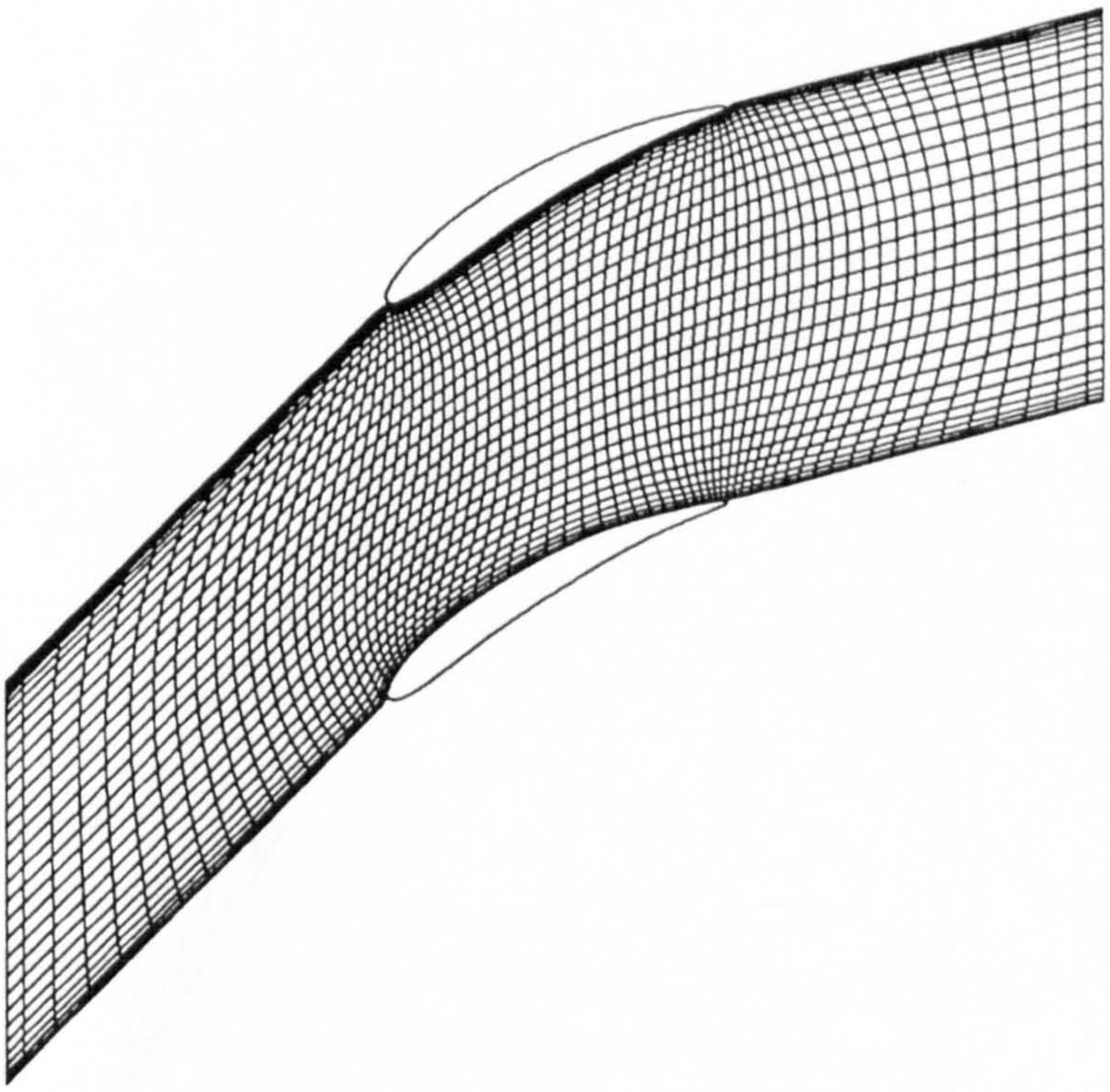

Figure 4.6 : Generated grid for NGTE 10C4/30C50 cascade, stagger angle = 30°.

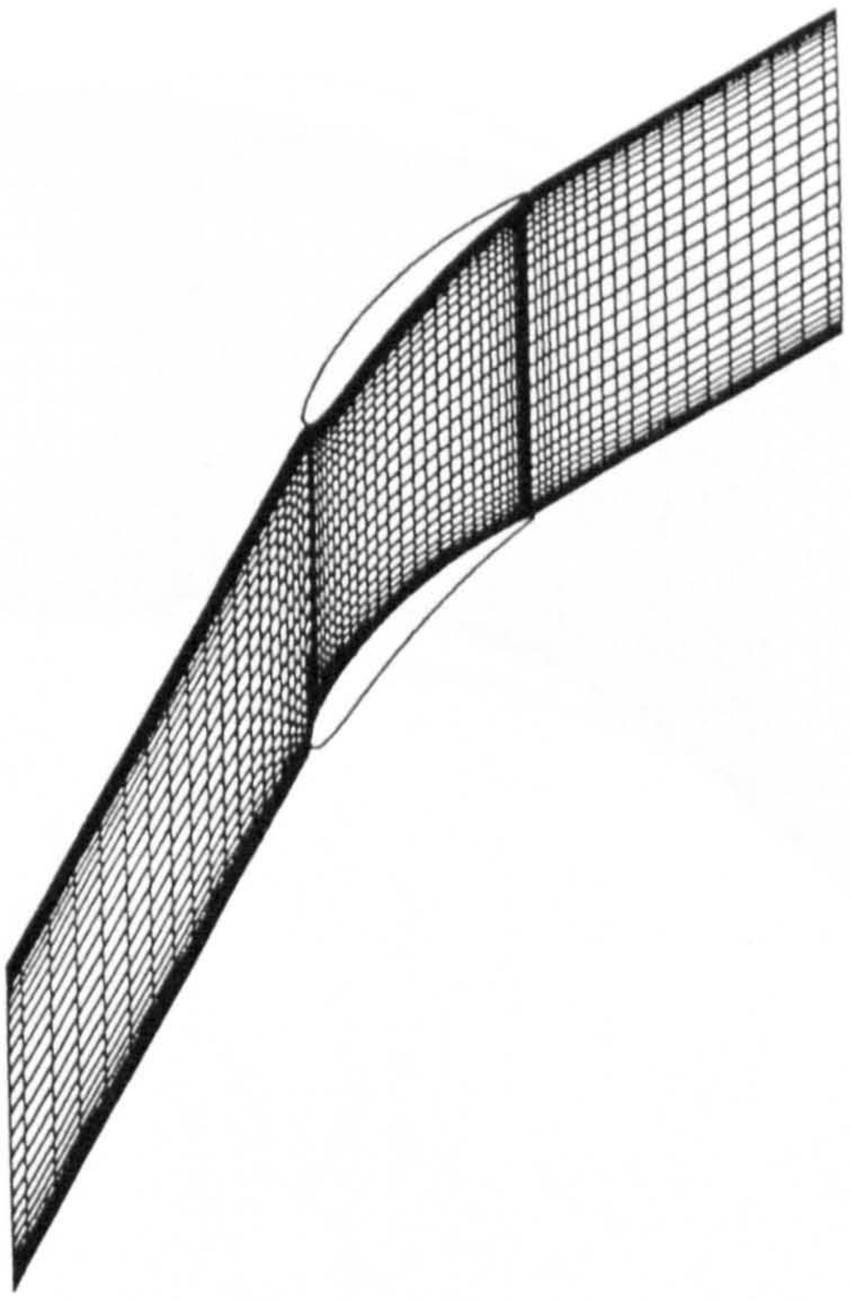

Figure 4.7 : Initial grid for NGTE 10C4/30C50 cascade, stagger angle = 45°.

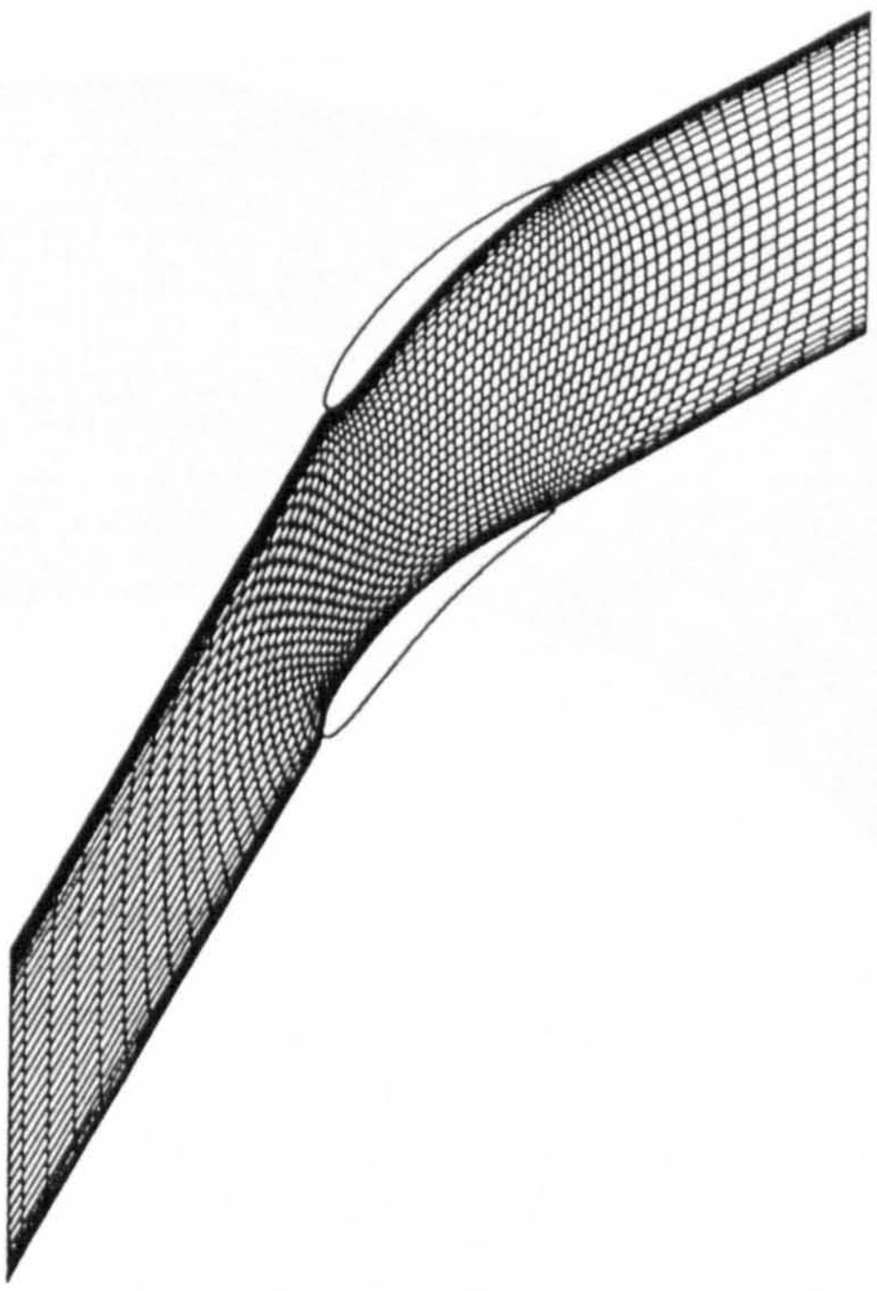

Figure 4.8 : Generated grid for NGTE 10C4/30C50 cascade, stagger angle = 45°.

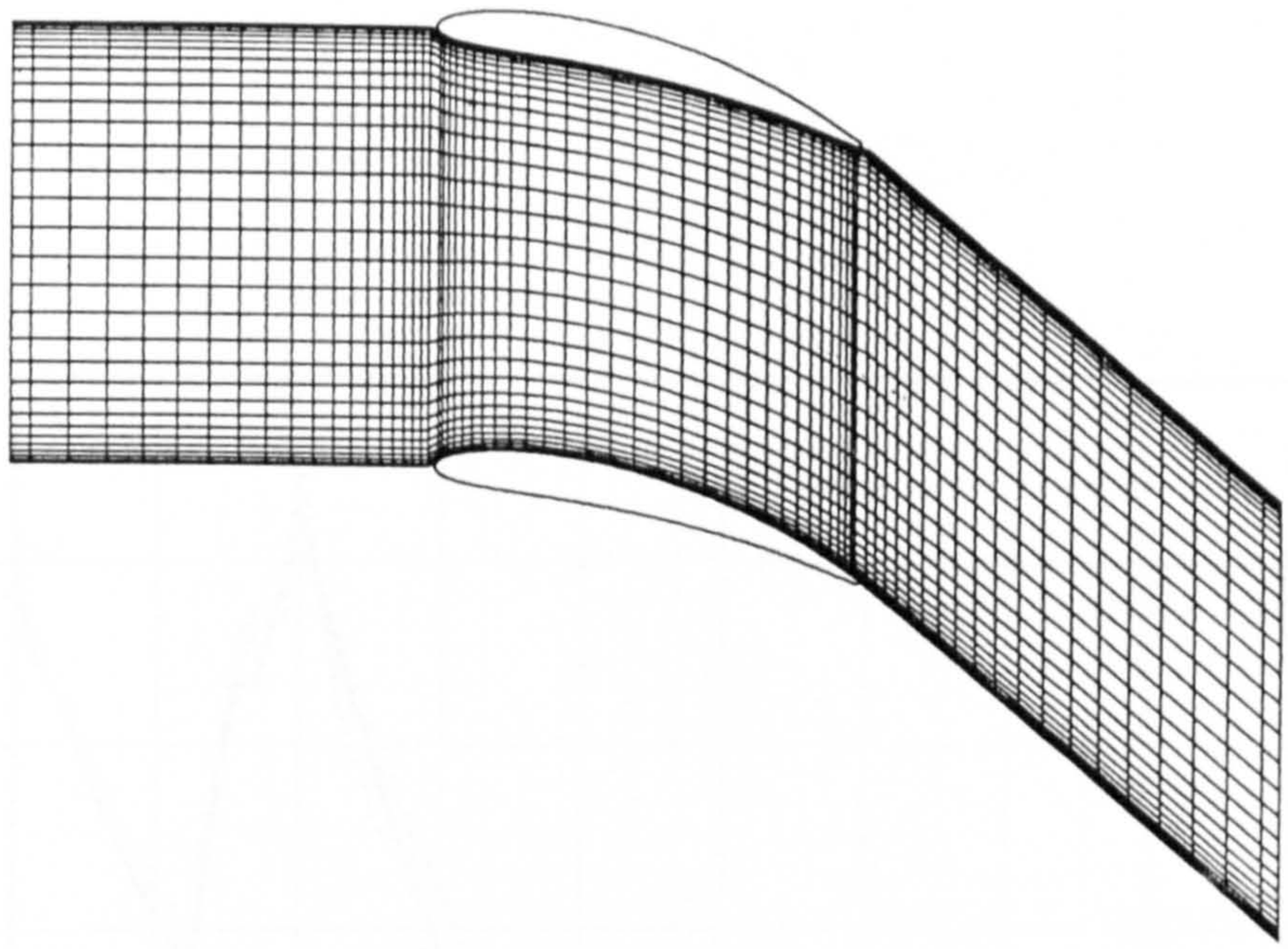

Figure 4.9 : Initial grid for NGTE 10C4/30C50 cascade, stagger angle = -15°.

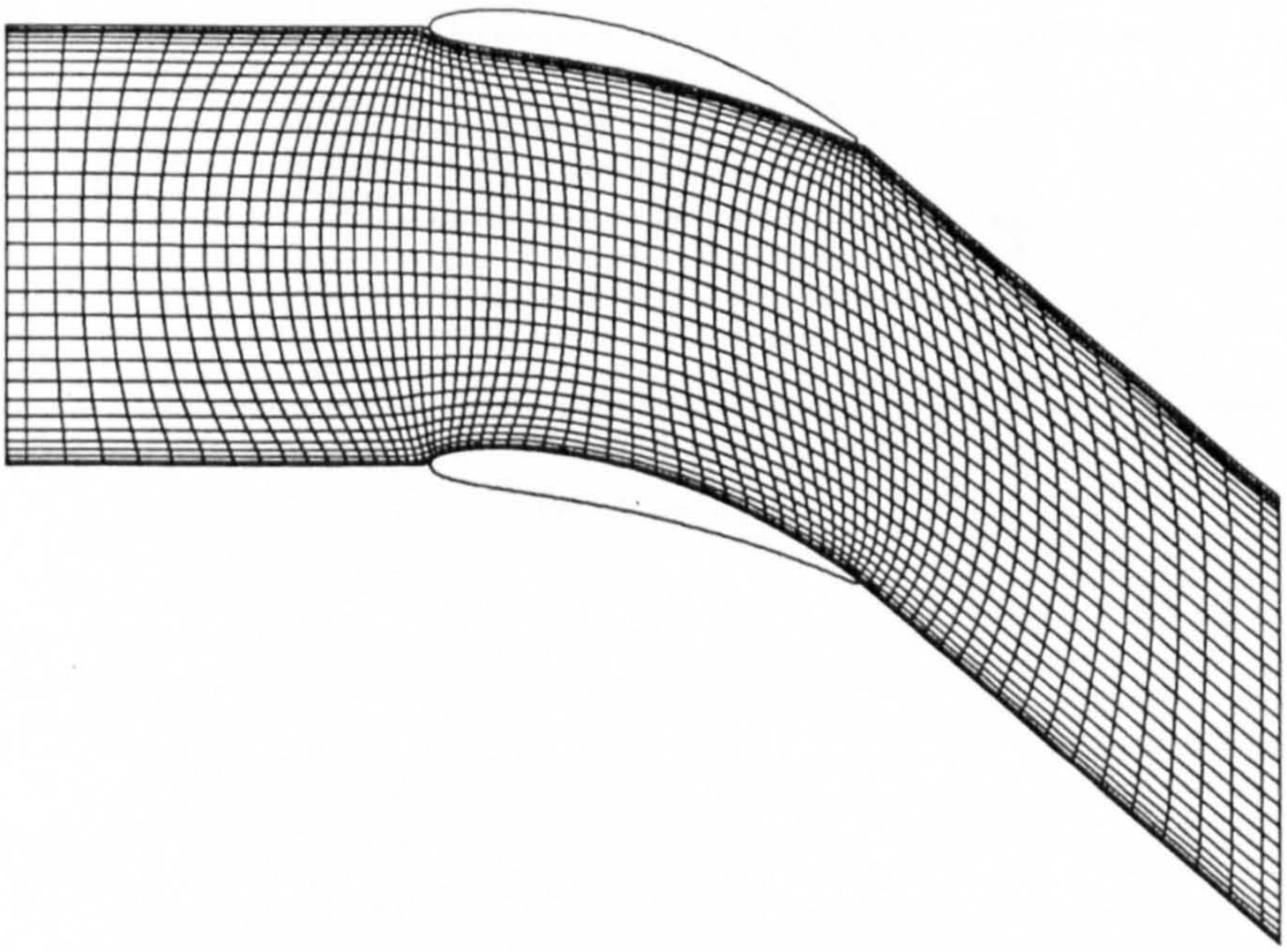

Figure 4.10 : Generated grid for NGTE 10C4/30C50 cascade, stagger angle = -15°.

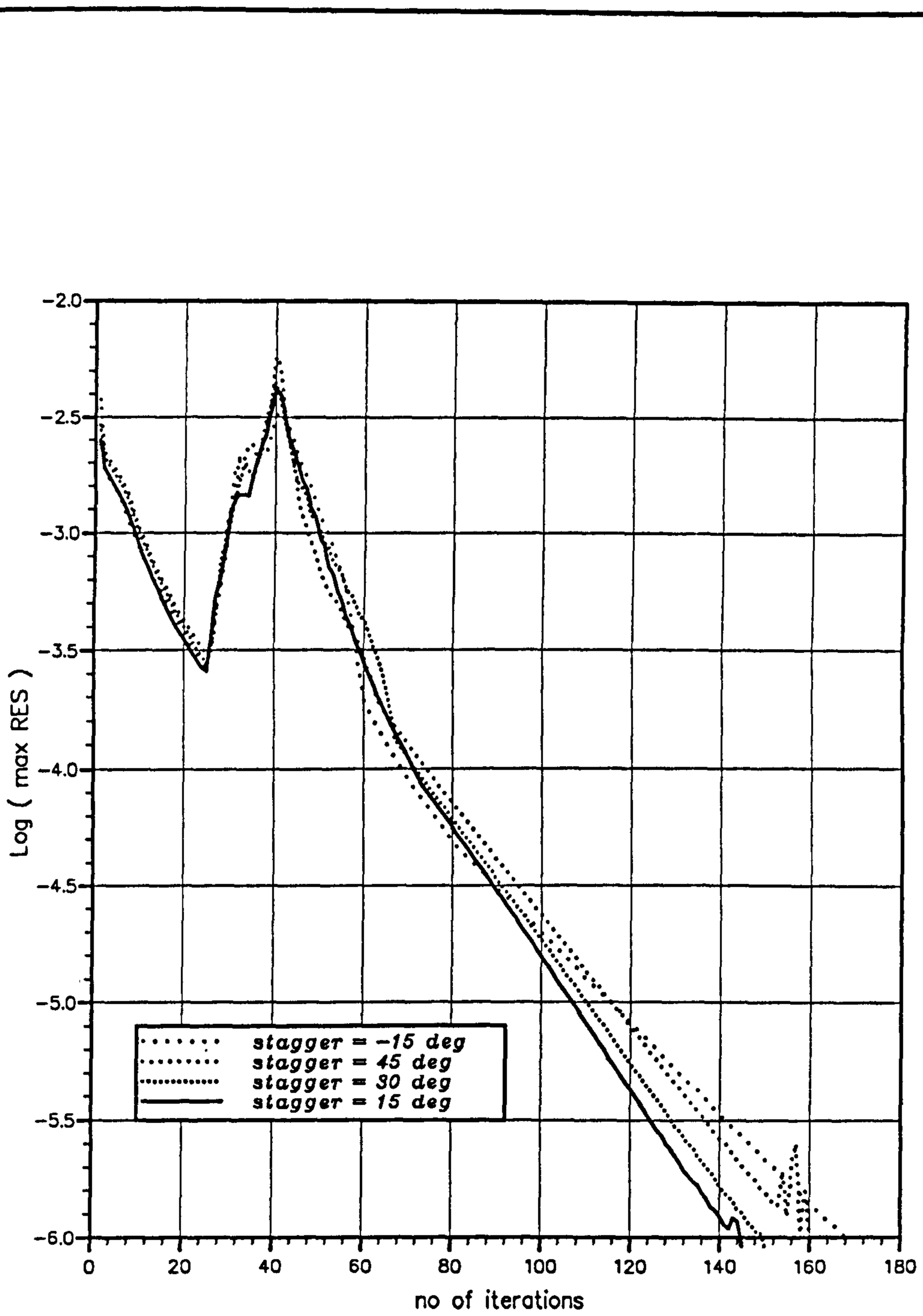

Figure 4.11 : Effect of stagger angle on convergence. 70 x 30 grid.

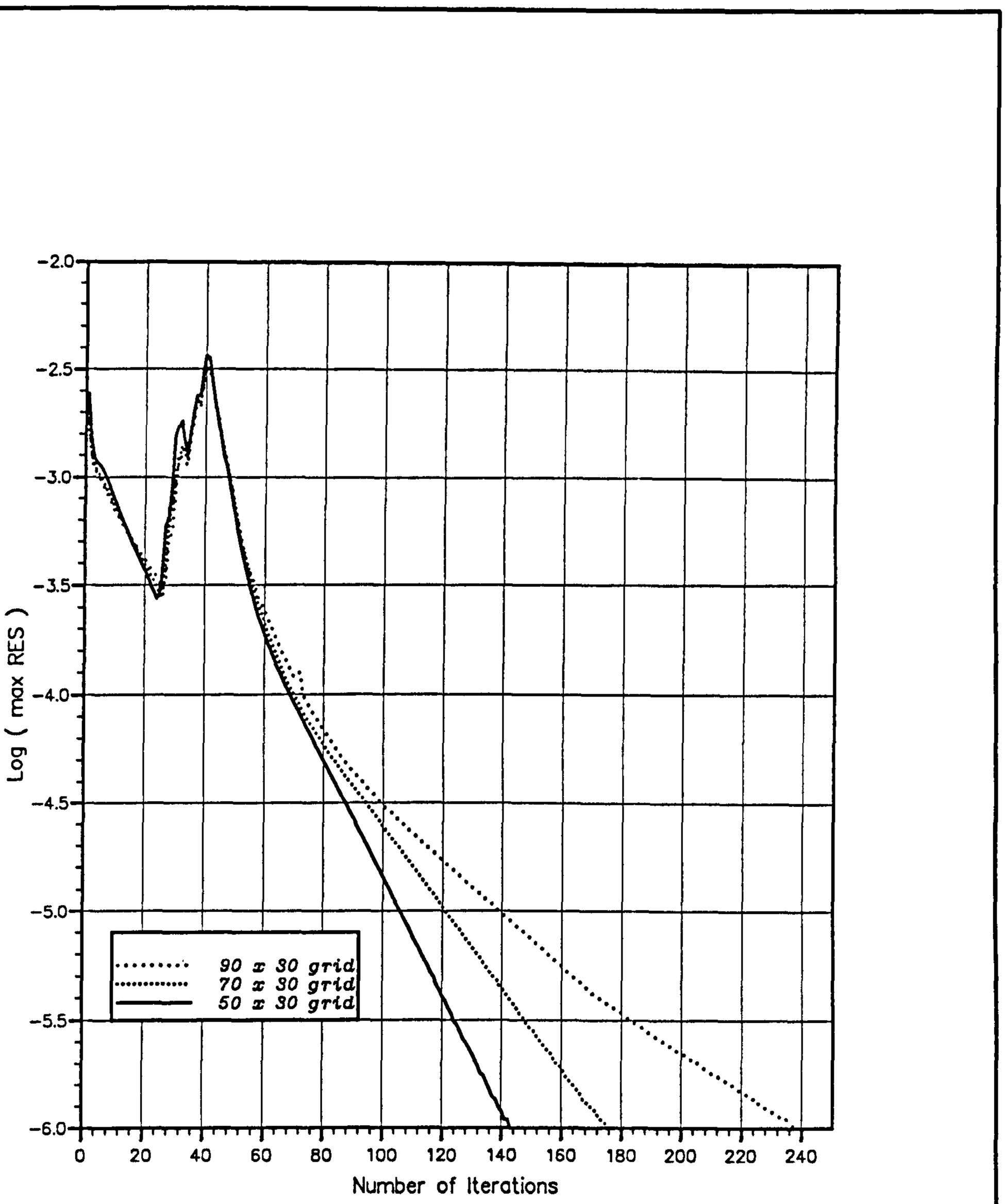

Figure 4.12 : Effect of grid size on convergence, stagger angle = 15°.

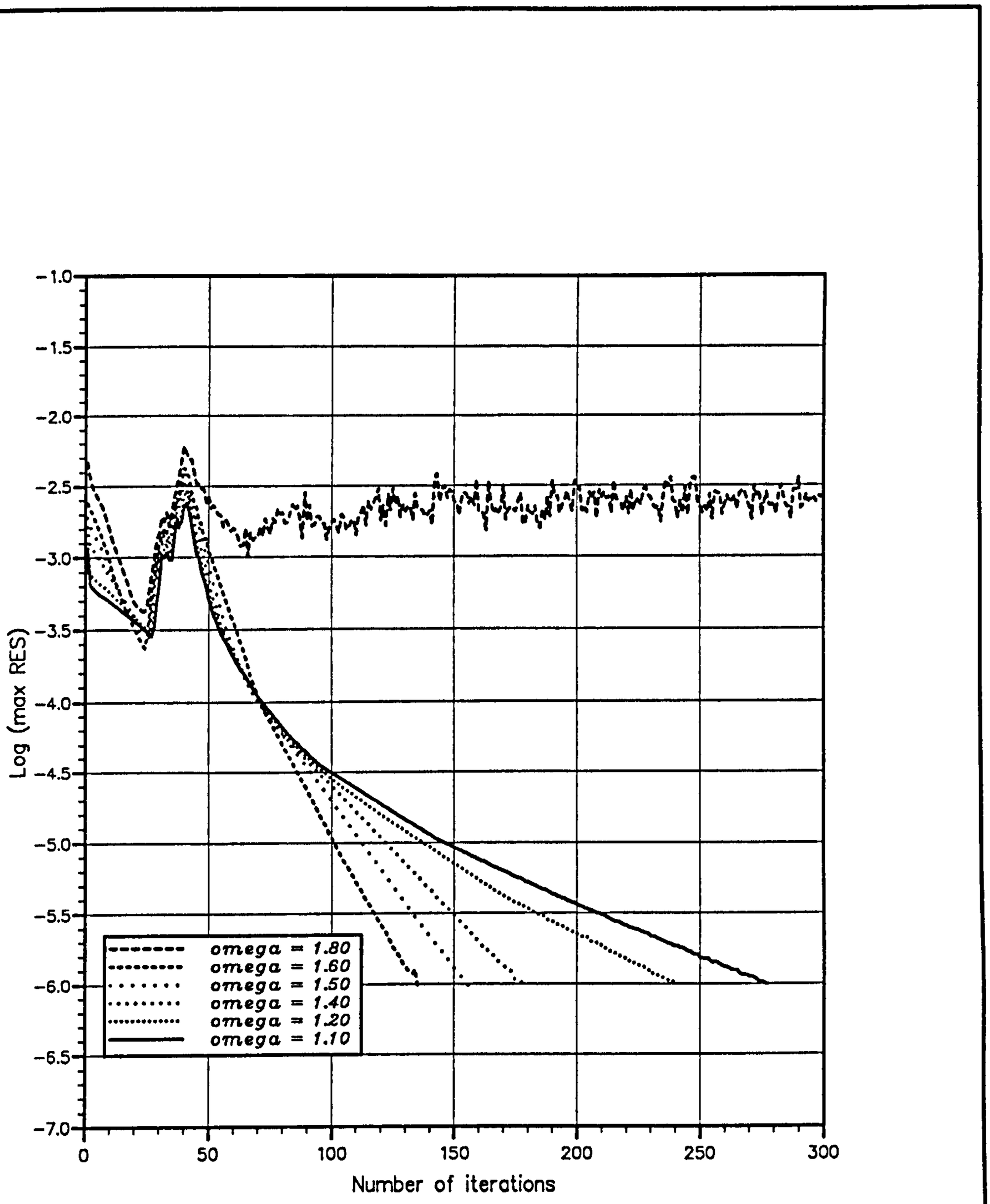

Figure 4.13 : Effect of over-relaxation factor ω on convergence history.

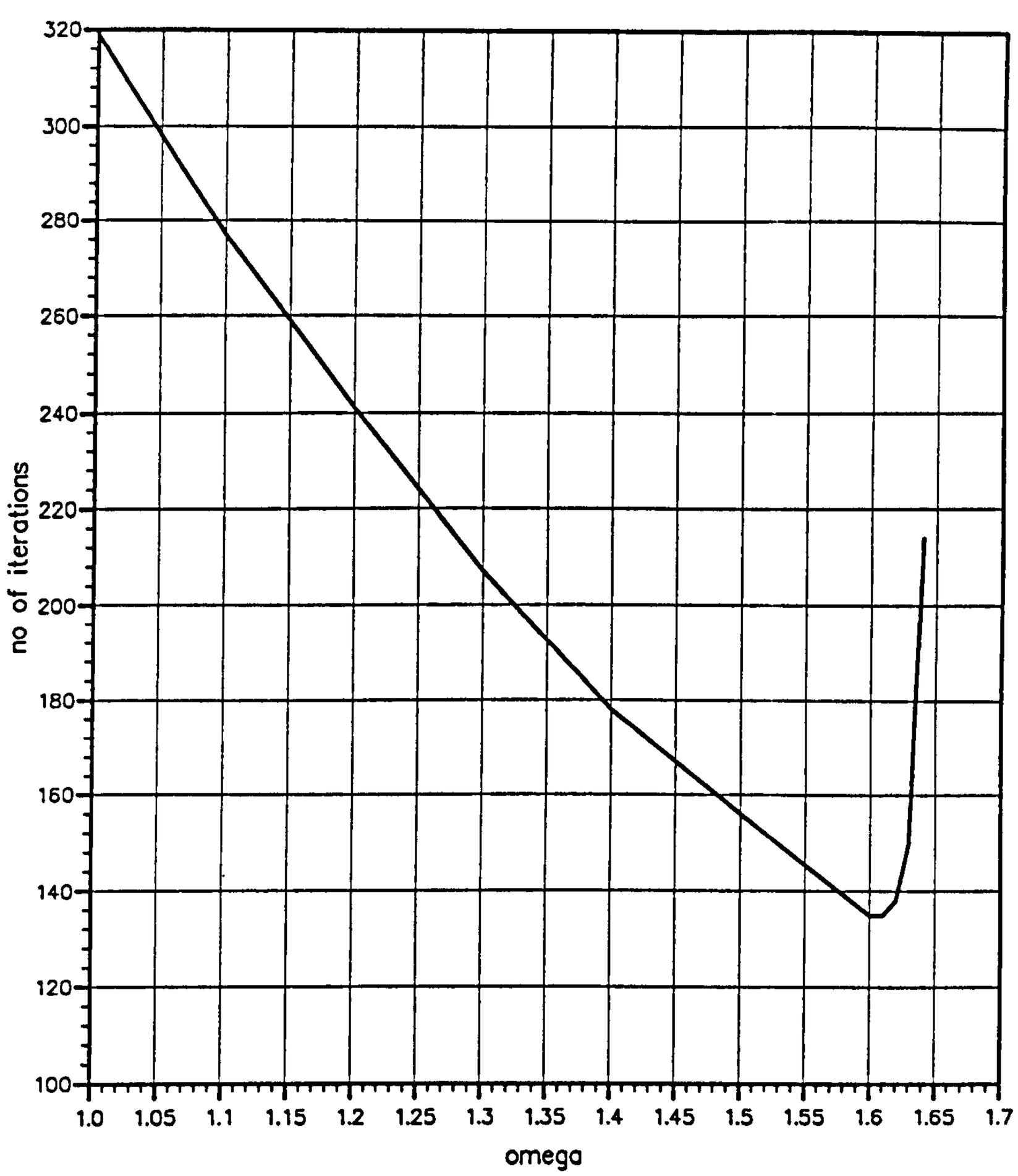

Figure 4.14 : Effect of over-relaxation factor ω on number of iterations for convergence. Convergence criterion $\epsilon_c = 1.0e\text{-}06$.

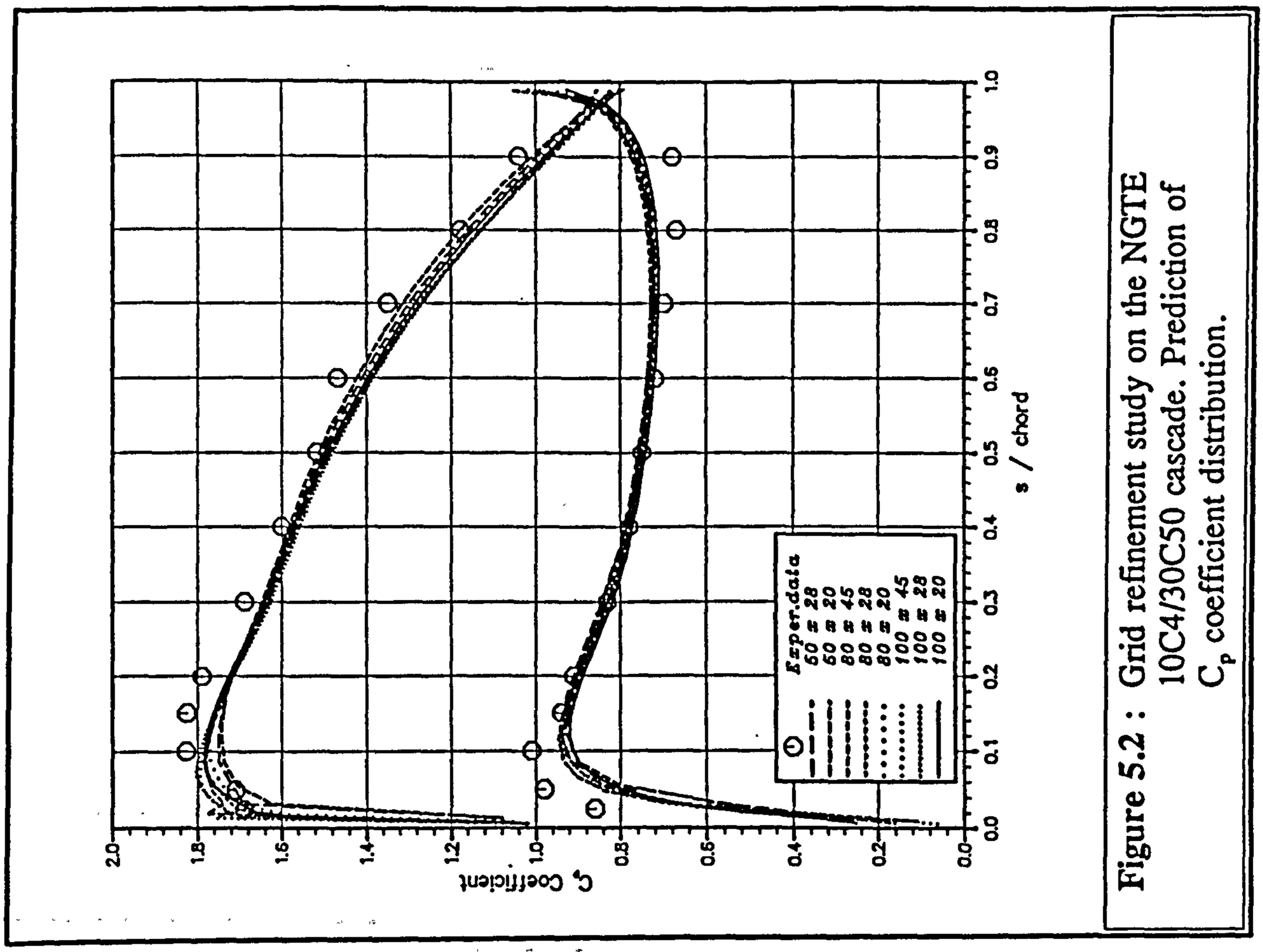

Figure 5.2 : Grid refinement study on the NGTE 10C4/30C50 cascade. Prediction of C_p coefficient distribution.

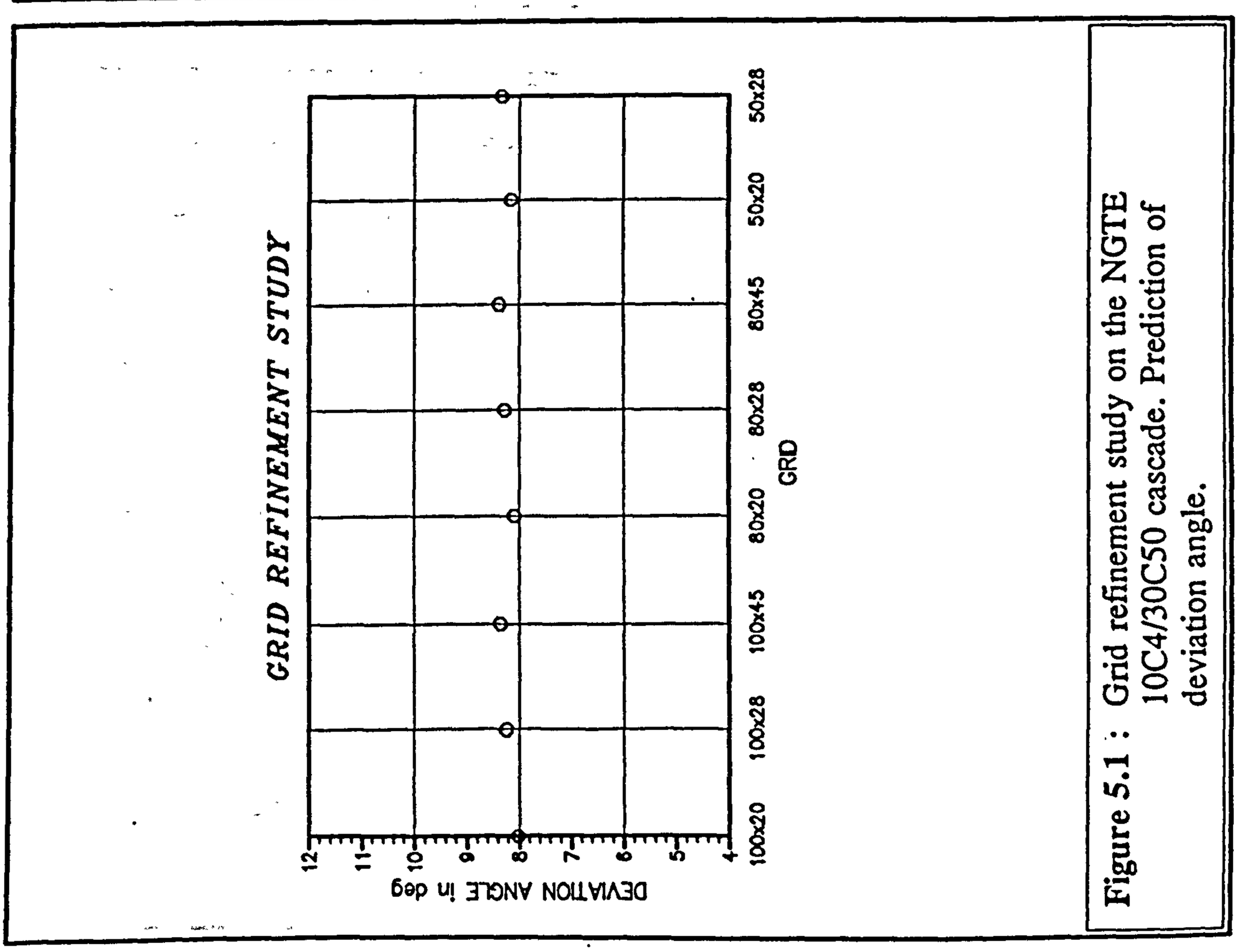

Figure 5.1 : Grid refinement study on the NGTE 10C4/30C50 cascade. Prediction of deviation angle.

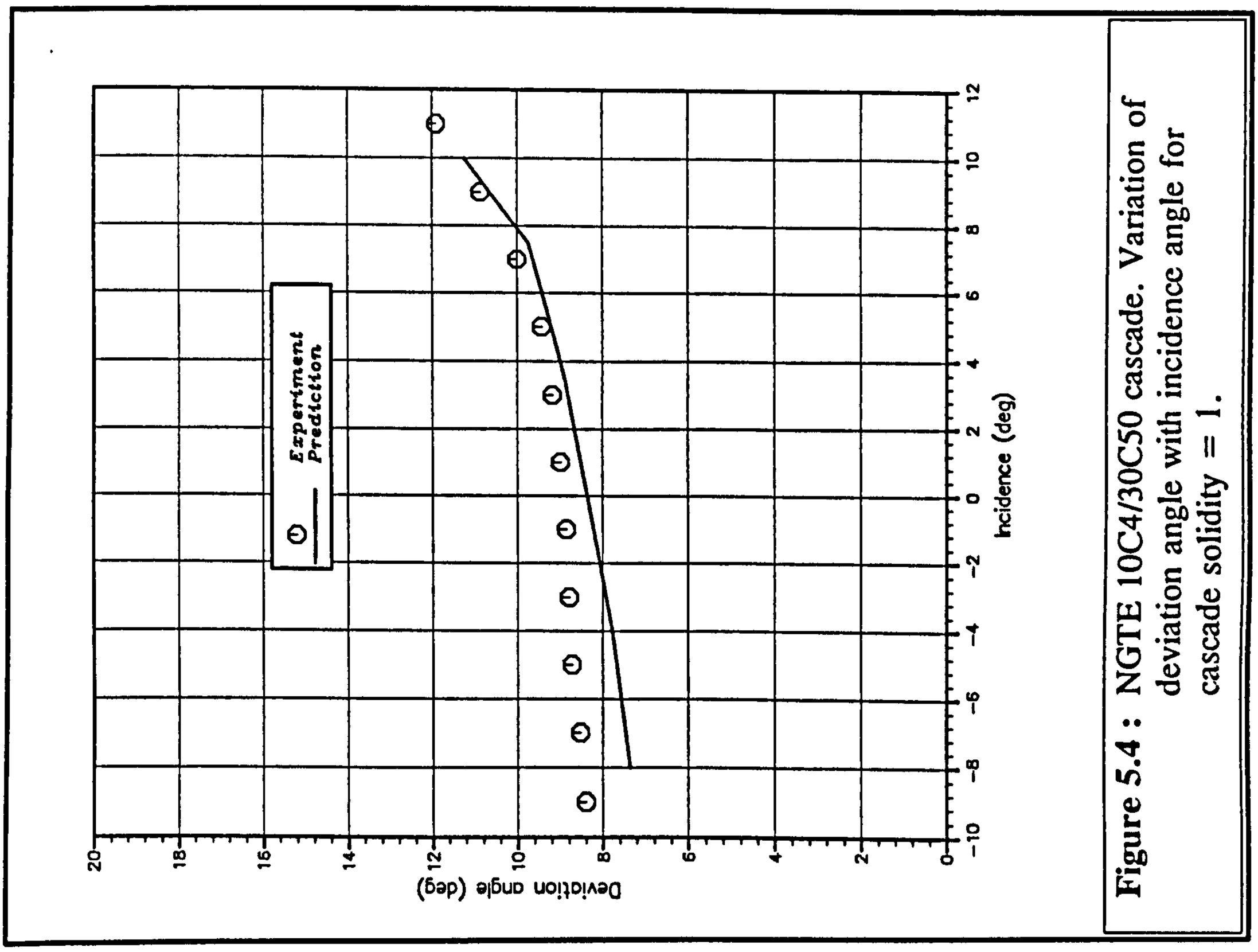

Figure 5.4 : NGTE 10C4/30C50 cascade. Variation of deviation angle with incidence angle for cascade solidity = 1.

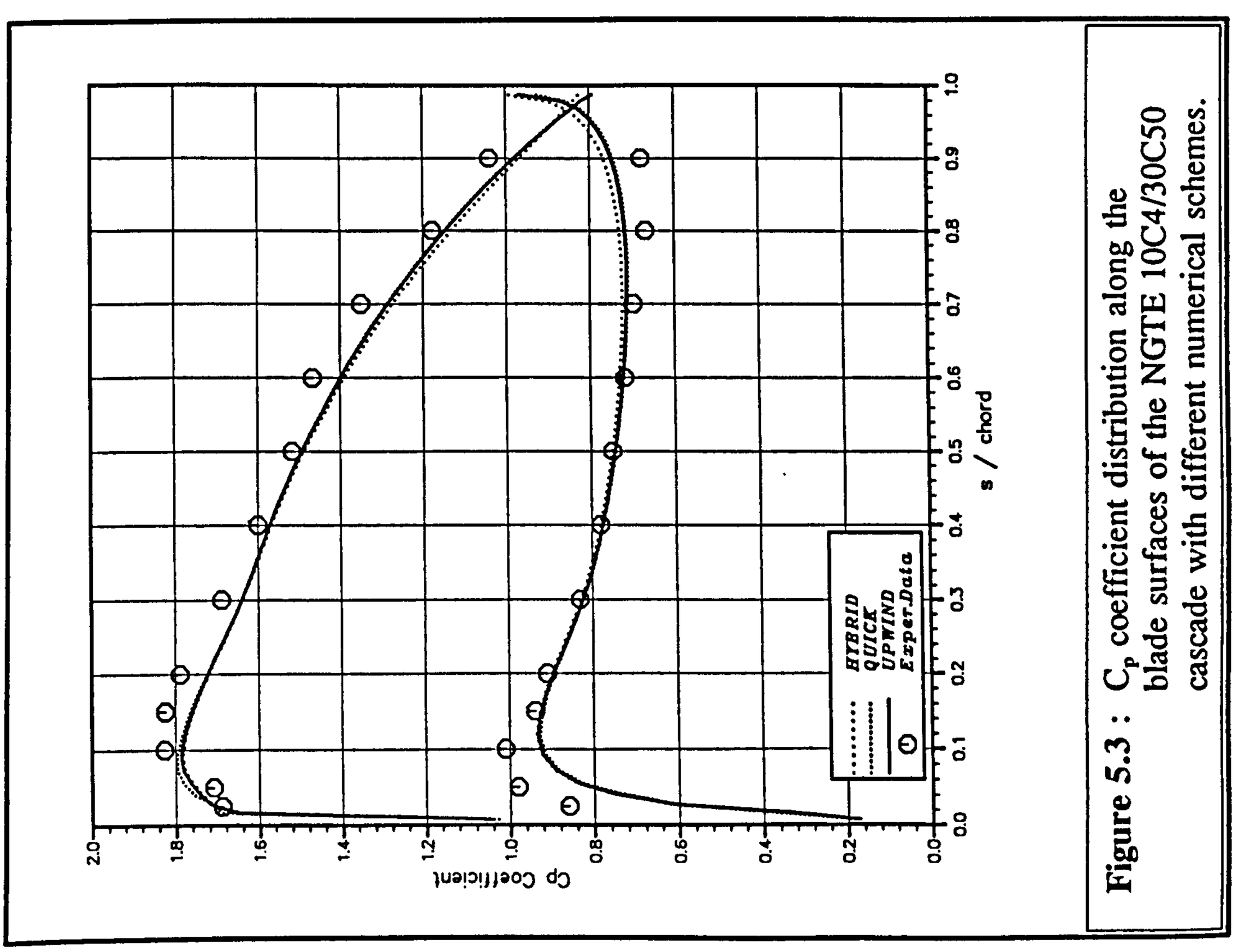

Figure 5.3 : C_p coefficient distribution along the blade surfaces of the NGTE 10C4/30C50 cascade with different numerical schemes.

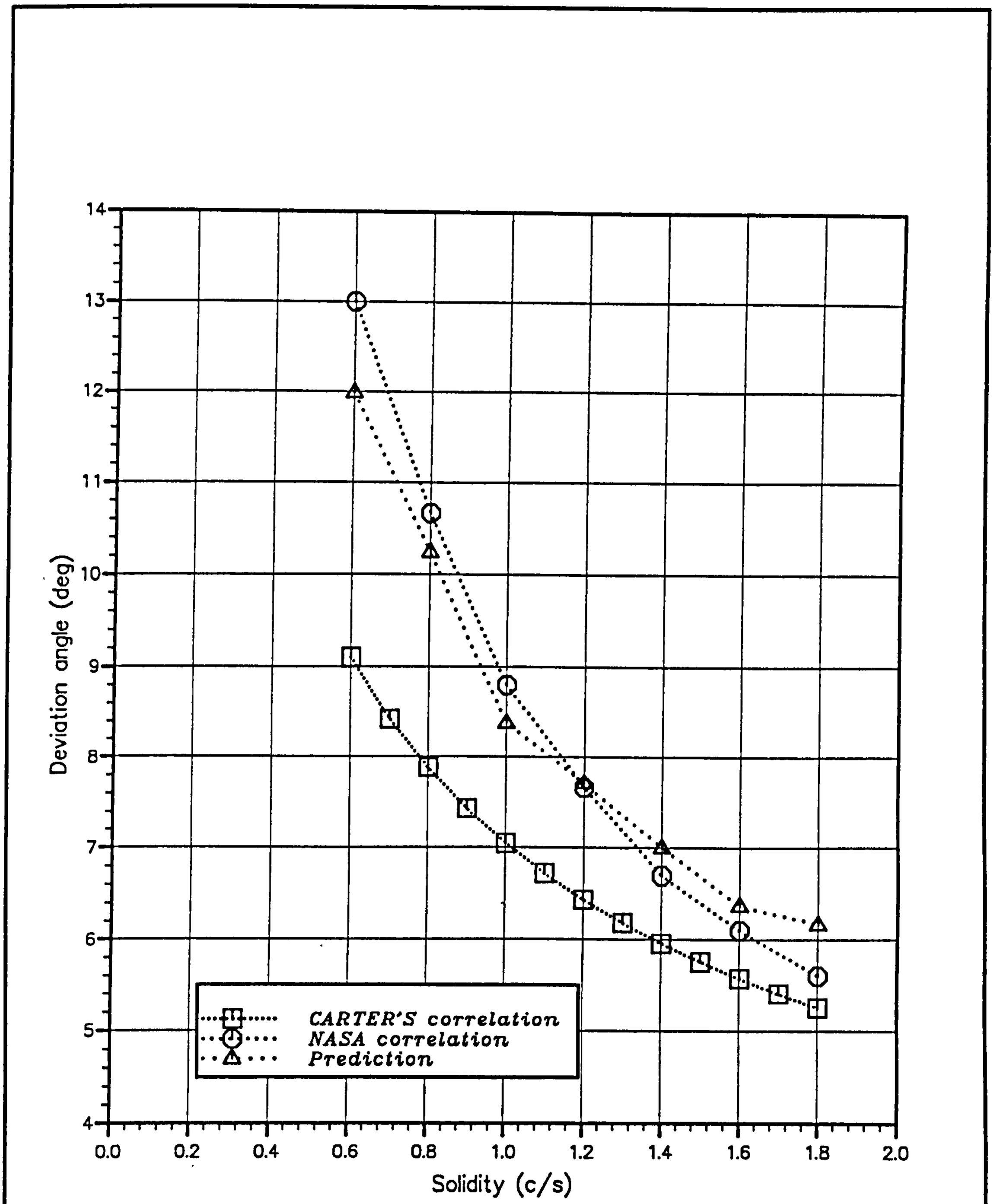

Figure 5.5 : NGTE 10C4/30C50 cascade. Variation of deviation angle with cascade solidity for stagger angle = 15°.

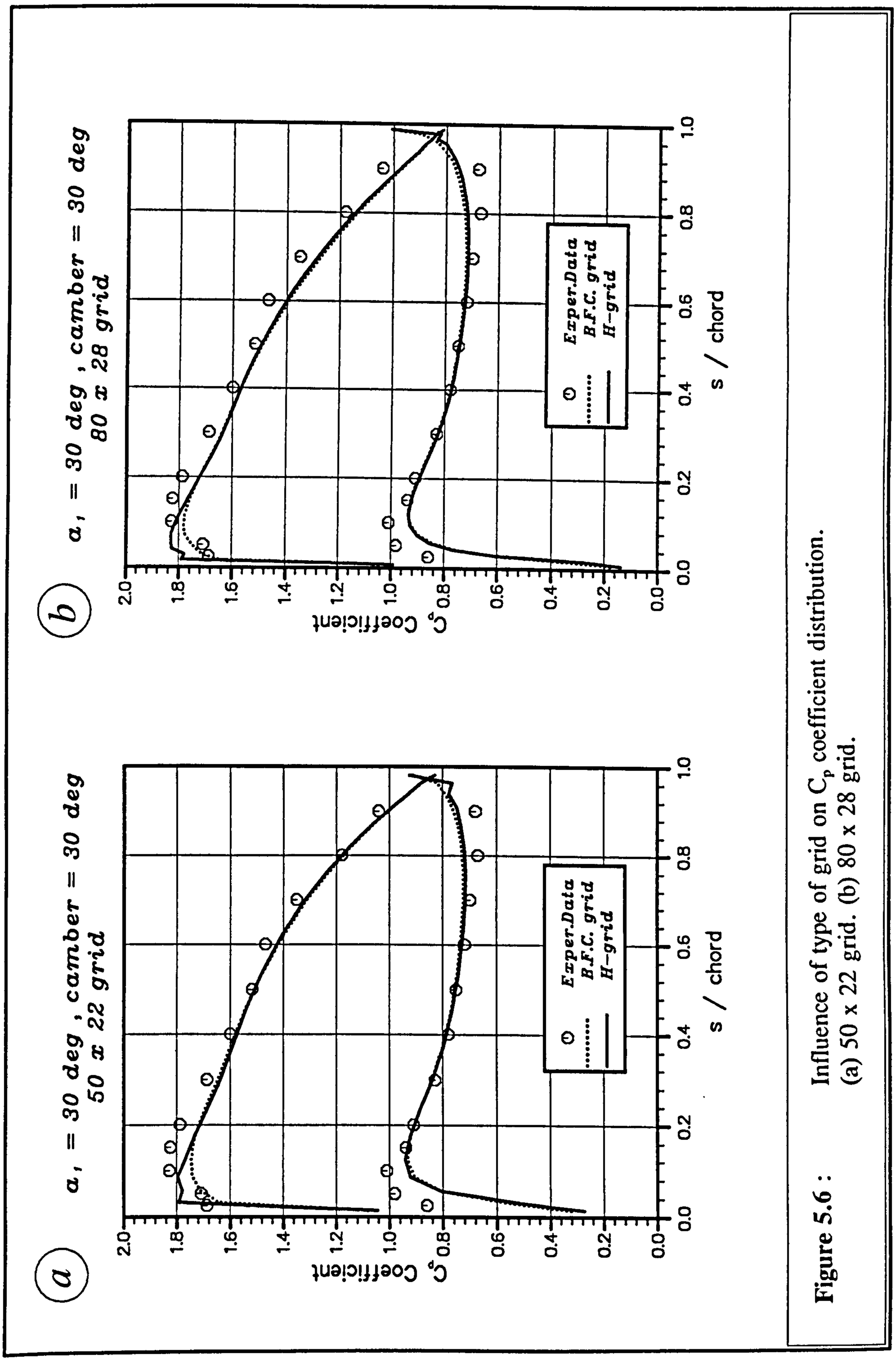

Influence of type of grid on C_p coefficient distribution.
(a) 50 x 22 grid. (b) 80 x 28 grid.

Figure 5.6 :

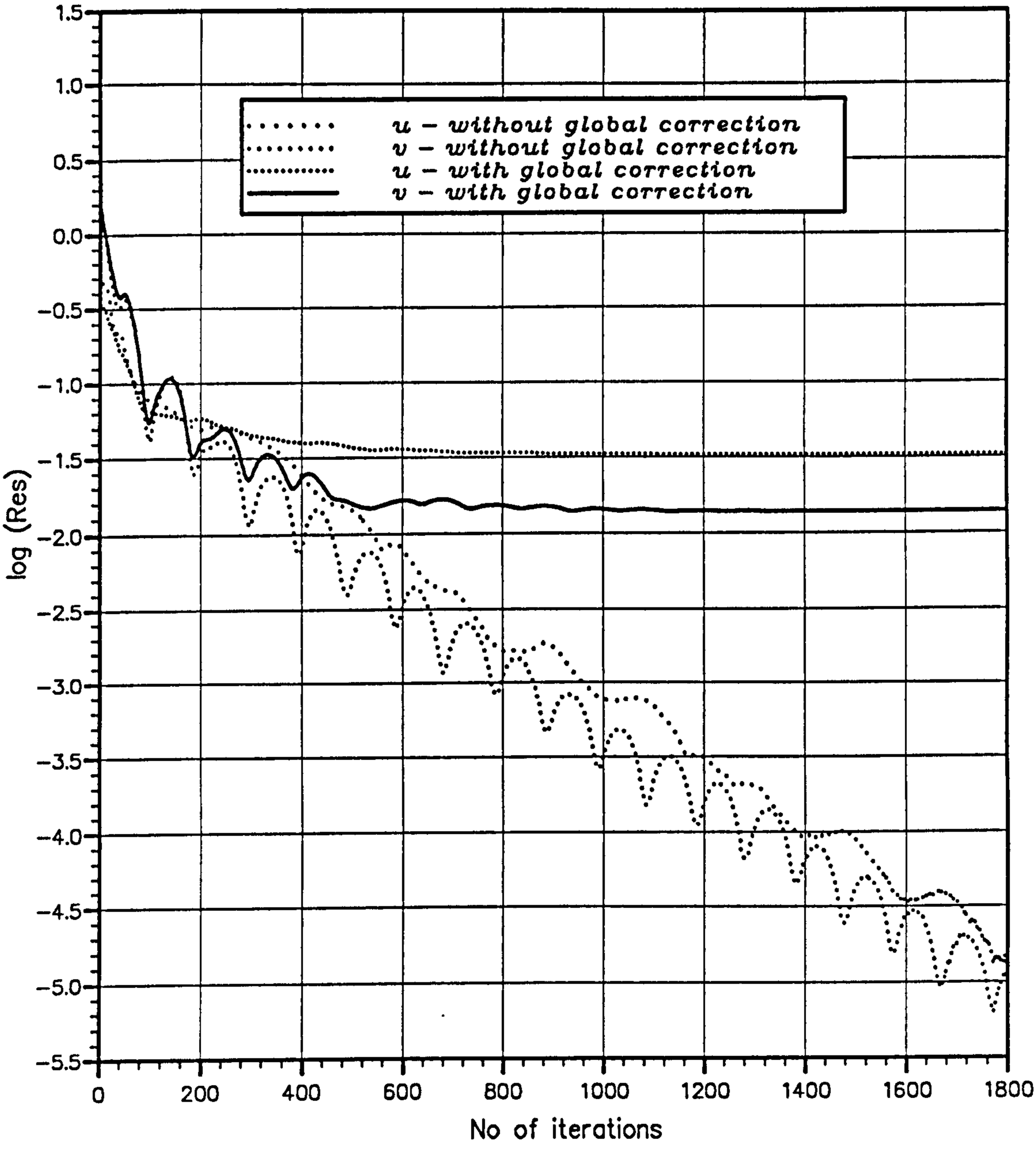

Figure 5.7 : Effect of global pressure correction on convergence history.

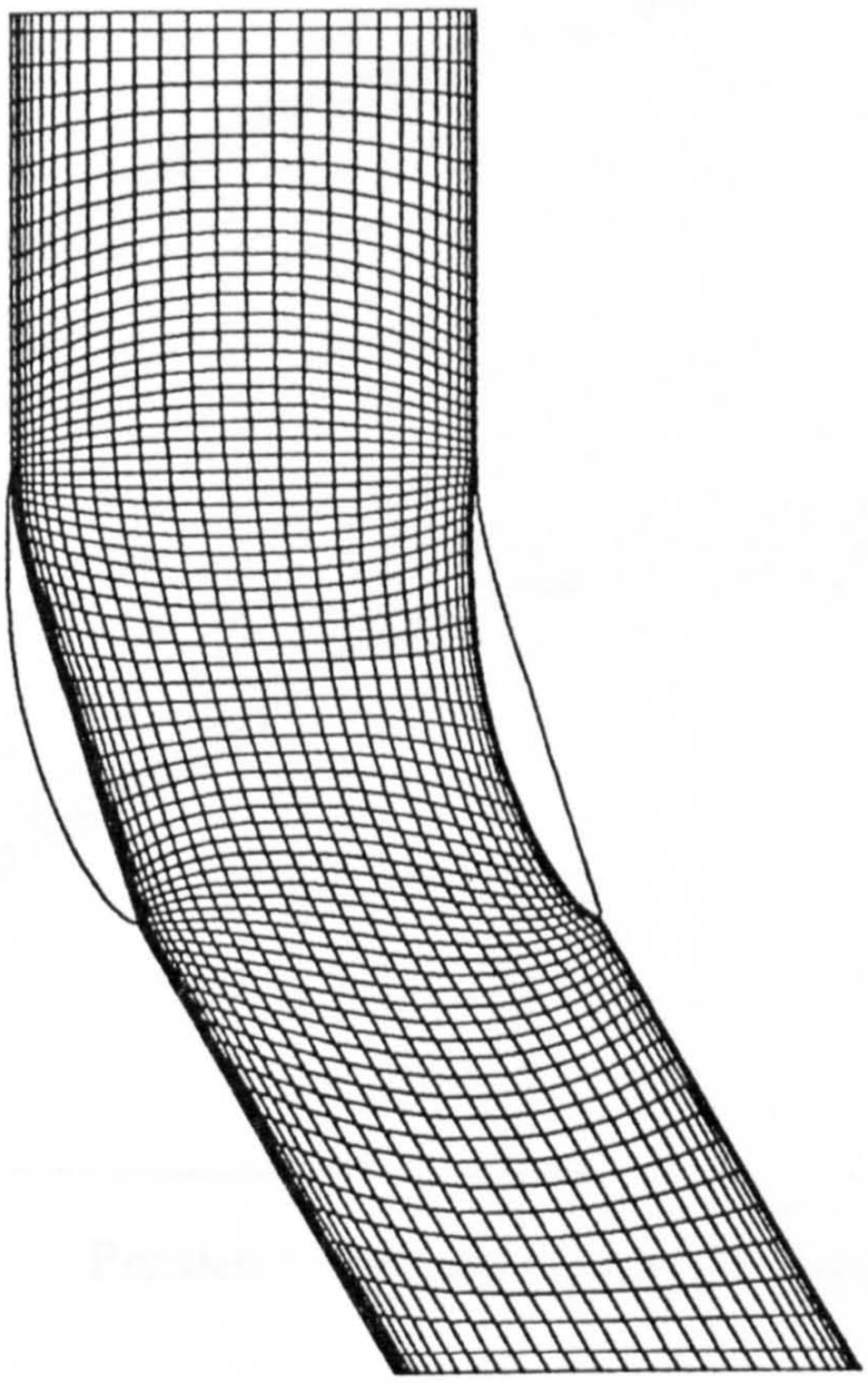

Figure 5.9 : Computational grid for the flow analysis in NACA 65-$(12A_{10})$10 cascade.

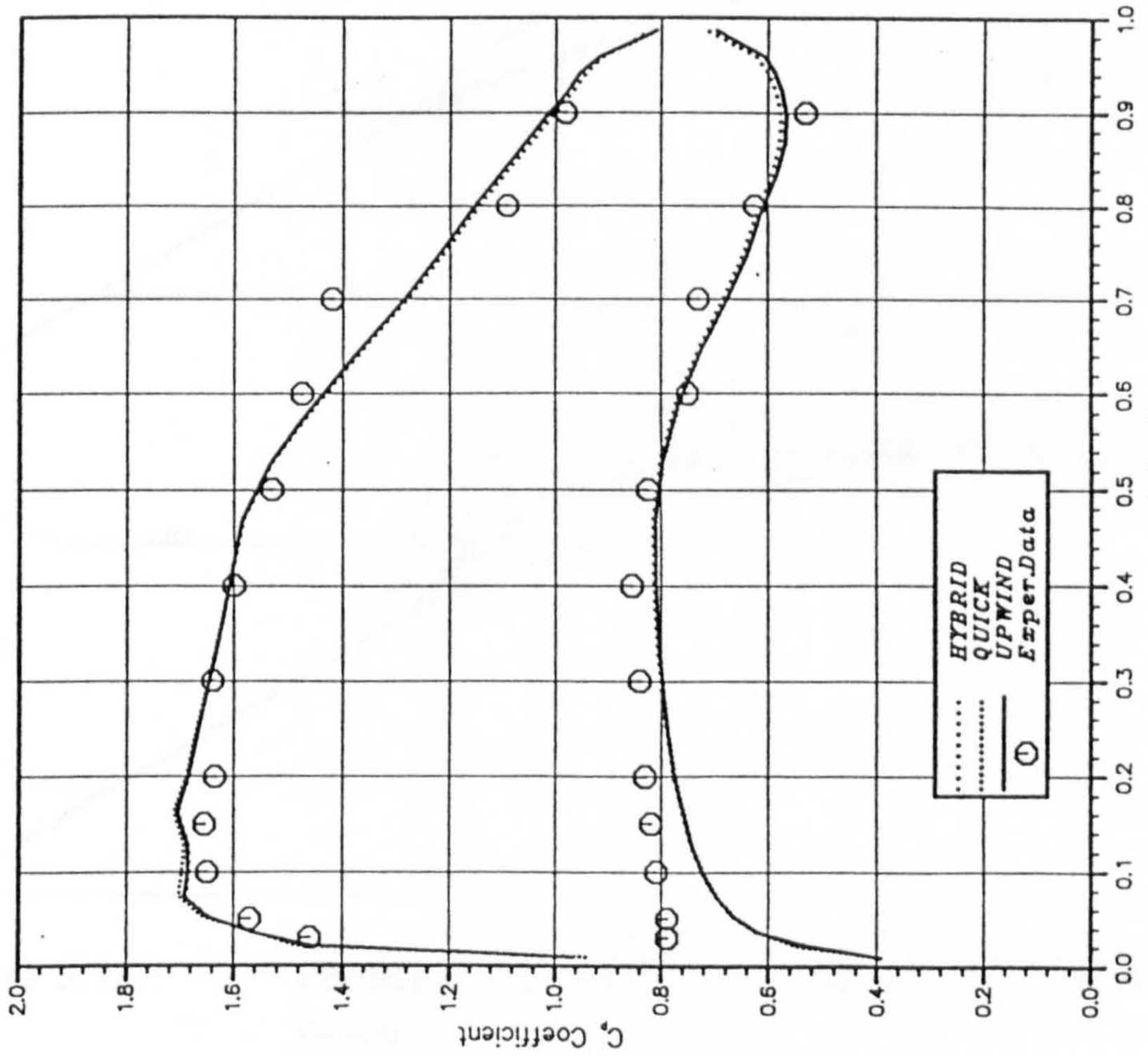

Figure 5.8 : C_p coefficient distribution along the blade surfaces of NACA 65-$(12A_{10})$10 cascade.

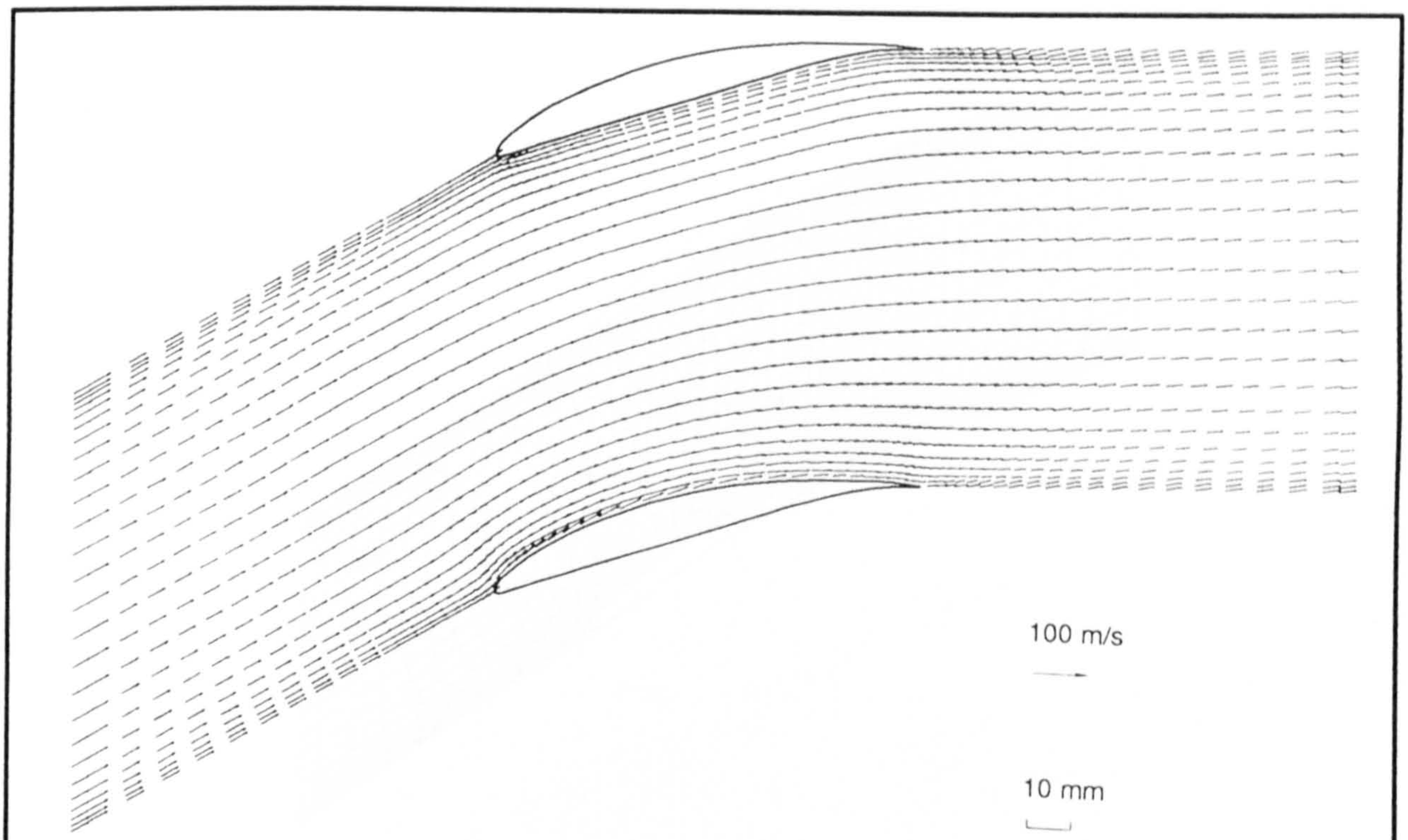

Figure 5.10 : Predicted velocity vectors in NACA 65-($12A_{10}$)10 cascade.

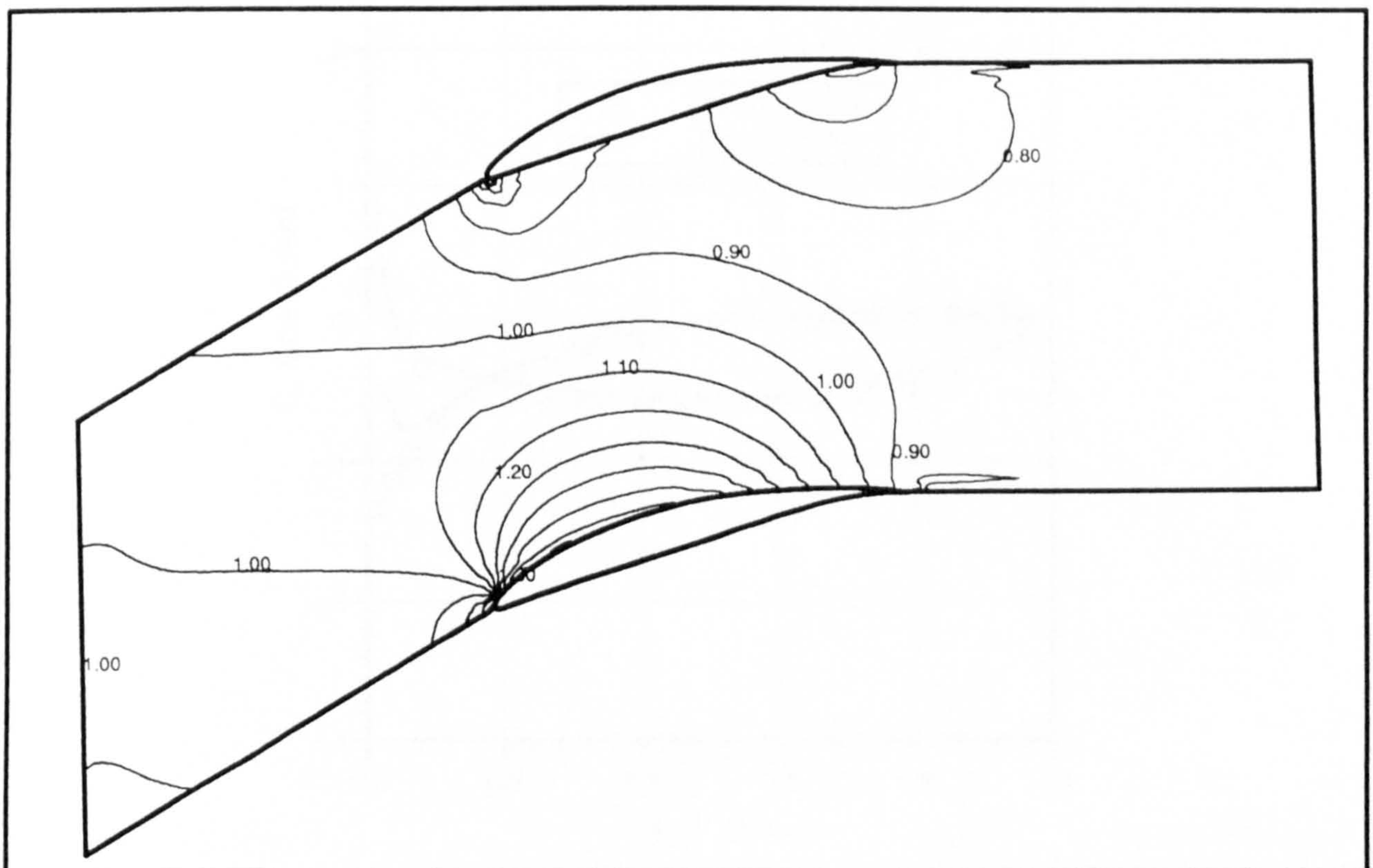

Figure 5.11 : Predicted C_p coefficient contours in NACA 65-($12A_{10}$)10 cascade.

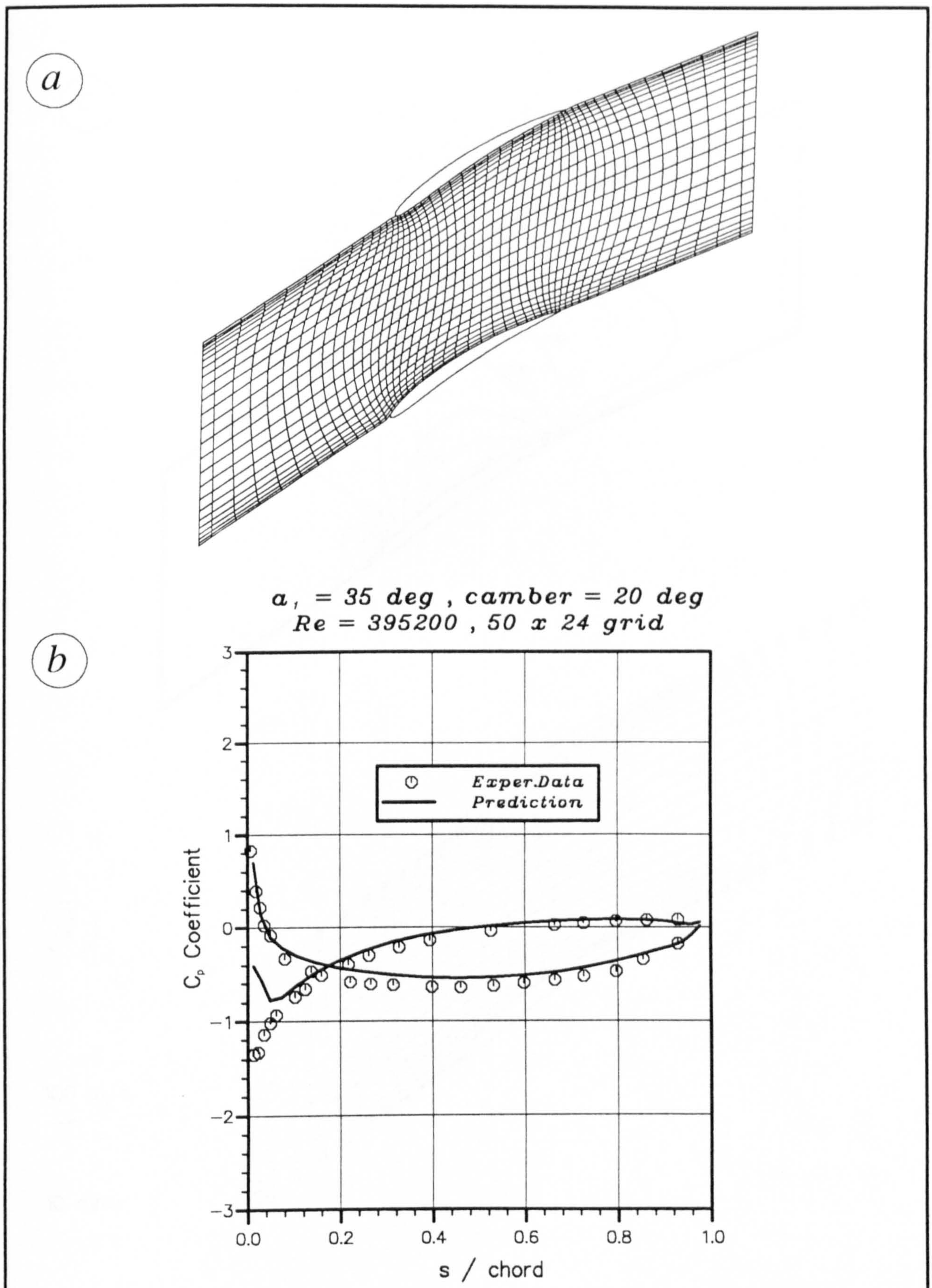

Figure 5.12 : Rhoden's cascade, 20° camber, $a_1 = 35°$. (a) Computational grid. (b) C_p coefficient along the blade surfaces.

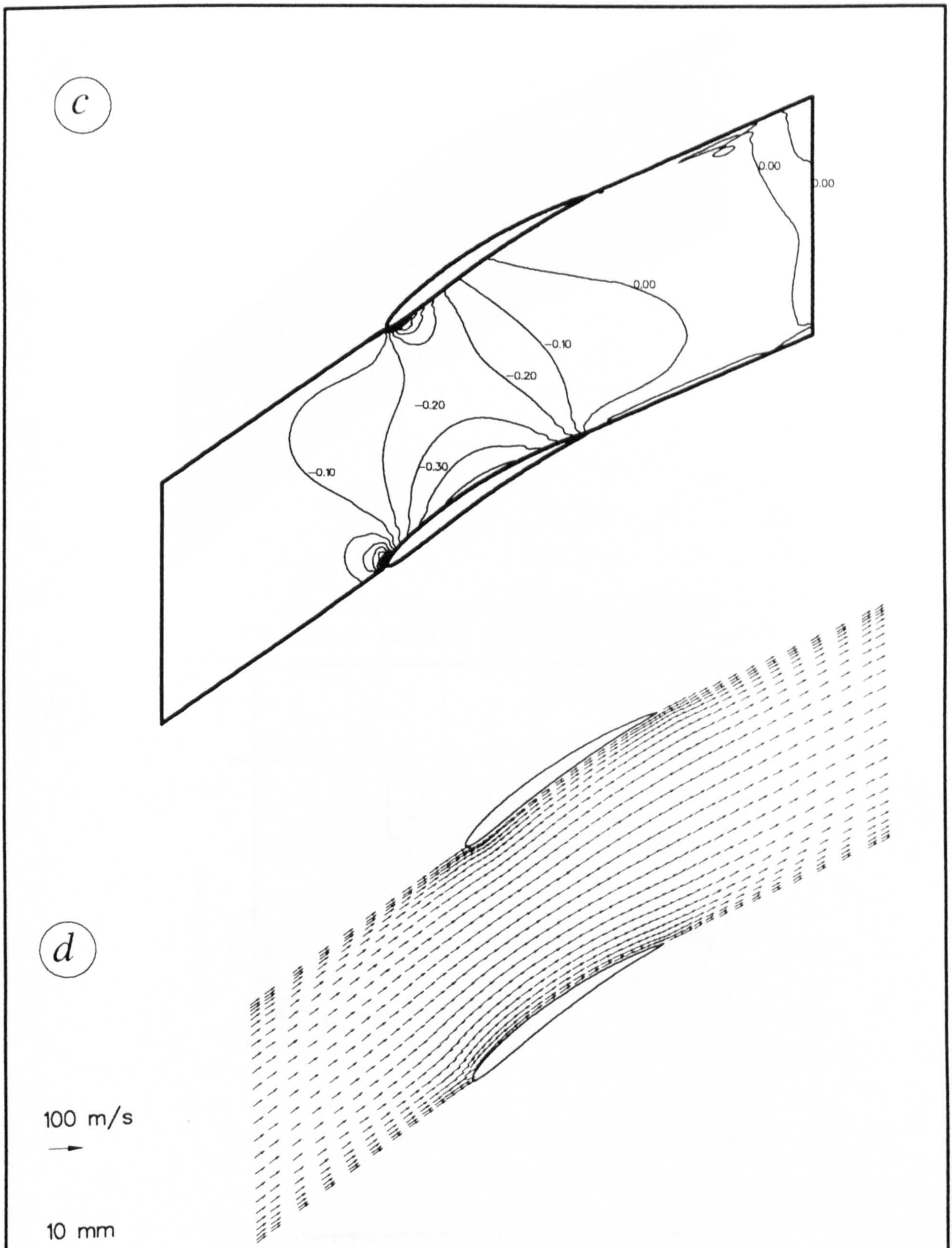

Figure 5.12 : Rhoden's cascade, 20° camber, $a_1 = 35°$. (c) Predicted C_p coefficient contours. (d) Predicted velocity vectors.

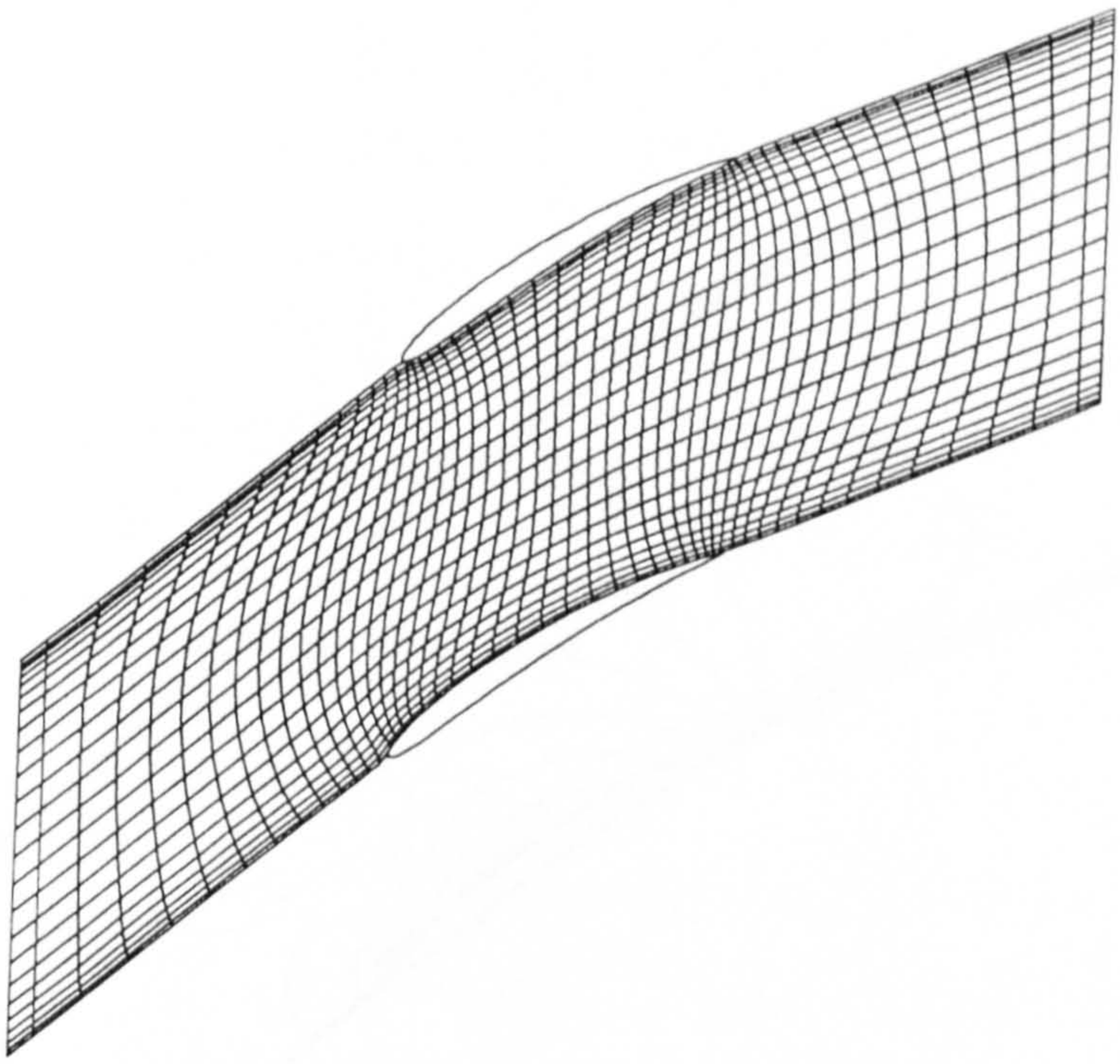

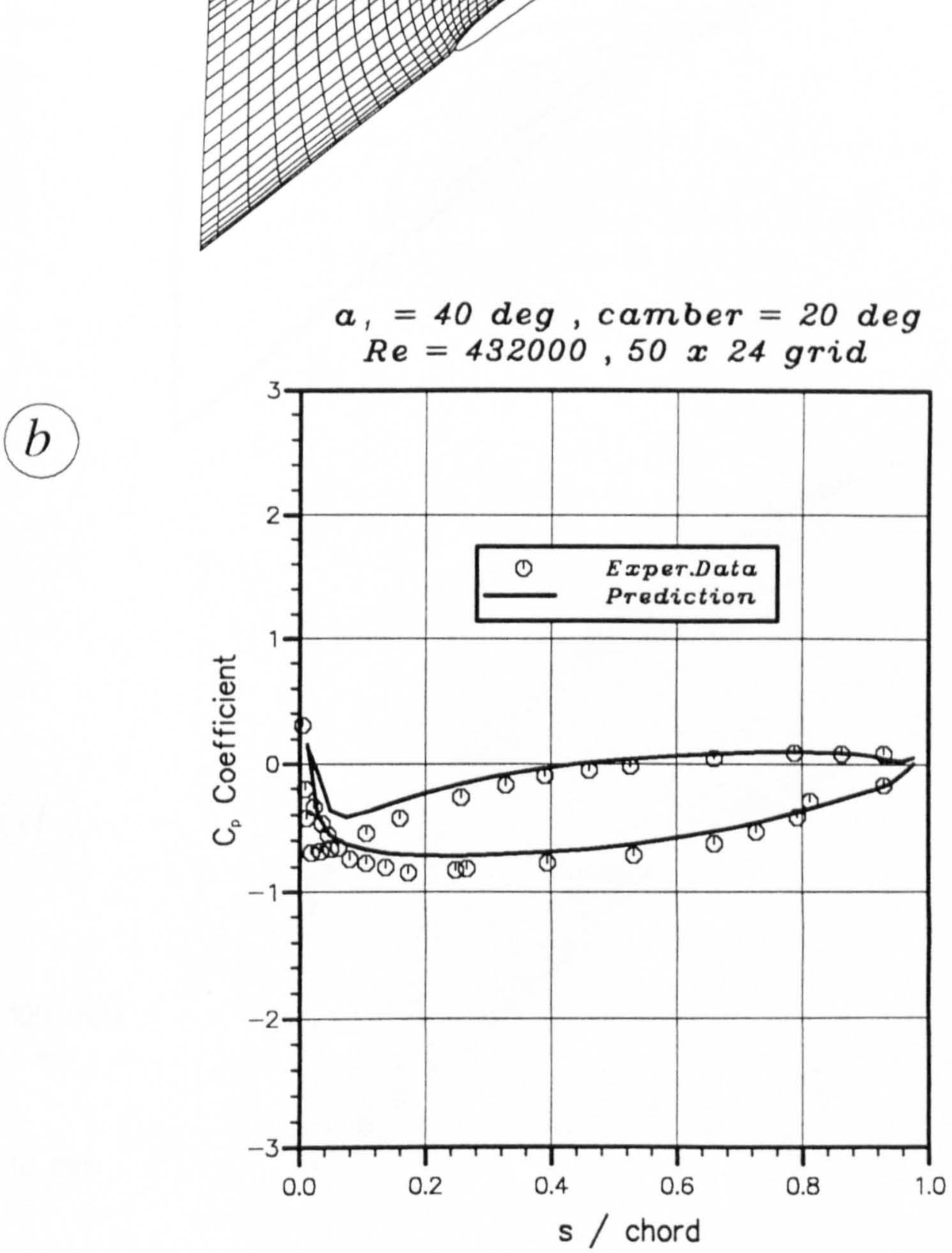

Figure 5.13 : Rhoden's cascade, 20° camber, $a_1 = 40°$. (a) Computational grid. (b) C_p coefficient along the blade surfaces.

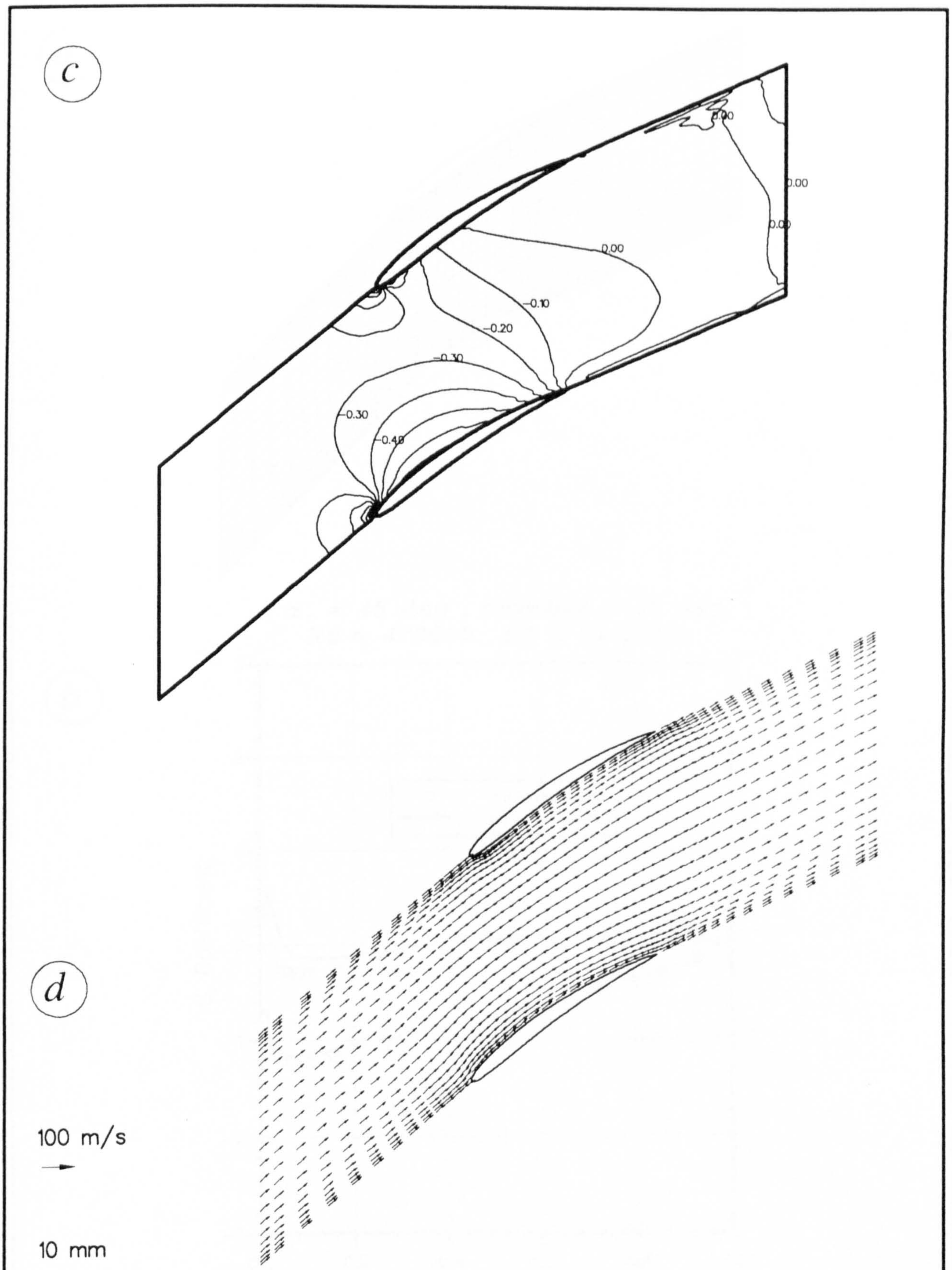

Figure 5.13 : Rhoden's cascade, 20° camber, $a_1 = 40°$. (c) Predicted C_p coefficient contours. (d) Predicted velocity vectors.

(a)

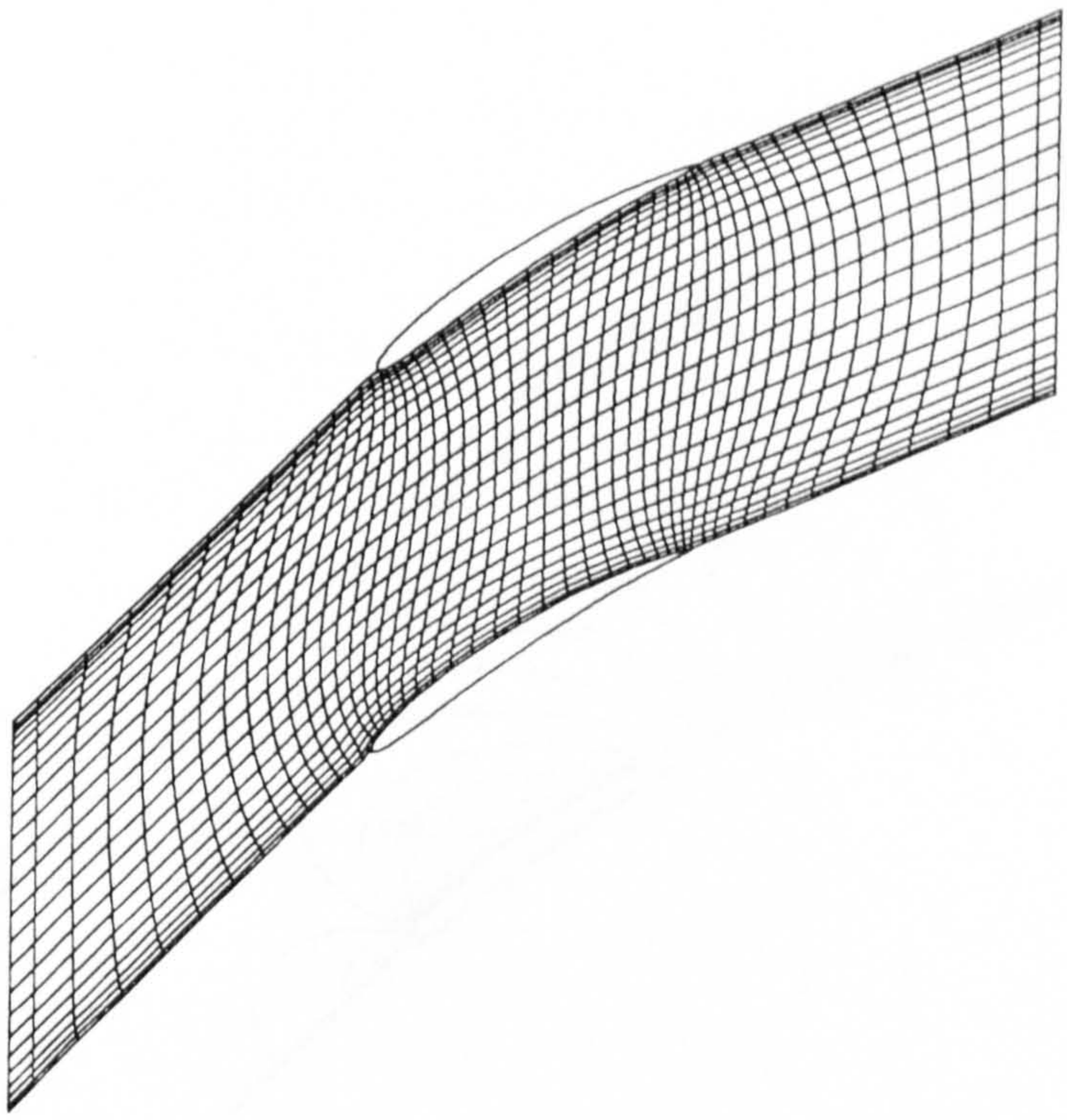

$a_1 = 45$ deg , camber = 20 deg
Re = 470000 , 50 x 24 grid

(b)

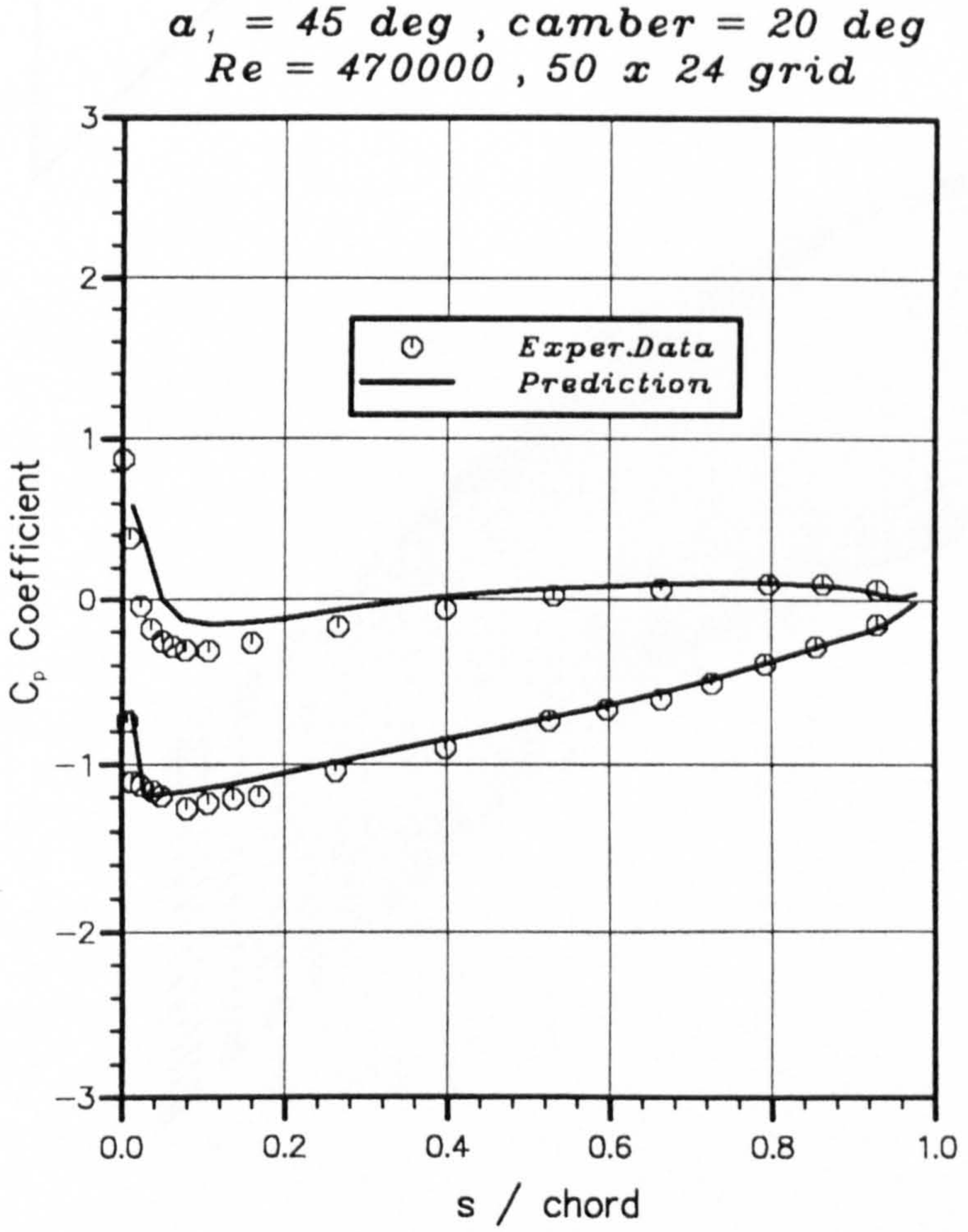

Figure 5.14 : Rhoden's cascade, 20° camber, $a_1 = 45°$. (a) Computational grid. (b) C_p coefficient along the blade surfaces.

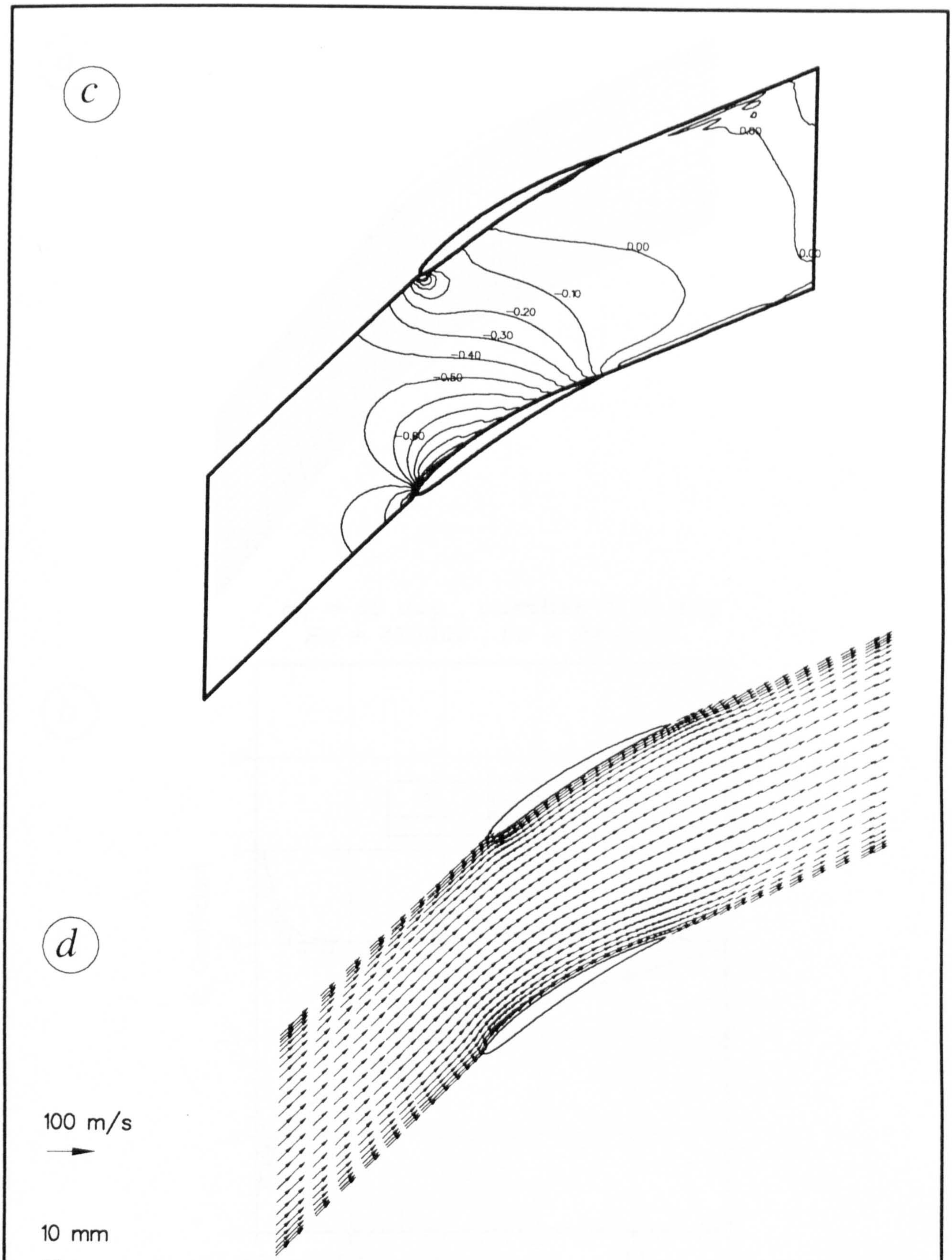

Figure 5.14 : Rhoden's cascade, 20° camber, $a_1 = 45°$. (c) Predicted C_p coefficient contours. (d) Predicted velocity vectors.

a

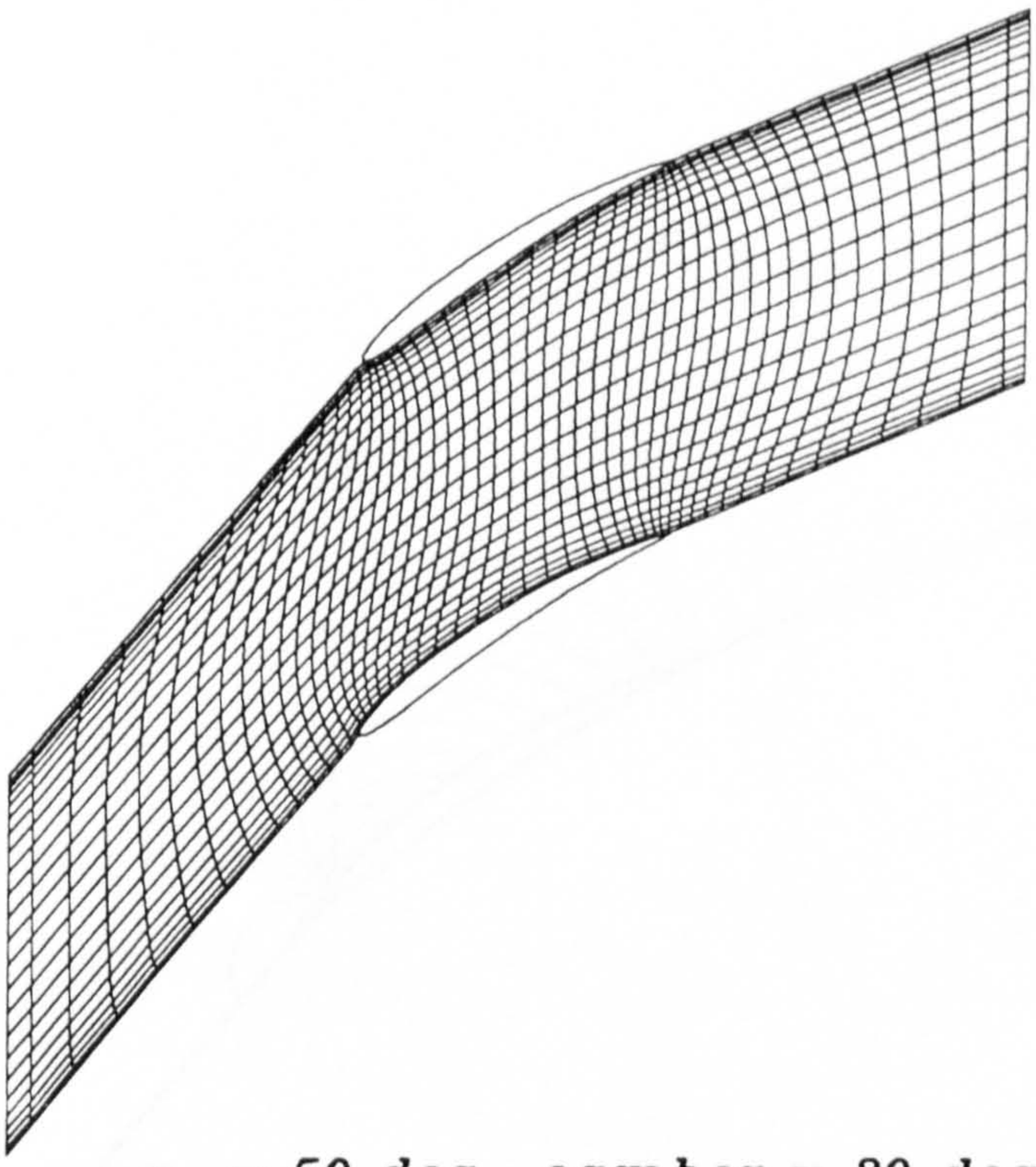

$a_1 = 50$ deg , camber = 20 deg
Re = 473000 , 50 x 24 grid

b

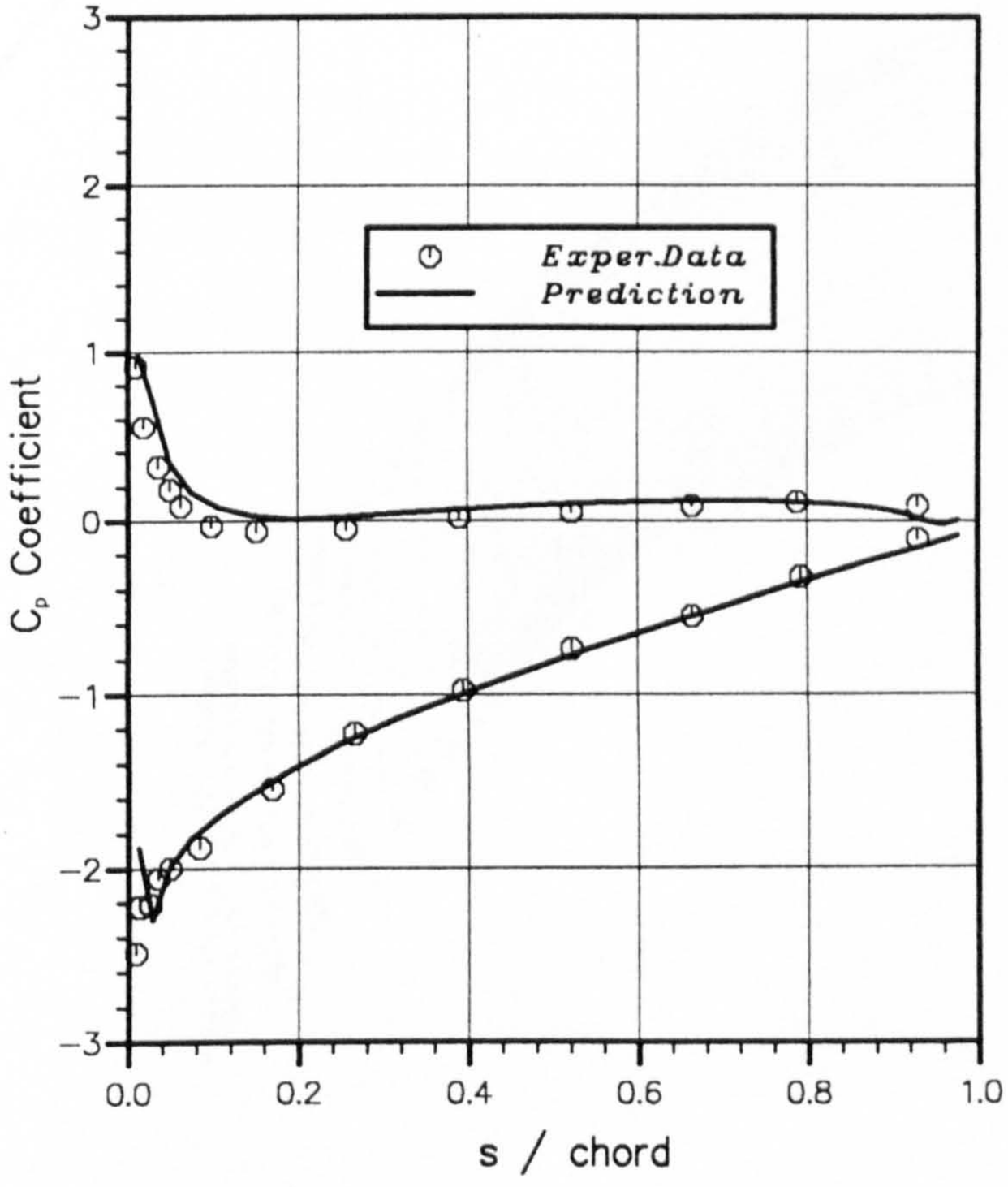

Figure 5.15 : Rhoden's cascade, 20° camber, $a_1 = 50°$. (a) Computational grid. (b) C_p coefficient along the blade surfaces.

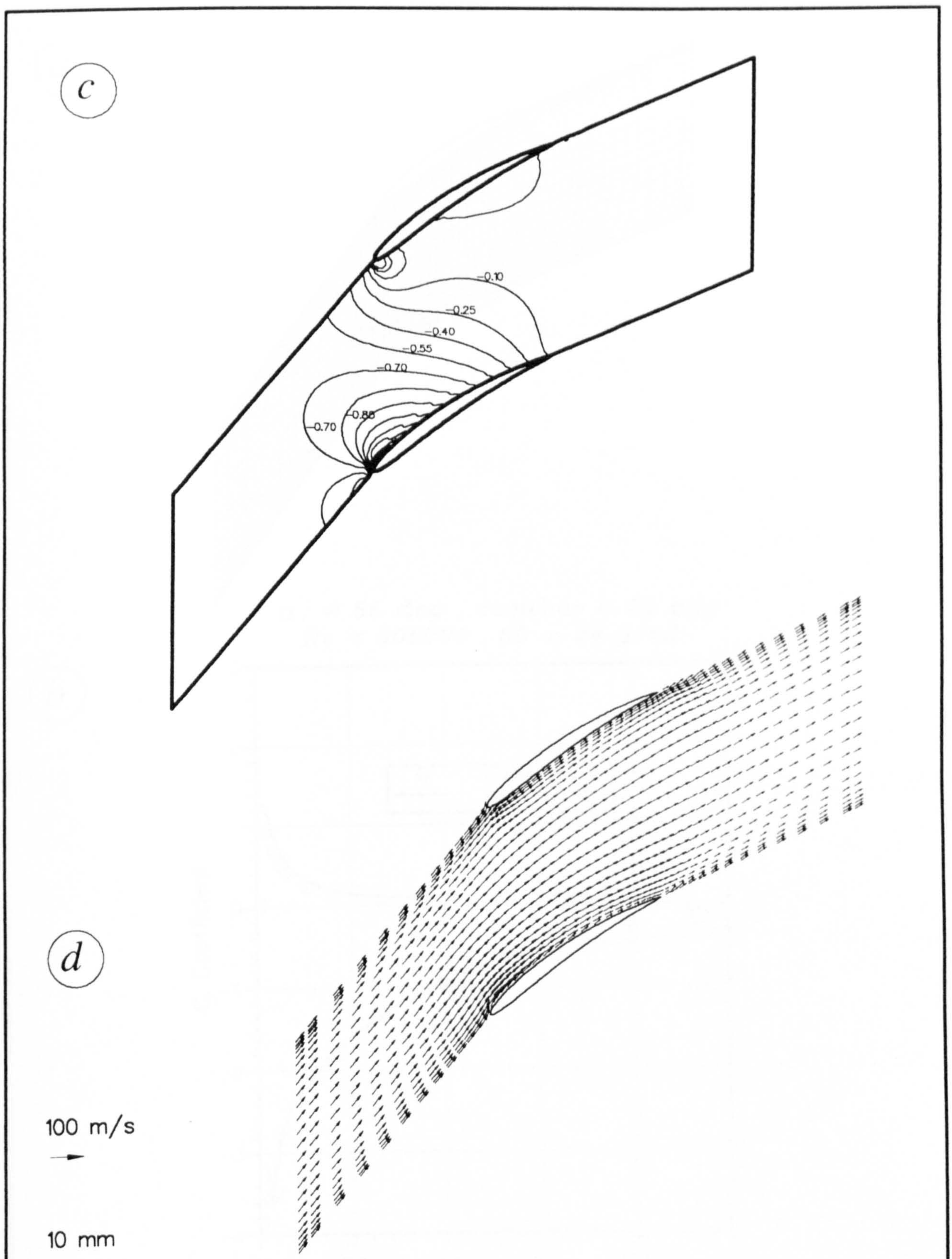

Figure 5.15 : Rhoden's cascade, 20° camber, $a_1 = 50°$. (c) Predicted C_p coefficient contours. (d) Predicted velocity vectors.

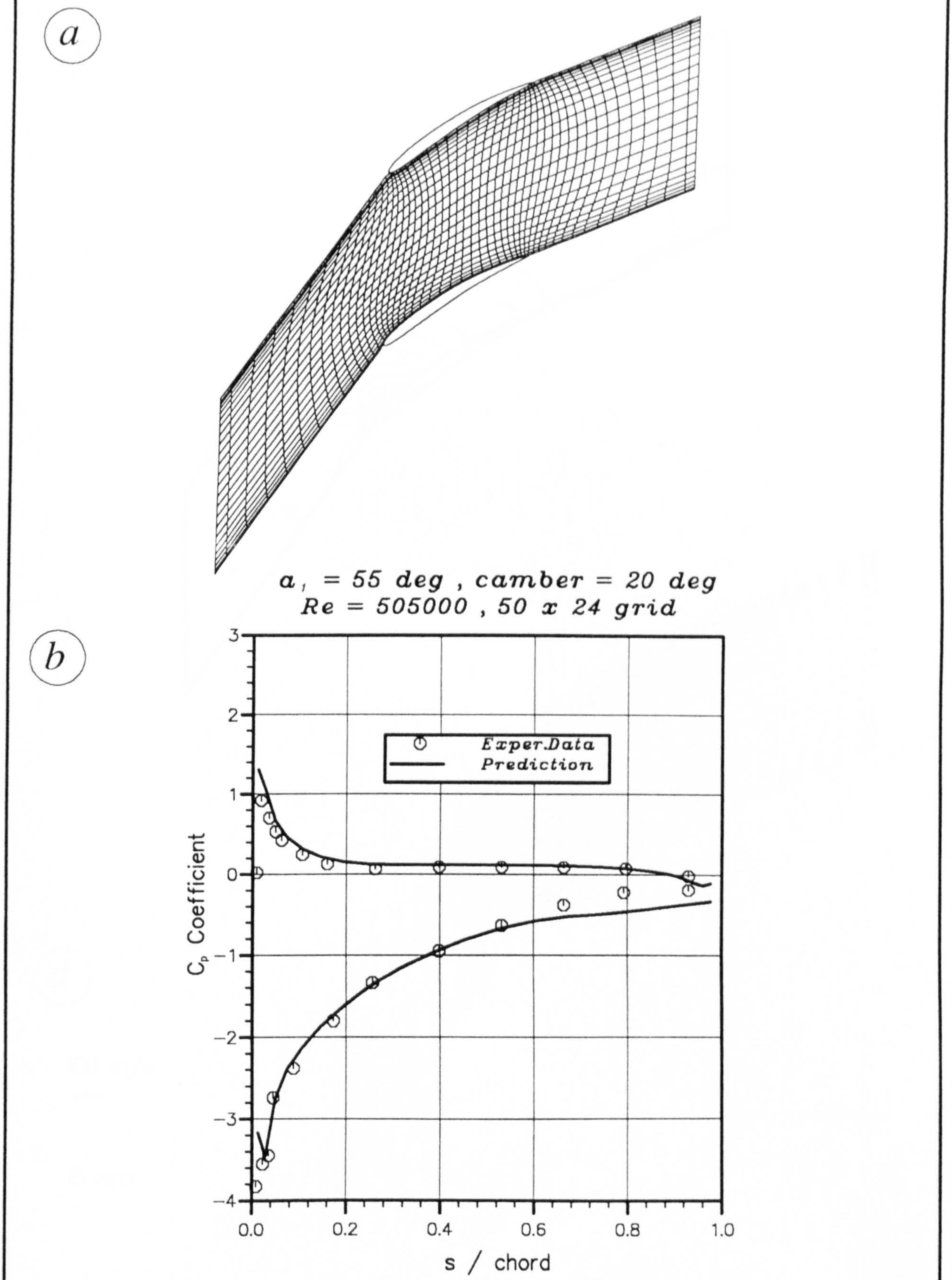

Figure 5.16 : Rhoden's cascade, 20° camber, $a_1 = 55°$. (a) Computational grid. (b) C_p coefficient along the blade surfaces.

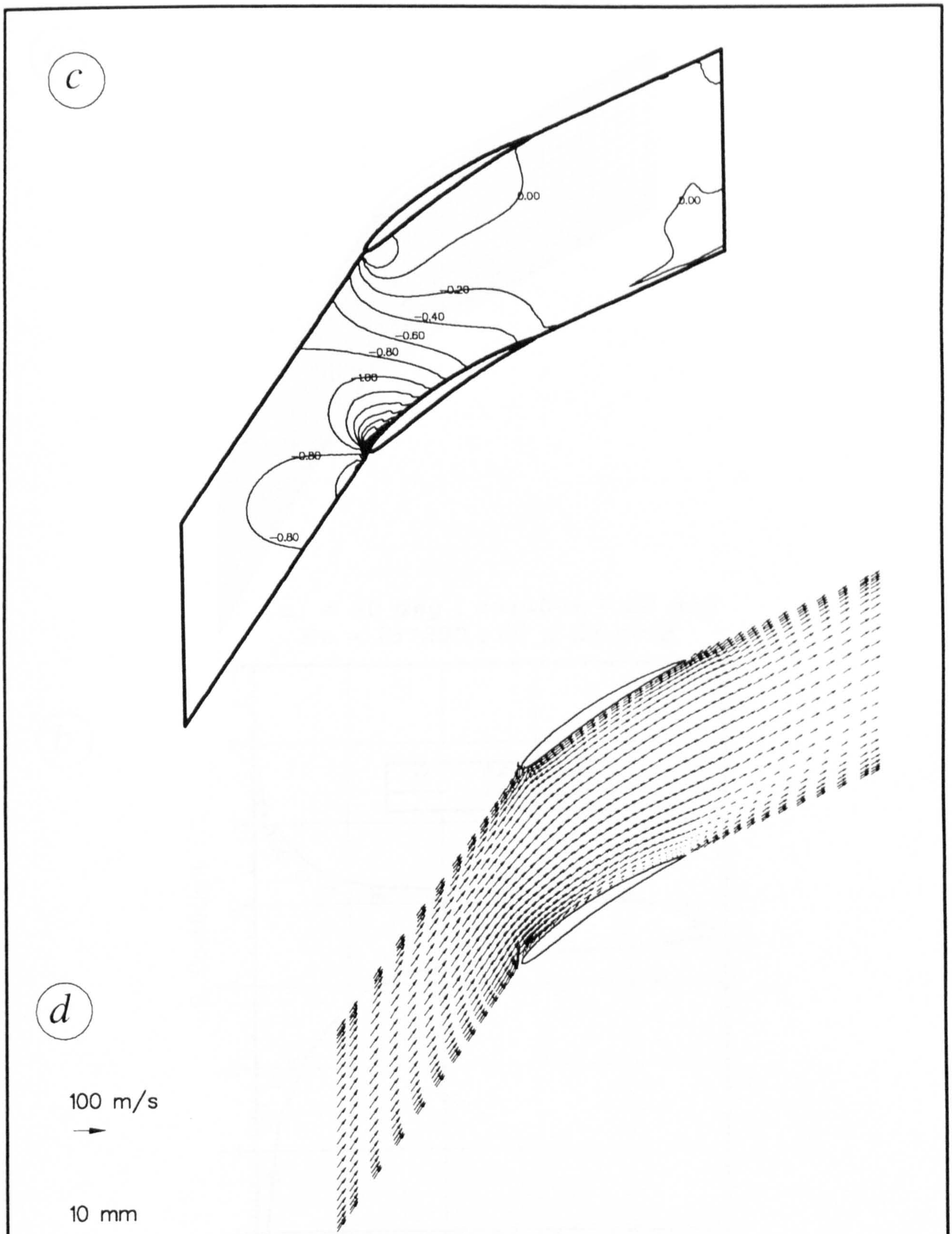

Figure 5.16 : Rhoden's cascade, 20° camber, $a_1 = 55°$. (c) Predicted C_p coefficient contours. (d) Predicted velocity vectors.

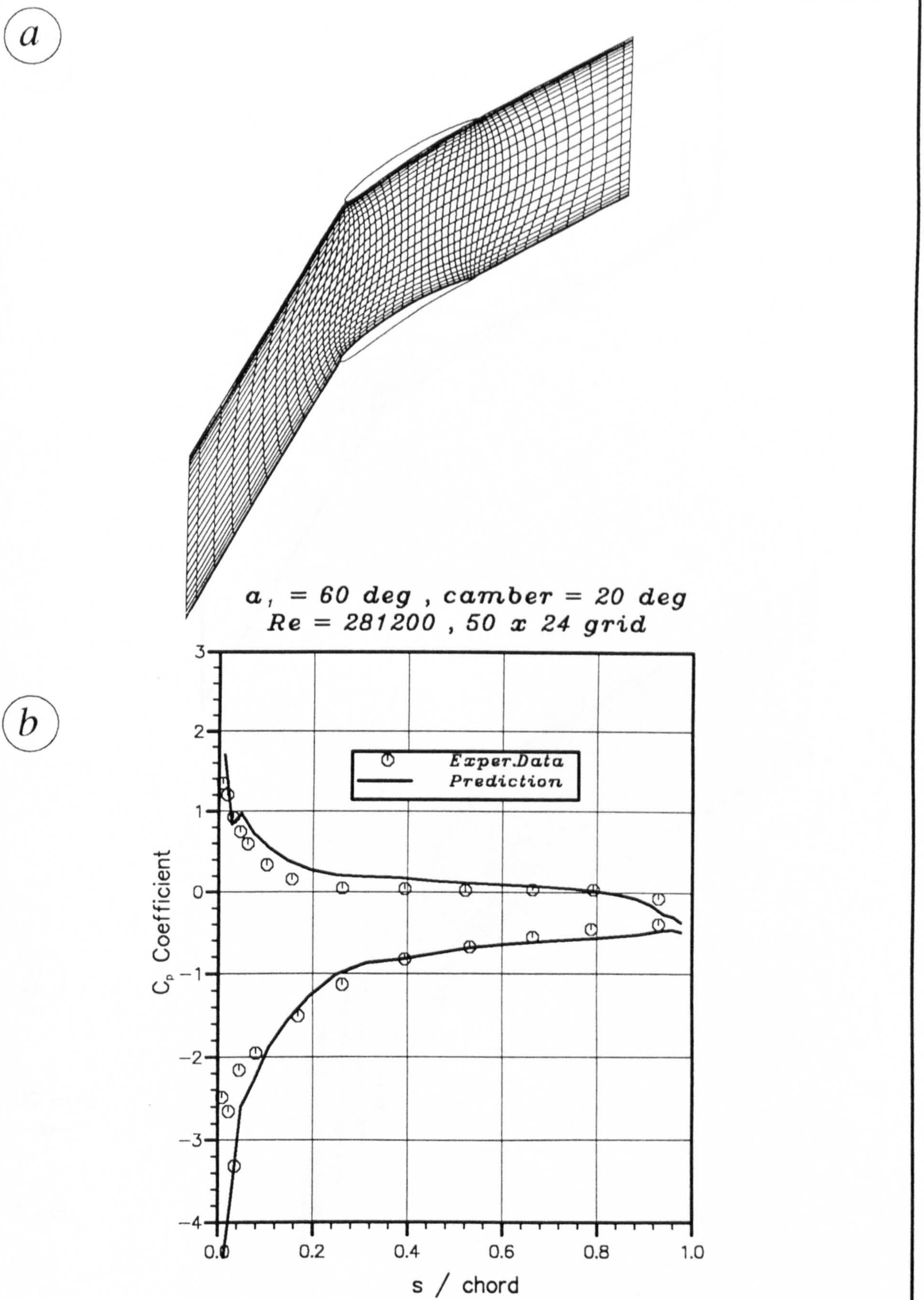

Figure 5.17 : Rhoden's cascade, 20° camber, $a_1 = 60°$. (a) Computational grid. (b) C_p coefficient along the blade surfaces.

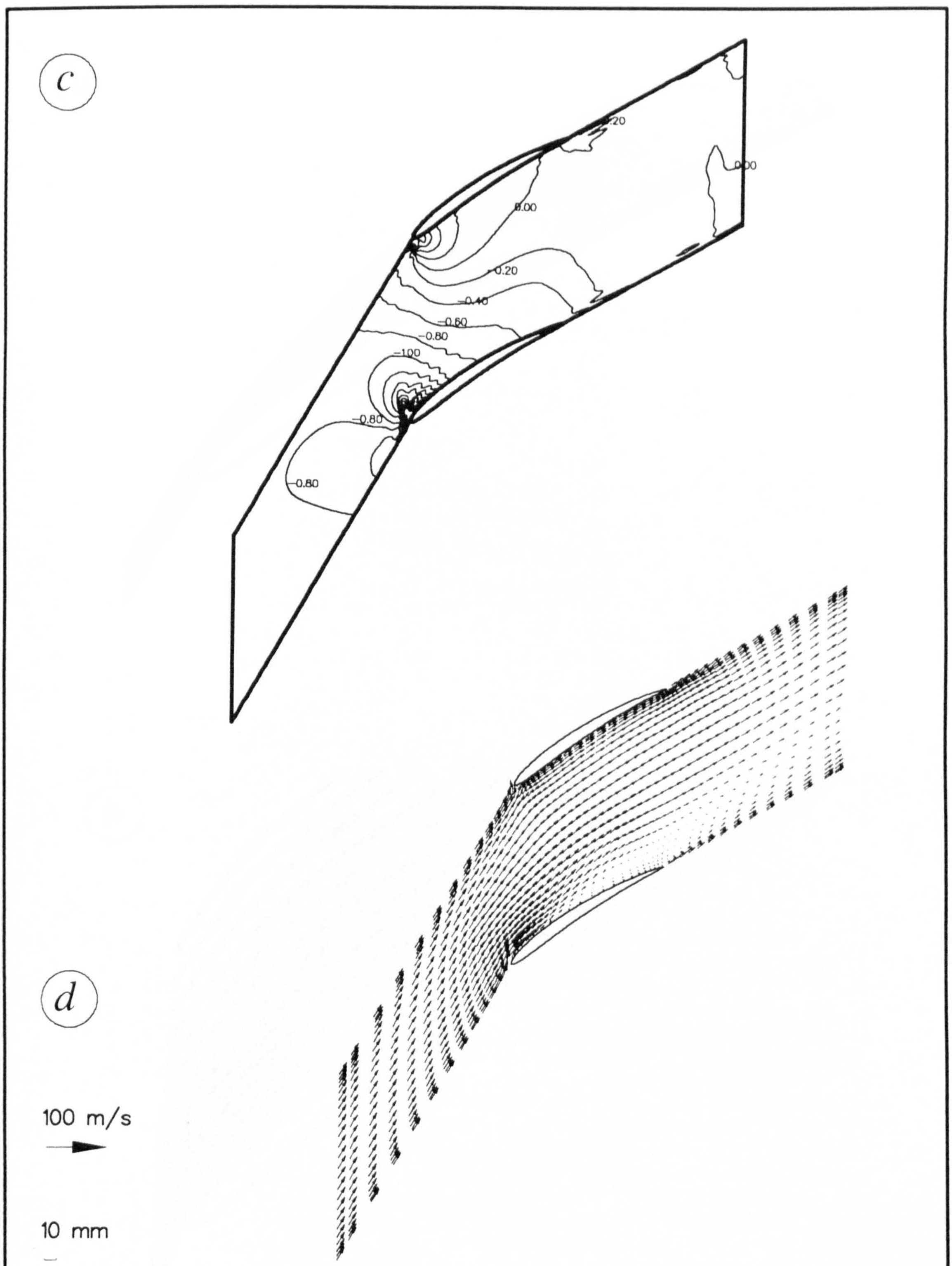

Figure 5.17 : Rhoden's cascade, 20° camber, $a_1 = 60°$. (c) Predicted C_p coefficient contours. (d) Predicted velocity vectors.

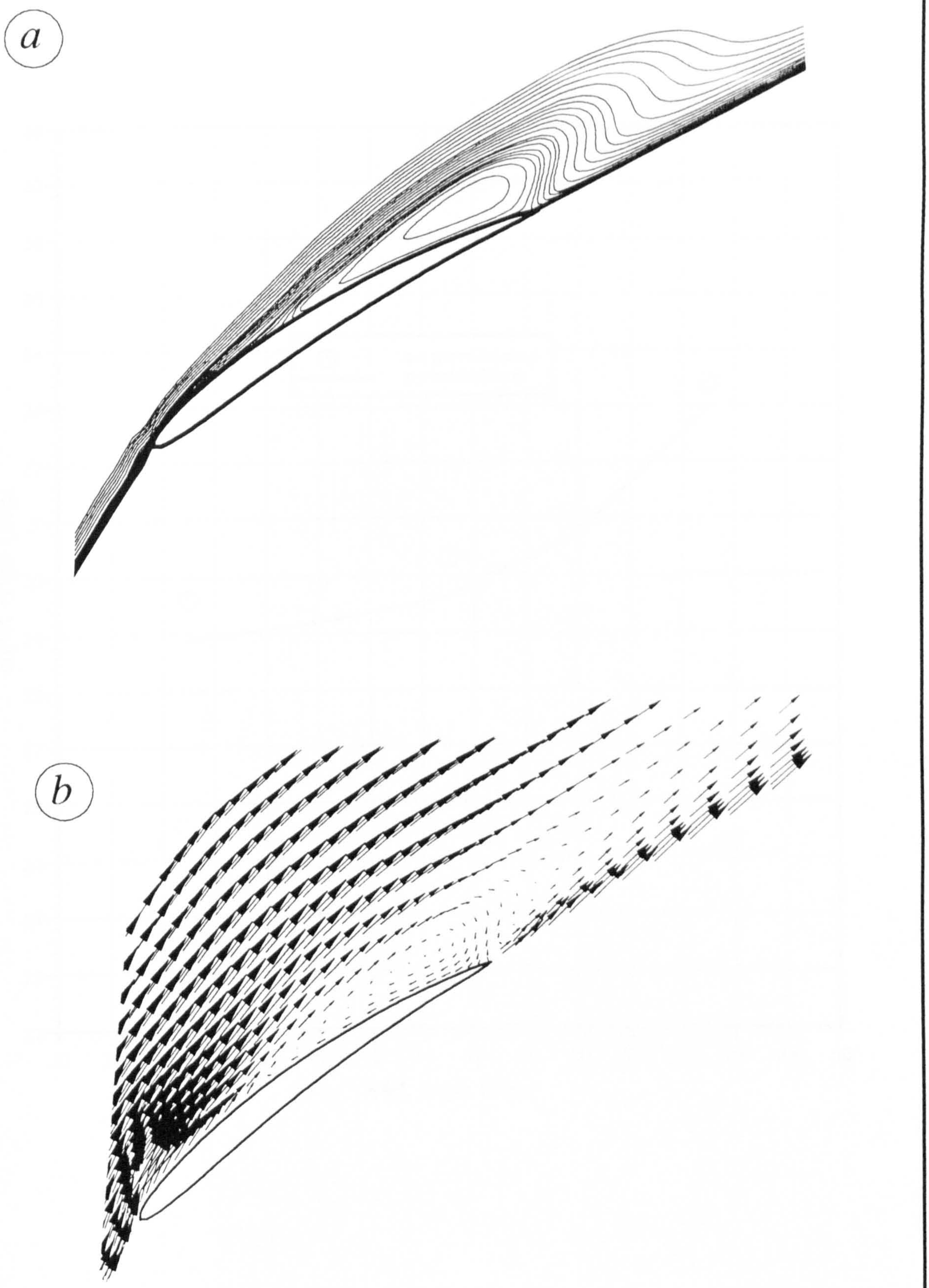

Figure 5.18 : Rhoden's cascade, 20° camber, $a_1 = 60°$. (a) Predicted streamlines along the suction side. (b) Predicted velocity vectors along the suction side.

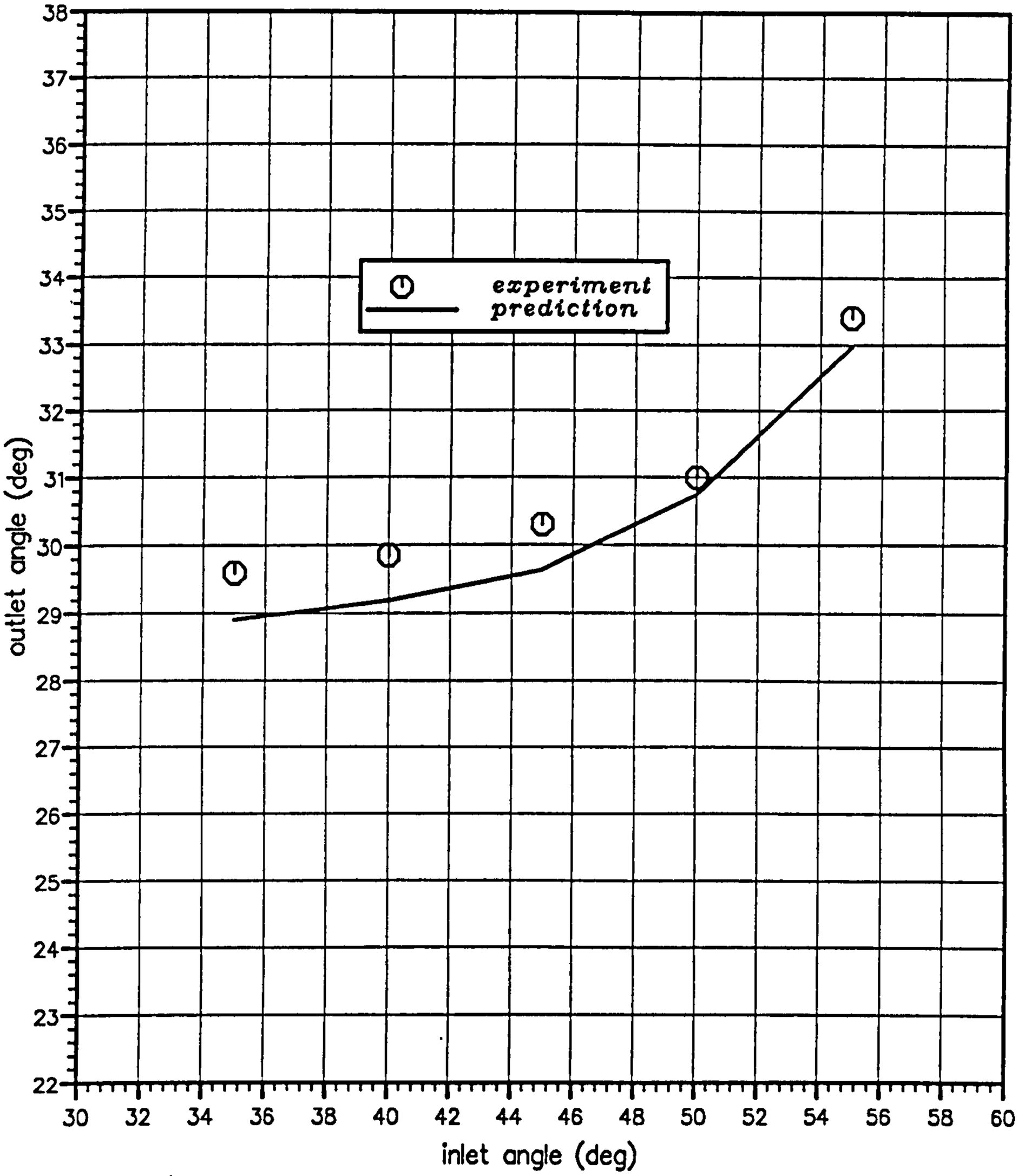

Figure 5.19 : Rhoden's cascade, 20° camber. Comparison between the measured and predicted outlet flow angle.

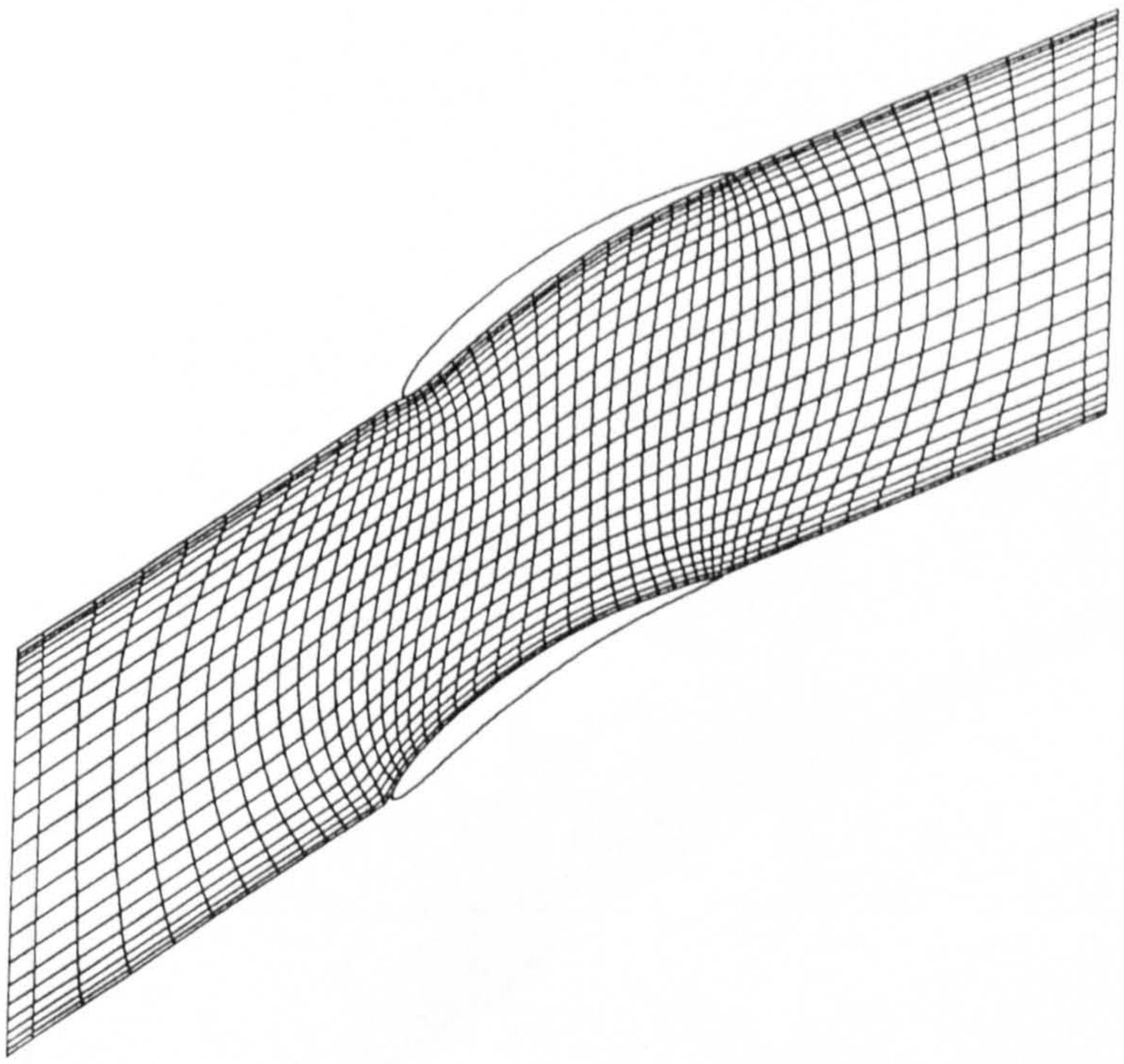

Figure 5.20 : Rhoden's cascade, 30° camber, $a_1 = 35°$. (a) Computational grid. (b) C_p coefficient along the blade surfaces.

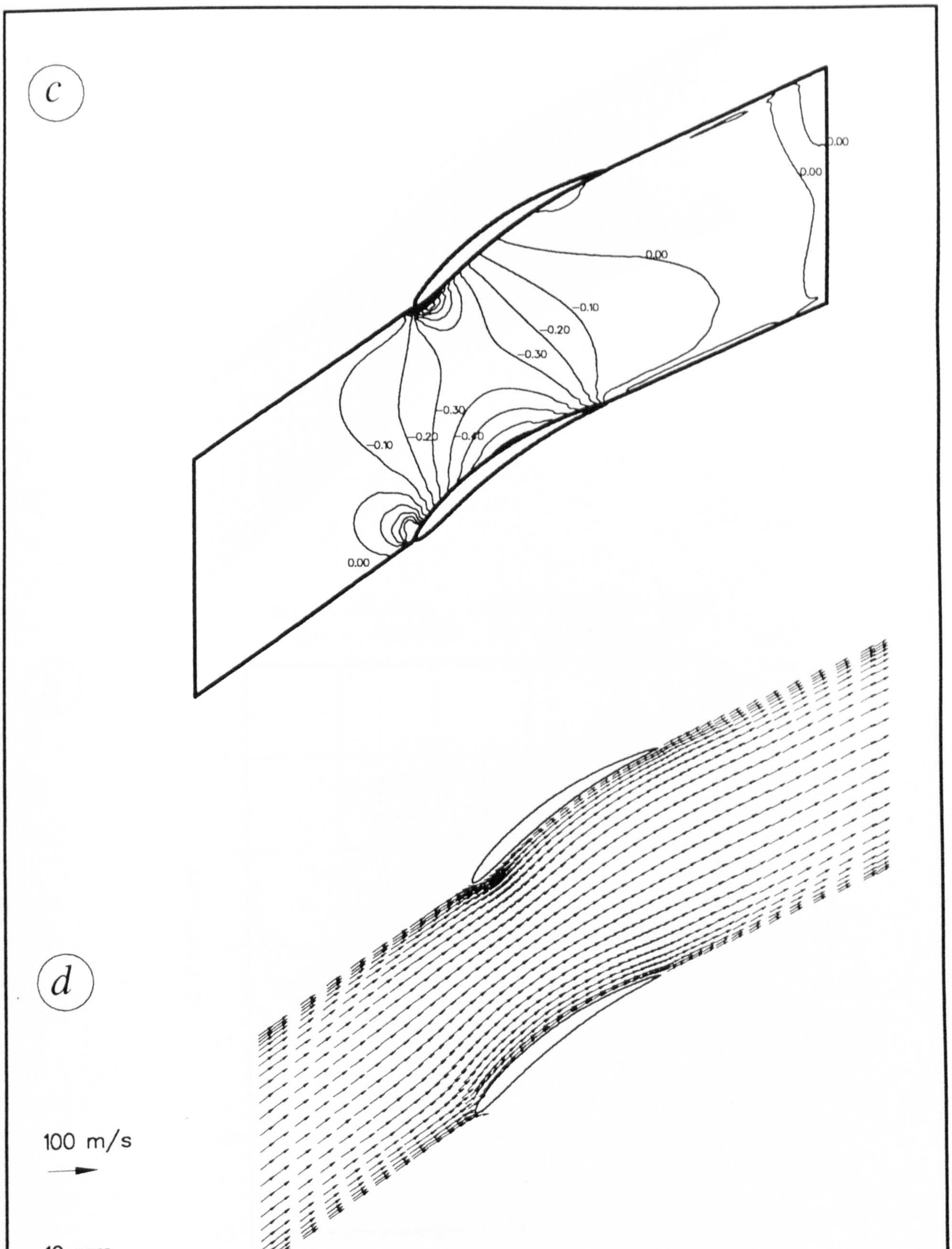

Figure 5.20 : Rhoden's cascade, 30° camber, $a_1 = 35°$. (c) Predicted C_p coefficient contours. (d) Predicted velocity vectors.

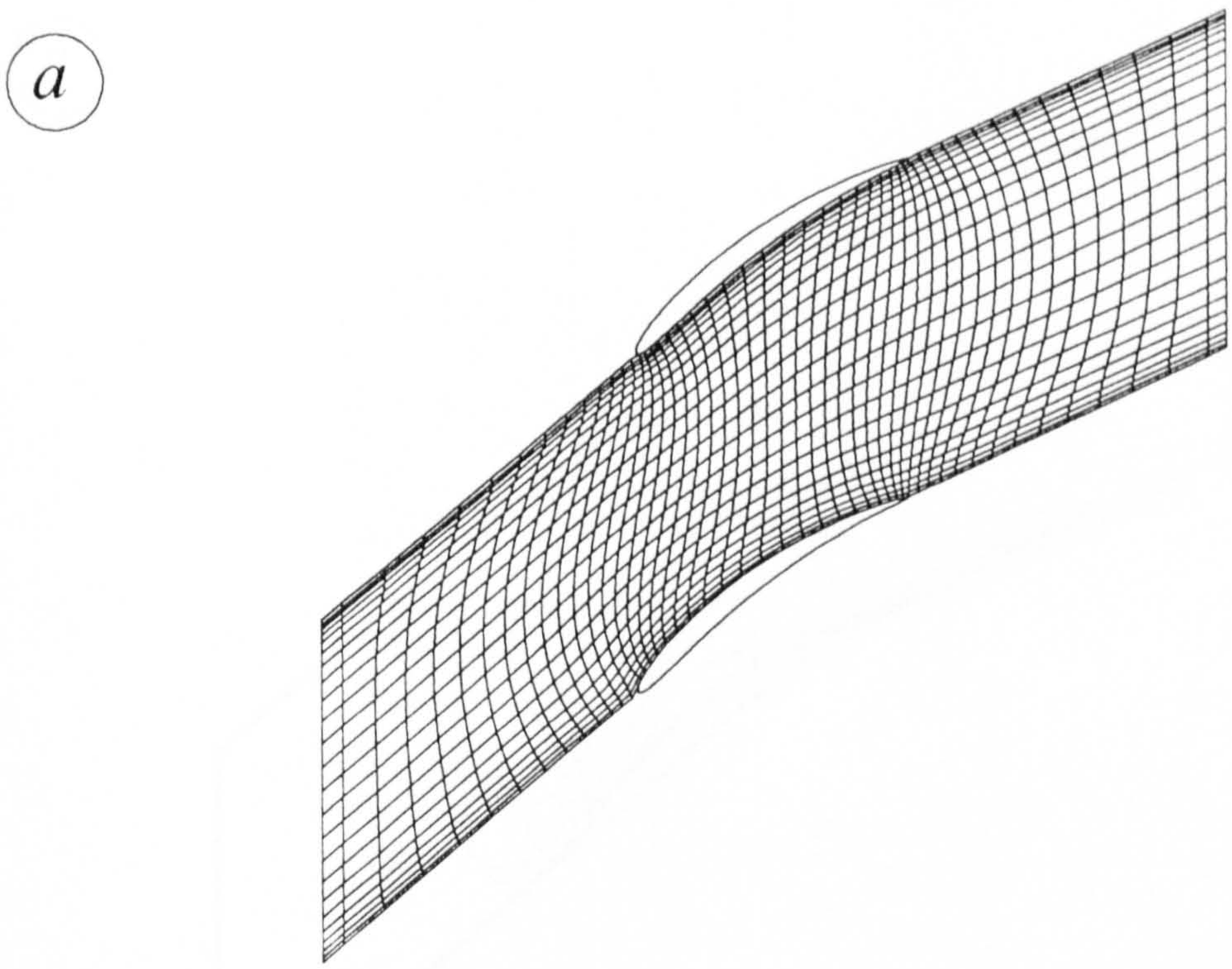

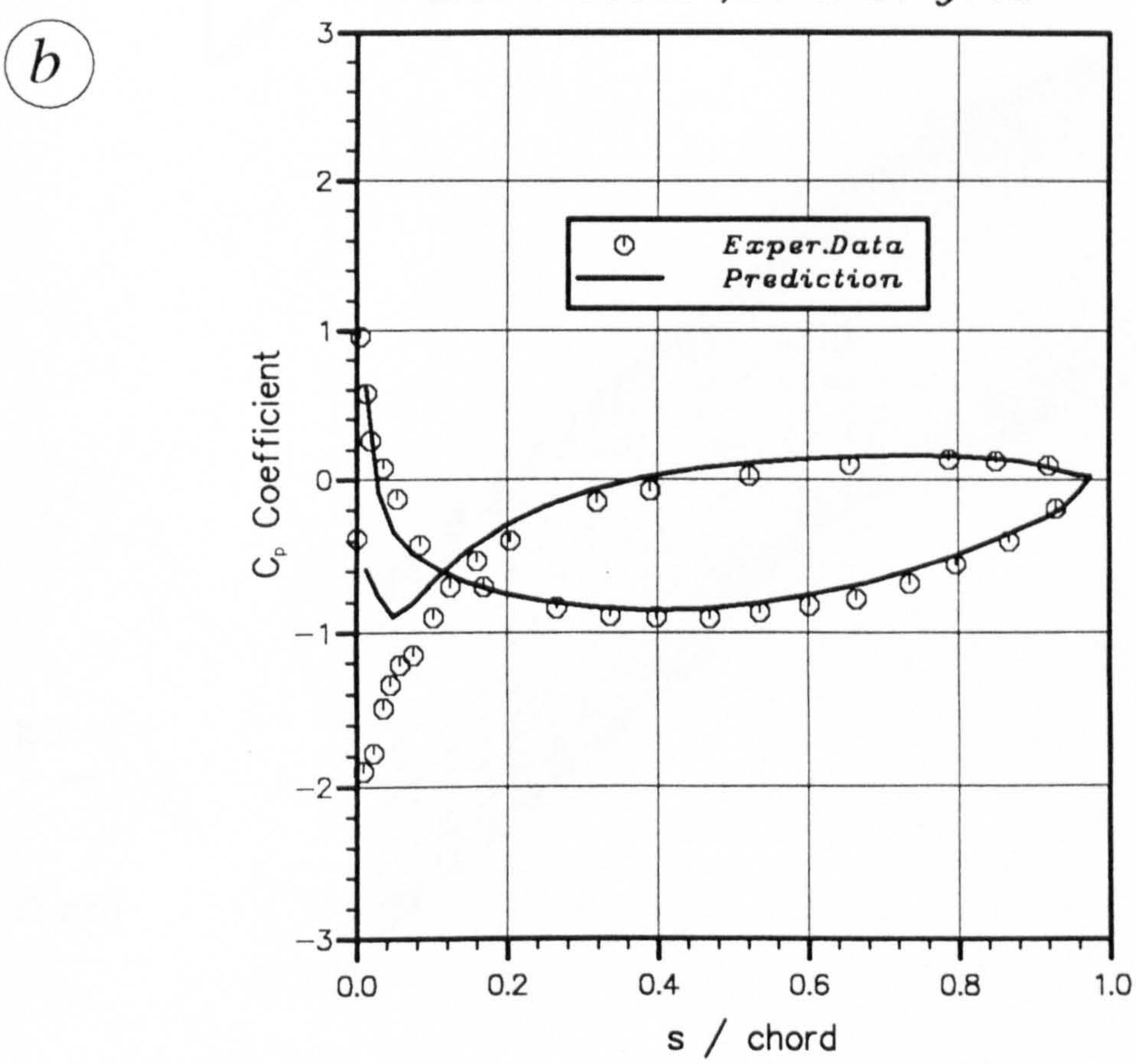

Figure 5.21 : Rhoden's cascade, 30° camber, $a_1 = 40°$. (a) Computational grid. (b) C_p coefficient along the blade surfaces.

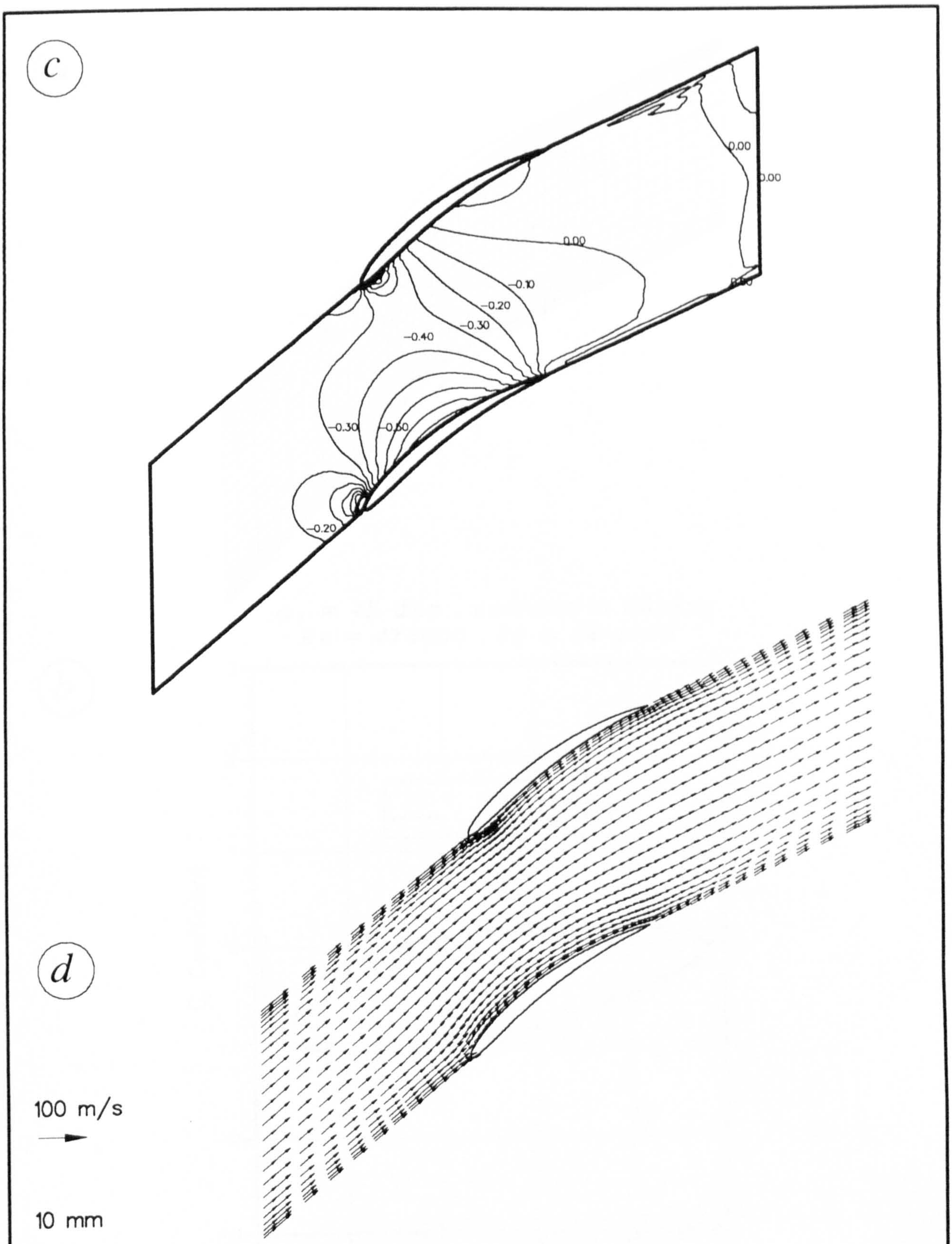

Figure 5.21 : Rhoden's cascade, 30° camber, $a_1 = 40°$. (c) Predicted C_p coefficient contours. (d) Predicted velocity vectors.

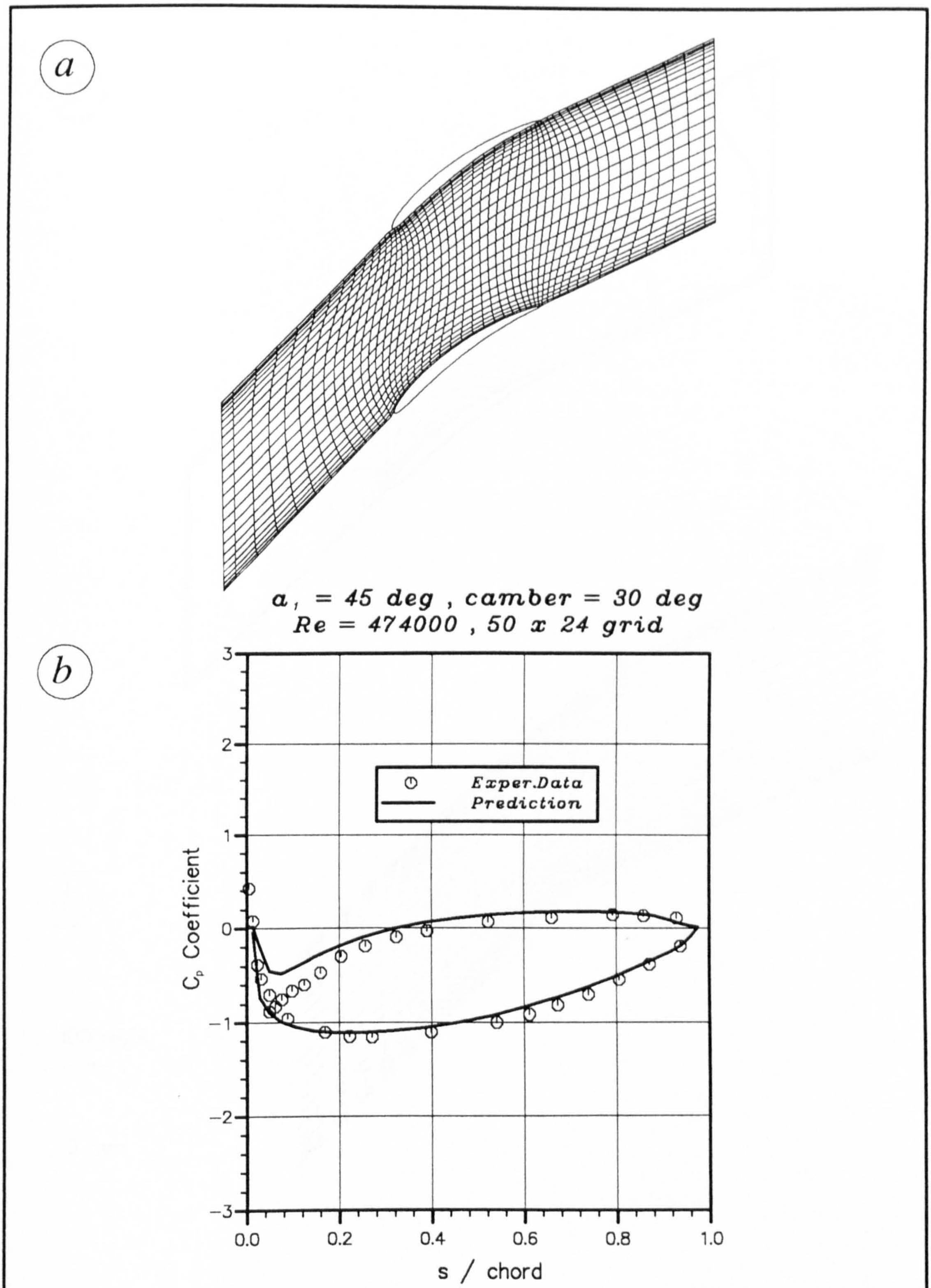

Figure 5.22 : Rhoden's cascade, 30° camber, $a_1 = 45°$. (a) Computational grid. (b) C_p coefficient along the blade surfaces.

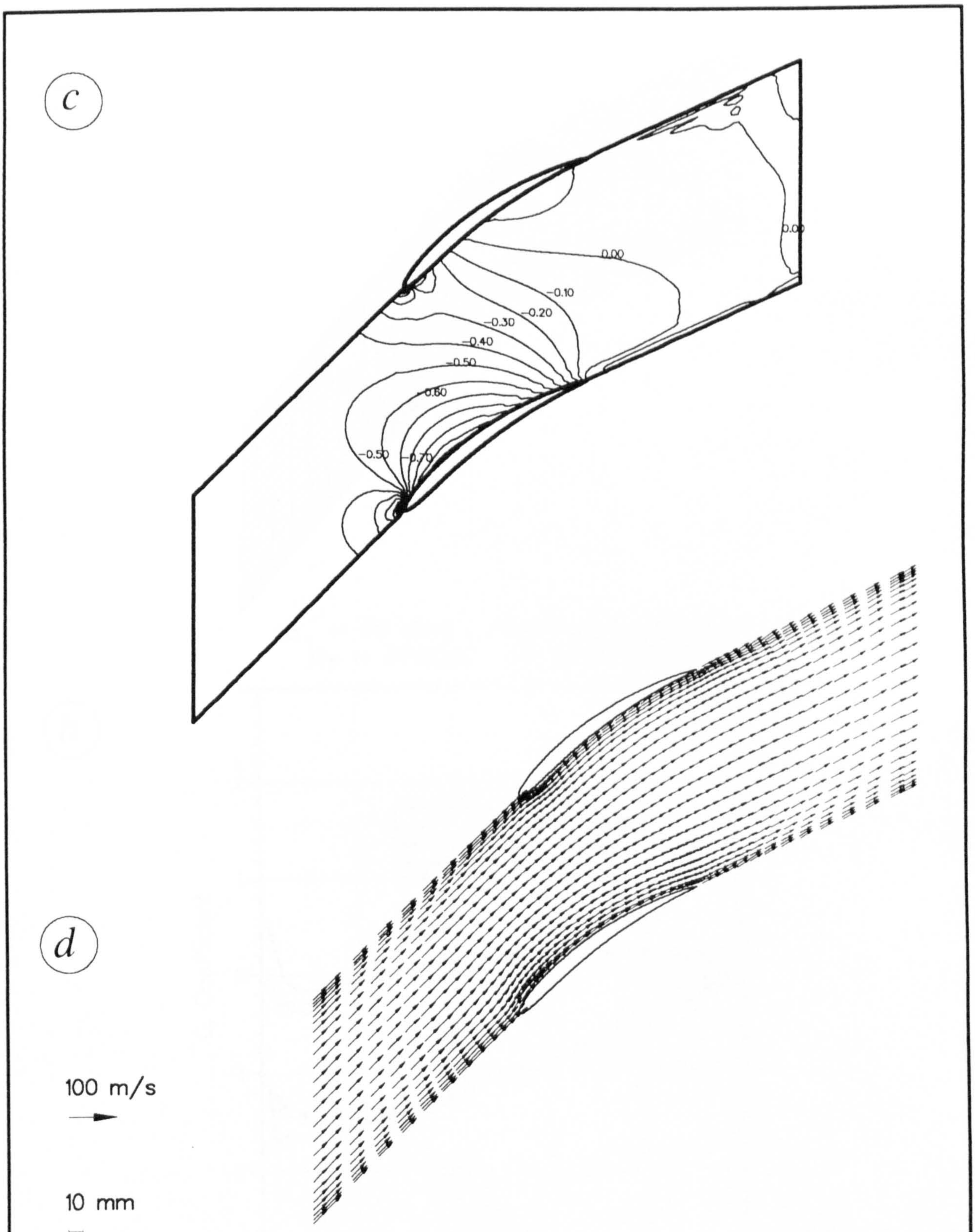

Figure 5.22 : Rhoden's cascade, 30° camber, $a_1 = 45°$. (c) Predicted C_P coefficient contours. (d) Predicted velocity vectors.

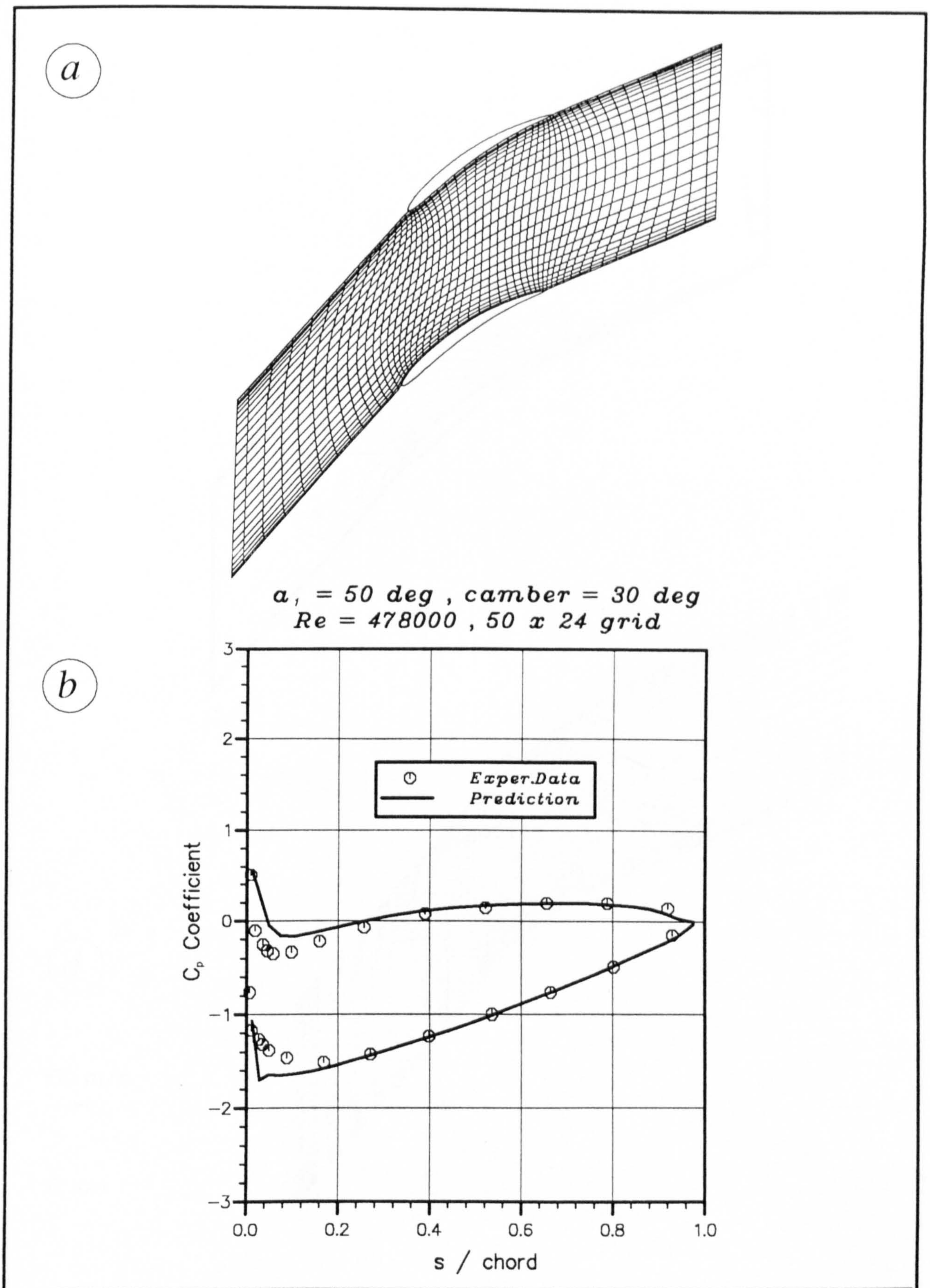

Figure 5.23 : Rhoden's cascade, 30° camber, $a_1 = 50°$. (a) Computational grid. (b) C_p coefficient along the blade surfaces.

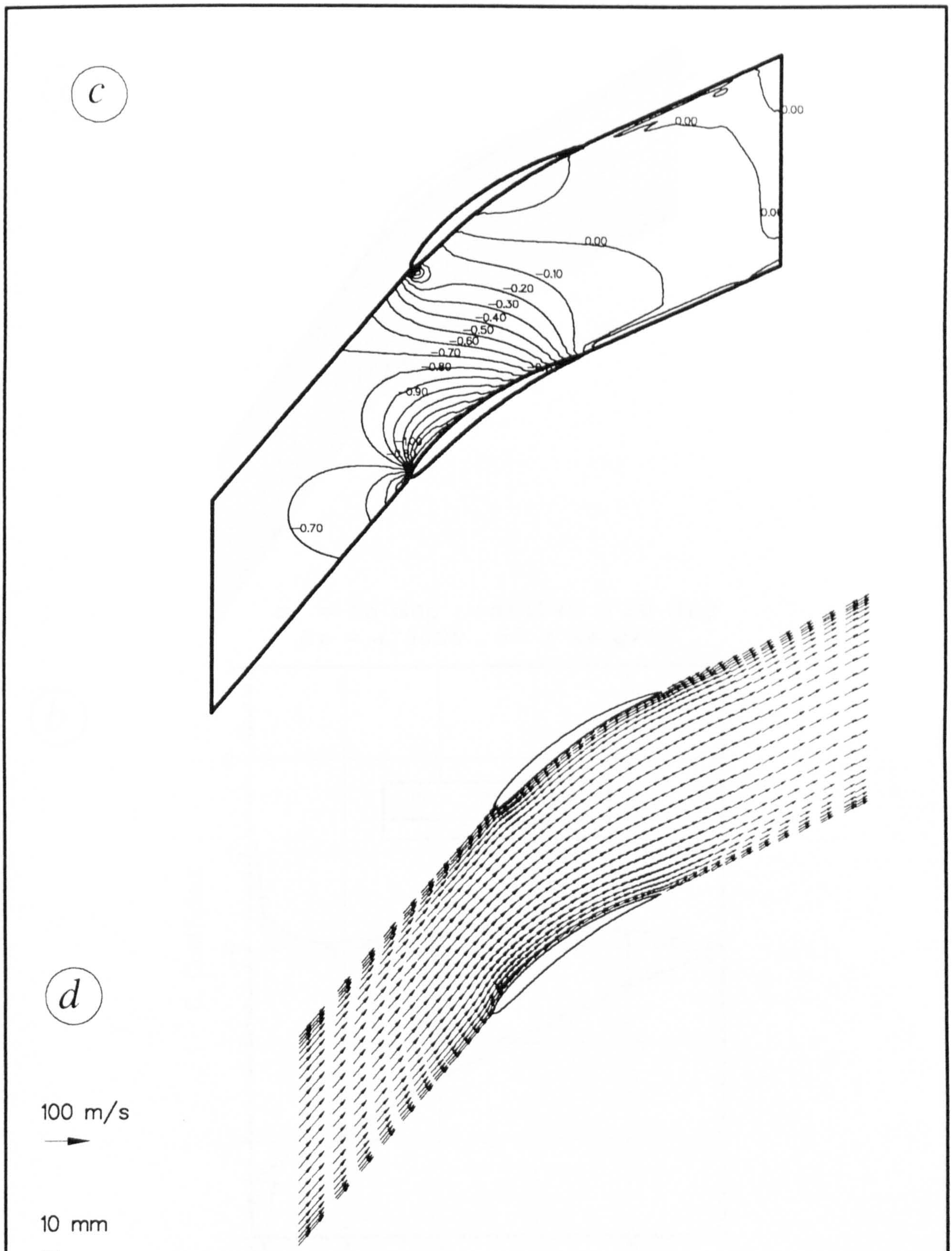

Figure 5.23 : Rhoden's cascade, 30° camber, $a_1 = 50°$. (c) Predicted C_p coefficient contours. (d) Predicted velocity vectors.

(a)

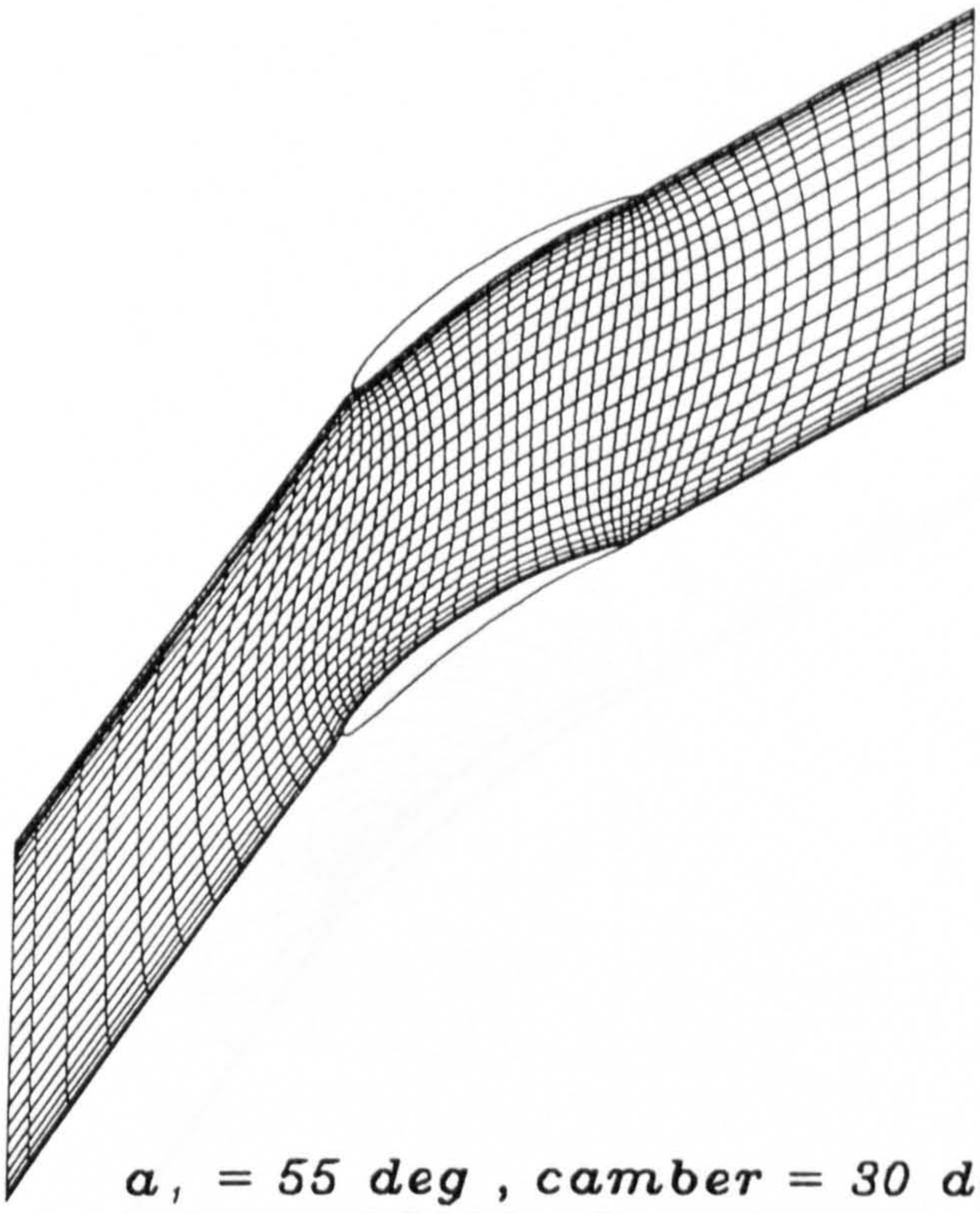

a, = 55 deg , camber = 30 deg
Re = 475000 , 50 x 24 grid

(b)

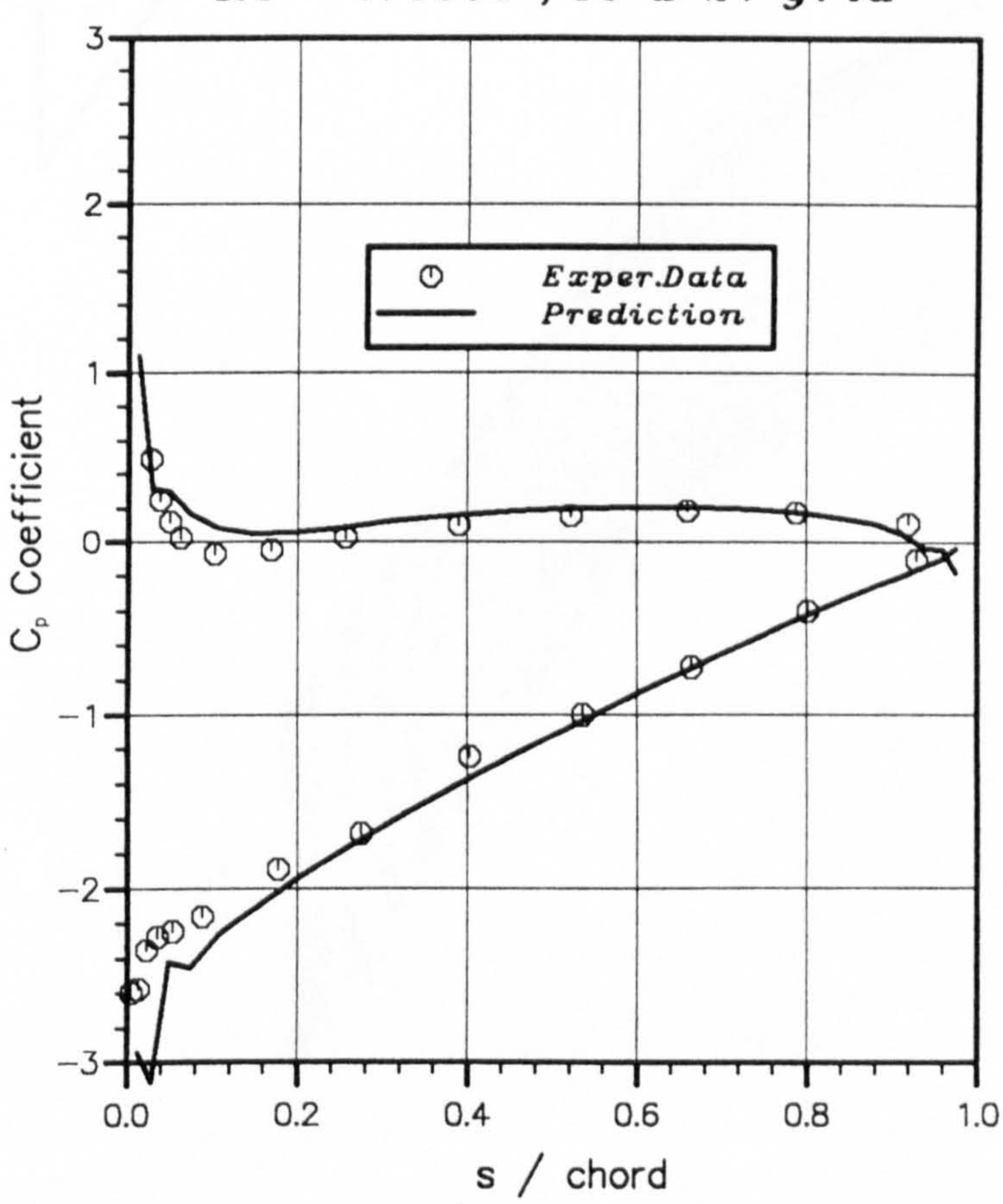

Figure 5.24 : Rhoden's cascade, 30° camber, $a_1 = 55°$. (a) Computational grid. (b) C_p coefficient along the blade surfaces.

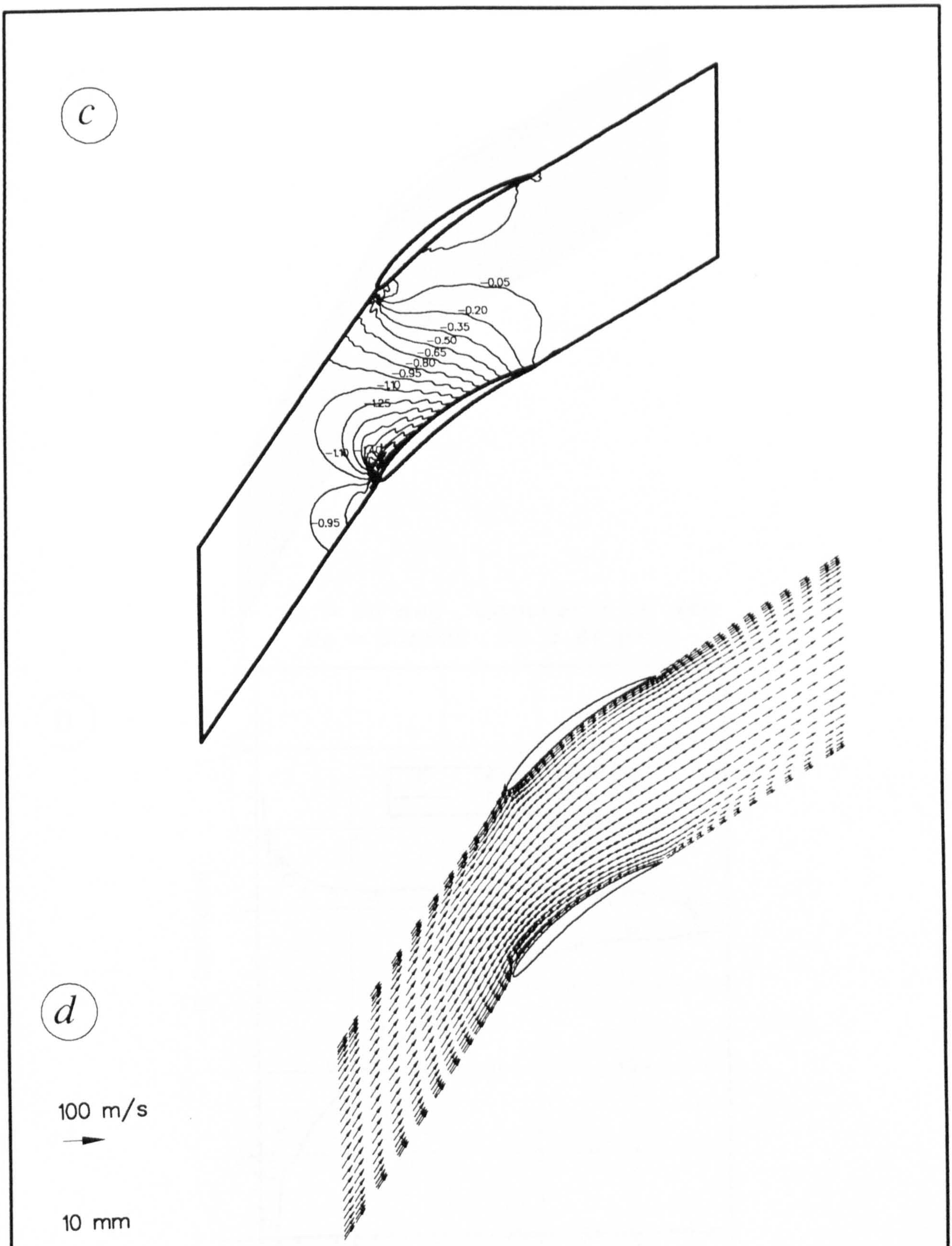

Figure 5.24 : Rhoden's cascade, 30° camber, $a_1 = 55°$. (c) Predicted C_p coefficient contours. (d) Predicted velocity vectors.

(a)

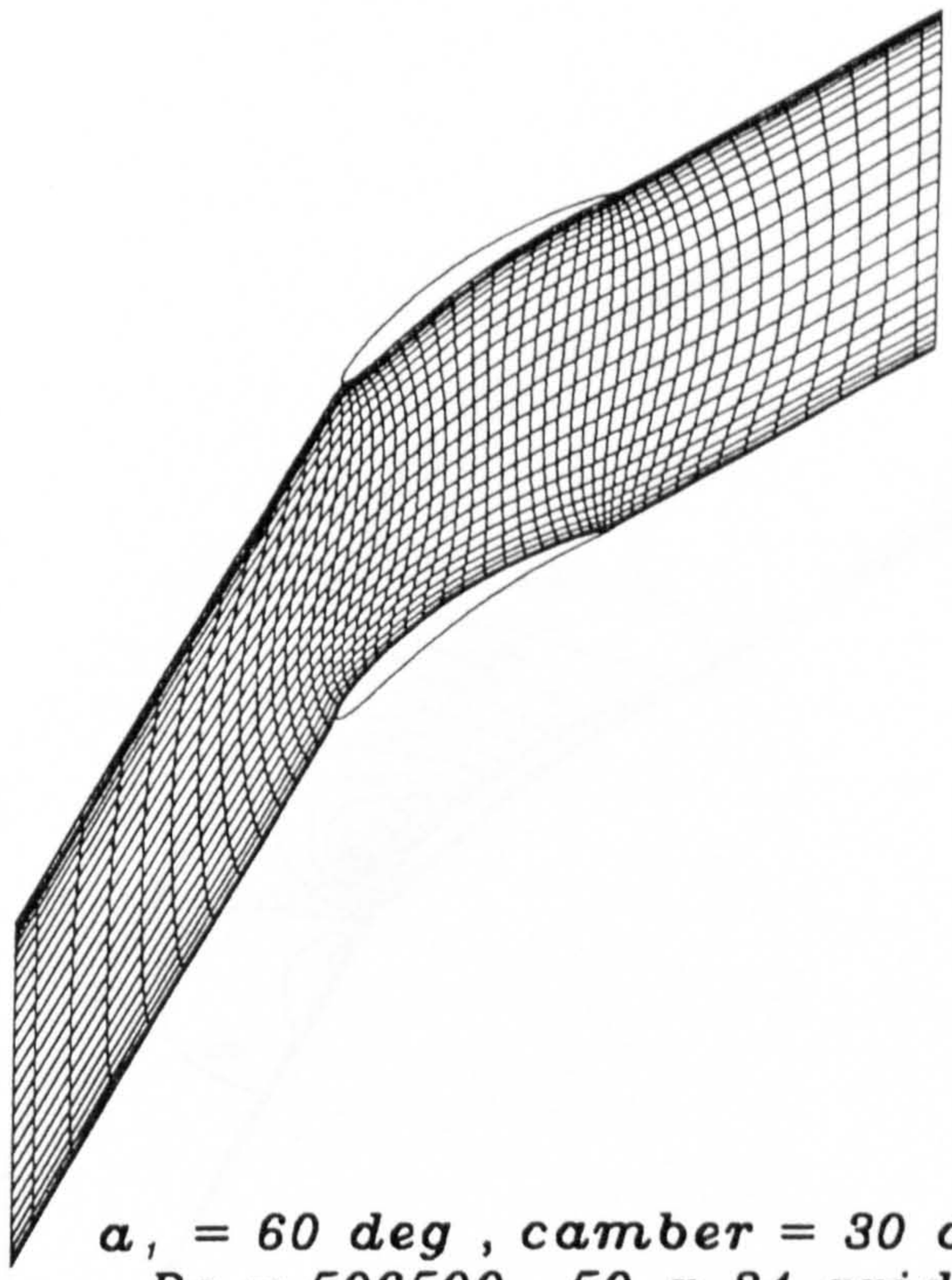

a, = 60 deg , camber = 30 deg
Re = 506500 , 50 x 24 grid

(b)

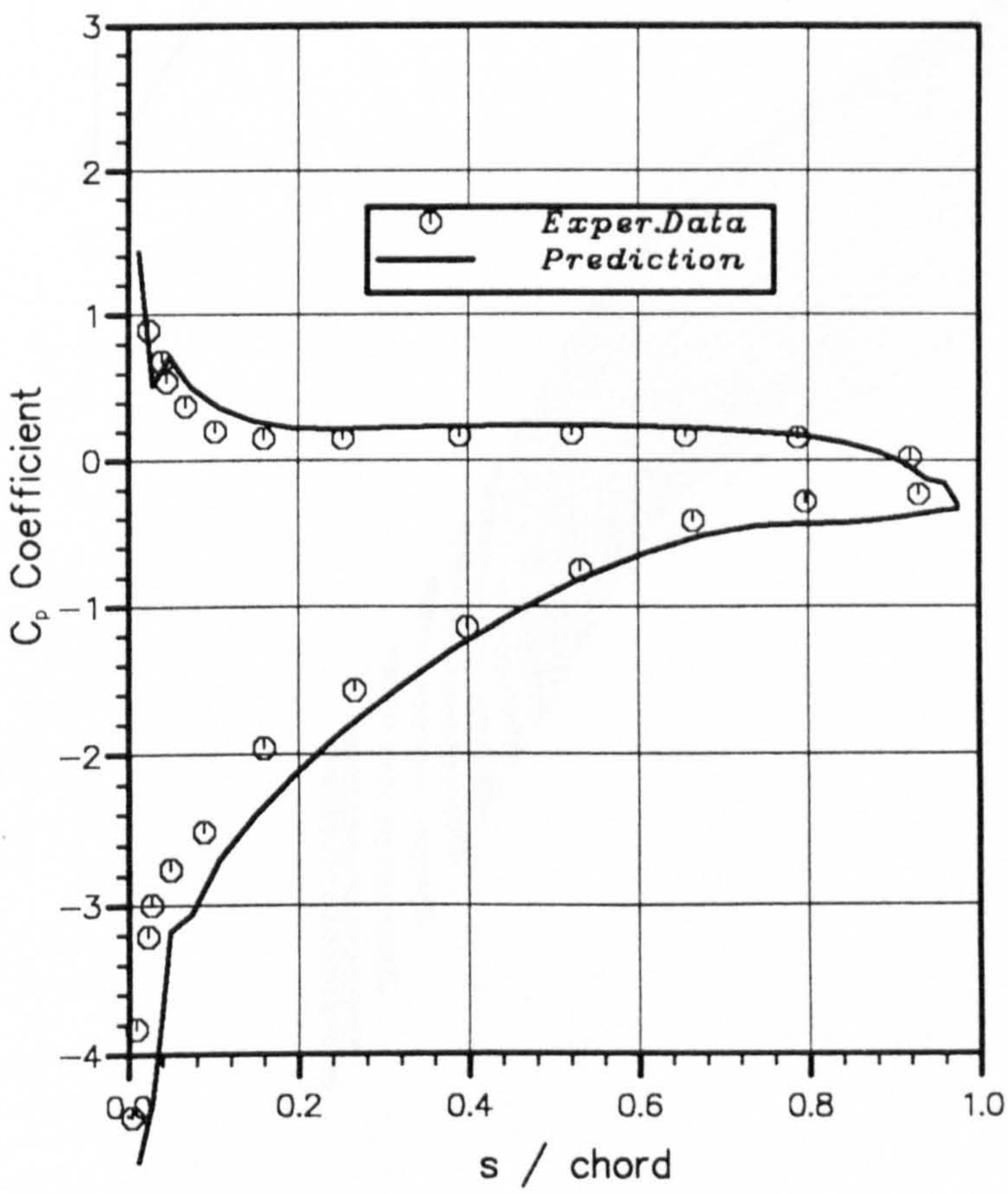

Figure 5.25 : Rhoden's cascade, 30° camber, $a_1 = 60°$. (a) Computational grid. (b) C_p coefficient along the blade surfaces.

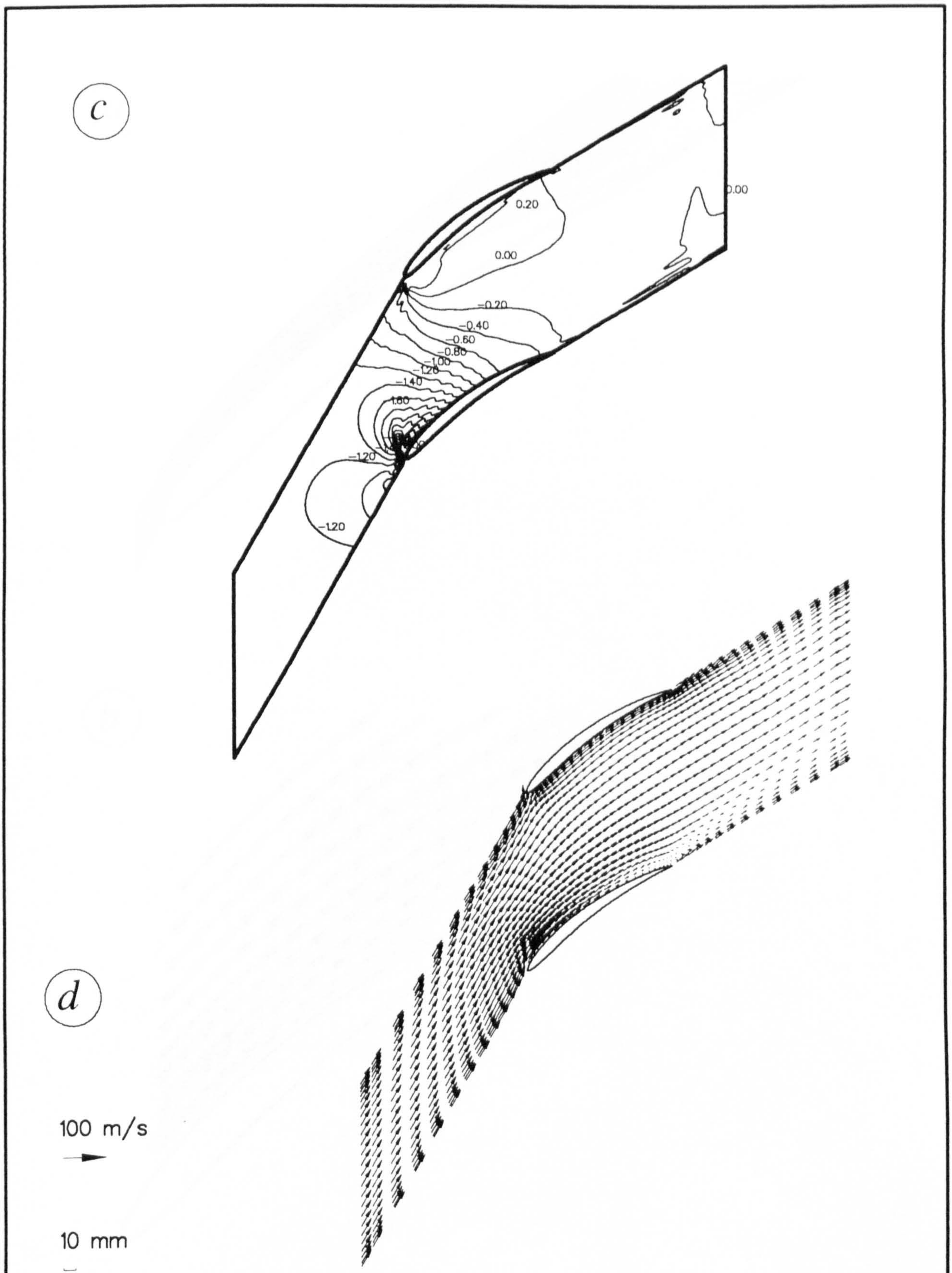

Figure 5.25 : Rhoden's cascade, 30° camber, $a_1 = 60°$. (c) Predicted C_p coefficient contours. (d) Predicted velocity vectors.

Figure 5.26 : Rhoden's cascade, 30° camber, $a_1 = 60°$. (a) Predicted streamlines along the suction side. (b) Predicted velocity vectors along the suction side.

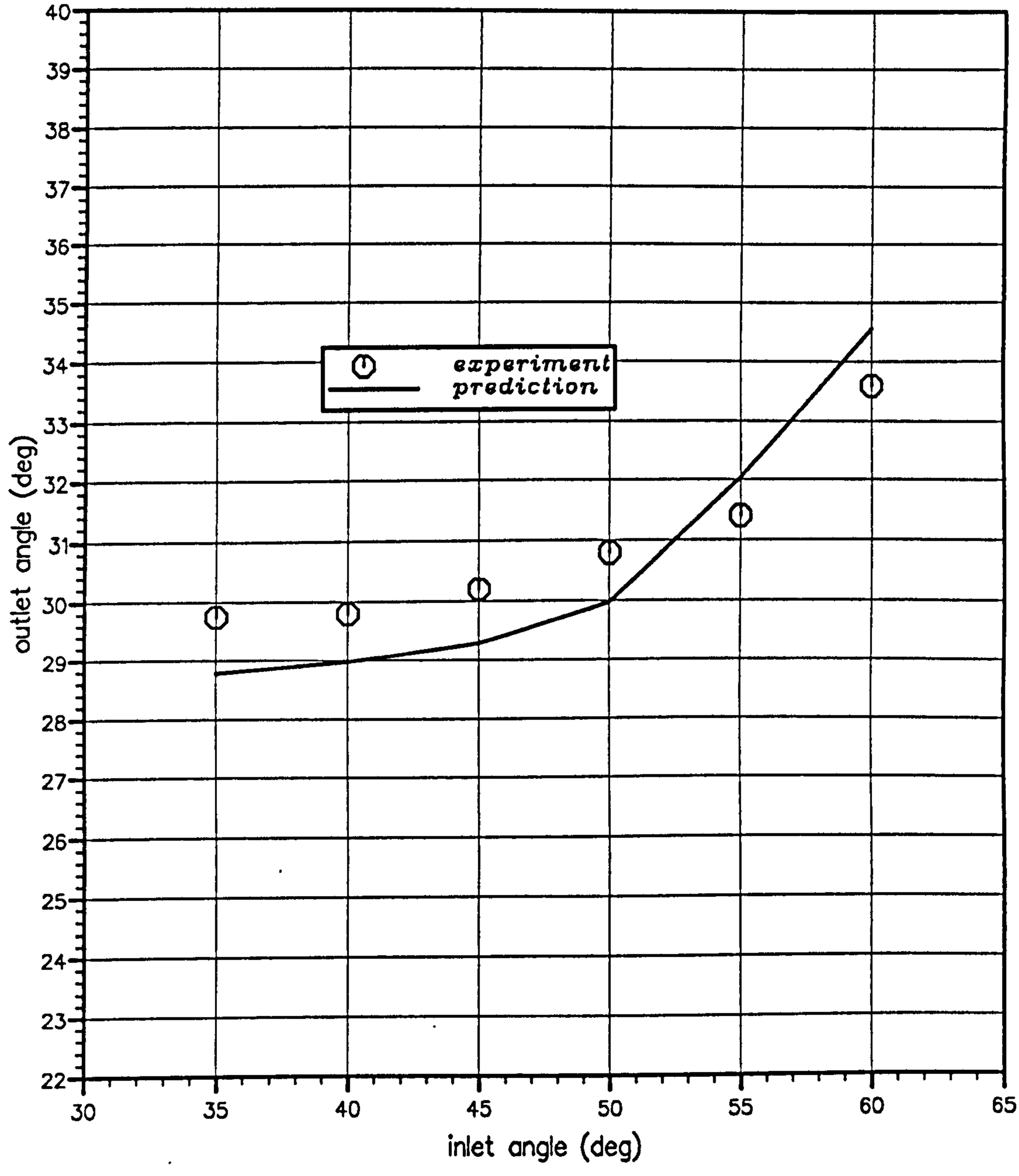

Figure 5.27 : Rhoden's cascade, 30° camber. Comparison between the measured and predicted outlet flow angle.

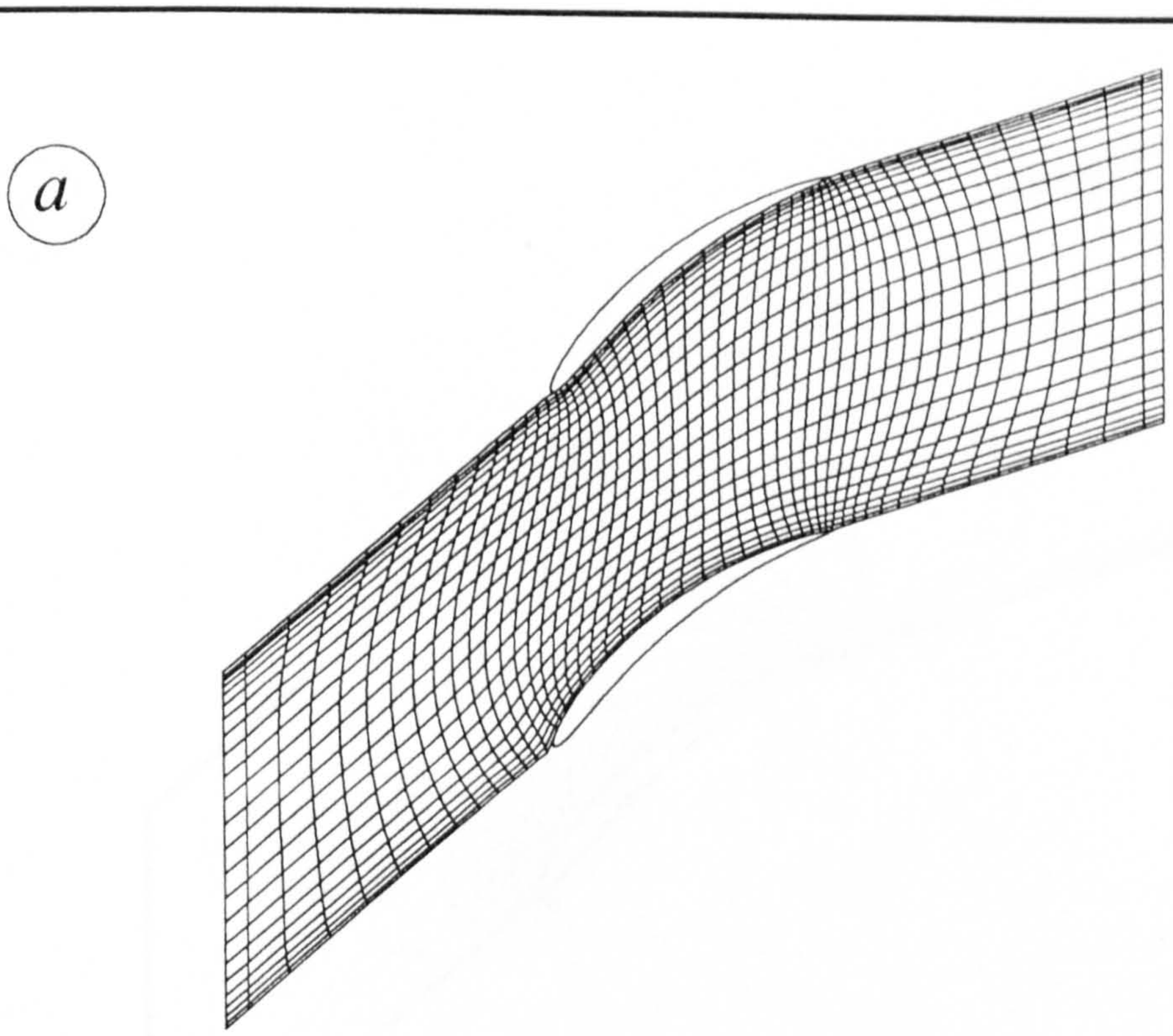

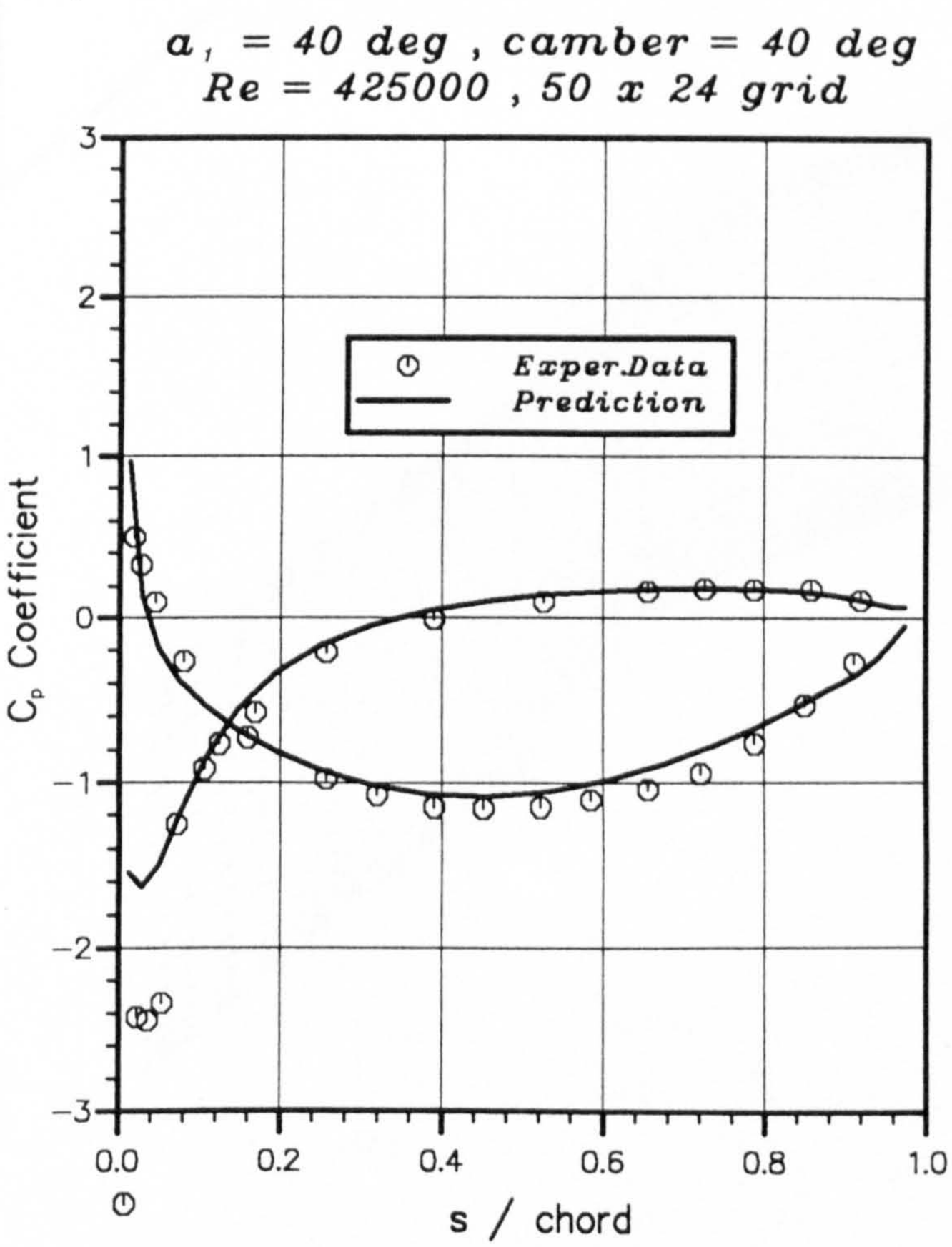

Figure 5.28 : Rhoden's cascade, 40° camber, $a_1 = 40°$. (a) Computational grid. (b) C_p coefficient along the blade surfaces.

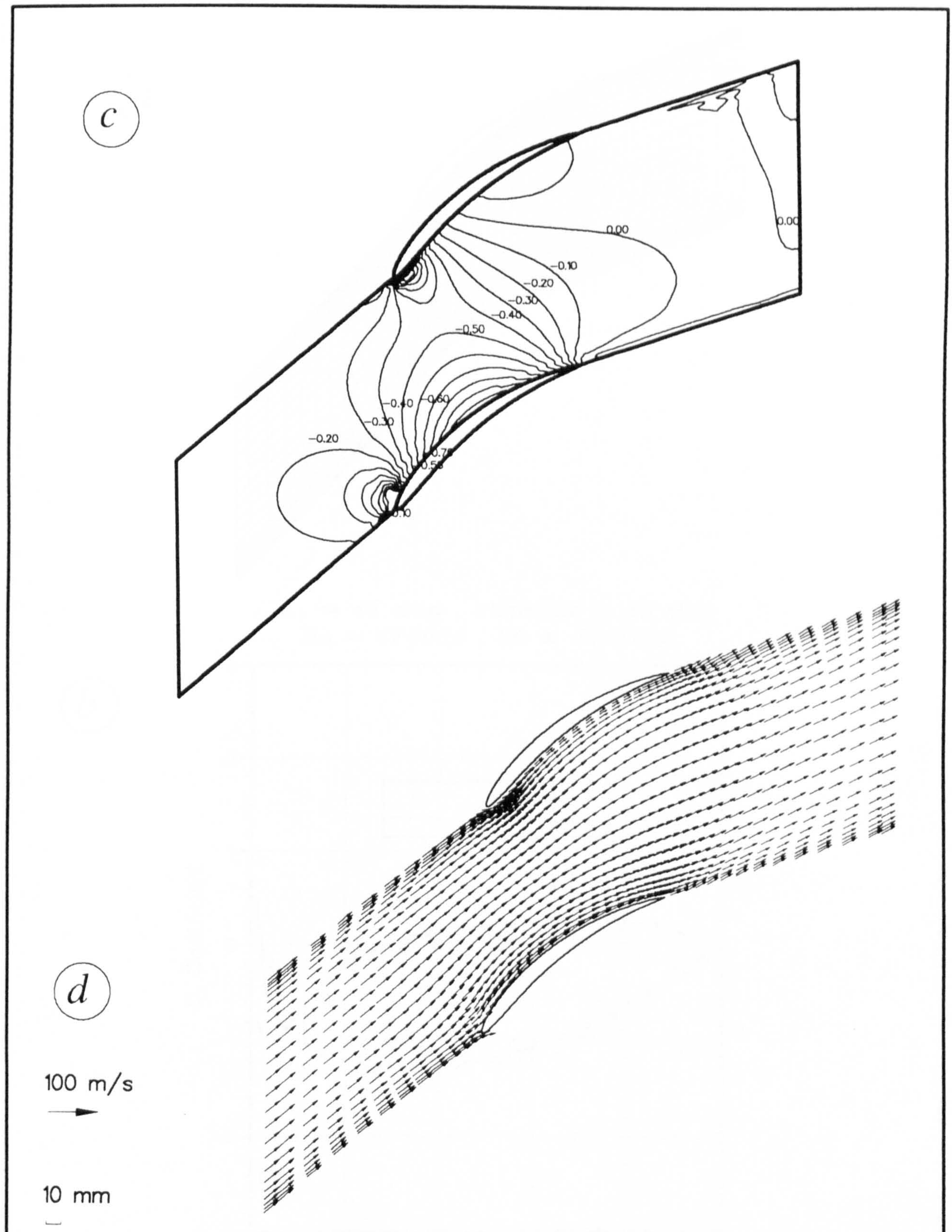

Figure 5.28 : Rhoden's cascade, 40° camber, $a_1 = 40°$. (c) Predicted C_p coefficient contours. (d) Predicted velocity vectors.

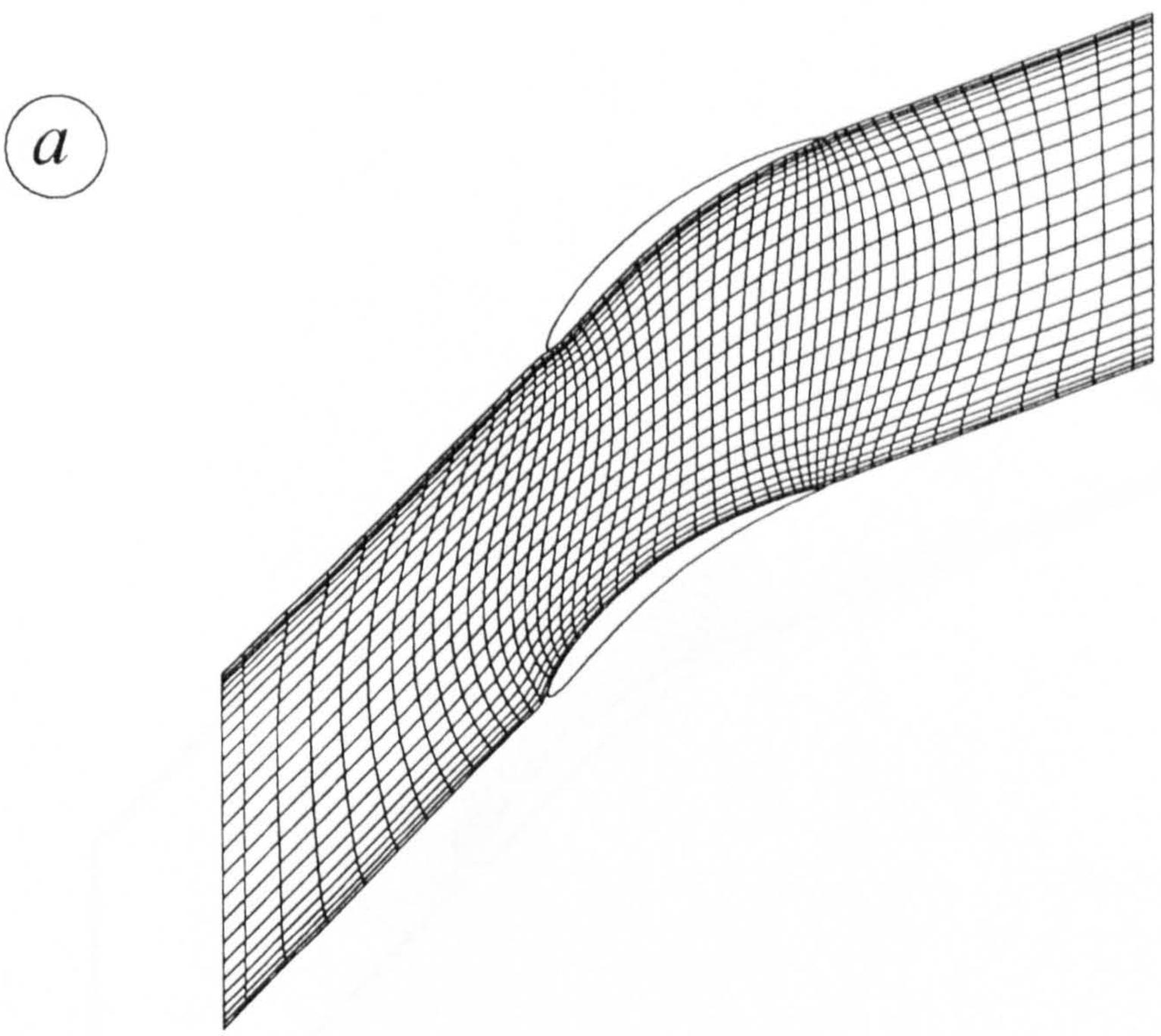

Figure 5.29 : Rhoden's cascade, 40° camber, $a_1 = 45°$. (a) Computational grid. (b) C_p coefficient along the blade surfaces.

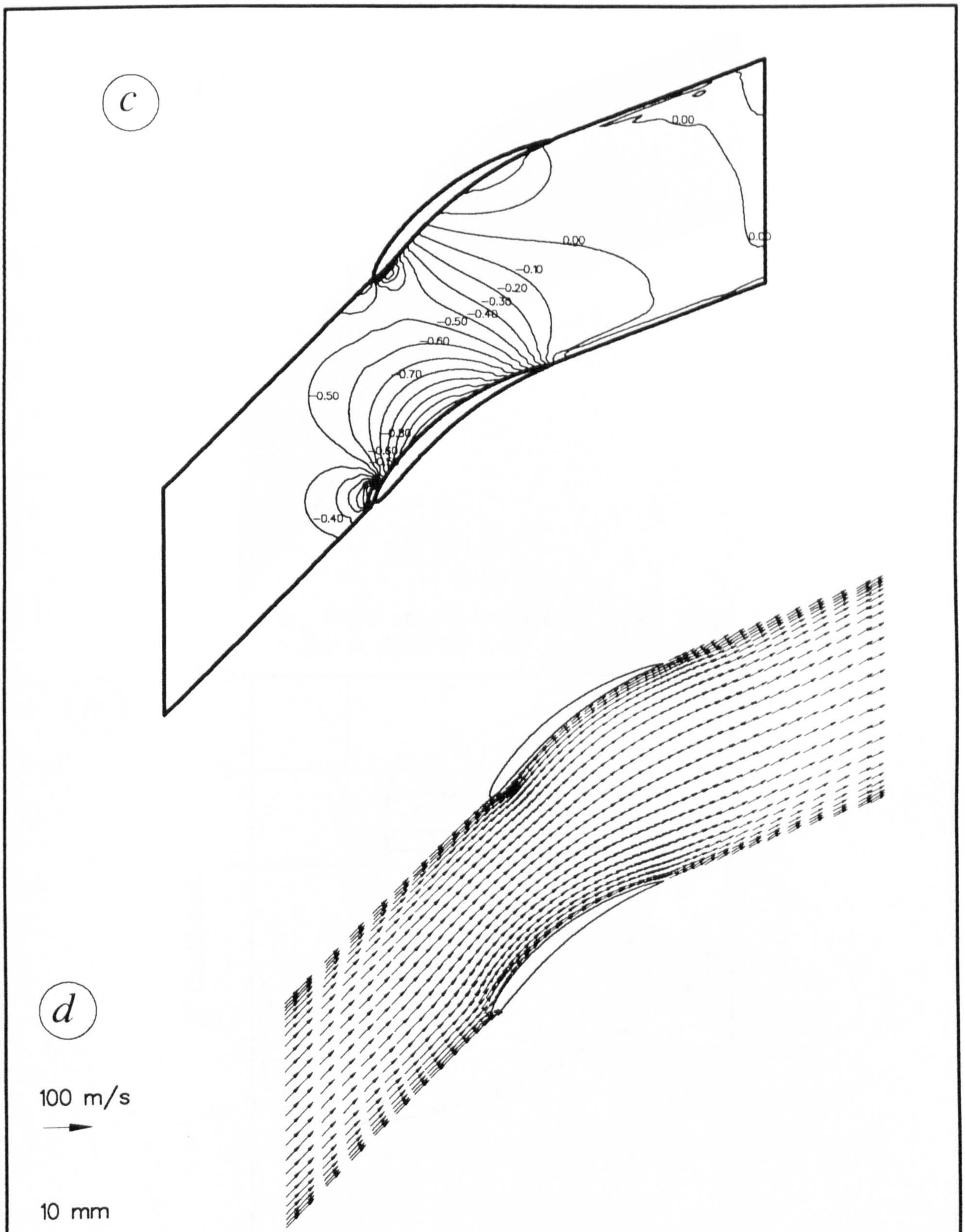

Figure 5.29 : Rhoden's cascade, 40° camber, $a_1 = 45°$. (c) Predicted C_p coefficient contours. (d) Predicted velocity vectors.

a

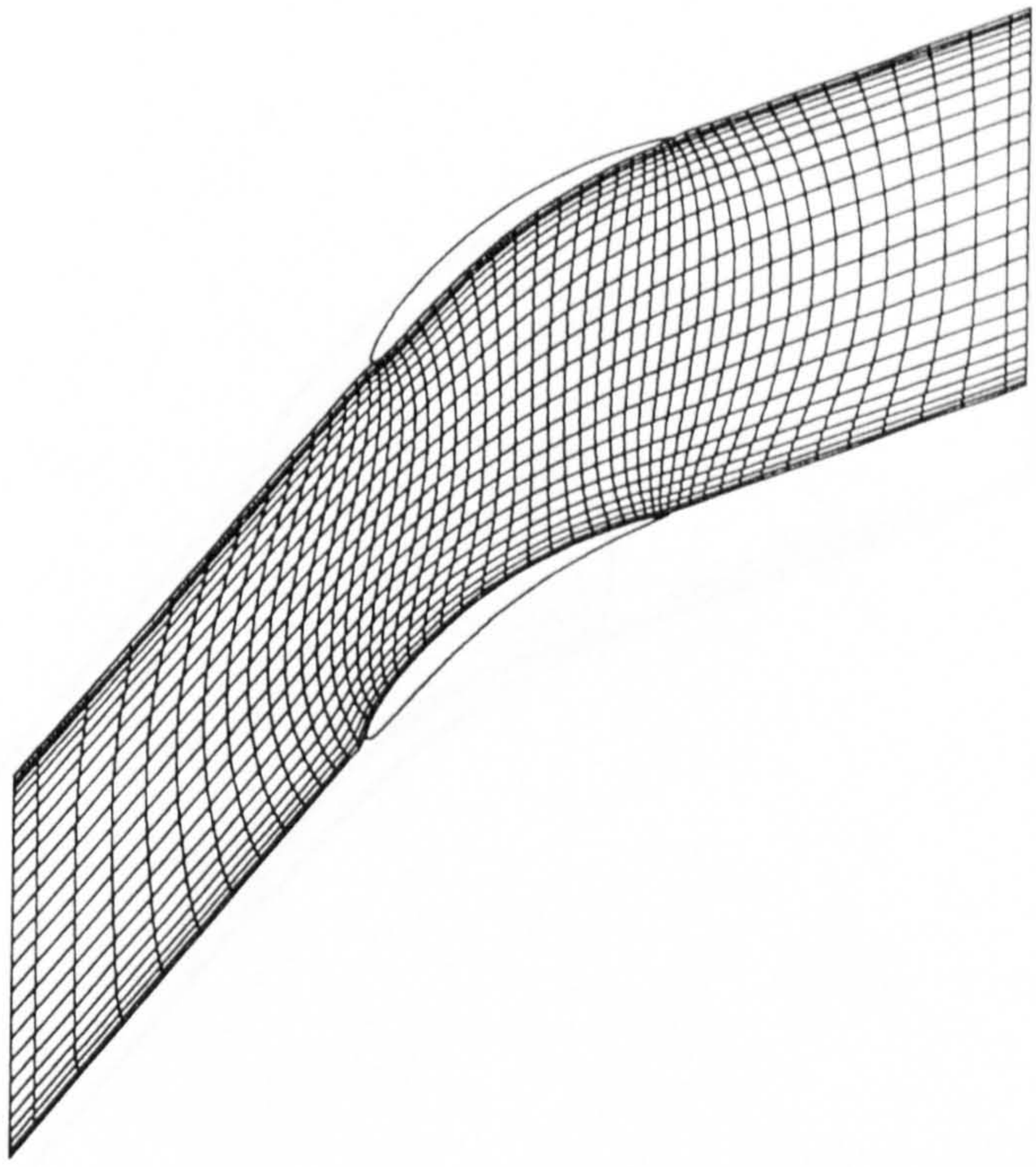

$a_1 = 50$ deg , camber = 40 deg
Re = 493000 , 50 x 24 grid

b

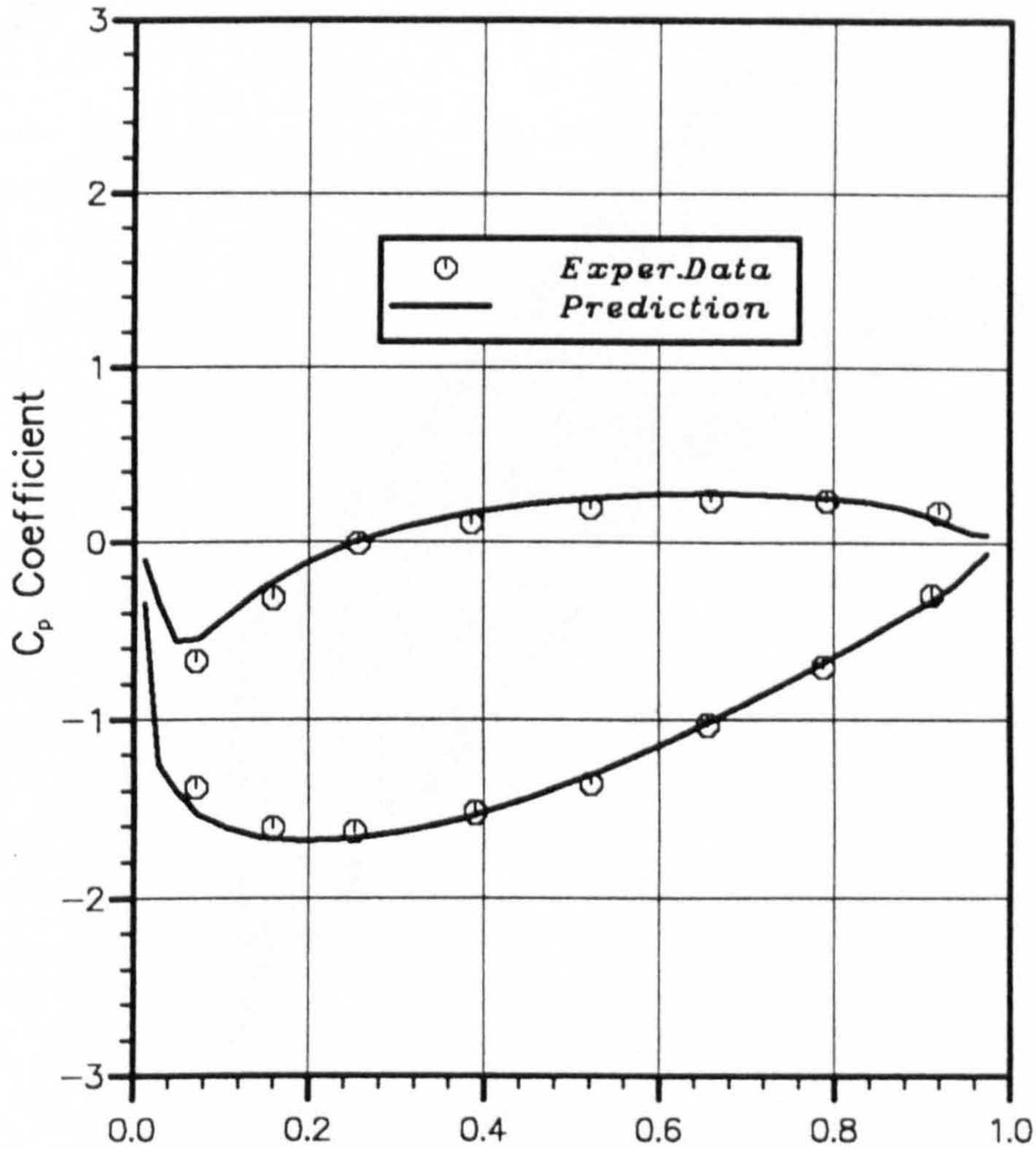

Figure 5.30 : Rhoden's cascade, 40° camber, $a_1 = 50°$. (a) Computational grid. (b) C_p coefficient along the blade surfaces.

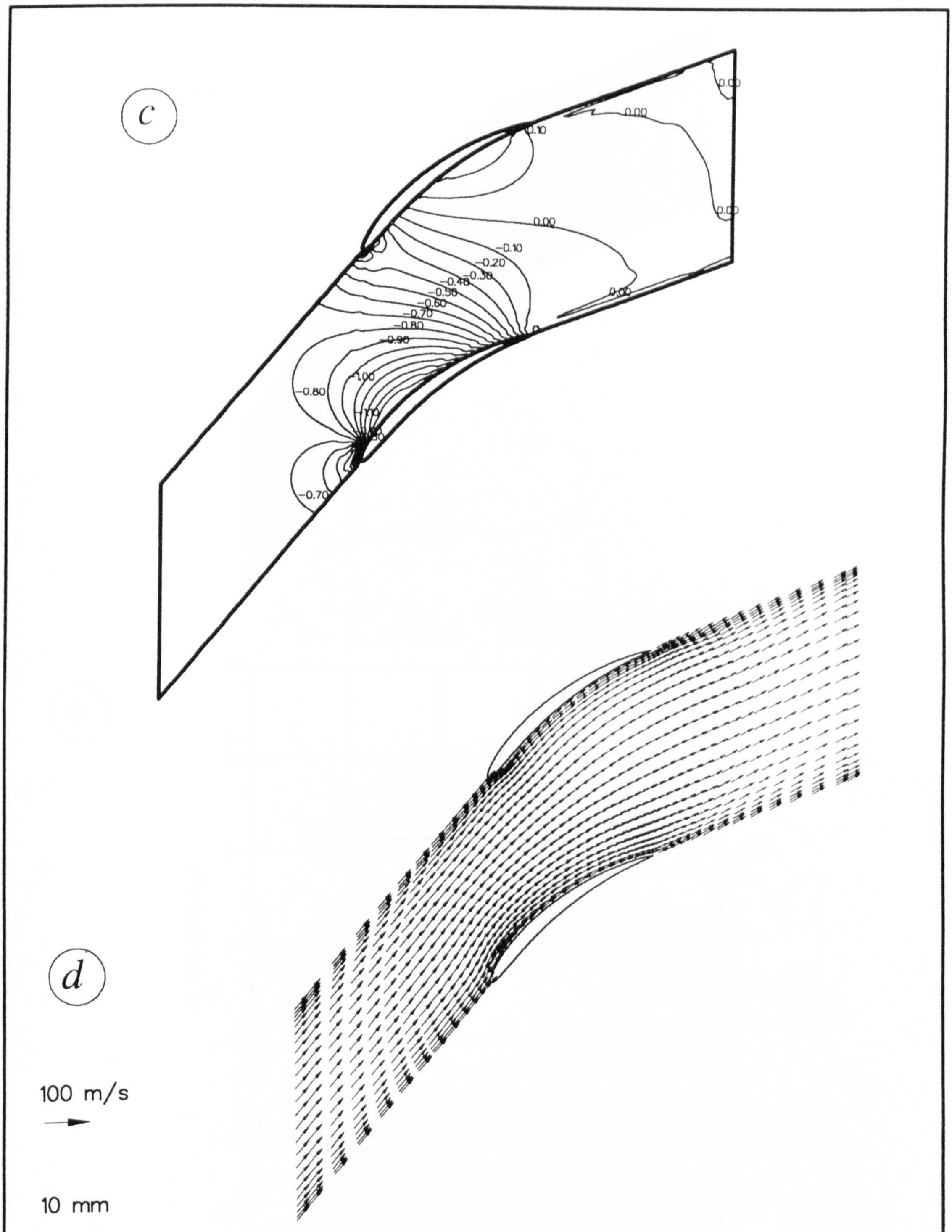

Figure 5.30 : Rhoden's cascade, 40° camber, $a_1 = 50°$. (c) Predicted C_p coefficient contours. (d) Predicted velocity vectors.

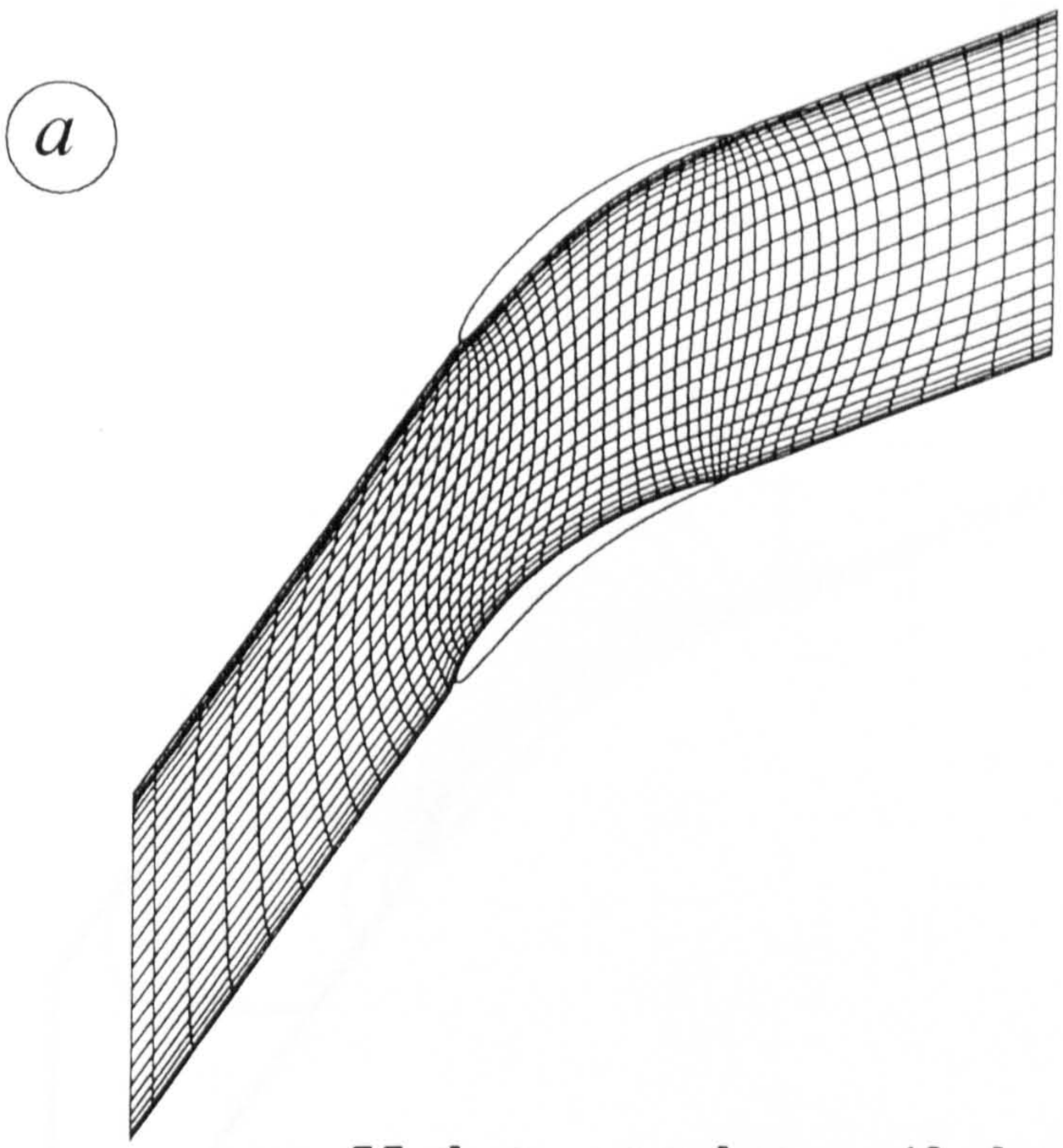

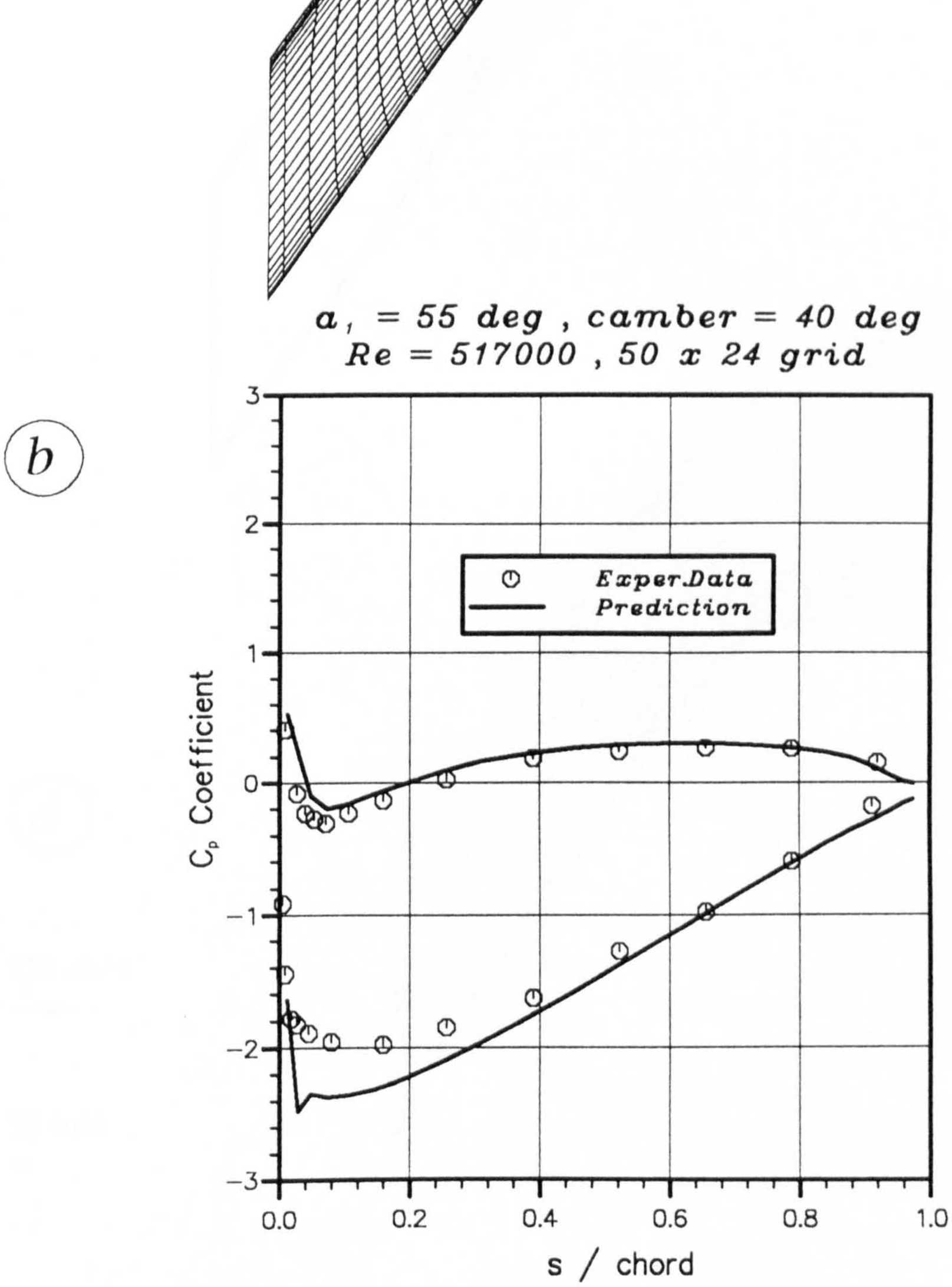

Figure 5.31 : Rhoden's cascade, 40° camber, $a_1 = 55°$. (a) Computational grid. (b) C_p coefficient along the blade surfaces.

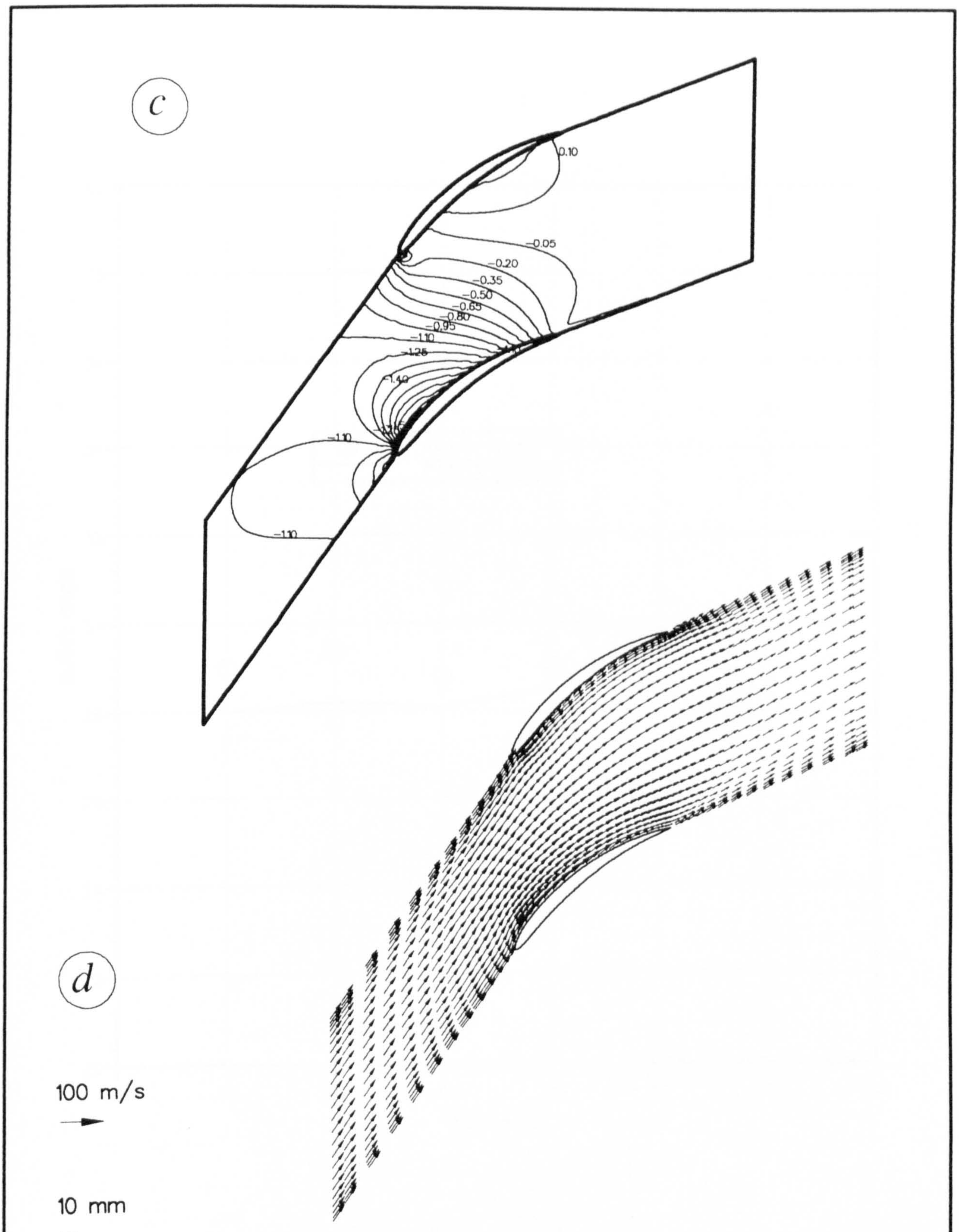

Figure 5.31 : Rhoden's cascade, 40° camber, $a_1 = 55°$. (c) Predicted C_p coefficient contours. (d) Predicted velocity vectors.

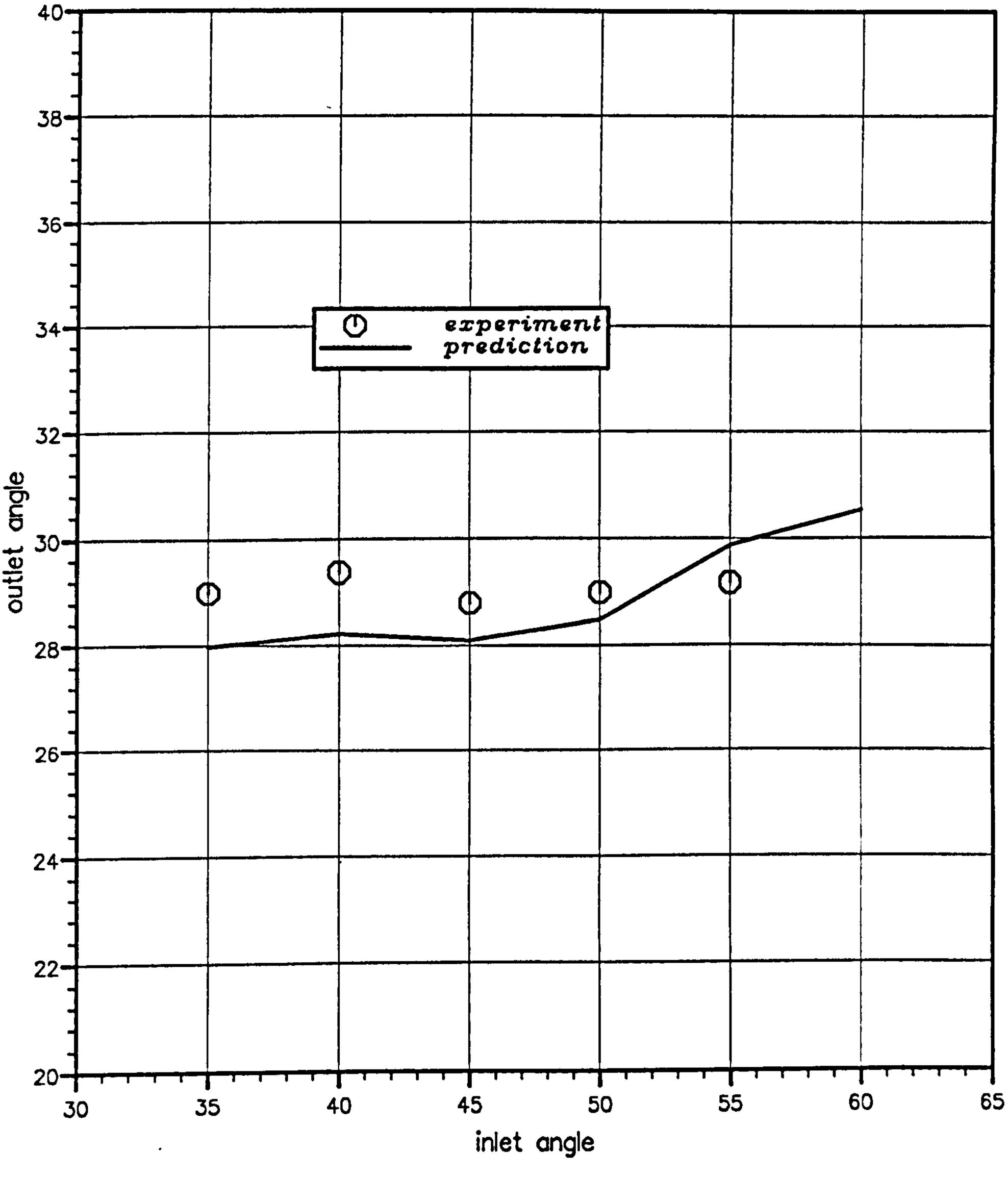

Figure 5.32 : Rhoden's cascade, 40° camber. Comparison between the measured and predicted outlet flow angle.

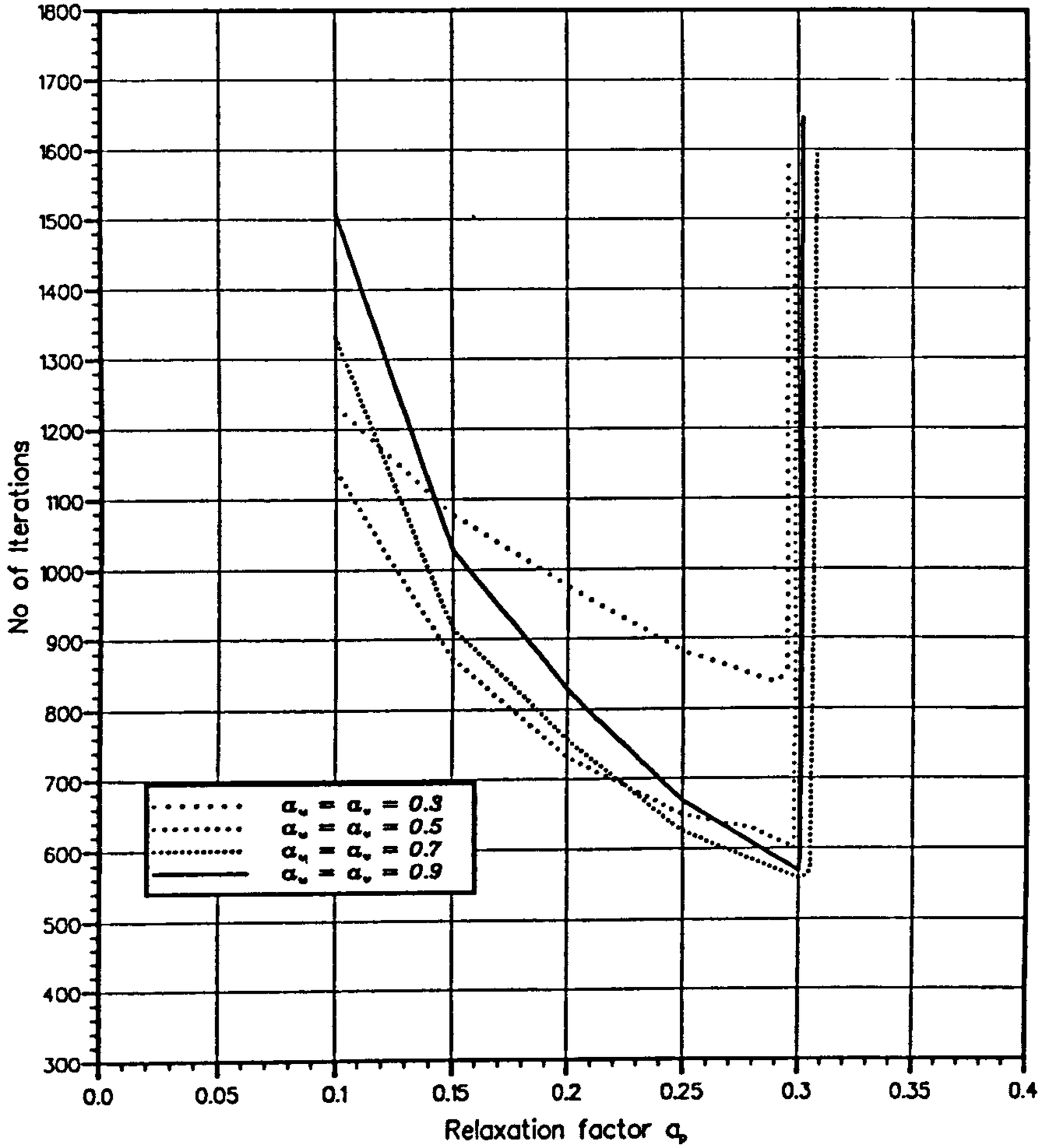

Figure 5.33 : Effect of under-relaxation factors on number of iterations for convergence.
Convergence criterion : ϵ_c=0.0001.

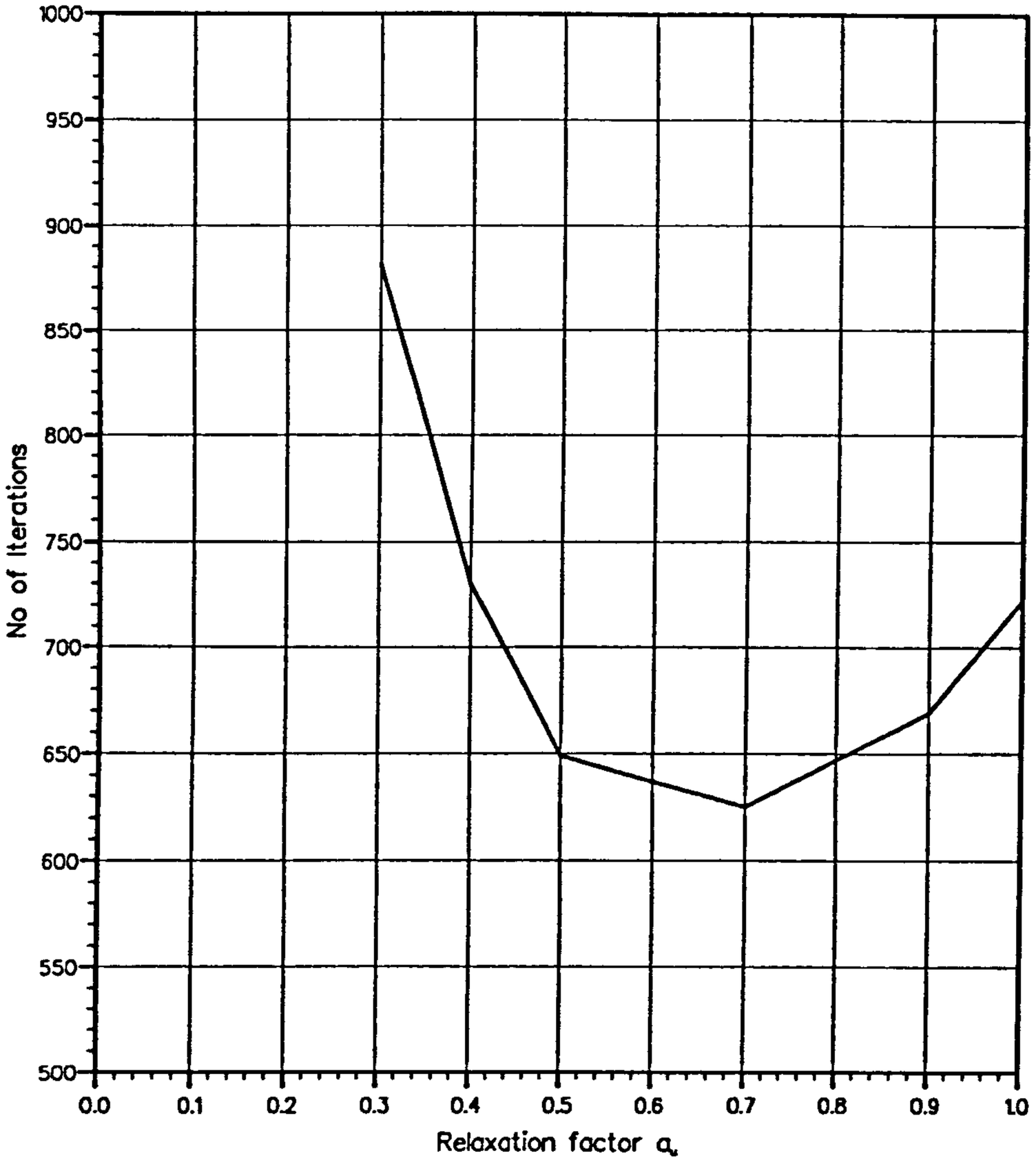

Figure 5.34 : Effect of under-relaxation factor α_u on number of iterations for convergence.
Convergence criterion : ϵ_c=0.0001, α_p=0.25.

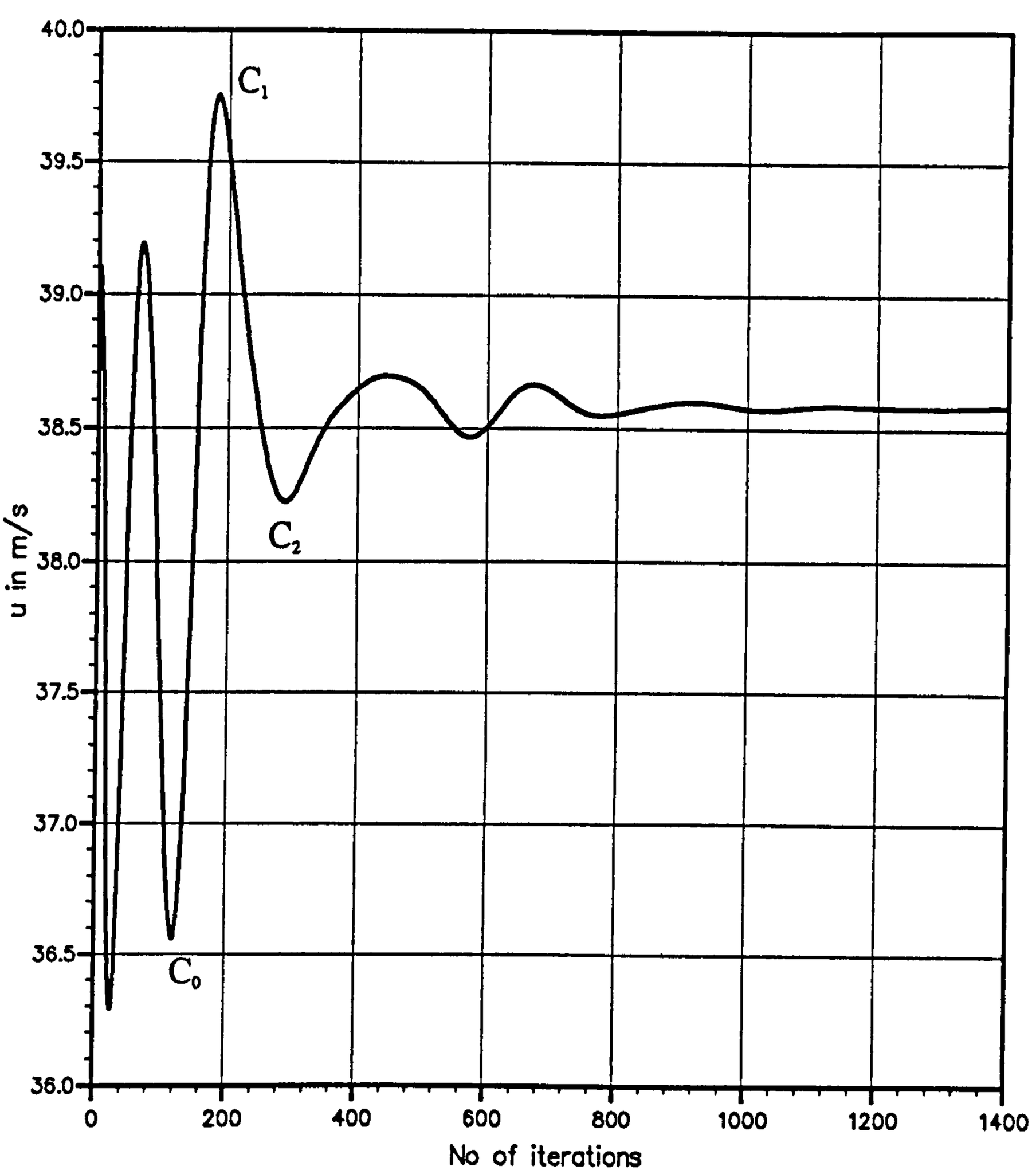

Figure 5.35 : Typical iterative path of velocity components at a certain grid location.

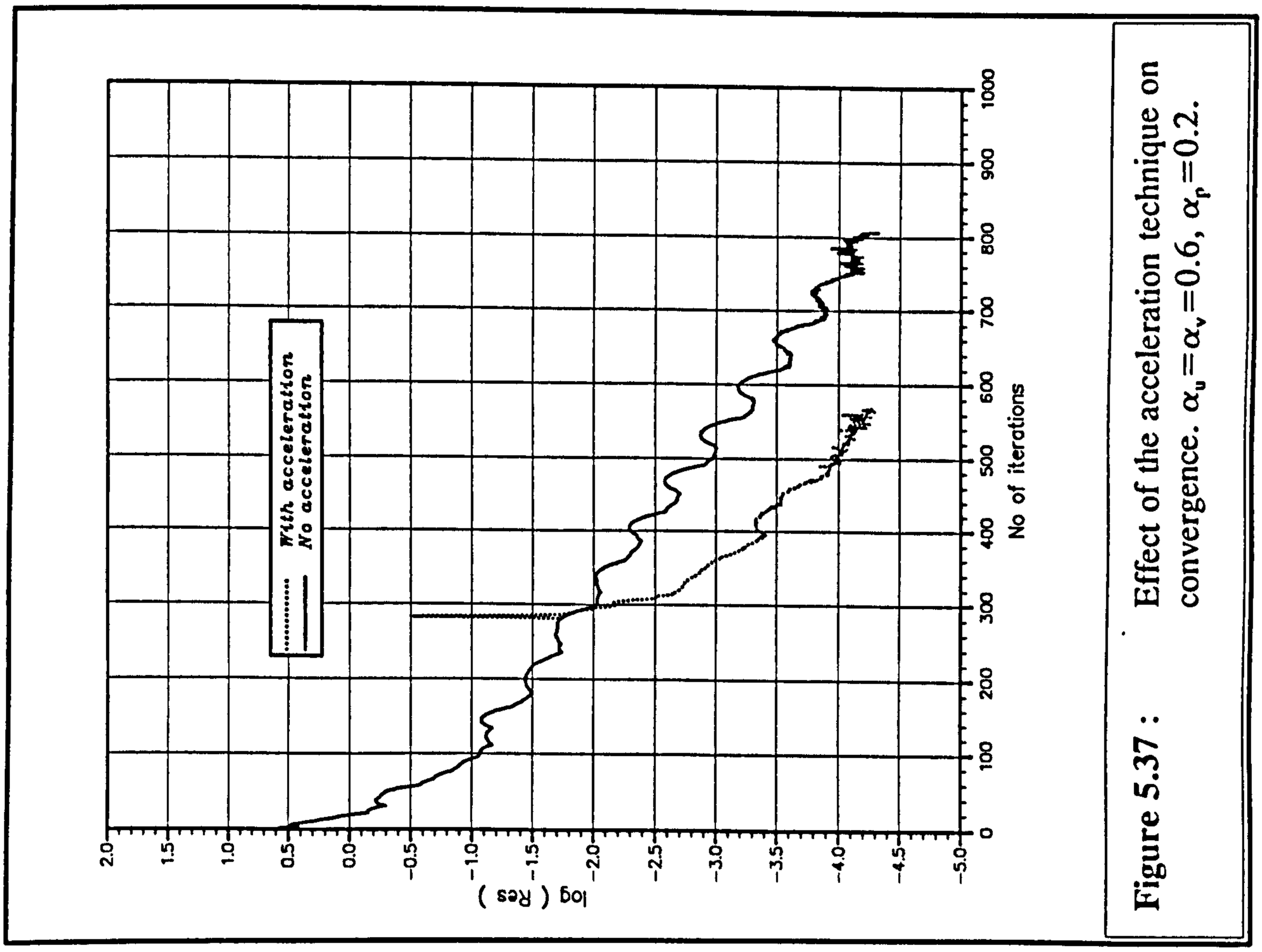

Figure 5.37 : Effect of the acceleration technique on convergence. $\alpha_u = \alpha_v = 0.6$, $\alpha_p = 0.2$.

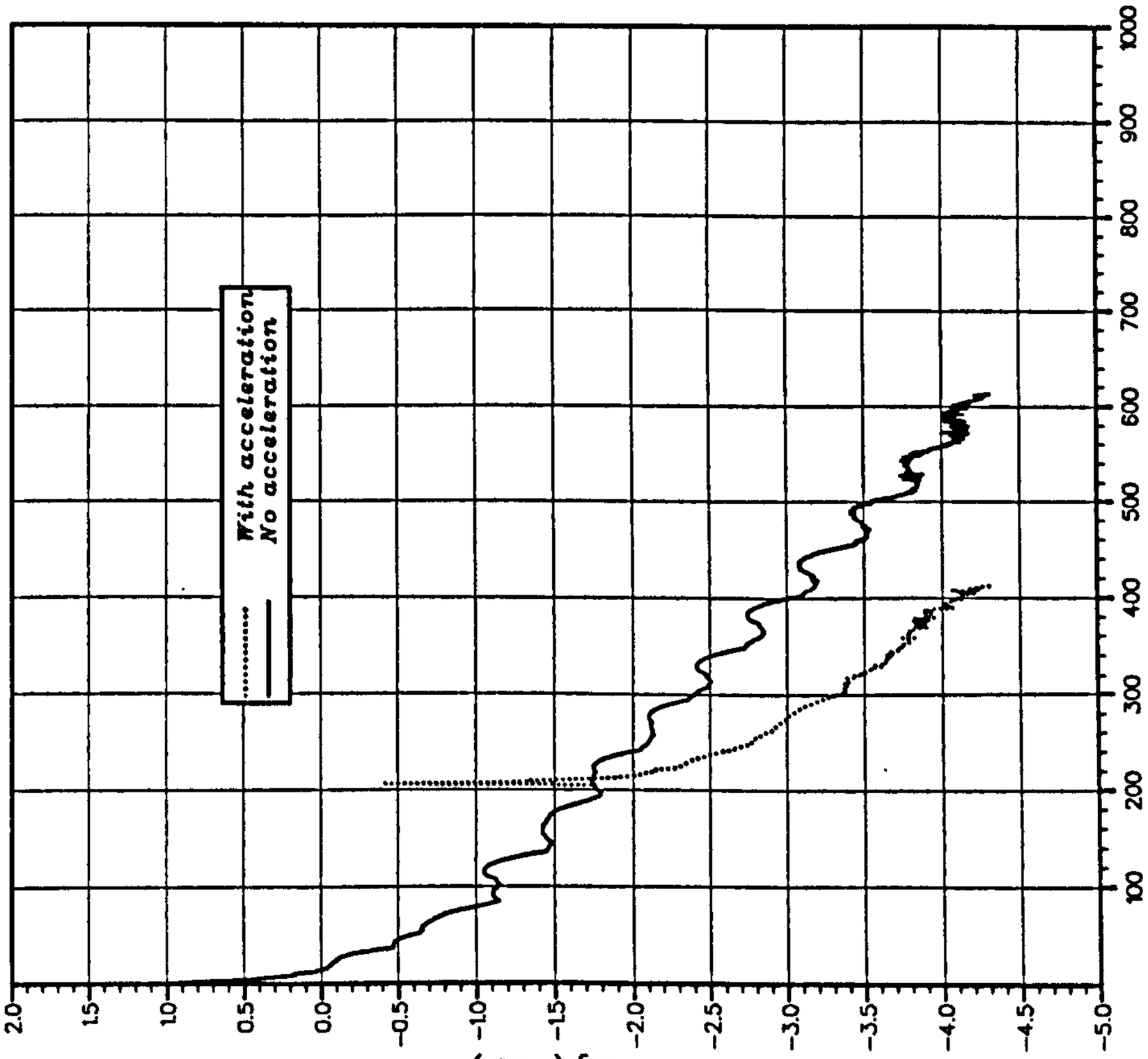

Figure 5.36 : Effect of the acceleration technique on convergence. $\alpha_u = \alpha_v = 0.8$, $\alpha_p = 0.3$.

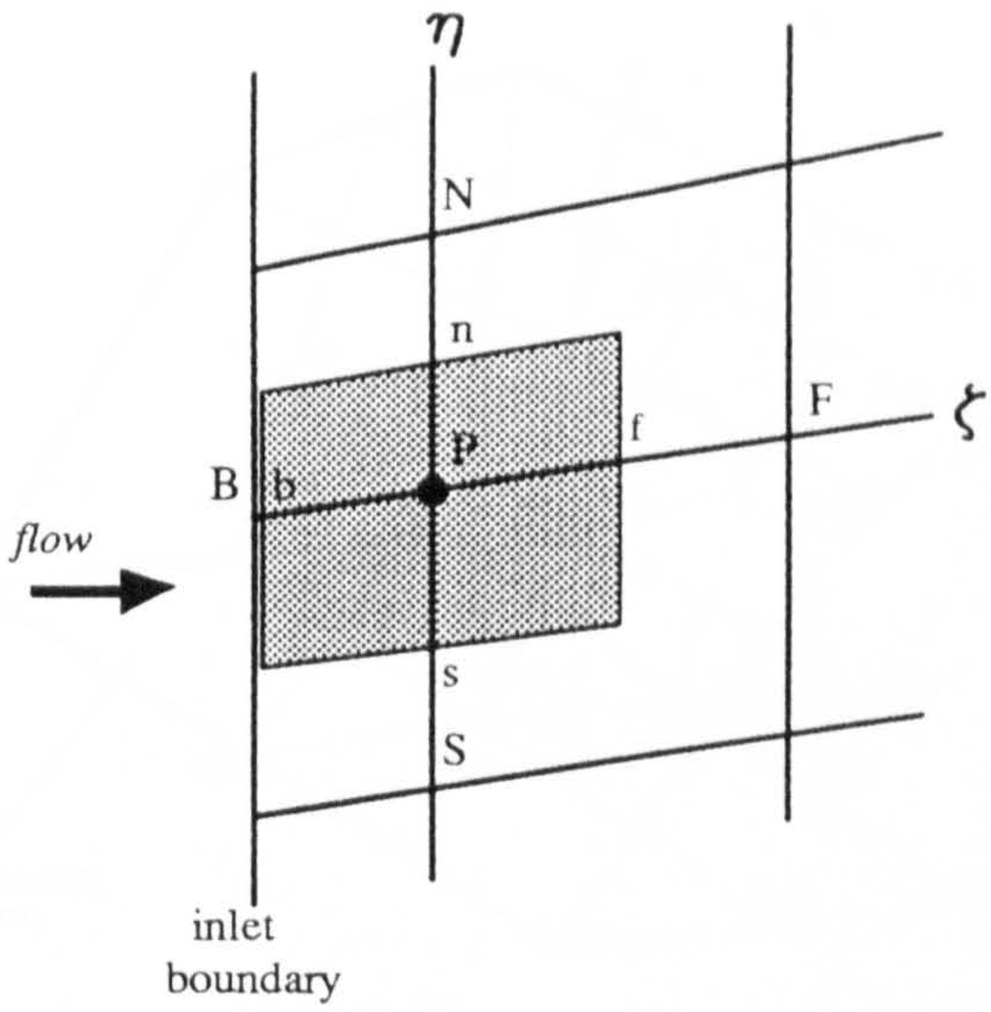

Figure 6.1 : Control volume next to an inlet boundary.

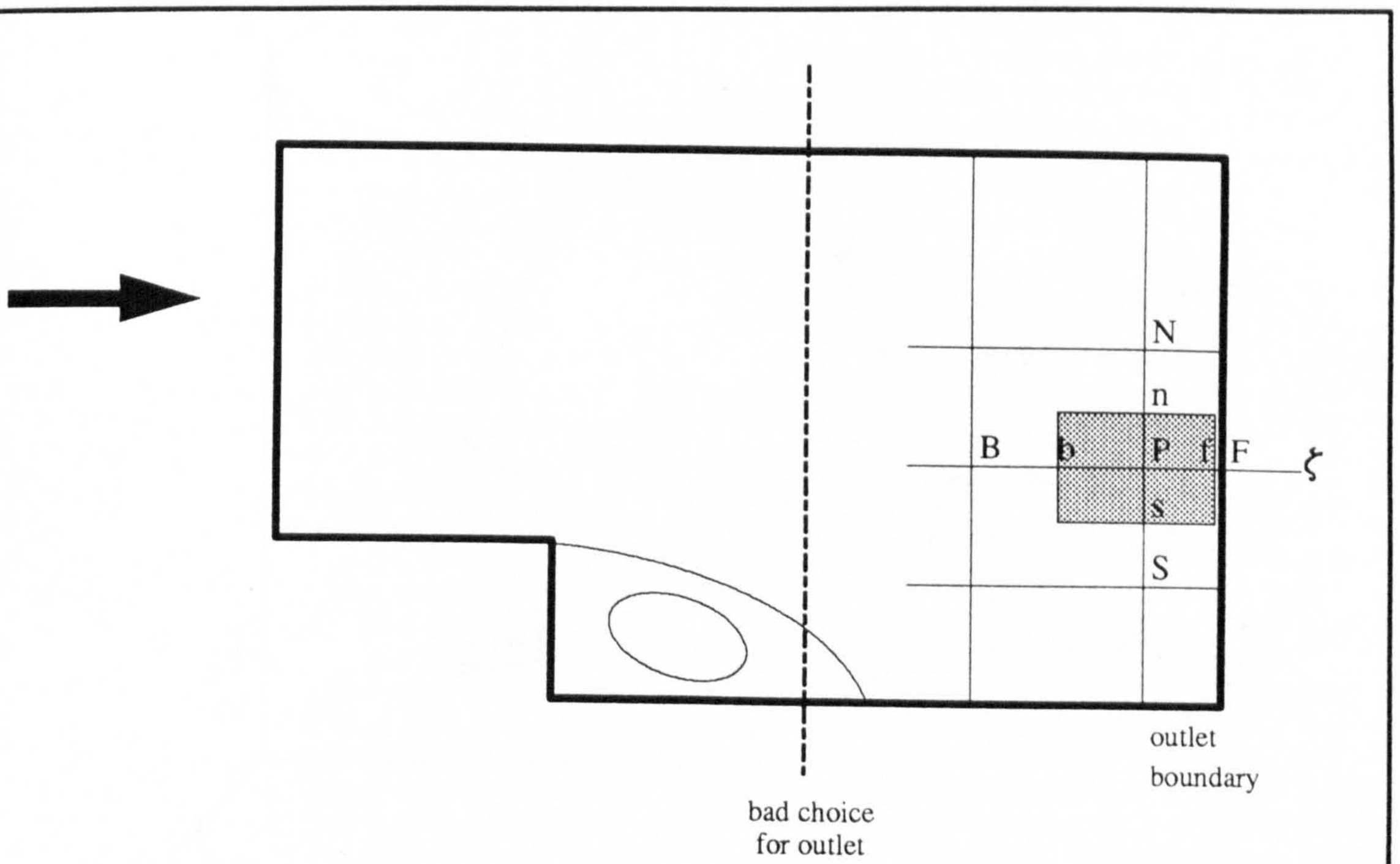

Figure 6.2 : Control volume next to an outlet boundary.

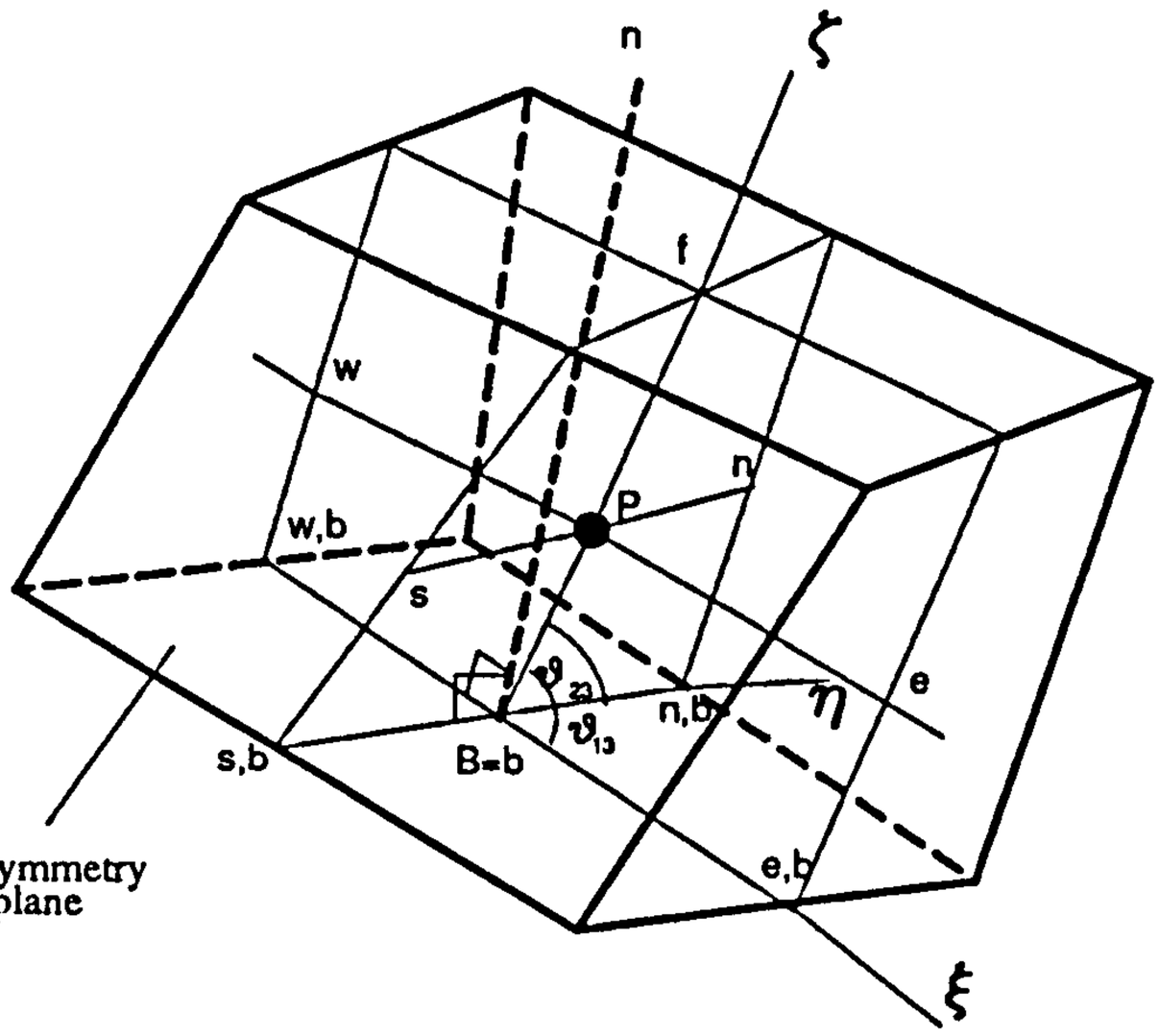

Figure 6.3 : Control volume next to a symmetric boundary.

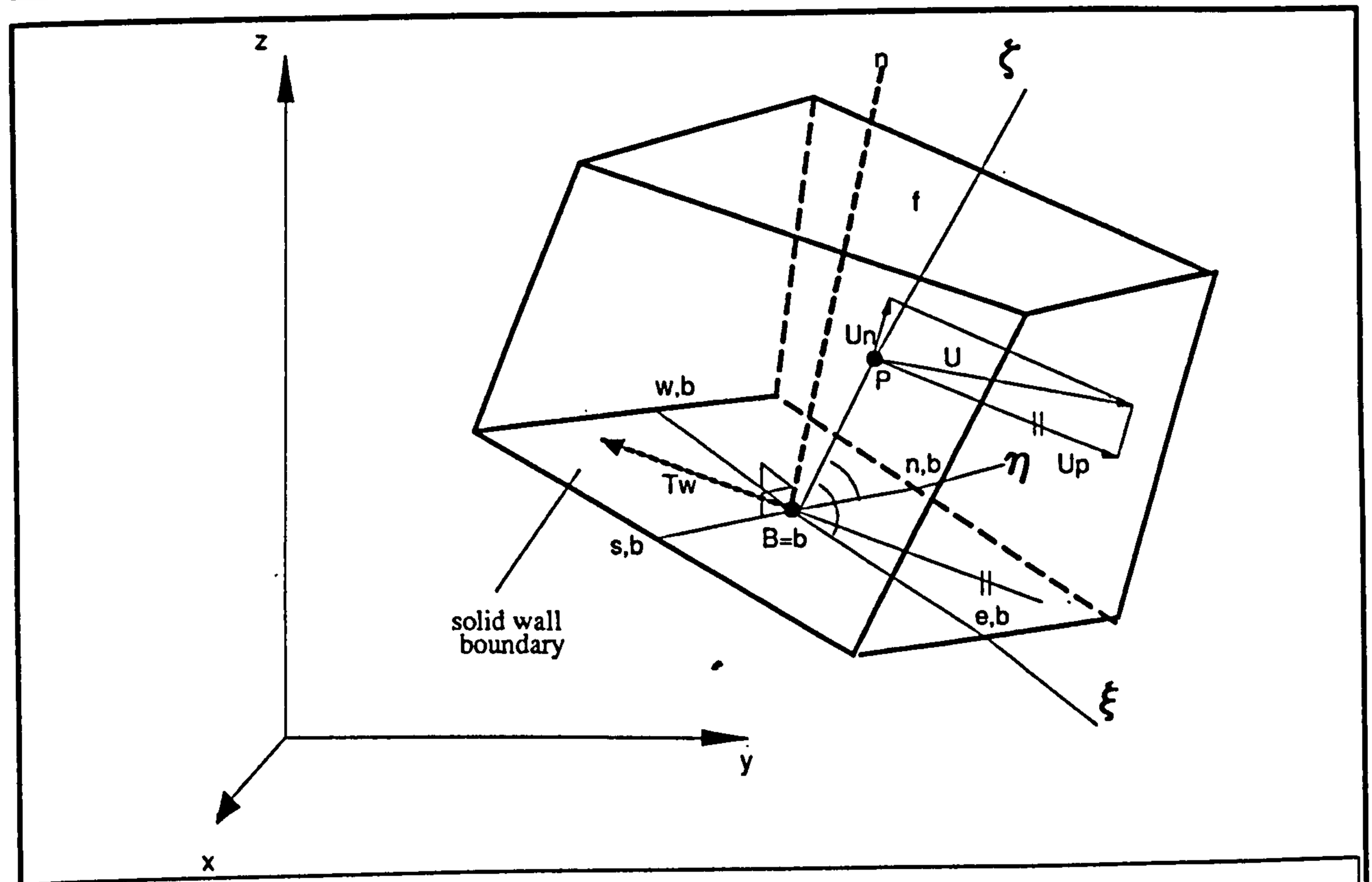

Figure 6.4 : Control volume next to a wall boundary.

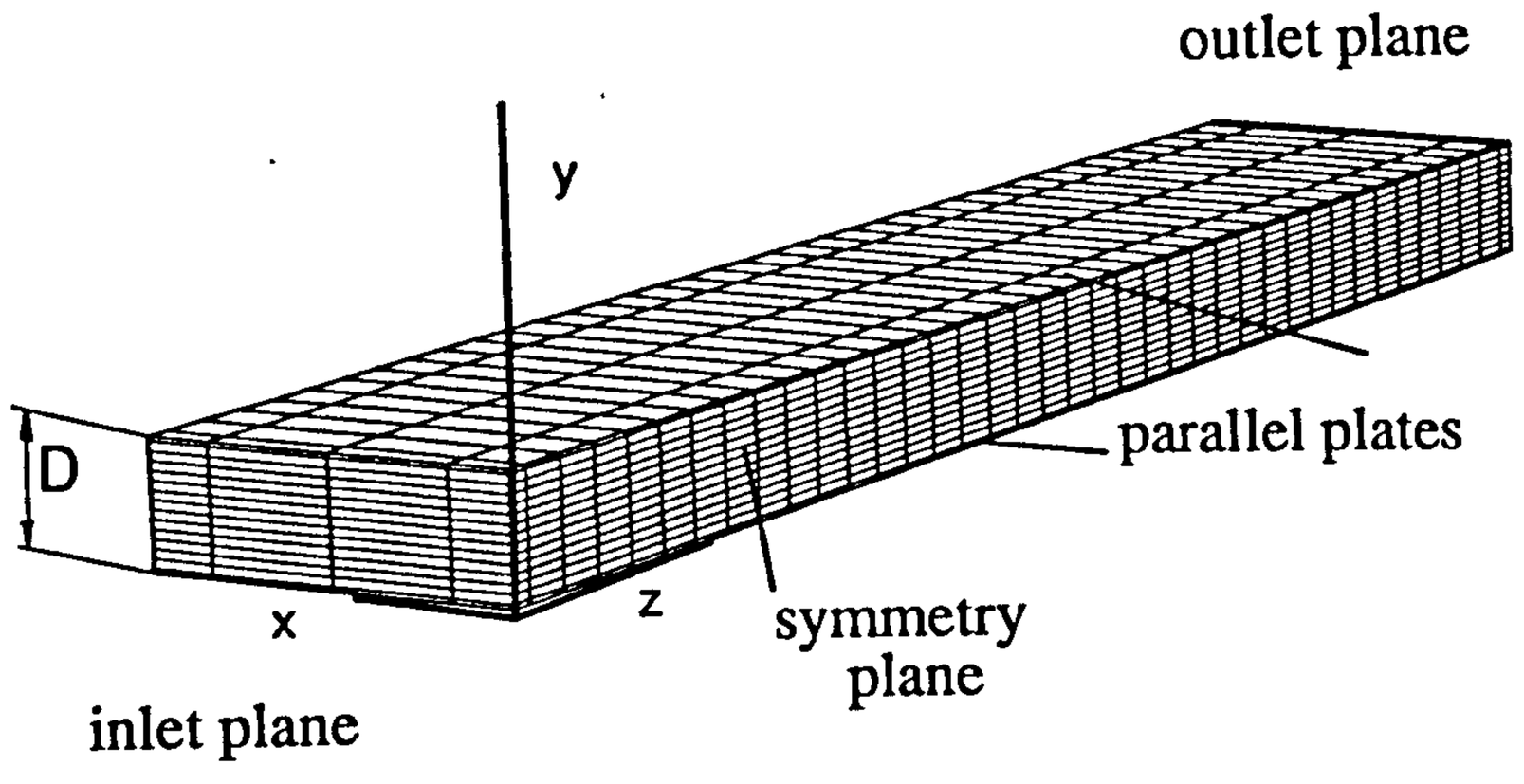

Figure 6.5 : Flow between two parallel plates.
Geometry and computational grid.

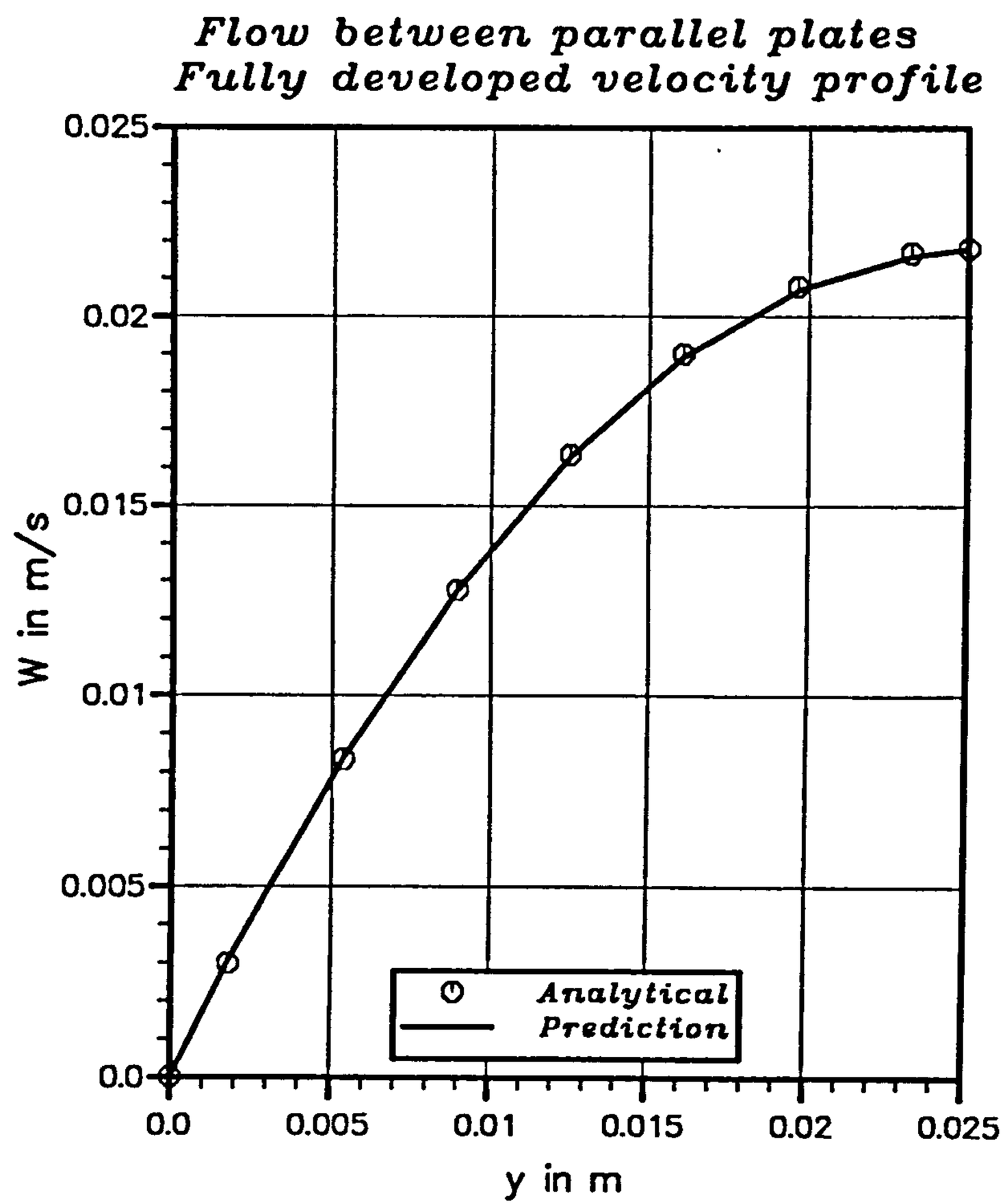

Figure 6.6 : Flow between parallel plates.
Fully developed laminar velocity profile.

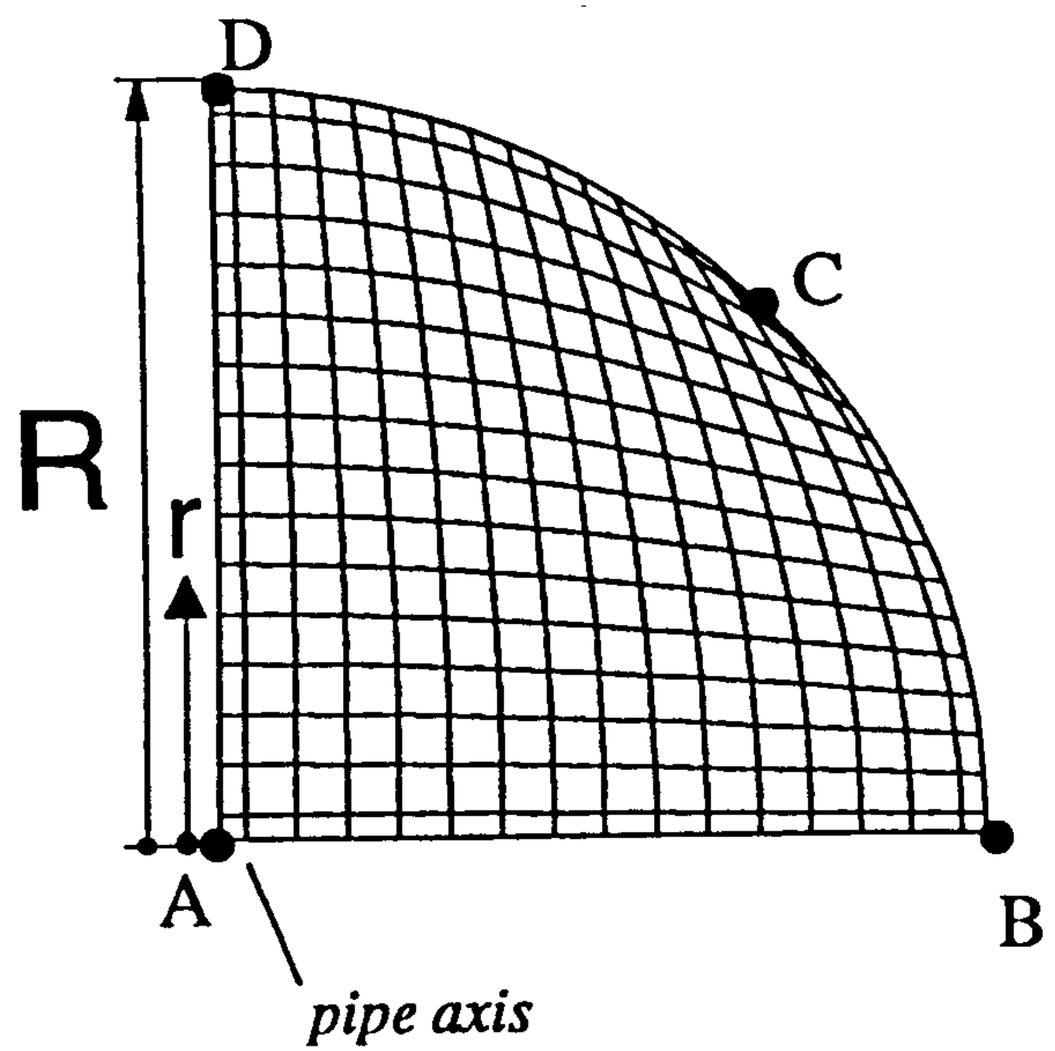

Figure 6.7: Laminar flow in a pipe. Computational grid on a cross-section of the pipe.

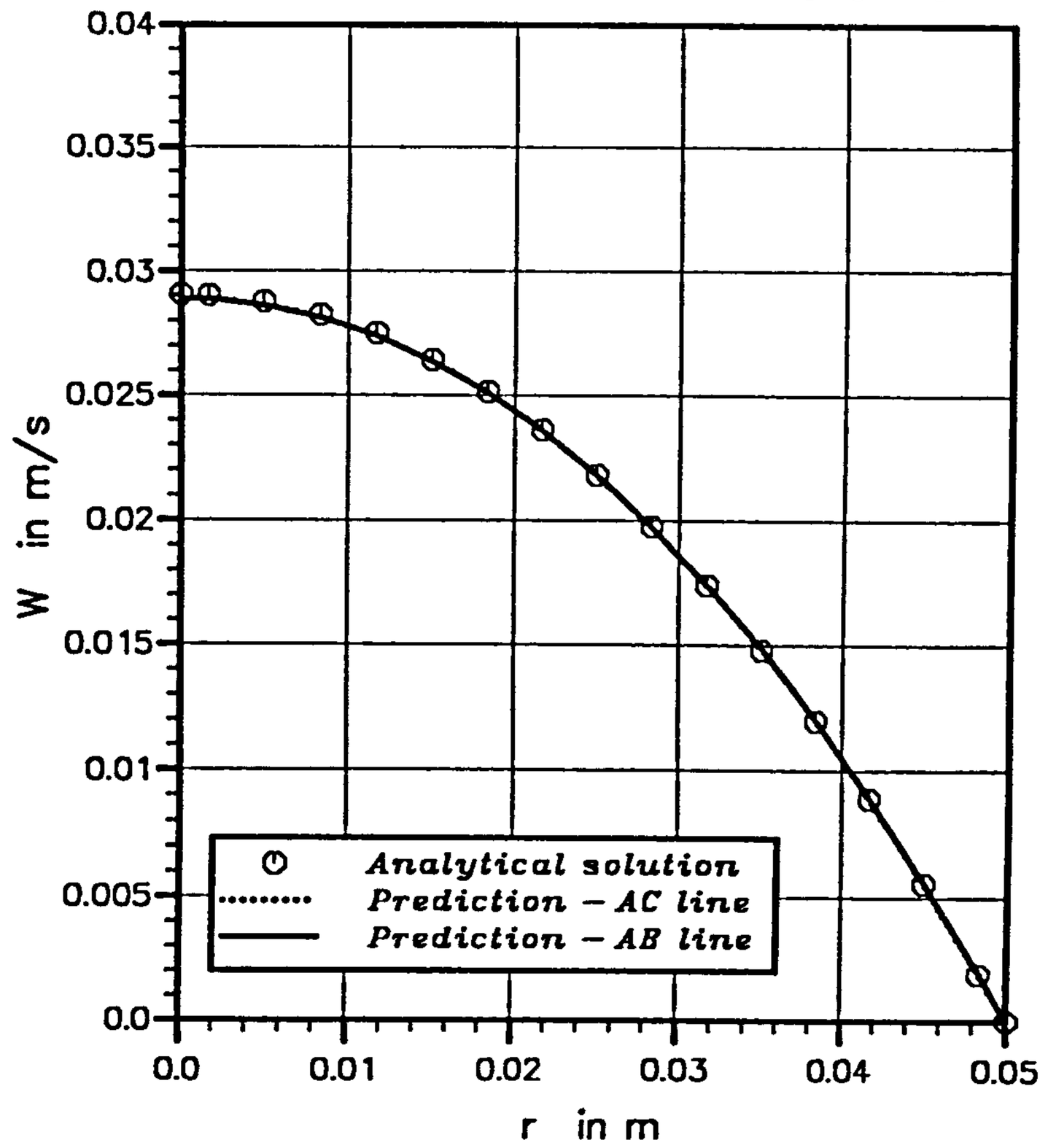

Figure 6.8 : Laminar flow in a pipe. Fully developed laminar velocity profile.

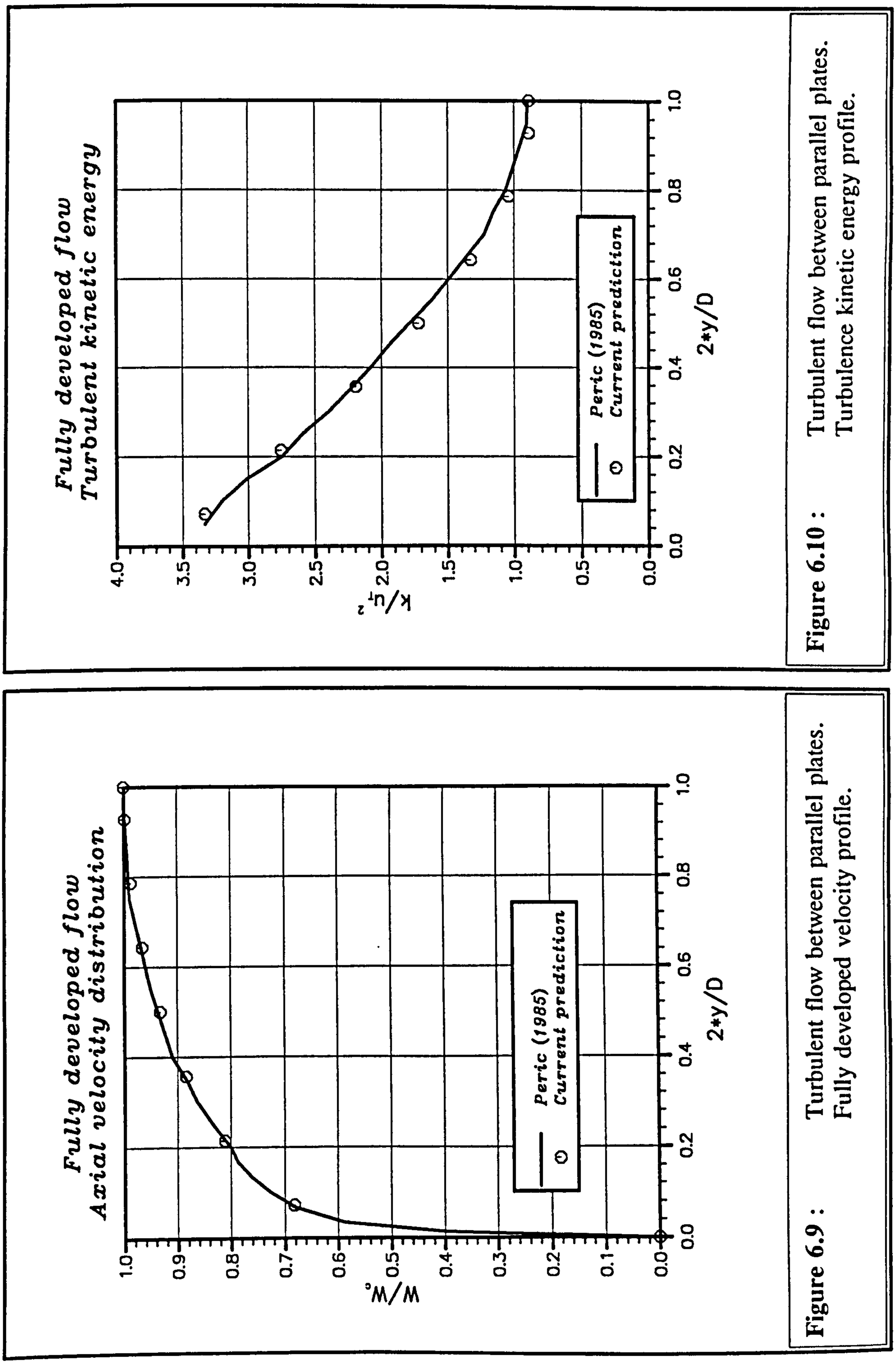

Figure 6.10 : Turbulent flow between parallel plates. Turbulence kinetic energy profile.

Figure 6.9 : Turbulent flow between parallel plates. Fully developed velocity profile.

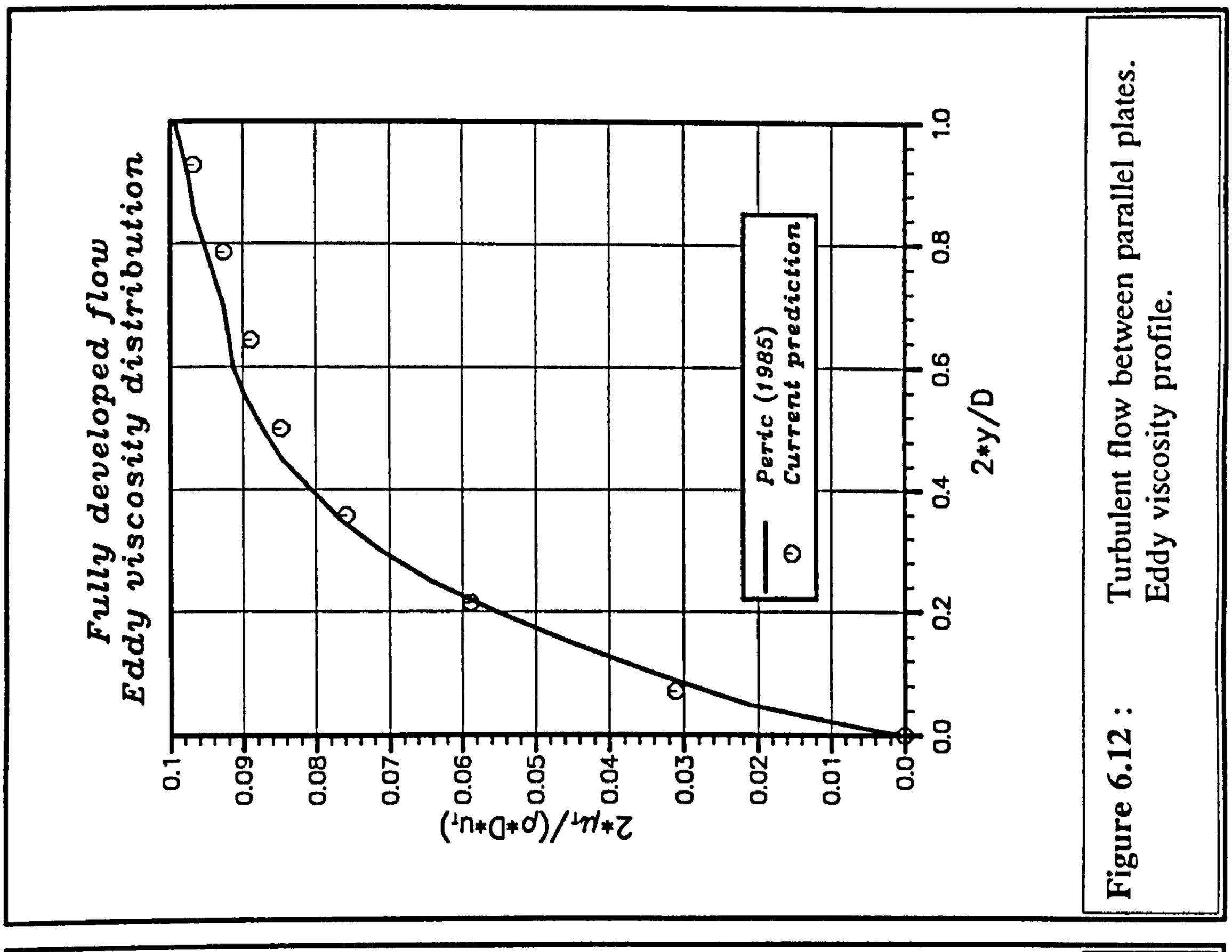

Figure 6.12 : Turbulent flow between parallel plates. Eddy viscosity profile.

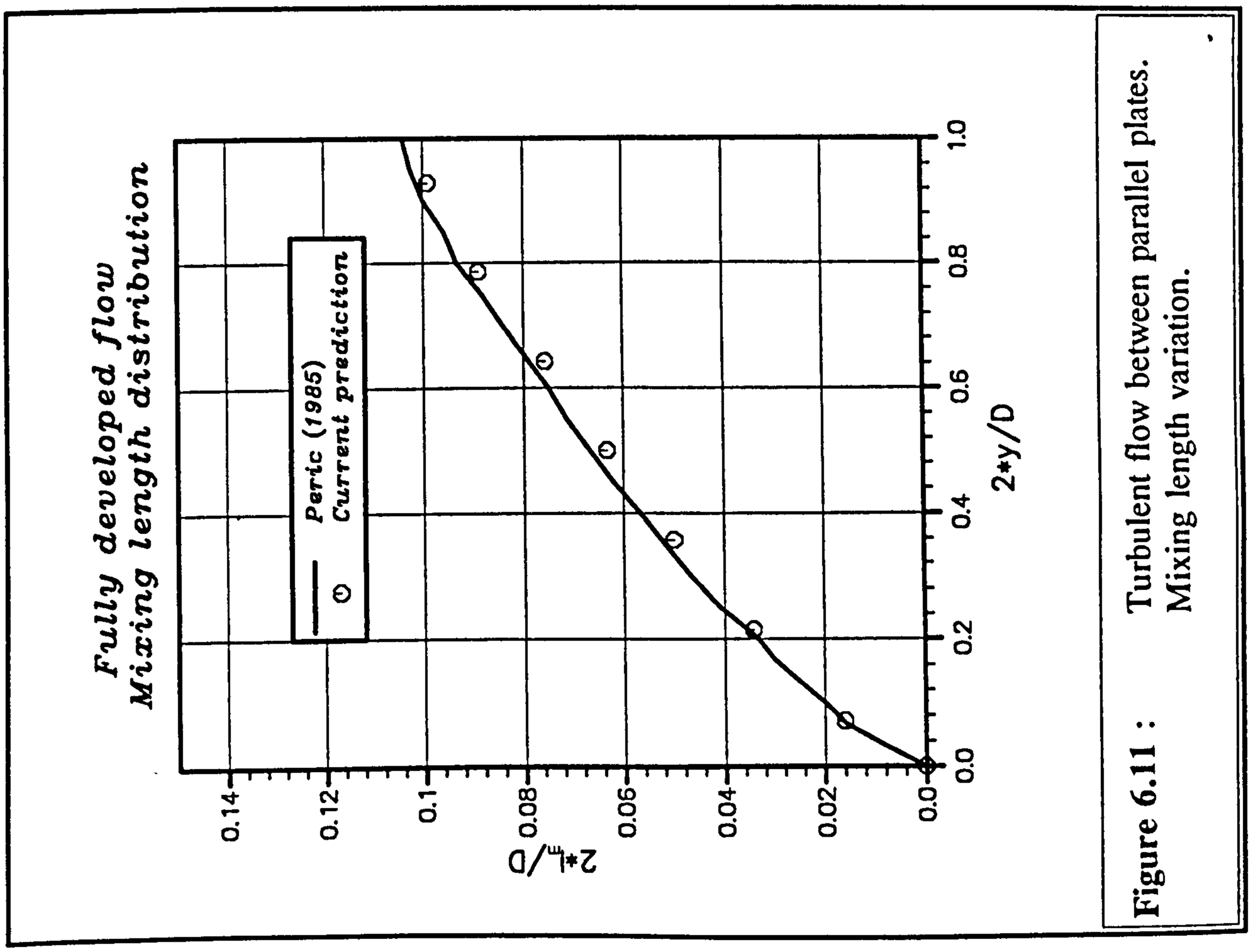

Figure 6.11 : Turbulent flow between parallel plates. Mixing length variation.

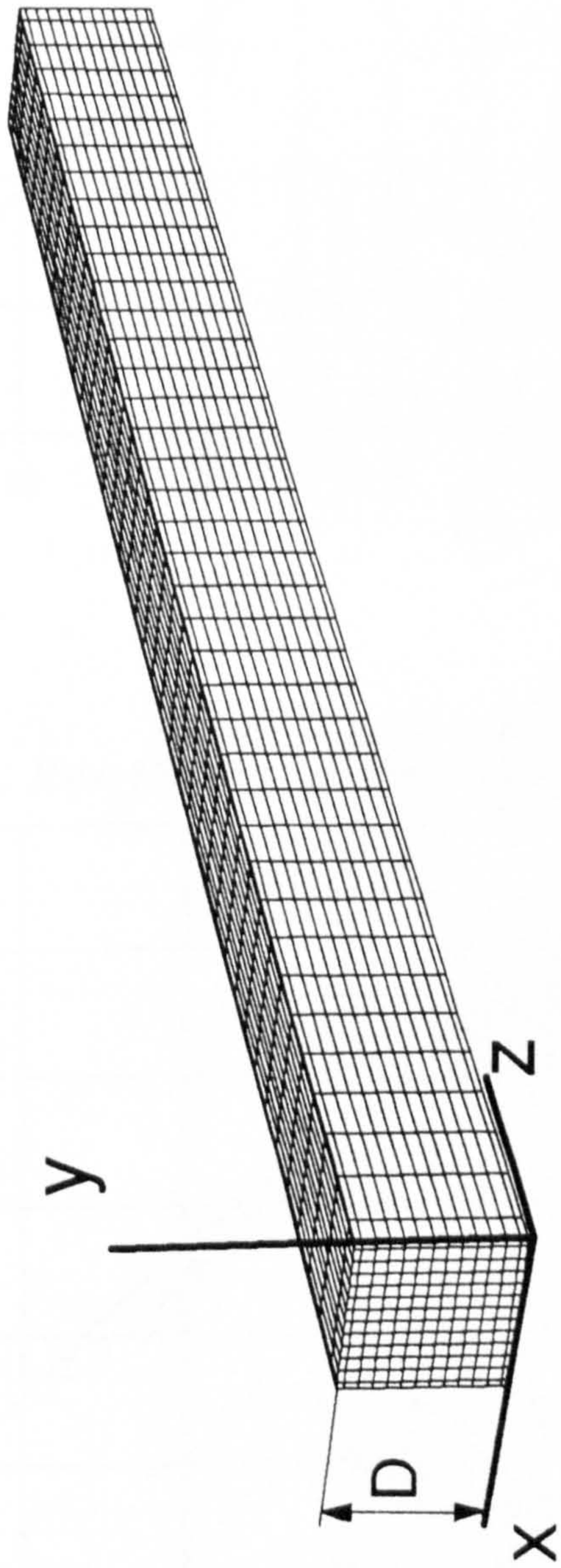

Flow in a square duct
Outline of the Grid

Figure 6.13 : Flow in a square duct.
Geometry and computational grid.

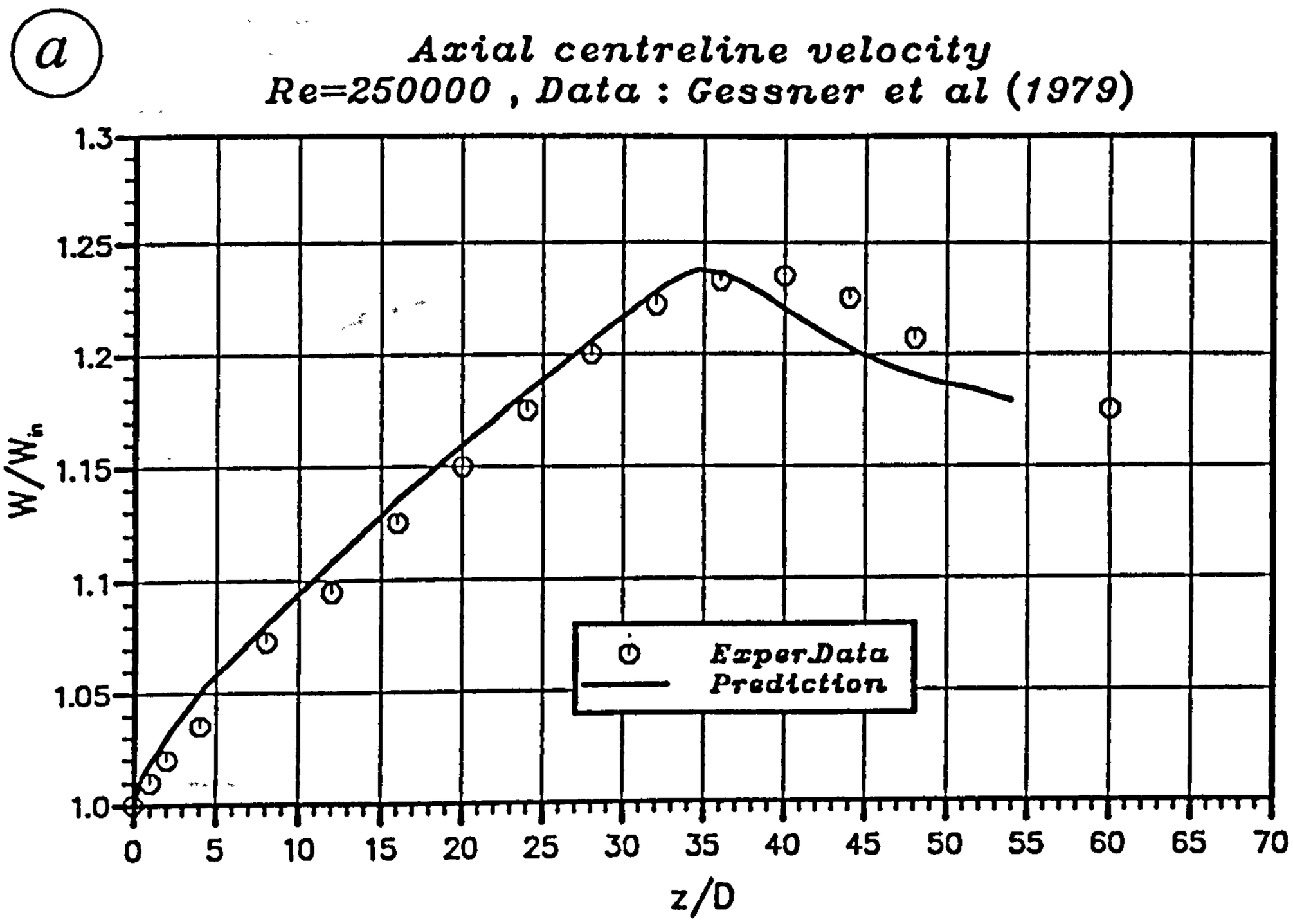

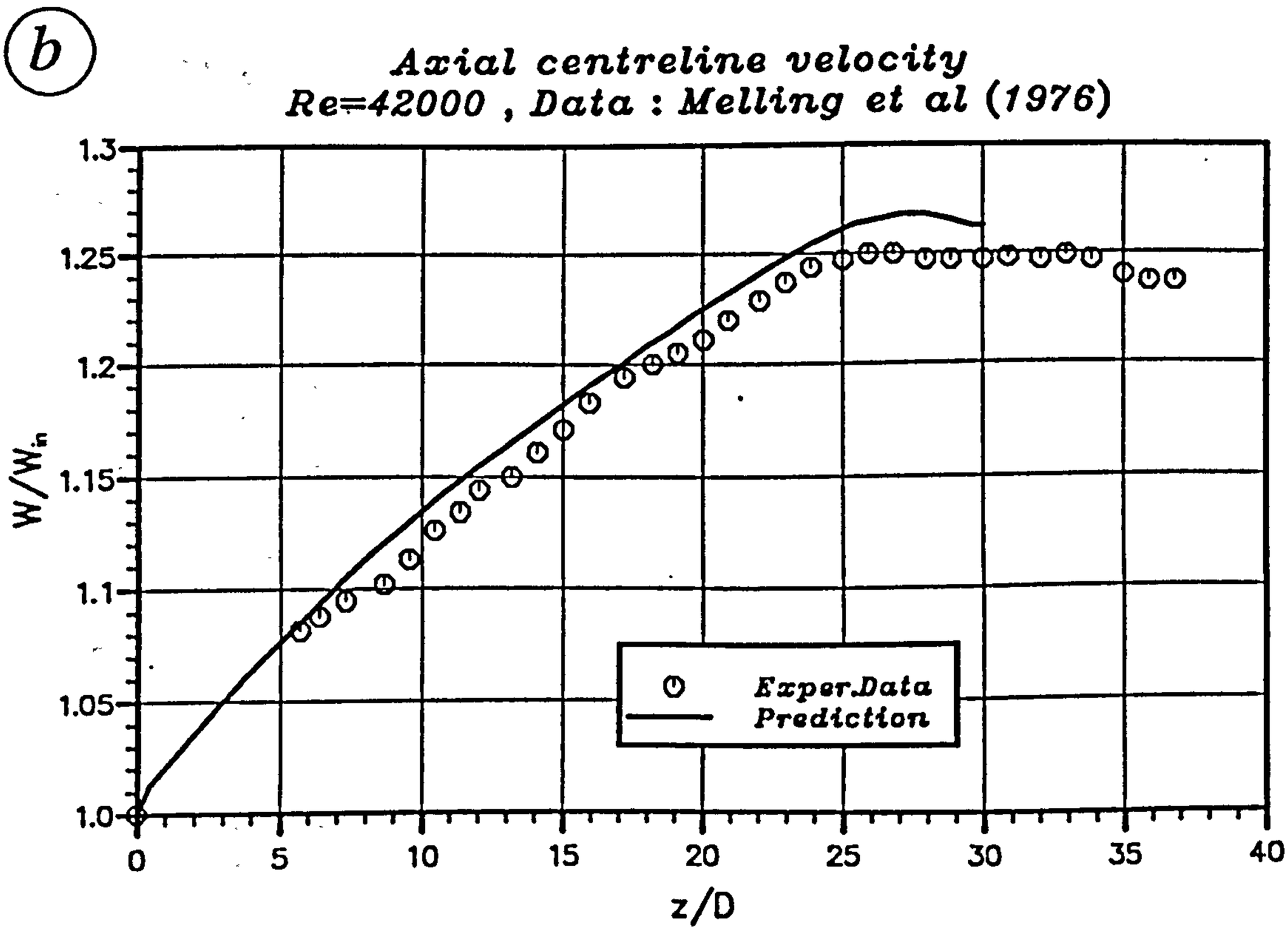

Figure 6.14 : Flow in a square duct. Axial centreline velocity at:
(a) Re = 250000, (b) Re = 42000.

(a) *Streamwise velocity distribution at Z/D=8*
Re = 250000 , Data : Gessner et al (1979)

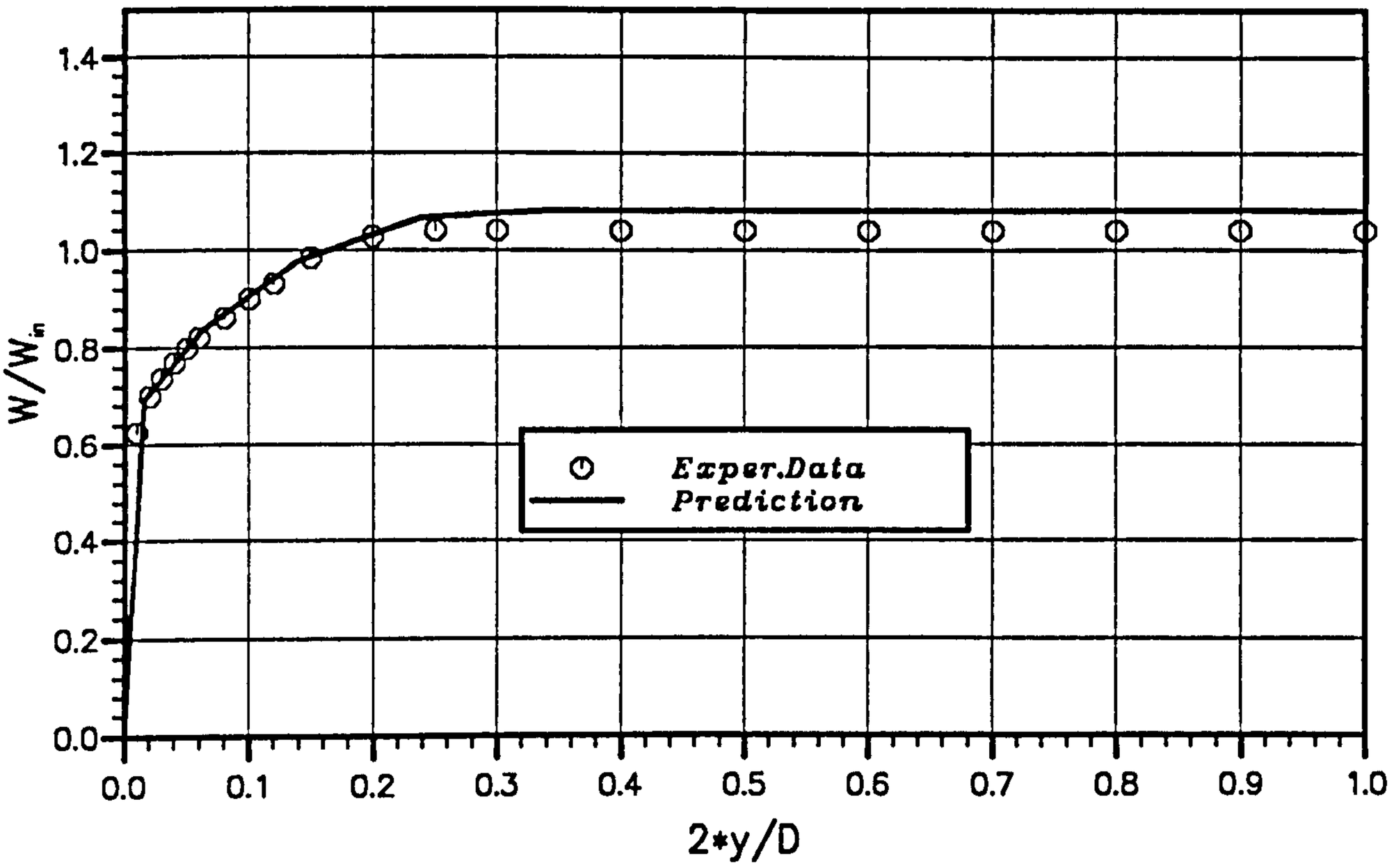

(b) *Streamwise velocity distribution at Z/D=16*
Re = 250000 , Data : Gessner et al (1979)

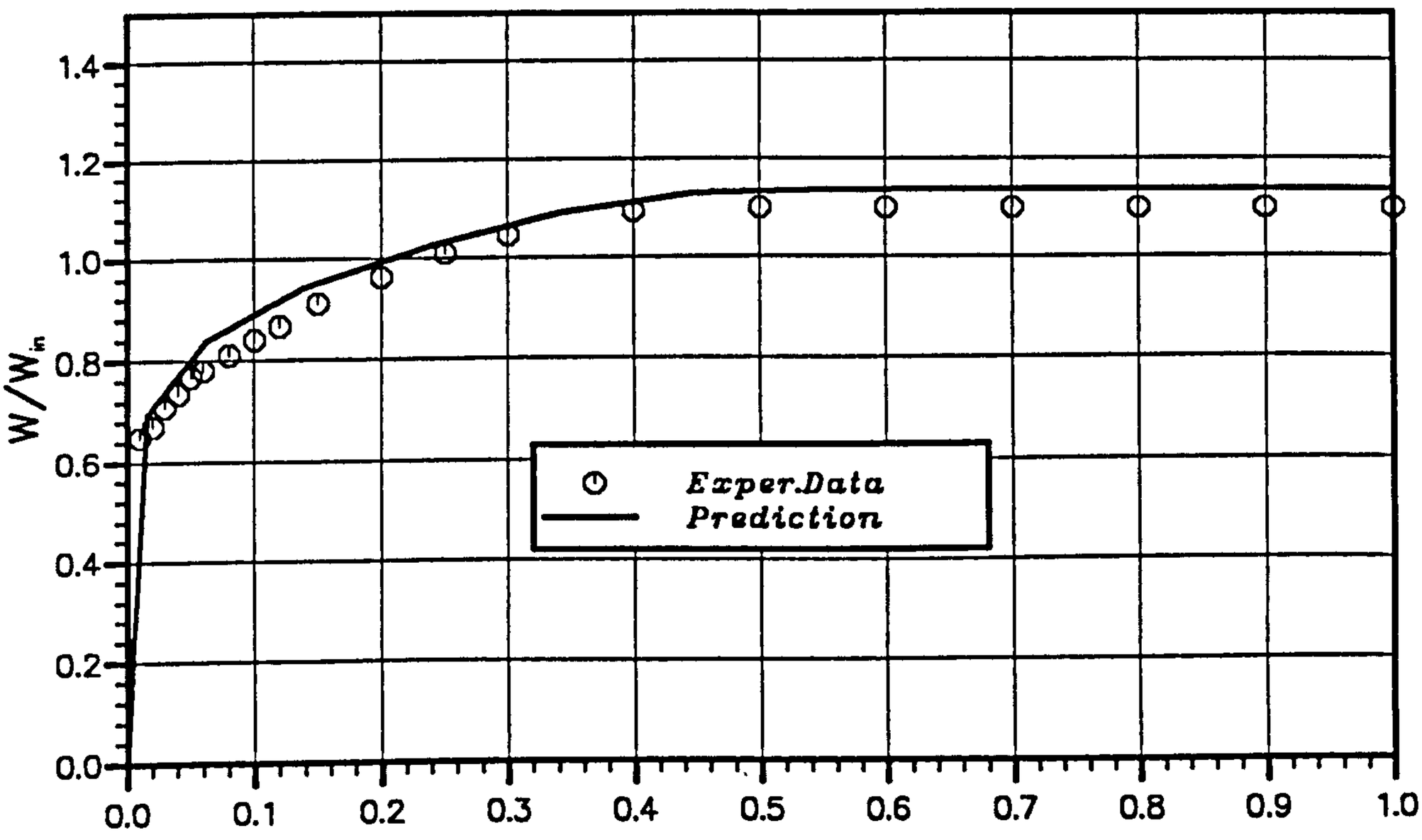

Figure 6.15 : Flow in a square duct. Steamwise velocity distribution at: (a) Z/D = 8, (b) Z/D = 16.

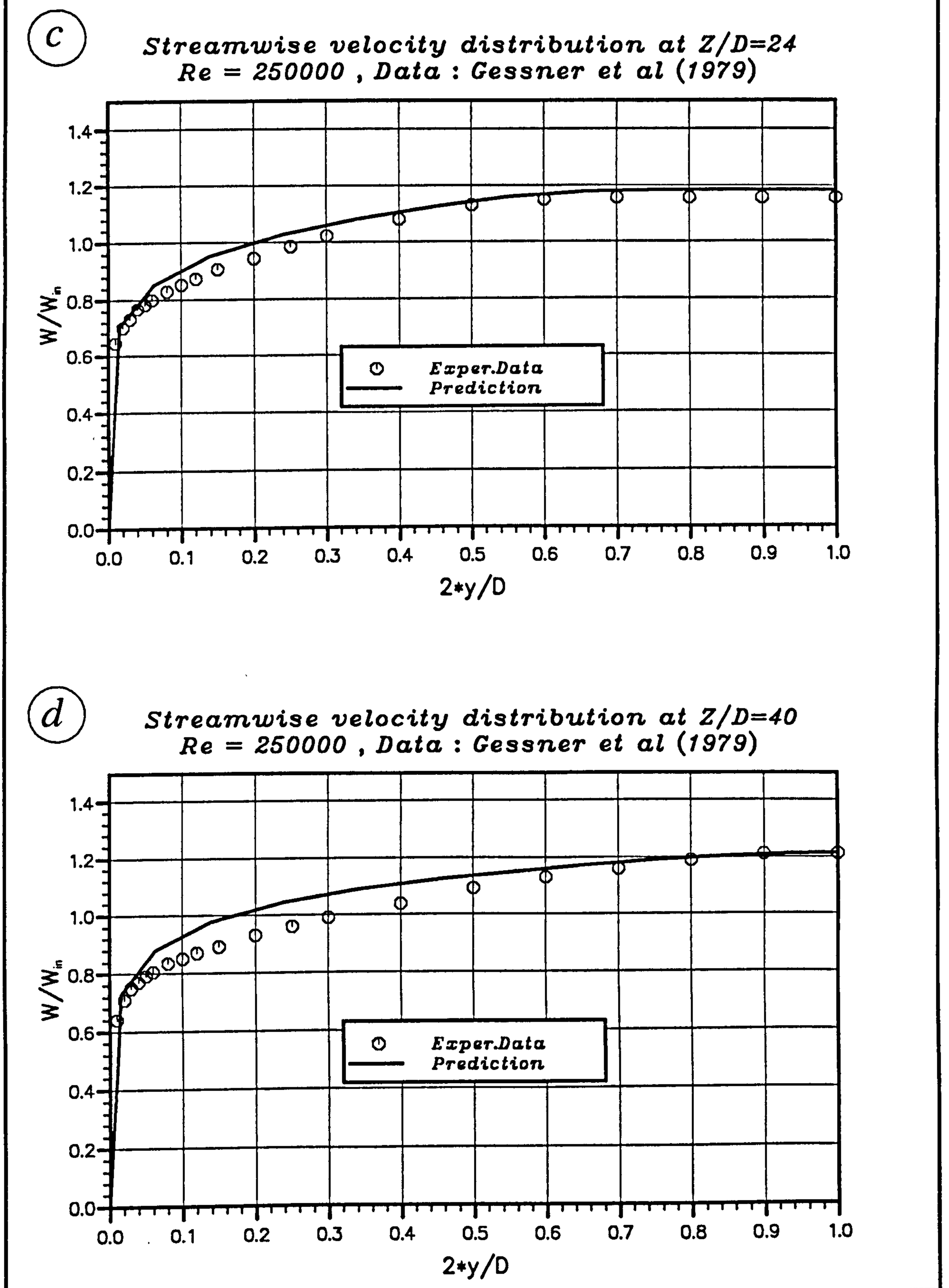

Figure 6.15 : Flow in a square duct. Streamwise velocity distribution at: (c) Z/D = 24, (d) Z/D = 40.

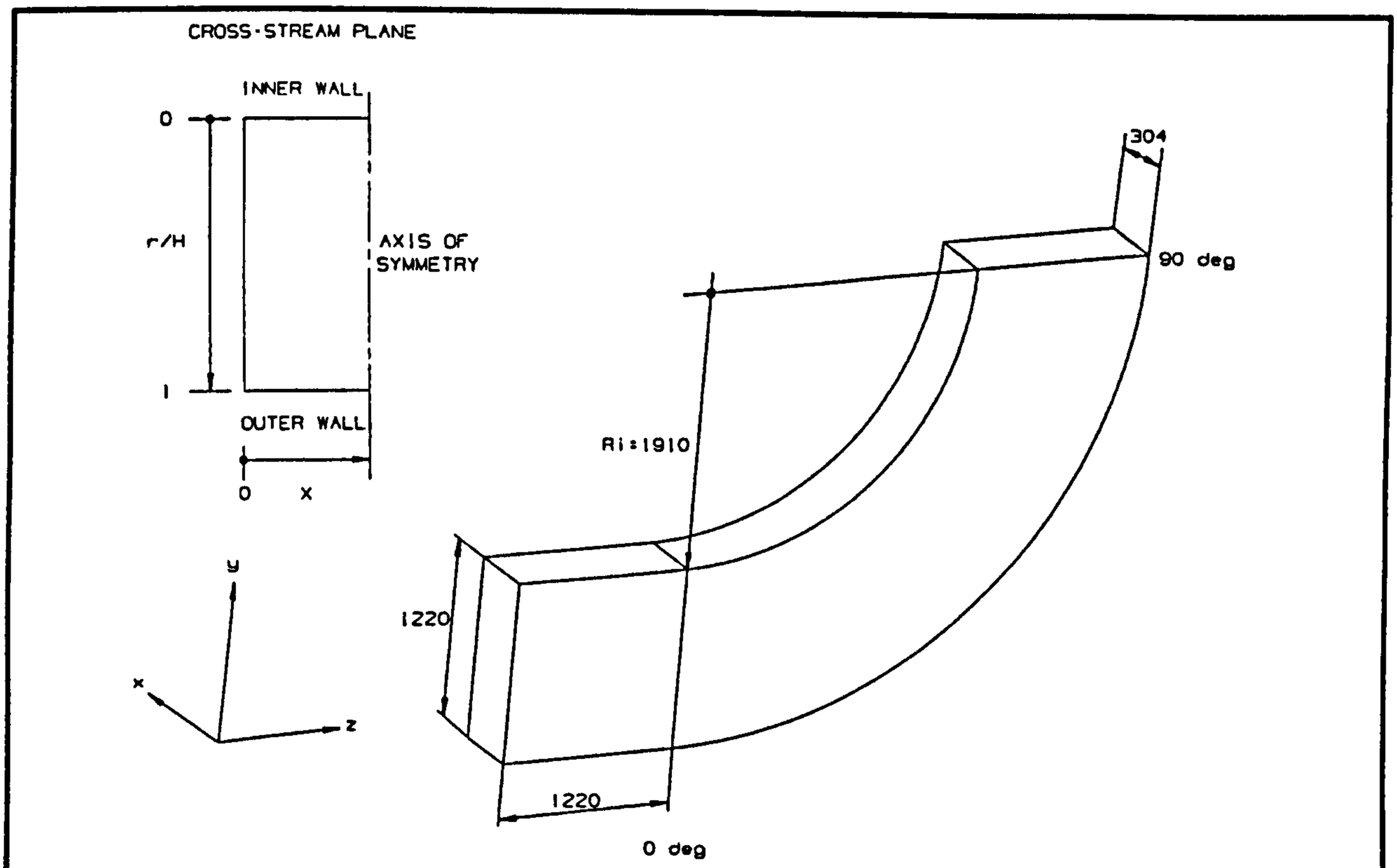

Figure 6.16 : Geometry of the 90° curved duct of rectangular cross-section.

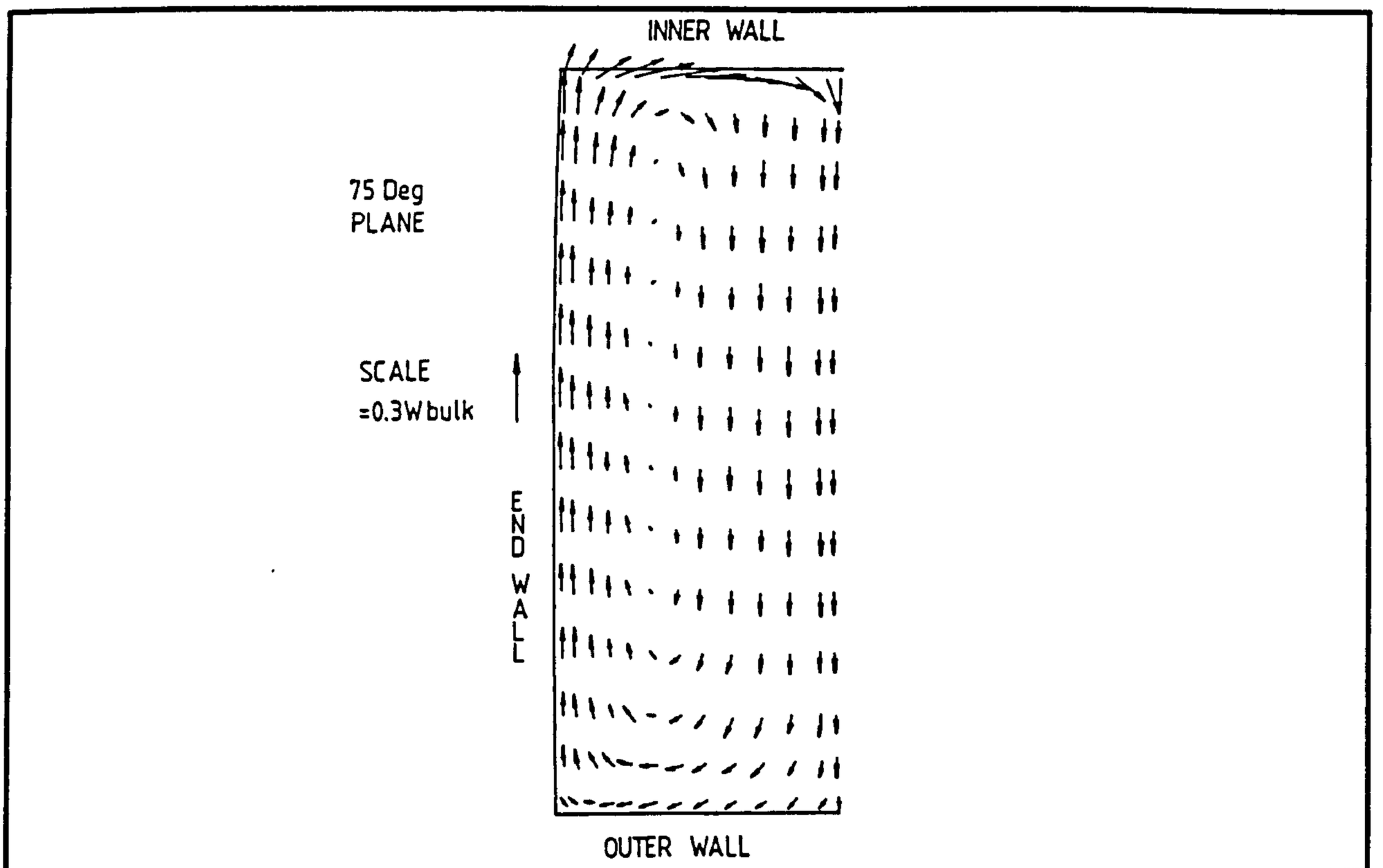

Figure 6.17 : Flow in a 90° curved duct.
Predicted secondary velocity pattern at the 75° plane.

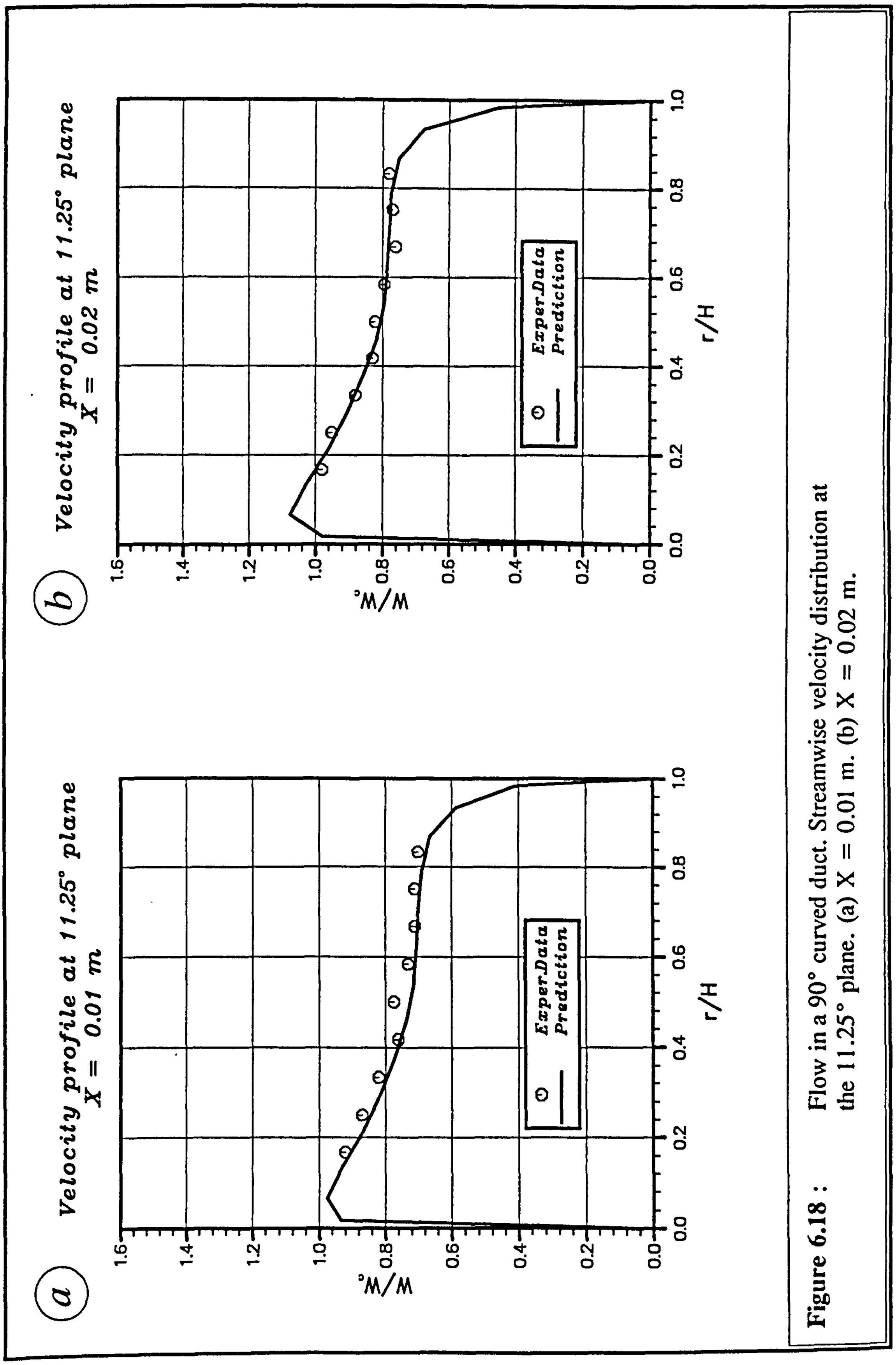

Figure 6.18 : Flow in a 90° curved duct. Streamwise velocity distribution at the 11.25° plane. (a) X = 0.01 m. (b) X = 0.02 m.

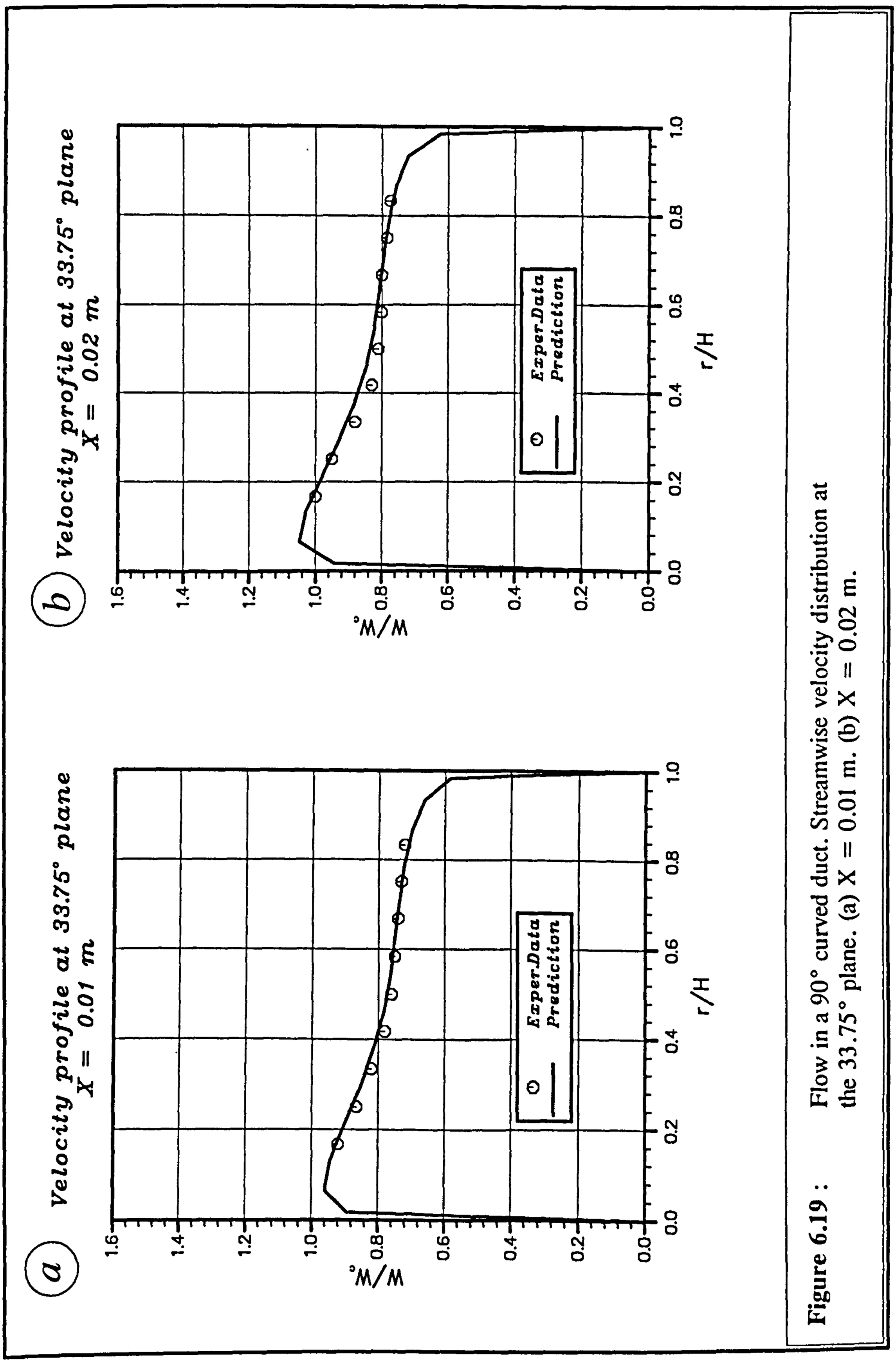

Figure 6.19 : Flow in a 90° curved duct. Streamwise velocity distribution at the 33.75° plane. (a) X = 0.01 m. (b) X = 0.02 m.

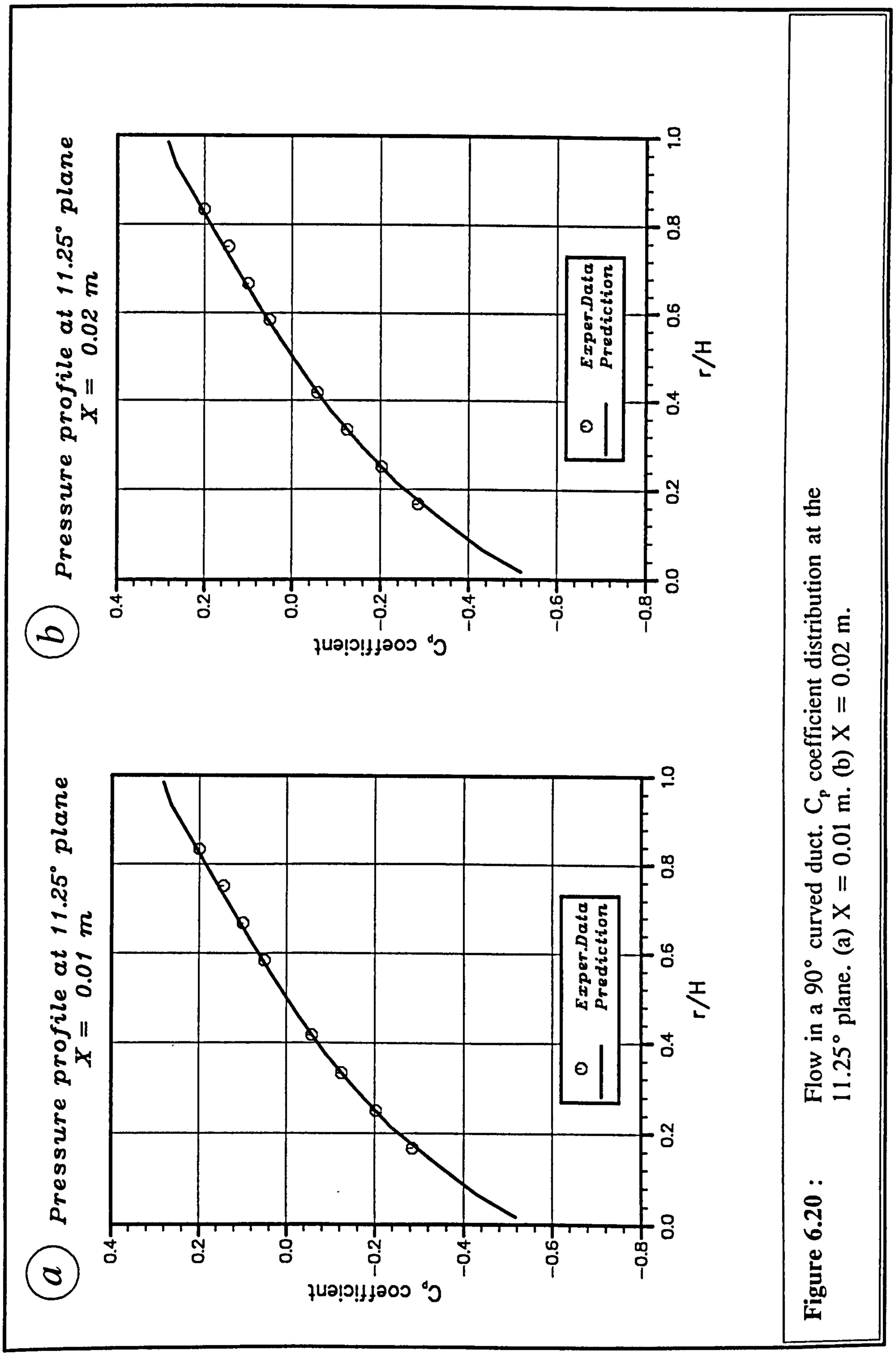

Figure 6.20 : Flow in a 90° curved duct. C_p coefficient distribution at the 11.25° plane. (a) X = 0.01 m. (b) X = 0.02 m.

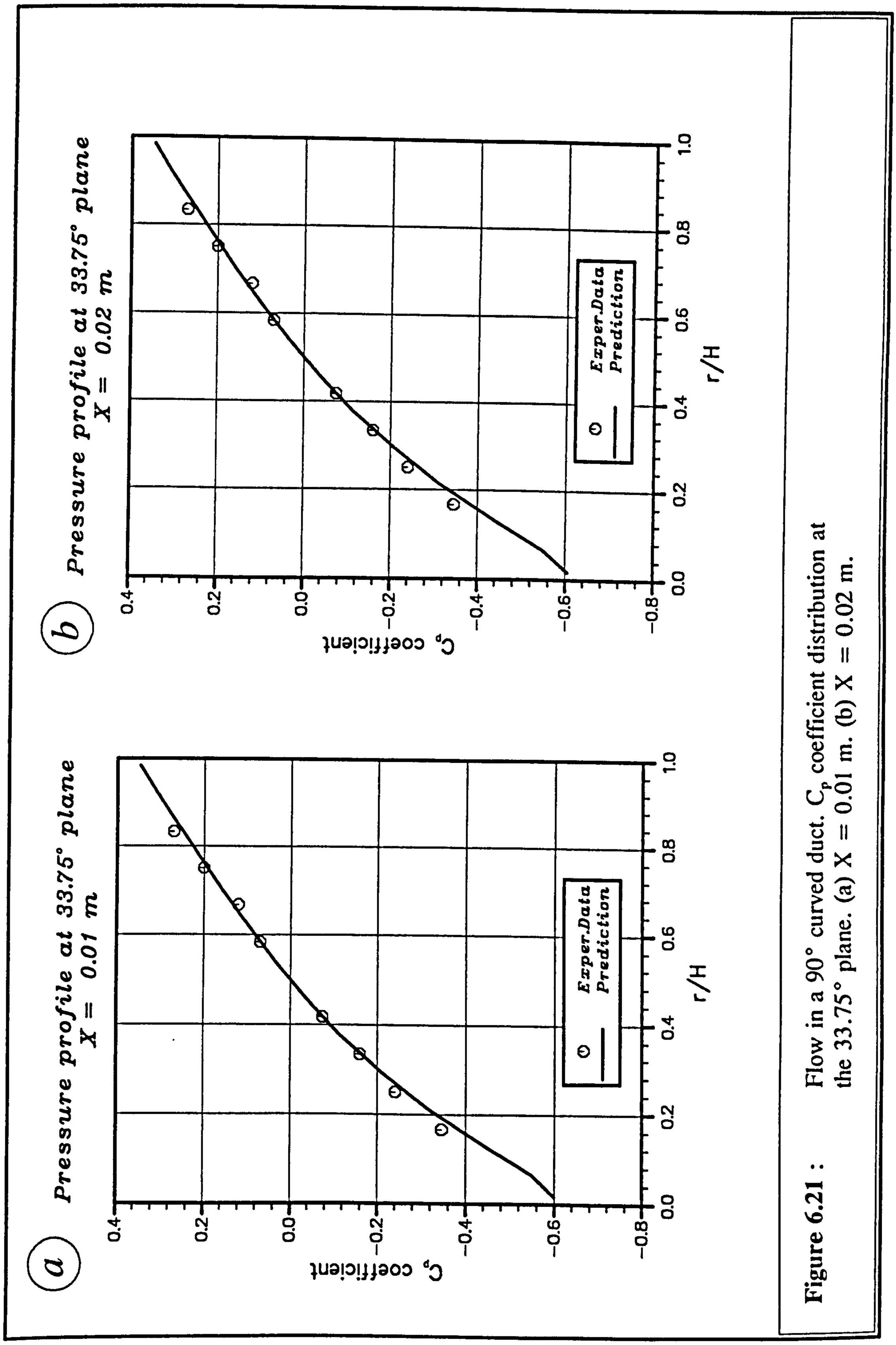

Flow in a 90° curved duct. C_p coefficient distribution at the 33.75° plane. (a) X = 0.01 m. (b) X = 0.02 m.

Figure 6.21 :

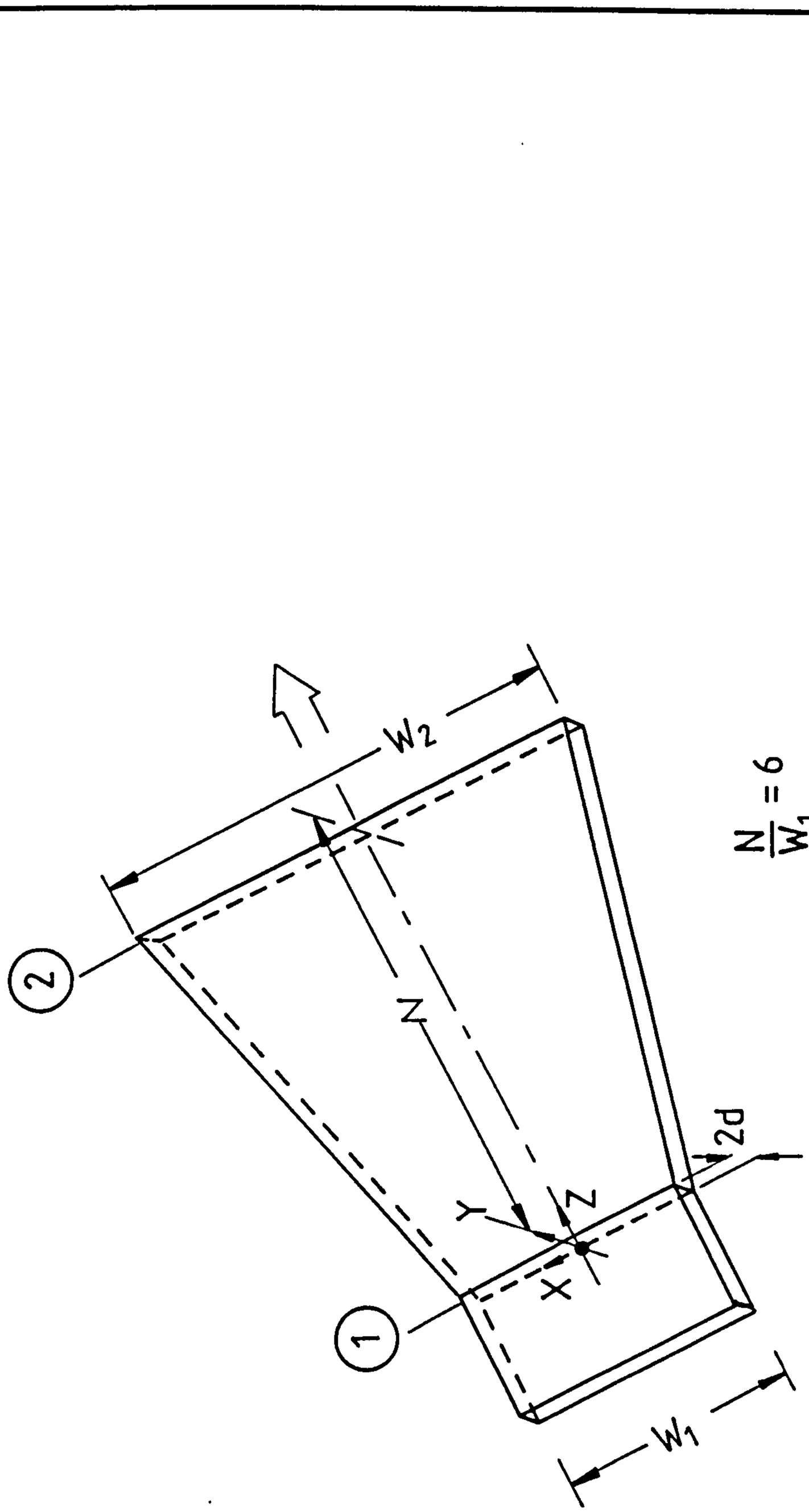

Figure 6.22 : Flow in a low-aspect-ratio diffuser. Outline of the geometry.

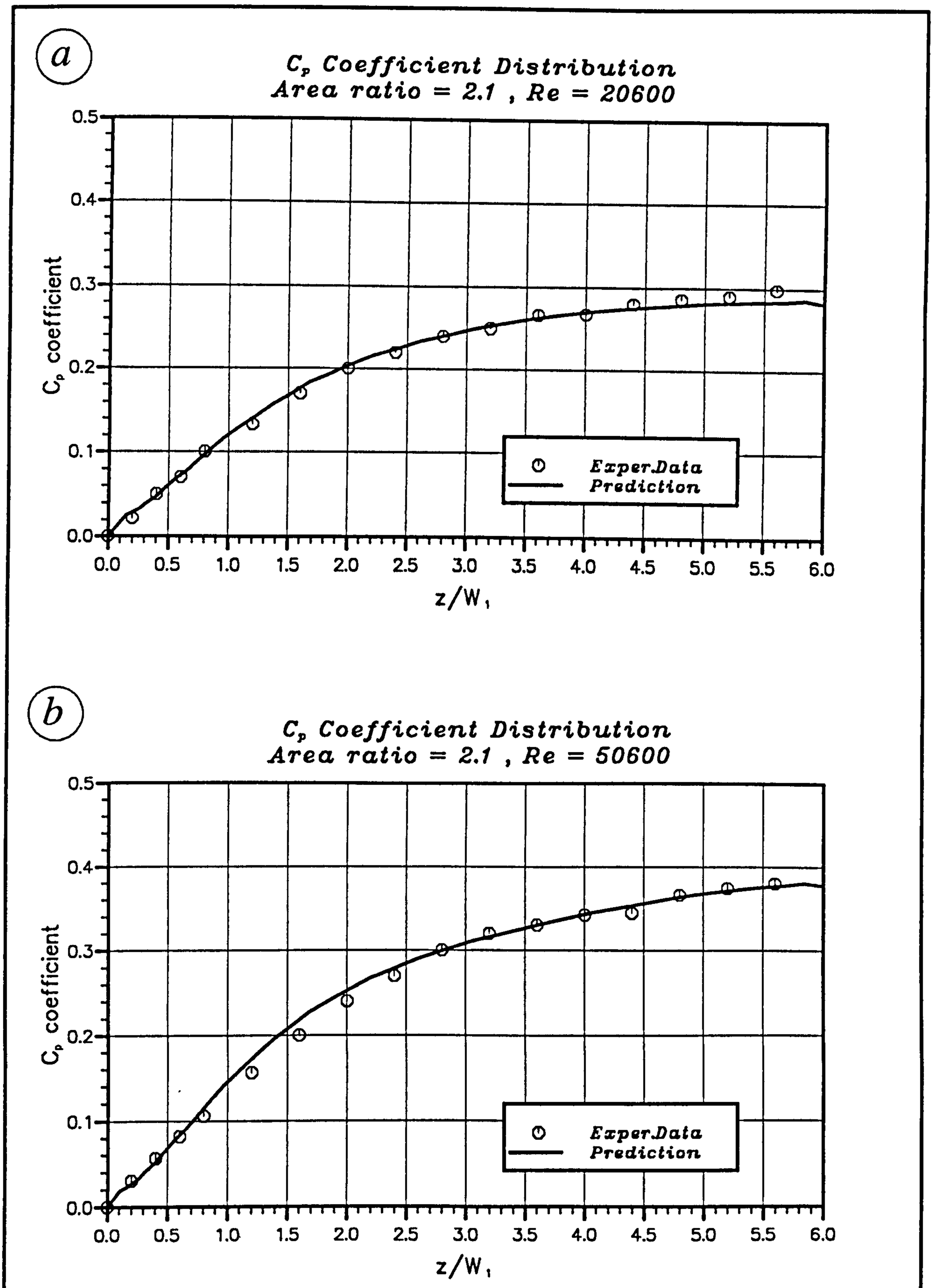

Figure 6.23 : C_p coefficient distribution along the diffuser.
Area ratio = 2.1. (a) Re = 20600. (b) Re = 50600.

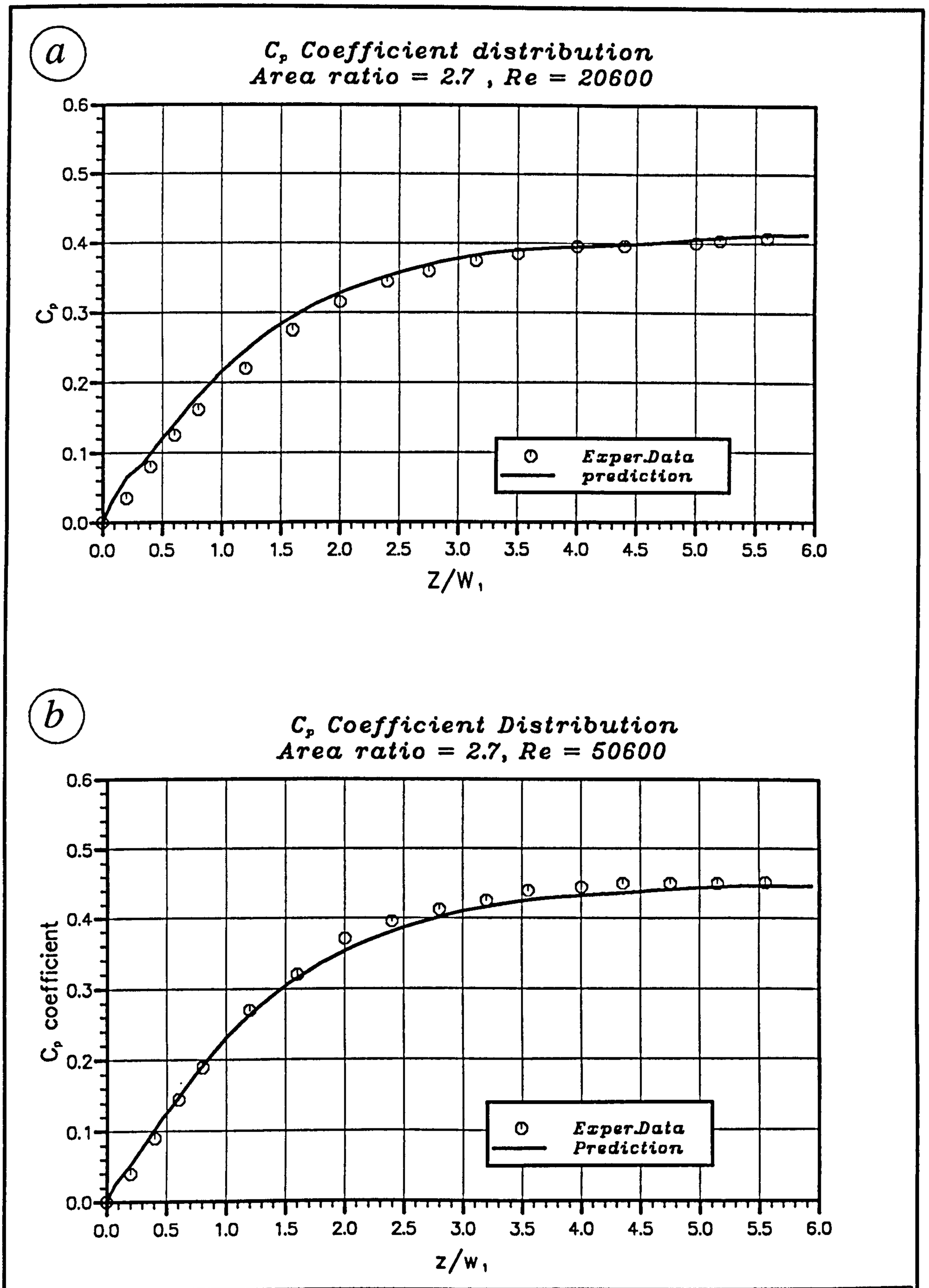

Figure 6.24 : C_p coefficient distribution along the diffuser.
Area ratio = 2.7. (a) Re = 20600. (b) Re = 50600.

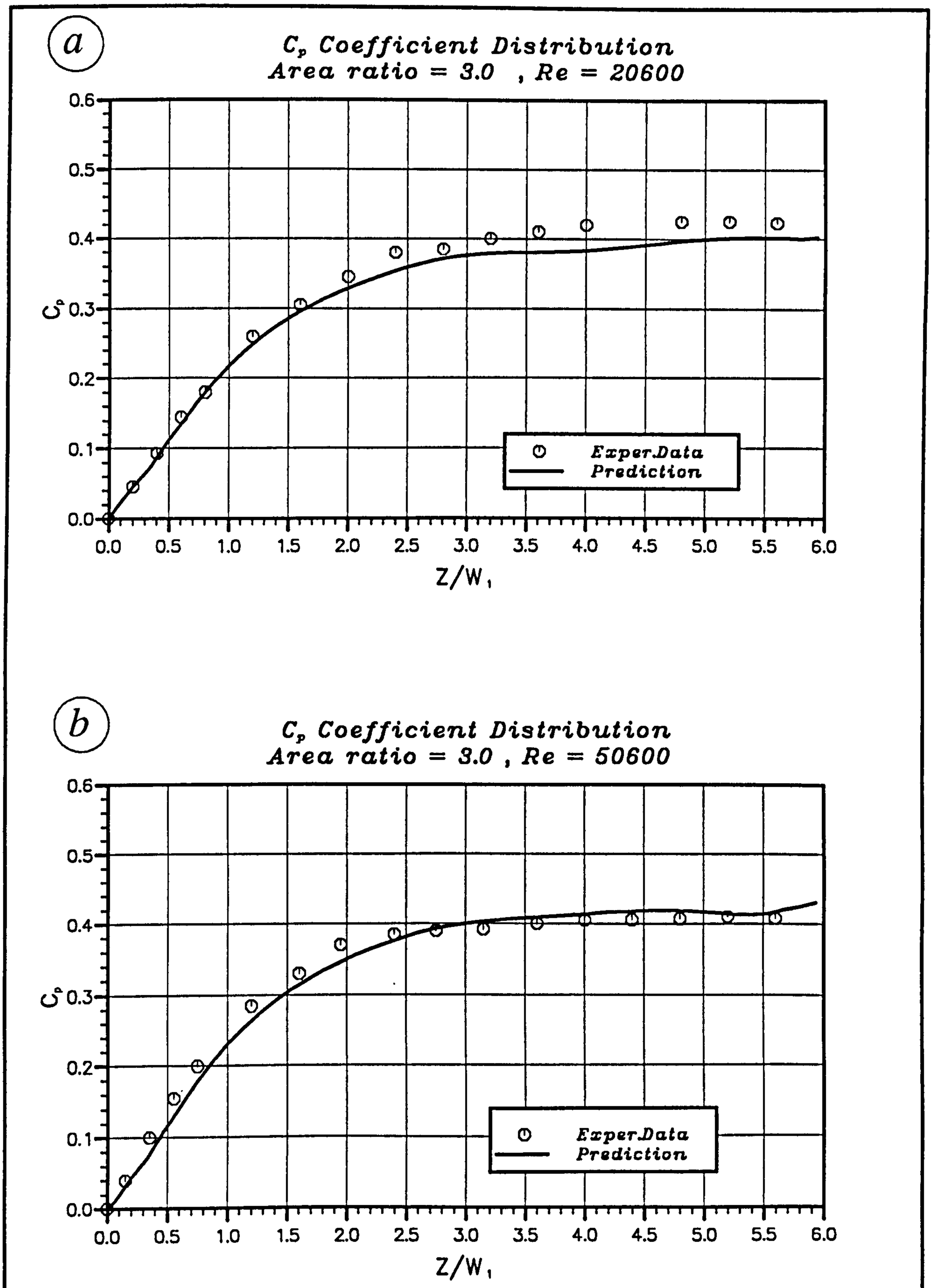

Figure 6.25 : C_p coefficient distribution along the diffuser.
Area ratio = 3.0. (a) Re = 20600. (b) Re = 50600.

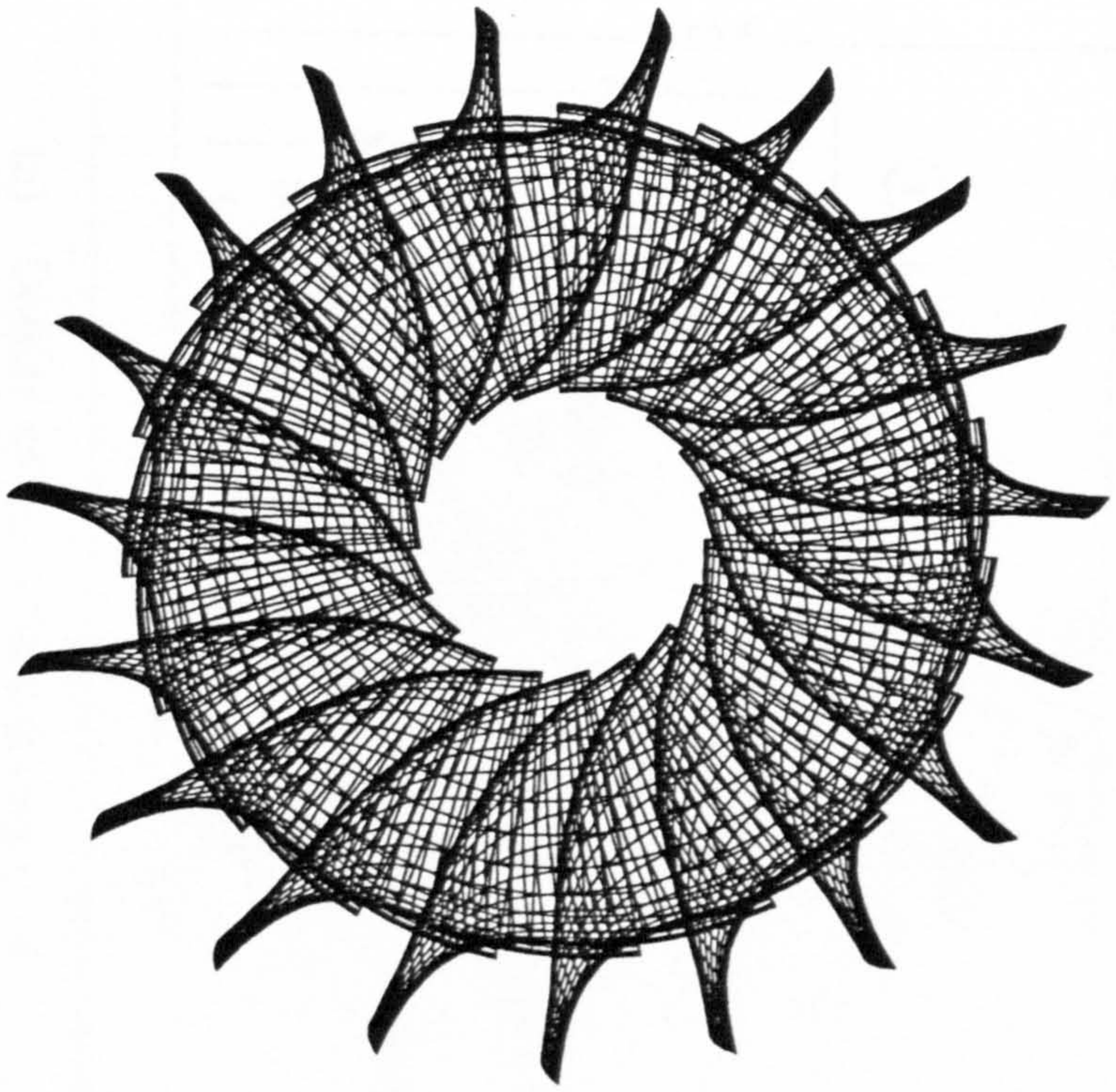

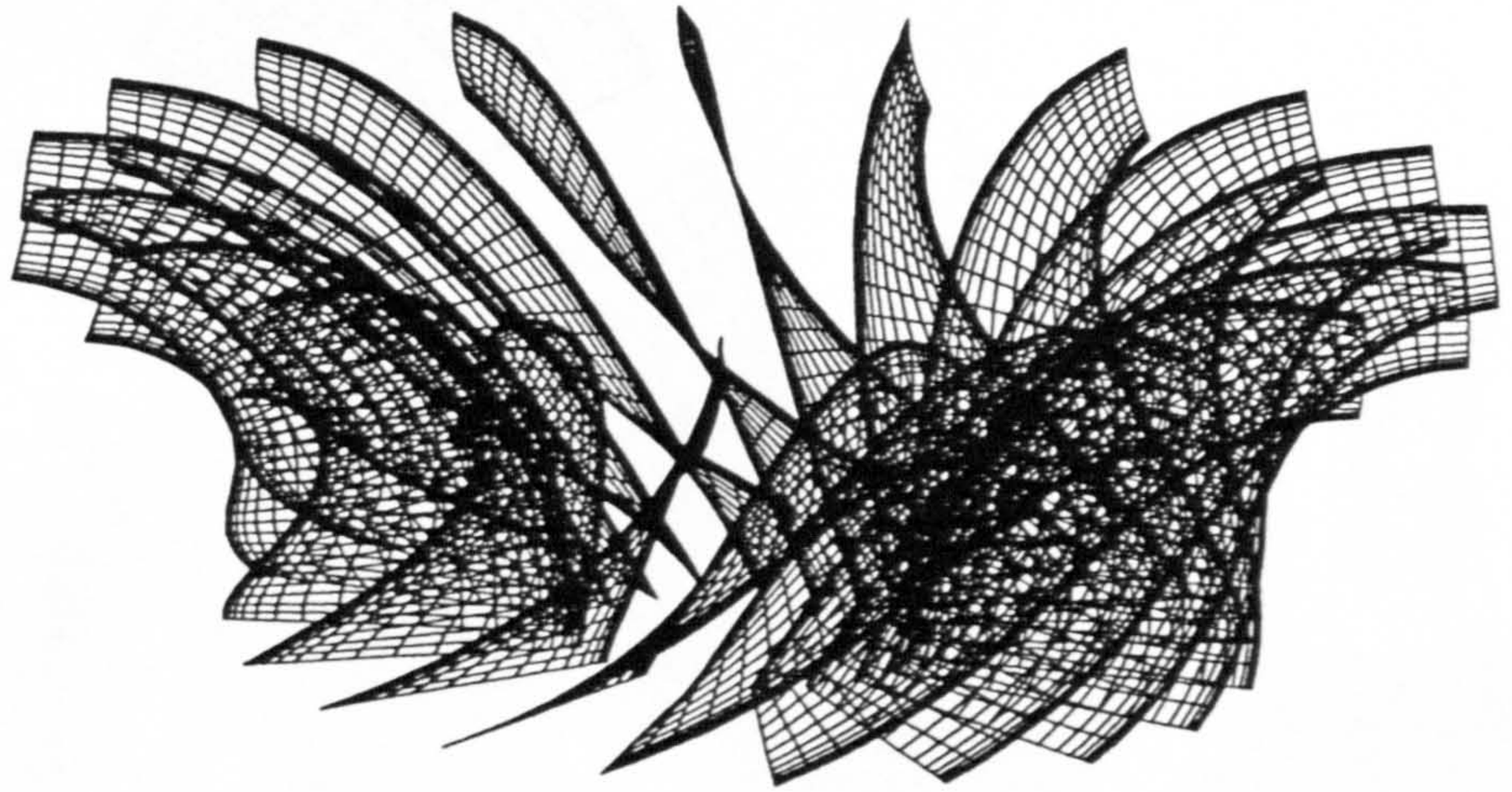

Figure 7.1 : Three-dimensional impeller geometry.

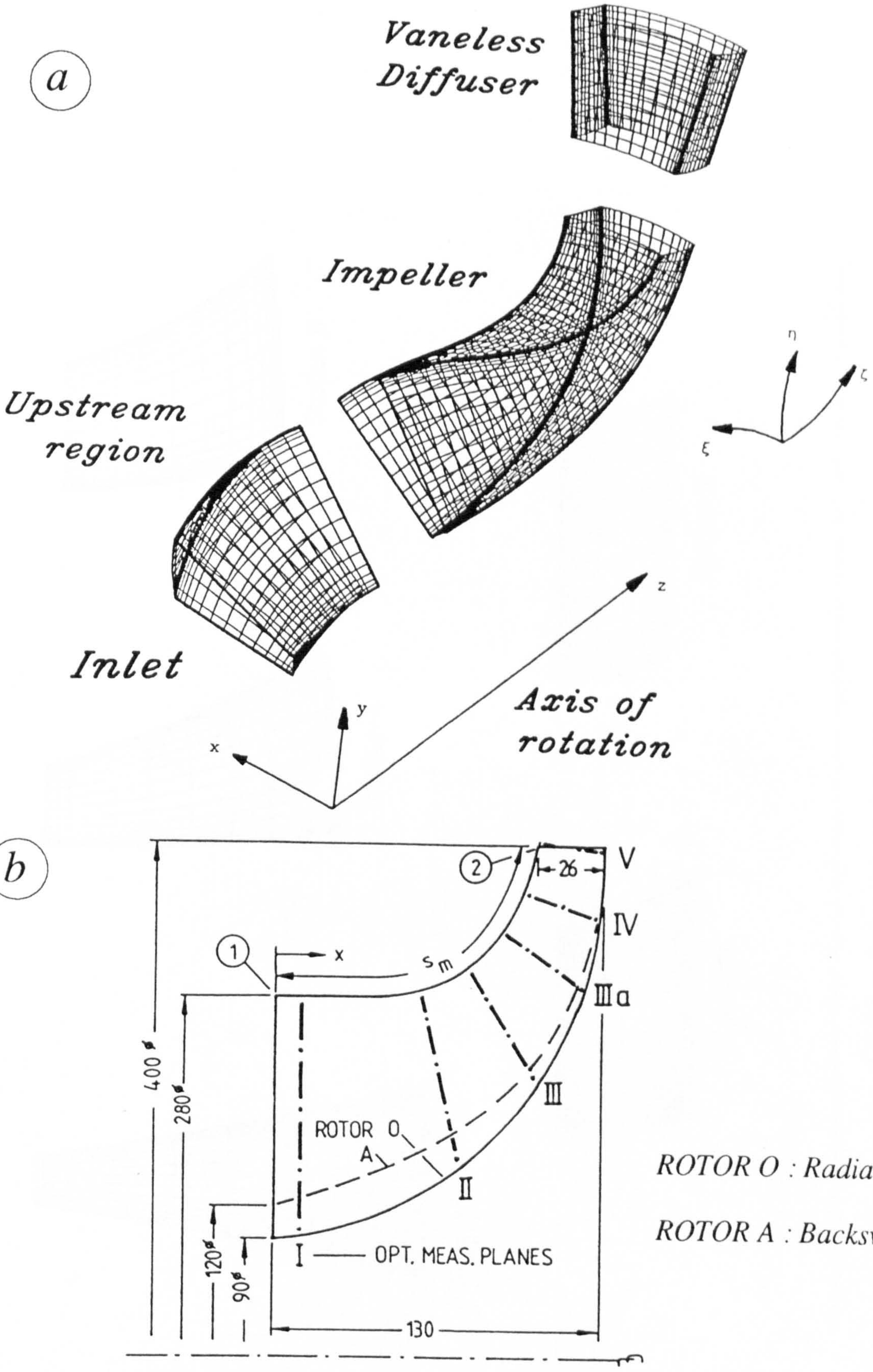

Figure 7.2 : (a) Outline of the computational grid
(b) Laser measurement planes

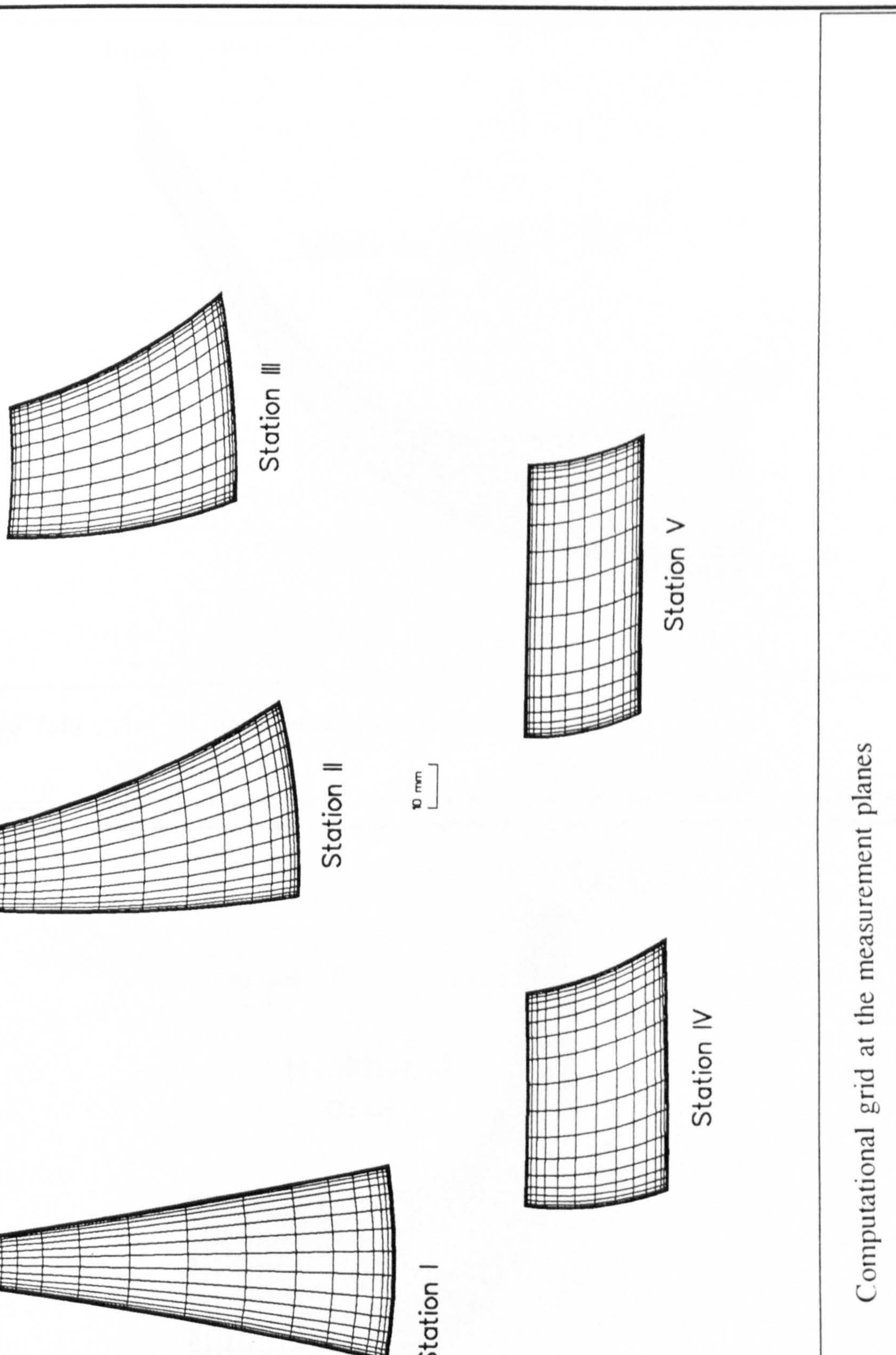

Figure 7.3 : Computational grid at the measurement planes

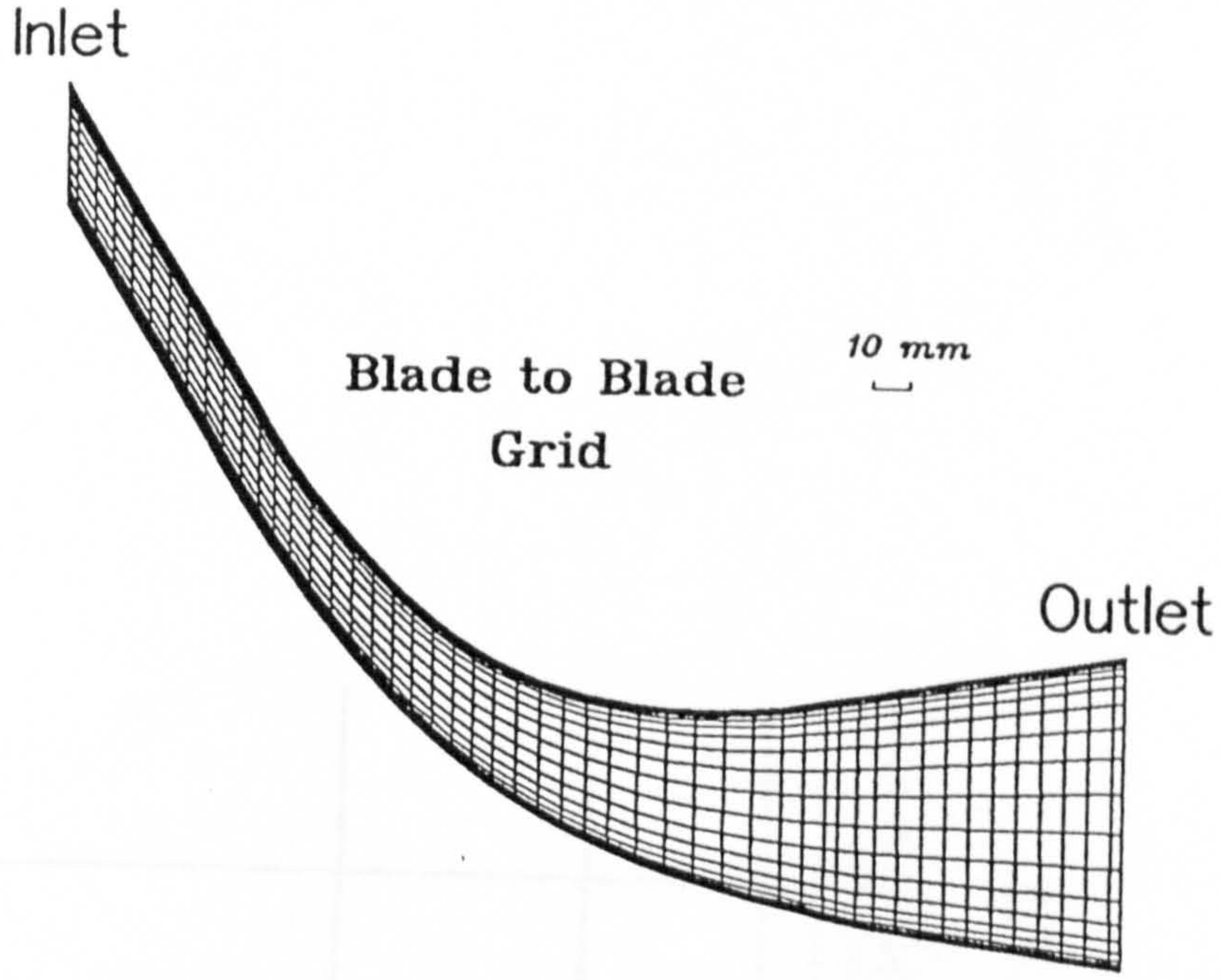

Figure 7.4a : Computational blade to blade grid

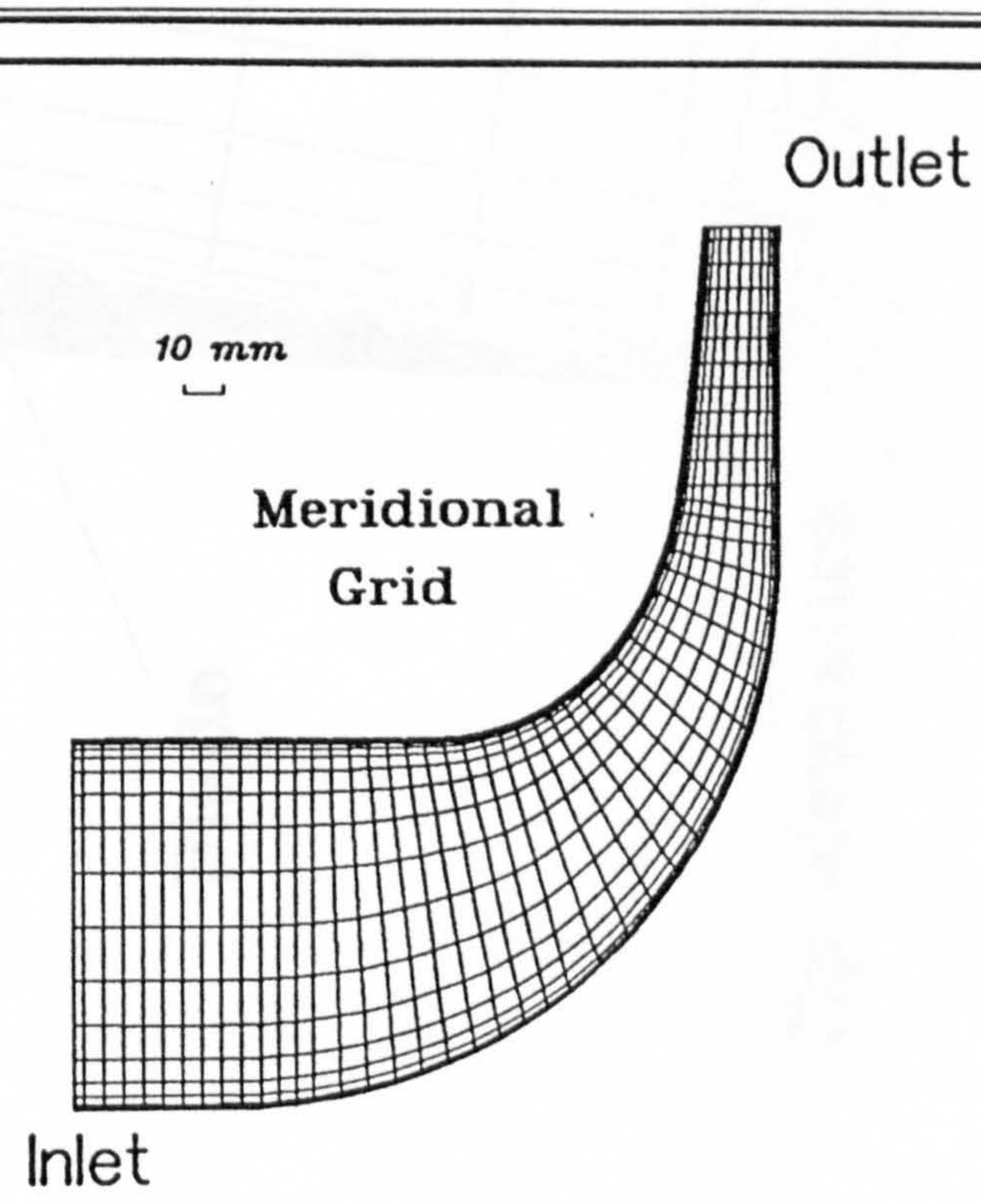

Figure 7.4b : Computational meridional grid

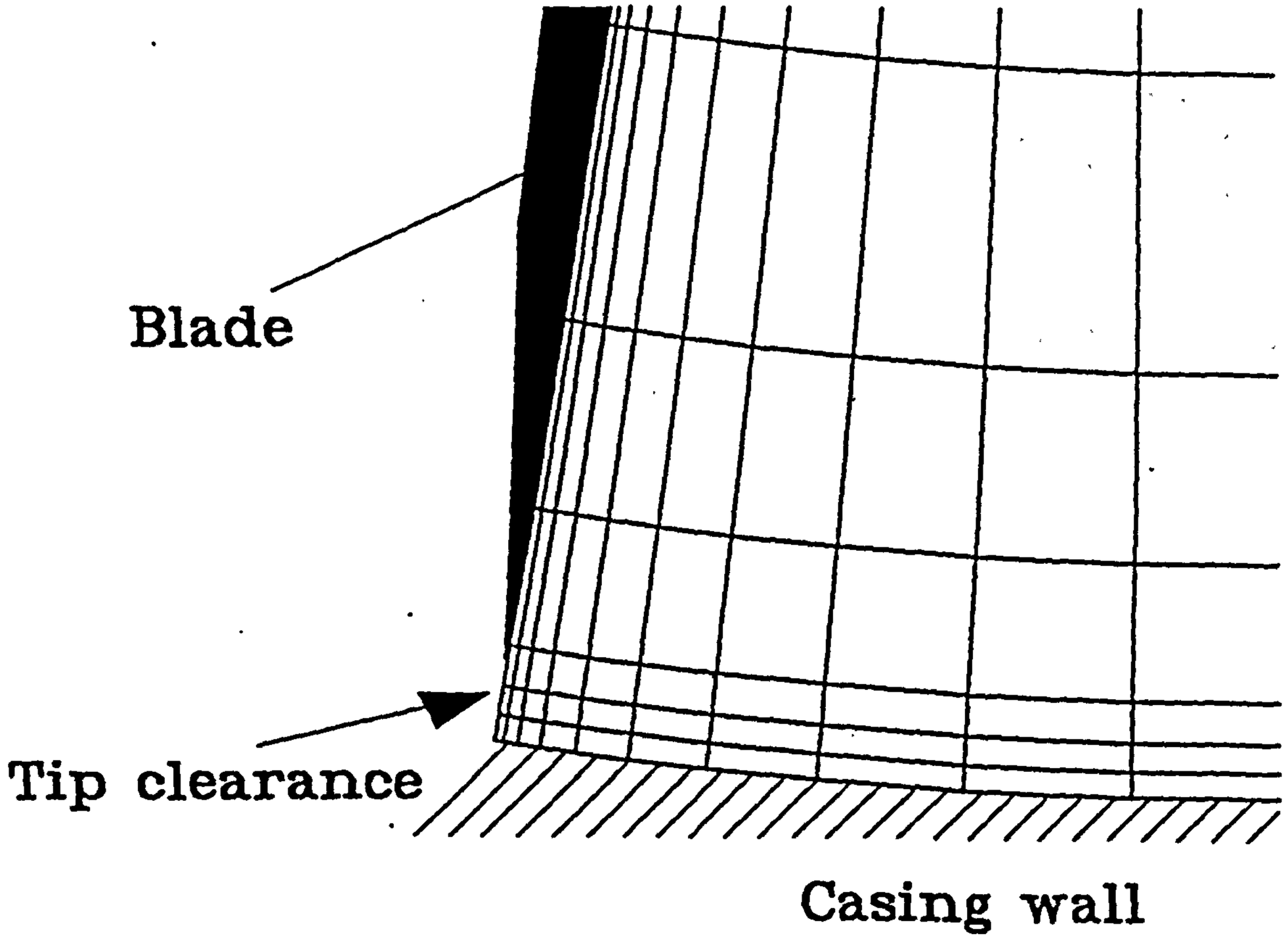

Figure 7.5 : Computational grid at the tip clearance gap.

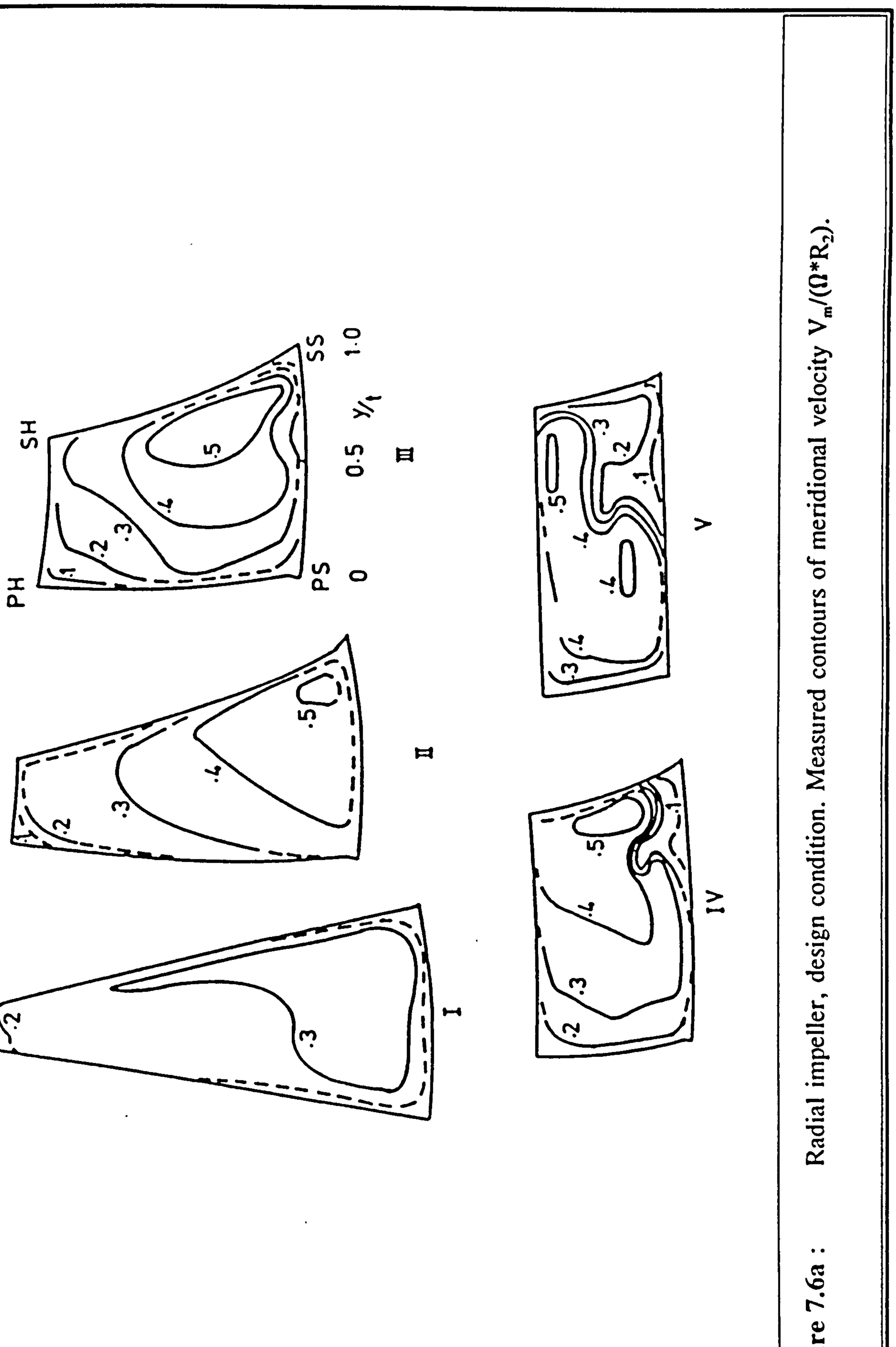

Figure 7.6a : Radial impeller, design condition. Measured contours of meridional velocity $V_m/(\Omega*R_2)$.

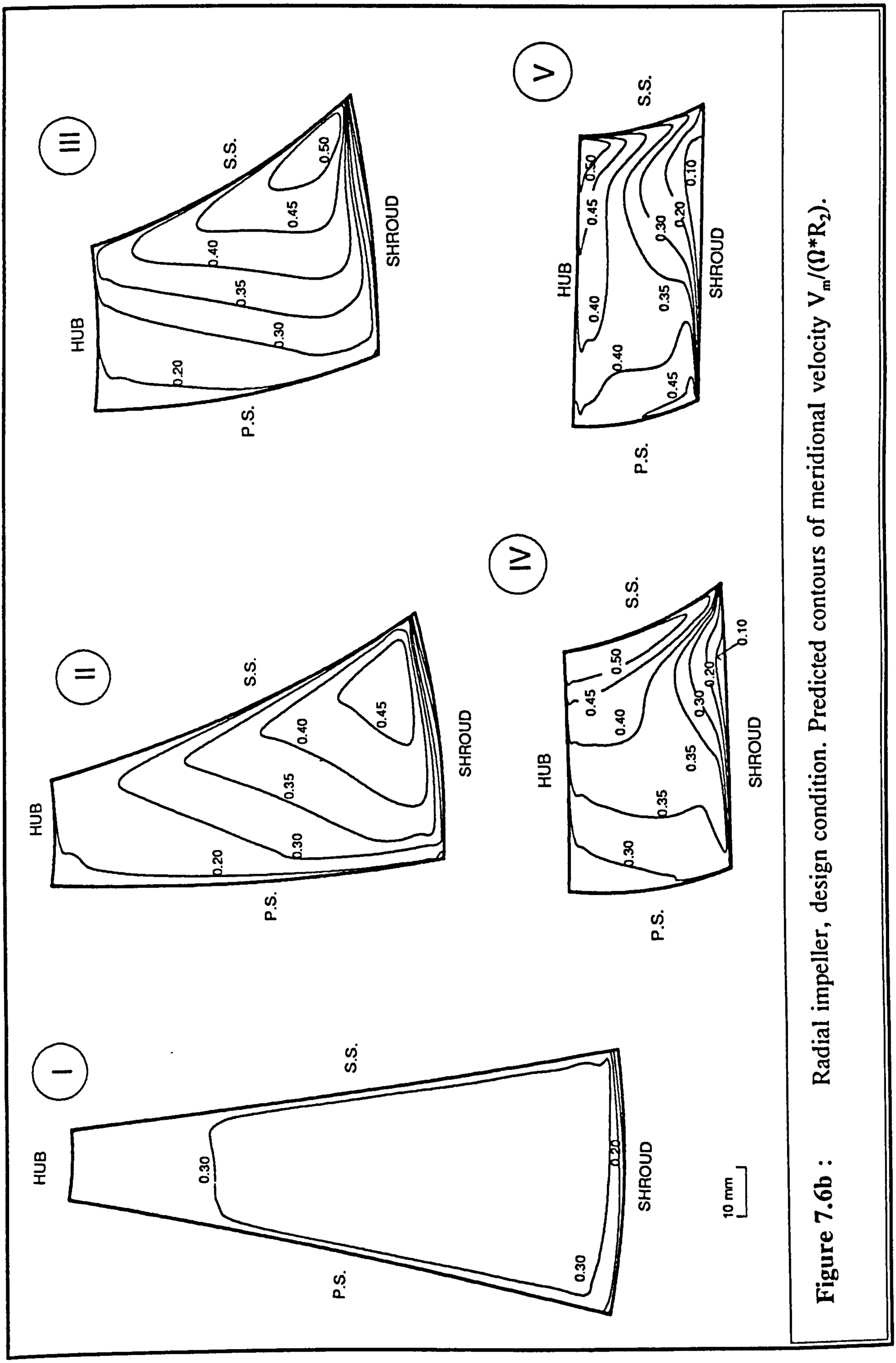

Figure 7.6b : Radial impeller, design condition. Predicted contours of meridional velocity $V_m/(\Omega*R_2)$.

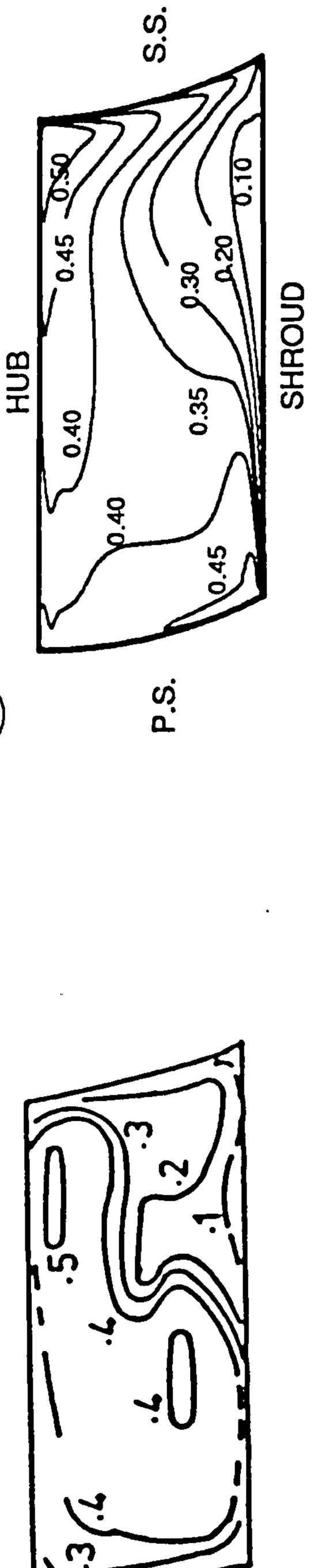

Figure 7.7 : Radial impeller, design condition. Contours of meridional velocity $V_m/(\Omega*R_2)$. (a) Measured. (b) Predicted. (c) Predicted by Moore et al (1980b).

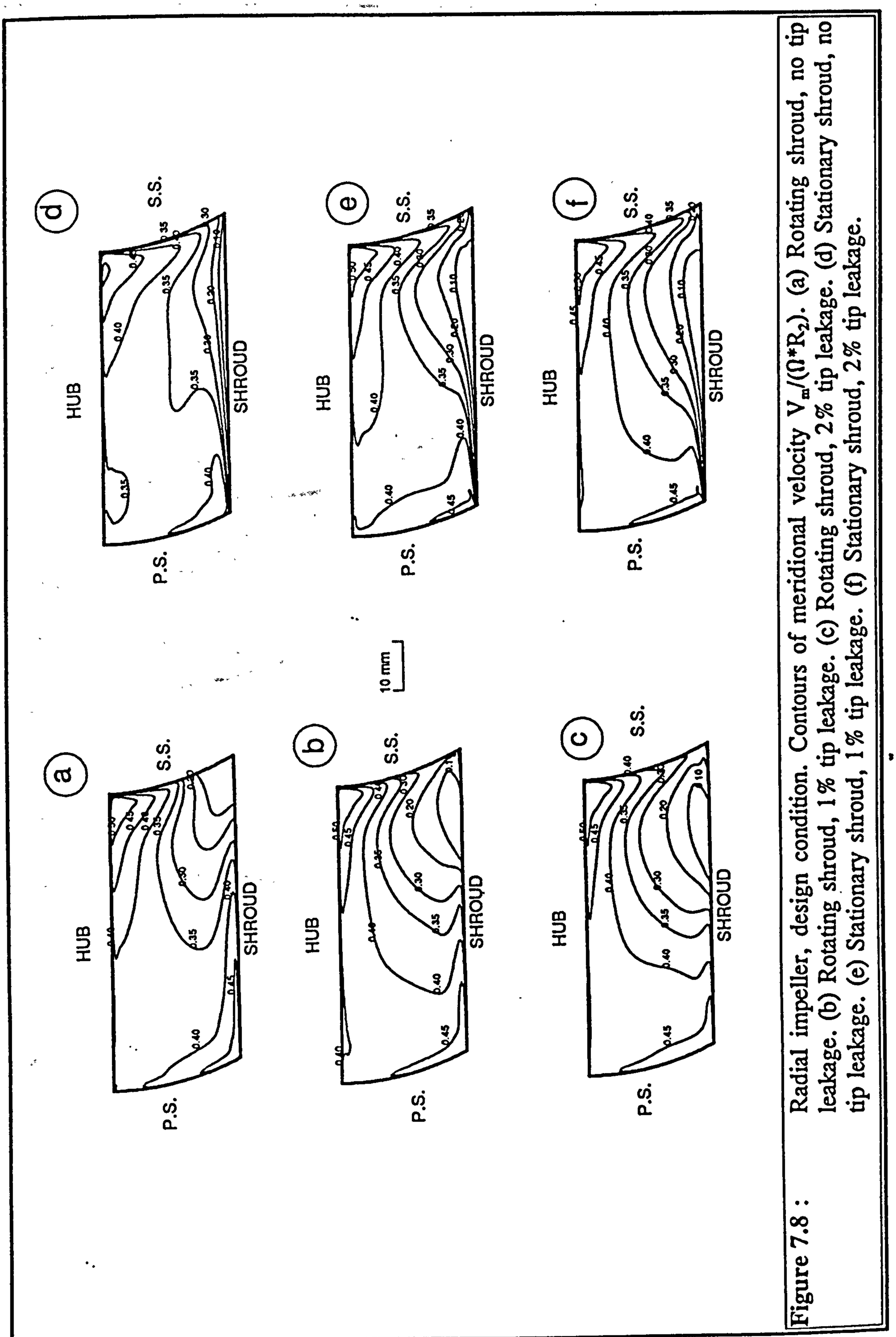

Figure 7.8 : Radial impeller, design condition. Contours of meridional velocity $V_m/(\Omega*R_2)$. (a) Rotating shroud, no tip leakage. (b) Rotating shroud, 2% tip leakage. (c) Rotating shroud, 1% tip leakage. (d) Stationary shroud, no tip leakage. (e) Stationary shroud, 2% tip leakage. (f) Stationary shroud, 1% tip leakage.

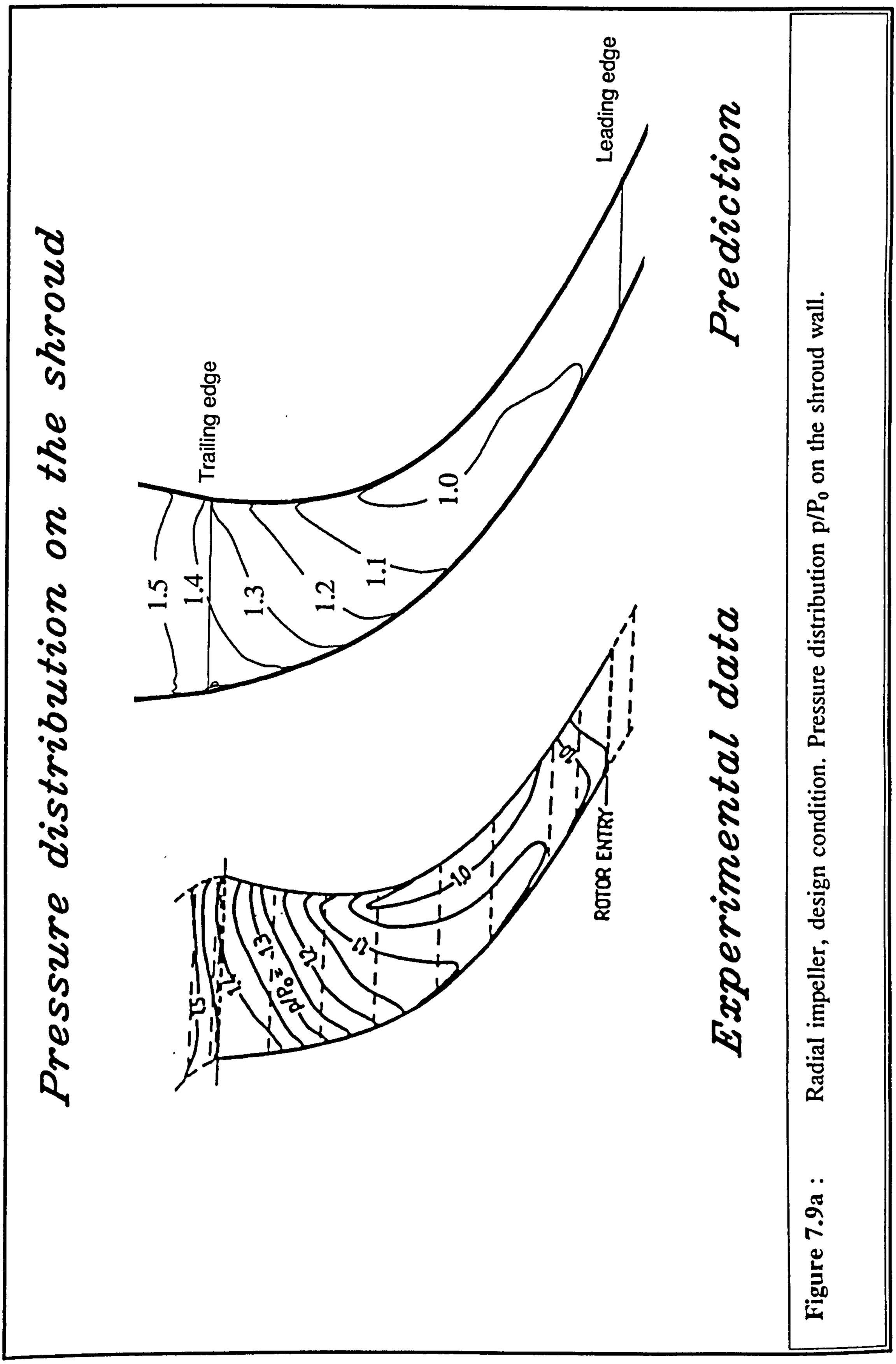

Figure 7.9a : Radial impeller, design condition. Pressure distribution p/P_0 on the shroud wall.

Eckardt Radial Impeller
Design Condition
Pressure p/P Distribution

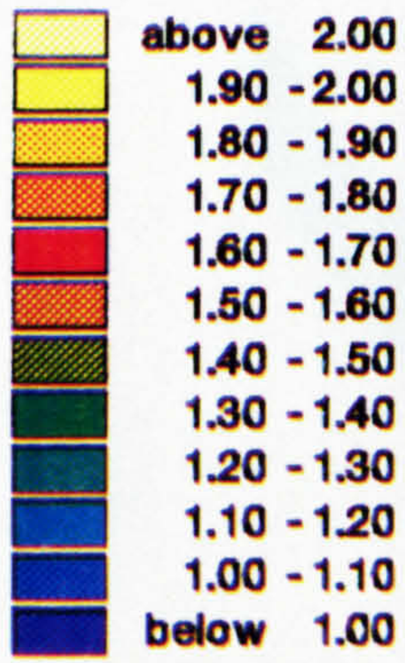

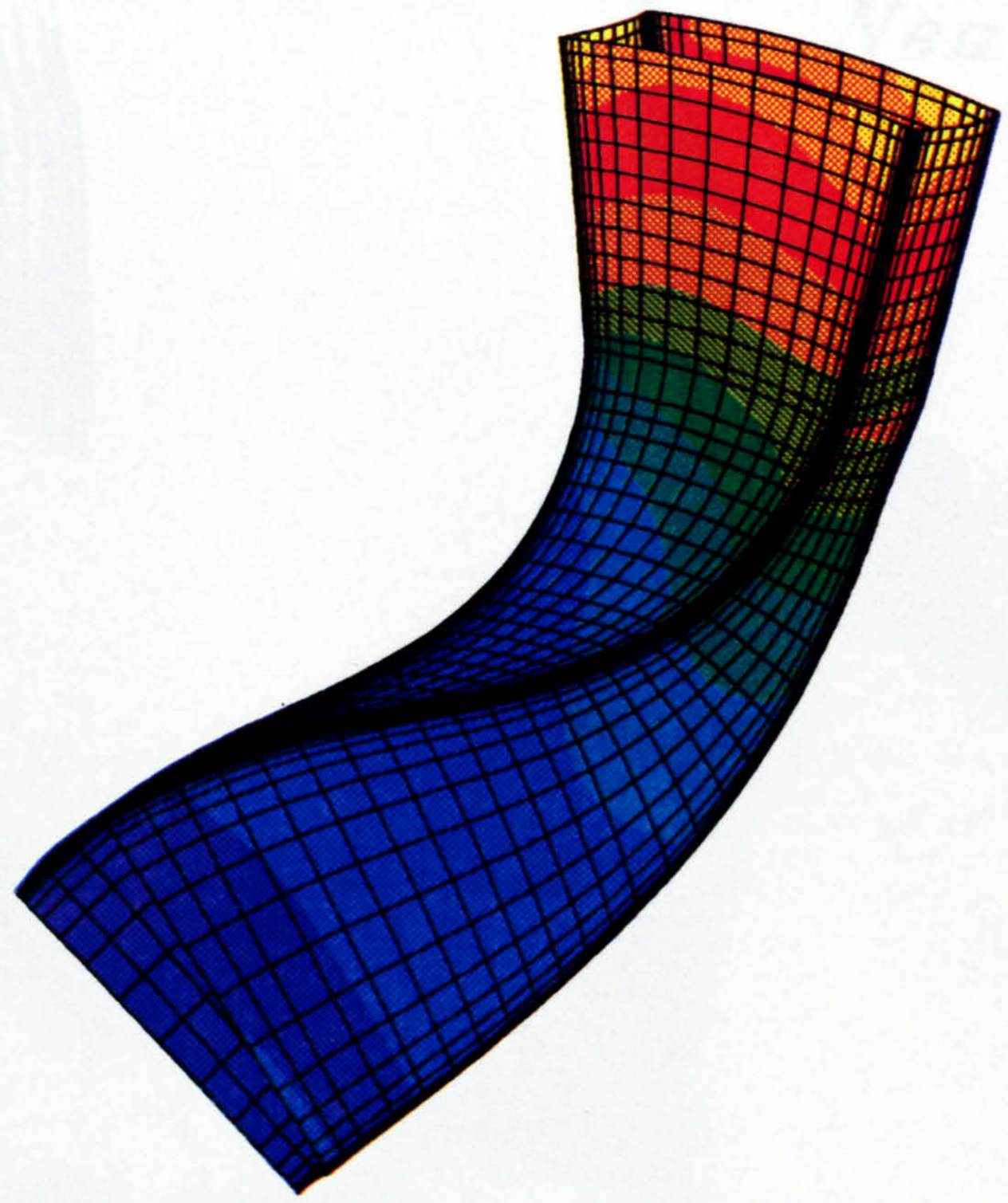

Figure 7.9b : Radial impeller, design condition. Three-dimensional pressure distribution p/P_0.

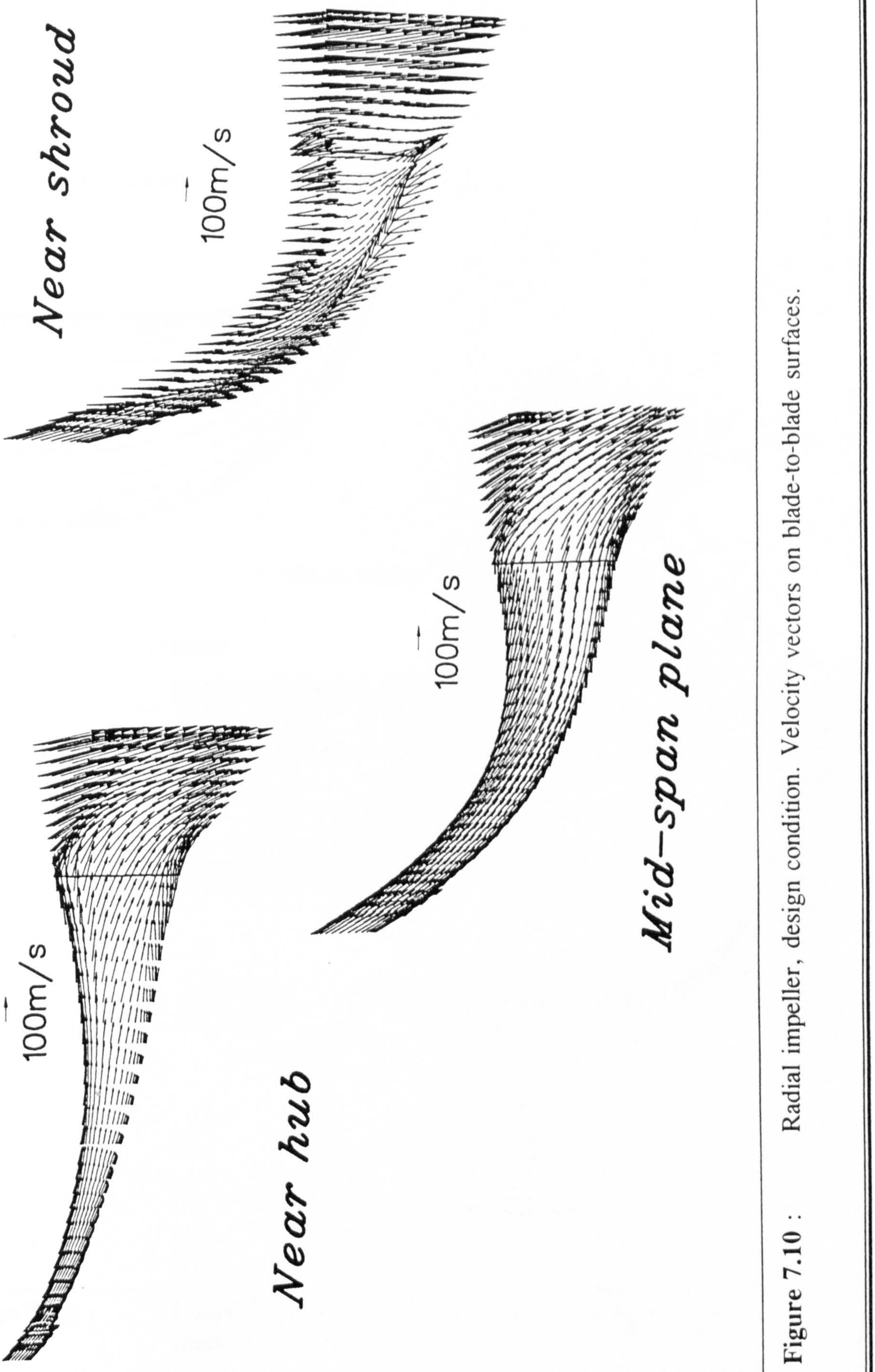

Figure 7.10 : Radial impeller, design condition. Velocity vectors on blade-to-blade surfaces.

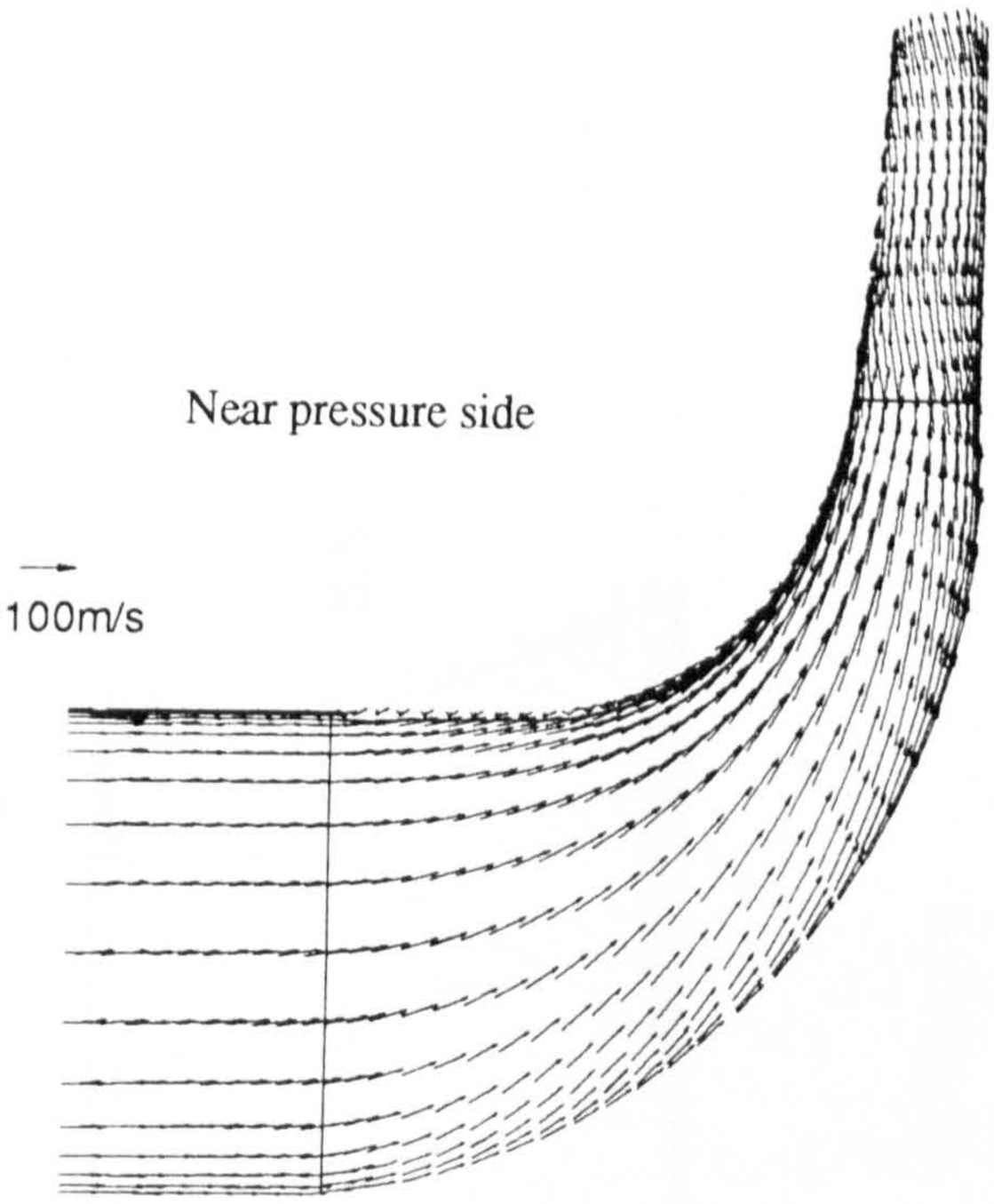

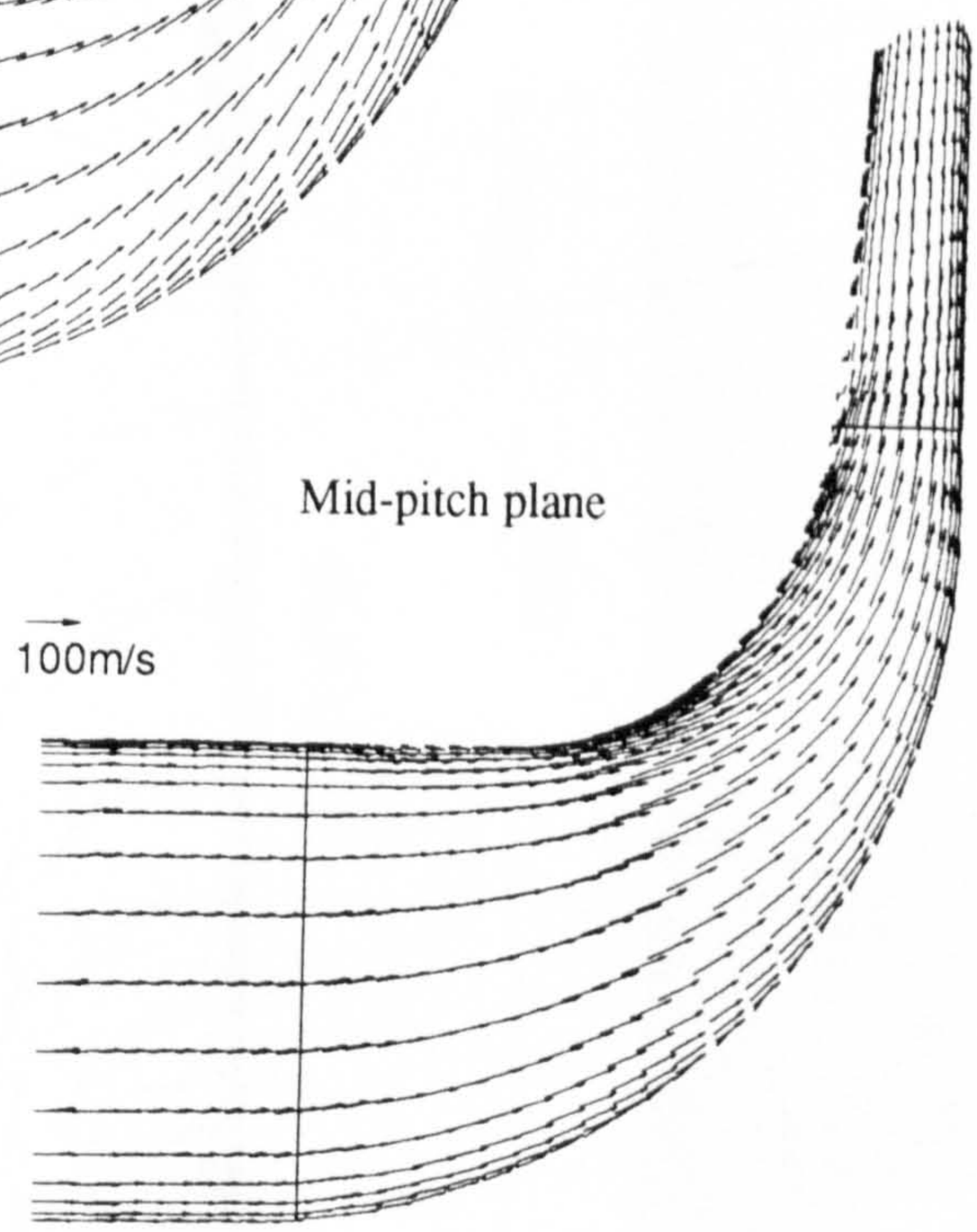

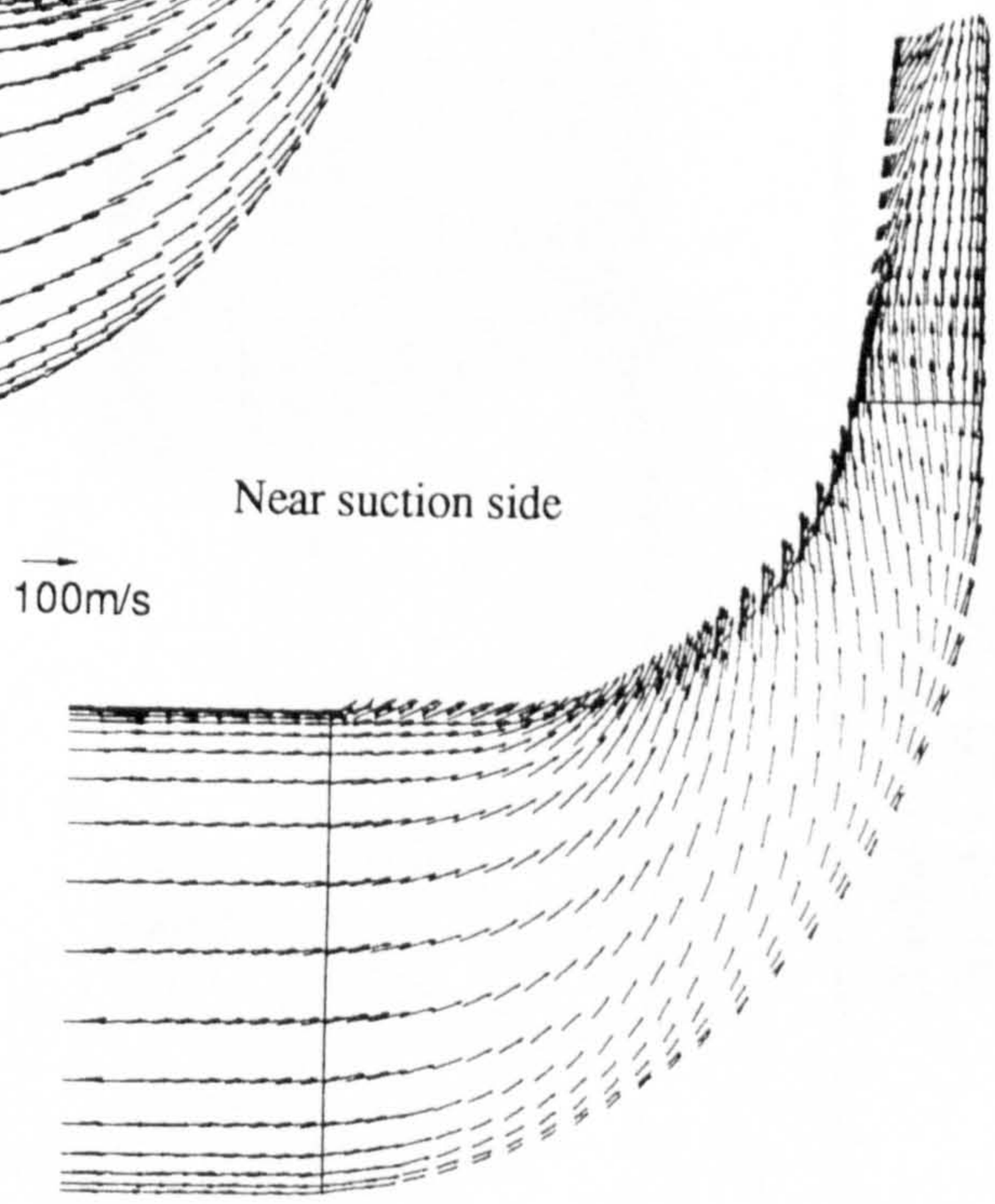

Figure 7.11 : Radial impeller, design condition. Velocity vectors on meridional surfaces.

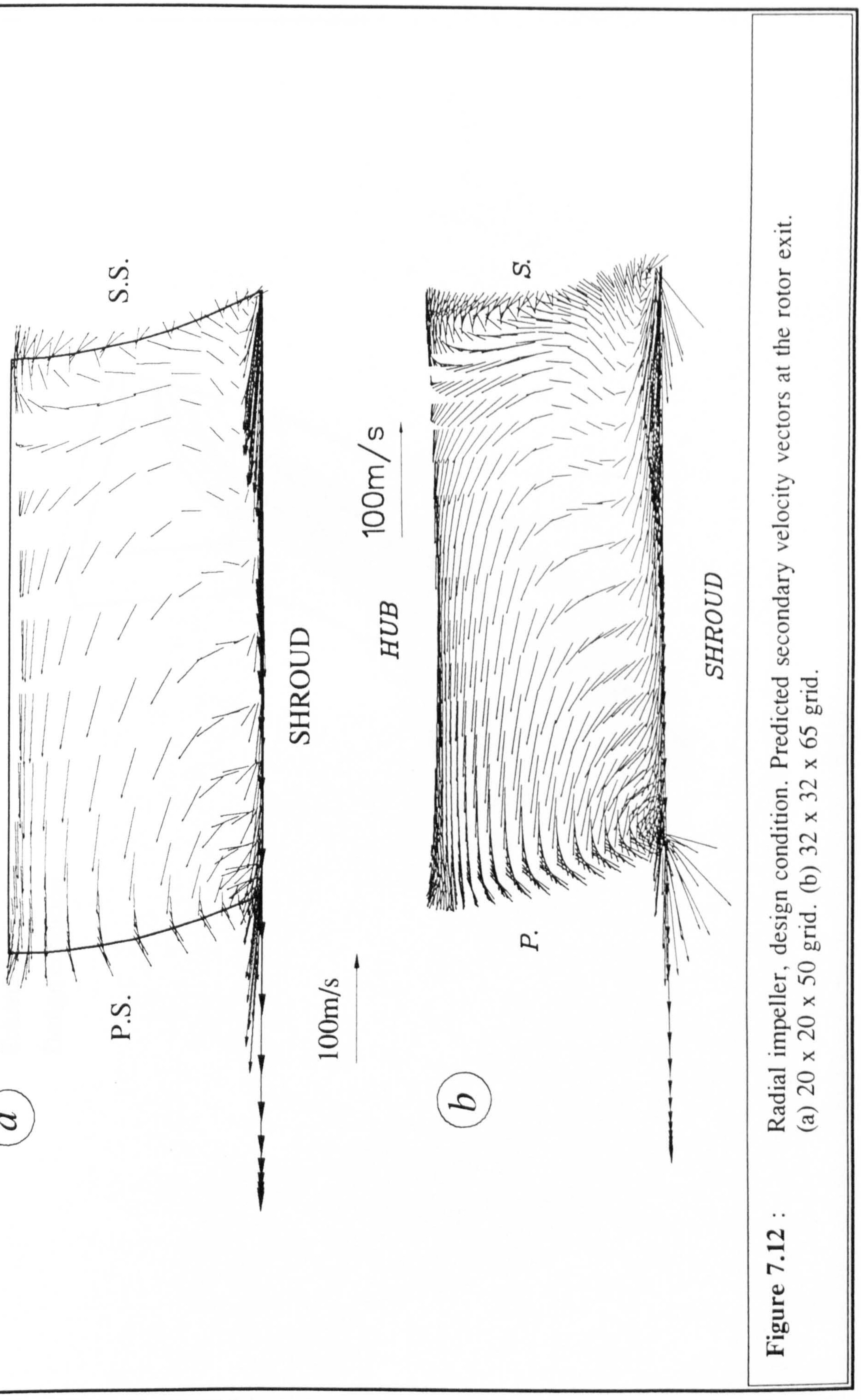

Figure 7.12 : Radial impeller, design condition. Predicted secondary velocity vectors at the rotor exit. (a) 20 x 50 x 20 grid. (b) 32 x 32 x 65 grid.

Eckardt Radial Impeller

Design condition

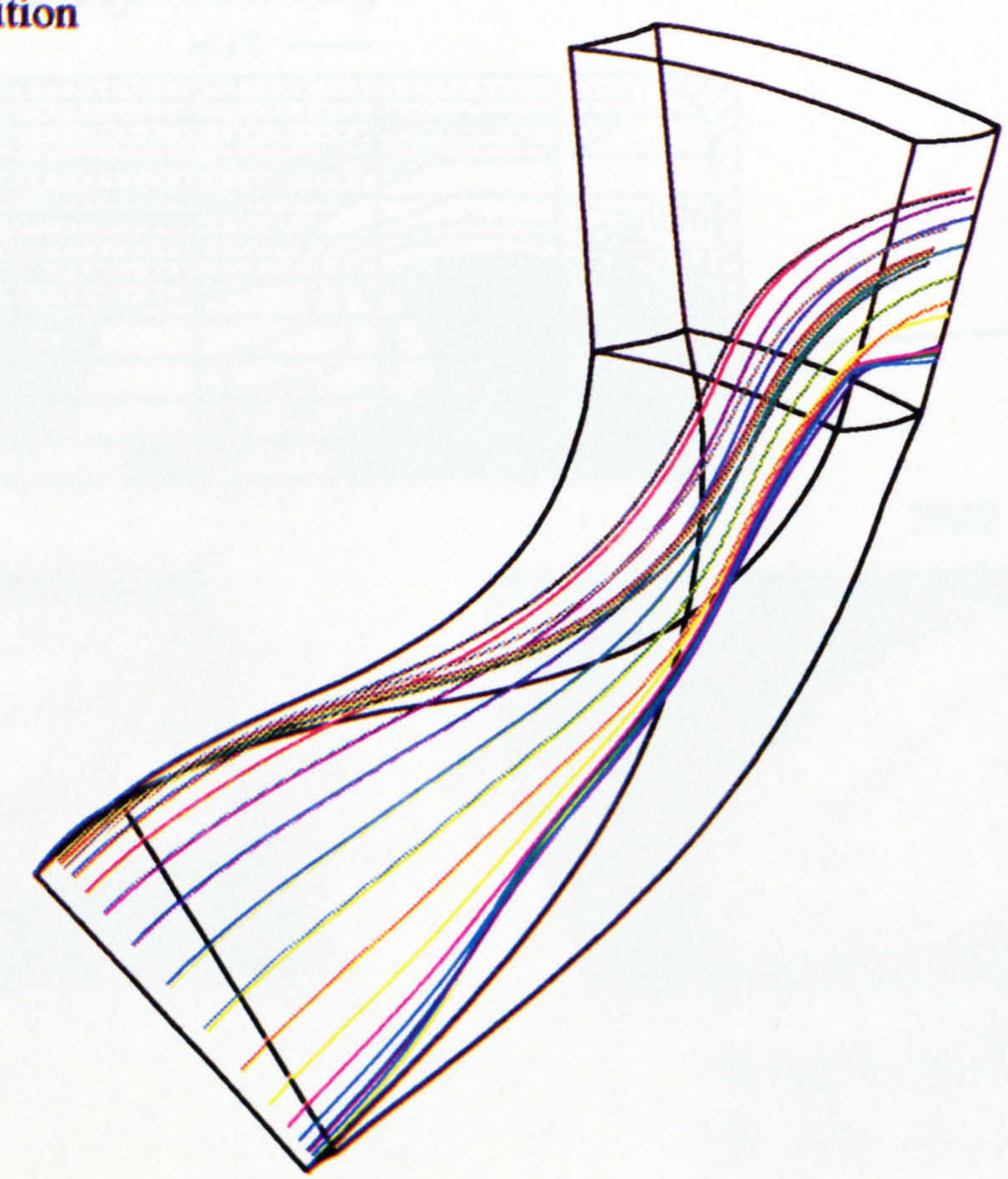

Figure 7.13 : Radial impeller, design condition. Predicted streamlines.

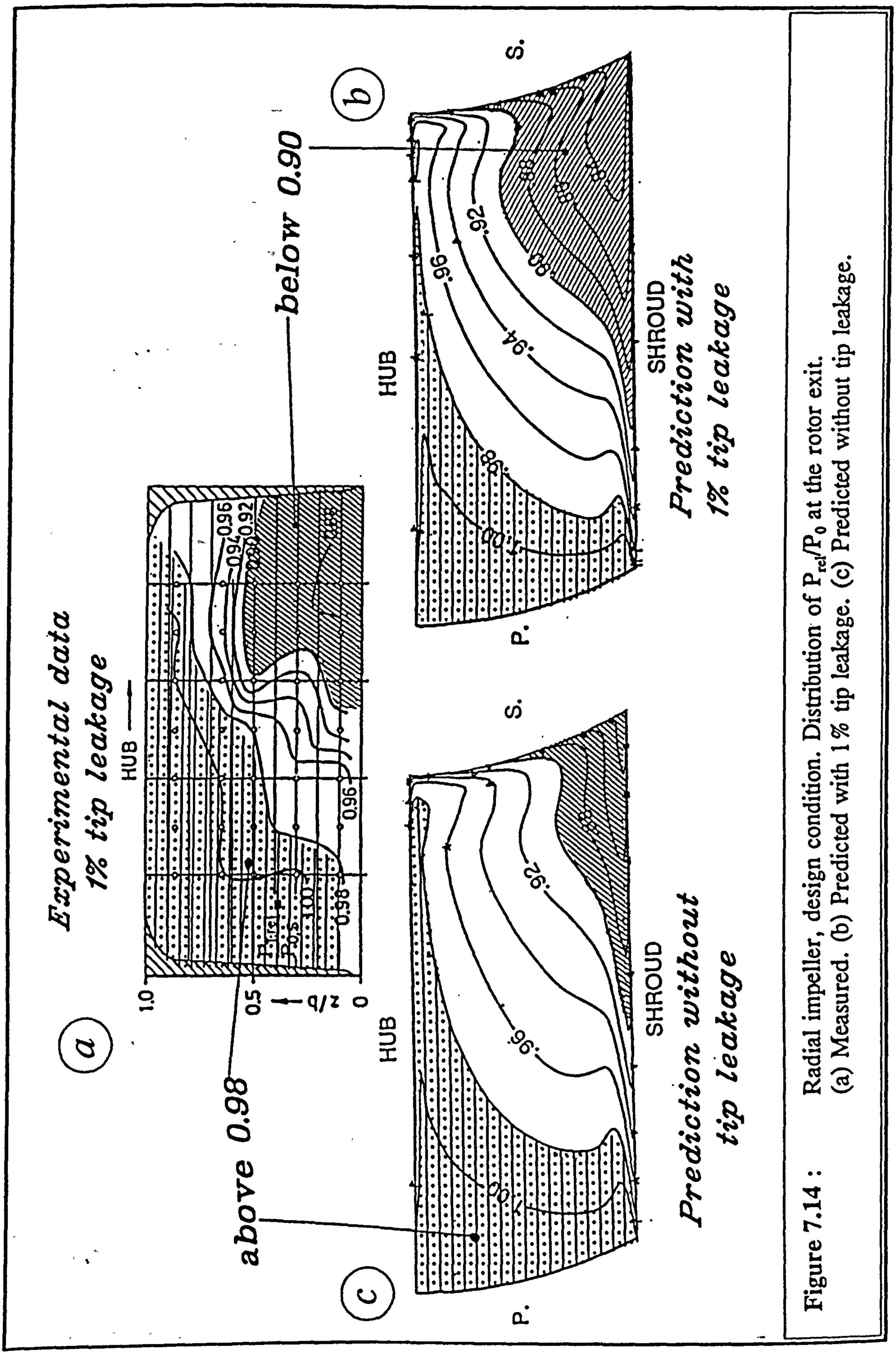

Figure 7.14 : Radial impeller, design condition. Distribution of P_{rel}/P_0 at the rotor exit. (a) Measured. (b) Predicted without tip leakage. (c) Predicted with 1% tip leakage.

(a)

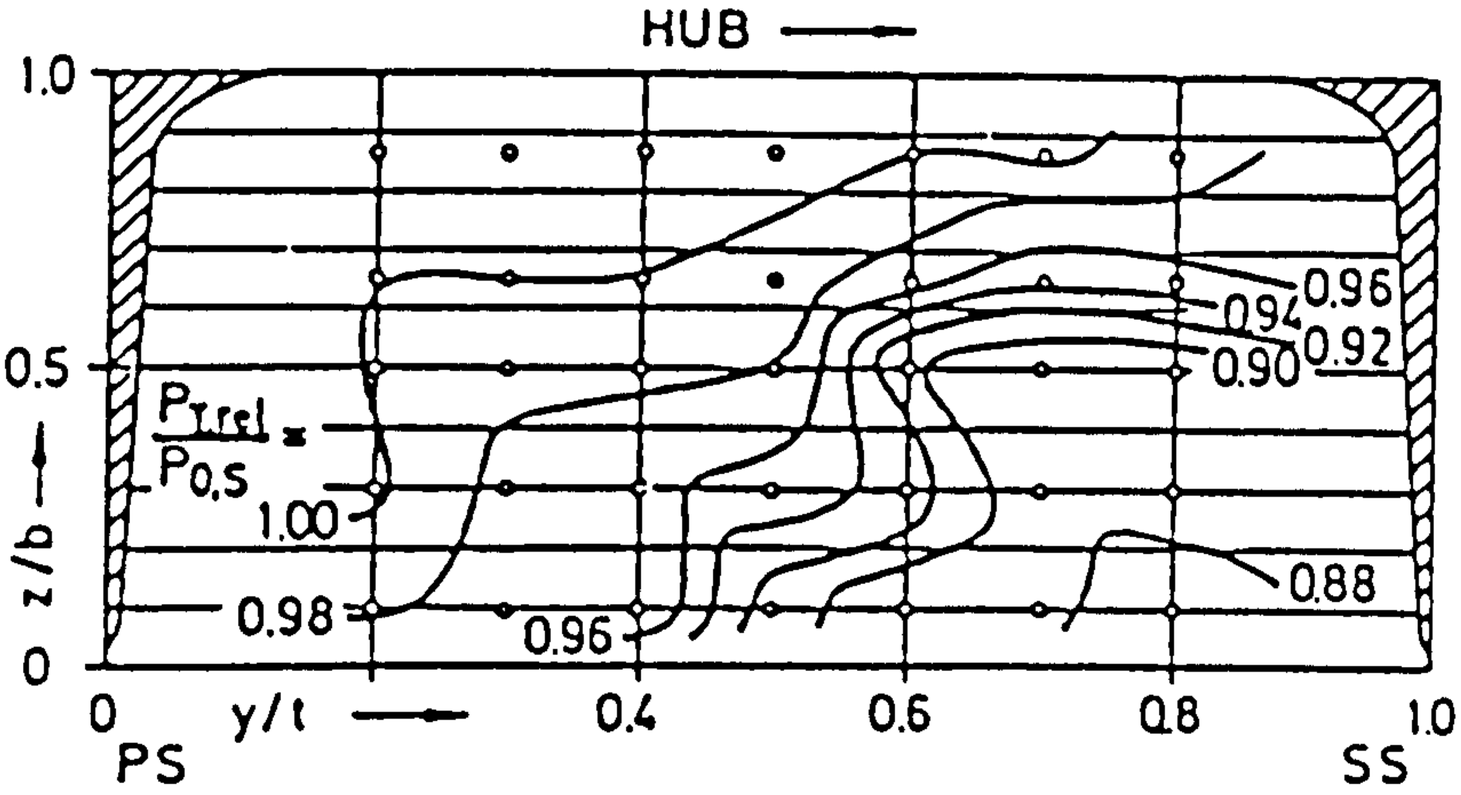

(b)

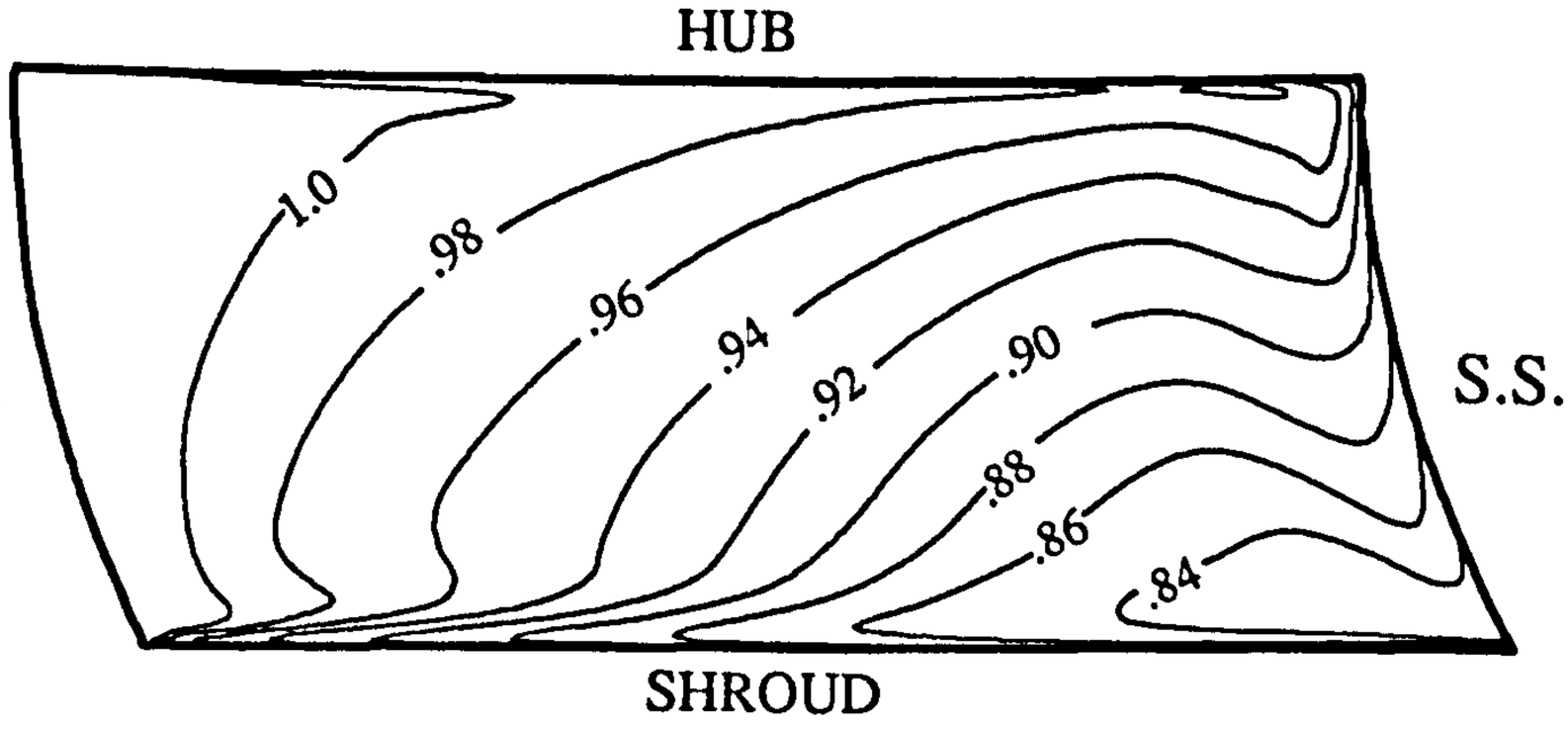

(d)

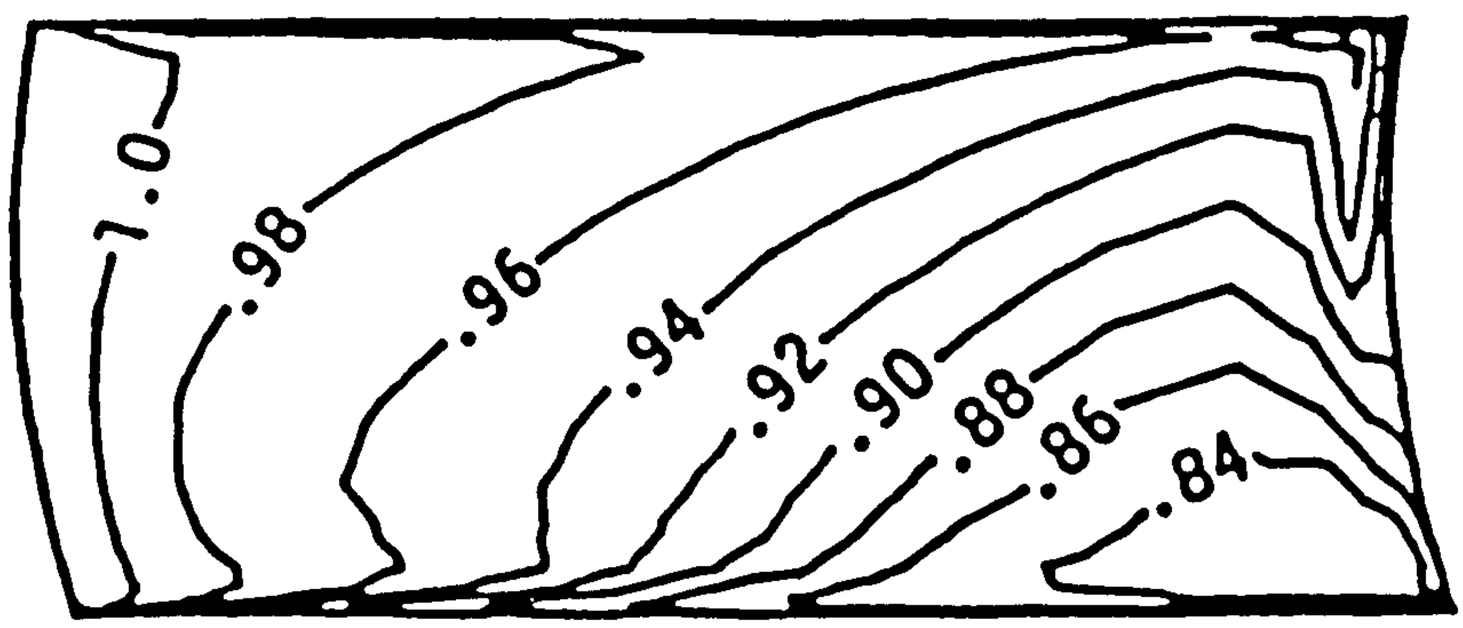

Figure 7.14 : Radial impeller, design condition. Distribution of P_{rel}/P_0 at the rotor exit: (a) Measured. (b) Predicted with 1% tip leakage. (d) Predicted by Rhie et al (1984).

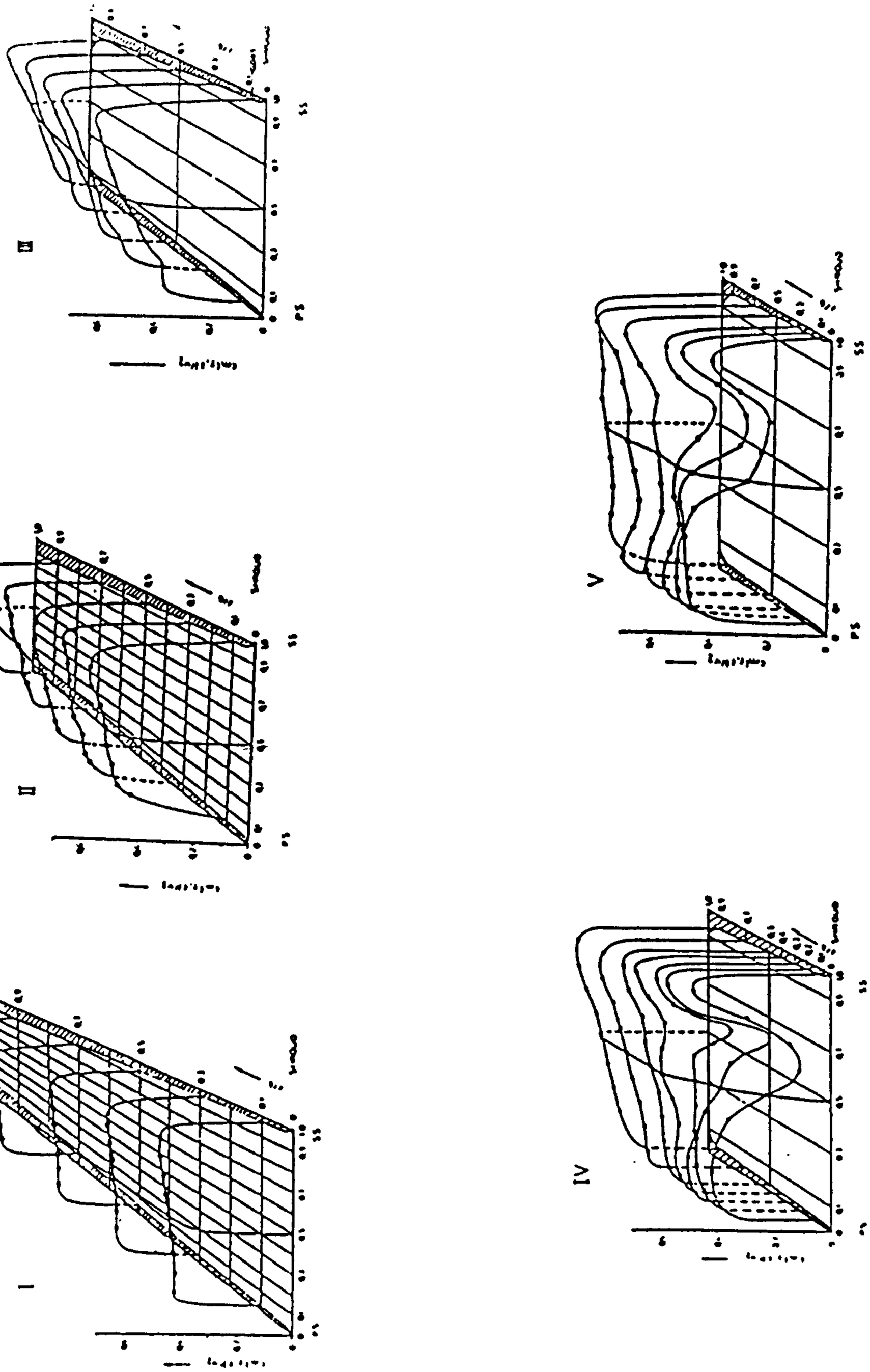

Figure 7.15a : Backswept impeller, design condition. Measured meridional velocity $V_m/(\Omega*R_2)$.

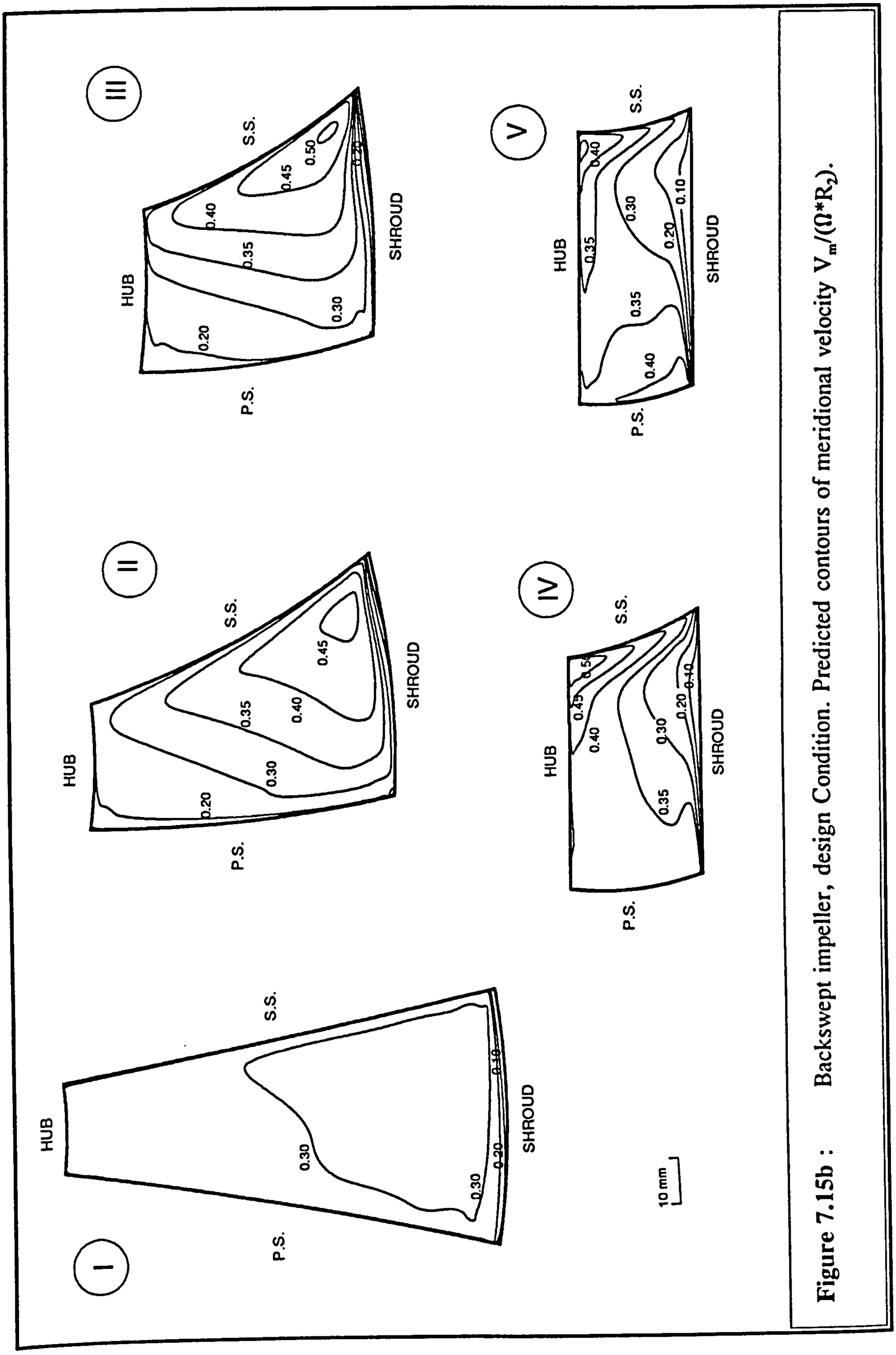

Figure 7.15b : Backswept impeller, design Condition. Predicted contours of meridional velocity $V_m/(\Omega*R_2)$.

(a)

Exper.data

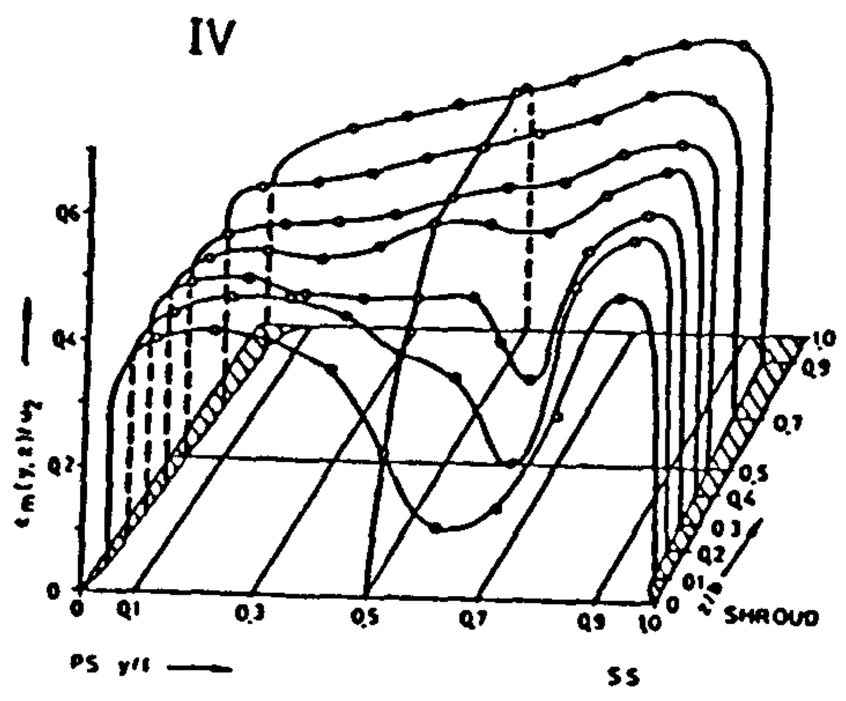

(b)

Prediction

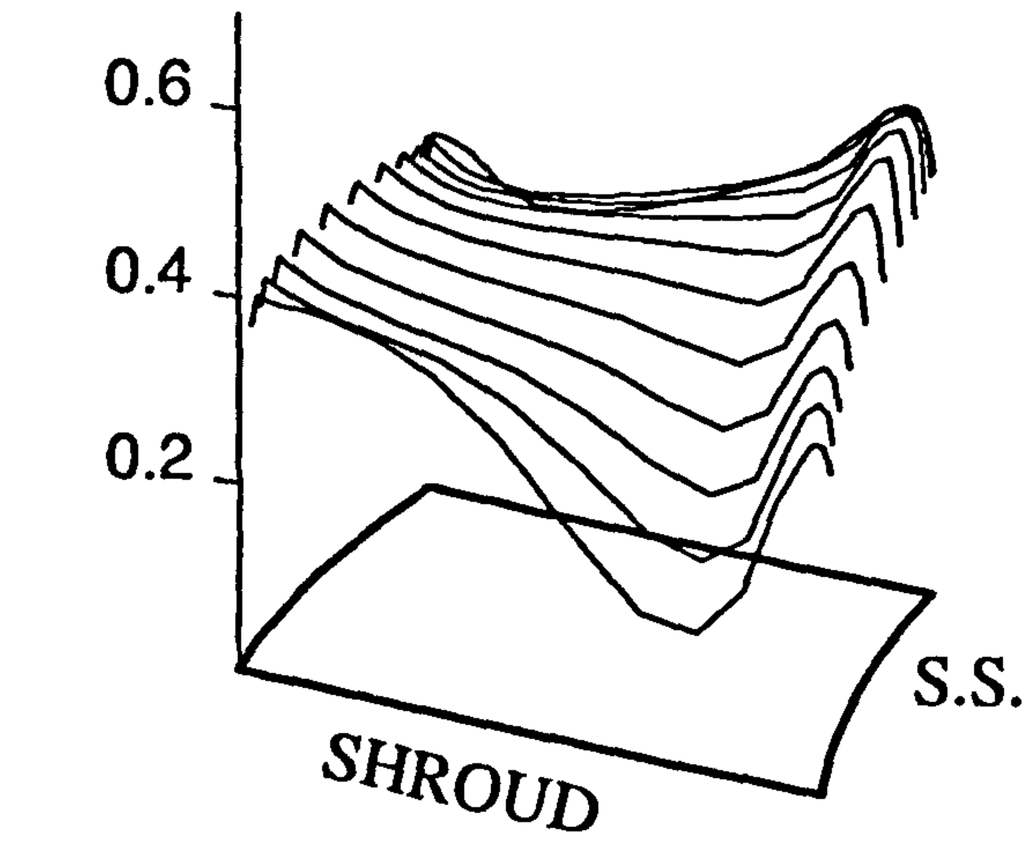

(c)

Hah et al (1988)

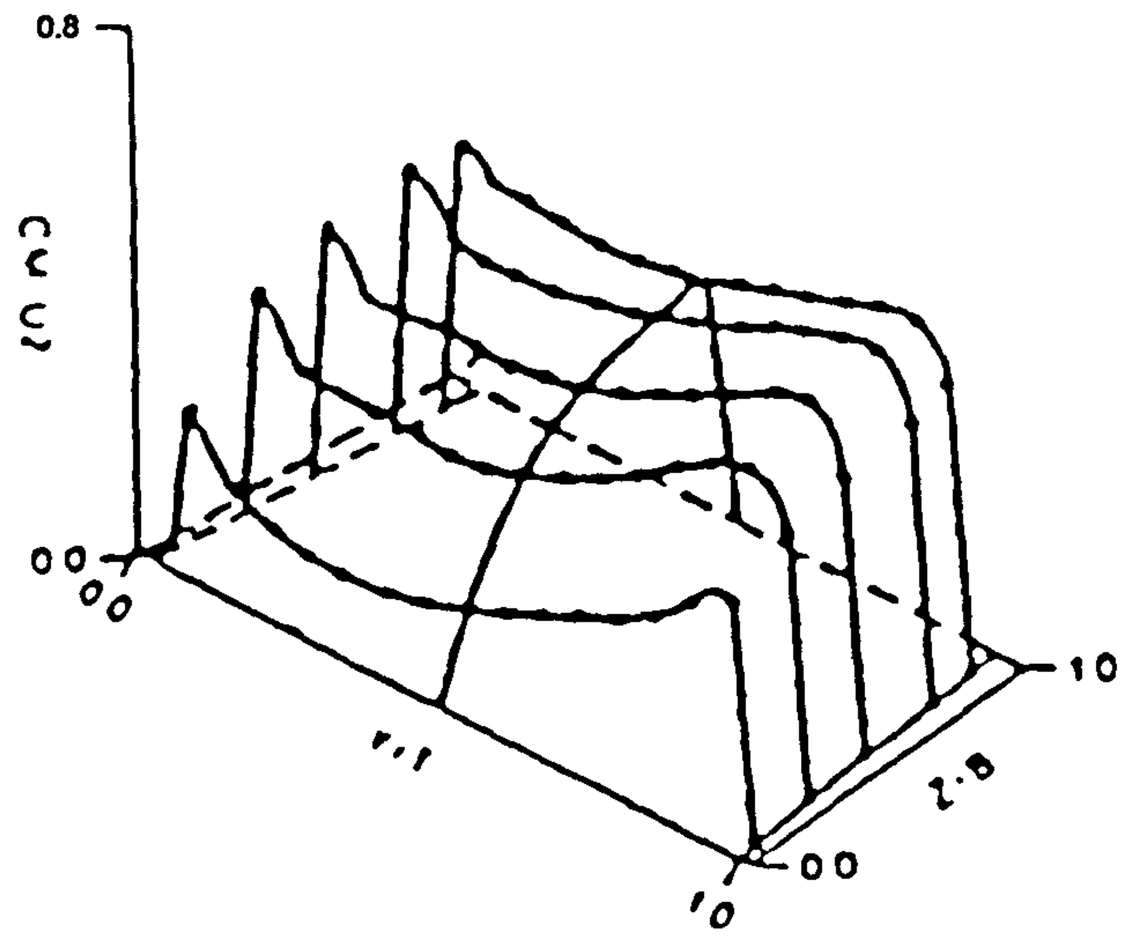

Design condition Plane IV

Figure 7.16 : Backswept impeller, design condition. Distribution of meridional velocity $V_m/(\Omega*R_2)$ at plane IV. (a) Measured. (b) Predicted. (c) Predicted by Hah et al (1988).

(a) *Exper.data*

(b) *Prediction*

(c) *Hah et al (1988)*

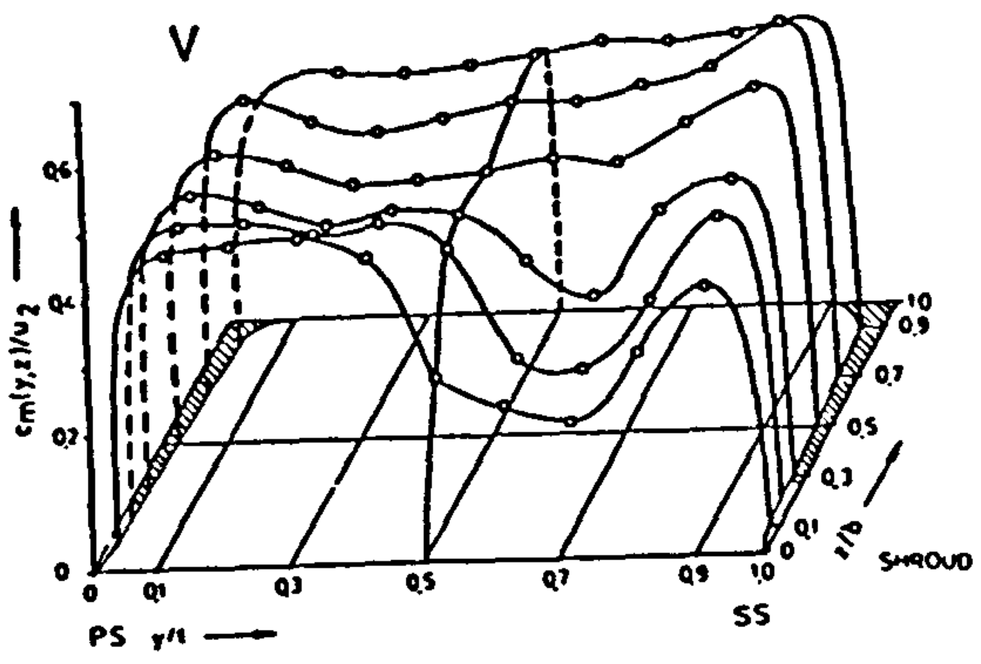

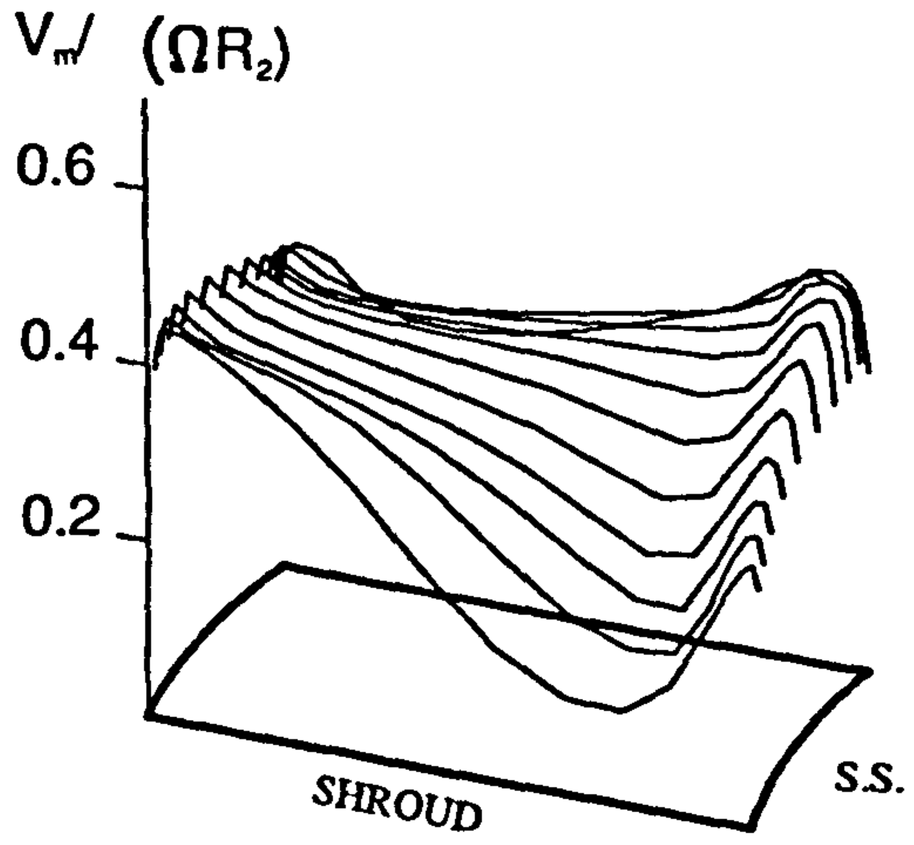

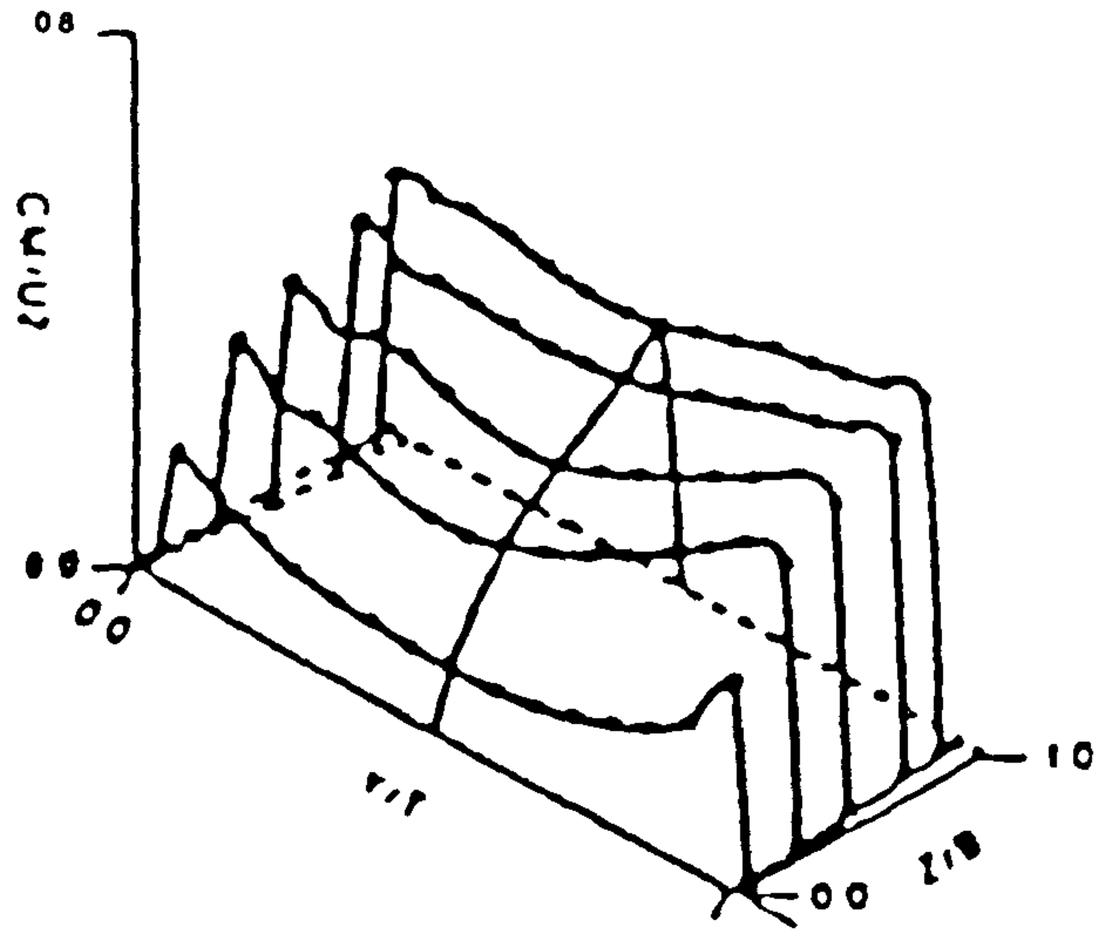

Design condition Plane V

Figure 7.17 : Backswept impeller, design condition. Distribution of meridional velocity $V_m/(\Omega * R_2)$ at plane V. (a) Measured. (b) Predicted. (c) Predicted by Hah et al (1988).

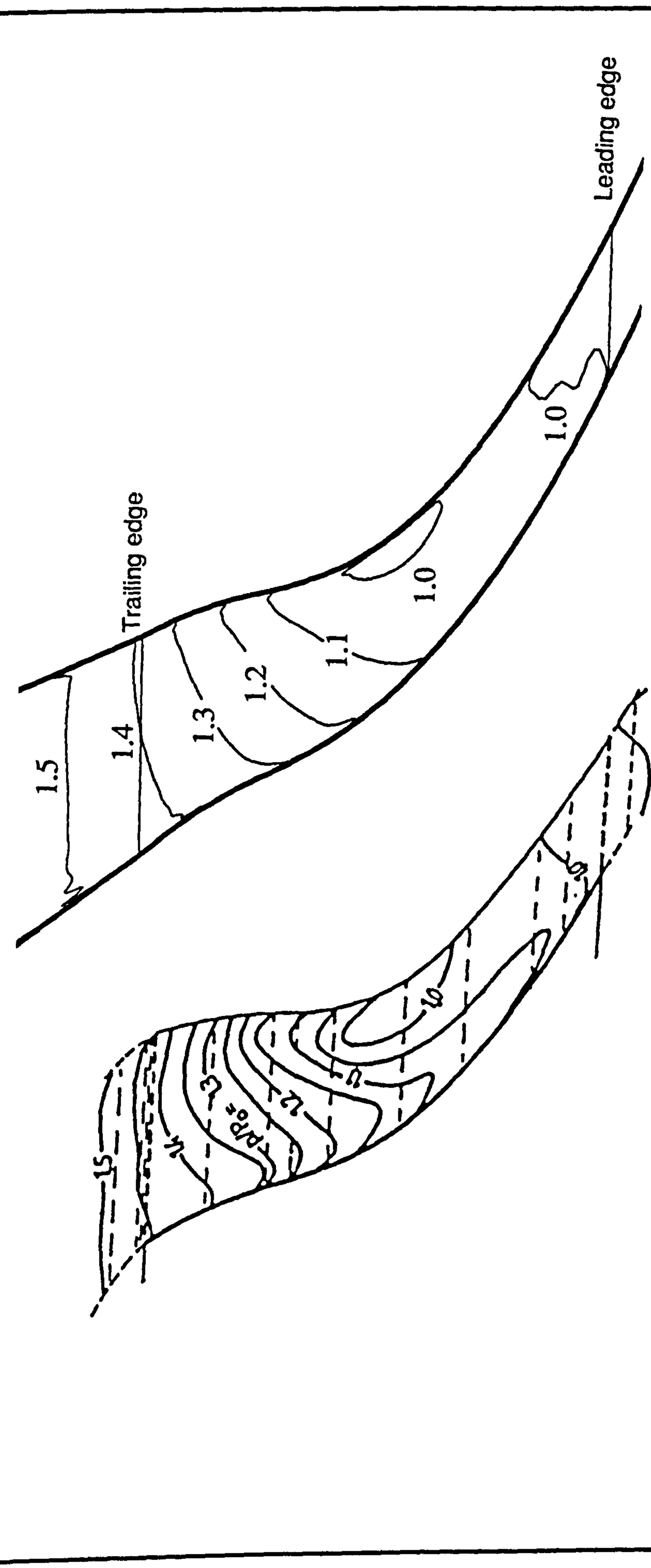

Figure 7.18a : Backswept impeller, design condition. Pressure distribution p/P_o on the shroud wall.

Eckardt Backswept Impeller
Design Condition
Pressure p/P Distribution

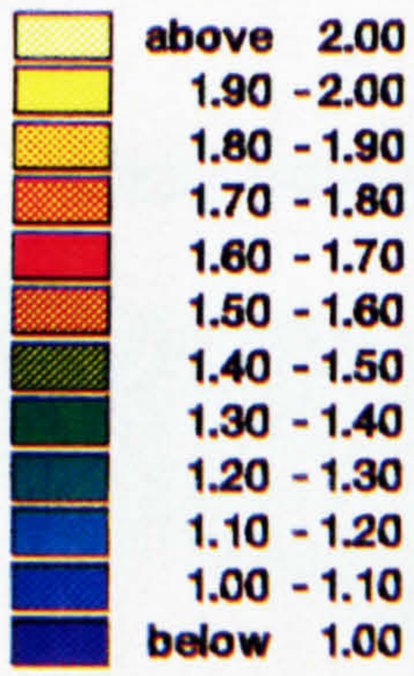

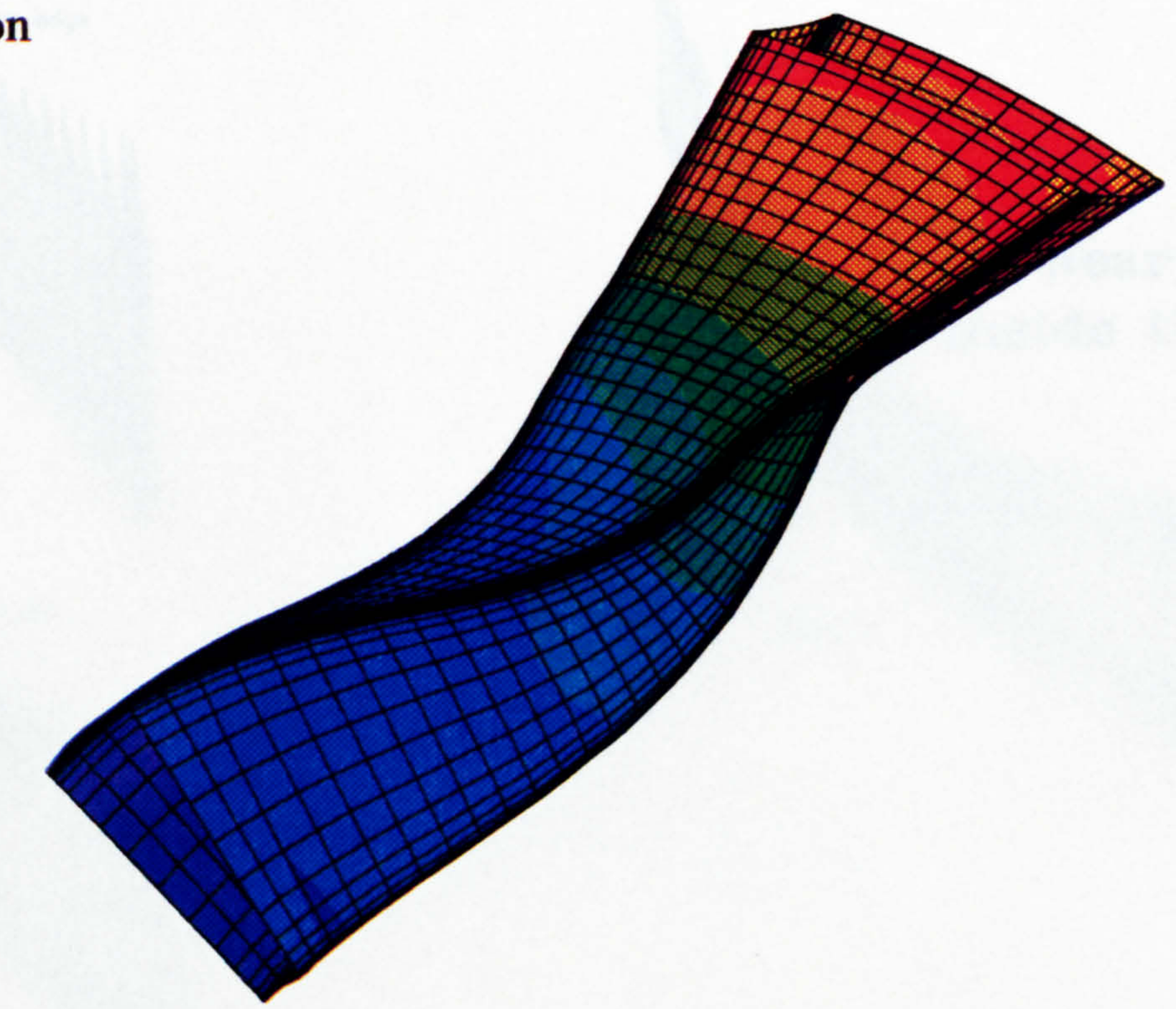

Figure 7.18b : Backswept impeller, design condition. Three dimensional pressure distribution p/P_0.

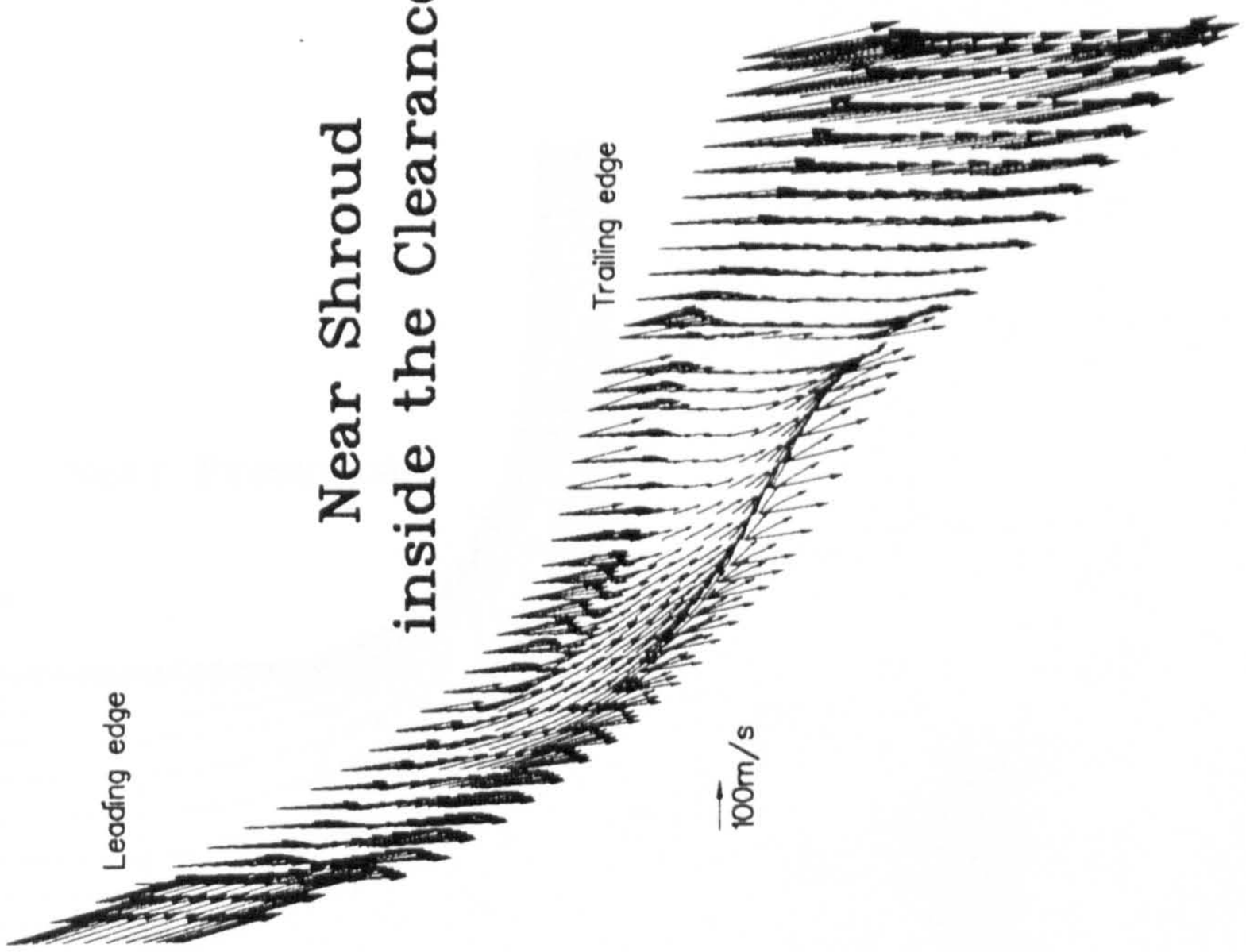

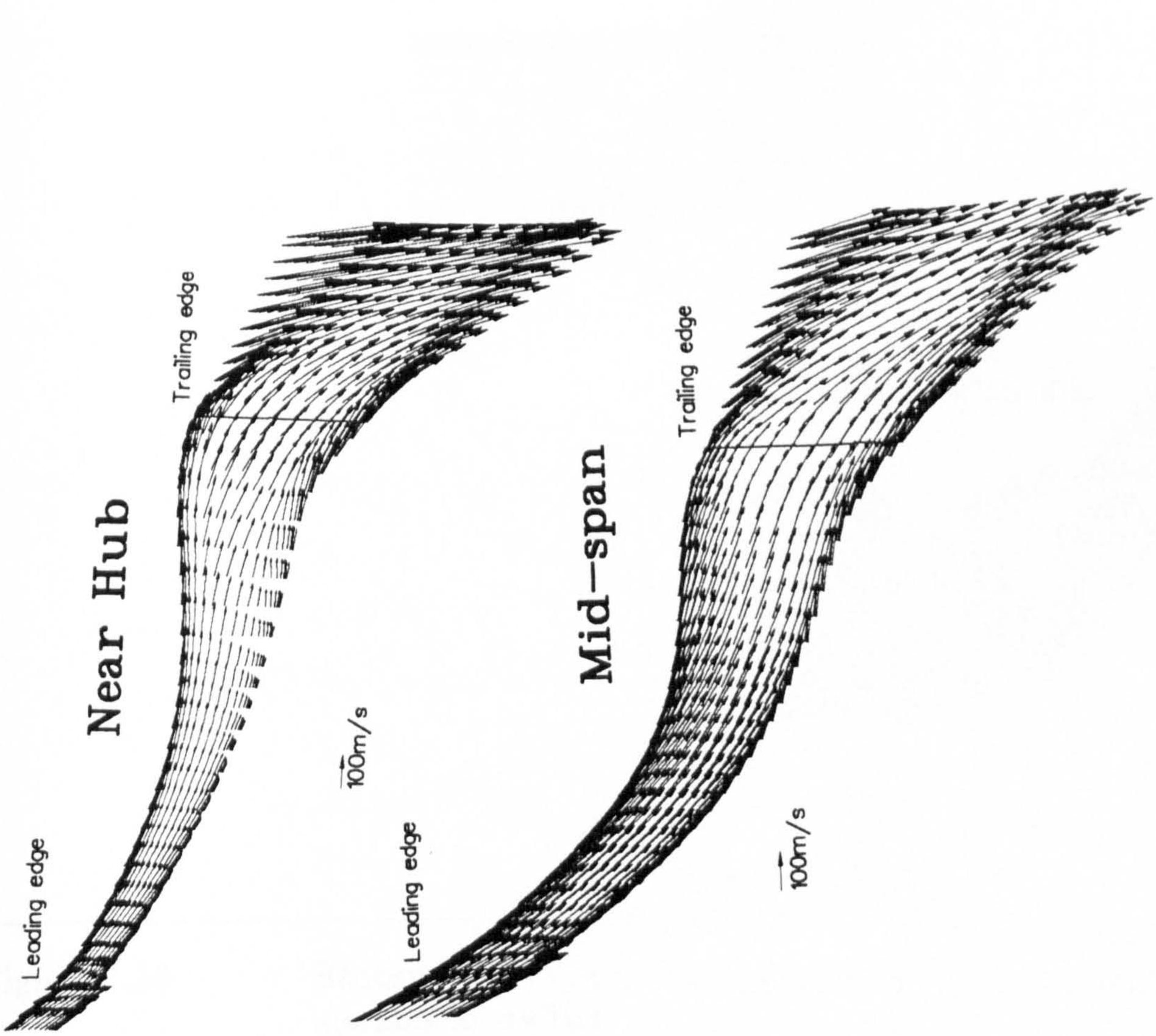

Figure 7.19 : Backswept impeller, design condition. Velocity vectors on blade-to-blade surfaces

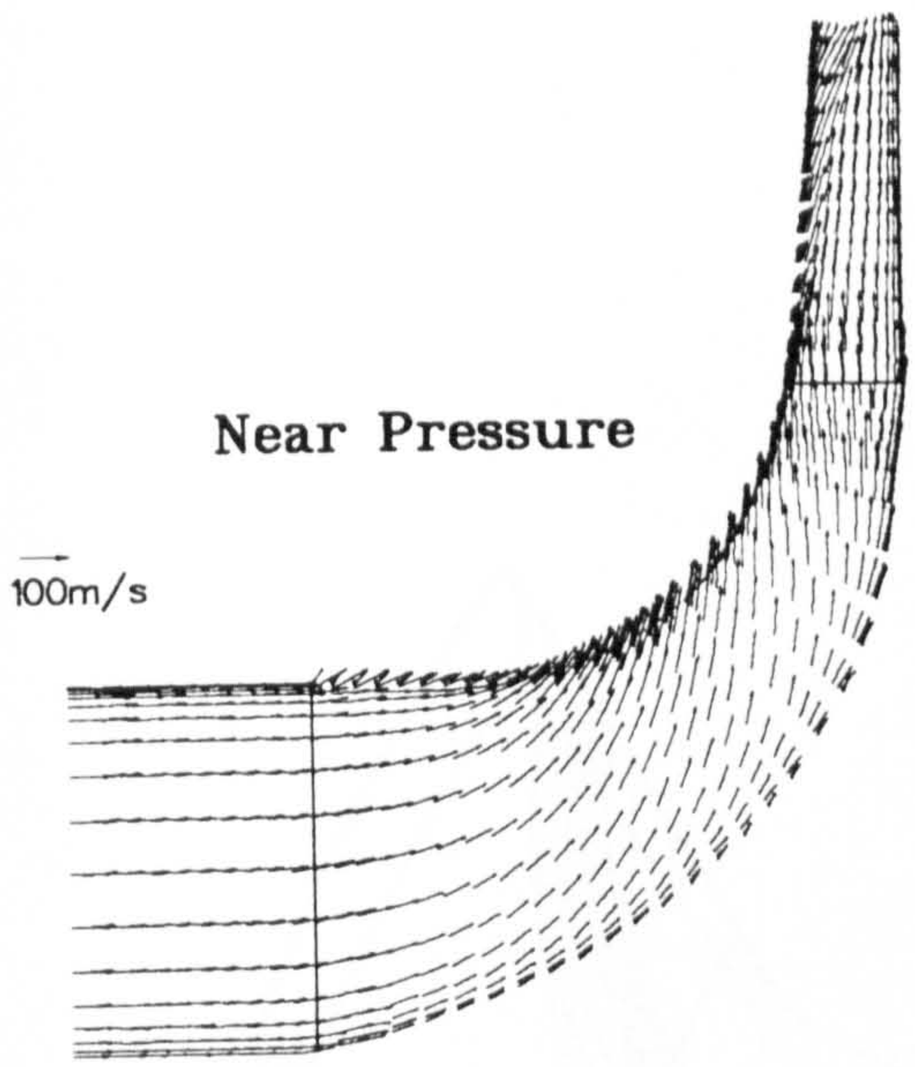

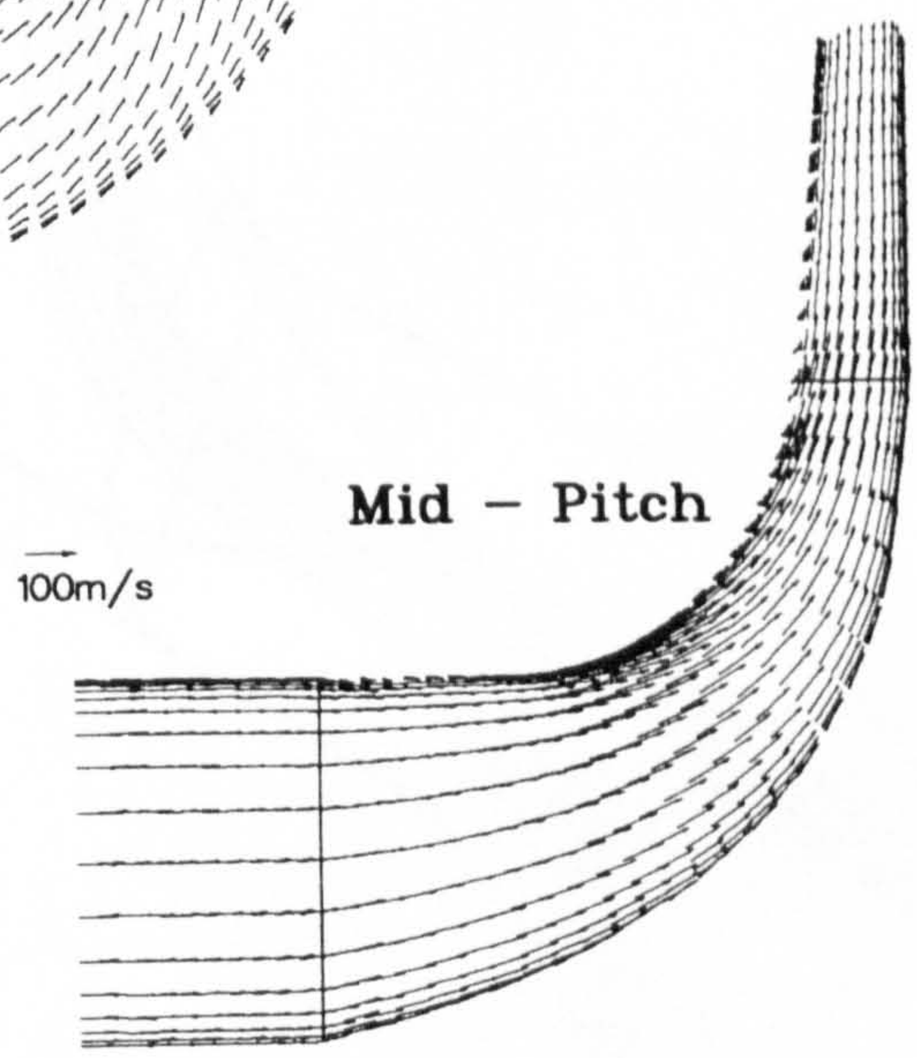

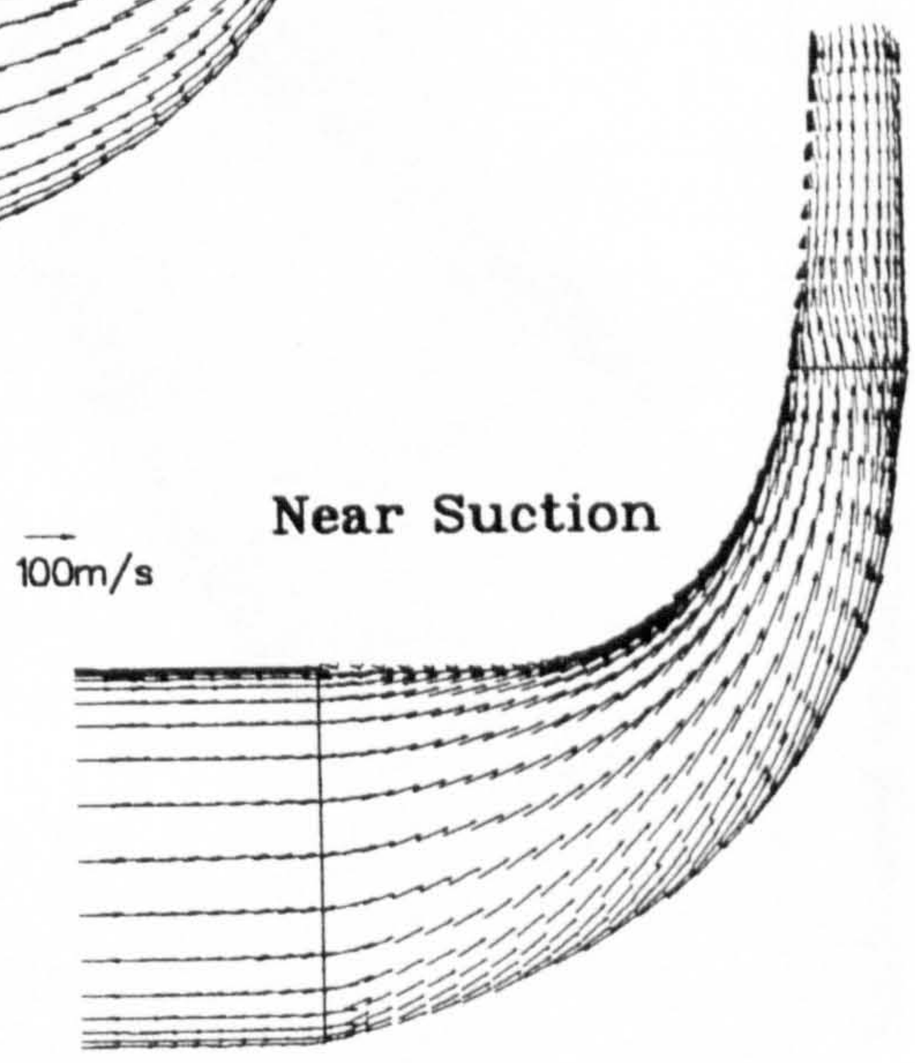

Figure 7.20 : Backswept impeller, design condition. Velocity vectors on meridional surfaces.

Eckardt Backswept Impeller

Design condition

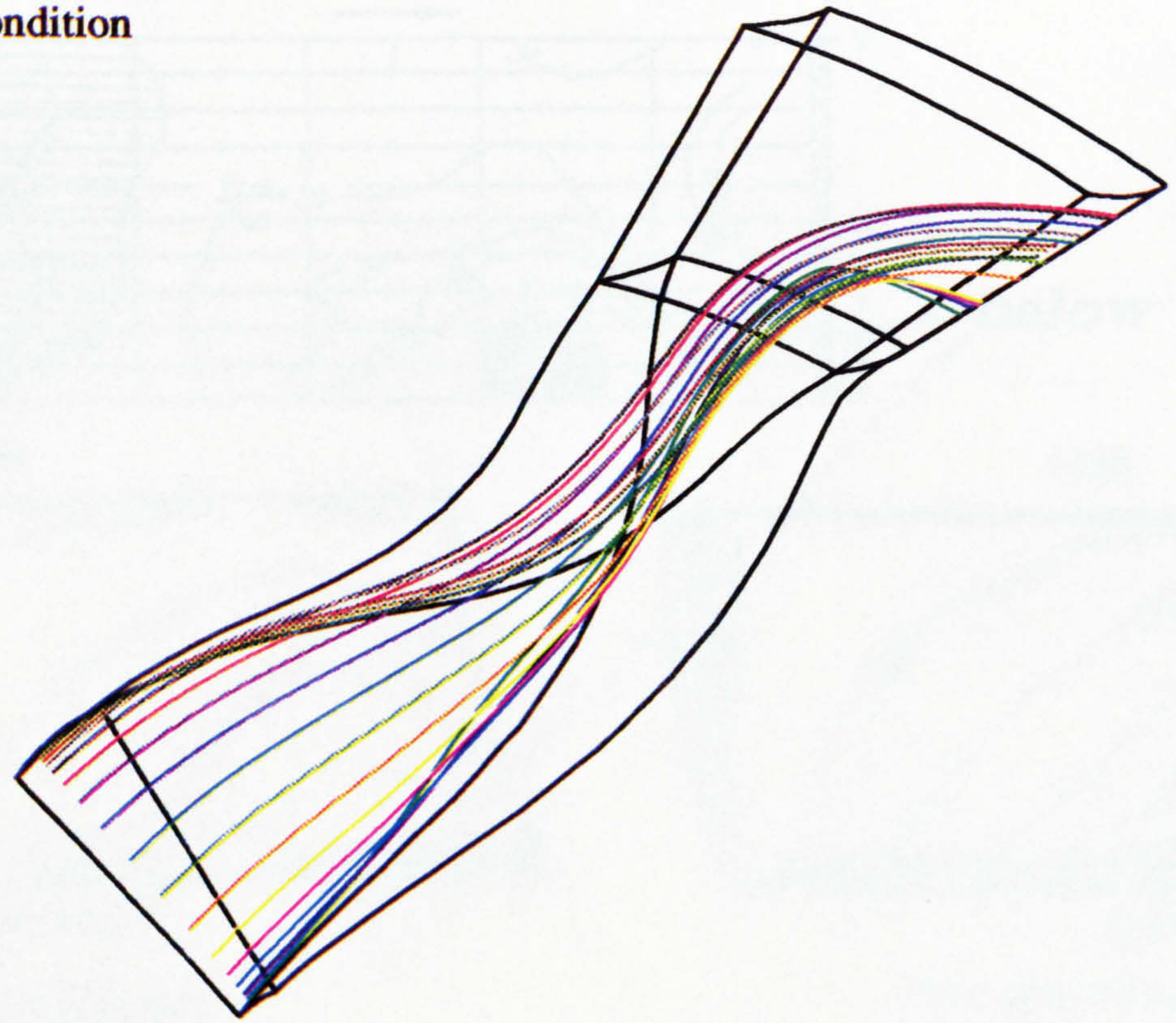

Figure 7.21 : Backswept impeller, design condition. Predicted streamlines.

Experimental data
1% tip leakage

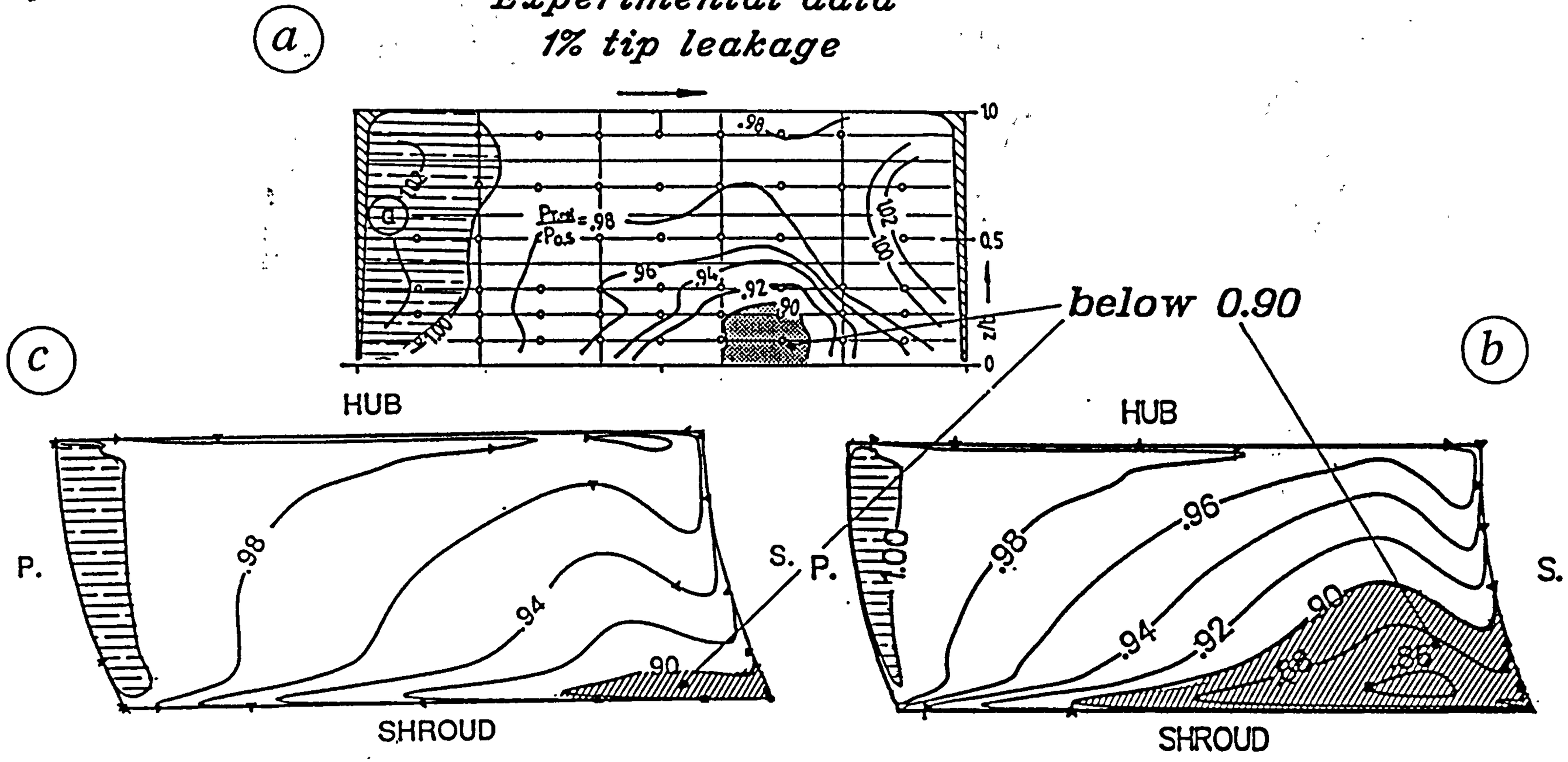

Figure 7.22 : Backswept impeller, choking condition. Distribution of P_{rel}/P_0 at the rotor exit.
(a) Measured, (b) Predicted with 1% tip leakage, (c) Predicted without tip leakage.

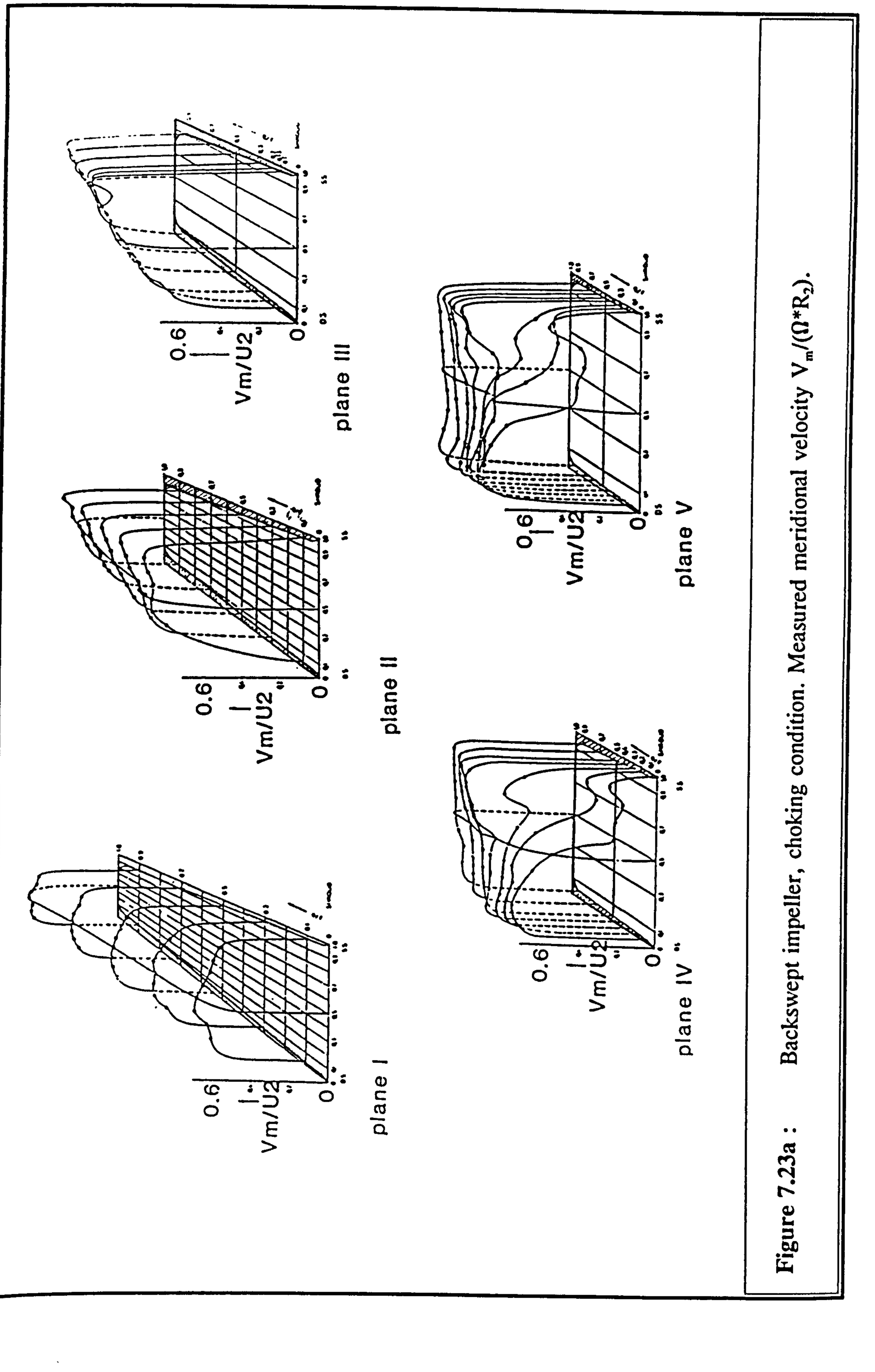

Figure 7.23a : Backswept impeller, choking condition. Measured meridional velocity $V_m/(\Omega*R_2)$.

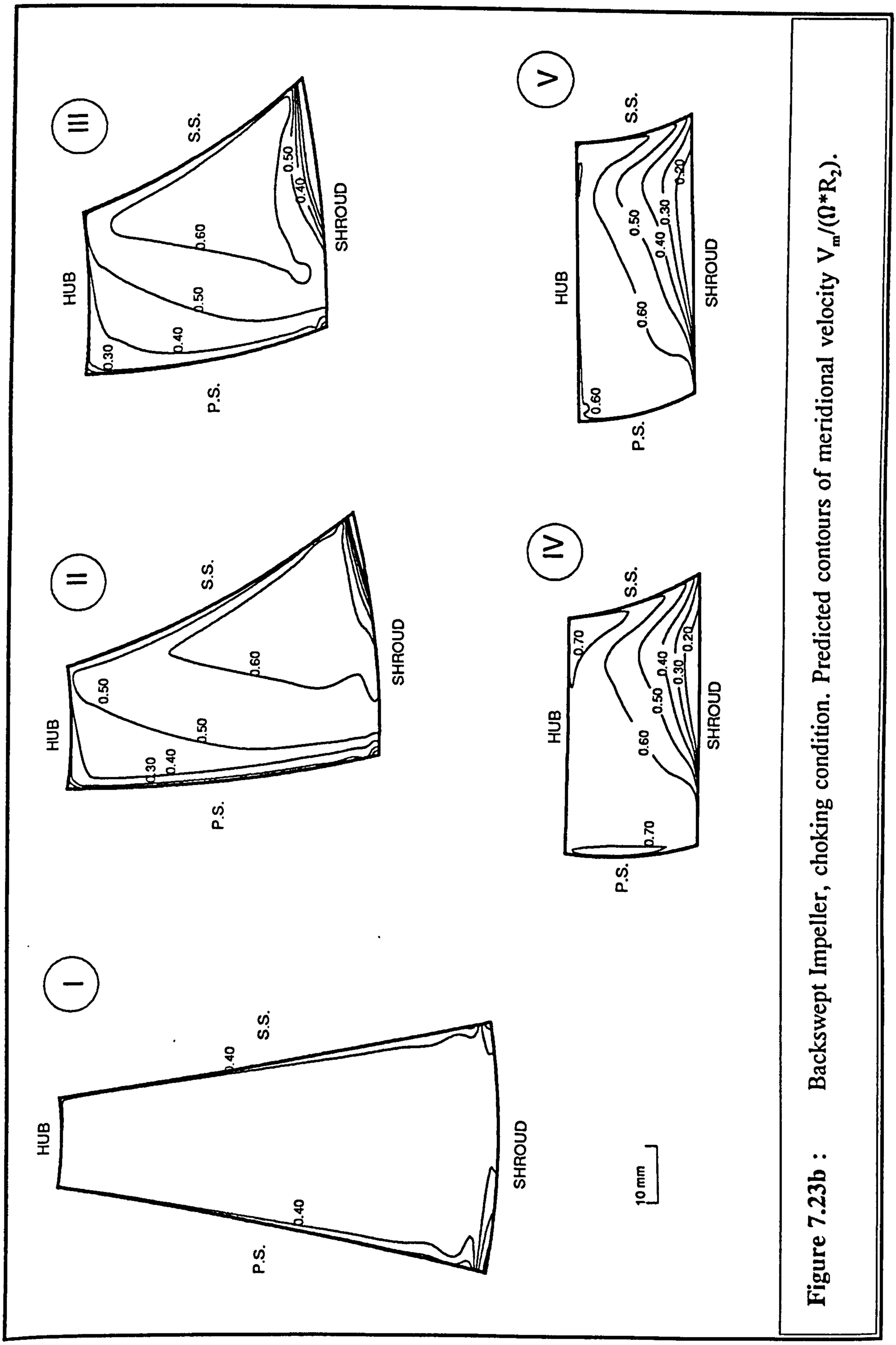

Figure 7.23b : Backswept Impeller, choking condition. Predicted contours of meridional velocity $V_m/(\Omega*R_2)$.

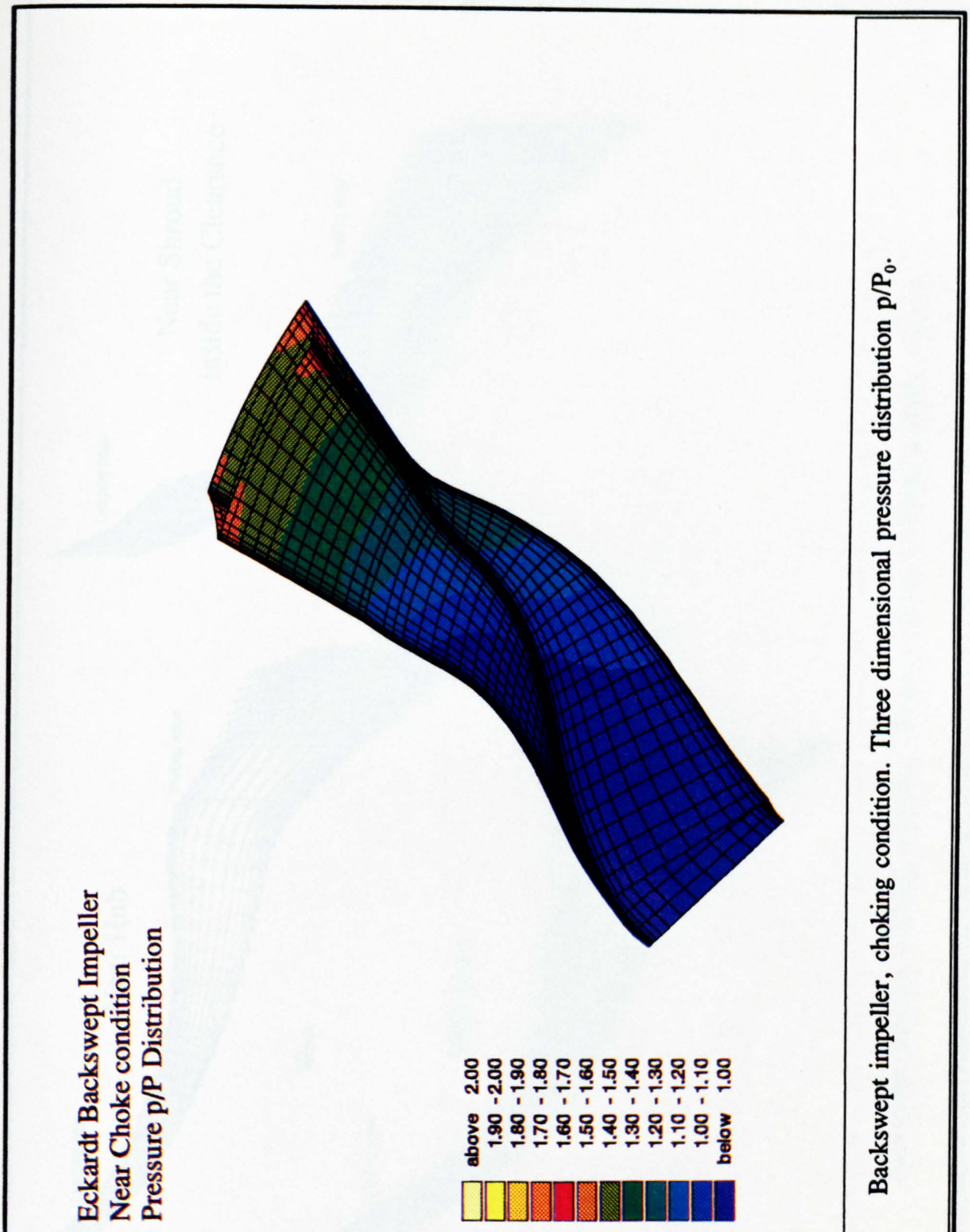

Figure 7.24 : Backswept impeller, choking condition. Three dimensional pressure distribution p/P_0.

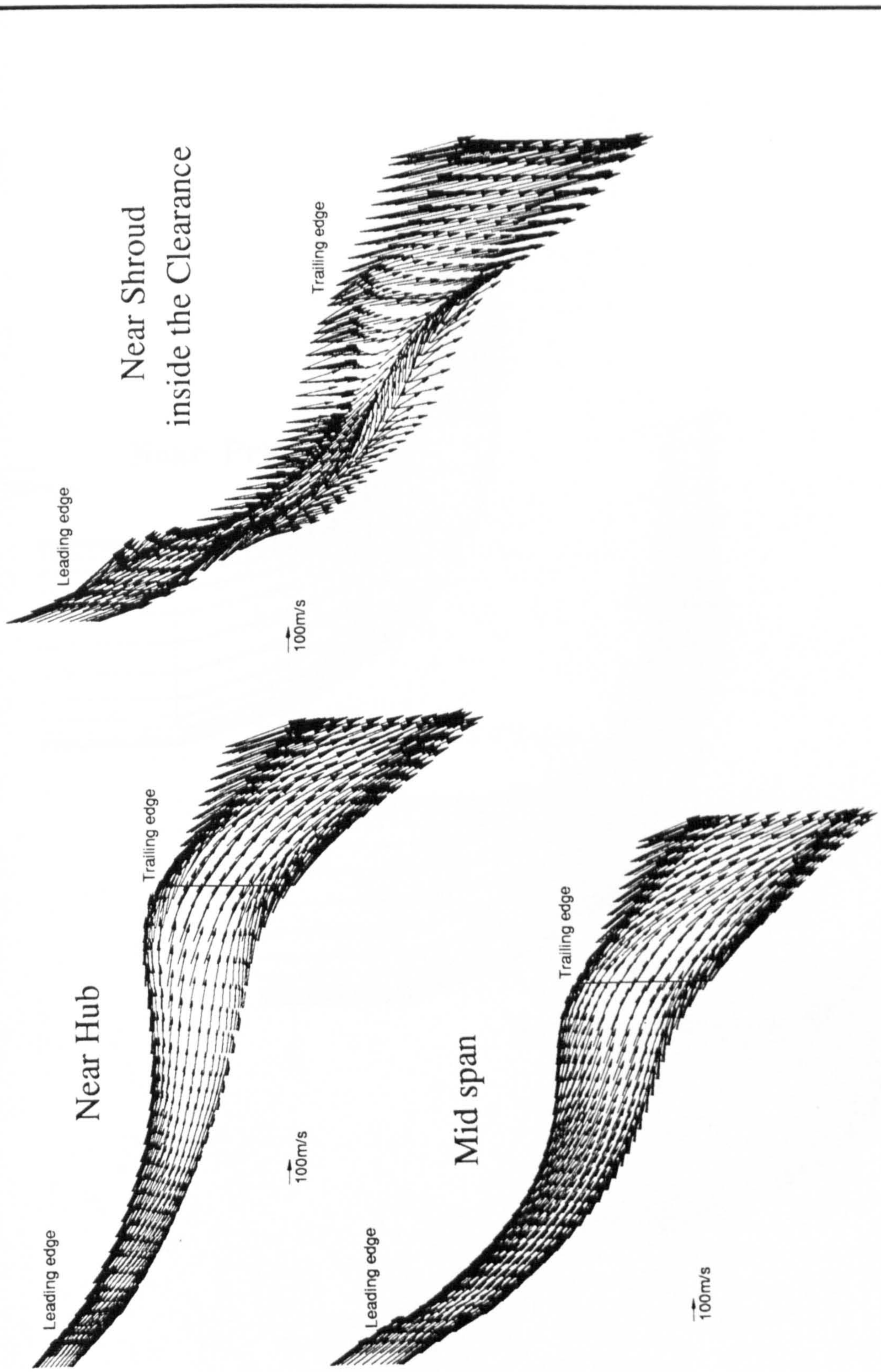

Figure 7.25 : Backswept impeller, choking condition. Velocity vectors on blade-to-blade surfaces.

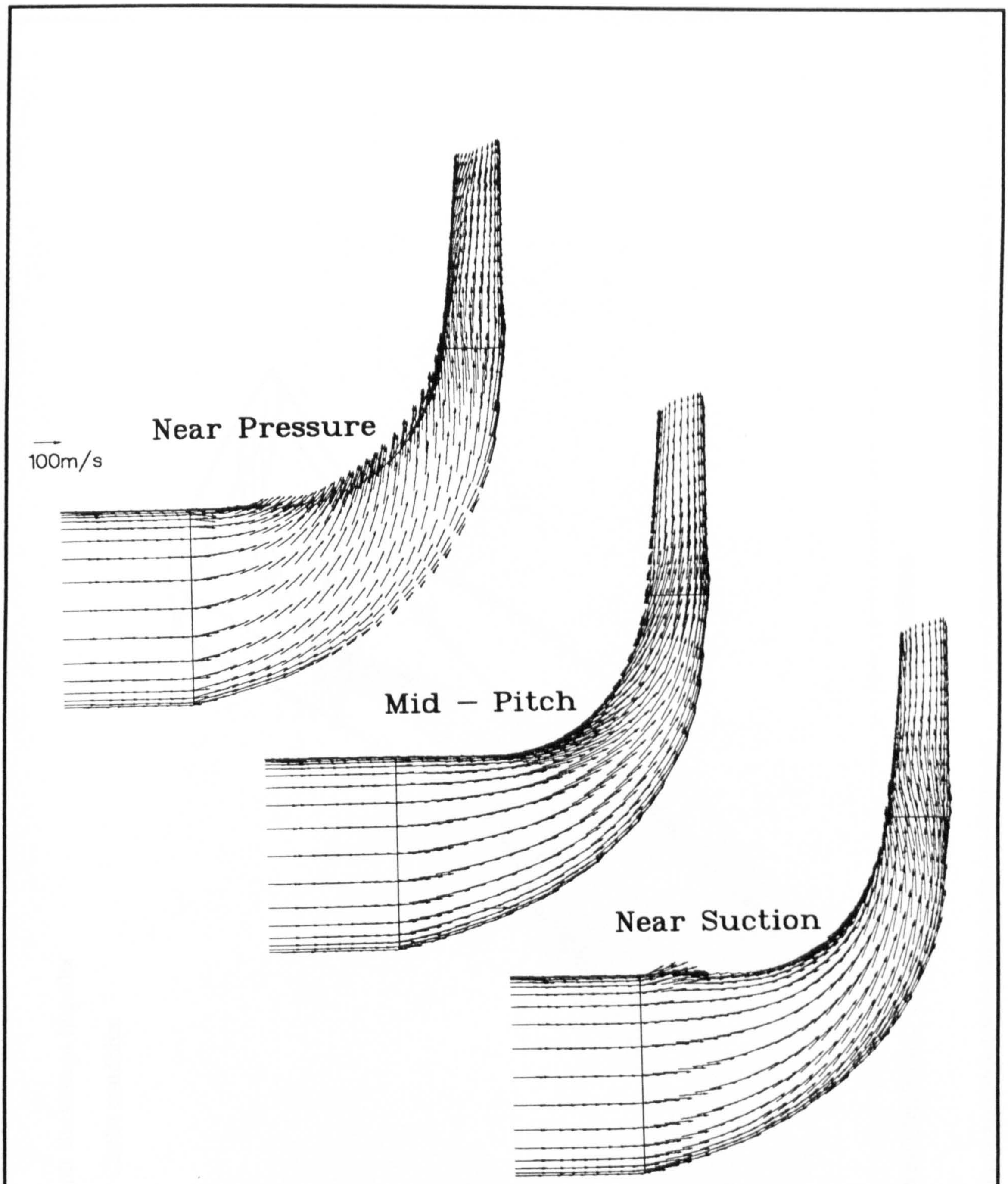

Figure 7.26 : Backswept impeller, choking condition. Velocity vectors on meridional surfaces.

Eckardt Backswept Impeller

Near Choke condition

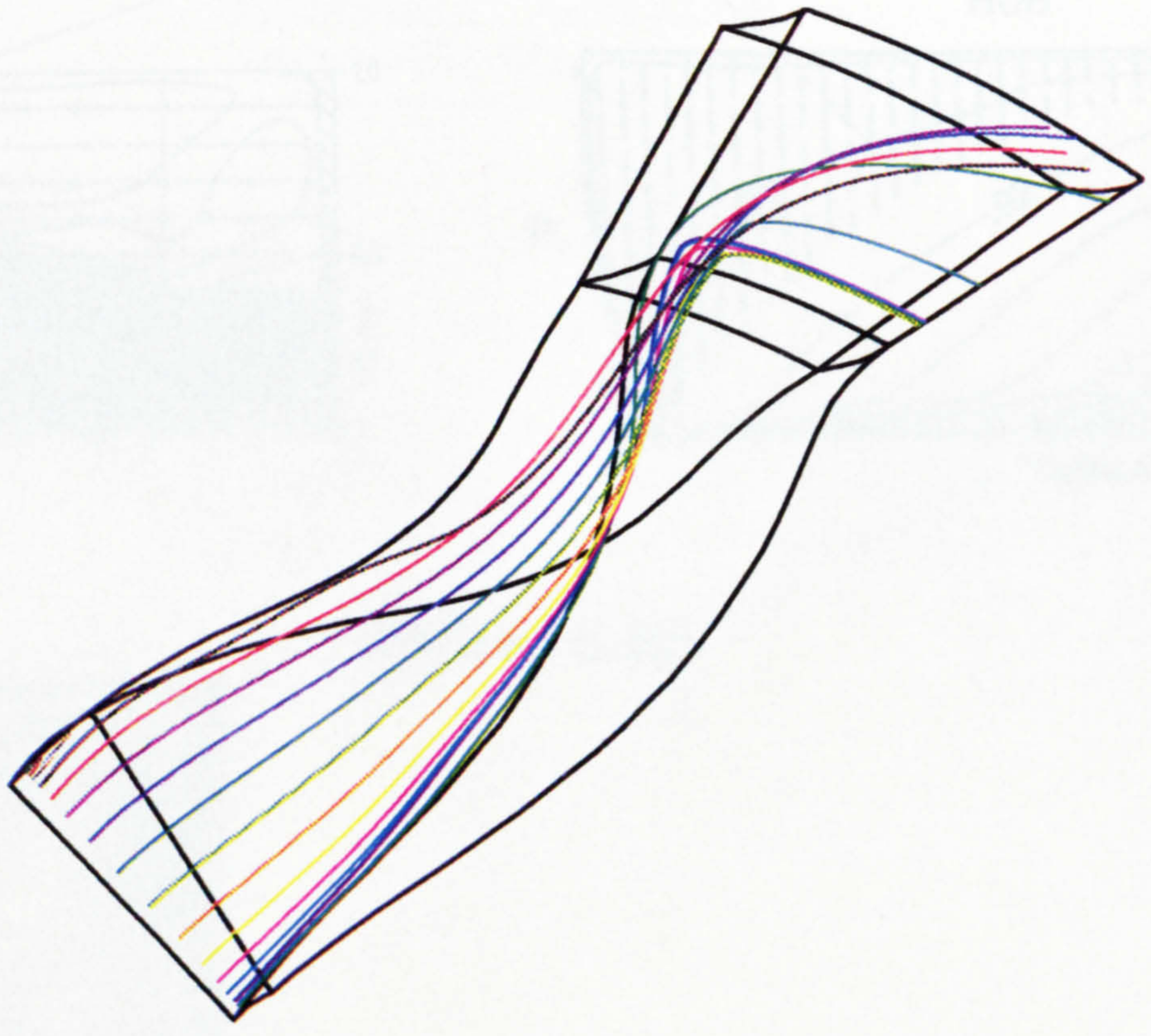

Figure 7.27 : Backswept impeller, choking condition. Predicted streamlines.

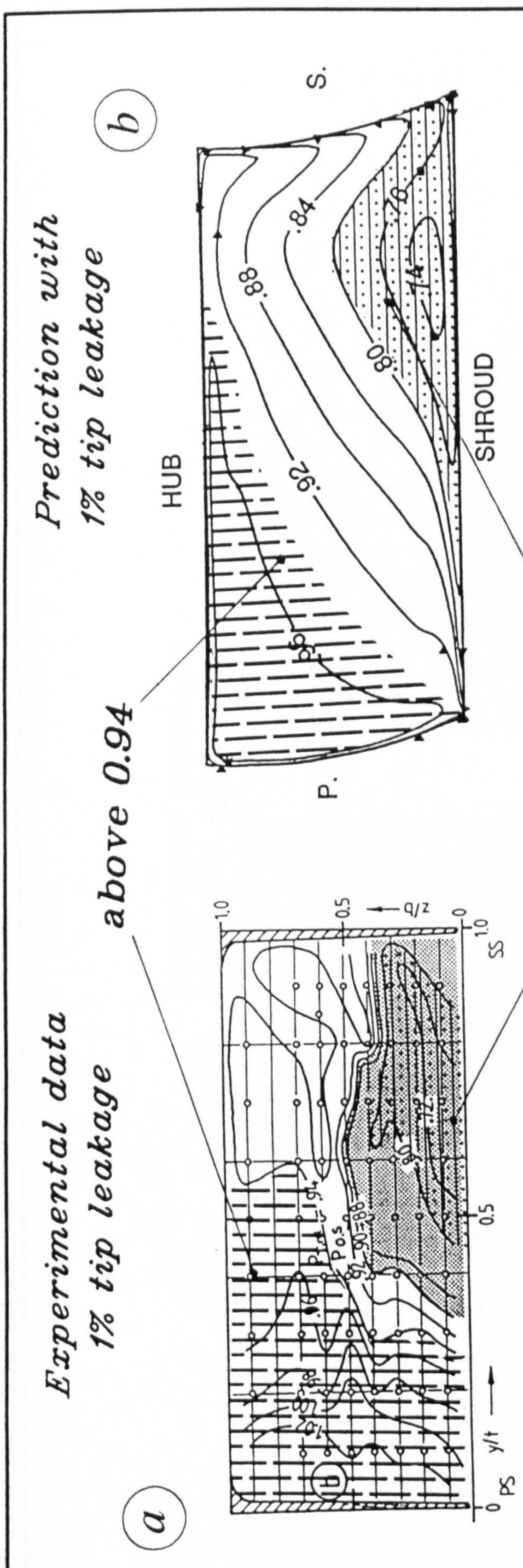

Figure 7.28 : Backswept impeller, choking condition. Distribution of P_{rel}/P_0 at the rotor exit. (a) Measured. (b) Predicted with 1 % tip leakage. (c) Predicted by Dawes (1987).

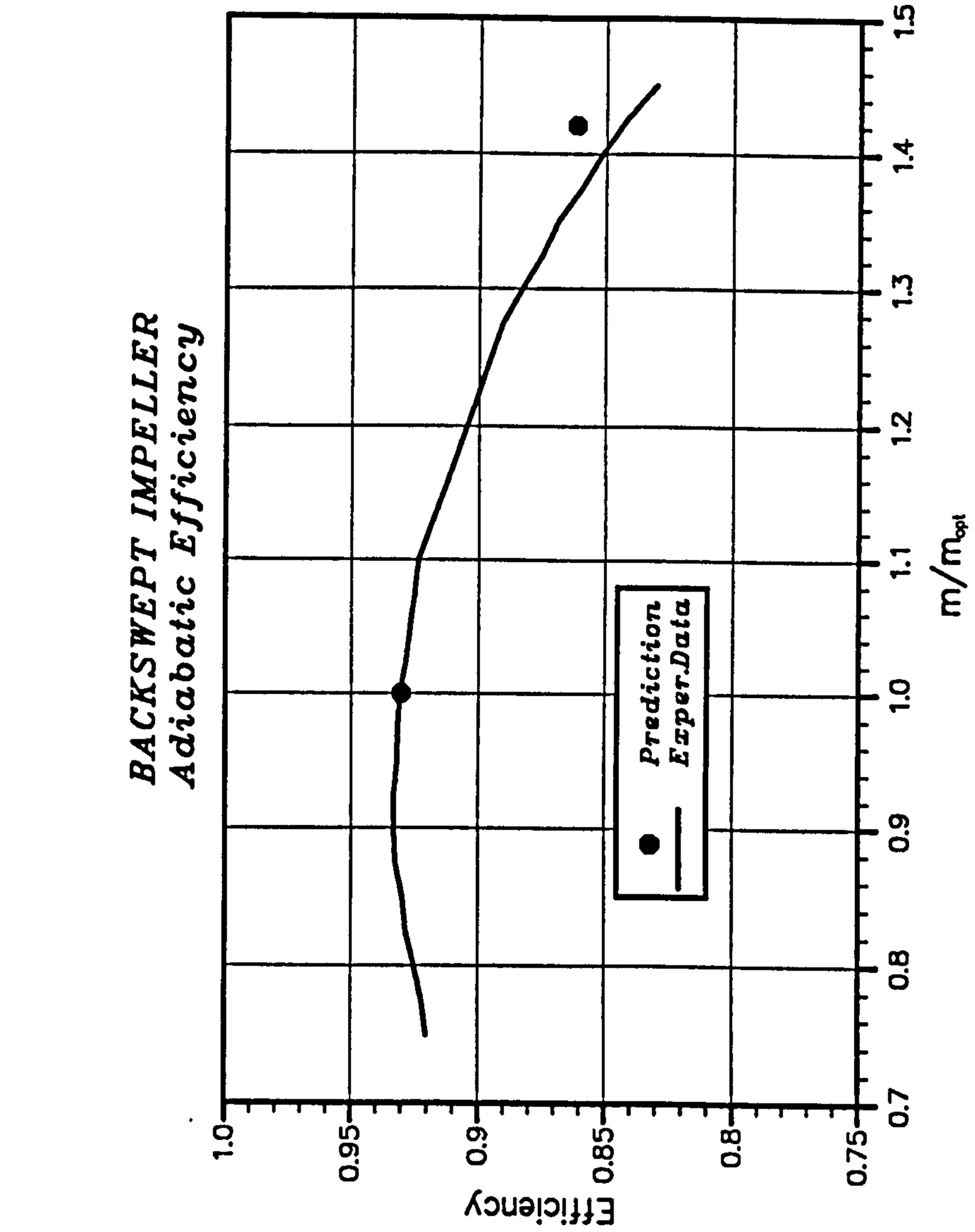

Backswept impeller, adiabatic efficiency.

Figure 7.29 :

(a)

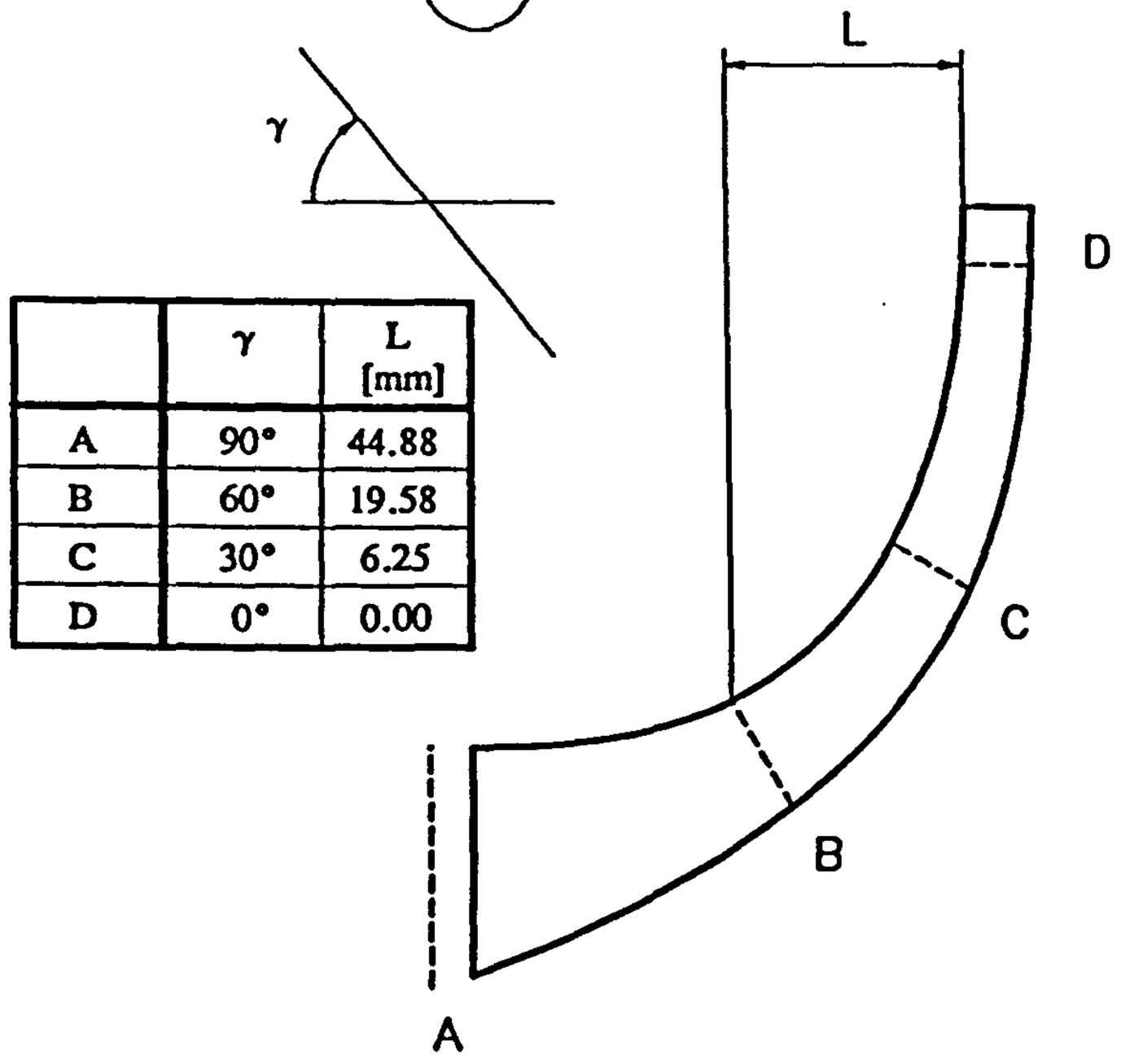

	γ	L [mm]
A	90°	44.88
B	60°	19.58
C	30°	6.25
D	0°	0.00

Measurement Planes

(b)

2–D measurements of:

– absolute velocity
– absolute flow angle

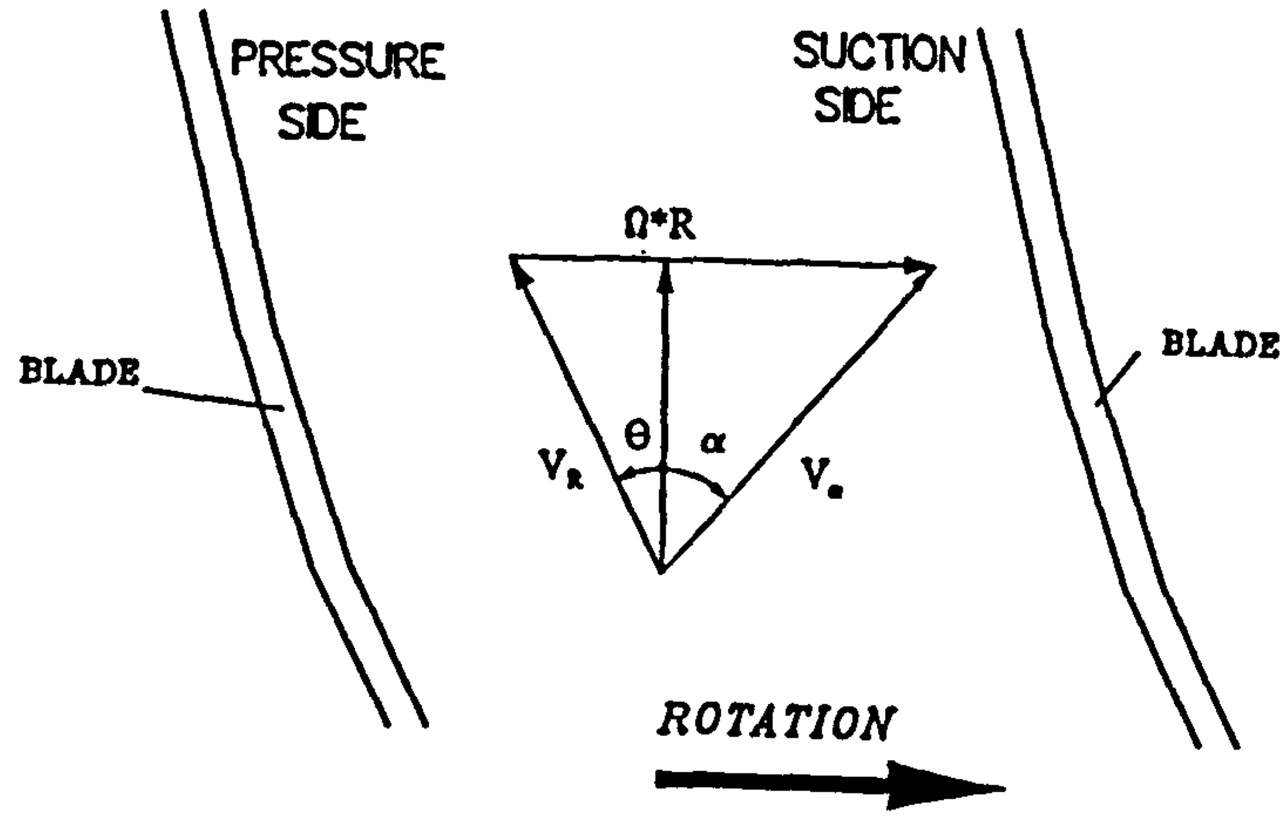

Figure 7.30 : GEM impeller. (a) Measurement Planes. (b) Velocity triangle.

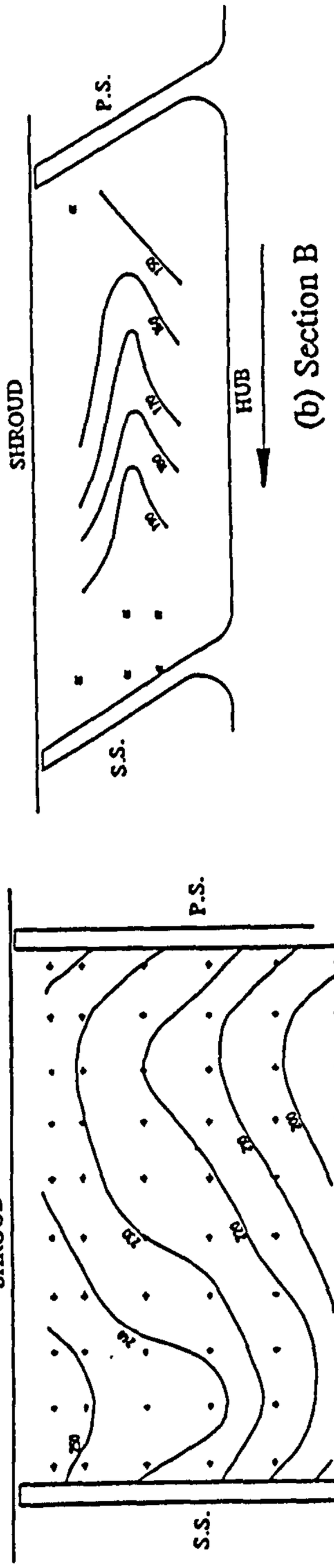

Figure 7.31a : GEM impeller, peak efficiency condition. Measured relative velocity V_R distribution in m/s.

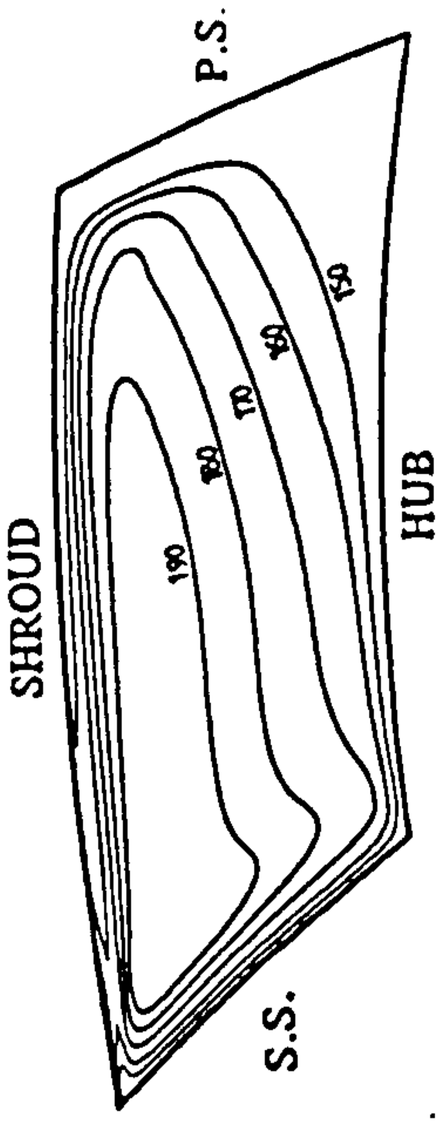

(b) Section B

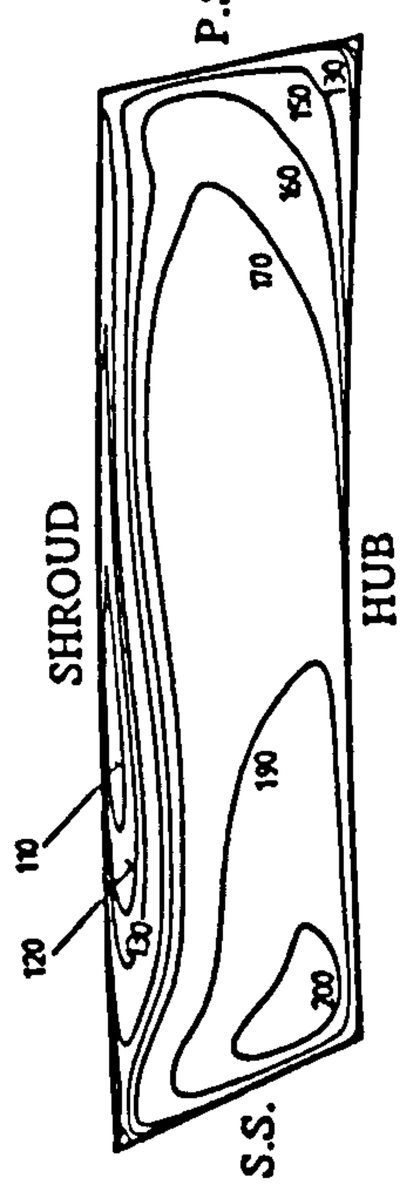

(c) Section C

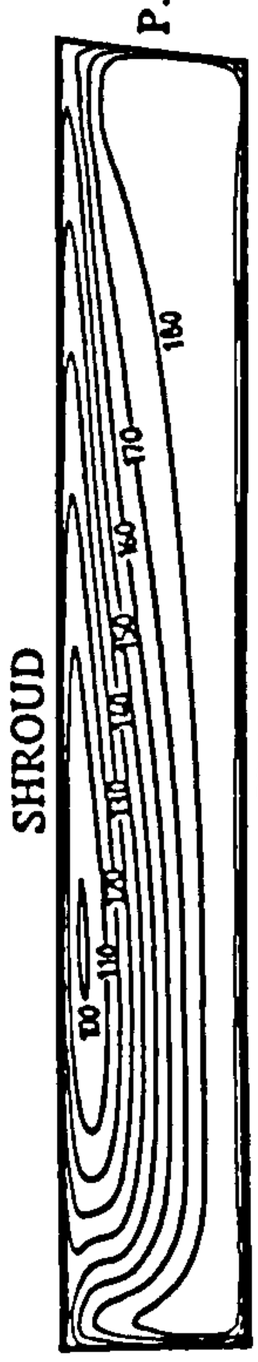

(d) Section D

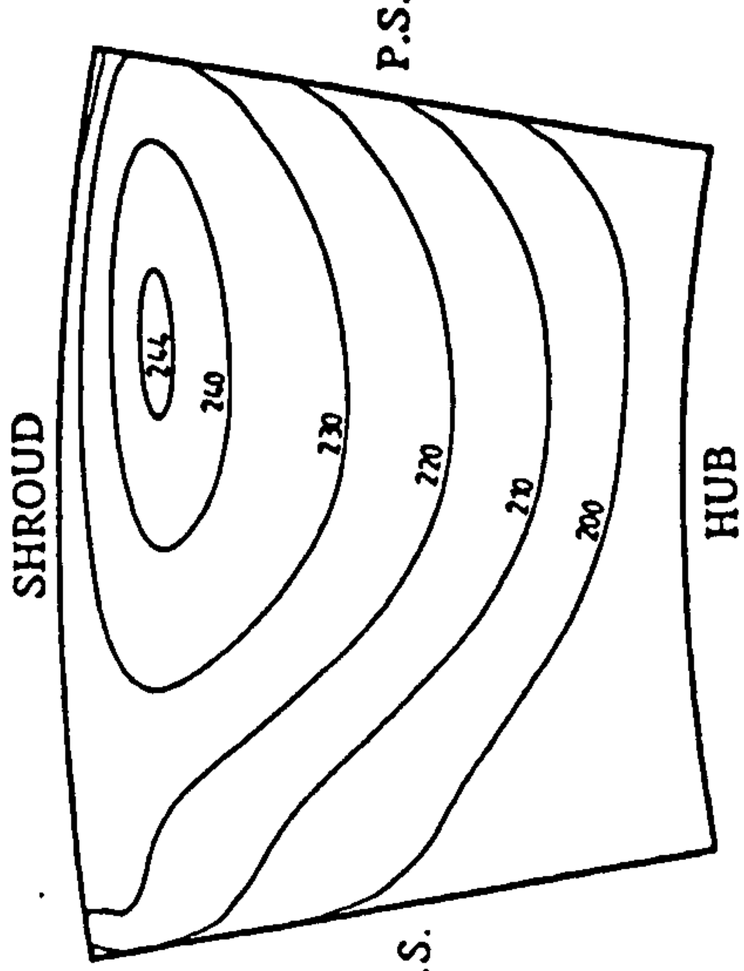

(a) Section A

Figure 7.31b : GEM impeller, peak efficiency condition. Predicted relative velocity V_R distribution in m/s.

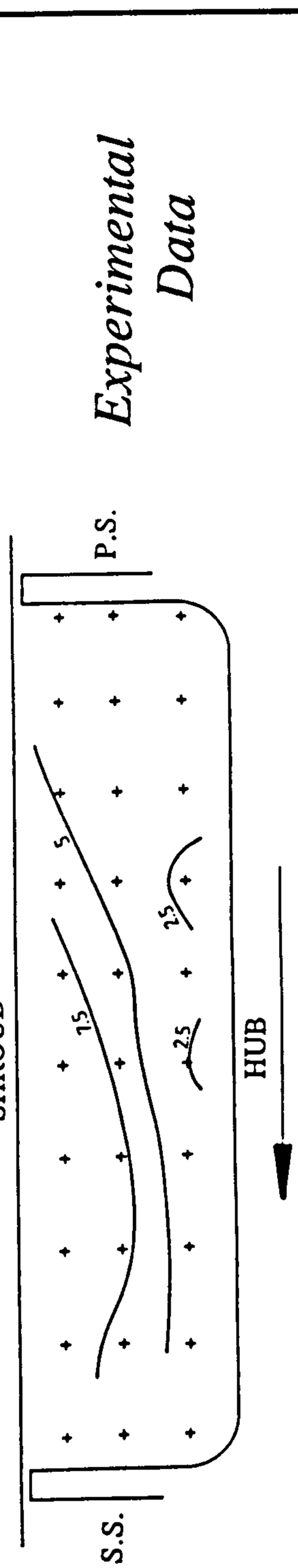

Figure 7.32 : GEM impeller, peak efficiency condition. Turbulence intensity % at section C.

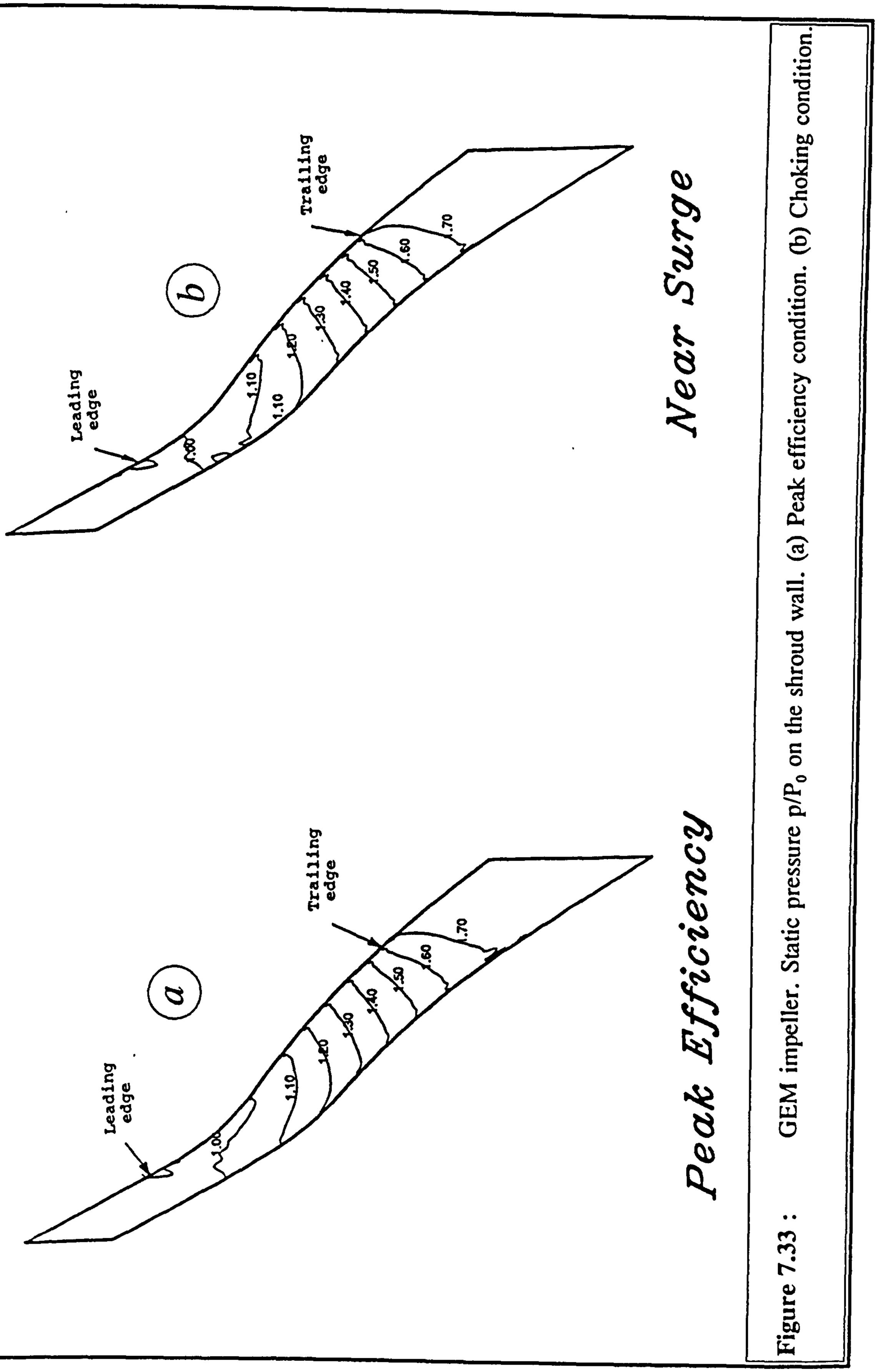

Figure 7.33 : GEM impeller. Static pressure p/P_0 on the shroud wall. (a) Peak efficiency condition. (b) Choking condition.

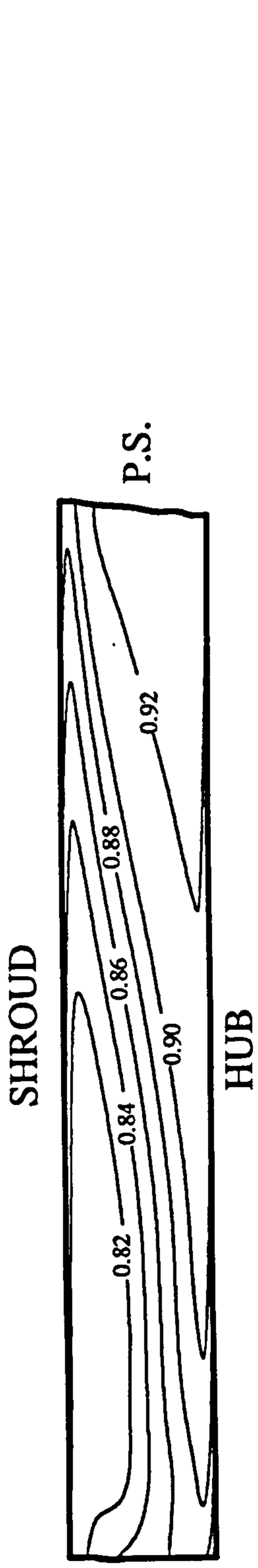

Figure 7.34 : GEM impeller, peak efficiency condition. Relative total pressure P_{rel}/P_0 at impeller exit.

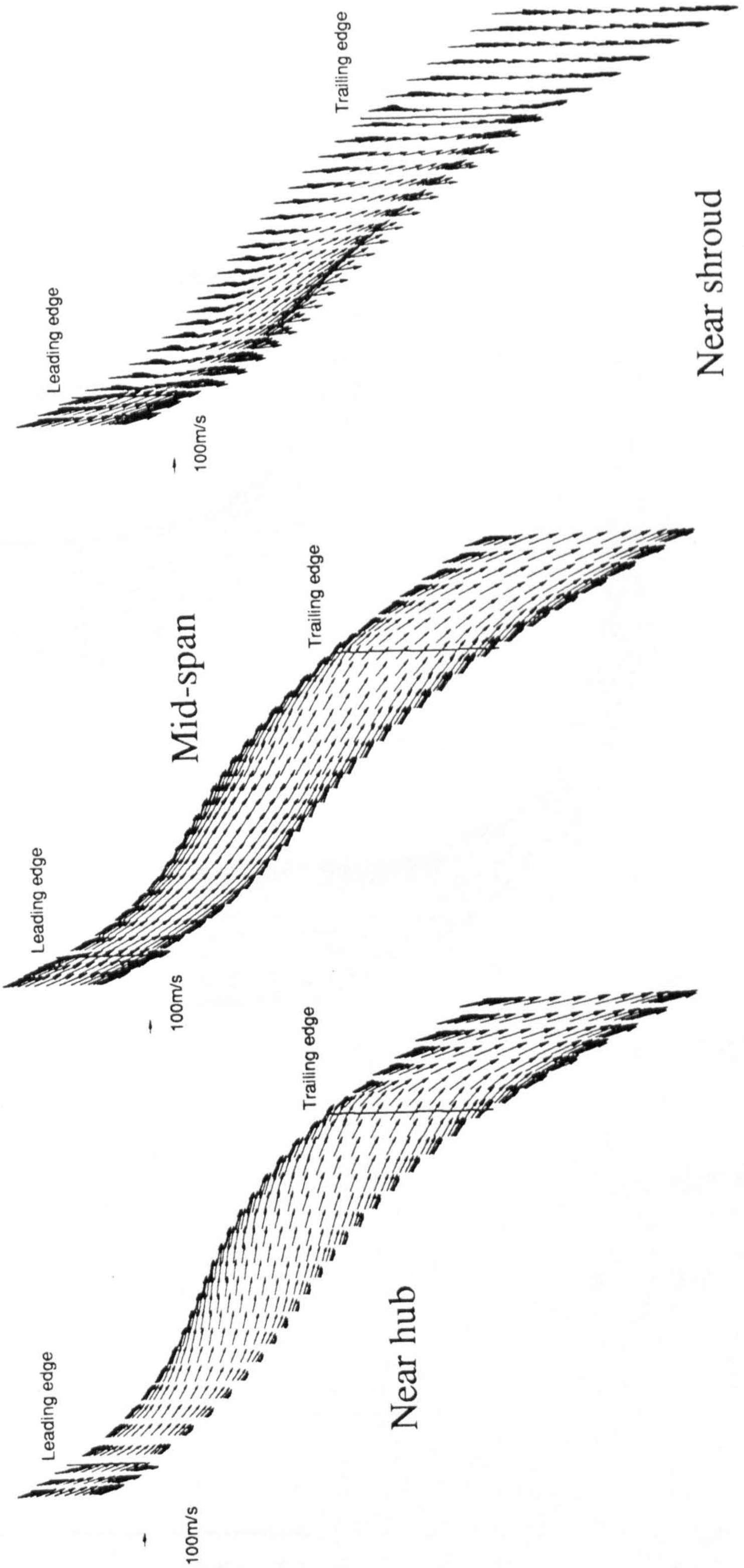

Figure 7.35 : GEM Impeller, peak efficiency condition. Velocity vectors on blade-to-blade surfaces.

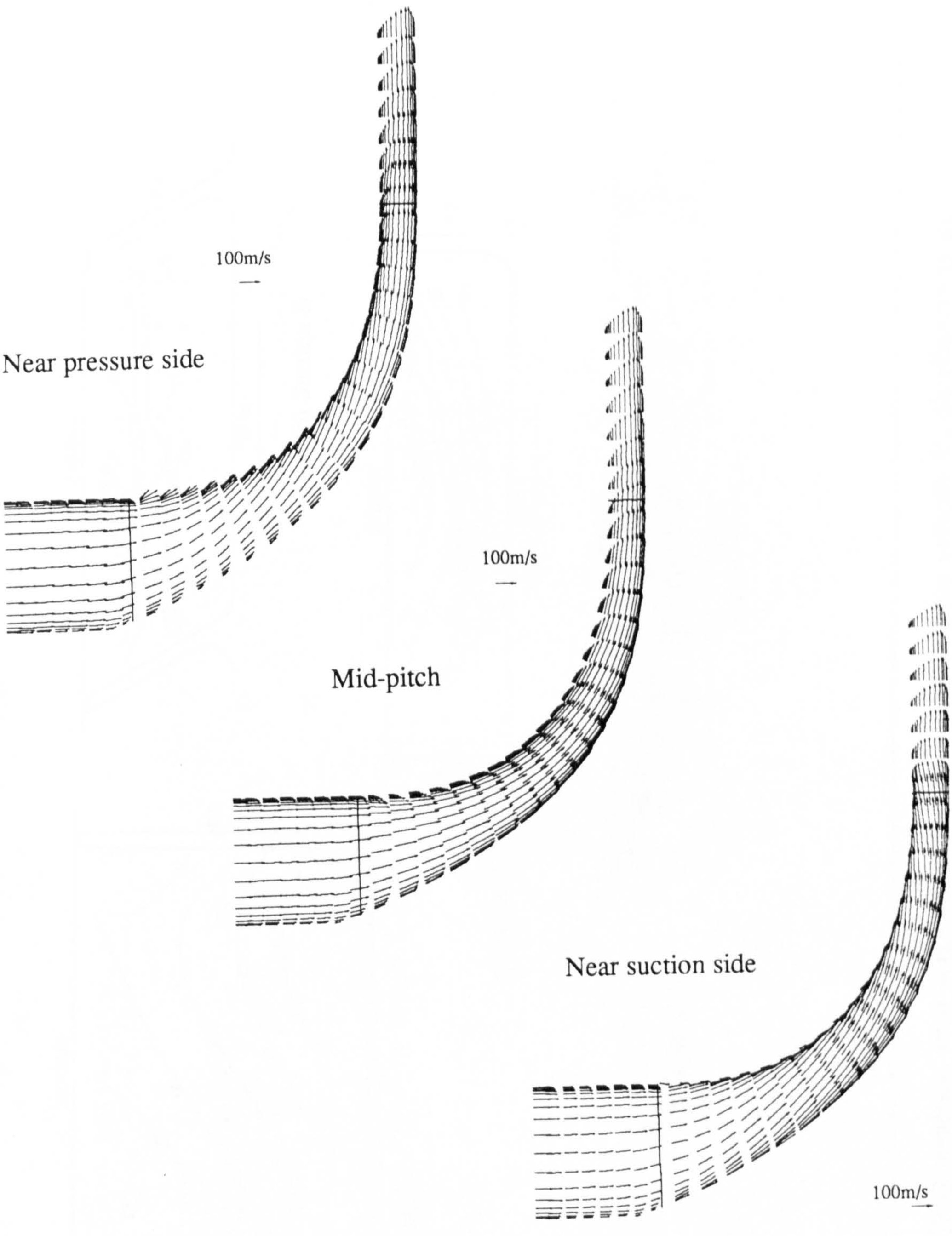

Figure 7.36 : GEM Impeller, peak efficiency condition. Velocity vectors on meridional surfaces.

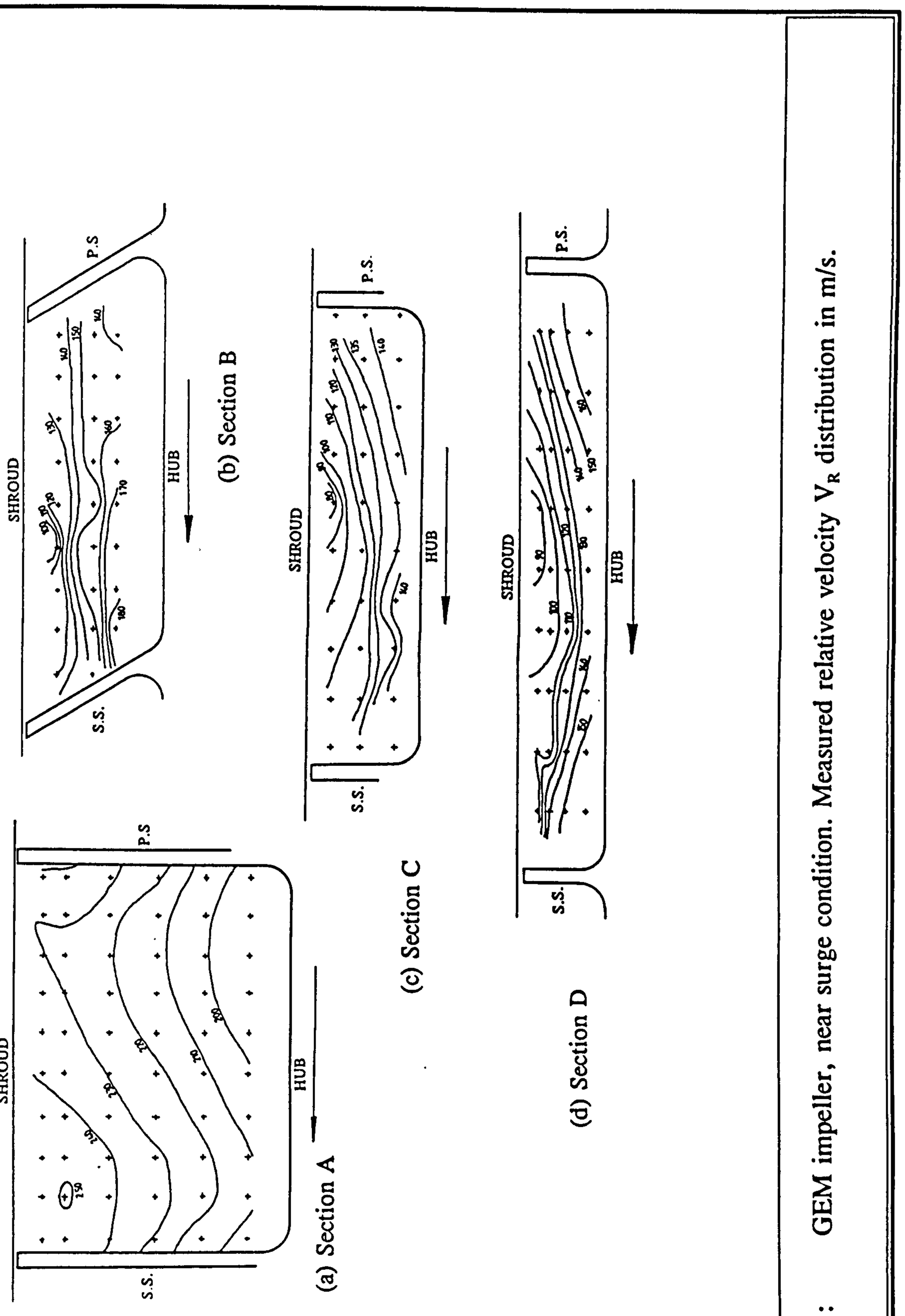

Figure 7.37a : GEM impeller, near surge condition. Measured relative velocity V_R distribution in m/s.

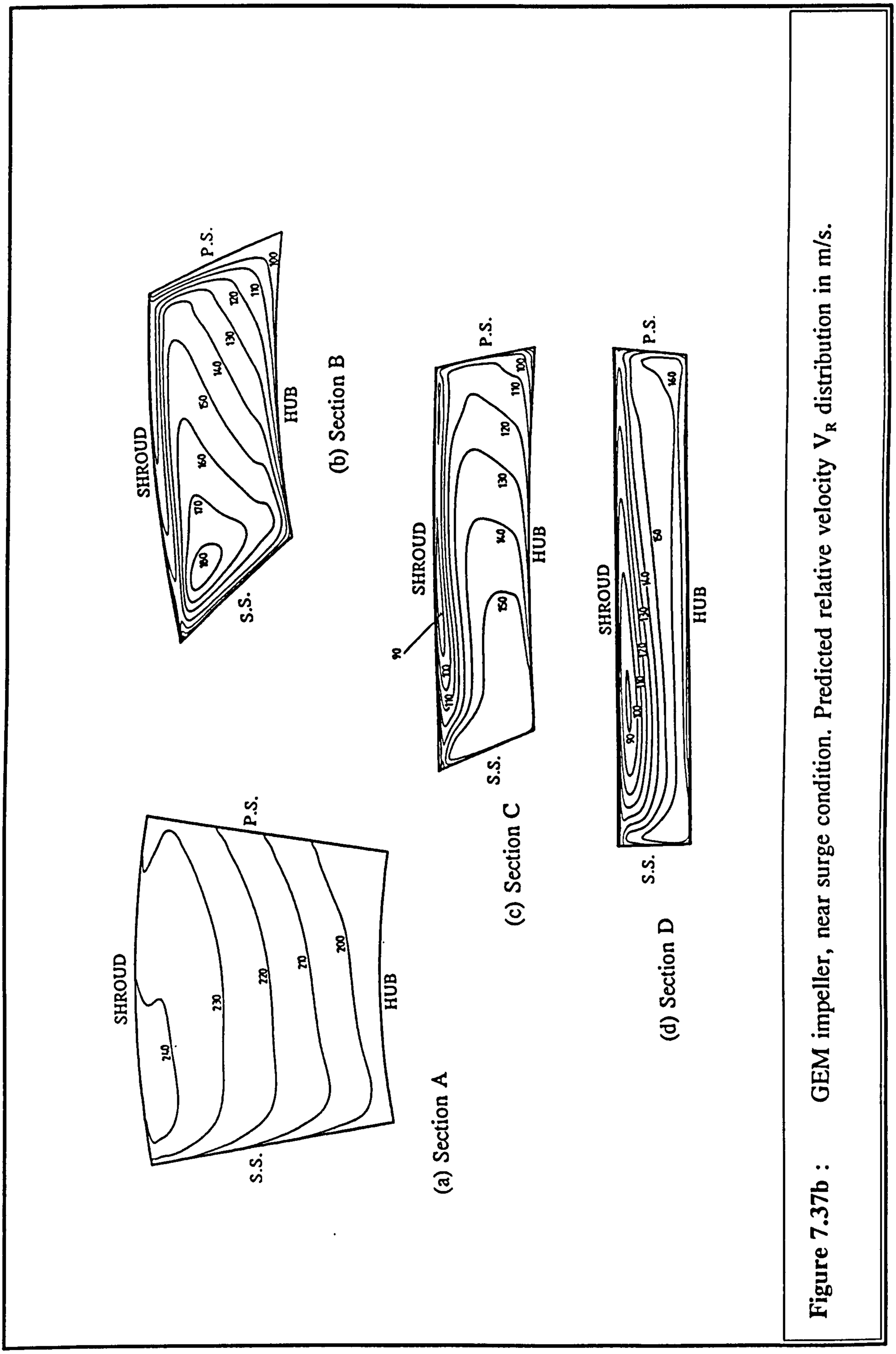

Figure 7.37b : GEM impeller, near surge condition. Predicted relative velocity V_R distribution in m/s.

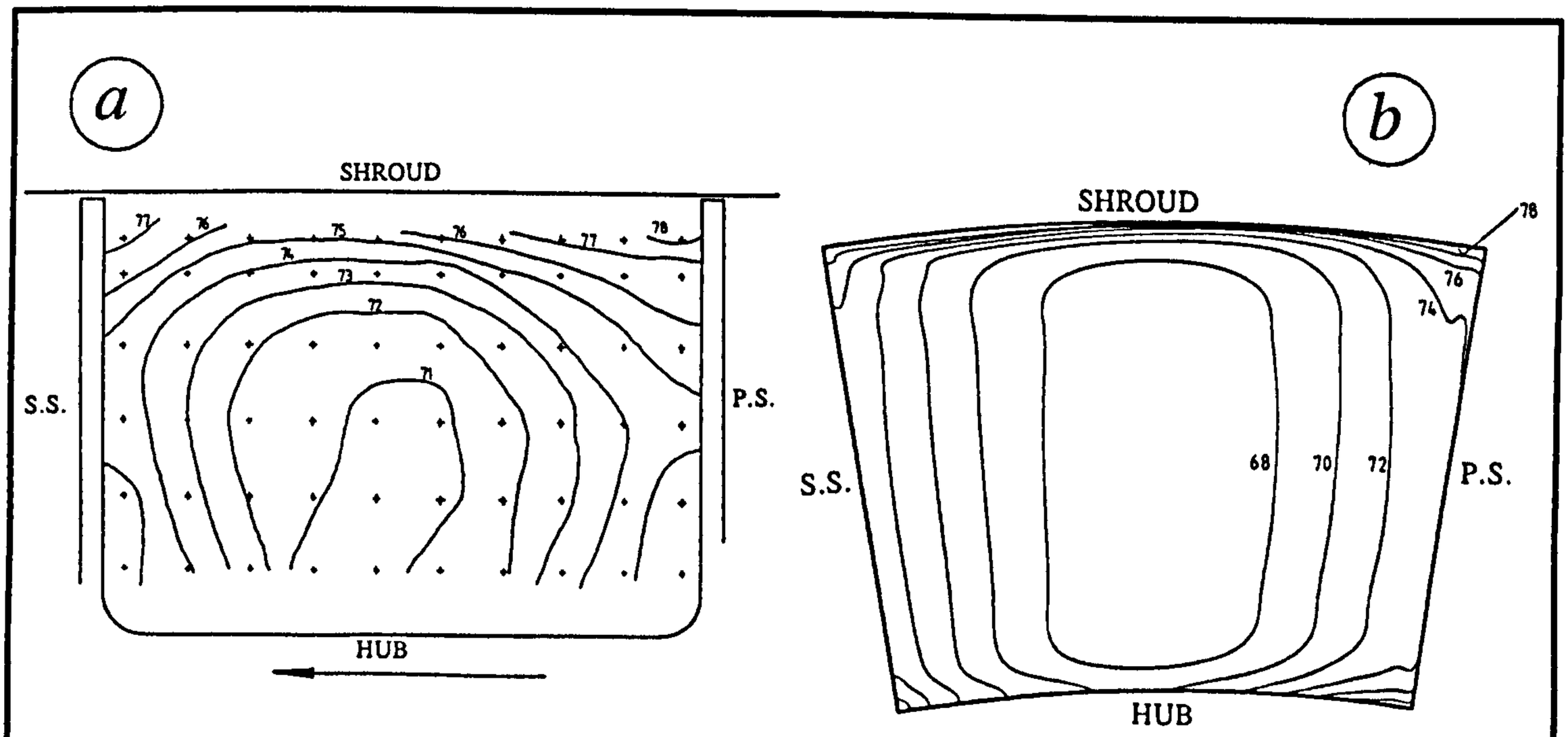

Figure 7.38 : GEM Impeller, near surge condition. Relative flow angle Θ distribution at section A. (a) Measured. (b) Predicted.

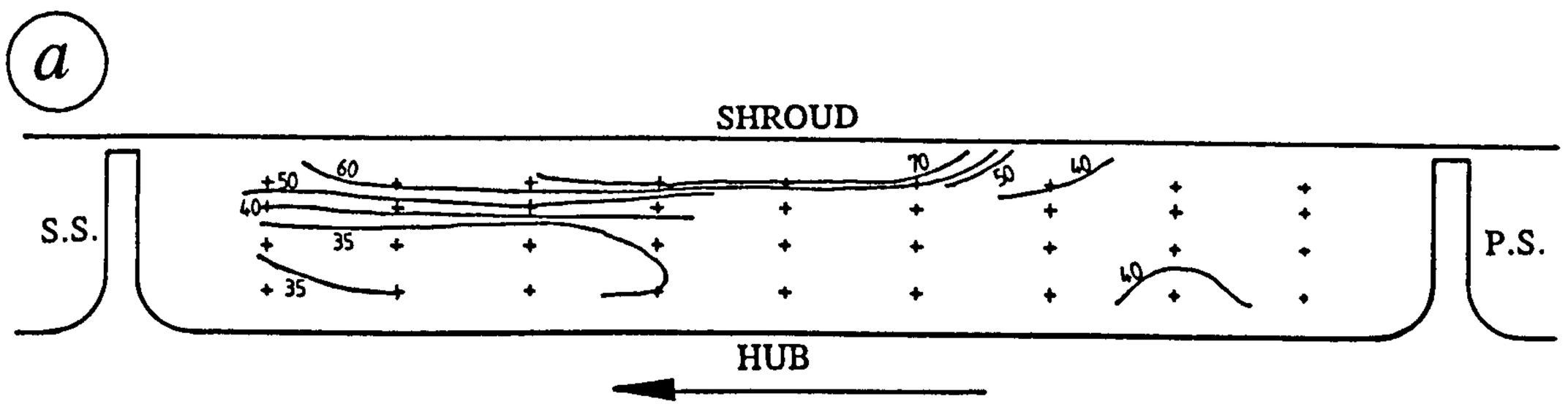

Figure 7.39 : GEM Impeller, near surge condition. Relative flow angle Θ distribution at section D. (a) measured. (b) Predicted.

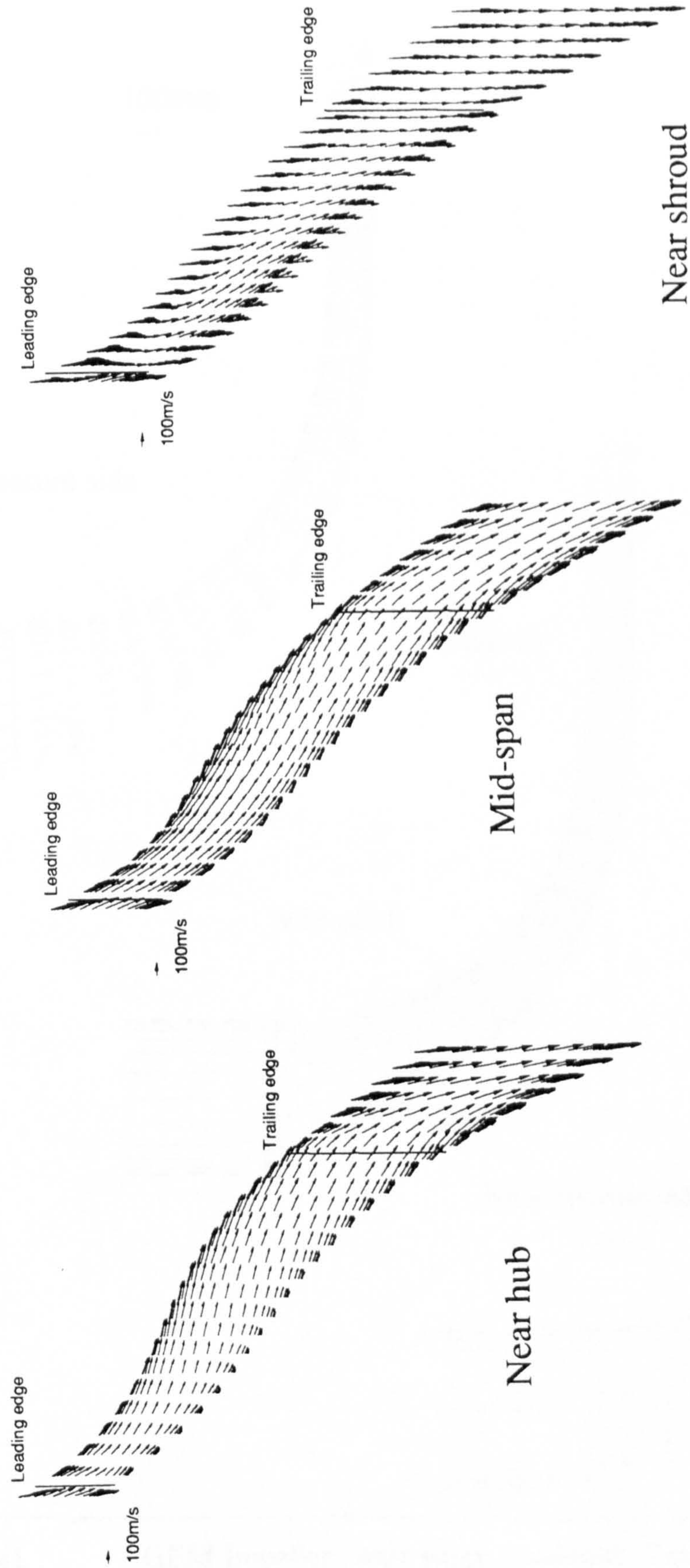

Figure 7.40 : GEM Impeller, near surge condition. Velocity vectors on blade-to-blade surfaces.

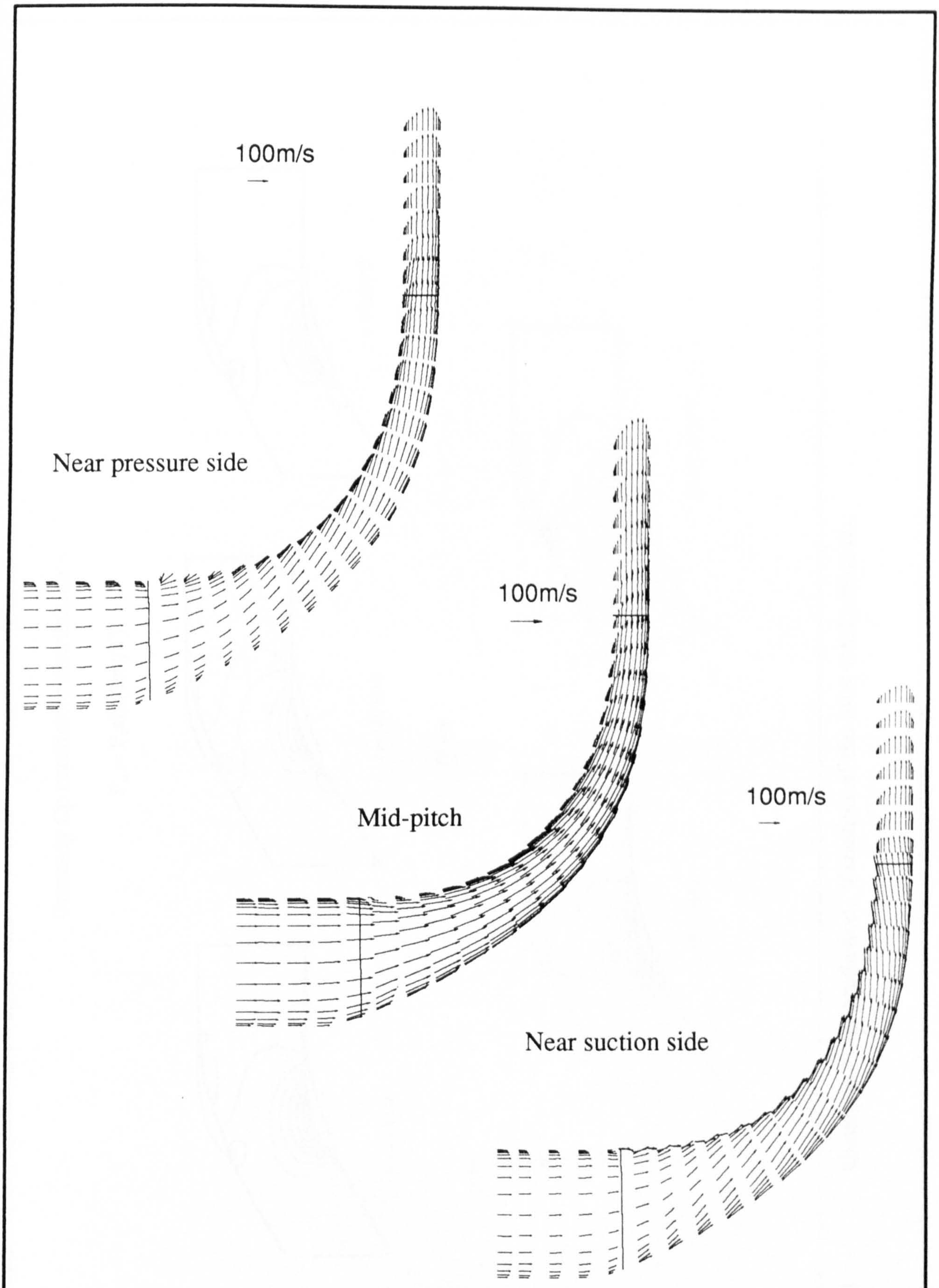

Figure 7.41 : GEM Impeller, near surge condition. Velocity vectors on meridional surfaces.

Unsteady Cp coefficient distribution

$P_{in} = P_o \sin(2\pi t/T)$

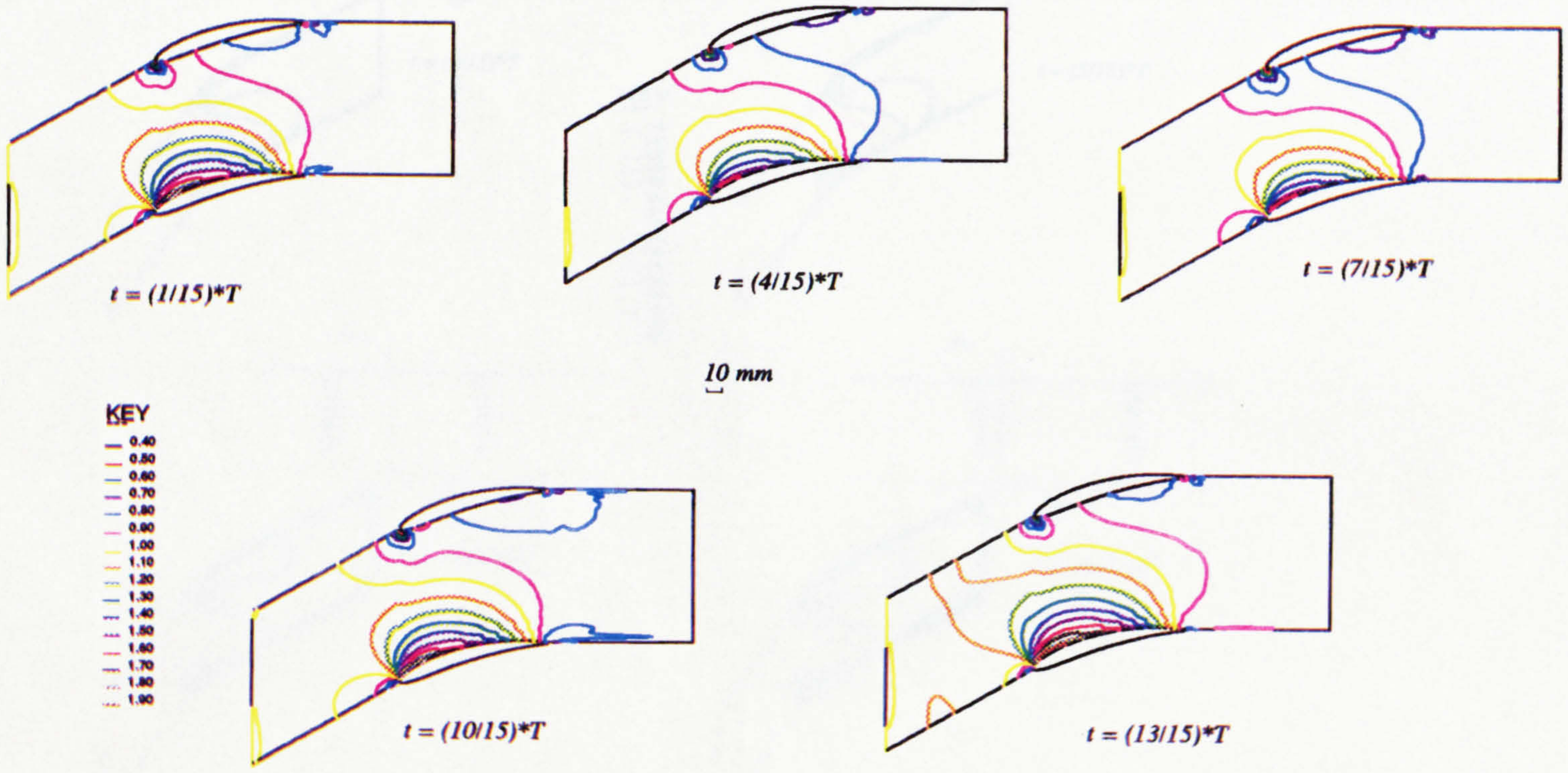

Figure 8.1 : Unsteady flow prediction. Variation of the inlet total pressure.

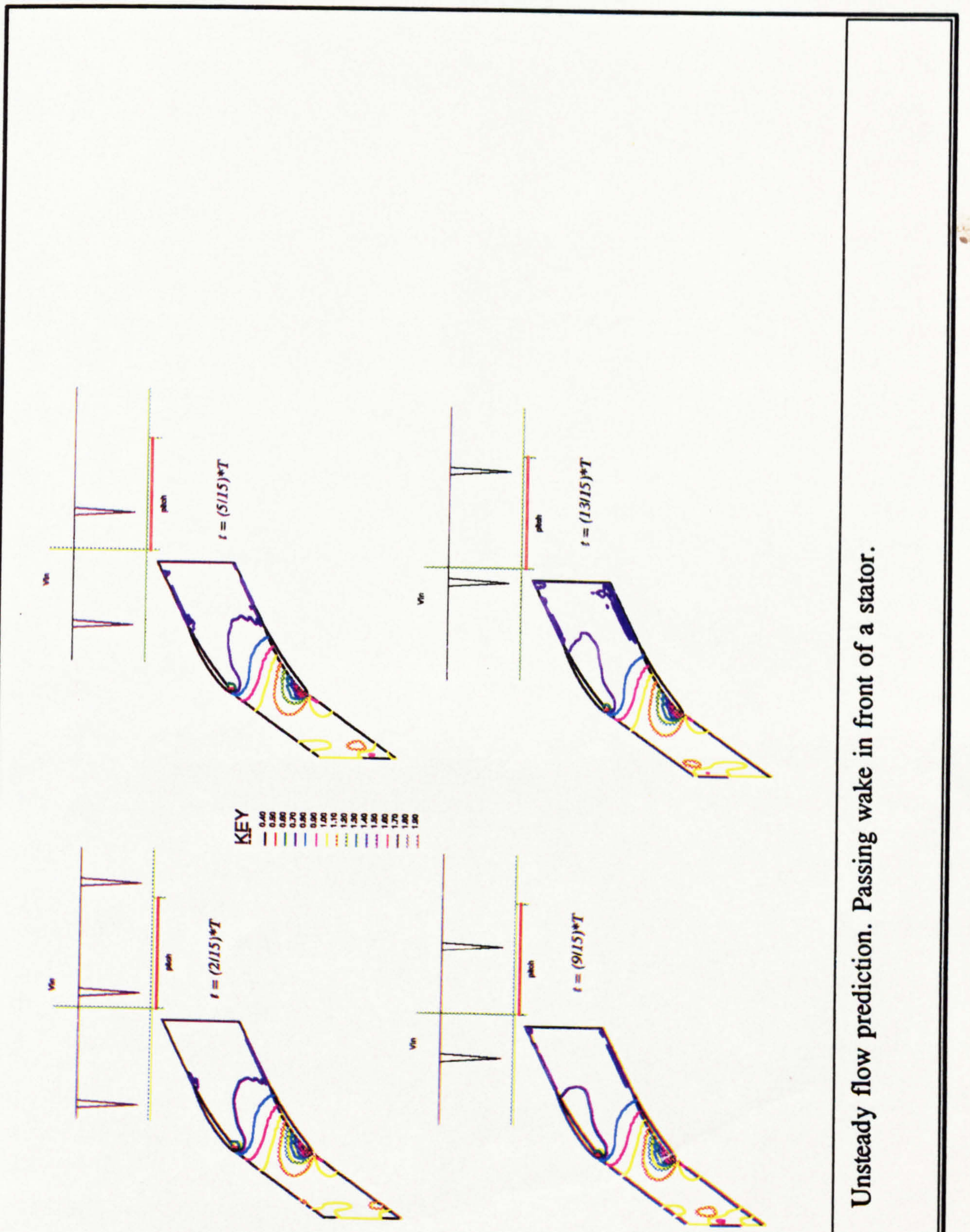

Figure 8.2 : Unsteady flow prediction. Passing wake in front of a stator.